Title
Structure of guests in MOF and their applications

Author
Kapustin, Ievgen

Publication Date
2018

Peer reviewed|Thesis/dissertation

Structure of Guests in MOF and Their Applications

by

Ievgen Kapustin

A dissertation submitted in partial satisfaction of the requirements for the degree of

Doctor of Philosophy

in

Chemistry

in the

Graduate Division

of the

University of California, Berkeley

Committee in charge:

Professor Omar M. Yaghi, Chair
Professor Peidong Yang
Professor Alex Zettl

Summer 2018

Abstract

Structure of Guests in MOF and Their Applications

by

Ievgen Kapustin

Doctor of Philosophy in Chemistry

University of California, Berkeley

Professor Omar M. Yaghi, Chair

Chapter 1. Introduction to the fundamentals of reticular chemistry, metal-organic frameworks (MOFs), crystallographic studies of MOFs, and sorption studies of MOFs.

Chapter 2. MOF-520 is used to coordinatively bind and align molecules of varying size, complexity, and functionality. The reduced motional degrees of freedom obtained with this coordinative alignment method allow the structures of molecules to be determined by single-crystal x-ray diffraction techniques. The chirality of the MOF backbone also serves as a reference in the structure solution for an unambiguous assignment of the absolute configuration of bound molecules. Sixteen molecules representing four common functional groups (primary alcohol, phenol, vicinal diol, and carboxylic acid), ranging in complexity from methanol to plant hormones (gibberellins, containing eight stereocenters), are crystallized and have their precise structure determined. Single and double bonds in gibberellins can be distinguished crystallographically. A racemic mixture of jasmonic acid is crystallized enantioselectively and its absolute configuration is determined for the first time.

Chapter 3. Despite numerous studies on chemical and thermal stability of MOF, mechanical stability remains largely undeveloped. To date, no strategy exists to control the mechanical deformation of MOFs under ultrahigh pressure. Here, we show that the mechanically unstable MOF-520 can be retrofitted by precise placement of a rigid 4,4′-biphenyldicarboxylate (BPDC) linker as a "girder" to afford a mechanically robust framework: MOF-520-BPDC. This retrofitting alters how the structure deforms under ultrahigh pressure and thus leads to a drastic enhancement of its mechanical robustness. While in the parent MOF-520 the pressure transmitting medium molecules diffuse into the pore and expand the structure from the inside upon compression, the girder in the new retrofitted MOF-520-BPDC prevents the framework from expansion by linking two adjacent secondary building units together. As a result, the modified MOF is stable under hydrostatic compression in a diamond-anvil cell up to 5.5

gigapascal. The increased mechanical stability of MOF-520-BPDC prohibits the typical amorphization observed for MOFs in this pressure range. Direct correlation between the orientation of these girders within the framework and its linear strain was estimated, providing new insights for the design of MOFs with optimized mechanical properties.

Chapter 4. Atmospheric water is a resource equivalent to ~10% of all fresh water in lakes on Earth. However, an efficient process for capturing and delivering water from air, especially at low humidity levels (down to 20%), has not been developed. We report the design and demonstration of a device based on a porous metal-organic framework {MOF-801, $[Zr_6O_4(OH)_4(fumarate)_6]$} that captures water from the atmosphere at ambient conditions by using low-grade heat from natural sunlight at a flux of less than 1 sun (1 kilowatt per square meter). This device is capable of harvesting 2.8 liters of water per kilogram of MOF daily at relative humidity levels as low as 20% and requires no additional input of energy.

Chapter 5. Water scarcity is a particularly severe challenge in arid and desert climates. While a substantial amount of water is present in the form of vapor in the atmosphere, harvesting this water by state-of-the-art dewing technology can be extremely energy intensive and impractical, particularly when the relative humidity (RH) is low (i.e., below ~40% RH). In contrast, atmospheric water generators that utilize sorbents enable capture of vapor at low RH conditions and can be driven by the abundant source of solar-thermal energy with higher efficiency. Here, we demonstrate an air-cooled sorbent-based atmospheric water harvesting device using the metal−organic framework (MOF)-801 operating in an exceptionally arid climate (10–40% RH) and sub-zero dew points (Tempe, Arizona, United States) with a thermal efficiency (solar input to water conversion) of ~14%. We predict that this device delivered over 0.25 L of water per kg of MOF for a single daily cycle.

Chapter 6. Energy-efficient production of water from desert air has not been developed. A proof-of-concept device for harvesting water at low relative humidity was reported; however, it only delivers droplets of water but not of sufficient quantity to be collected. Here, we report a laboratory-to-desert experiment where a prototype employing up to 1.2 kg of metal-organic framework-801 was tested in the laboratory and later in the desert of Arizona, United States. It produced 100 grams of water per kilogram of MOF-801 per day-and-night cycle, using only natural cooling and ambient sunlight as a source of energy. We also report an aluminum-based MOF-303, which delivers more than twice the amount of water. The desert experiment uncovered key parameters pertaining to the energy, material, and air requirements for efficient production of water from desert air, even at a sub-zero dew point.

Structure of Guests in MOF and Their Applications

Table of Contents

Chapter 1

Reticular Chemistry of MOF and its Crystallographic and Sorptive Aspects

1.1 Introduction

Reticular chemistry links molecular building units *via* strong bonds to make crystalline, extended structures such as metal-organic frameworks (MOFs)[1]. Since the discovery that MOFs can exhibit permanent porosity[2], this chemistry has become one of the most rapidly expanding fields of science due to their various potential applications. Reticular chemistry advanced the field of solid materials in three major ways: (i) it demonstrated the concept of joining organic and inorganic components through strong bonds to access robust, extended, crystalline, porous materials; (ii) it revealed that the functionalities and metrics of such solids can be tuned by varying the building blocks, while maintaining the underlying structural network; (iii) it enabled the post-synthetic modification of such extended structures. Because the vast majority of reticulated structures are crystalline and porous, characterization of their crystallographic and adsorptive properties has been crucial to the development of reticular chemistry. For example, single-crystal X-ray diffraction (SXRD) analysis is the central tool in establishing the structures of MOFs. In fact, the determination of average atomic positions, the canonical application of SXRD, in the crystal structures of MOFs is often just the starting point – as we show in Chapters 2 and 3, the post-synthetic modification of MOF-520 can only be revealed by means of SXRD. Furthermore, the intrinsic porosity of crystallized three-dimensional MOFs could (and should) be characterized *via* the typical arsenal of sorption techniques, such as nitrogen and argon at cryotemperatures, and carbon dioxide, methane, and hydrogen at ambient temperatures. As of now, MOFs stand as the state of the art for hydrogen, methane, carbon dioxide, and (logically) all other gas capacities as a result of their record-breaking porosities[3]. It follows naturally that adsorption of water vapor, the solvent of life, is another prolific and rapidly expanding application of MOFs. Potential applications include desalination, adsorption-driven heat exchange, dehumidification, indoor humidity control, and as we discuss in Chapters 4, 5, and 6, water harvesting from arid regions with severe water scarcity.[4–6].

1.2 Metal-Organic Frameworks (MOFs)

MOFs are constructed by linking inorganic and organic units by strong bonds – a synthetic process termed as reticular synthesis. By its principles, reticular synthesis can tolerate a vast degree of variation across individual constituents' geometries, sizes, and functionalities, which has led to more than 20,000 different MOFs being reported and studied within the past decade[1]. The organic units are di- or polytopic organic carboxylates (and other similar anionic molecules), which, when linked to metal-containing units, yield architecturally robust crystalline MOF structures with a characteristic porosity of greater than 50% of the crystal volume. The surface area values of such MOFs typically range from 1000 to 10,000 $m^2\ g^{-1}$, thus exceeding those of classic porous materials such as zeolites and carbon alloptropes[7]. To date, MOFs with permanent porosities are more extensive in their variety and multiplicities than any other class of porous materials. These aspects have earned MOFs the reputation of being ideal candidates for the storage of fuels (hydrogen and methane)[8], capture of carbon dioxide[9], and applications in catalysis[10].

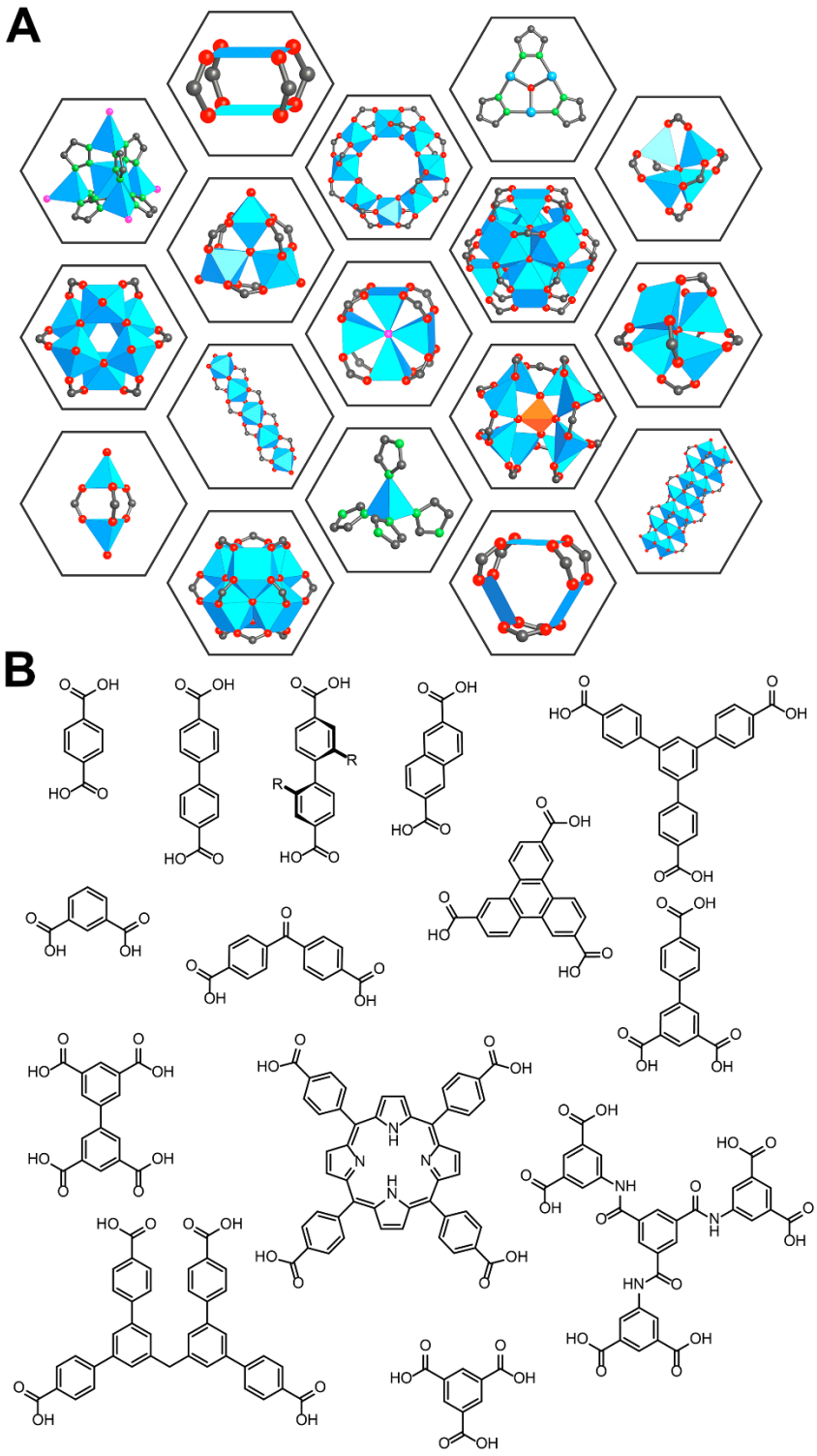

Figure 1.1. A representative library of inorganic multimetallic secondary building units (**A**) and of multitopic organic linkers (**B**) reported in common metal-organic frameworks.

The most prominent feature of MOFs is the rich library of secondary building units (SBUs) and organic linkers, which combinatorially generate vast types of structures (Figure 1.1). The former component, SBUs, segregates MOFs from other classes of coordination polymers – SBUs are polyatomic, while coordination polymers feature chelation of single metal atoms – and provides the remarkable architectural stability of the frameworks. For example, 12 Zn-O bonds must be broken to excise one inorganic SBU and therefore linkage vertex from MOF-5. In contrast, a tetrahedral coordination polymer may lose one linkage vertex simply by breaking four M–L bonds to release one metal cation. Metal–carboxylate bonds are also much more thermodynamically stable than M–N (neutral linker) bonds, increasing the architectural and thermal stabilities of MOFs. SBUs are also rigid and geometrically well-defined, which enables MOFs to be predesigned based on structural principles. These properties of SBUs combined make them ideal building units for targeting and realizing a wide range of porous crystalline frameworks. Using this SBU approach, one can design MOFs by the judicious choice of rigid building blocks, therefore limiting the formation of other structures. Though subsequent optimizations including changes in concentration, solvent polarities, pHs and temperatures are usually required, designed MOFs can typically be acquired.

The second component of MOF chemistry is the organic linkers. Typically, a linker can be proposed based on desirable size, shape, and connectivity, and accessed *via* methods established in modern synthetic organic chemistry. Over the past 20 years, organic linkers with various geometries (linear, triangular, squarer, rectangular, tetrahedral, hexagonal, etc.) and connectivities (ditopic, tritopic, tetratopic, hexatopic, etc.) have been reported. Similar to SBUs, the multitopicity of organic linkers contributes to the overall stability of MOF structures. Because organic linkers are typically rigid and have defined geometries of coordination, a prudent choice in organic linker is just as important as a reasonable choice in SBU.

For reference, we show several important MOFs which have shifted the paradigm of MOF chemistry in unique ways (Figure 1.2). MOF-5 is the first exceptionally stable MOFs with a very high surface area[11]. Its discovery also simplified the idea of the isoreticular expansion of MOFs, due to its primitive cubic topology and non-interpenetrated structure[12]. Another exceptional MOF, HKUST-1, was reported almost simultaneously with MOF-5, and possesses open-metal sites on its copper-based paddlewheel SBUs[13]. Despite being reported almost 20 years ago, HKUST-1 still holds the highest record for methane working capacity[14]. MOF-177, which possesses the 'queen of MOFs' topology, demonstrated that maximizing the number of interactions with guest molecules could yield groundbreaking surface area values[15]. MOF-801, built from simple organic fumarate linkers and zirconium salts, showed the exceptional hydrolytic stability that MOFs can achieve and was the first MOF implemented into a water harvester[16]. MOF-808 constitutes the first example where targeted sulfation of MOFs led to the formation of superacids in its framework – an exceptional material for heterogeneous catalysis[17]. MIL-53 stands as a prototypical framework for many hydrolytically stable MOFs, where water uptake can be tuned in terms of the inflection point of the isotherm, and also showed novel breathing dynamics[18]. Finally, MOF-74 had an enormous combined impact on reticular chemistry, from its isoreticular expansion to IRMOF-74-XI[19], to the selective capture of CO_2 in presence of water[9], and of course, the multivariate SBUs present in the parent MOF[20].

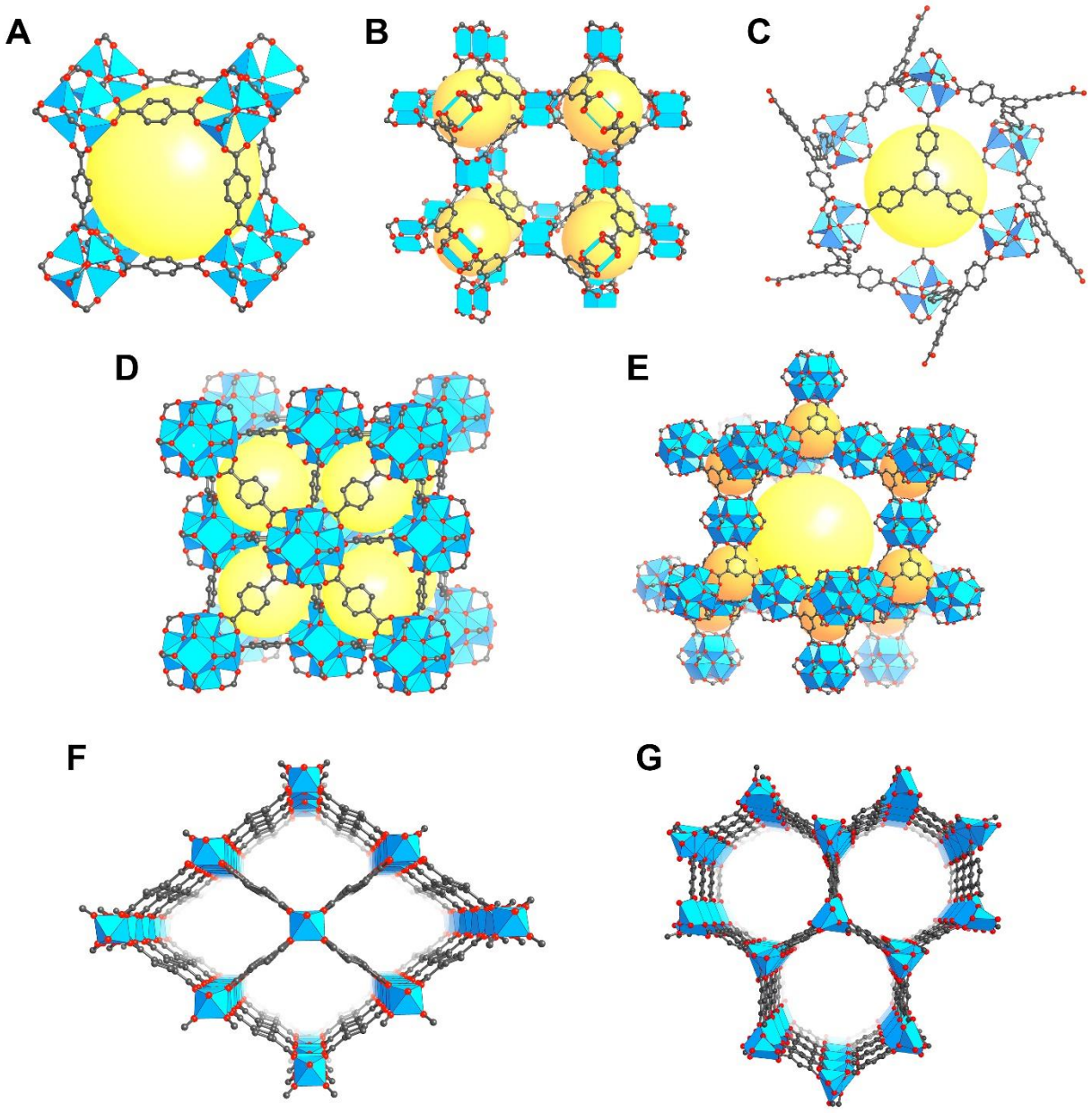

Figure 1.2. Prototypical MOFs. (**A**) MOF-5 [$Zn_4O(BDC)_3$]. (**B**) HKUST-1 [$Cu_3(BTC)_2$]. (**C**) MOF-177 [$Zn_4O(BTB)_3$]. (**D**) MOF-801 [$Zr_6O_4(OH)_4$(fumarate)$_6$]. (**E**) MOF-808 [$Zr_6O_4(OH)_4(BTC)_2(HCOO)_2$] (**F**) MIL-53 (Al) [Al(OH)BDC]. (**G**) MOF-74 (Mg) [Mg_2(DOT)]. Abbreviations: BDC = 1,4-benzenedicarboxylate; BTC = benzene-1,3,5-tricarboxylate; BTB = 4,4',4''-benzene1,3,5-triyl-tribenzoate]; DOT = dioxidoterephthalate. Color scheme: C, gray; O, red, metal polyhedral, blue. Yellow spheres display the accessible pore. Hydrogen atoms are omitted for clarity.

1.3 Crystallography of guests in MOFs

At the inception of MOF chemistry, SXRD was merely a tool to determine the average crystal structure of obtained MOF crystals. It was, however, clear that this method would eventually evolve to be the most powerful tool to determine the positions of guest molecules in as-synthesized and post-synthetically modified MOFs[21]. For example, an SXRD study of an MOF-808-2.3(SO_4) single crystal provided unequivocal evidence for metal-bound sulfate groups

incorporated into a crystalline, porous MOF, where ~2.3 bound sulfates are observed per Zr SBU[17] (Figure 1.3). Another prominent example of an SXRD study of guest molecules in MOFs is the observation of a number of different gases in Co-MOF-74, where the atomic positions of nitrogen, carbon dioxide, oxygen, carbon monoxide, methane, argon, and white phosphorous can be located[22].

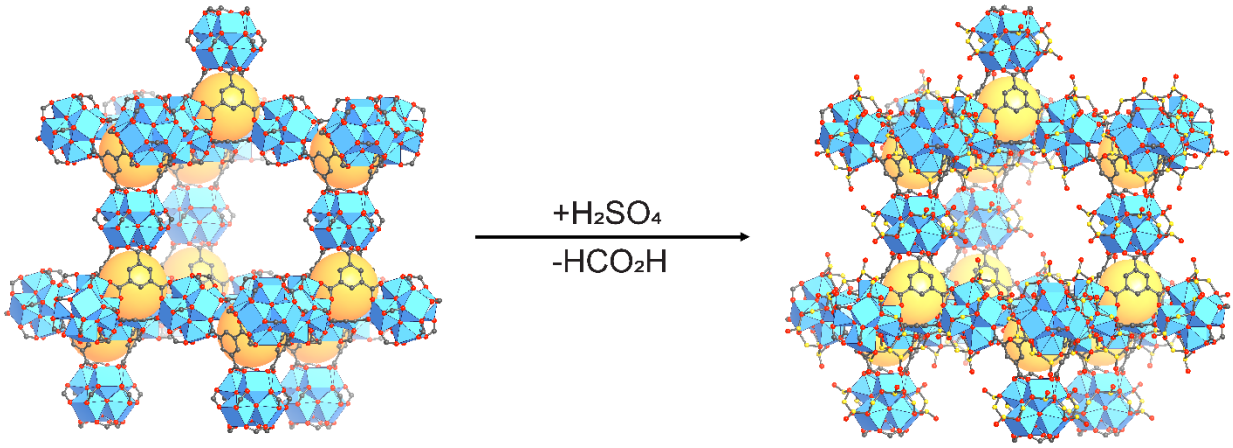

Figure 1.3. Sulfation of MOF-808 was performed by replacement the formate sites at the $Zr_6O_4(OH)_4(-CO_2)_6(HCOO)_6$ SBU by immersion of crystalline MOF-808 into aqueous sulfuric acid. The presence of disordered sulfate group at the SBU was confirmed by SXRD.

2013 marked a major breakthrough in the crystallography of guests in extended structures when a crystalline sponge method was introduced for the first time[23]. In this report, authors suggested a protocol for crystallization-free analysis of molecules using the so-called crystalline sponge (extended coordination polymer), which can be soaked with the noncrystalline guest. These guests diffuse into the sponge and are oriented within the pores *via* weak intermolecular interactions, ordering them and rendering them amenable for the single-crystal X-ray diffraction analysis. However, the drawbacks of the crystalline sponge method were revealed in the very first report: (i) the precision of crystal structures was low due to significant thermal vibrations of molecules which were not bound covalently to the interior of the sponge, and (ii) the incorrect assignment of the absolute structure of natural product miyakosyne A[24] (Figure 1.4). Both of these issues have been addressed in the coordinative alignment method described in Chapter 2, where the guest molecules are bound using strong bonds and the chiral framework stands as an enantiodiscriminating reference for the "crystallized" molecules, enabling unambiguous assignment of stereochemistry. Then in Chapter 3, a guest molecule is introduced to the MOF and aligned using the coordinative alignment method, similar to the post-syntheteic sulfation of MOF-808. This guest improved the properties of the MOF, particularly in terms of its mechanical stiffness. Therefore, the coordinative alignment method has been demonstrated as a means to improve the parent MOF, while the crystalline sponge method is limited to the simple SXRD determination of guest molecules.

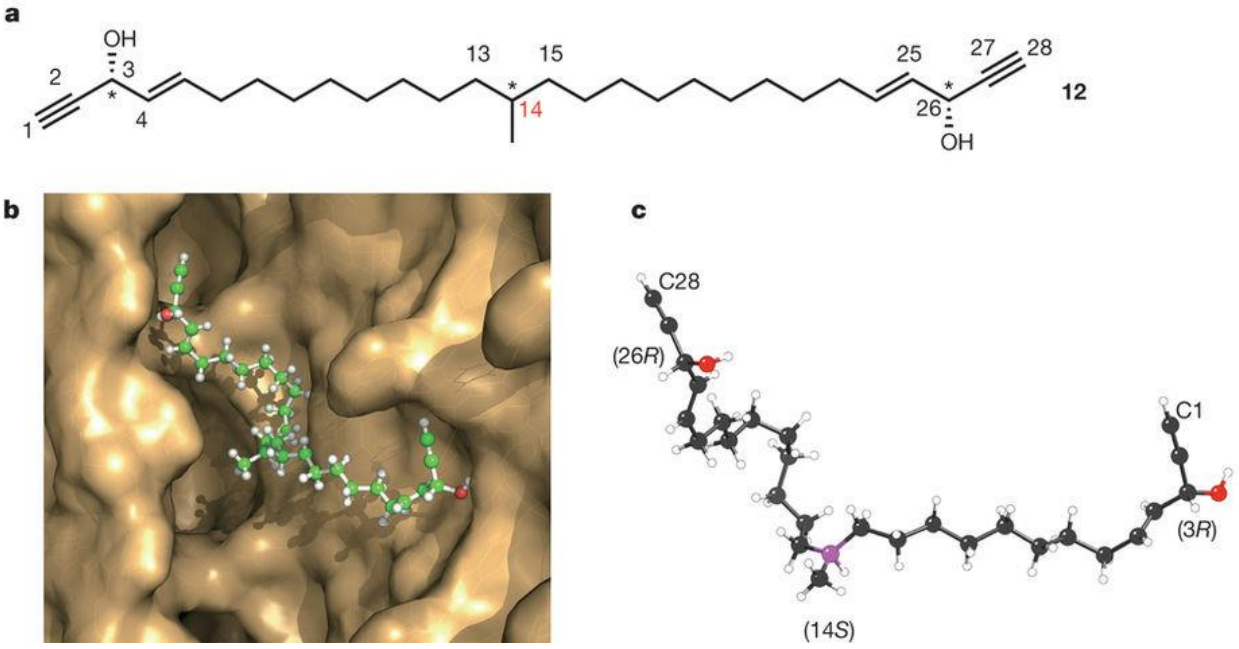

Figure 1.4. Crystal structure of miyakosyne A – a natural product whose absolute structure was incorrectly assigned in the original report. (**A**) Chemical structure of miyakosyne A. (**B**) Orientation of miyakosyne A enclathrated in the pore of crystalline sponge. (**C**) The absolute structure of miyakosyne A determined by relative configuration to C3 and C26. The chiral center C14 is drawn in magenta.

1.4 Water sorption in MOFs

Since the seminal report of permanent porosity in MOFs in 1998, innumerable publications have been dedicated to the measurements of nitrogen[11], argon[11], carbon dioxide[9], methane[25], hydrogen[26], ammonia[27], carbon monoxide[28], oxygen[29], acetylene[30], xylenes,[31] etc. sorption. However, there was a consistent and prominent vacancy in the field of water sorption in MOFs. This was primarily due to two reasons: (i) MOFs synthesized in this era were not hydrothermally stable, and (ii) trace water molecules typically bind more tightly to the interior of the frameworks than other gases, decreasing the capacities and selectivities of MOFs towards other gases[32]. In fact, the first promising measurement of water sorption in MOFs in our group was conducted serendipitously while in pursuit of a material which could efficiently separate carbon dioxide from flue gas in presence of water[9,32]. The targeted MOF, MOF-801, did not show high affinity to carbon dioxide; instead, it had a remarkable 'S'-shaped Type V isotherm[33] (Figure 1.5). At P/P_0 = 0.1 (or 10% of relative humidity at 25 °C) the water uptake in this MOF was found to be higher than 20 wt% - the highest capacity at that moment for any known hydrothermally stable and recyclable material.

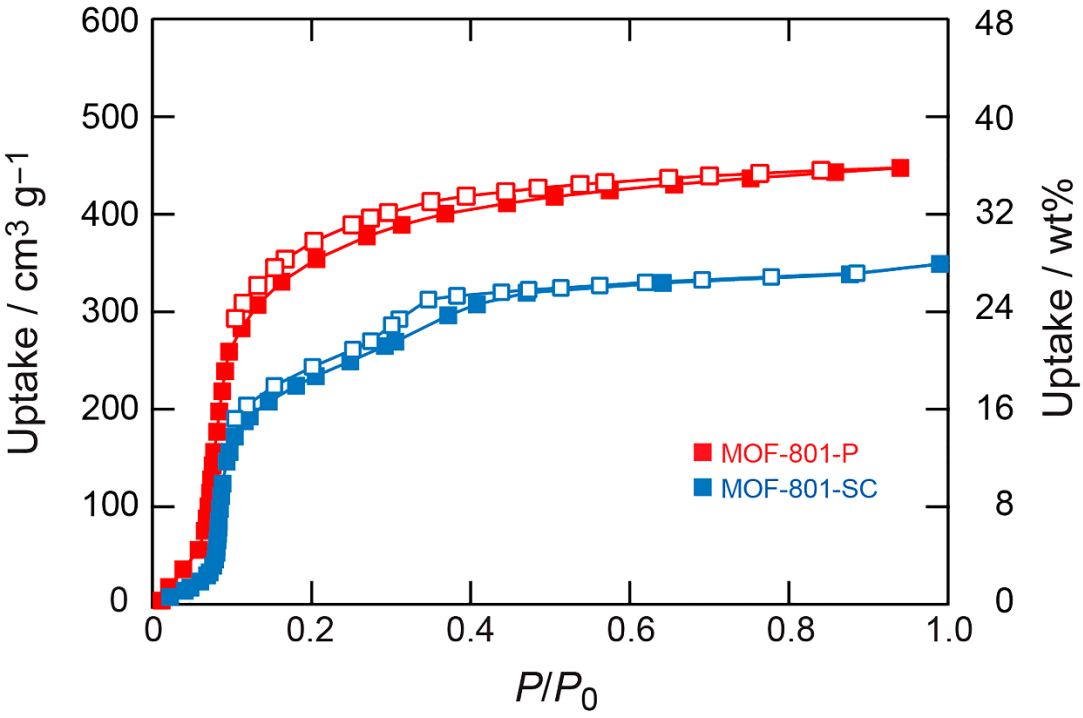

Figure 1.5. Water isotherms of microcrystalline powder (red) and single-crystalline (blue) MOF-801 measured at 25 °C. The drastic increase in uptake at low relative humidity value makes it ideal for water harvesting at arid regions.

More impactful than the amount of water up take was that after five consecutive cycles of adsorption/desorption, the capacity of this MOF does not decrease. This is in stark contrast to zeolite 13X (and other zeolites) which is typically used for water adsorption chillers[34]. This observation lead to the systematic study of water sorption in Zr-based MOFs with different organic linkers (both polar and non-polar), topologies and pore sizes (Figure 1.6).

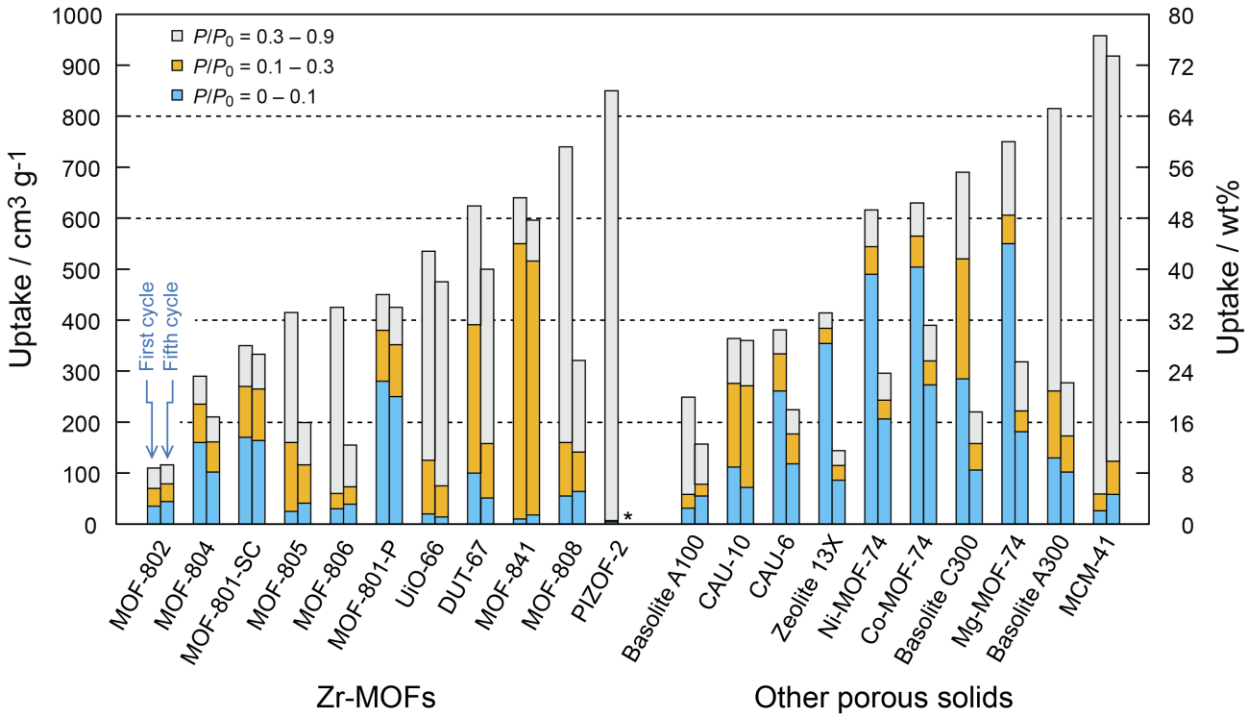

Figure 1.6. Water uptake capacity of zirconium MOFs (left) and other representative porous materials (right) in different pressure ranges. The large water uptake capacity indicates that the pore filling or condensation occurs in this pressure range.

As a result of this study, three important criteria were defined for MOFs to be considered as good water capture performers: (i) they should be hydrolytically stable, (ii) they should not lose capacity from adsorption/desorption cycling, and (iii) they should be easily regenerated at ambient temperatures. Furthermore, the temperature dependence of water uptake was measured for the first time in this work. It was found that the that the maximum uptake capacity is not significantly influenced by the temperature, indicating that water molecules are easily condensed within the MOF pores. The isosteric heat of adsorption estimated from the isotherms measured at various temperatures was approximately 60 kJ per mol for MOF-801, which is about 25% higher than the latent energy of water and much lower than of that in zeolites[35]. At the conclusions of this work, authors briefly mentioned arguably the most important application of MOFs — water harvesting from air. It was hypothesized that MOF-801 can be applied for temperature-triggered water capture and release, where atmospheric water could be captured during cool nights and delivered during hot days. This would be particularly effective for areas with a significant contrast in temperature between day and night, which is often the case for very arid regions. For example, in the city of Tabuk in Saudi Arabia, the typical summer temperature and relative humidity during day time are respectively 40 °C and 5%, drastically changing at night to 25 °C and 35%. Assuming $P/P_0 \times 100$ = RH %, the working capacity of MOF-801 between P/P_0 = 0.05−0.35 is more than 30 wt %. If 15 kg of MOF-801 is deployed in Tabuk under these optimal conditions, it should be able to deliver *ca*. 5 L of pure water per day. Chapters 3-5 describe the efforts towards harvesting water from air, using only the power of sunlight. Discussion of the principles of water harvesting, as well as the thermodynamic considerations for such a MOF-based water harvester and the parameters which are important to consider are also presented, which are anticipated to enable practical water production from desert air.

References for Chapter 1

(1) Furukawa, H.; Cordova, K. E.; O'Keeffe, M.; Yaghi, O. M. *Science* **2013**, *341*, 1230444.

(2) Li, H.; Eddaoudi, M.; Groy, T. L.; Yaghi, O. M. *J. Am. Chem. Soc.* **1998**, *120*, 8571-8572.

(3) Furukawa, H.; Ko, N.; Go, Y. B.; Aratani, N.; Choi, S. B.; Choi, E.; Yazaydin, A. O.; Snurr, R. Q.; O'Keeffe, M.; Kim, J.; Yaghi, O. M. *Science* **2010**, *329*, 424–428.

(4) Canivet, J.; Fateeva, A.; Guo, Y.; Coasne, B.; Farrusseng, D. *Chem. Soc. Rev.* **2014**, *43*, 5594–5617.

(5) Kim, H.; Yang, S.; Rao, S. R.; Narayanan, S.; Kapustin, E. A.; Furukawa, H.; Umans, A. S.; Yaghi, O. M.; Wang, E. N. *Science* **2017**, *356*, 430–434.

(6) de Lange, M. F.; Verouden, K. J. F. M.; Vlugt, T. J. H.; Gascon, J.; Kapteijn, F. *Chem. Rev.* **2015**, *115*, 12205–12250.

(7) Farha, O. K.; Eryazici, I.; Jeong, N. C.; Hauser, B. G.; Wilmer, C. E.; Sarjeant, A. A.; Snurr, R. Q.; Nguyen, S. T.; Yazaydın, A. Ö.; Hupp, J. T. *J. Am. Chem. Soc.* **2012**, *134*, 15016–15021.

(8) Zhao, X.; Xiao, B.; Fletcher, A. J.; Thomas, K. M.; Bradshaw, D.; Rosseinsky, M. J. *Science* **2004**, *306*, 1012–1015.

(9) Fracaroli, A. M.; Furukawa, H.; Suzuki, M.; Dodd, M.; Okajima, S.; Gándara, F.; Reimer, J. A.; Yaghi, O. M. *J. Am. Chem. Soc.* **2014**, *136*, 8863–8866.

(10) Rungtaweevoranit, B.; Baek, J.; Araujo, J. R.; Archanjo, B. S.; Choi, K. M.; Yaghi, O. M.; Somorjai, G. A. *Nano Lett.* **2016**, *16*, 7645–7649.

(11) Yaghi, O. M.; Li, H.; Eddaoudi, M.; O'Keeffe, M. *Nature* **1999**, *402*, 276–279.

(12) Eddaoudi, M.; Kim, J.; Rosi, N.; Vodak, D.; Wachter, J.; O'Keeffe, M.; Yaghi, O. M. *Science* **2002**, *295*, 469–472.

(13) Chui, S. S.-Y.; Lo, S. M.-F.; Charmant, J. P. H.; Orpen, A. G.; Williams, I. D. *Science* **1999**, *283*, 1148–1150.

(14) Tian, T.; Zeng, Z.; Vulpe, D.; Casco, M. E.; Divitini, G.; Midgley, P. A.; Silvestre-Albero, J.; Tan, J.-C.; Moghadam, P. Z.; Fairen-Jimenez, D. *Nat. Mater.* **2017**, *17*, 174–179.

(15) Chae, H. K.; Siberio-Pérez, D. Y.; Kim, J.; Go, Y.; Eddaoudi, M.; Matzger, A. J.; O'Keeffe, M.; Yaghi, O. M. *Nature* **2004**, *427*, 523–527.

(16) Furukawa, H.; Gándara, F.; Zhang, Y.-B.; Jiang, J.; Queen, W. L.; Hudson, M. R.; Yaghi, O. M. *J. Am. Chem. Soc.* **2014**, *136*, 4369–4381.

(17) Jiang, J.; Gándara, F.; Zhang, Y.-B.; Na, K.; Yaghi, O. M.; Klemperer, W. G. *J. Am. Chem. Soc.* **2014**, *136*, 12844–12847.

(18) Serre, C.; Millange, F.; Tshouvenot, C.; Noguès, M.; Marsolier, G.; Louër, D.; Férey, G. *J. Am. Chem. Soc.* **2002**, *124*, 13519–13526.

(19) Deng, H.; Grunder, S.; Cordova, K. E.; Valente, C.; Furukawa, H.; Hmadeh, M.; Gandara, F.; Whalley, A. C.; Liu, Z.; Asahina, S.; Kazumori, H.; O'Keeffe, M.; Terasaki, O.; Stoddart, J. F.; Yaghi, O. M. *Science* **2012**, *336*, 1018–1023.

(20) Wang, L. J.; Deng, H.; Furukawa, H.; Gándara, F.; Cordova, K. E.; Peri, D.; Yaghi, O. M. *Inorg. Chem.* **2014**, *53*, 5881–5883.

(21) Öhrström, L. *ACS Cent. Sci.* **2017**, *3*, 528–530.

(22) Gonzalez, M. I.; Mason, J. A.; Bloch, E. D.; Teat, S. J.; Gagnon, K. J.; Morrison, G. Y.; Queen, W. L.; Long, J. R. *Chem. Sci.* **2017**, *8*, 4387–4398.

(23) Inokuma, Y.; Yoshioka, S.; Ariyoshi, J.; Arai, T.; Hitora, Y.; Takada, K.; Matsunaga, S.; Rissanen, K.; Fujita, M. *Nature* **2013**, *495*, 461–466.

(24) Inokuma, Y.; Yoshioka, S.; Ariyoshi, J.; Arai, T.; Hitora, Y.; Takada, K.; Matsunaga, S.; Rissanen, K.; Fujita, M. *Nature* **2013**, *501*, 262–262.

(25) Gándara, F.; Furukawa, H.; Lee, S.; Yaghi, O. M. *J. Am. Chem. Soc.* **2014**, *136*, 5271–5274.

(26) Spencer, E. C.; Howard, J. A. K.; McIntyre, G. J.; Rowsell, J. L. C.; Yaghi, O. M. *Chem. Commun.* **2006**, 278–280.

(27) Doonan, C. J.; Tranchemontagne, D. J.; Glover, T. G.; Hunt, J. R.; Yaghi, O. M. *Nat. Chem.* **2010**, *2*, 235–238.

(28) Reed, D. A.; Keitz, B. K.; Oktawiec, J.; Mason, J. A.; Runčevski, T.; Xiao, D. J.; Darago, L. E.; Crocellà, V.; Bordiga, S.; Long, J. R. *Nature* **2017**, *550*, 96–99.

(29) DeCoste, J. B.; Weston, M. H.; Fuller, P. E.; Tovar, T. M.; Peterson, G. W.; LeVan, M. D.; Farha, O. K. *Angew. Chemie Int. Ed.* **2014**, *53*, 14092–14095.

(30) Wang, J.; Xie, D.; Zhang, Z.; Yang, Q.; Xing, H.; Yang, Y.; Ren, Q.; Bao, Z. *AIChE J.* **2017**, *63*, 2165–2175.

(31) Gonzalez, M. I.; Kapelewski, M. T.; Bloch, E. D.; Milner, P. J.; Reed, D. A.; Hudson, M. R.; Mason, J. A.; Barin, G.; Brown, C. M.; Long, J. R. *J. Am. Chem. Soc.* **2018**, *140*, 3412–3422.

(32) Nguyen, N. T. T.; Furukawa, H.; Gándara, F.; Nguyen, H. T.; Cordova, K. E.; Yaghi, O. M. *Angew. Chemie* **2014**, *126*, 10821–10824.

(33) Thommes, M.; Kaneko, K.; Neimark, A. V; Olivier, J. P.; Rodriguez-Reinoso, F.; Rouquerol, J.; Sing, K. S. W. *Pure Appl. Chem* **2015**.

(34) Hauer, A. *Adsorption* **2007**, *13*, 399–405.

(35) Kim, H.; Cho, H. J.; Narayanan, S.; Yang, S.; Furukawa, H.; Schiffres, S.; Li, X.; Zhang, Y.-B.; Jiang, J.; Yaghi, O. M.; Wang, E. N. *Sci. Rep.* **2016**, *6*, 19097.

Chapter 2

Coordinative Alignment of Molecules in Chiral Metal–Organic Frameworks

Portions of this chapter have been previously published in:
Lee, S., Kapustin, E. A. & Yaghi, O. M. Coordinative Alignement of Molecules in Chiral Metal–Organic Frameworks. *Science* **353,** 808–811 (2016).

2.1 Preface

Knowledge of three-dimensional (3D) molecular structures is crucial for scientific advances in fields ranging from materials chemistry to medicine. First-generation MOF-based structure determination matrices were based solely on the void properties and are known as crystalline sponges. However, this technique relies primarily on weak interactions to induce crystalline order of the included molecules. In this Chapter, a chiral metal-organic framework, MOF-520, was used to coordinatively bind and align molecules of varying size, complexity, and functionality. The reduced motional degrees of freedom obtained with this coordinative alignment method allowed the structures of molecules to be determined by single-crystal x-ray diffraction techniques. The chirality of the MOF backbone also served as a reference in the structure solution for an unambiguous assignment of the absolute configuration of bound molecules. Sixteen molecules representing four common functional groups (primary alcohol, phenol, vicinal diol, and carboxylic acid), ranging in complexity from methanol to plant hormones (gibberellins, containing eight stereocenters), were crystallized and had their precise structure determined. We distinguished single and double bonds in gibberellins, and we enantioselectively crystallized racemic jasmonic acid, whose absolute configuration had only been inferred from derivatives. This work was done in collaboration with Seungkyu Lee.

2.2 Introduction

Single-crystal x-ray diffraction is a powerful technique for the definitive identification of chemical structures. Although most molecules and molecular complexes can be crystallized, often enthalpic and entropic factors introduce orientational disorder that prevents determination of a high-resolution structure[1]. Several strategies based on the inclusion of guests in a host framework that helps maintain molecular orientation have been used to overcome this challenge[2–4]. However, most of these methods rely primarily on weak interactions to induce crystalline order of the included molecules. Here, we demonstrate a strategy for crystallization of molecules within the pores of chiral metal-organic frameworks (MOFs)[5]. This strategy provides the following advantages: (i) The molecules make covalent bonds to well-defined metal sites of the MOF; these bonds anchor them and lower their motional degrees of freedom, thereby promoting their alignment into an ordered pattern across the interior of the crystalline framework. (ii) The absolute structure of the chiral MOF serves as a reference for the direct determination of the absolute configuration of bound chiral molecules[6]. This latter feature avoids the reported pseudosymmetry problems that have obscured the absolute structures that specify the enantiomorph in achiral host framework systems[7–9].

Specifically, we used this coordinative alignment (CAL) method to successfully crystallize 16 different molecules in the interior of MOF-520 [$Al_8(\mu\text{-}OH)_8(HCOO)_4(BTB)_4$; BTB = 1,3,5-benzenetribenzoate][10]. These molecules represent a range of functionality, flexibility, and complexity. The first 12 are relatively simple molecules: benzoic acid **1**, methanol **2**, ethylene glycol **3**, 3-nitrophenol **4**, heptanoic acid **5**, 3-hydroxybenzoic acid **6**, 3,5-diaminobenzoic acid **7**, trimesic acid **8**, 4-bromophenol **9**, 2-(2,6-dichloranilino)phenylacetic acid (diclofenac) **10**, 5,7-dihydroxy-3-(4-hydroxyphenyl)chromen-4-one (genistein) **11**, and *tert*-butyloxycarbonyl-(*RS*)-3-amino-1,2-propanediol **12**. In addition, this method allowed us to successfully crystallize two different plant hormone types within the MOF: gibberellins (form A_1, **13**, and form A_3, **14**) with eight stereocenters, and (±)-jasmonic acid (**15**, **16**). The precision of the crystal structures with only 30% occupancy of the bound gibberellins enabled us to distinguish the single bond in **13**

from the double bond in **14**, this being the only difference between the two complex molecules. The crystal structure of (±)-jasmonic acid, whose absolute configuration had only been inferred from derivatives, was obtained enantioselectively, with each enantiomorph of the MOF binding only one enantiomer of jasmonic acid from a racemic mixture.

2.3 MOF-520 system

We chose MOF-520 as the framework for implementing the CAL method of crystallization because of its high crystallinity, robustness, and chirality (Figure 2.1). Its secondary building units (SBUs) are rings of eight aluminum octahedra sharing corners through eight m-OHs and four formate ligands. Each of these SBUs is linked by 12 BTB units, and each BTB is linked to three SBUs to make a three-dimensional, extended porous framework.

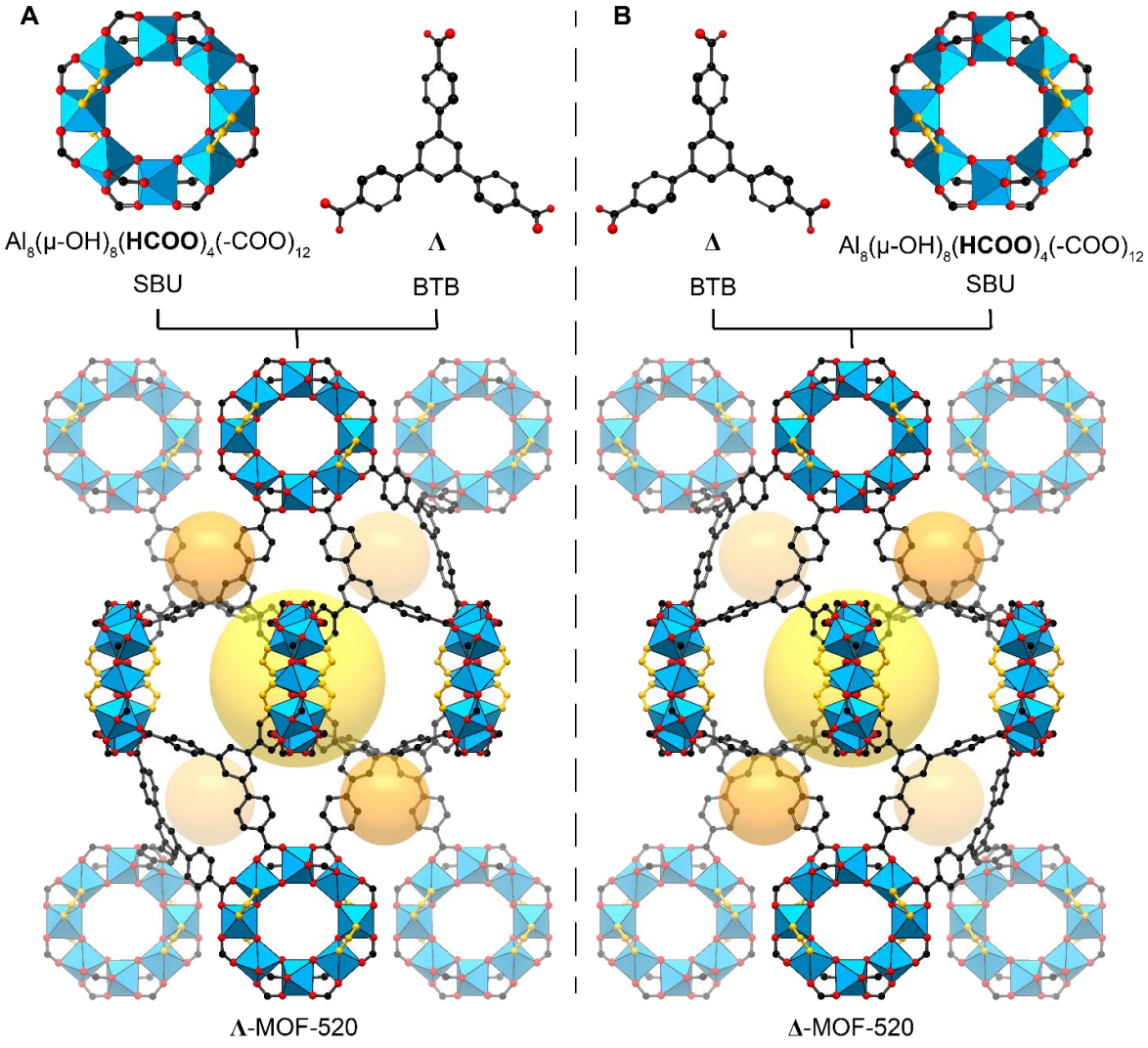

Figure 2.1. Structures of MOF-520 enantiomorphs and their building units. MOF-520 comprises the SBU, $Al_8(\mu\text{-}OH)_8(HCOO)_4(\text{-}COO)_{12}$, and BTB linker. Each SBU is coordinated by 16 carboxylates, 12 from BTB linkers and 4 from formate ligands (highlighted in yellow on the SBU). The absolute structure descriptors Λ-MOF-520 (**A**) and Δ-MOF-520 (**B**) are assigned on the basis of absolute configuration of the BTB linker. The large yellow and small orange balls represent the octahedral and tetrahedral pores, respectively. Color code: black, C; red, O; blue polyhedra, Al.

Two types of ellipsoidal pores are formed from elongated arrangements of SBUs that are octahedral (10.01 Å × 10.01 Å × 23.23 Å) and tetrahedral (5.89 Å × 5.89 Å × 6.21 Å). The framework of MOF-520 crystallizes in the noncentrosymmetric space group $P4_22_12$, with a chiral atomic arrangement. The absolute structure of each enantiomorph is designated as Λ or Δ according to the chirality of the BTB linker in the respective crystal structure (Figure 2.1, A and B). Although each single crystal is nearly enantiomorphically pure according to the Flack parameters of the refined structures — 0.049(17) for Λ and 0.031(11) for Δ — the overall bulk sample is a racemic conglomerate containing both enantiomorphs (see Tables S2.1 to S2.3 in the Supporting Information of this Chapter)[11].

The distinctive nature of this MOF lies in each of the aluminum SBUs having four formate ligands in addition to 12 carboxyl units from BTB linkers to complete the octahedral coordination sites of the aluminum centers. These formate ligands occupy two sites on each face of the SBU in a chiral tetrahedral arrangement with D_2 symmetry. We anticipated that through acid-base chemistry, we could substitute these formates with incoming organic molecules such as carboxylates, alkoxides, and phenolates (Figure 2.2A). Given that the interior of the MOF has large octahedral pores, it is reasonable to expect molecules of varying size and complexity to diffuse into this space and covalently bind to the metal sites (Figure 2.2B), thereby aligning themselves within the MOF to be amenable to x-ray structure determination (see below).

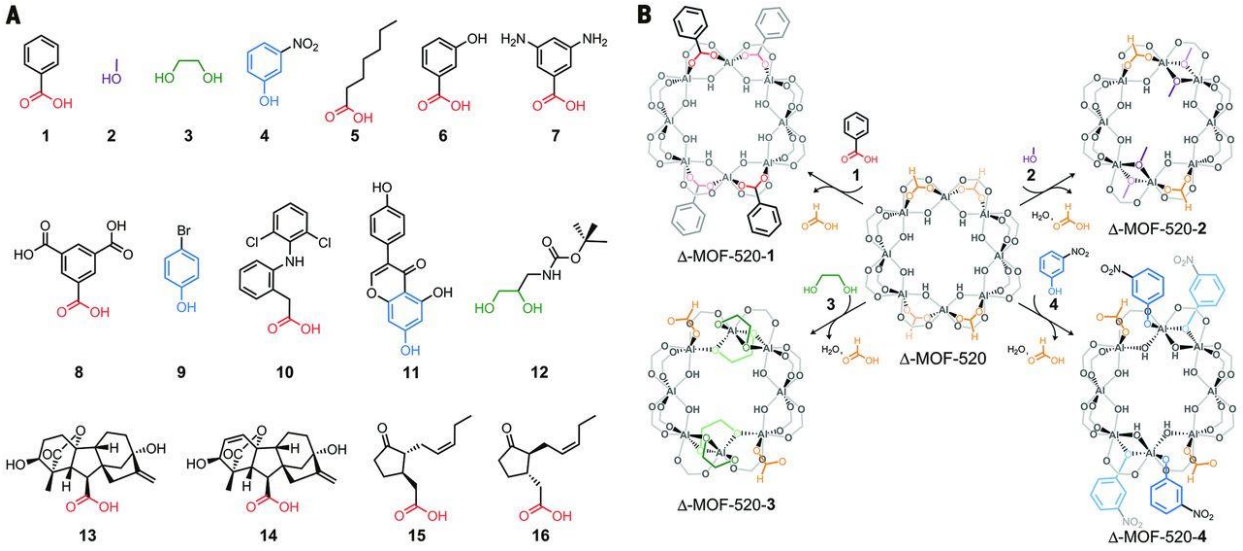

Figure 2.2. Structures of incoming molecules (1 to 16) and coordination modes of their deprotonated forms on the SBU of Δ-MOF-520. (**A**) The structures of **1** to **16** represent the molecules binding to the SBU, where their functionalities are highlighted with colors: red, carboxylic acid; purple, primary alcohol; green, vicinal diol; blue, phenol. (**B**) The SBU of Δ-MOF-520 is shown in the center, with the four formate ligands (yellow) highlighted. The deprotonated forms of **1** to **4** replace all (**1**) or some (**2** to **4**) of the formate ligands and μ-OH on the SBU; the resulting coordination modes and the functionalities of the molecules are colored. For clarity, the chiralities of Λ-MOF-520-**2** and -**4** are converted to Δ configuration.

Before examining the incorporation of molecules into the pores of MOF-520, we used single-crystal x-ray diffraction (SXRD) techniques to ensure full characterization of the structure of the MOF. We confirmed the chemical composition of the evacuated MOF-520 by ^{1}H nuclear magnetic resonance (NMR) of digested samples (calculated formate/BTB ratio, 1:1; found, 1:0.93) and by elemental analysis [calculated weight percent (wt %), C 58.81, H 3.14, N 0.0;

found wt %, C 59.20, H 3.19, N < 0.2]. The porosity of MOF-520 was confirmed by measurement of N_2 type I isotherm at 77 K, which led to a final uptake of 770 $cm^3\ g^{-1}$ at 1 atm, similar to a calculated uptake, 821 $cm^3\ g^{-1}$, based on the structure obtained from the SXRD data (both values at standard temperature and pressure). The MOF-520 samples were also characterized by infrared spectroscopy to ensure the absence of solvent in the pores, thermal gravimetric analysis to confirm the thermal stability of the MOF, and powder x-ray diffraction to confirm the bulk purity of the crystals (see the Supporting Information).

2.4 Alignment of molecules with different functionalities

Molecules **1** to **16** have functionalities that include primary alcohol, phenol, vicinal diol, and carboxylic acid (Figure 2.2A). These molecules were covalently bonded to the MOF by immersion of single crystals of MOF-520 in a concentrated solution of the respective molecule followed by heating (40° to 100°C) for at least 12 hours. One of the single crystals in the resulting racemic conglomerate batch was chosen and SXRD data were collected. The architectural robustness and high chemical stability of MOF-520 enabled the substitution of the symmetrically equivalent four formates in the SBU with the carboxylates of incoming molecules and their covalent binding to the SBUs with full retention of crystallinity. In the case of alkoxides and phenolates, only two formates on the same face of the SBU were replaced in addition to μ-OHs (Figure 2.2B). This substitution pattern led to a doubling of the unit cell in the *c*-direction without affecting the connectivity of the MOF backbone. Consecutive SBUs along *c* were substituted strictly on the opposite face of the ring, leading to a change in the space groups of the Λ and Δ-frameworks, $P4_22_12$, to an enantiomorphic pair, $P4_32_12$ (Λ) and $P4_12_12$ (Δ), respectively.

Relatively small achiral molecules were chosen to describe in detail the four different binding modes in Δ-MOF-520 for all incoming molecules: benzoic acid **1** as a carboxylic acid, methanol **2** as a primary alcohol, ethylene glycol **3** as a vicinal diol, and 3-nitrophenol **4** as a phenol. Benzoic acid shared the same binding mode as formate, where for **2**, two methoxides replaced two formates on the same face of the ring and doubly bridged the Al in a μ^2 manner, thus changing the corner-sharing Al octahedra to edge-sharing. This change in geometry induced further substitution of two μ-OHs with the methoxides. Overall, four alkoxides replaced two formates and two μ-OHs, with two coordinated formates remaining on the C_2 symmetric SBU. The binding mode of **3** was similar to that of **2**, where the formates and μ-OHs were substituted and the same geometry change of the SBU occurred. The main difference is that the remaining two formates are now bonded to the SBU as terminal ligands, which had previously been bridging ligands on the SBU of Δ-MOF-520. In the case of **4**, two different binding modes were observed with positional disorder; one is similar to that of **2**, and the other is shown in Figure 2.2B (two of four phenolic oxygen atoms are bridging).

The resulting substituted frameworks, MOF-520-**2** and MOF-520-**3**, have a larger pore width relative to the original MOF-520 [distance between the Al atoms of adjacent SBUs = 14.70 ± 0.04 Å and 14.13 ± 0.05 Å, respectively, versus 13.73 ± 0.04 Å for MOF-520] (Figure 2.3). Thus, we used MOF-520 for the crystallization of incoming molecules **1** to **10**, **12**, **15**, and **16**; MOF-520-**2** for **11**; and MOF-520-**3** for **13** and **14**.

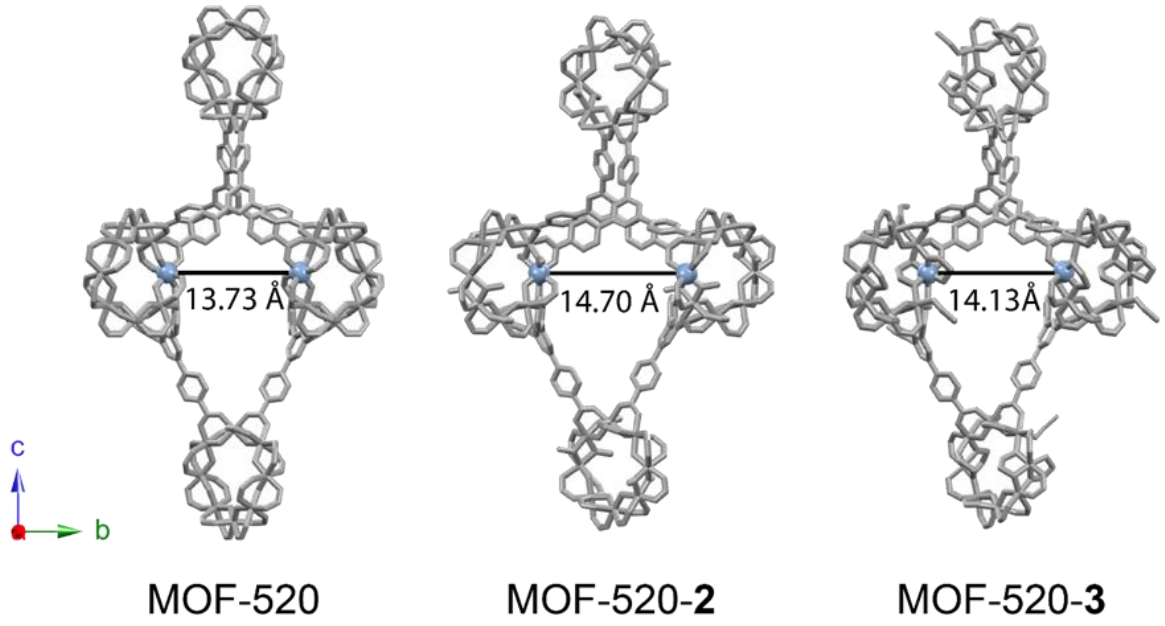

Figure 2.3. Channel width comparison between MOF-520, MOF-520-2, and -3. The frameworks are indicated with gray stick models and the Al on adjacent SBUs are indicated with blue sphere. The unit cell axes are shown in the bottom left corner.

2.5 Crystallographic details of molecules crystallized using CAL method

The crystal structures of all molecules bound to the MOF were determined by SXRD and show the binding modes outlined above. All of the structures were refined anisotropically (Figure 2.4). In general, the value of anisotropic displacement parameters of the incorporated molecules increased with their distance from the binding sites; this was expected, because the orientations of the bound molecules are mainly governed by a single site of covalent attachment. Those parts of the bound molecules that are far from the binding sites are stabilized by noncovalent interactions such as π-π interactions and weak hydrogen bonds with the aromatic rings and carboxylates of the framework (Figure 2.4 and Table 2.1).

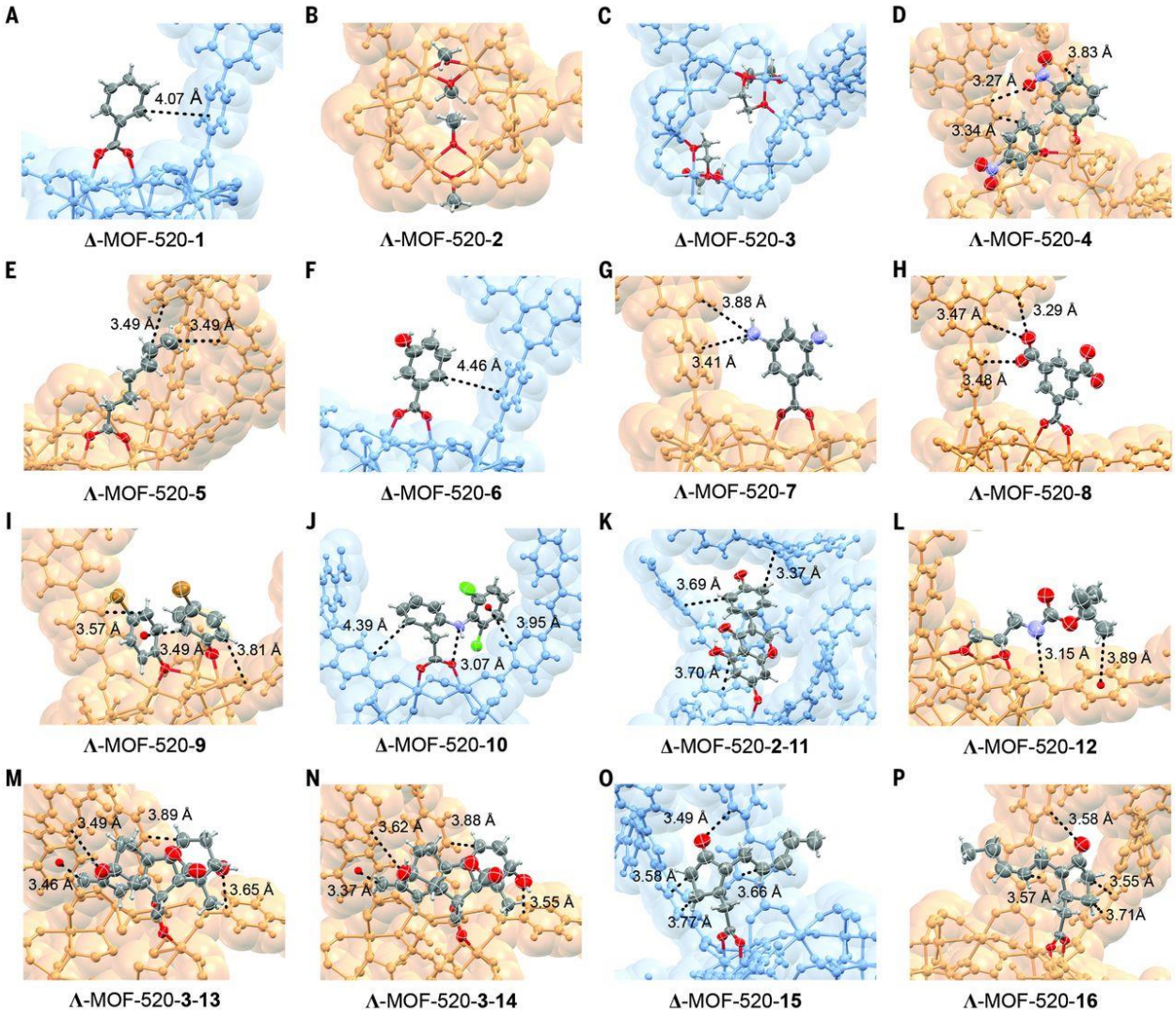

Figure 2.4. Refined structures of 1 to 16 crystallized in Λ- or Δ-MOF-520. (**A** to **P**) The refined structures of the molecules obtained from SXRD data are indicated with 50% probability thermal ellipsoids. The surroundings of the coordination sites of Λ- and Δ-MOF-520 are shown with orange and blue space-filling models, respectively. Intramolecular interactions [except for (**A**) and (**F**)] between the moieties of the molecules and the surroundings of the coordination sites are indicated with dotted lines and distances (Å). In cases with positional disorder, only one conformation of bound molecules is shown for clarity. Color code: gray, C; red, O; white, H; pale violet, N; green, Cl; brown, Br.

The bound molecules **1**, **2**, **3**, and **6** are simple and small in their structure; their ordering within the MOF is sustained only by covalent bonds to aluminum, with no evidence for weak interactions with the framework observed (Figure 2.4, A, B, C, and F). The covalent binding is sufficient to anchor these molecules and lower their degrees of freedom, an aspect that is present in all crystal structures of **1** to **16**; weak interactions play a role for some molecules but not all. For example, in Δ-MOF-520-**6**, the closest distance from the covalent bond **6** to the framework is 4.46 Å, which corresponds to the distance between the *ortho*-carbon of **6** and the adjacent aromatic ring of the MOF; this indicates that there are no contributing secondary interactions with the framework (Figure 2.4F). However, the entire structure of **6** was solved without

ambiguity. The OH group of **6** is pointing away from the framework, which suggests a possible repulsive interaction with the adjacent aromatic ring of the linker. No detectable residual electron density was observed in the structure refinement for the second OH group at the other *meta* position.

Within the MOF, molecules **10** and **11** were also ordered by anchoring through covalent bonding to aluminum, but their order was further enhanced by the presence of π- π (T-shaped for **10** and parallel-displaced for **11**) and hydrogen bonding (N–H···O for **10** and O–H··· π for **11**) interactions to the framework (Figure 2.4, J and K). Similar interactions were also observed for the molecules **4**, **5**, **7** to **9**, and **12** to **16**. Details of the structural information (including the covalent bond distances, the types of closest noncovalent interactions between the bound molecules and the framework, and refinement parameters) are given in Table 2.1.

Table 2.1. The distances of covalent bonding and types of intramolecular interactions in all structures with their crystallographic refinement parameters. Superscript ***a***: more than one covalent interactions are indicated by the range of the distances, ***b***: the types of interactions are estimated considering the functional groups and the distance between them, ***c***: parallel-displaced, ***d***: T-shaped configuration.

Structure	MOF-bound molecule Al–O distance [a]/ Å	Types of non-covalent interactions [b]	R [I>2σ(I)]	S
Δ-MOF-520-**1**	1.913(4) 1.994(4)	N/A	0.0508	0.965
Λ-MOF-520-**2**	1.8648(12) 1.9008(12)	N/A	0.0334	0.982
Δ-MOF-520-**3**	1.882(3) 1.941(3)	N/A	0.0385	0.916
Λ-MOF-520-**4**	1.876(3) 1.944(3)	π–π (P) [c]	0.0560	1.051
Λ-MOF-520-**5**	1.9084(16) 1.9268(16)	CH–π	0.0372	1.024
Δ-MOF-520-**6**	1.904(3) 1.918(3)	N/A	0.0542	1.025
Λ-MOF-520-**7**	1.8978(18) 1.8986(19)	NH–π	0.0418	1.002
Λ-MOF-520-**8**	1.900(7) 1.966(8)	OH–π	0.0620	0.988
Λ-MOF-520-**9**	1.889(3) 1.911(3)	π–π (P), π–π (T) [d]	0.0613	1.018
Δ-MOF-520-**10**	1.907(6) 1.921(6)	π–π (T), NH–O	0.0532	1.050
Δ-MOF-520-**2**-**11**	1.878(3)	π–π (P), π–π (T), OH- π	0.0516	1.081
Λ -MOF-520-**12**	1.873(3) 1.922(3)	CH–π, NH–O	0.0523	1.024
Λ -MOF-520-**3**-**13**	1.9106(18) 1.9238(17)	CH–π, OH–π	0.0568	1.082

Λ -MOF-520-**3**-**14**	1.909(3) 1.918(3)	CH–π, OH–π	0.0580	0.942
Δ-MOF-520-**15**	1.9025(18) 1.9299(17)	CH–π, CH–O	0.0474	1.040
Λ -MOF-520-**16**	1.9099(16) 1.9255(15)	CH–π, CH–O	0.0460	1.082

2.6 Crystal structures of gibberellins A_1 and A_3 as an example of CAL method precision

Because the CAL method yields highly ordered arrangements for molecules within the MOF, their structure can be determined even with low occupancy at the binding sites. This feature makes it possible to obtain structures of larger and more complex molecules with high accuracy and to determine the absolute configuration of chiral molecules with high certainty. The structures of gibberellins **13** and **14**, two derivatives of a natural plant hormone, illustrate the power of the CAL method (Figure 2.4, M and N, and Figure 2.5). All nonhydrogen atoms of these complex molecules with eight stereocenters could be assigned from an occupancy of only 30%. The final structures were refined without any geometrical constraints or restraints applied on the gibberellin molecules (see Tables S2.16 and S2.17 in the Supporting Information). The accuracy of our method is documented by the characterization of the subtle structure difference between **13** and **14**, where we find C_1–C_2 to be a single bond (1.57 ± 0.02 Å) in **13** and a double bond (1.30 ± 0.03 Å) in **14**. The C–C–C bond angles at C_1 and C_2 are 105.0° ± 1.5° and 113.3° ± 1.4°in **13** and 121.6° ± 1.7° and 117.8° ± 1.8° in **14**, indicative of sp^3 and sp^2 hybridization, respectively. Ball-and-stick representations of the structures are superimposed for direct comparison in Figure 2.5.

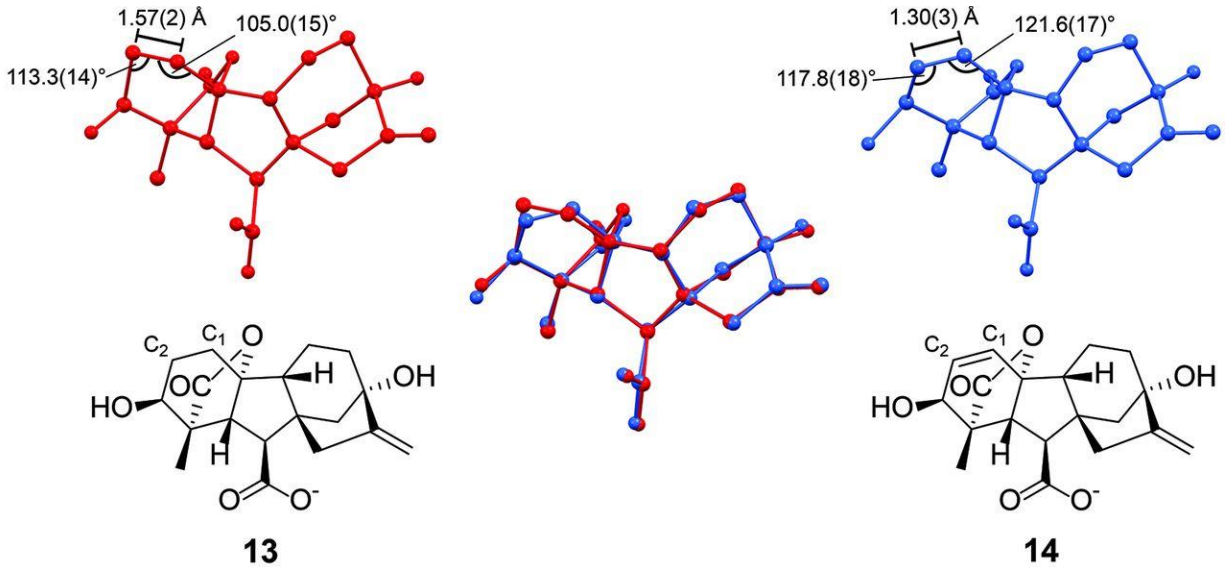

Figure 2.5. Comparison of the molecular geometries of 13 and 14. Ball-and-stick models of the structures of **13** and **14** crystallized in Λ-MOF-520-**3** are shown in red and blue, respectively. Their conformations are overlaid in the middle. The structural difference, a single bond between C_1 and C_2 for **13** and a double bond for **14**, can be distinguished from the distances and the angles indicated on the models. For clarity, only atoms C_1 and C_2 are labeled.

2.7 Absolute structure determination with CAL method

The absolute structures of Λ-MOF-520-3-**13** and -**14** were assigned based on their Flack parameters — 0.063(9) and 0.05(2), respectively — despite the low occupancies of the molecules. In previous reports, the absolute configurations of the guests were determined in achiral host frameworks[7–9,12]. In those methods, pseudocentrosymmetry problems were reported and the absolute structure determinations were obscured, even though the structures of the guests were identified in the structure solution. This problem may be caused by several factors, such as low guest occupancy[7–9], lack of high-angle reflections because of disorder of the guest[9,13], and the nearly centrosymmetric nature of the guest[8,9,14]. The chiral MOFs show anomalous scattering from the framework itself, regardless of any included chiral molecules[14,15]. The strong enantiomorph-distinguishing power originates mainly from the scattering of the chiral framework and is enhanced by chiral and achiral bound molecules. It is sufficient for determining the absolute structure of the resulting crystal, including the absolute configuration of the bound molecule, even when the occupancy of the latter is low.

One advantage of the CAL method for the determination of the absolute configuration of molecules is that it may reduce dependence on the absolute structure parameters of the inclusion crystal data. For example, when a single crystal with absolute structure Λ has been determined by SXRD and subsequently used in the inclusion, the absolute configuration of the incorporated molecule can be directly deduced from the predetermined Λ structure. In this case, the correctness of the absolute configuration of incorporated molecules is highly dependent on the predetermined absolute structure and the knowledge of the enantiopurity of the single crystal used for the inclusion[6].

Finally, to demonstrate that the chirality of the binding sites of MOF-520 can separate enantiomers when one of them interacts more favorably with the binding site of one of the enantiomorphs of the MOF, we determined the absolute configuration of another plant hormone, jasmonic acid, for which a crystal structure has heretofore not been reported. A solution of a racemic mixture of (–)-jasmonic acid **15** and (+)-jasmonic acid **16** was reacted with a racemic conglomerate of MOF-520, and SXRD data for two enantiomorphic crystals were collected after the reaction. The molecules **15** and **16** selectively attached to Δ-MOF-520 and Λ-MOF-520, respectively (Figure 2.4, O and P). The positions of the last three carbons were not clearly defined, presumably because of their conformational flexibility, the low occupancy of 33%, and the ensuing overlap with the electron density of residual disordered solvent. However, the atoms defining the stereocenters of **15** and their absolute configurations, *R* for C_3 and *R* for C_7, were observed unambiguously with a Flack parameter of 0.037(8). This result corresponds to that deduced from the absolute configurations of a derivative of **15**, (–)-methyl jasmonate, which were determined by a synthetic approach[16]. The enantiomer **16** attached to Λ-MOF-520 showed the opposite absolute configuration, as indicated by a refined Flack parameter of 0.040(8). We note that the enantiomerically pure molecules **13** and **14** had an occupancy that was sufficiently high for unambiguous structure and absolute configuration determination only in one of the two enantiomorphs. This enantioselective binding can potentially be applied to the absolute configuration determination of samples that contain a minor enantiomer, without the need for chiral high-performance liquid chromatography separation before carrying out the inclusion procedure[7].

Supporting Information for Chapter 2

Materials

Aluminum nitrate nonahydrate, $Al(NO_3)_3 \cdot 9H_2O$, N,N-dimethylformamide (DMF) (purity ≥ 99.9 %) were purchased form Sigma Aldrich Co. 1,3,5-benzenetribenzoic acid (H_3BTB) was purchased from TCI America. Formic acid (99.8 %) was obtained from EMD Chemicals. Anhydrous acetone (purity ≥ 99.8 %, extra dry with AcroSeal) was purchased from Acros Organics. All chemicals obtained were used without further purification. Scintillation vials (20 mL) and polypropylene cabs with foil liner were purchased form Wheaton.

Instrumentation

Attenuated total reflectance (ATR) FTIR spectra of neat samples were performed on a Bruker ALPHA Platinum ATR-FTIR Spectrometer equipped with a single reflection diamond ATR module (Section S1.1). Carbon, hydrogen, nitrogen elemental microanalyses (EA) were performed in the Microanalytical Laboratory of the College of Chemistry at UC Berkeley, using a Perkin Elmer 2400 Series II CHNS elemental analyzer (Section S1.1). Single-crystal X-ray diffraction (SXRD) data was collected using synchrotron radiation in beamline 11.3.1 of the Advanced Light Source, Lawrence Berkeley National Laboratory (LBNL), a Bruker MicroSTAR-H APEX II diffractometer and a Bruker D-8-Venture diffractometer (Sections S1.2 and S2.2). Beamline 11.3.1. is equipped with a PHOTO100 CMOS detector operating in shutterless mode equipped, and the radiation is monochromated using silicon (111). The Bruker MicroSTAR-H APEX II diffractometer is equipped with a CCD area detector and a micro-focus rotating anode X-ray source with a Cu-target (λ = 1.54178 Å). The Bruker D8-Venture diffractometer is equipped with a PHOTON100 CMOS detector and a micro-focus X-ray tube with a Cu-target (λ = 1.54178 Å). Powder X-ray diffraction (PXRD) patterns were acquired with a Bruker D8 Advance diffractometer (Cu Kα radiation, λ = 1.54056 Å). N_2 adsorption isotherms were recorded on a Quantachrome Autosorb-1 volumetric gas adsorption analyzer. Thermogrametric analysis (TGA) traces were collected on a TA Instruments Q-500 series thermal gravimetric analyzer. Solution ^1H NMR spectra were acquired on a Bruker Advance-500 MHz NMR spectrometer in Molecular Foundry in LBNL.

Synthesis of MOF-520 single crystals

MOF-520, **$Al_8(OH)_8(HCOO)_4BTB_4$.** In a 20 mL scintillation vial, the mixture solution of $Al(NO_3)_3 \cdot 9H_2O$ (90.0 mg, 0.240 mmol), H_3BTB (75.0 mg, 0.170 mmol) in DMF (17 mL) was prepared. The solution was sonicated for 1 min and formic acid (1.40 mL, 0.0310 mol) was added to the solution. The vial was capped and placed in the preheated 140 °C oven. After 4 days, block shaped clear single crystals with size range 50 to 100 μm were obtained on the wall of the vial. Subtle temperature difference can affect the quality of the single crystals. It is recommended that several vials containing the solution be set together and placed in different locations in the oven. The vial with the best single crystals was chosen and the single crystals were used for the inclusion of the molecules. For the characterization of MOF-520, the rest of the crystals were further processed.

Solvent exchange and guest removal activation procedure: The single crystals were washed with DMF (10.0 mL) three times per day for three days to remove the unreacted reagents in the pores. DMF solvent in the pore was exchanged with anhydrous acetone by washing the crystals with anhydrous acetone (10.0 mL) three times per day for three days. For supercritical CO_2 drying (SCD) activation, the acetone was decanted and acetone in the crystals was thoroughly exchanged with liquid CO_2 in the chamber of a Tousimis Samdri PVT-3D critical point dryer. The sample was subsequently kept in a supercritical CO_2 atmosphere (typical conditions of 40 °C and 1200 psi) for 30 min and then the supercritical CO_2 was slowly vented over the course of 6 hours. To remove the residual molecules in the pores, the crystals were evacuated for 6 h at 120 °C under 30 mTorr. Yield: 16 % based on Al. ATR-FTIR (cm^{-1}): 3059 (w), 1613 (s), 1600 (s), 1565 (m), 1517 (w), 1456 (s), 1423 (s), 1293 (w), 1183 (m), 1153 (w), 1105 (w), 1018 (w), 977 (m), 858 (w), 819 (w), 787 (s), 712 (m), 678 (m), 640 (s), 589 (s), 548 (s), 498 (m), 446 (w). EA: Found (wt %): C: 59.20; H: 3.19; N: < 0.2. Calculated (wt %): C: 58.81; H: 3.14; N: 0.0.

Single crystal X-ray diffraction analysis of MOF-520

Single-crystalline samples were mounted on MiTeGen® kapton loops in LV CryoOil® and placed in a 100(2) K nitrogen cold stream from Oxford Cryosystems Cryostream equipment. In all cases, the raw data were processed with the Bruker APEX2 software package. The data were first integrated using the SAINT procedure and then corrected for absorption with SADABS procedure. The structures were solved by direct methods (XS-2008) and the refinement was done by full-matrix least squares on F^2 (SHELXL-2014), using the Olex2 software package [17,18]. Mercury software was used for structure visualization[19].

Λ-MOF-520. A truncated octahedron-shaped crystal (80 x 60 x 60 μm^3) of as-synthesized **Λ**-MOF-520 was measured at beamline 11.3.1 at the ALS with radiation of λ = 1.0333 Å. According to intensity statistics table for the whole dataset (PRP file), the resolution was cut off to 0.83 Å. Solvent masking was applied during structure refinement. Before solvent masking instruction, structure was refined anisotropically and hydrogen atoms were placed into positions calculated geometrically. The connected asymmetric unit was defined inside the unit cell: MOVE command was applied to all atoms. The weighting scheme is refined as well as the extinction coefficient. The void volume is estimated to be 8963 $Å^3$ with 9196 electrons removed during masking. Some reflections were omitted due to non-ideal solvent masking, beam stop clipping and the minor presence of diffuse scattering. The threshold $(I_{obs}-I_{calc})/\sigma(W)>10$ was chosen for omitting these reflections. Omission of these reflections did not affect the refinement; the fraction of omitted reflections is less than 0.1% of the whole dataset.

Table S2.1. Crystal data, data collection, and structure refinement parameters for **Λ**-MOF-520.

Name	**Λ**-MOF-520
Chemical composition of MOF per asymmetric unit	$Al_2\ C_{28}\ H_{18}\ O_{10}$
Chemical formula of bound molecule	none
Bound molecule occupancy	0%
Formula mass	568.38
Crystal system	Tetragonal
Space group	$P4_22_12$
a, Å	18.5370(6)
c, Å	37.4217(15)
V, Å^3	12858.9(10)
d, g cm^{-3}	0.587
μ, mm^{-1}	0.210
Z	8
Measured reflections	75723
Independent reflections	11665
Observed reflections	10335
θ_{min} , ^{o}	2.248
θ_{max} , ^{o}	38.523
h	-22 to 18
k	-22 to 22
l	-33 to 43
R int	0.0550
$R\ [F^2>2\sigma(F^2)]$	0.0290
$wR(F^2)$	0.0800
S	0.991
Parameters	373
Geometrical restraints on the molecule	0
Occupational constraints on the molecule	0
Geometrical constraints on the molecule	0
Flack parameter	0.049(17)
$\Delta\rho_{max}$, e Å^{-3}	0.144
$\Delta\rho_{min}$, e Å^{-3}	-0.114
Crystal size, mm^3	0.080 x 0.060 x 0.060
Radiation, Å	1.0333
Temperature, K	100

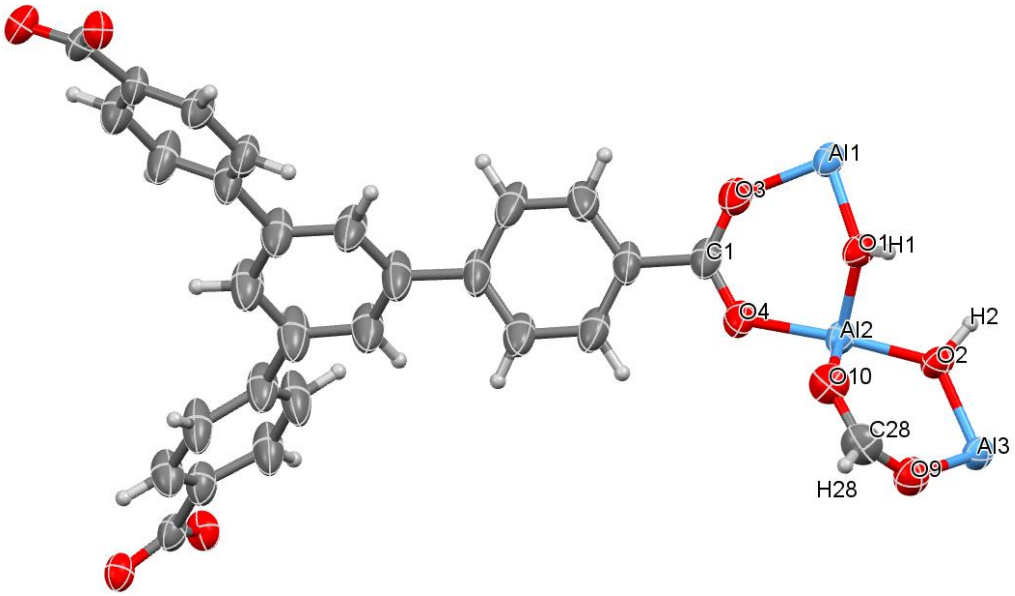

Figure S2.1. Asymmetric unit in the single crystal structure of **Λ**-MOF-520. Thermal ellipsoids are drawn with 50% probability.

Δ-MOF-520. A colorless truncated octahedron-shaped crystal (80 x 60 x 60 μm^3) of as-synthesized **Δ**-MOF-520 was measured at Bruker MicroSTAR-H APEX II diffractometer with radiation of λ = 1.54178 Å. According to intensity statistics table for the whole dataset (PRP file), the resolution was cut off to 0.83 Å. Solvent masking was applied during structure refinement. Before solvent masking instruction, structure was refined anisotropically and hydrogen atoms were placed into positions calculated geometrically. The connected asymmetric unit was defined inside the unit cell: MOVE command was applied to all atoms. The weighting scheme is refined as well as the extinction coefficient. The void volume is estimated to be 8913 $Å^3$ with 8417 electrons removed during masking. Some reflections were omitted due to non-ideal solvent masking, beam stop clipping and the minor presence of diffuse scattering. The threshold $(I_{obs}-I_{calc})/\sigma(W)>10$ was chosen for omitting these reflections. Omission of these reflections did not affect the refinement; the fraction of omitted reflections is less than 0.1% of the whole dataset.

Table S2.2. Crystal data, data collection, and structure refinement parameters for **Δ**-MOF-520.

Name	**Δ**-MOF-520
Chemical composition of MOF per asymmetric unit	$Al_2\ C_{28}\ H_{18}\ O_{10}$
Chemical formula of bound molecule	none
Bound molecule occupancy	0%
Formula mass	568.38
Crystal system	Tetragonal
Space group	$P4_22_12$
a, Å	18.4753(4)
c, Å	37.4264(9)
V, Å^3	12775.0(6)
d, g cm^{-3}	0.662
μ, mm^{-1}	0.324
Z	8
Measured reflections	49798
Independent reflections	11725
Observed reflections	10446
θ_{min} , ^{o}	2.667
θ_{max} , ^{o}	68.374
h	-22 to 20
k	-21 to 15
l	-45 to 44
R int	0.0335
R [$F^2>2\sigma(F^2)$]	0.0339
wR(F^2)	0.0897
S	0.989
Parameters	373
Geometrical restraints on the molecule	0
Occupational constraints on the molecule	0
Geometrical constraints on the molecule	0
Flack parameter	0.031(11)
$\Delta\rho_{max}$, e Å^{-3}	0.403
$\Delta\rho_{min}$, e Å^{-3}	-0.165
Crystal size, mm^3	0.080 x 0.070 x 0.070
Radiation, Å	1.54178
Temperature, K	100

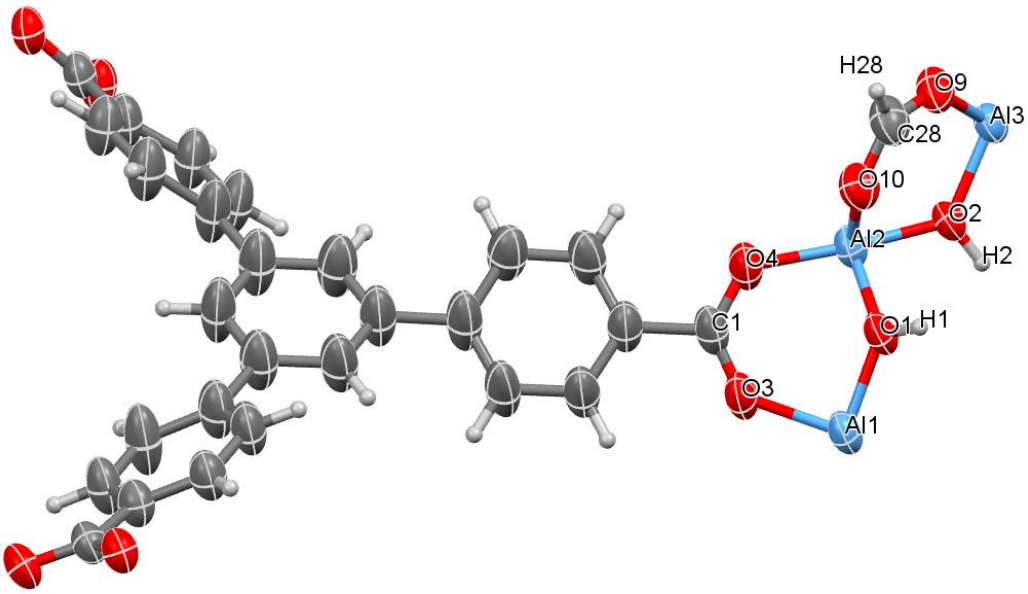

Figure S2.2. Asymmetric unit in the single crystal structure of **Λ**-MOF-520. Thermal ellipsoids are drawn with 50% probability.

Table S2.3. The structure refinement parameters for MOF-520 from statistical experiment to estimate the racemic character for twenty one single-crystalline samples (thirteen **Δ** and eight **Λ** forms).

Form	*R* int	*R* [*I*>2*σ*(*I*)]	*S*	*Flack parameter, **x**(u)*
Δ (delta)	0.0415	0.0310	1.092	0.106(9)
Δ (delta)	0.0716	0.0411	0.950	-0.01(8)
Δ (delta)	0.0566	0.0333	0.890	0.01(2)
Δ (delta)	0.0820	0.0414	0.963	-0.01(7)
Δ (delta)	0.0490	0.0289	1.027	0.073(19)
Δ (delta)	0.0414	0.0286	1.053	0.077(11)
Δ (delta)	0.0409	0.0390	0.938	0.05(3)
Δ (delta)	0.0299	0.0378	0.928	0.08(4)
Δ (delta)	0.0307	0.0418	0.956	0.11(4)
Δ (delta)	0.0204	0.0343	1.119	0.15(4)
Δ (delta)	0.0391	0.0404	0.920	0.05(6)
Δ (delta)	0.0595	0.0498	1.055	0.08(6)
Δ (delta)	0.0430	0.0348	1.010	0.10(1)
Λ (lambda)	0.0356	0.0305	1.054	0.040(13)
Λ (lambda)	0.0479	0.0325	1.072	0.03(4)
Λ (lambda)	0.0650	0.0281	1.074	0.11(3)
Λ (lambda)	0.0892	0.0432	1.056	0.06(2)
Λ (lambda)	0.0661	0.0331	1.035	0.13(3)
Λ (lambda)	0.0596	0.0336	0.969	0.06(3)
Λ (lambda)	0.0497	0.0461	0.910	-0.12(5)
Λ (lambda)	0.0382	0.0289	1.103	0.07(1)

Powder X-ray diffraction analysis

Guest free single crystals were used for PXRD experiment. Ground sample was placed on a quartz sample holder and was mounted on the diffractometer. The data was collected from 2 to 50 degrees by 0.02 step for total 60 minutes data collection time.

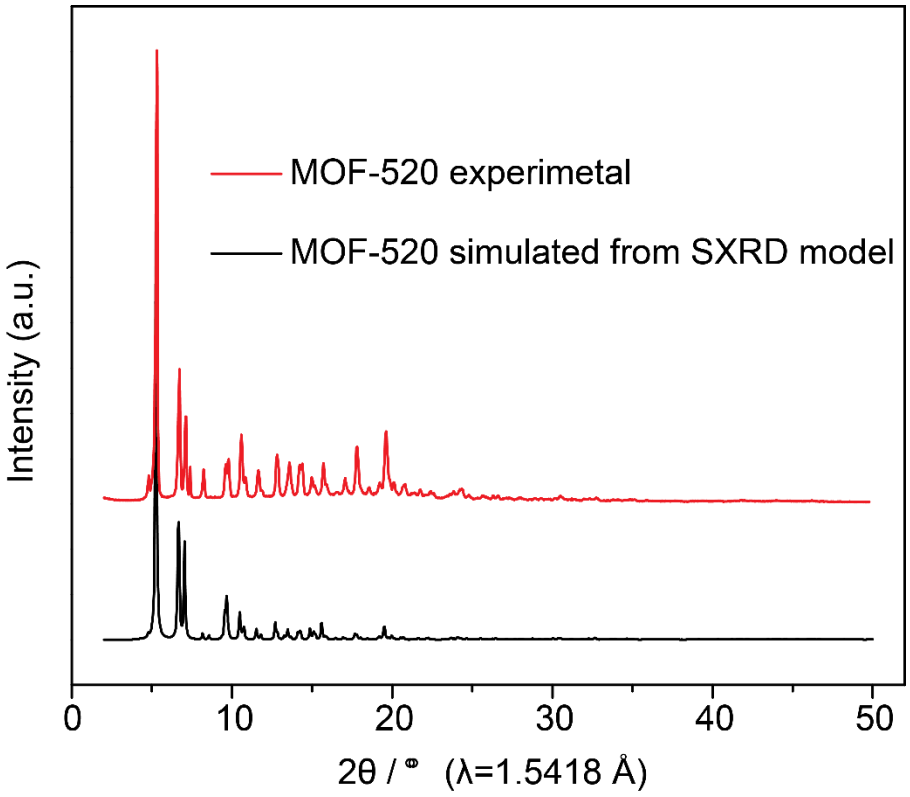

Figure S2.3. PXRD pattern of MOF-520 and the simulated pattern of MOF-520 structure from SXRD data.

N_2 isotherm

40 mg of guest free samples in 9 mm bulb gas cell was charged with Ar to avoid air contamination and the cell was mounted on the instrument. Liquid nitrogen bath was used for the measurements at 77 K. Helium was used for the estimation of dead space for gas adsorption measurements. Ultra-high-purity grade N_2 and He gases (Praxair, 99.999% purity) were used throughout the adsorption experiments. 46 adsorption and 16 desorption points were collected.

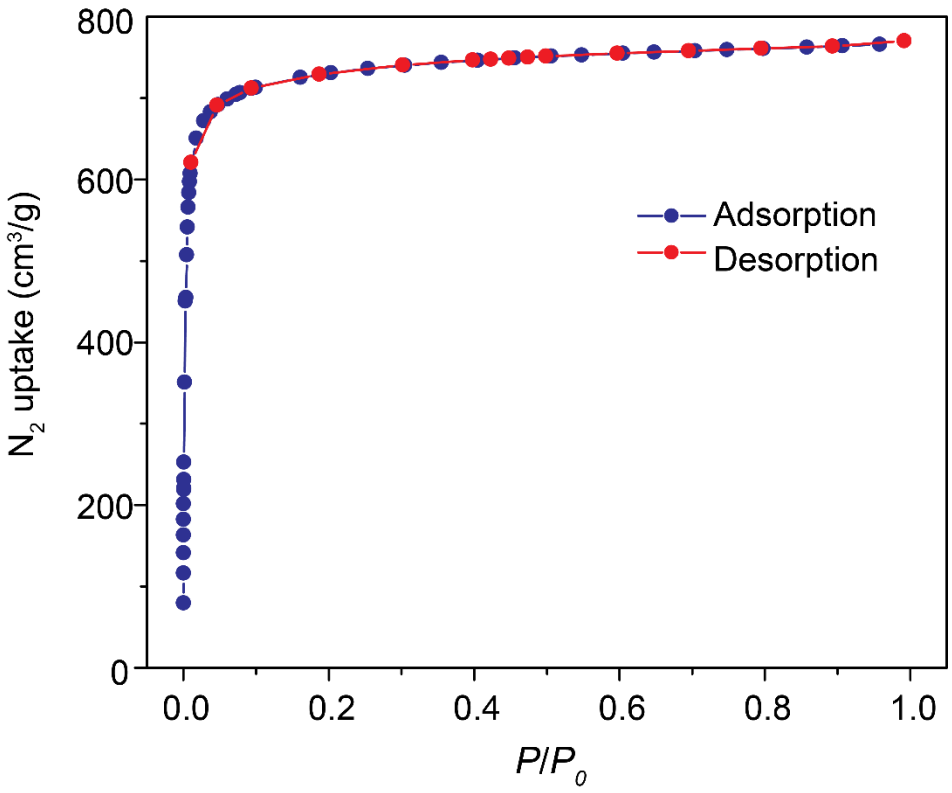

Figure S2.4. N_2 isotherm of MOF-520 at 77K.

Thermogravimetric analysis

The guest free sample was held in a platinum pan under nitrogen atmosphere with a flow rate of 40 mL/min. Temperature was controlled by the furnace heating from 25 °C up to 800 °C with a ramp rate of 5 °C/ min.

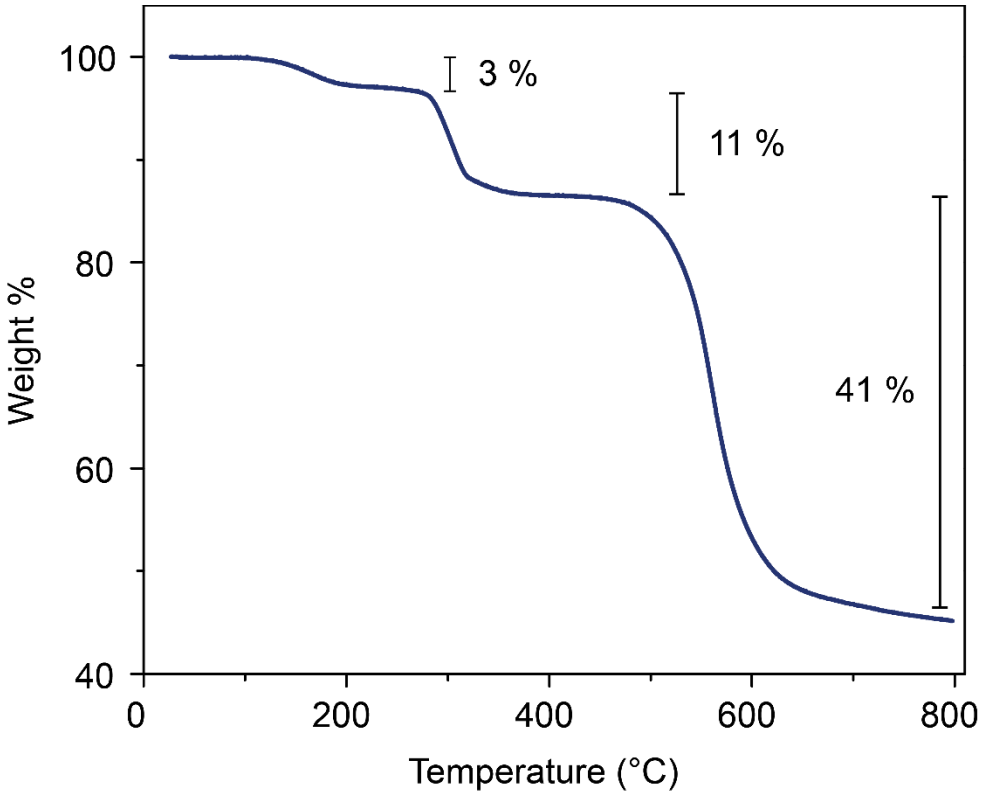

Figure S2.5. TGA data of the guest free MOF-520.

^{1}H NMR

The guest free sample (1 mg) was transferred to a 4 mL vial. Deuterated dimethyl sulfoxide (d_6-DMSO) (600 µL) was add to the vial followed by the addition of 20 µL of NaOH (1 M in D_2O). The solution was sonicated for 10 min to digest the crystals. The vial was capped and placed in a preheated 120 °C oven for 20 min to completely dissolve the crystals. The final clear solution was used for the ^{1}H NMR experiment.

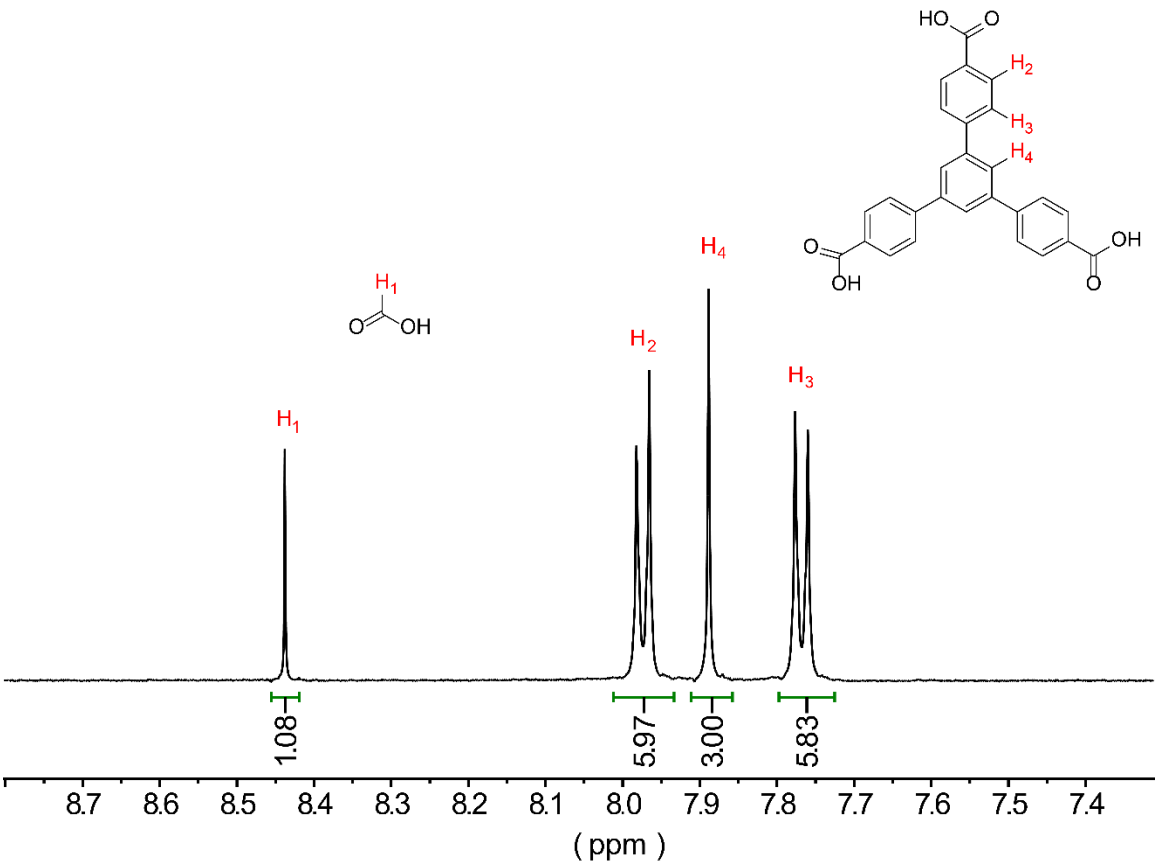

Figure S2.6. ^{1}H NMR data of digested guest free MOF-520 in d_6-DMSO.

Inclusion procedures and single crystal X-ray diffraction analyses

Diclofenac sodium salt, benzoic acid, heptanoic acid, anhydrous ethylene glycol (99.8 %), and anhydrous methanol (99.8 %) were purchased form Sigma Aldrich Co. 3-hydroxybenzoic acid, gibberellin A_3, genistein, (±)-jasmonic acid, 4-bromophenol, 1,3,5-benzentricarboxylic acid , 3-nitrophenol, and 3,5-diaminobenzoic acid were purchased from TCI America. Boc-(RS)-3-amino-1,2-propanediol was purchased from AnaSec Inc. Gibberellin A_1 was purchased from Santa Cruze Biotechnology, Inc. All chemicals obtained were used without further purification.

MOF-520 single crystal preparation. As-synthesized MOF-520 single crystals were washed with fresh DMF (10 mL), three times per day for three days to remove unreacted starting materials in the pore. Between each washing procedure, the crystals were kept in fresh DMF (18 mL in a 20 mL vial). Otherwise mentioned in the detail procedure, MOF-520 single crystals impregnated with DMF were used for the molecule showing better solubility in DMF. When the molecules dissolve better in acetone, MOF-520 single crystals impregnated with acetone were prepared by exchanging DMF in the pore with fresh acetone following the solvent exchange procedure in Section S1.1. Since the bulk sample is a racemic conglomerate, a mixture of both enantiomers was used for the inclusion.

General inclusion procedure. In general, the introduction of the molecules into MOF-520 was carried out by soaking MOF-520 single crystals impregnated with fresh DMF or acetone in a saturated solution of the molecule in DMF or acetone, respectively. The choice of the solvent of the solution was decided by the solubility of the molecules. The mixture of MOF-520 and the molecule solution was prepared in a scintillation vial. The vial was closed with a polypropylene cap having foil liner and placed in a preheated isothermal oven, 40 °C for acetone solution and 100 °C for DMF solution. After several days, SXRD data collection was carried out with the resulting single crystals. To confirm the incorporation of molecules along with SXRD data, ^{1}H NMR data was collected for MOF-520-**1** to -**5.** They represent the whole functionalities though which the molecules, **1** to **16**, bind to Al. Although the incorporation can be confirmed from the NMR data, some of the integration ratio, molecule to H_3BTB linker, show deviation from the occupancy in the refined structures. This can be explained by that the molecule incorporation in a single crystal does not represent the whole batch of the sample.

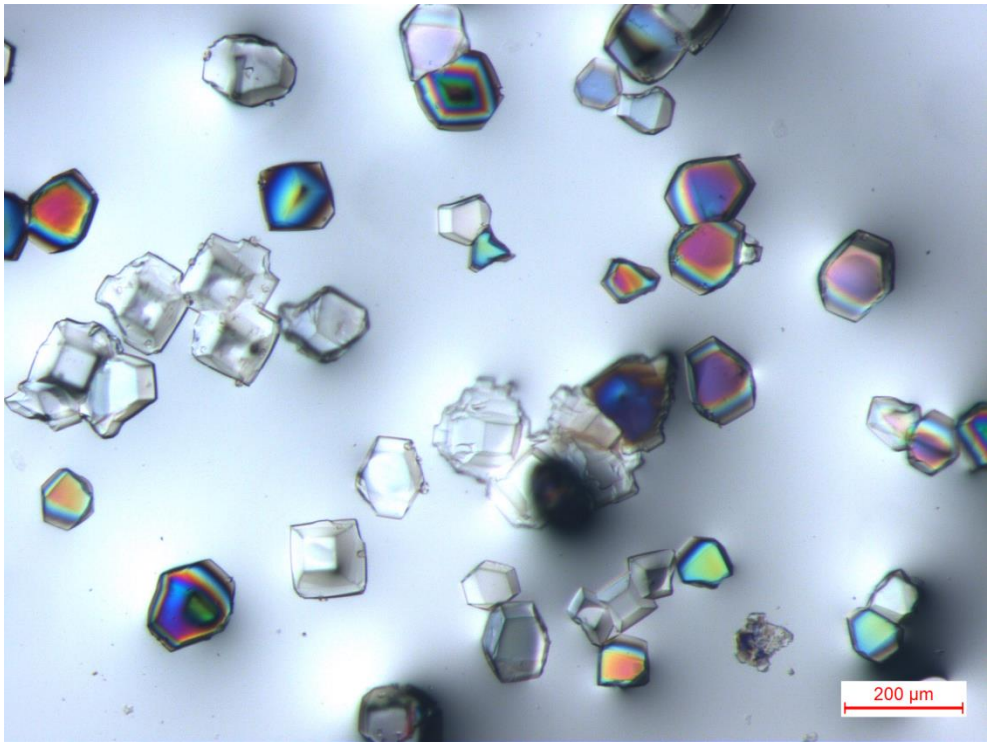

Figure S2.7. As-synthesized MOF-520 single crystals image obtained from optical microscope under polarized light.

MOF-520-1 (**1** = benzoic acid). Benzoic acid solution was prepared by adding benzoic acid (40.0 mg, 0.326 mmol) to DMF (200.0 µL) in a 4 mL vial and the solution was sonicated for 10 min to dissolve the material. MOF-520 single crystals (1.0 mg) impregnated with DMF were added to the solution. The vial was closed and placed in the preheated 100 °C oven. After 12 hours, the vial was kept at room temperature to slowly cool down the solution. SXRD data was collected with a single crystal from the vial.

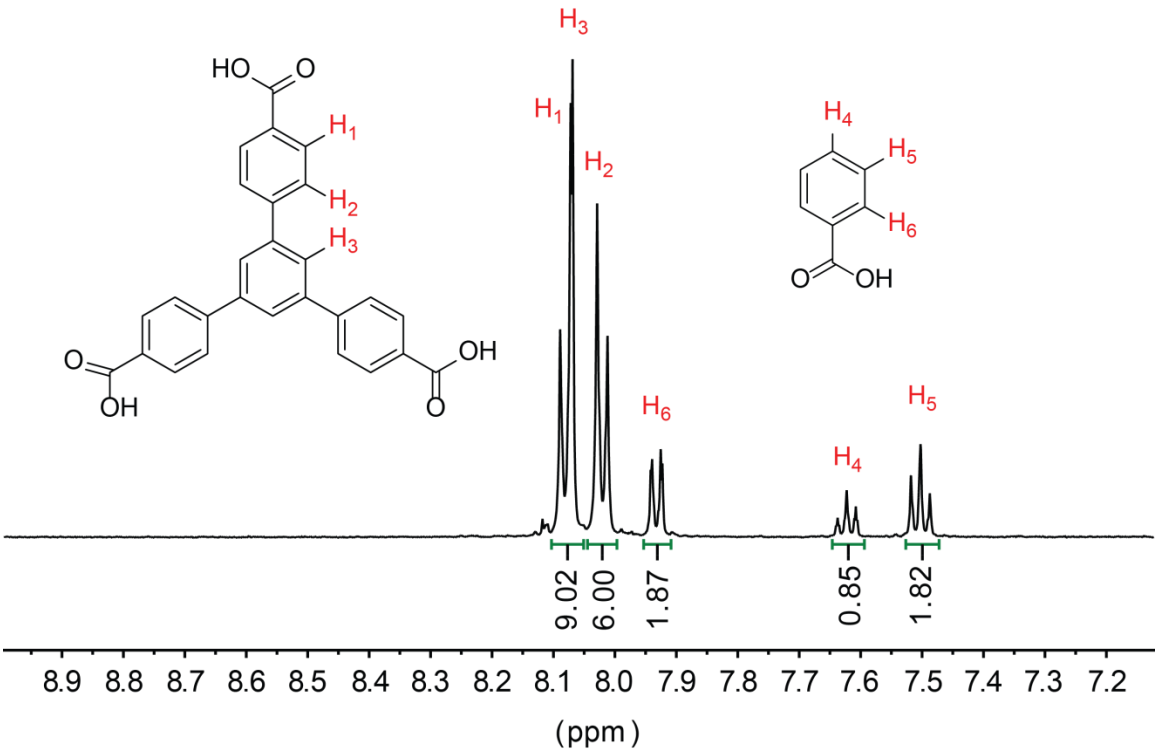

Figure S2.8. ^{1}H NMR data of digested guest free MOF-520-**1** in d_6-DMSO.

MOF-520-2 (**2** = methanol). The activated guest free single crystals of MOF-520 (50 mg) were soaked in anhydrous methanol (10 mL) in a 20 mL vial. The vial was kept in a preheated 40 °C oven for 15 days. After the reaction, the vial was cooled down at room temperature. One of the single crystals was used for SXRD analysis and rest of the crystals were activated to evacuate the pore. The same solvent exchange and activation procedure for MOF-520 was applied.

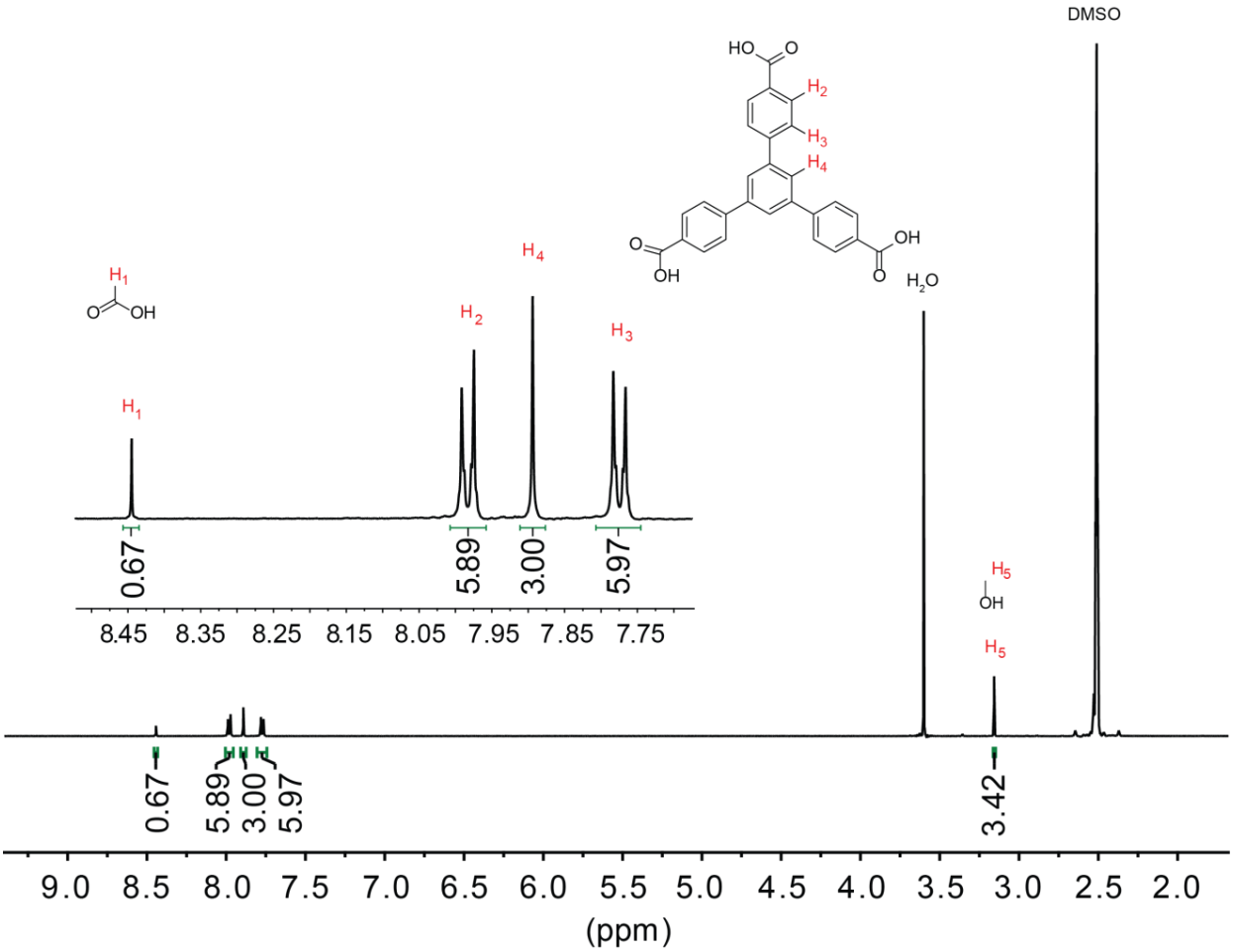

Figure S2.9. ^{1}H NMR data of digested guest free MOF-520-**2** in d_6-DMSO.

MOF-520-**3** (**3** = ethylene glycol). The activated single crystals of MOF-520 (50 mg) were soaked in ethylene glycol (10 mL) in a 20 mL vial. The vial was kept in a preheated 100 °C oven for 5 days. After the reaction, one of the single crystals was used for SXRD analysis and rest of the crystals were activated to evacuate the pore. The same solvent exchange and activation procedure for MOF-520 was applied.

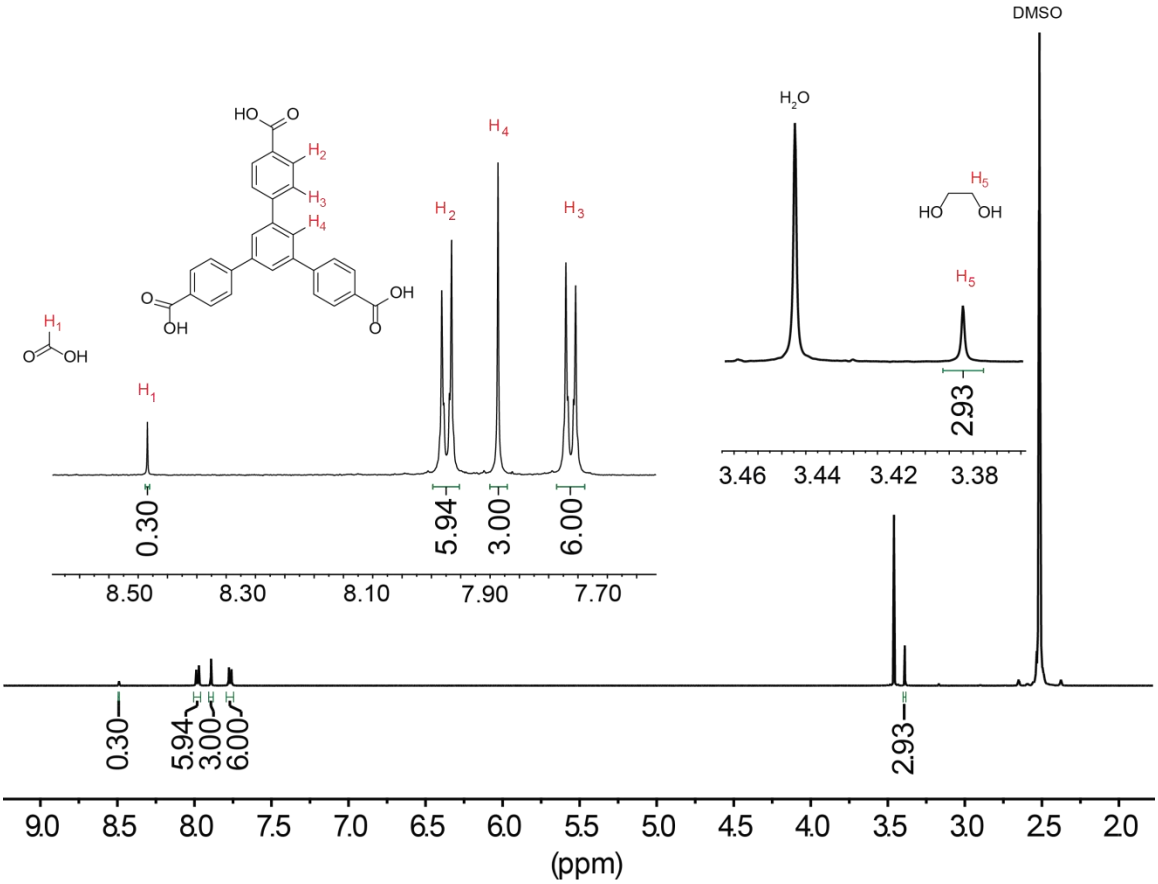

Figure S2.10. ^{1}H NMR data of digested guest free MOF-520-**3** in d_6-DMSO.

MOF-520-4 (4 = 3-nitrophenol). 3-nitrophenol solution was prepared by adding 3-nitrophenol (60.0 mg, 0.432 mmol) to anhydrous acetone (200.0 µL) in a 4 mL vial followed by adding triethylamine (2.0 µL) into the solution. MOF-520 single crystals (1.0 mg) impregnated with acetone were added to the solution. The vial was capped and placed in the room temperature for 10 days. SXRD data was collected with a single crystal from the vial.

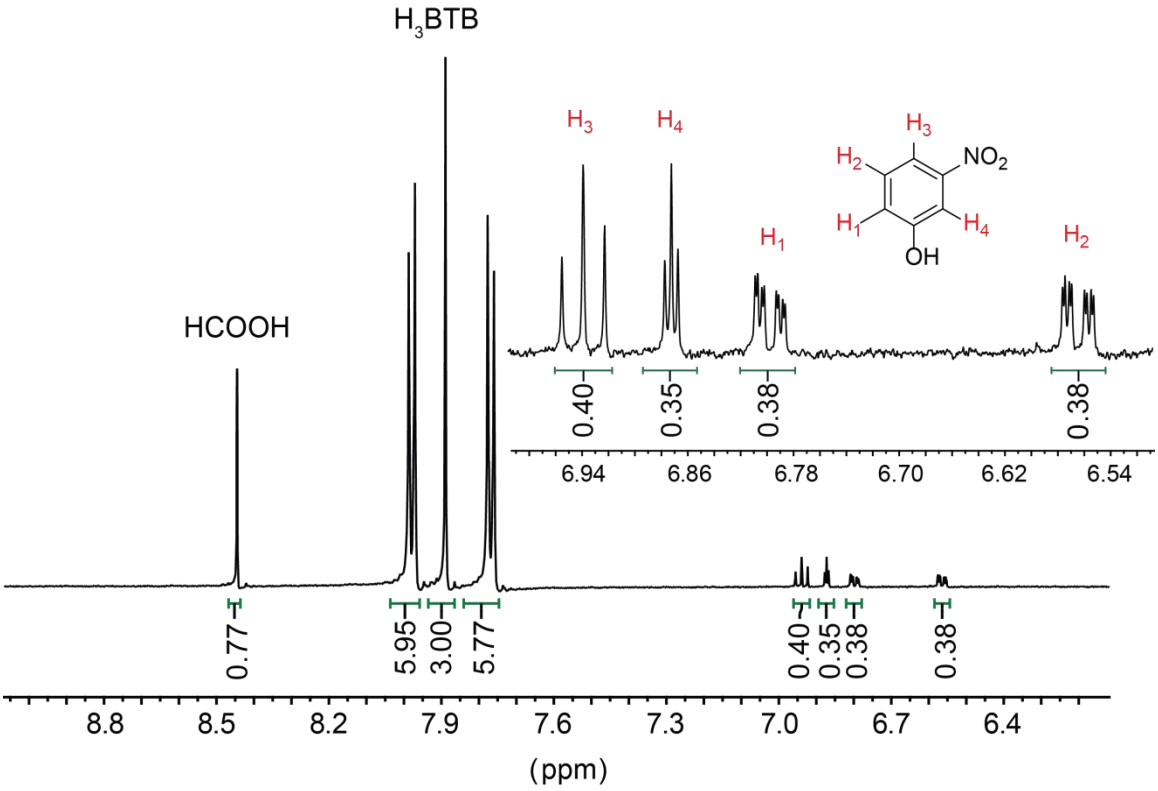

Figure S2.11. ^{1}H NMR data of digested guest free MOF-520-**4** in d_6-DMSO.

MOF-520-5 (5= heptanoic acid). Heptanoic acid solution was prepared by adding heptanoic acid (60.0 µL, 0.424 mmol) to anhydrous DMF (200.0 µL) in a 4 mL vial. MOF-520 single crystals (1.0 mg) impregnated with DMF were added to the solution. The vial was closed and placed in the preheated 100 °C oven. After 2 days, SXRD data was collected with a single crystal from the vial.

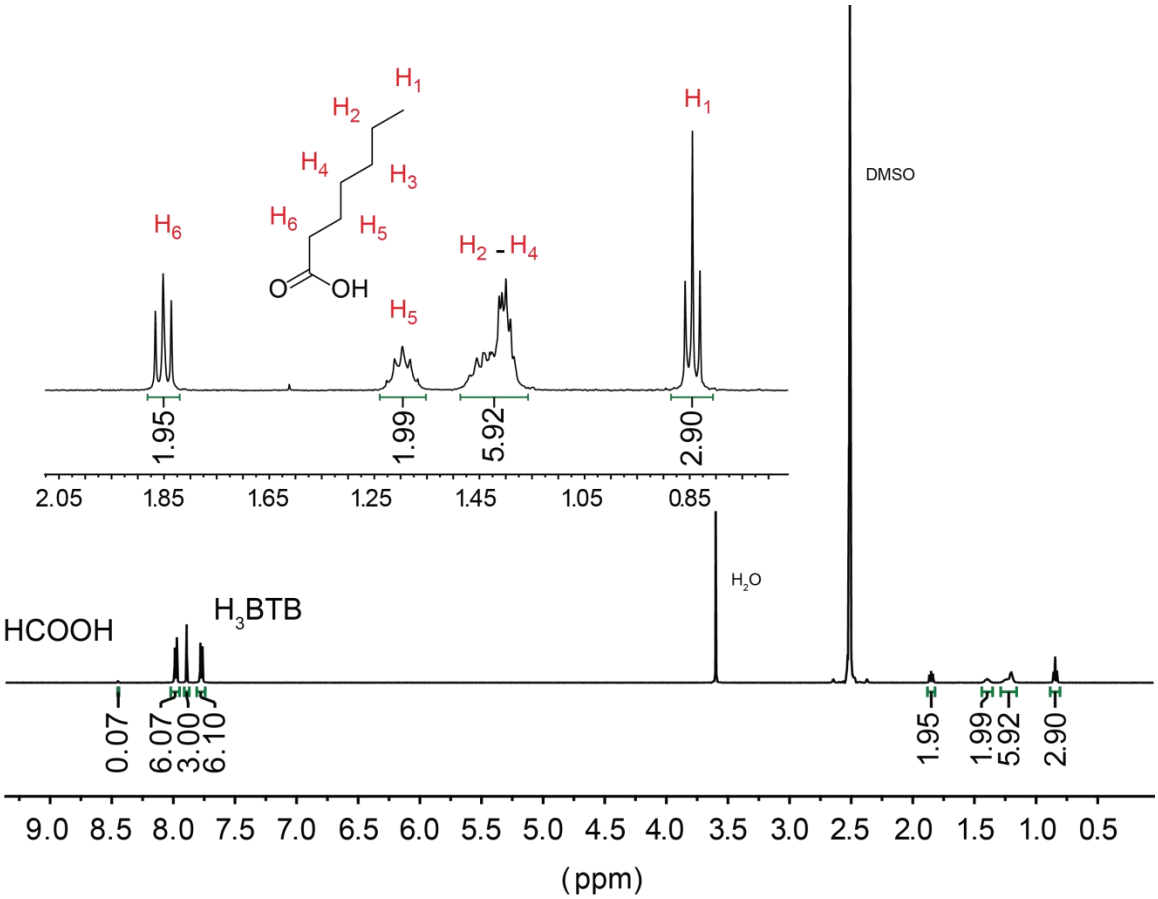

Figure S2.12. ^{1}H NMR data of digested guest free MOF-520-**5** in d_6-DMSO.

MOF-520-6 (6 = 3-hydroxybenzoic acid). 3-hydroxybenzoic acid (60.0 mg, 0.434 mmol) was added to DMF (200.0 µL) in a 4 mL vial and the solution was sonicated for 10 min to dissolve the material. MOF-520 single crystals (1.0 mg) impregnated with DMF were added to the solution. The vial was capped and placed in preheated 100 °C oven for 24 hrs. SXRD data was collected with a single crystal from the vial.

MOF-520-7 (7 = 3,5-diaminobenzoic acid). 3-hydroxybenzoic acid (60.0 mg, 0.394 mmol) was added to anhydrous acetone (200.0 µL) in a 4 mL vial and the solution was sonicated for 10 min to dissolve the material. MOF-520 single crystals (1.0 mg) impregnated with acetone were added to the solution. The vial was capped and placed in preheated 40 °C oven for 2 days. SXRD data was collected with a single crystal from the vial.

MOF-520-8 (8 = Trimesic acid). Trimesic acid (50.0 mg, 0.238 mmol) was added to DMF (200.0 µL) in a 4 mL vial and the solution was sonicated for 10 min to dissolve the material. MOF-520 single crystals (1.0 mg) impregnated with DMF were added to the solution. The vial was capped and placed in preheated 100 °C oven for 24 hrs. SXRD data was collected with a single crystal from the vial.

MOF-520-9 (9 = 4-bromophenol). 4-bromophenol solution was prepared by adding 4-bromophenol (60.0 mg, 0.432 mmol) to anhydrous acetone (200.0 µL) in a 4 mL vial followed

by adding triethylamine (2.0 µL) into the solution and the solution was sonicated for 10 min to dissolve the material. MOF-520 single crystals (1.0 mg) impregnated with acetone were added to the solution and the vial was placed in the preheated 40 °C oven for 10 days. SXRD data was collected with a single crystal from the vial.

MOF-520-10 (10 = diclofenac). Diclofenac solution was prepared by adding sodium diclofenac sodium salt (30.0 mg, 0.094 mmol) to anhydrous DMF (150.0 µL) in a Pyrex tube measuring 10 × 8 mm (o.d × i.d) and the solution was sonicated for 10 min to dissolve the material. MOF-520 single crystals (2.0 mg) impregnated with DMF were added to the solution. The tube was sealed by freeze-pump- thaw method (30 mTorr) and placed in the preheated 100 °C oven for 3 days. SXRD data was collected with a single crystal from the tube.

MOF-520-2-11 (11 = genistein). Genistein solution was prepared by adding genistein (10.0 mg, 0.0370 mmol) to anhydrous acetone (400.0 µL) in a 4 mL vial followed by adding triethylamine (10 µL), and the solution was sonicated for 10 min to dissolve the material. MOF-520-**2** single crystals (3.0 mg) impregnated with acetone were added to the solution. The vial was capped and placed in the preheated 45 °C oven for 5 days. SXRD data was collected with a single crystal from the vial.

MOF-520-12 (12 = Boc-(RS)-3-amino-1,2-propanediol). Boc-(RS)-3-amino-1,2-propanediol solution was prepared by adding Boc-(RS)-3-amino-1,2-propanediol (50.0 mg, 0.094 mmol) to DMF (300.0 µL) and the solution was sonicated for 10 min to dissolve the material. MOF-520 single crystals (1.0 mg) impregnated with DMF were added to the solution. The vial was capped and placed in preheated 100 °C oven for 3 days. SXRD data was collected with a single crystal from the vial.

MOF-520-3-13 (13 = gibberellin A_1). Gibberellin A_1 solutions was prepared by adding gibberellin A_1 (15.0 mg, 0.0433 mmol) to DMF (200.0 µL) in a 4 mL vial, and the solution was sonicated for 10 min to dissolve the material. MOF-520-**3** single crystals (5.0 mg) impregnated with DMF were added to the solution. The vial was capped and placed in the preheated 100 °C oven for 5 days. SXRD data was collected with a single crystal from the vial.

MOF-520-3-14 (14 = gibberellin A_3). Gibberellin A_3 solutions was prepared by adding gibberellin A_3 (15.0 mg, 0.0433 mmol) to DMF (200.0 µL) in 10 mm opening Pyrex tube, and the solution was sonicated for 10 min to dissolve the material. MOF-520-**3** single crystals (5.0 mg) impregnated with DMF were added to the solution. The tube was sealed by freeze-pump-thaw method (50 mTorr) and placed in the preheated 100 °C oven for 4 days. SXRD data was collected with a single crystal from the tube.

MOF-520-15 and -16 (15 = (-)-jasmonic acid, 16 = (+)-jasmonic acid). (±)−Jasmonic acid solution was prepared by adding (±)-jasmoic acid (100 µL) to anhydrous DMF (100.0 µL) in the Pyrex tube, and the solution was sonicated for 1 min to dissolve the material. MOF-520 single crystals (2.0 mg) impregnated with DMF were added to the solution. The tube was sealed by freeze-pump- thaw method (30 mTorr) and placed in the preheated 100 °C oven for 4 days. SXRD data was collected with a single crystal from the tube.

Single crystal X-ray analysis of inclusion crystals

After the inclusion of the molecules, several single crystals from each batch were mounted on the diffractometer and SXRD data was collected. In a typical experiment the single-crystalline sample was mounted on MiTeGen® kapton loops in LV CryoOil® and placed in a 100(2) K nitrogen cold stream from Oxford Cryosystems Cryostream equipment. The best data in terms of the occupancy of the molecules incorporated was chosen and reported here. Since the chirality of a single crystal could not be distinguished by inspection of the shape of the crystal or by polarized light, the choice of the chirality of the inclusion crystal from the batch was not in control. The resolution obtained for all samples was limited due to inherent disorder in the crystals; in order to improve the refinement of the model, the resolution was cut off, according to intensity statistics table. In case of measurements with synchrotron radiation, i.e. the wavelength is not CuK$_\alpha$, the DISP command was used to set the f′, f″, and μ values for atoms in the structures.

The refinement procedure can be divided into several parts: the anisotropic refinement of the MOF structure, the localization and assignment of the bound molecule, the anisotropic refinement of the bound molecule, and solvent masking procedure. First, the structure of MOF is refined anisotropically and all hydrogen atoms are placed into geometrically calculated positions. The connected asymmetric unit was defined inside the unit cell: MOVE command was applied to all atoms. The weighting scheme is refined as well as the extinction coefficient. After this step, we started to assign the electron density peaks, which are closest to the binding site, and can be interpreted as a part of the bound molecule. The assigned atoms are refined with U^{iso} = 0.05. Once assignment of large part of the molecule is done, the occupancy of the bound molecule is estimated with a free variable and isotropic displacement parameters were refined freely. Once the refinement has run to convergence, the resulting occupancy is fixed throughout the whole bound molecule. Typically, standard deviations of U^{iso}'s tend to increase with increasing distance from the binding site. The occupancy of binding carboxylate group or alcoholic or phenolic oxygen atoms are given unit value. Once the whole molecule is localized and fixed, a step-by-step anisotropic refinement is carried out: the closest atom to the binding site is refined first followed by the refinement of further atom. Once all non-hydrogen atoms are refined anisotropically, hydrogen atoms present at the target molecule are placed into geometrically calculated positions. The electron density due to the presence the highly disordered solvent molecule of DMF within the pore, is accounted for by a solvent masking procedure[20]. Note that due to partial occupancy of the target molecule at the binding site of the SBU, the electron density of the target molecule is superimposed by some solvent density, which cannot be taken into account by the solvent masking procedure. In addition, it needs to be considered that obscuring of low-angle reflections significantly affects the amount of unassigned electron density, accounted by solvent masking procedure, but not the geometry of bound molecule. Before and after solvent masking, the Flack parameters are within the 3σ error range, i.e.

$$|x_{\text{before masking}} - x_{\text{after masking}}| < 3[(u_{\text{before masking}})^2 + (u_{\text{after masking}})^2]^{1/2}$$

Where x is the absolute Flack parameter value and u is its estimated standard deviation[21].

All geometrical restraints and occupational constraints, applied to non-hydrogen atoms of bound molecules, are listed in the CIF files as well as on the corresponding table of each structure.

Δ-MOF-520-1. A colorless truncated octahedron-shaped crystal (110 x 80 x 80 μm^3) of **Δ**-MOF-520-**1** was measured at a Bruker D-8-Venture diffractometer with radiation of λ = 1.54178 Å. According to intensity statistics table for the whole dataset (PRP file), the resolution was cut off to 1.00 Å. Solvent masking was applied during structure refinement. Before solvent masking instruction, structure was refined anisotropically and hydrogen atoms were placed into positions calculated geometrically. The molecule of benzoic acid was found to be positionally disordered (two parts with 0.5 occupancy). Solvent masking was applied during structure refinement. Before solvent masking instruction, structure was refined anisotropically and hydrogen atoms were placed into positions calculated geometrically. The connected asymmetric unit was defined inside the unit cell: MOVE command was applied to all atoms. The weighting scheme is refined as well as the extinction coefficient. The void volume is estimated to be 8312 $Å^3$ with 5692 electrons. Some reflections were omitted due to non-ideal solvent masking, beam stop clipping and the minor presence of diffuse scattering. The threshold $(I_{obs}-I_{calc})/\sigma(W)>10$ was chosen for omitting these reflections. Omission of these reflections did not affect the refinement; the fraction of omitted reflections is less than 0.1% of the whole dataset.

Table S2.4. Crystal data, data collection, and structure refinement parameters for **Δ**-MOF-520-**1**.

Name	**Δ**-MOF-520-**1**
Chemical composition of MOF per asymmetric unit	$Al_2\ C_{27}\ H_{17}\ O_8$
Chemical formula of bound molecule	$C_7\ H_5\ O_2$
Bound molecule occupancy	100%
Formula mass	644.47
Crystal system	Tetragonal
Space group	$P4_22_12$
a, Å	18.9406(5)
c, Å	36.6364(11)
V, Å^3	13143.2(8)
d, g cm^{-3}	0.651
μ, mm^{-1}	0.642
Z	8
Measured reflections	40325
Independent reflections	6901
Observed reflections	5022
θ_{min} , º	2.412
θ_{max} , º	50.498
h	-16 to 18
k	-18 to 14
l	-21 to 36
R int	0.0582
R [$F^2>2\sigma(F^2)$]	0.0508
wR(F^2)	0.1265
S	0.965
Parameters	471
Geometrical restraints on the molecule	96
Occupational constraints on the molecule	2
Geometrical constraints on the molecule	0
Flack parameter	0.076(15)
$\Delta\rho_{max}$, e Å^{-3}	0.193
$\Delta\rho_{min}$, e Å^{-3}	-0.349
Crystal size, mm^3	0.110 x 0.080 x 0.080
Radiation, Å	1.54178
Temperature, K	100

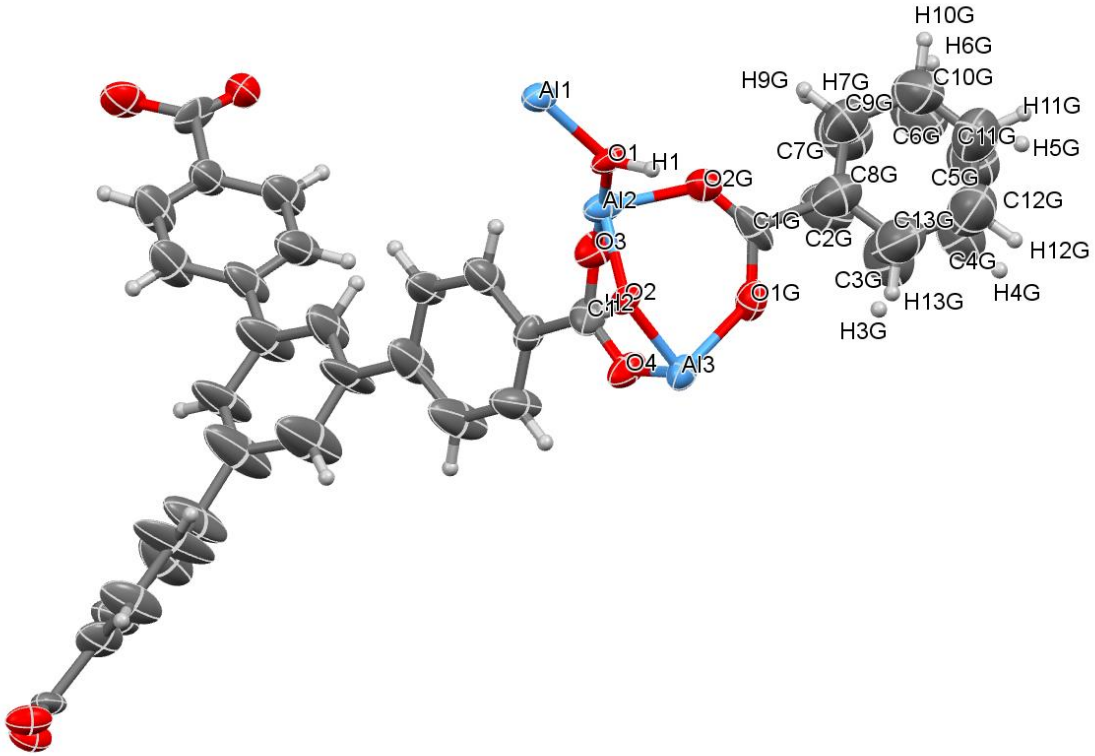

Figure S2.13. Asymmetric unit in the single crystal structure of **Λ**-MOF-520-**1**. Thermal ellipsoids are drawn with 50% probability.

Λ-MOF-520-2. A colorless truncated octahedron-shaped crystal (60 x 40 x 40 μm^3) of **Λ**-MOF-520-**2** was measured at a beamline 11.3.1 at the ALS with radiation of λ = 1.0332 Å. According to intensity statistics table for the whole dataset (PRP file), the resolution was cut off to 0.84 Å. Solvent masking was applied during structure refinement. Before solvent masking instruction, structure was refined anisotropically and hydrogen atoms were placed into positions calculated geometrically. The connected asymmetric unit was defined inside the unit cell: MOVE command was applied to all atoms. The weighting scheme is refined as well as the extinction coefficient. The void volume is estimated to be 19048 $Å^3$ with 5013 electrons removed during masking. The occupancy for 2 bound molecules of methanol was constrained to 1. Some reflections were omitted due to non-ideal solvent masking, beam stop clipping and the minor presence of diffuse scattering. The threshold $(I_{obs}\text{-}I_{calc})/\sigma(W)>10$ was chosen for omitting these reflections. Omission of these reflections did not affect the refinement; the fraction of omitted reflections is less than 0.1% of the whole dataset.

Table S2.5. Crystal data, data collection, and structure refinement parameters for **Λ**-MOF-520-**2**.

Name	**Λ**-MOF-520-**2**.
Chemical composition of MOF per asymmetric unit	$Al_4\ C_{55}\ H_{34}\ O_{17}$
Chemical formula of bound molecule	$C_1H_3O_1$
Bound molecule occupancy	2 molecules of 100 %
Formula mass	1136.81
Crystal system	Tetragonal
Space group	$P4_32_12$
a, Å	19.5333(8)
c, Å	69.876(3)
V, Å^3	26661(2)
d, g cm^{-3}	0.566
μ, mm^{-1}	0.180
Z	8
Measured reflections	201862
Independent reflections	23574
Observed reflections	20791
θ_{min} , º	2.143
θ_{max} , º	37.992
h	-23 to 23
k	-23 to 23
l	-83 to 83
R int	0.0582
$R\ [F^2>2\sigma(F^2)]$	0.0334
$wR(F^2)$	0.0853
S	0.982
Parameters	723
Geometrical restraints on the molecule	0
Occupational constraints on the molecule	2
Geometrical constraints on the molecule	0
Flack parameter	0.059(14)
$\Delta\rho_{max}$, e Å^{-3}	0.330
$\Delta\rho_{min}$, e Å^{-3}	-0.404
Crystal size, mm^3	0.060 x 0.040 x 0.040
Radiation, Å	1.0332
Temperature, K	100

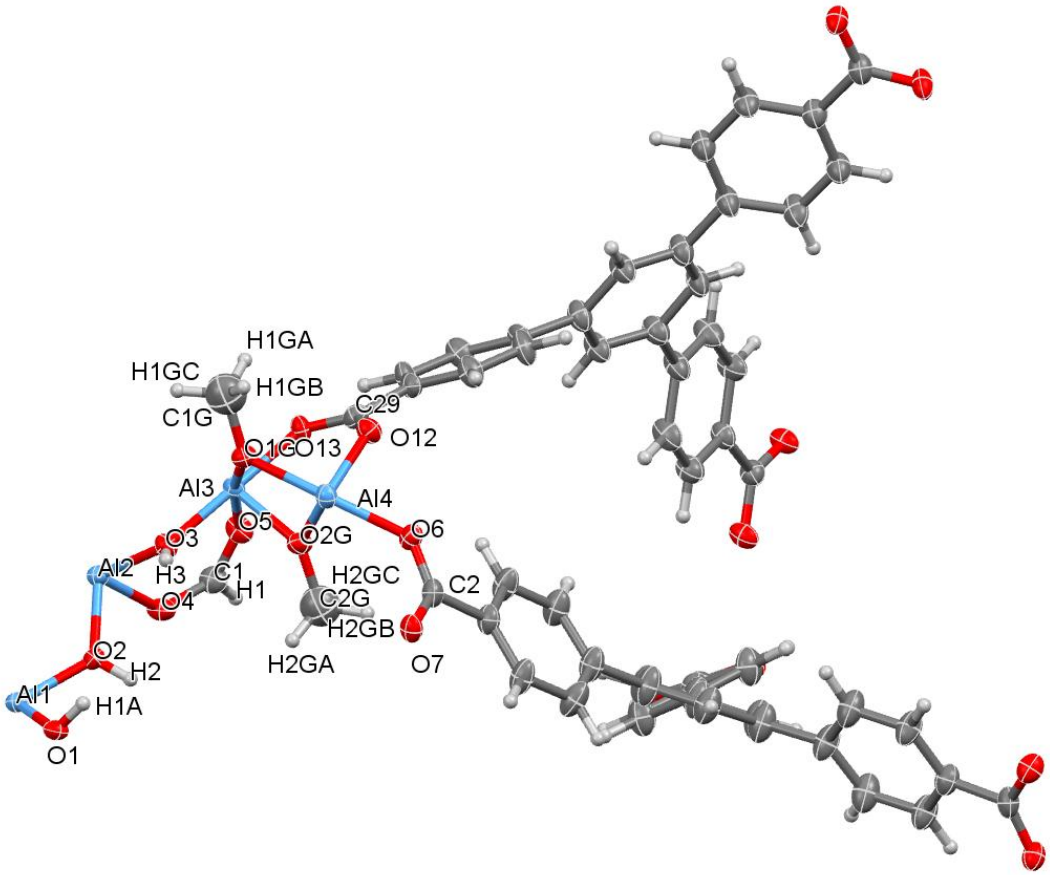

Figure S2.14. Asymmetric unit in the single crystal structure of **Λ**-MOF-520-**2**. Thermal ellipsoids are drawn with 50% probability.

Δ-MOF-520-3. A colorless truncated octahedron-shaped crystal (100 x 85 x 85 μm^3) of **Δ**-MOF-520-**3** was measured at a beamline 11.3.1 at the ALS with radiation of λ = 1.23990 Å. According to intensity statistics table for the whole dataset (PRP file), the resolution was cut off to 0.97 Å. The occupancy of each ethylene glycol was found through adding a new variable and then constrained to 1.0. The occupancy of the dangling moiety of the formic acid was set to 0.4. Solvent masking was applied during structure refinement. Before solvent masking instruction, structure was refined anisotropically and hydrogen atoms were placed into positions calculated geometrically. The connected asymmetric unit was defined inside the unit cell: MOVE command was applied to all atoms. The weighting scheme is refined as well as the extinction coefficient. The void volume is estimated to be 17397 $Å^3$ with 18733 electrons removed during masking. Some reflections were omitted due to non-ideal solvent masking, beam stop clipping and the minor presence of diffuse scattering. The threshold $(I_{obs}-I_{calc})/\sigma(W)>10$ was chosen for omitting these reflections. Omission of these reflections did not affect the refinement; the fraction of omitted reflections is less than 0.1% of the whole dataset.

Table S2.6. Crystal data, data collection, and structure refinement parameters for **Δ**-MOF-520-**3**.

Name	**Δ**-MOF-520-**3**
Chemical composition of MOF per asymmetric unit	$Al_4\ C_{54.4}\ H_{32.4}\ O_{15.4}$
Chemical formula of bound molecule	$C_2H_4O_2$
Bound molecule occupancy	2 molecules of 100 %
Formula mass	1160.42
Crystal system	Tetragonal
Space group	$P4_12_12$
a, Å	18.9175(19)
c, Å	71.908(7)
V, Å^3	25734(6)
d, g cm^{-3}	0.599
μ, mm^{-1}	0.319
Z	8
Measured reflections	108909
Independent reflections	14339
Observed reflections	10577
θ_{min} , º	2.122
θ_{max} , º	39.274
h	-19 to 19
k	-19 to 19
l	-73 to 73
R int	0.1373
$R\ [F^2>2\sigma(F^2)]$	0.0385
$wR(F^2)$	0.0837
S	0.916
Parameters	748
Geometrical restraints on the molecule	2
Occupational constraints on the molecule	3
Geometrical constraints on the molecule	0
Flack parameter	0.10(3)
$\Delta\rho_{max}$, e Å^{-3}	0.156
$\Delta\rho_{min}$, e Å^{-3}	-0.186
Crystal size, mm^3	0.100 x 0.085 x 0.085
Radiation, Å	1.2399
Temperature, K	100

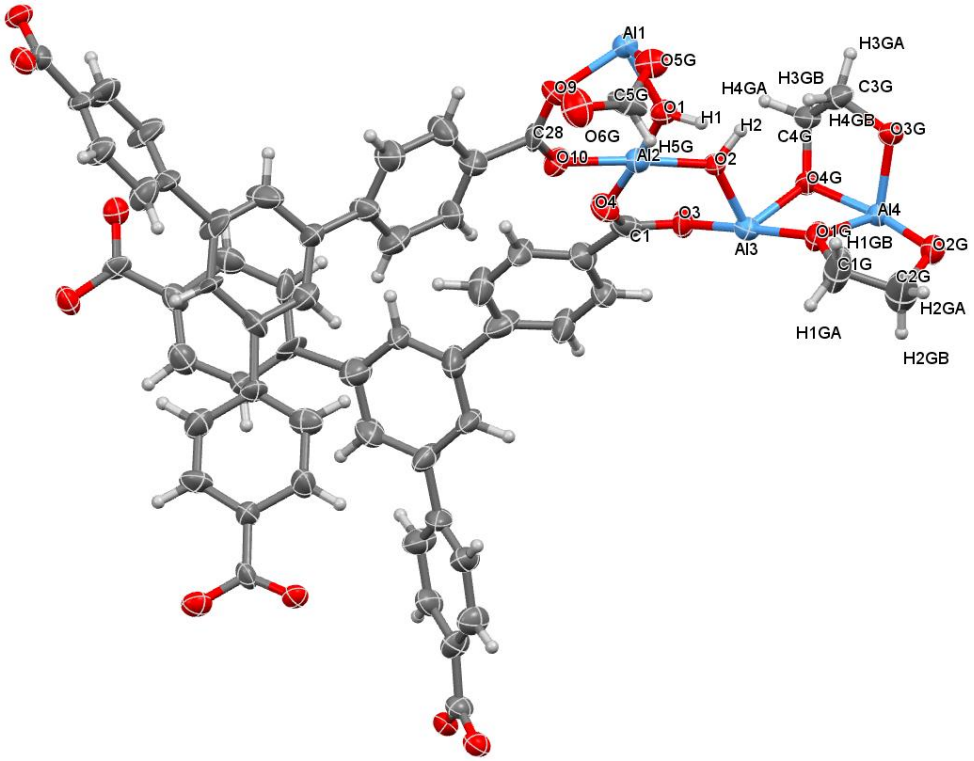

Figure S2.15. Asymmetric unit in the single crystal structure of **Λ**-MOF-520-**3**. Thermal ellipsoids are drawn with 50% probability.

Λ-MOF-520-4. A colorless truncated octahedron-shaped crystal (80 x 60 x 60 μm^3) of **Λ**-MOF-520-**4** was measured at a beamline 11.3.1 at the ALS with radiation of λ = 0.88560 Å. According to intensity statistics table for the whole dataset (PRP file), the resolution was cut off to 1.00 Å. The occupancy of each 3-nitrophenol was found through adding a new variable and then constrained to 0.65, 0.35 and 0.5 values. The occupancy of the dangling moiety of the formic acid was set to 0.5. Solvent masking was applied during structure refinement. Before solvent masking instruction, structure was refined anisotropically and hydrogen atoms were placed into positions calculated geometrically. The connected asymmetric unit was defined inside the unit cell: MOVE command was applied to all atoms. The weighting scheme is refined as well as the extinction coefficient. Once solvent masking instruction was introduced, the weight scheme was refined to convergence. The void volume is estimated to be 15573 $Å^3$ with 3598 electrons removed during masking. Some reflections were omitted due to non-ideal solvent masking, beam stop clipping and the minor presence of diffuse scattering. The threshold (I_{obs}-I_{calc})/σ(W)>10 was chosen for omitting these reflections. Omission of these reflections did not affect the refinement; the fraction of omitted reflections is less than 0.1% of the whole dataset.

Table S2.7. Crystal data, data collection, and structure refinement parameters for **Λ**-MOF-520-**4**

Name	**Λ**-MOF-520-**4**
Chemical composition of MOF per asymmetric unit	$Al_4\ C_{55}\ H_{33}\ O_{18}$
Chemical formula of bound molecule	$C_6H_4O_3N_1$
Bound molecule occupancy	1 molecule of 65 %, 1 molecule of 50%, 1 molecule of 35%
Formula mass	1296.89
Crystal system	Tetragonal
Space group	$P4_32_12$
a, Å	19.342(5)
c, Å	70.335(17)
V, Å^3	26312(14)
d, g cm^{-3}	0.655
μ, mm^{-1}	0.134
Z	8
Measured reflections	120352
Independent reflections	13783
Observed reflections	12462
θ_{min} , ^{o}	2.588
θ_{max} , ^{o}	26.311
h	-19 to 19
k	-19 to 19
l	-70 to 70
R int	0.0667
$R\ [F^2>2\sigma(F^2)]$	0.0560
$wR(F^2)$	0.1556
S	1.048
Parameters	965
Geometrical restraints on the molecule	70
Occupational constraints on the molecule	4
Geometrical constraints on the molecule	0
Flack parameter	0.07(4)
$\Delta\rho_{max}$, e Å^{-3}	0.295
$\Delta\rho_{min}$, e Å^{-3}	-0.316
Crystal size, mm^3	0.080 x 0.060 x 0.060
Radiation, Å	0.88560
Temperature, K	100

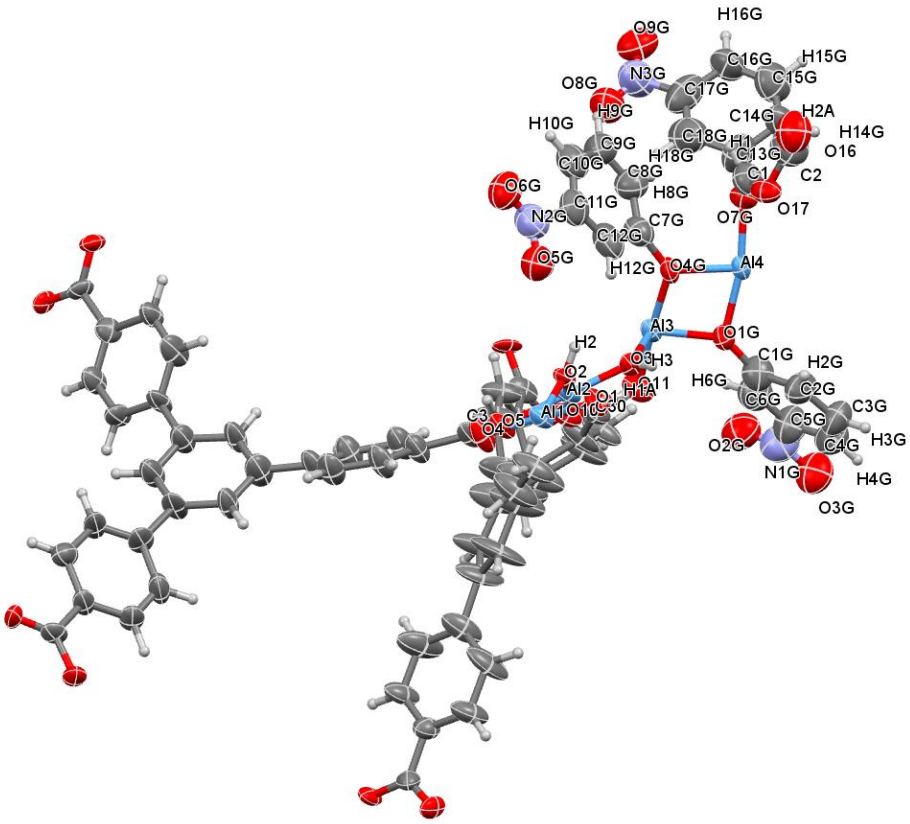

Figure S2.16. Asymmetric unit in the single crystal structure of **Λ**-MOF-520-**4**. Thermal ellipsoids are drawn with 50% probability.

Λ-MOF-520-5. A colorless truncated octahedron-shaped crystal (90 x 60 x 60 μm^3) of **Λ**-MOF-520-**5** was measured at a beamline 11.3.1 at the ALS with radiation of λ = 1.23990 Å. According to intensity statistics table for the whole dataset (PRP file), the resolution was cut off to 0.80 Å. The occupancy of heptanoic acid was found to be 0.55 for the most of the structure and this occupancy value was set for the whole molecule. Solvent masking was applied during structure refinement. Before solvent masking instruction, structure was refined anisotropically and hydrogen atoms were placed into positions calculated geometrically. The connected asymmetric unit was defined inside the unit cell: MOVE command was applied to all atoms. The weighting scheme is refined as well as the extinction coefficient. Once solvent masking instruction was introduced, the weight scheme was refined to convergence. The C7G, C6G and C5G atoms are heavily overlapped with the solvent present in the crystal, so they were initially put into calculated positions using DFIX and DELU restraints. The void volume is estimated to be 8446 $Å^3$ with 5312 electrons removed during masking. Some reflections were omitted due to non-ideal solvent masking, beam stop clipping and the minor presence of diffuse scattering. The threshold $(I_{obs}-I_{calc})/\sigma(W)>10$ was chosen for omitting these reflections. Omission of these reflections did not affect the refinement; the fraction of omitted reflections is less than 0.1% of the whole dataset.

Table S2.8. Crystal data, data collection, and structure refinement parameters for **Λ**-MOF-520-**5**.

Name	**Λ**-MOF-520-**5**
Chemical composition of MOF per asymmetric unit	$Al_2\ C_{27.45}\ H_{17}\ O_{8.9}$
Chemical formula of bound molecule	$C_7H_{13}O_2$
Bound molecule occupancy	55 %
Formula mass	614.21
Crystal system	Tetragonal
Space group	$P4_22_12$
a, Å	18.6010(6)
c, Å	37.3859(13)
V, Å^3	12935.4(9)
d, g cm^{-3}	0.631
μ, mm^{-1}	0.326
Z	8
Measured reflections	246186
Independent reflections	13281
Observed reflections	11445
θ_{min} , º	2.695
θ_{max} , º	50.900
h	-23 to 23
k	-23 to 23
l	-46 to 46
R int	0.0699
R [$F^2>2\sigma(F^2)$]	0.0372
wR(F^2)	0.1074
S	1.024
Parameters	417
Geometrical restraints on the molecule	15
Occupational constraints on the molecule	1
Geometrical constraints on the molecule	0
Flack parameter	0.064(8)
$\Delta\rho_{max}$, e Å^{-3}	0.203
$\Delta\rho_{min}$, e Å^{-3}	-0.299
Crystal size, mm^3	0.090 x 0.060 x 0.060
Radiation, Å	1.23990
Temperature, K	100

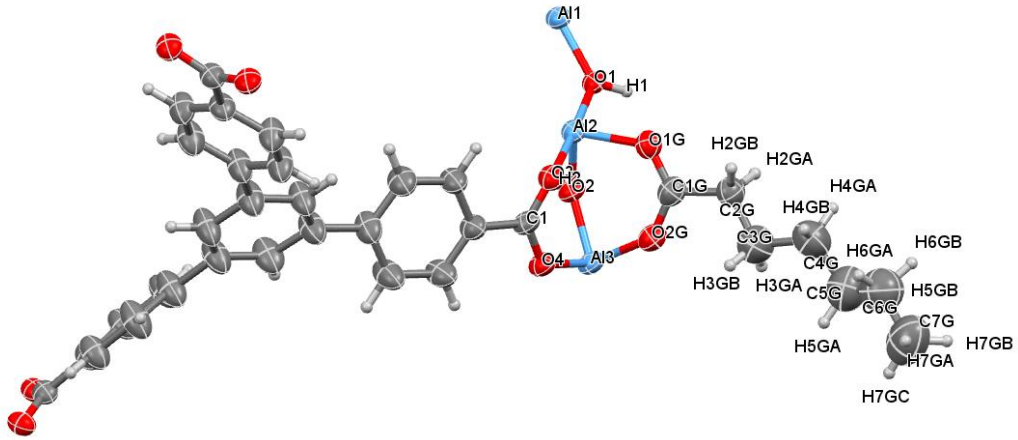

Figure S2.17. Asymmetric unit in the single crystal structure of **Λ**-MOF-520-**5**. Thermal ellipsoids are drawn with 50% probability.

Δ-MOF-520-6. A colorless truncated octahedron-shaped crystal (100 x 80 x 80 μm^3) of **Δ**-MOF-520-**6** was measured at a beamline 11.3.1 at the ALS with radiation of λ = 0.77490 Å. According to intensity statistics table for the whole dataset (PRP file), the resolution was cut off to 0.83 Å. The overall occupancy of 3-hydroxybenzoic acid was constrained to 1. The molecule of 3,5-diaminobenzoic acid was found to be positionally disordered. The occupancy of each part of 3-hydroxybenzoic acid was found through adding a new variable: 0.58 and 0.42, respectively Solvent masking was applied during structure refinement. Before solvent masking instruction, structure was refined anisotropically and hydrogen atoms were placed into positions calculated geometrically. The connected asymmetric unit was defined inside the unit cell: MOVE command was applied to all atoms. The weighting scheme is refined as well as the extinction coefficient. Once solvent masking instruction was introduced, the weight scheme was refined to convergence. The void volume is estimated to be 7952 $Å^3$ with 1165 electrons removed during masking. Some reflections were omitted due to non-ideal solvent masking, beam stop clipping and the minor presence of diffuse scattering. The threshold $(I_{obs}-I_{calc})/\sigma(W)>10$ was chosen for omitting these reflections. Omission of these reflections did not affect the refinement; the fraction of omitted reflections is less than 0.1% of the whole dataset.

Table S2.9. Crystal data, data collection, and structure refinement parameters for **Δ**-MOF-520-**6**.

Name	**Δ**-MOF-520-**6**
Chemical composition of MOF per asymmetric unit	$Al_2\ C_{27}\ H_{17}\ O_8$
Chemical formula of bound molecule	$C_7H_5O_3$
Bound molecule occupancy	100 %
Formula mass	660.47
Crystal system	Tetragonal
Space group	$P4_22_12$
a, Å	18.7200(7)
c, Å	36.8786(15)
V, Å^3	12923.7(11)
d, g cm^{-3}	0.679
μ, mm^{-1}	0.093
Z	8
Measured reflections	168732
Independent reflections	11871
Observed reflections	9717
θ_{min} , º	2.065
θ_{max} , º	27.844
h	-22 to 22
k	-22 to 22
l	-44 to 44
R int	0.0674
$R\ [F^2>2\sigma(F^2)]$	0.0542
$wR(F^2)$	0.1569
S	1.025
Parameters	491
Geometrical restraints on the molecule	75
Occupational constraints on the molecule	1
Geometrical constraints on the molecule	0
Flack parameter	0.07(3)
$\Delta\rho_{max}$, e Å^{-3}	0.478
$\Delta\rho_{min}$, e Å^{-3}	-0.272
Crystal size, mm^3	0.100 x 0.080 x 0.080
Radiation, Å	0.77490
Temperature, K	100

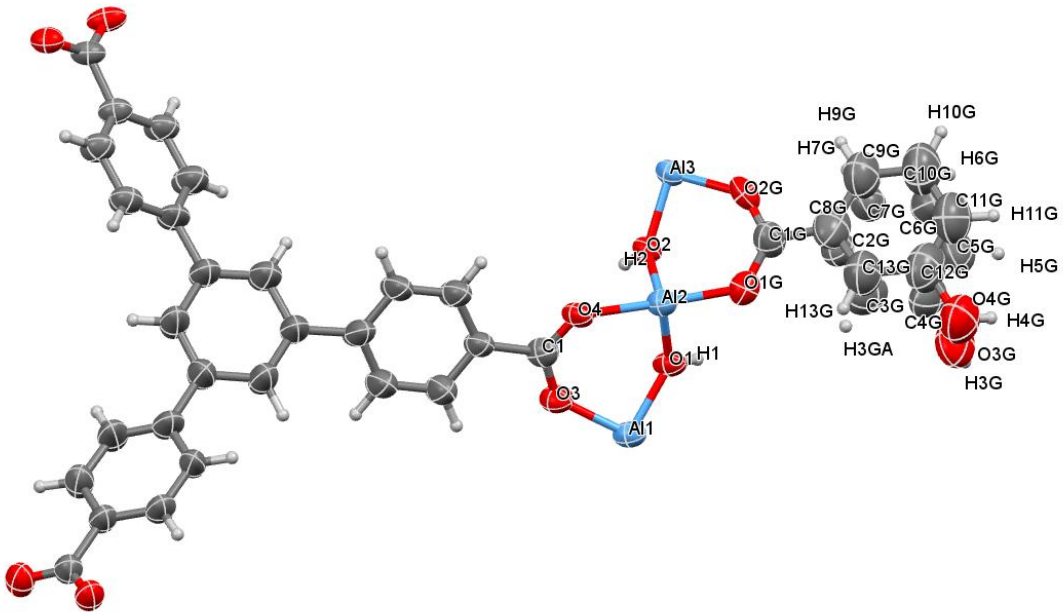

Figure S2.18. Asymmetric unit in the single crystal structure of **Λ**-MOF-520-**6**. Thermal ellipsoids are drawn with 50% probability.

Λ-MOF-520-7. A colorless truncated octahedron-shaped crystal (80 x 50 x 50 μm^3) of **Λ**-MOF-520-**7** was measured at a beamline 11.3.1 at the ALS with radiation of λ = 0.77490 Å. According to intensity statistics table for the whole dataset (PRP file), the resolution was cut off to 0.83 Å. The molecule of 3,5-diaminobenzoic acid was found to be positionally disordered. The occupancy of each part of 3,5-diaminobenzoic acid was found through adding a new variable and then constrained to 0.5. Solvent masking was applied during structure refinement. Before solvent masking instruction, structure was refined anisotropically and hydrogen atoms were placed into positions calculated geometrically. The connected asymmetric unit was defined inside the unit cell: MOVE command was applied to all atoms. The weighting scheme is refined as well as the extinction coefficient. Once solvent masking instruction was introduced, the weight scheme was refined to convergence. The void volume is estimated to be 8064 $Å^3$ with 1078 electrons removed during masking. Some reflections were omitted due to non-ideal solvent masking, beam stop clipping and the minor presence of diffuse scattering. The threshold (I_{obs}-I_{calc})/σ(W)>10 was chosen for omitting these reflections. Omission of these reflections did not affect the refinement; the fraction of omitted reflections is less than 0.1% of the whole dataset.

Table S2.10. Crystal data, data collection, and structure refinement parameters for **Λ**-MOF-520-**7**.

Name	**Λ**-MOF-520-**7**
Chemical composition of MOF per asymmetric unit	$Al_2\ C_{27}\ H_{17}\ O_8$
Chemical formula of bound molecule	$C_7H_3O_2N_2$
Bound molecule occupancy	100 %
Formula mass	674.51
Crystal system	Tetragonal
Space group	$P4_22_12$
a, Å	19.008(4)
c, Å	36.526(7)
V, Å^3	13197(6)
d, g cm^{-3}	0.679
μ, mm^{-1}	0.091
Z	8
Measured reflections	102464
Independent reflections	12073
Observed reflections	10831
θ_{min} , ^{o}	2.682
θ_{max} , ^{o}	27.864
h	-22 to 22
k	-22 to 22
l	-43 to 44
R int	0.0727
R [$F^2>2\sigma(F^2)$]	0.0418
$wR(F^2)$	0.1146
S	1.002
Parameters	507
Geometrical restraints on the molecule	0
Occupational constraints on the molecule	2
Geometrical constraints on the molecule	0
Flack parameter	0.06(4)
$\Delta\rho_{max}$, e Å^{-3}	0.165
$\Delta\rho_{min}$, e Å^{-3}	-0.297
Crystal size, mm^3	0.080 x 0.050 x 0.050
Radiation, Å	0.77490
Temperature, K	100

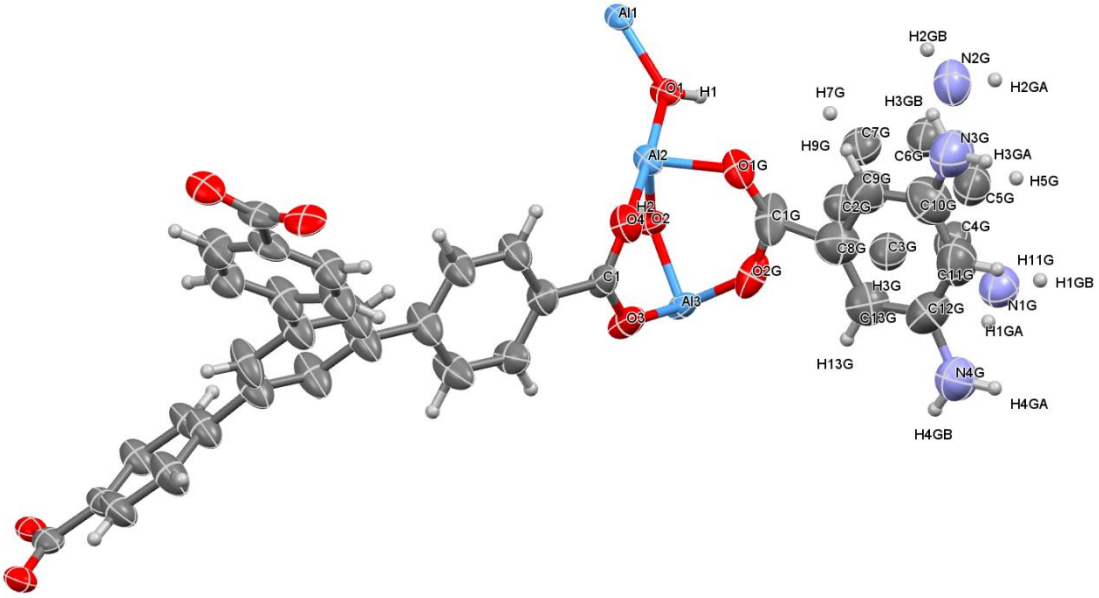

Figure S2.19. Asymmetric unit in the single crystal structure of **Λ**-MOF-520-**7**. Thermal ellipsoids are drawn with 50% probability.

Λ-MOF-520-8. A colorless truncated octahedron-shaped crystal (110 x 90 x 90 μm^3) of **Λ**-MOF-520-**7** was measured at a Bruker D-8-Venture diffractometer with radiation of λ = 1.54178 Å. According to intensity statistics table for the whole dataset (PRP file), the resolution was cut off to 1.09 Å. The occupancy of trimesic acid was found through adding a new variable and then constrained to 0.75. Before solvent masking instruction, structure was refined anisotropically and hydrogen atoms were placed into positions calculated geometrically. The connected asymmetric unit was defined inside the unit cell: MOVE command was applied to all atoms. The weighting scheme is refined as well as the extinction coefficient. Once solvent masking instruction was introduced, the weight scheme was refined to convergence. The void volume is estimated to be 7995 $Å^3$ with 4902 electrons removed during masking. Some reflections were omitted due to non-ideal solvent masking, beam stop clipping and the minor presence of diffuse scattering. The threshold $(I_{obs}-I_{calc})/\sigma(W)>10$ was chosen for omitting these reflections. Omission of these reflections did not affect the refinement; the fraction of omitted reflections is less than 0.1% of the whole dataset.

Table S2.11. Crystal data, data collection, and structure refinement parameters for **Λ**-MOF-520-**8**.

Name	**Λ**-MOF-520-**8**
Chemical composition of MOF per asymmetric unit	$Al_2\ C_{27.25}\ H_{17}\ O_{8.5}$
Chemical formula of bound molecule	$C_9H_3O_6$
Bound molecule occupancy	75 %
Formula mass	689.70
Crystal system	Tetragonal
Space group	$P4_22_12$
a, Å	19.0082(15)
c, Å	36.661(3)
V, Å^3	13246(2)
d, g cm^{-3}	0.692
μ, mm^{-1}	0.692
Z	8
Measured reflections	28689
Independent reflections	5149
Observed reflections	3575
θ_{min} , º	2.62
θ_{max} , º	44.536
h	-15 to 17
k	-17 to 17
l	-32 to 33
R int	0.1017
$R\ [F^2>2\sigma(F^2)]$	0.0620
$wR(F^2)$	0.1573
S	0.986
Parameters	446
Geometrical restraints on the molecule	53
Occupational constraints on the molecule	1
Geometrical constraints on the molecule	0
Flack parameter	0.10(3)
$\Delta\rho_{max}$, e Å^{-3}	0.224
$\Delta\rho_{min}$, e Å^{-3}	-0.290
Crystal size, mm^3	0.110 x 0.090 x 0.090
Radiation, Å	1.54178
Temperature, K	100

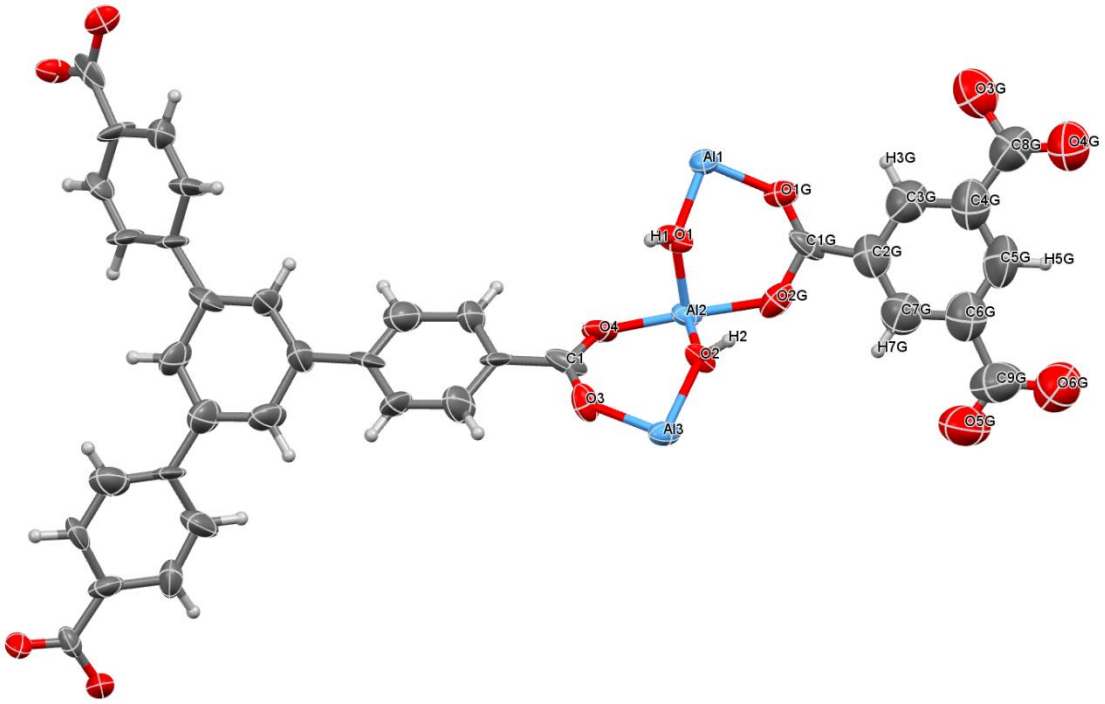

Figure S2.20. Asymmetric unit in the single crystal structure of **Λ**-MOF-520-**8**. Thermal ellipsoids are drawn with 50% probability.

Λ-MOF-520-9. A colorless truncated octahedron-shaped crystal (100 x 80 x 80 μm^3) of **Λ**-MOF-520-**9** was measured at a beamline 11.3.1 at the ALS with radiation of λ = 0.95370 Å. According to intensity statistics table for the whole dataset (PRP file), the resolution was cut off to 0.83 Å. The occupancy of 4-bromophenol was found through adding a new variable and then constrained to 0.3 and 0.2. Before solvent masking instruction, structure was refined anisotropically and hydrogen atoms were placed into positions calculated geometrically. The connected asymmetric unit was defined inside the unit cell: MOVE command was applied to all atoms. The weighting scheme is refined as well as the extinction coefficient. Once solvent masking instruction was introduced, the weight scheme was refined to convergence. Since the amount of significant anomalous scatterers within the pore was not significant, the application of the solvent masking procedure was valid. The flack parameters for MOF-520-**9** before solvent masking and after was within 3σ error range: before, 0.010(2) and after, 0.010(3). The void volume is estimated to be 16409 $Å^3$ with 4945 electrons removed during masking. Some reflections were omitted due to non-ideal solvent masking, beam stop clipping and the minor presence of diffuse scattering. The threshold $(I_{obs}-I_{calc})/\sigma(W)>10$ was chosen for omitting these reflections. Omission of these reflections did not affect the refinement; the fraction of omitted reflections is less than 0.1% of the whole dataset.

Table S2.12. Crystal data, data collection, and structure refinement parameters for **Λ**-MOF-520-**9**.

Name	**Λ**-MOF-520-**9**
Chemical composition of MOF per asymmetric unit	$Al_4\ C_{54.8}\ H_{34.6}\ O_{36.5}$
Chemical formula of bound molecule	$C_6H_4O_1Br_1$
Bound molecule occupancy	1 molecule with 30 %, 1 molecule with 20 %
Formula mass	1183.15
Crystal system	Tetragonal
Space group	$P4_32_12$
a, Å	19.1308(5)
c, Å	70.677(2)
V, Å^3	25866.9(16)
d, g cm^{-3}	0.608
μ, mm^{-1}	0.196
Z	8
Measured reflections	142101
Independent reflections	23641
Observed reflections	17574
θ_{min} , º	2.54
θ_{max} , º	33.04
h	-23 to 21
k	-24 to 24
l	-90 to 90
R int	0.0904
R [$F^2>2\sigma(F^2)$]	0.0613
wR(F^2)	0.1625
S	1.018
Parameters	829
Geometrical restraints on the molecule	99
Occupational constraints on the molecule	2
Geometrical constraints on the molecule	0
Flack parameter	0.10(3)
$\Delta\rho_{max}$, e Å^{-3}	0.440
$\Delta\rho_{min}$, e Å^{-3}	-0.321
Crystal size, mm^3	0.100 x 0.080 x 0.080
Radiation, Å	0.95370
Temperature, K	100

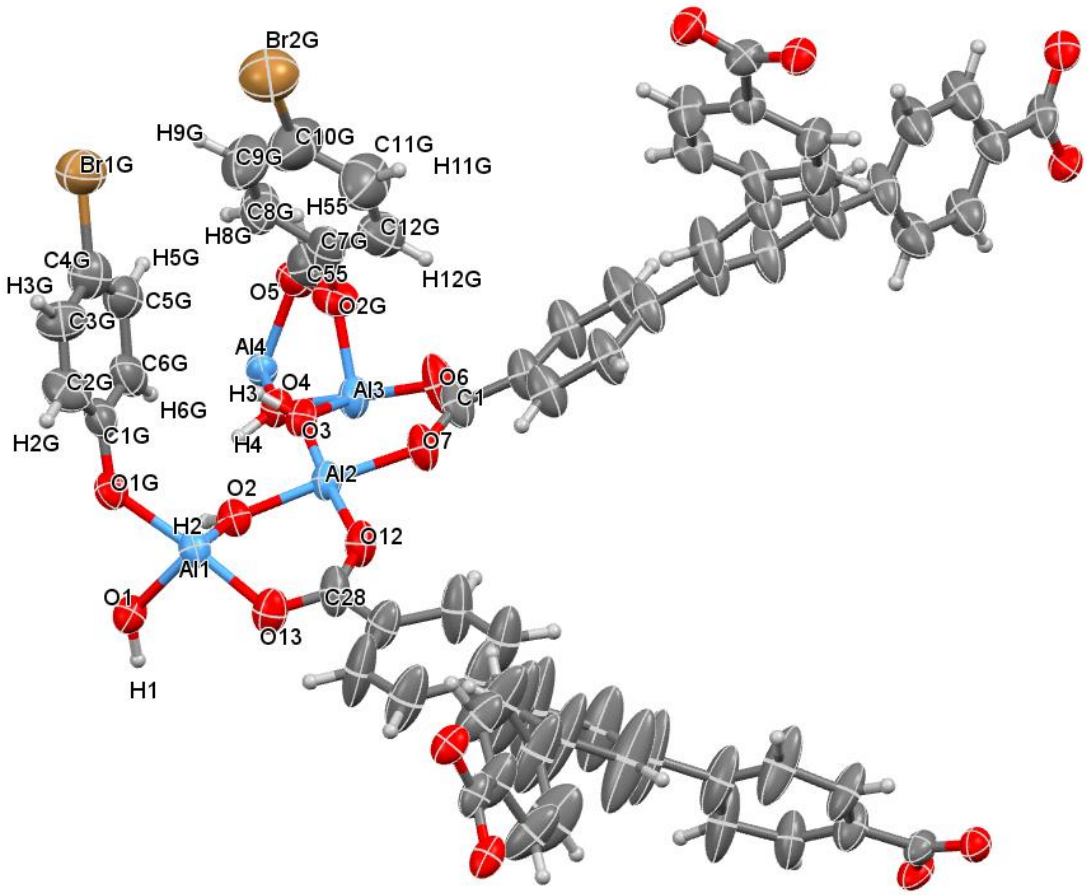

Figure S2.21. Asymmetric unit in the single crystal structure of **Λ**-MOF-520-**9**. Thermal ellipsoids are drawn with 50% probability.

Δ-MOF-520-10. A colorless truncated octahedron-shaped crystal (70 x 55 x 55 μm^3) of **Δ**-MOF-520-**10** was measured at a beamline 11.3.1 at the ALS with radiation of λ = 1.0332 Å. According to intensity statistics table for the whole dataset (PRP file), the resolution was cut off to 0.83 Å. The occupancy of diclofenac was found through adding a new variable and then constrained to 0.35. Before solvent masking instruction, structure was refined anisotropically and hydrogen atoms were placed into positions calculated geometrically. The connected asymmetric unit was defined inside the unit cell: MOVE command was applied to all atoms. The weighting scheme is refined as well as the extinction coefficient. Once solvent masking instruction was introduced, the weight scheme was refined to convergence. Since the amount of significant anomalous scatterers within the pore was not significant, the application of the solvent masking procedure was valid. The flack parameters for MOF-520-**10** before solvent masking and after was within 3σ error range: before, 0.09(2) and after, 0.013(2). The void volume is estimated to be 16371 $Å^3$ with 13287 electrons removed during masking. The large value of unassigned electron density within the unit cell is due to missing of some low-angle observations. Some reflections were omitted due to non-ideal solvent masking, beam stop clipping and the minor presence of diffuse scattering. The threshold $(I_{obs}-I_{calc})/\sigma(W)>10$ was chosen for omitting these

reflections. Omission of these reflections did not affect the refinement; the fraction of omitted reflections is less than 0.1% of the whole dataset.

Table S2.13. Crystal data, data collection, and structure refinement parameters for **Δ**-MOF-520-**10**.

Name	**Δ**-MOF-520-**10**
Chemical composition of MOF per asymmetric unit	$Al_4\ C_{55.3}\ H_{34}\ O_{18.3}$
Chemical formula of bound molecule	$C_{14}H_{10}O_2N_1Cl_2$
Bound molecule occupancy	35%
Formula mass	1202.44
Crystal system	Tetragonal
Space group	$P4_12_12$
a, Å	19.0123(9)
c, Å	71.393(4)
V, Å^3	25806(3)
d, g cm^{-3}	0.619
μ, mm^{-1}	0.232
Z	8
Measured reflections	214744
Independent reflections	23593
Observed reflections	15541
θ_{min} , º	2.202
θ_{max} , º	38.503
h	-22 to 22
k	-22 to 22
l	-85 to 85
R int	0.1020
$R\ [F^2>2\sigma(F^2)]$	0.0532
$wR(F^2)$	0.1355
S	1.050
Parameters	856
Geometrical restraints on the molecule	120
Occupational constraints on the molecule	1
Geometrical constraints on the molecule	0
Flack parameter	0.13(2)
$\Delta\rho_{max}$, e Å^{-3}	0.335
$\Delta\rho_{min}$, e Å^{-3}	-0.227
Crystal size, mm^3	0.070 x 0.055 x 0.055
Radiation, Å	1.0332
Temperature, K	100

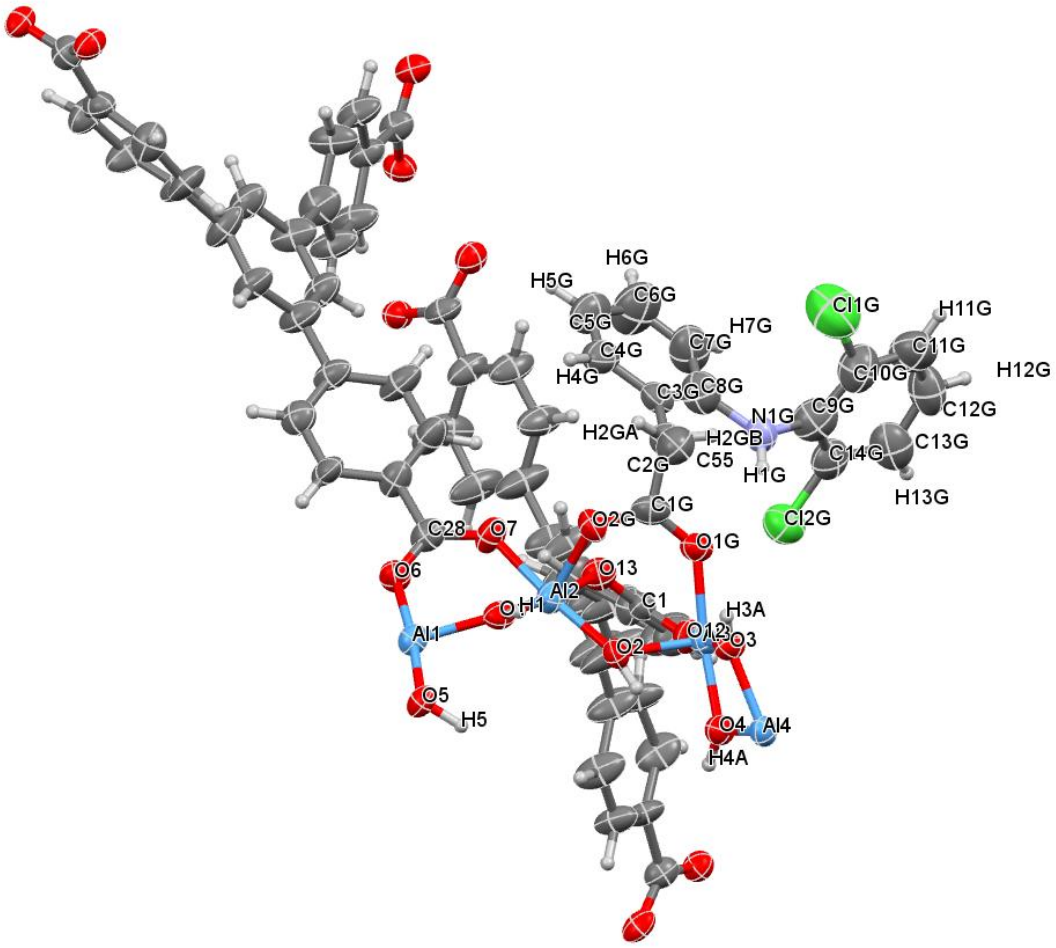

Figure S2.22. Asymmetric unit in the single crystal structure of **Δ**-MOF-520-**10**. Thermal ellipsoids are drawn with 50% probability.

Δ-MOF-520-2-11. A colorless truncated octahedron-shaped crystal (85 x 55 x 55 μm^3) of **Δ**-MOF-520-**2-11** was measured at a beamline 11.3.1 at the ALS with radiation of λ = 1.2398 Å. According to intensity statistics table for the whole dataset (PRP file), the resolution was cut off to 0.89 Å. The occupancy of genistein was found through adding a new variable and then constrained to 0.40. The occupancy of 2 molecules of methanol was constrained to 0.50. The occupancy of dangling moiety was constrained to 0.40. Before solvent masking instruction, structure was refined anisotropically and hydrogen atoms were placed into positions calculated geometrically. After refining the framework anisotropically, **11** was found initially assigning C1G and C2G carbons in the electron density difference map. The connected asymmetric unit was defined inside the unit cell: MOVE command was applied to all atoms. The weighting scheme is refined as well as the extinction coefficient. Once solvent masking instruction was introduced, the weight scheme was refined to convergence. The FLAT command was used to set the planar geometry for part of the bound molecule. The void volume is estimated to be 16326 $Å^3$ with 12794 electrons removed during masking. The large value of unassigned electron density within the unit cell is due to missing of some low-angle observations. Some reflections were omitted due to non-ideal solvent masking, beam stop clipping and the minor presence of diffuse scattering. The threshold $(I_{obs}-I_{calc})/\sigma(W)>10$ was chosen for omitting these reflections.

Omission of these reflections did not affect the refinement; the fraction of omitted reflections is less than 0.1% of the whole dataset.

Table S2.14. Crystal data, data collection, and structure refinement parameters for **Δ**-MOF-520-**2**-**11**.

Name	**Δ**-MOF-520-**2**-**11**
Chemical composition of MOF per asymmetric unit	$Al_4\ C_{56}\ H_{37.4}\ O_{19}$
Chemical formula of bound molecule	$C_{15}H_9O_5$
Bound molecule occupancy	40%
Formula mass	1229.46
Crystal system	Tetragonal
Space group	$P4_12_12$
a, Å	19.3467(7)
c, Å	70.207(3)
V, Å^3	26278(2)
d, g cm^{-3}	0.622
μ, mm^{-1}	0.325
Z	8
Measured reflections	152095
Independent reflections	19266
Observed reflections	13969
θ_{min} , º	2.097
θ_{max} , º	43.945
h	-21 to 21
k	-21 to 21
l	-78 to 78
R int	0.0717
$R\ [F^2>2\sigma(F^2)]$	0.0516
$wR(F^2)$	0.1412
S	1.081
Parameters	914
Geometrical restraints on the molecule	147
Occupational constraints on the molecule	4
Geometrical constraints on the molecule	0
Flack parameter	0.144(16)
$\Delta\rho_{max}$, e Å^{-3}	0.222
$\Delta\rho_{min}$, e Å^{-3}	-0.319
Crystal size, mm^3	0.085 x 0.055 x 0.055
Radiation, Å	1.2398
Temperature, K	100

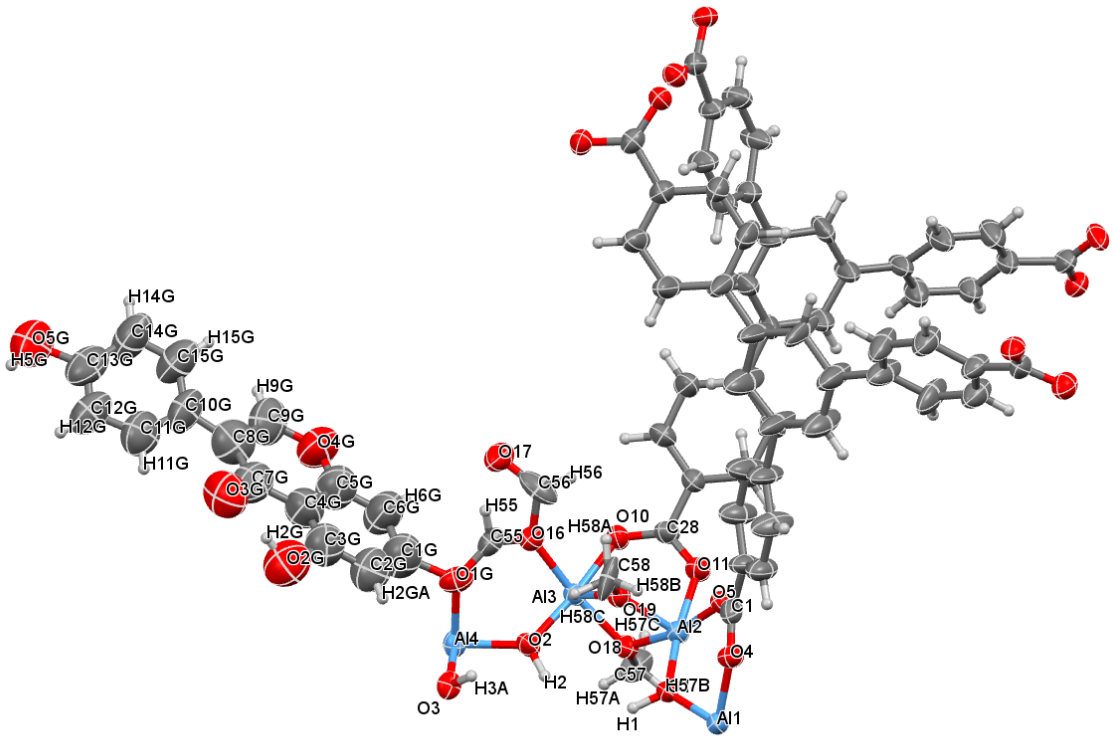

Figure S2.23. Asymmetric unit in the single crystal structure of **Λ**-MOF-520-**2**-**11**. Thermal ellipsoids are drawn with 50% probability.

Λ-MOF-520-12. A colorless truncated octahedron-shaped crystal (90 x 60 x 60 μm^3) of **Λ**-MOF-520-**9** was measured at a beamline 11.3.1 at the ALS with radiation of λ = 1.2398 Å. According to intensity statistics table for the whole dataset (PRP file), the resolution was cut off to 1.00 Å. The occupancy of Boc-(RS)-3-amino-1,2-propanediol was found through adding a new variable and then constrained to 0.80. Before solvent masking instruction, structure was refined anisotropically and hydrogen atoms were placed into positions calculated geometrically. The connected asymmetric unit was defined inside the unit cell: MOVE command was applied to all atoms. The weighting scheme is refined as well as the extinction coefficient. Once solvent masking instruction was introduced, the weight scheme was refined to convergence. The tert-butyl part of the bound molecule was found to be disordered and overlapped with solvent, so DFIX command was used to fix the geometry this fragment. The void volume is estimated to be 7968 $Å^3$ with 3223. Some reflections were omitted due to non-ideal solvent masking, beam stop clipping and the minor presence of diffuse scattering. The threshold $(I_{obs}\text{-}I_{calc})/\sigma(W)>10$ was chosen for omitting these reflections. Omission of these reflections did not affect the refinement; the fraction of omitted reflections is less than 0.1% of the whole dataset.

Table S2.15. Crystal data, data collection, and structure refinement parameters for **Λ**-MOF-520-**12**.

Name	**Λ**-MOF-520-**12**
Chemical composition of MOF per asymmetric unit	$Al_2\ C_{27}\ H_{16}\ O_{7.4}$
Chemical formula of bound molecule	$C_8H_{15}O_4N_1$
Bound molecule occupancy	80%
Formula mass	664.12
Crystal system	Tetragonal
Space group	$P4_22_12$
a, Å	19.5071(9)
c, Å	34.2595(18)
V, Å^3	13036.7(14)
d, g cm^{-3}	0.677
μ, mm^{-1}	0.339
Z	8
Measured reflections	80057
Independent reflections	6854
Observed reflections	6065
θ_{min} , º	2.576
θ_{max} , º	38.336
h	-19 to 19
k	-19 to 19
l	-34 to 34
R int	0.0431
R [$F^2>2\sigma(F^2)$]	0.0523
wR(F^2)	0.1489
S	1.024
Parameters	446
Geometrical restraints on the molecule	9
Occupational constraints on the molecule	1
Geometrical constraints on the molecule	0
Flack parameter	0.040(15)
$\Delta\rho_{max}$, e Å^{-3}	0.209
$\Delta\rho_{min}$, e Å^{-3}	-0.240
Crystal size, mm^3	0.090 x 0.060 x 0.060
Radiation, Å	1.2398
Temperature, K	100

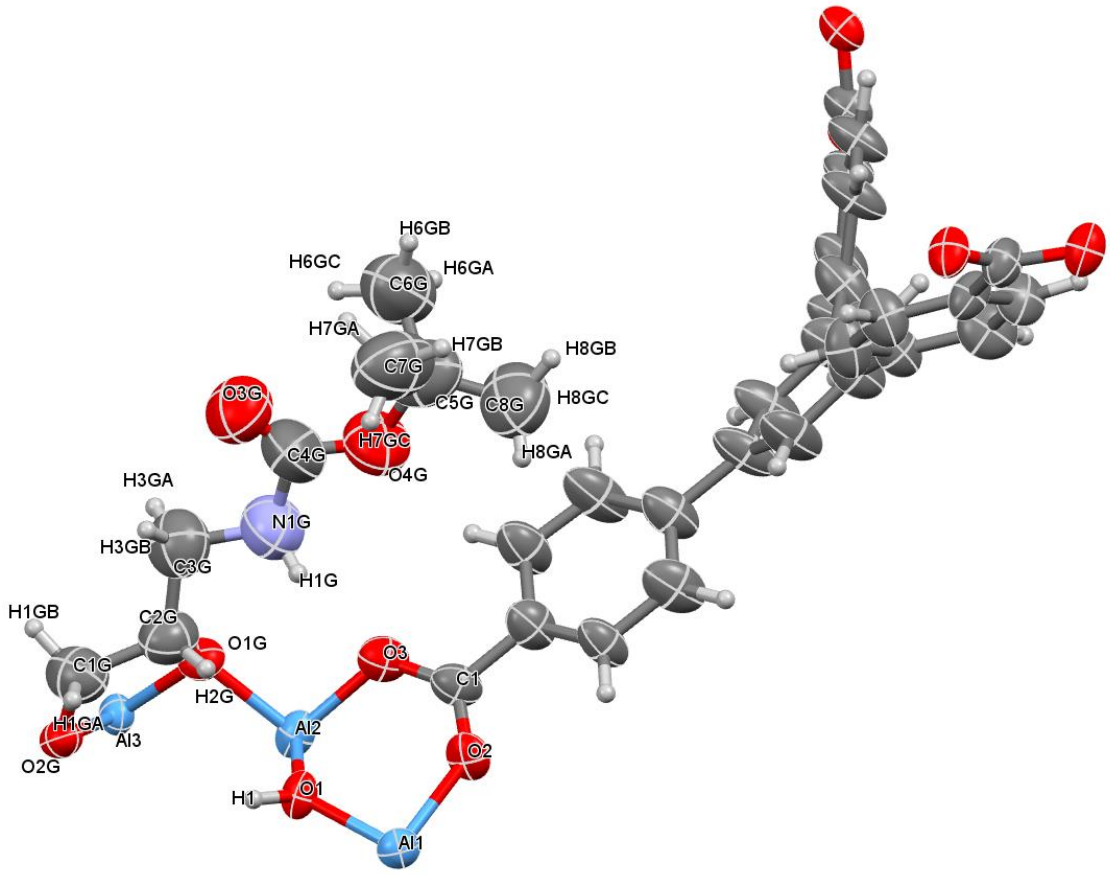

Figure S2.24. Asymmetric unit in the single crystal structure of **Λ**-MOF-520-**12**. Thermal ellipsoids are drawn with 50% probability.

Λ-MOF-520-3-13. A colorless truncated octahedron-shaped crystal (80 x 55 x 55 μm^3) of **Λ**-MOF-520-**3-13** was measured at a beamline 11.3.1 at the ALS with radiation of λ = 1.03320 Å. According to intensity statistics table for the whole dataset (PRP file), the resolution was cut off to 0.70 Å. The occupancy of gibberellin A_1 was found through adding a new variable and then constrained to 0.30. Before solvent masking instruction, structure was refined anisotropically and hydrogen atoms were placed into positions calculated geometrically. The connected asymmetric unit was defined inside the unit cell: MOVE command was applied to all atoms. The weighting scheme is refined as well as the extinction coefficient. Once solvent masking instruction was introduced, the weight scheme was refined to convergence. The FREE command was used to remove the connectivity due to partial overlap of two molecules within the asymmetric unit. The void volume is estimated to be 6432 $Å^3$ with 2832 electrons removed during masking. Some reflections were omitted due to non-ideal solvent masking, beam stop clipping and the minor presence of diffuse scattering. The threshold $(I_{obs}-I_{calc})/\sigma(W)>10$ was chosen for omitting these reflections. Omission of these reflections did not affect the refinement; the fraction of omitted reflections is less than 0.1% of the whole dataset.

Table S2.16. Crystal data, data collection, and structure refinement parameters for **Λ**-MOF-520-**3**-**13**.

Name	**Λ**-MOF-520-**3**-**13**
Chemical composition of MOF per asymmetric unit	$Al_2\ C_{27.7}\ H_{16}\ O_{9.4}$
Chemical formula of bound molecule	$C_{19}H_{23}O_6$
Bound molecule occupancy	30%
Formula mass	658.38
Crystal system	Tetragonal
Space group	$P4_22_12$
a, Å	18.0631(8)
c, Å	37.9654(16)
V, Å^3	12387.2(12)
d, g cm^{-3}	0.706
μ, mm^{-1}	0.212
Z	8
Measured reflections	289571
Independent reflections	18927
Observed reflections	15661
θ_{min} , º	2.263
θ_{max} , º	47.596
h	-25 to 25
k	-25 to 25
l	-52 to 54
R int	0.0427
R [$F^2>2\sigma(F^2)$]	0.0568
wR(F^2)	0.1729
S	1.082
Parameters	563
Geometrical restraints on the molecule	0
Occupational constraints on the molecule	1
Geometrical constraints on the molecule	0
Flack parameter	0.063(9)
$\Delta\rho_{max}$, e Å^{-3}	0.460
$\Delta\rho_{min}$, e Å^{-3}	-0.307
Crystal size, mm^3	0.080 x 0.055 x 0.055
Radiation, Å	1.0332
Temperature, K	100

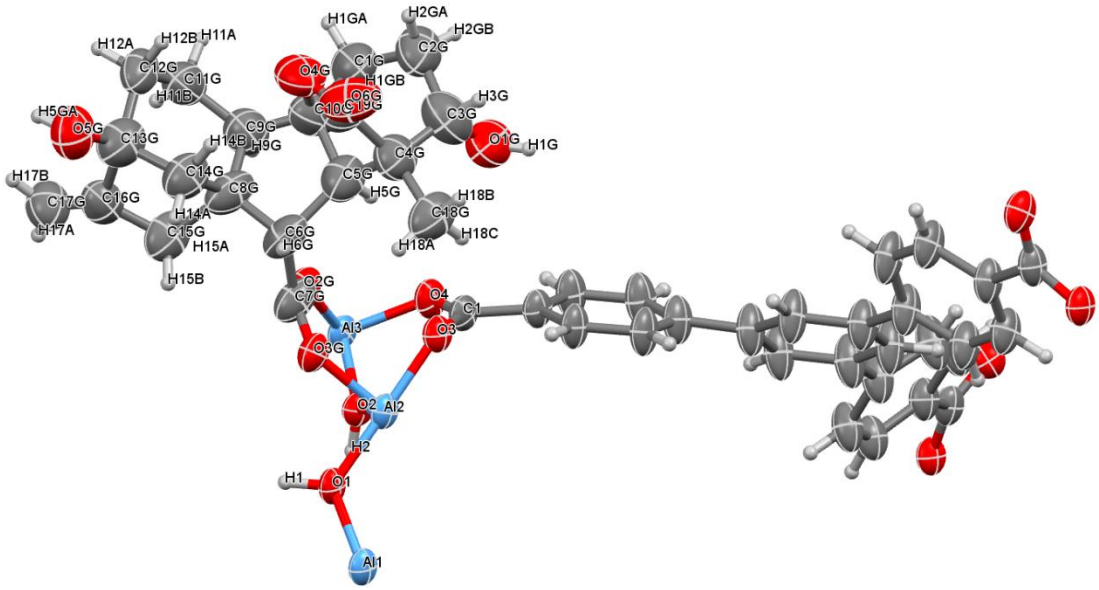

Figure S2.25. Asymmetric unit in the single crystal structure of **Λ**-MOF-520-**3-13**. Thermal ellipsoids are drawn with 50% probability.

Λ-MOF-520-3-14. A colorless truncated octahedron-shaped crystal (80 x 65 x 65 μm^3) of **Λ**-MOF-520-**3-14** was measured at a beamline 11.3.1 at the ALS with radiation of λ = 0.8856 Å. According to intensity statistics table for the whole dataset (PRP file), the resolution was cut off to 0.76 Å. The occupancy of gibberellin A_3 was found through adding a new variable and then constrained to 0.30. The occupancy of ethylene glycol molecule was set to 0.50. Before solvent masking instruction, structure was refined anisotropically and hydrogen atoms were placed into positions calculated geometrically. The connected asymmetric unit was defined inside the unit cell: MOVE command was applied to all atoms. The weighting scheme is refined as well as the extinction coefficient. Once solvent masking instruction was introduced, the weight scheme was refined to convergence. The FREE command was used to remove the connectivity due to partial overlap of two molecules within the asymmetric unit. The void volume is estimated to be 6633 $Å^3$ with 1488 electrons removed during masking. Some reflections were omitted due to non-ideal solvent masking, beam stop clipping and the minor presence of diffuse scattering. The threshold $(I_{obs}-I_{calc})/\sigma(W)>10$ was chosen for omitting these reflections. Omission of these reflections did not affect the refinement; the fraction of omitted reflections is less than 0.1% of the whole dataset.

Table S2.17. Crystal data, data collection, and structure refinement parameters for **Λ**-MOF-520-**3**-**14**.

Name	**Λ**-MOF-520-**3**-**14**
Chemical composition of MOF per asymmetric unit	$Al_2\ C_{28.7}\ H_{16}\ O_{9.4}$
Chemical formula of bound molecule	$C_{19}H_{21}O_6$
Bound molecule occupancy	30%
Formula mass	669.79
Crystal system	Tetragonal
Space group	$P4_22_12$
a, Å	18.6064(8)
c, Å	37.2099(18)
V, Å^3	12882.0(13)
d, g cm^{-3}	0.691
μ, mm^{-1}	0.134
Z	8
Measured reflections	164629
Independent reflections	15378
Observed reflections	10565
θ_{min} , º	2.362
θ_{max} , º	35.660
h	-24 to 24
k	-24 to 24
l	-48 to 48
R int	0.0605
R [$F^2>2\sigma(F^2)$]	0.0580
wR(F^2)	0.1604
S	0.942
Parameters	582
Geometrical restraints on the molecule	0
Occupational constraints on the molecule	2
Geometrical constraints on the molecule	0
Flack parameter	0.05(2)
$\Delta\rho_{max}$, e Å^{-3}	0.358
$\Delta\rho_{min}$, e Å^{-3}	-0.232
Crystal size, mm^3	0.080 x 0.065 x 0.065
Radiation, Å	0.8856
Temperature, K	100

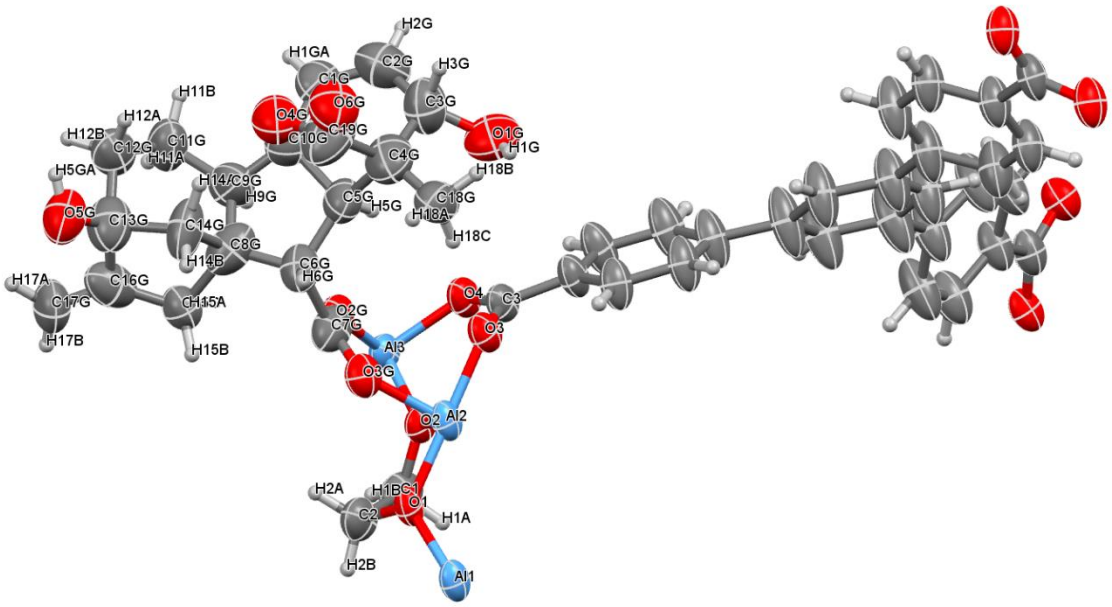

Figure S2.26. Asymmetric unit in the single crystal structure of **Λ**-MOF-520-**3-14**. Thermal ellipsoids are drawn with 50% probability.

Δ-MOF-520-15. A colorless truncated octahedron-shaped crystal (60 x 40 x 40 μm^3) of **Δ**-MOF-520-**15**. was measured at a beamline 11.3.1 at the ALS with radiation of λ = 1.03330 Å. According to intensity statistics table for the whole dataset (PRP file), the resolution was cut off to 0.80 Å. The occupancy of (-)-jasmonic acid was found through adding a new variable and then constrained to 0.33. Before solvent masking instruction, structure was refined anisotropically and hydrogen atoms were placed into positions calculated geometrically. The connected asymmetric unit was defined inside the unit cell: MOVE command was applied to all atoms. The weighting scheme is refined as well as the extinction coefficient. Once solvent masking instruction was introduced, the weight scheme was refined to convergence. Last three carbon atoms of the bound molecule (C12G, C11G and C10G) are heavily overlapped with solvent molecule so they were placed initially into geometrically calculated positions. DFIX and DANG commands were used to set the geometry of this fragment. The void volume is estimated to be 7465 $Å^3$ with 3732 electrons removed during masking. Some reflections were omitted due to non-ideal solvent masking, beam stop clipping and the minor presence of diffuse scattering. The threshold (I_{obs}-I_{calc})/σ(W)>10 was chosen for omitting these reflections. Omission of these reflections did not affect the refinement; the fraction of omitted reflections is less than 0.1% of the whole dataset.

Table S2.18. Crystal data, data collection, and structure refinement parameters for **Δ**-MOF-520-**15**.

Name	**Δ**-MOF-520-**15**
Chemical composition of MOF per asymmetric unit	$Al_2\ C_{27.67}\ H_{17}\ O_{9.34}$
Chemical formula of bound molecule	$C_{12}H_{17}O_3$
Bound molecule occupancy	33%
Formula mass	622.40
Crystal system	Tetragonal
Space group	$P4_22_12$
a, Å	18.5251(7)
c, Å	37.4577(15)
V, Å^3	12854.7(11)
d, g cm^{-3}	0.642
μ, mm^{-1}	0.197
Z	8
Measured reflections	318021
Independent reflections	13161
Observed reflections	12455
θ_{min} , º	2.248
θ_{max} , º	40.224
h	-24 to 24
k	-24 to 24
l	-49 to 49
R int	0.0417
R [$F^2>2\sigma(F^2)$]	0.0474
wR(F^2)	0.1430
S	1.046
Parameters	472
Geometrical restraints on the molecule	8
Occupational constraints on the molecule	1
Geometrical constraints on the molecule	0
Flack parameter	0.037(8)
$\Delta\rho_{max}$, e Å^{-3}	0.583
$\Delta\rho_{min}$, e Å^{-3}	-0.322
Crystal size, mm^3	0.060 x 0.040 x 0.040
Radiation, Å	1.0333
Temperature, K	100

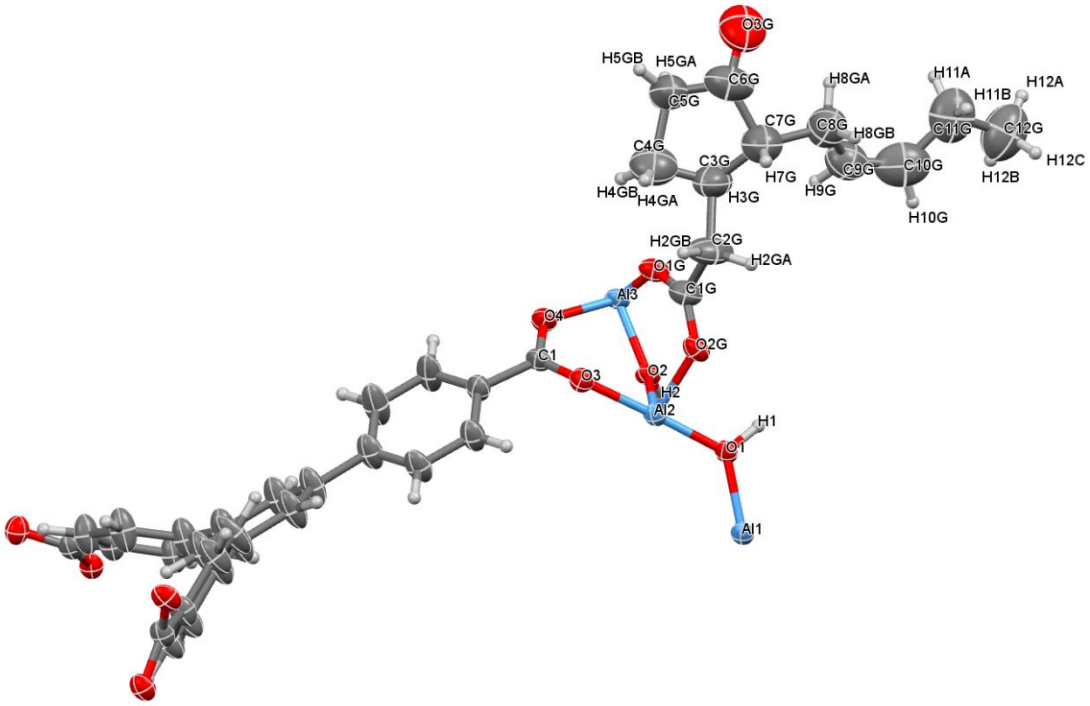

Figure S2.27. Asymmetric unit in the single crystal structure of **Λ**-MOF-520-**15**. Thermal ellipsoids are drawn with 50% probability.

Λ-MOF-520-16. A colorless truncated octahedron-shaped crystal (60 x 40 x 40 μm^3) of **Λ**-MOF-520-**16** was measured at a beamline 11.3.1 at the ALS with radiation of λ = 1.03330 Å. According to intensity statistics table for the whole dataset (PRP file), the resolution was cut off to 0.80 Å. The occupancy of (+)-jasmonic acid was found through adding a new variable and then constrained to 0.33 Before solvent masking instruction, structure was refined anisotropically and hydrogen atoms were placed into positions calculated geometrically. The connected asymmetric unit was defined inside the unit cell: MOVE command was applied to all atoms. The weighting scheme is refined as well as the extinction coefficient. Once solvent masking instruction was introduced, the weight scheme was refined to convergence. Last three carbon atoms of the bound molecule (C12G, C11G and C10G) are heavily overlapped with solvent molecule so they were placed initially into geometrically calculated positions. DFIX and DANG commands were used to set the geometry of this fragment. ISOR command was used to restrain the thermal parameters of these carbon atoms. The void volume is estimated to be 7652$Å^3$ with 3862 electrons removed during masking. Some reflections were omitted due to non-ideal solvent masking, beam stop clipping and the minor presence of diffuse scattering. The threshold (I_{obs}-I_{calc})/σ(W)>10 was chosen for omitting these reflections. Omission of these reflections did not affect the refinement; the fraction of omitted reflections is less than 0.1% of the whole dataset.

Table S2.19. Crystal data, data collection, and structure refinement parameters for **Λ**-MOF-520-**16**.

Name	**Λ**-MOF-520-**16**
Chemical composition of MOF per asymmetric unit	$Al_2\ C_{27.67}\ H_{17}\ O_{9.34}$
Chemical formula of bound molecule	$C_{12}H_{17}O_3$
Bound molecule occupancy	33%
Formula mass	622.40
Crystal system	Tetragonal
Space group	$P4_22_12$
a, Å	18.7304(7)
c, Å	37.2104(15)
V, Å^3	13054.4(11)
d, g cm^{-3}	0.632
μ, mm^{-1}	0.194
Z	8
Measured reflections	359086
Independent reflections	13361
Observed reflections	12453
θ_{min} , º	2.236
θ_{max} , º	40.223
h	-28 to 28
k	-28 to 28
l	-56 to 56
R int	0.0526
R [$F^2>2\sigma(F^2)$]	0.0460
wR(F^2)	0.1400
S	1.084
Parameters	472
Geometrical restraints on the molecule	50
Occupational constraints on the molecule	1
Geometrical constraints on the molecule	0
Flack parameter	0.040(8)
$\Delta\rho_{max}$, e Å^{-3}	0.454
$\Delta\rho_{min}$, e Å^{-3}	-0.289
Crystal size, mm^3	0.060 x 0.040 x 0.040
Radiation, Å	1.0333
Temperature, K	100

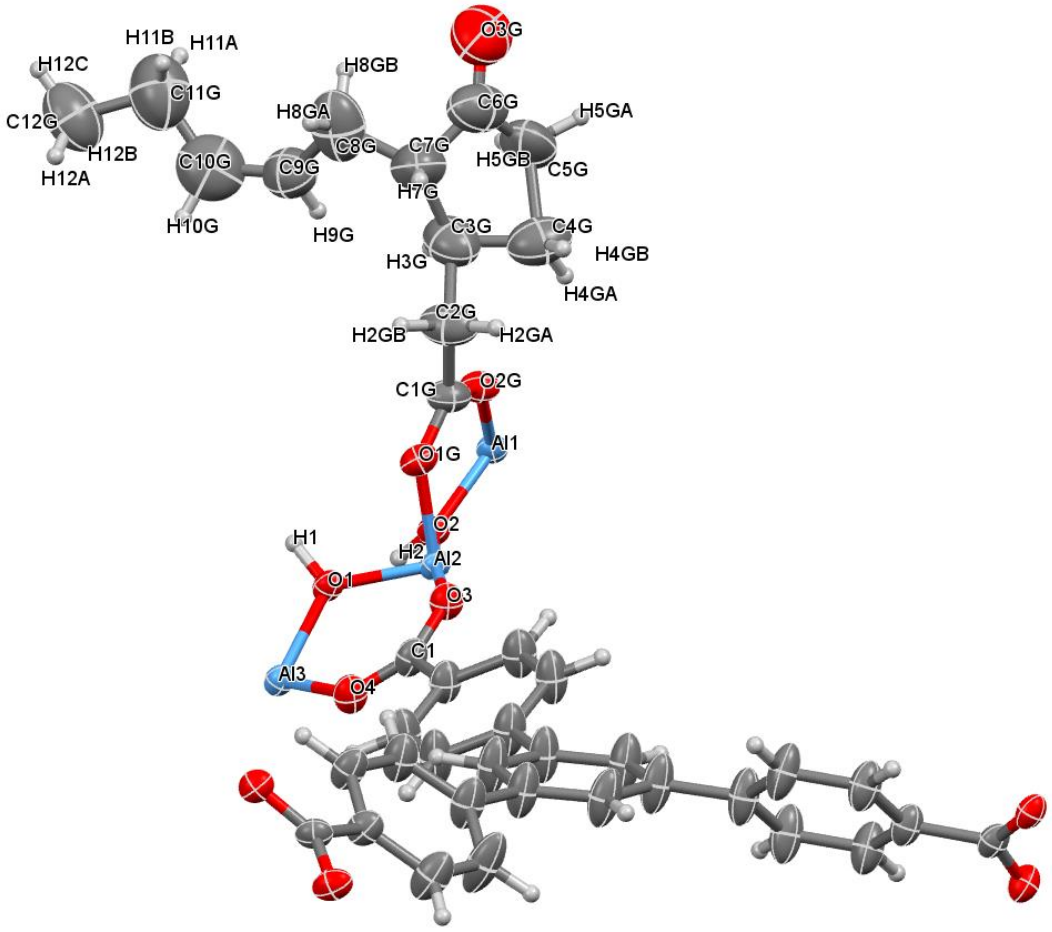

Figure S2.28. Asymmetric unit in the single crystal structure of **Λ**-MOF-520-**16**. Thermal ellipsoids are drawn with 50% probability.

References for Chapter 2

(1) Holden, A.; Morrison, P. *Crystals and crystal growing*; MIT Press, 1982.

(2) Atwood, J. L.; Davies, J. E. D.; MacNicol, D. D. *Inclusion compounds*; Academic Press, 1984.

(3) Legrand, Y.-M.; van der Lee, A.; Barboiu, M. *Science* **2010**, *329*, 299–302.

(4) Inokuma, Y.; Yoshioka, S.; Ariyoshi, J.; Arai, T.; Hitora, Y.; Takada, K.; Matsunaga, S.; Rissanen, K.; Fujita, M. *Nature* **2013**, *495*, 461–466.

(5) Furukawa, H.; Cordova, K. E.; O'Keeffe, M.; Yaghi, O. M. *Science* **2013**, *341*, 1230444.

(6) Flack, H. D.; Bernardinelli, G. *Acta Crystallogr. Sect. A Found. Crystallogr.* **1999**, *55*, 908–915.

(7) Yoshioka, S.; Inokuma, Y.; Hoshino, M.; Sato, T.; Fujita, M. *Chem. Sci.* **2015**, *6*, 3765–3768.

(8) Sanna, E.; Escudero-Adán, E. C.; Bauzá, A.; Ballester, P.; Frontera, A.; Rotger, C.; Costa, A. *Chem. Sci.* **2015**, *6*, 5466–5472.

(9) Hoshino, M.; Khutia, A.; Xing, H.; Inokuma, Y.; Fujita, M. *IUCrJ* **2016**, *3*, 139–151.

(10) Gándara, F.; Furukawa, H.; Lee, S.; Yaghi, O. M. *J. Am. Chem. Soc.* **2014**, *136*, 5271–5274.

(11) Flack, H. D.; Bernardinelli, G. *J. Appl. Crystallogr.* **2000**, *33*, 1143–1148.

(12) Ramadhar, T. R.; Zheng, S.-L.; Chen, Y.-S.; Clardy, J. *Acta Crystallogr. Sect. A Found. Adv.* **2015**, *71*, 46–58.

(13) Flack, H. D.; Bernardinelli, G.; Clemente, D. A.; Linden, A.; Spek, A. L. *Acta Crystallogr. Sect. B Struct. Sci.* **2006**, *62*, 695–701.

(14) Flack, H. D.; Shmueli, U. *Acta Crystallogr. Sect. A Found. Crystallogr.* **2007**, *63*, 257–265.

(15) Bijvoet, J. M.; Peerdeman, A. F.; van Bommel, A. J. *Nature* **1951**, *168*, 271–272.

(16) Hill, R. K.; Edwards, A. G. *Tetrahedron* **1965**, *21*, 1501–1507.

(17) Sheldrick, G. M. *Acta Crystallogr. Sect. A Found. Crystallogr.* **2008**, *64*, 112–122.

(18) Dolomanov, O. V.; Bourhis, L. J.; Gildea, R. J.; Howard, J. A. K.; Puschmann, H. *J. Appl. Crystallogr.* **2009**, *42*, 339–341.

(19) Macrae, C. F.; Edgington, P. R.; McCabe, P.; Pidcock, E.; Shields, G. P.; Taylor, R.; Towler, M.; van de Streek, J. *J. Appl. Crystallogr.* **2006**, *39*, 453–457.

(20) Rees, B.; Jenner, L.; Yusupov, M. *Acta Crystallogr. Sect. D Biol. Crystallogr.* **2005**, *61*, 1299–1301.

(21) Spek, A. L. *Acta Crystallogr. Sect. C Struct. Chem.* **2015**, *71*, 9–18.

Chapter 3

Molecular Retrofitting Adapts a Metal−Organic Framework to Extreme Pressure

Portions of this chapter have been previously published in:
Kapustin, E. A., Lee, S., Alshammari, A. S. & Yaghi, O. M. Molecular Retrofitting Adapts a Metal–Organic Framework to Extreme Pressure. *ACS Cent. Sci.* **3,** 662–667 (2017).

3.1 Preface

In the previous Chapter 2, we showed how to coordinatively bind and align different guest molecules which allows for their structural determination. Here, we demonstrate the alignment of guests can also improve the properties of the MOF itself, in particular, mechanical properties. Despite numerous studies on chemical and thermal stability of MOFs, mechanical stability remains largely undeveloped. No strategy existed to control the mechanical deformation of MOFs under ultrahigh pressure until this research was published. Specifically, the mechanically unstable MOF-520 was retrofitted by precise placement of a rigid 4,4′-biphenyldicarboxylate (BPDC) linker as a "girder" to afford a mechanically robust framework: MOF-520-BPDC. This retrofitting alters how the structure deforms under ultrahigh pressure and thus leads to a drastic enhancement of its mechanical robustness. While in the parent MOF-520 the pressure transmitting medium molecules diffused into the pore and expanded the structure from the inside upon compression, the girder in the new retrofitted MOF-520-BPDC prevented the framework from expansion by linking two adjacent secondary building units together. As a result, the modified MOF was stable under hydrostatic compression in a diamond-anvil cell up to 5.5 gigapascal. This work was done in collaboration with Seungkyu Lee and Dr. Ahmad S. Alshammari.

3.2. Introduction

A unique feature of MOFs is that they have "pores without walls", where the internal space is encompassed by multimetallic junctions and organic linkers rather than continuous impenetrable walls as in traditional porous materials. This junction-and-linker arrangement maximally exposes the adsorptive sites and increases their number, leading to ultrahigh surface areas for MOFs[1–3]. Thus, having pores without walls couples the high storage capacity with the facile diffusion of molecules in and out of the pores, making MOFs useful in natural gas storage, separation of gas mixtures, and selective catalysis[4–7]. It is remarkable that, even with the vast openness of MOF structures, they have been shown to be architecturally, thermally, and chemically stable: properties that are essential for their development from basic science to applications and commercialization[8]. As more applications come online, the next challenge is to show how these open structures withstand mechanical stress, to which they inevitably will be subjected during their operation and long-term use. In this context, the question of what is the breaking point of a given framework becomes paramount. Here, we show how applying extreme pressure (*ca.* 10,000 atm, 1 gigapascal) onto MOF crystals provides means for identifying the weakest component of the framework. We also introduce the concept of molecular retrofitting and demonstrate its use in adapting such a framework to extreme mechanical stress (Figure 3.1).

Specifically, we examined the mechanical response of porous MOF-520 crystal structure, $Al_8(\mu\text{-}OH)_8(HCOO)_4(BTB)_4$ (BTB = 1,3,5-benzenetribenzoate), to hydrostatic pressures from ambient up to 3 gigapascal (GPa)[9]. We observed expansion of the framework along two crystallographic axes as a function of pressure, and thereby identified the most vulnerable element of this MOF. We proceeded to introduce 4,4′-biphenyldicarboxylate (BPDC) linkers as molecular "girders" of ideal size and shape to covalently fit into the backbone of MOF-520. In this way, the original fragile MOF-520 was retrofitted by BPDC to become a mechanically robust framework as evidenced by the fact that it remains crystalline up to 5.5 GPa and on subsequent decompression. Typically, the extreme pressure regime is achieved by loading of

single-crystalline or powder sample between the two minuscule culets of opposing diamonds of a diamond-anvil cell (DAC)[10]. A pressure transmitting medium (PTM) uniformly surrounds the sample to provide hydrostaticity[11]. Usually the crystal structures of MOFs under these conditions experience significant distortions, both in the multimetallic SBUs and in the organic linkers, and even undergo reversible/irreversible phase transitions[12–18]. The possibility of having the pressure medium molecules diffuse into the MOF pores is unique as it allows study and evaluation of framework deformity. In most cases, the penetration of solvent molecules under extreme pressure inside the MOF (termed overhydration effect) creates internal pressure, which expands the already filled MOF[19–22]. At initial compression, the framework expands, but then contracts at higher pressures. The behavior of the framework under these conditions provides an opportunity to identify its weakest points. However, the overhydration effect usually results in reduction of long-range order in the crystal, and the sample becomes irreversibly amorphous. Typically, this lack of crystallinity under pressure has prohibited the study of framework distortions by means of single-crystal X-ray diffraction techniques. These challenges are addressed in the present study.

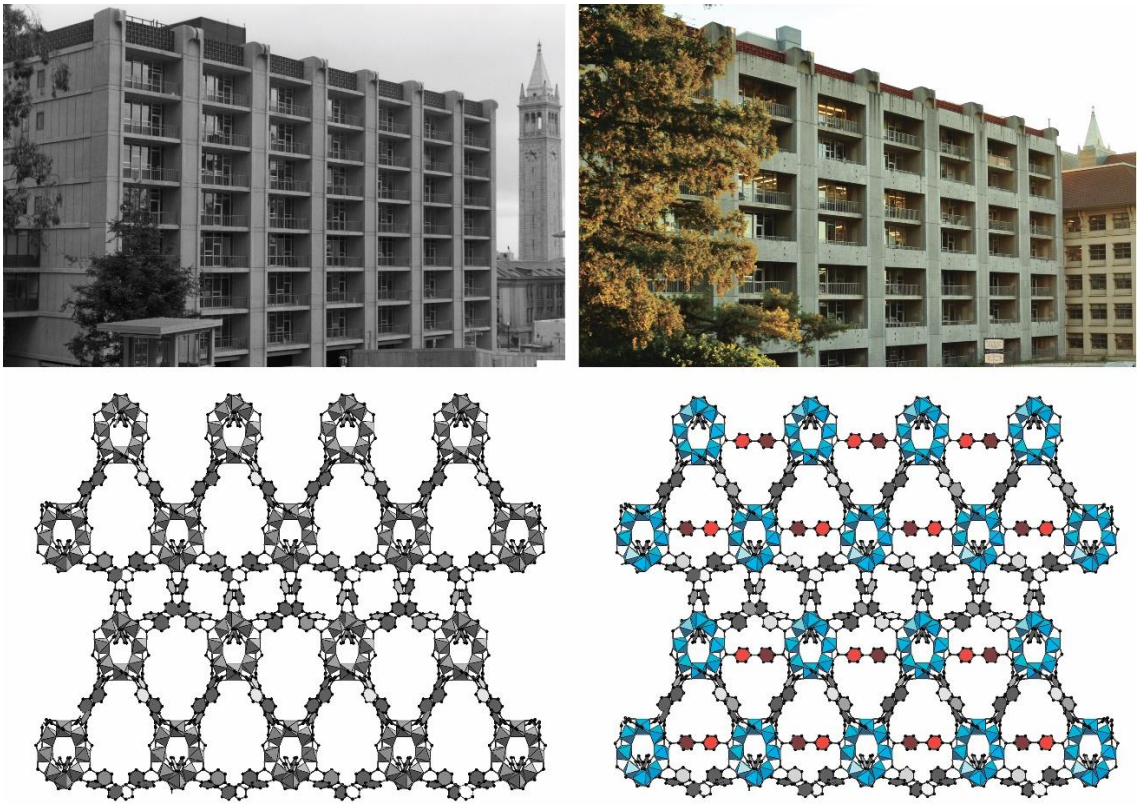

Figure 3.1. Visualization of the retrofitting approach in architecture (top) and on a molecular level (bottom). The images of Latimer Hall at UC Berkeley before and after retrofitting are shown for conceptual clarity. The single-crystal X-ray diffraction structures of pristine MOF-520 in gray versus the retrofitted MOF-520-BPDC with BPDC girders shown in red.

3.3 Mechanical damage of MOF-520 under extreme pressure

First, we studied the mechanical response of the crystal structure of MOF-520 toward the increase of the hydrostatic pressure in methanol/ethanol pressure transmitting media in a DAC.

MOF-520 is composed of Al-based SBUs linked together with BTB linkers. The secondary building units in MOF-520 are octametallic rings with Al octahedra sharing corners through eight −OHs and four formate ligands. Every SBU is linked by 12 BTBs, resulting in a (12,3)-connected net with **fon** topology (Figure 3.2)[23]. MOF-520 crystallizes in the non-centrosymmetric space group $P4_22_12$ with unit cell parameters of 18.3754(6) Å (*a*) and 37.6893(12) Å (*c*) and a unit cell volume of 12726.0(9) Å^3.

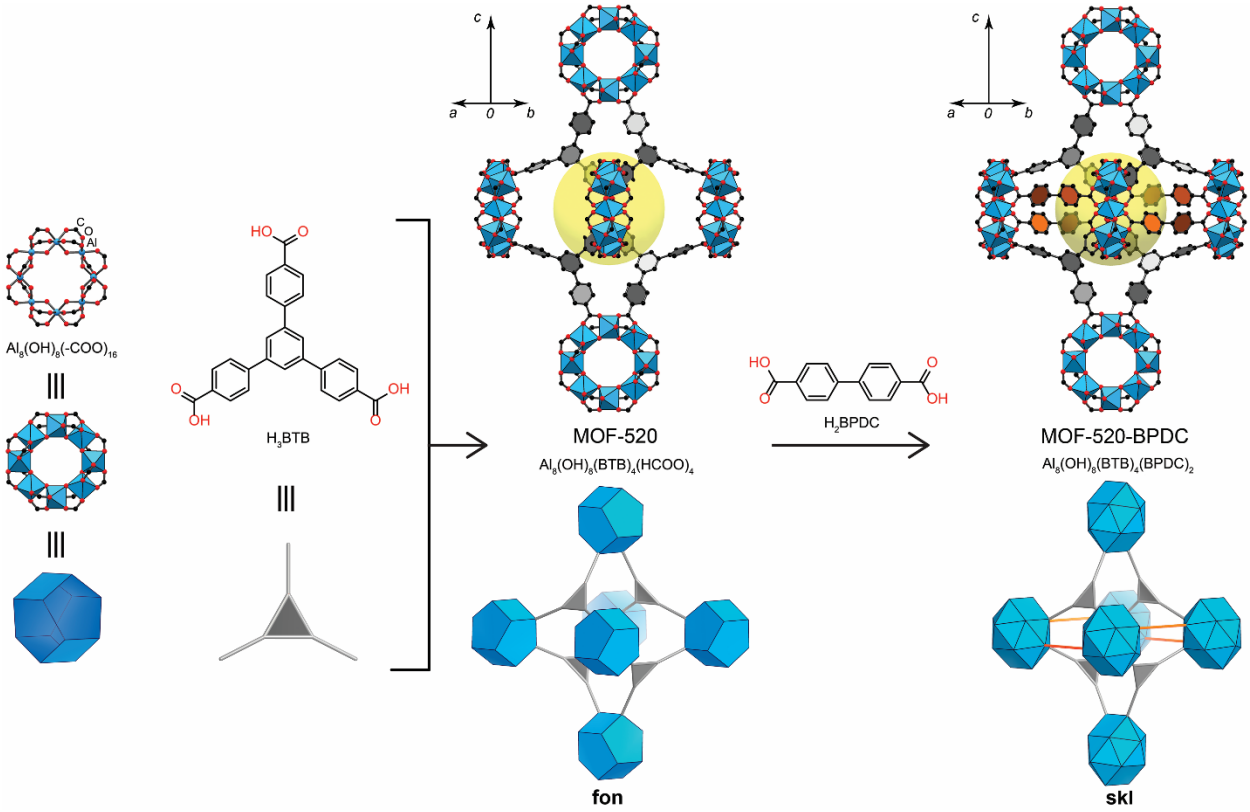

Figure 3.2. **MOF-520 is built from Al-based octametallic secondary building units and organic BTB linkers**. Introduction of H_2BPDC by the CAL method into MOF-520 leads to the new retrofitted MOF-520-BPDC possessing new **skl** topology. BTB organic linkers are reduced to gray triangles, BPDC girders to orange links, and Al-based SBU to blue polyhedra. Atom color scheme: C, black; O, red; Al, blue polyhedra. H atoms are omitted for clarity. Yellow balls indicate the space in the octahedral arrangement of building units in the framework.

The single-crystalline sample of MOF-520 was placed into a DAC with a culet size of 500 μm, a tungsten gasket, and a methanol/ethanol mixture (4:1) as a penetrating PTM at room temperature. Several rubies were also placed next to the MOF crystal to monitor the pressure using the ruby fluorescence method[24]. The sample was immersed in the PTM for solvent exchange for at least a week prior to single-crystal X-ray data collection. High-pressure data was collected at the 12.2.2 high-pressure beamline at the Advanced Light Source synchrotron (LBNL). The crystal structure was solved and refined at 10^{-4}, 0.15(2), 0.86(2), 1.47(2), 2.24(2), and 2.82(2) GPa upon compression of MOF. At pressures higher than 2.82 GPa, the sample turned amorphous, and the deterioration of the data prevented the structure solution and refinement. Upon further decompression, the data collection was unsuccessful due to complete degradation of the sample: the crystal cracked and disintegrated into several pieces (see Figure S3.9 in the Supporting Information for this Chapter). The crystallographic data and the pore

environment information are shown in Table 3.1. The pore volume and electron count of unassigned electron density within the pore were calculated using the SQUEEZE algorithm[25].

Table 3.1. Crystallographic data and pore metrics of MOF-520 before retrofitting as a function of hydrostatic pressure

Pressure / GPa	*a* / Å	*c* / Å	Unit cell volume / Å^3	Pore volume / Å^3	Electron count / e$^-$	Electron count per pore volume / e$^-$ Å^{-3}
0.0001	18.920(3)	37.190(7)	13313(5)	9391.5	9172	~0.98
0.15(2)	19.070(3)	36.930(7)	13430(5)	9653.7	15064	~1.56
0.86(2)	19.196(3)	36.569(7)	13475(4)	9629.5	10558	~1.10
1.47(2)	19.182(3)	36.534(7)	13443(4)	9495.8	13890	~1.46
2.24(2)	19.130(3)	36.480(7)	13350(4)	9528.4	12753	~1.33
2.81(2)	19.070(3)	36.409(7)	13241(5)	9441.1	11252	~1.19

The bulk strain of MOF-520 crystal structure in the range from 10^{-4} to 3 GPa was found to be non-monotonic (Figure 3.3). Upon initial compression up to 0.86 GPa, the crystal structure of MOF expands by almost 1% due to the overhydration effect. A similar observation was reported before for prototypical frameworks, such as MOF-5, ZIF-8, HKUST-1, and UiO-67[19–22]. The amount of unassigned electron density, corresponding to PTM molecules, increases by almost 40% from 9299 electrons after DAC loading to 15064 at 0.15(2) GPa, signaling the penetration of the solvent inside the pore. Despite the uncertainty in the calculation of the electron density by SQUEEZE algorithm caused by the poor quality of the experimental data (low resolution, lack of low-angle reflections, overlap with the reflections from two diamonds), this observation is consistent with the pore volume increase by almost 300 Å^3 due to internal pressure. The analysis of anisotropy of compression reveals that the structural expansion along *a* and *b* crystallographic axes prevails the contraction along the *c* direction. Upon further increase of pressure, MOF-520 starts to compress along all directions, resulting in the overall decrease in the unit cell volume. Thus, the relative change in volume reaches −0.5% at 2.82(2) GPa. The pore shrinks in size monotonically, leading to the "activation" of the porous material: the number of methanol molecules inside the pore at 2.82(2) GPa is even smaller than such at 0.15(2) GPa. The analogous "activation" was previously reported for ZIF-8 under pressure[21].

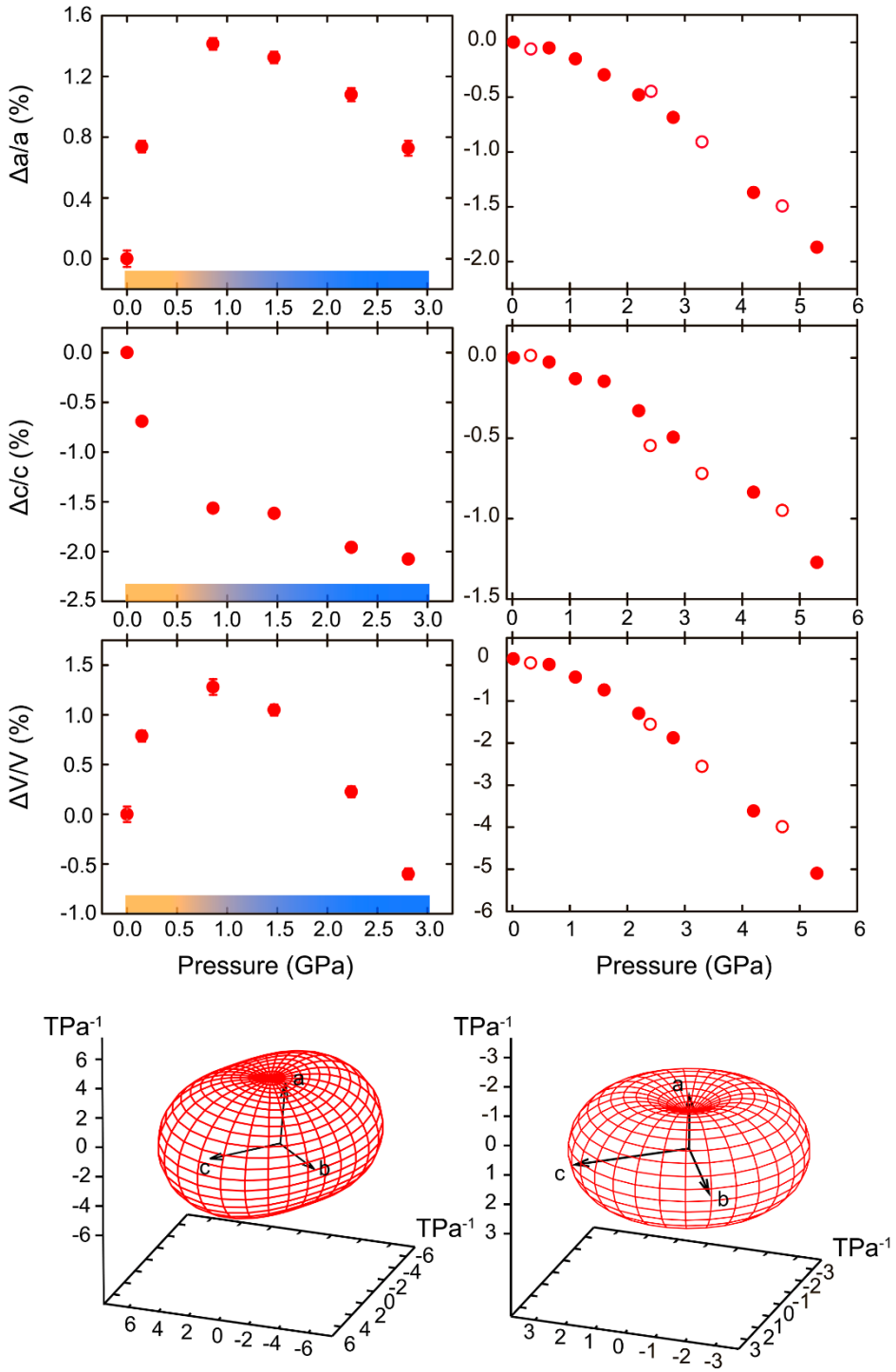

Figure 3.3. Relative changes in unit cell parameters of MOF-520 (left) and MOF-520-BPDC (right) with pressure. Filled and open symbols correspond to increasing pressure and decompression data, respectively. The standard deviations of values are smaller than the size of symbols. The two different regimes of compression in MOF-520 are highlighted with yellow and blue, respectively. The ellipsoids of strain in red are calculated for both structures using PASCal software[26]; only the regime of compression was used for the calculation of ellipsoid for MOF-520.

3.4 Introduction of the 4,4′-biphenyldicarboxylate (BPDC) linkers as girders

The formate ligands at the SBU of MOF-520 were fully replaced with carboxylic functionalities following the protocol of the coordinative alignment (CAL) method[27]. The distance between formate ligands of two adjacent SBUs is *ca*. 9.5 Å in MOF-520, which allows the precise fitting of the 4,4′-biphenyldicarboxylate of comparable length (10.1 Å). Thus, by soaking MOF-520 single crystals in a saturated solution of H_2BPDC, it was possible to replace two formates, linking two SBUs by a rigid molecular girder. The loading rate of this new organic linker was monitored by digested ^{1}H NMR. After 4 days, the crystals of the resulting MOF-520-BPDC, $Al_8(\mu\text{-}OH)_8(BPDC)_2(BTB)_4$, were washed with anhydrous *N*,*N*-dimethylformamide, and the SXRD data were collected at 100 K at ambient pressure. Noteworthy, the introduction of the new linker does not decrease the crystallinity of the sample: the resolution of the data collected at 100 K for MOF-520-BPDC is comparable with such for pristine MOF-520 (see Tables S3.1 and S3.2 in the Supporting Information). Since the NMR spectra represent the whole batch of the material but not the individual single crystal, during the structure solution and refinement, the occupancy of BPDC girder was estimated by means of SXRD. The sample was fully characterized in terms of surface area, thermal stability, and composition after activation in order to directly compare the MOFs before and after girder installation. The introduction of the 4,4′-biphenyldicarboxylate girder does not change the symmetry of the MOF, and the space group of MOF-520-BPDC remains $P4_22_12$. At the same time, the structure is expanded along the crystallographic axes *a* and *b* by 0.8 Å but compressed along the longest axis *c* by 1 Å (Table 3.2). This structural modification leads to the overall expansion of the unit cell by more than 700 Å^3. As expected, the crystallographic density of the framework is increased after modification by just 0.05 g cm^{-3} due to the expansion of the unit cell. The pore volume estimated from the nitrogen adsorption measurement at 77 K is decreased by almost 25% from 1.28 cm^3 g^{-1} for MOF-520 to 0.91 cm^3 g^{-1} for MOF-520- BPDC. Similar reduction of the BET surface area was observed: 3630 and 2548 m^2 g^{-1}for MOF-520 and MOF-520-BPDC, respectively; attributable to the addition of the girder. Despite of the overall decrease in porosity, the pores in the MOF-520- BPDC are still accessible for the methanol/ethanol mixture as a pressure transmitting medium. In the retrofitted MOF, each SBU is now linked by four BPDCs in addition to 12 BTBs, resulting in a new (16,3)-connected net. While the overall symmetry of the unit cell is preserved during the modification, the retrofitted MOF possesses the new and thus far unreported **skl** topology (Figure 3.2). In MOF-520-BPDC the girders are directed along the crystallographic axes *a* and *b*, while the *c* direction remains unchanged. The distance between two adjacent SBUs is increased by almost 0.6 Å due to the incorporation of the BPDC linker.

Table 3.2. Crystallographic data and pore metrics of MOF-520 after retrofitting with BPDC, MOF-520-BPDC, as a function of hydrostatic pressure

Pressure / GPa	*a* / Å	*c* / Å	Unit cell volume / Å^3	Pore volume / Å^3	Electron count / e$^-$	Electron count per pore volume / e$^-$ Å^{-3}
0.0001	19.215(4)	36.779(4)	13580(6)	9104.1	8612	~0.95

0.32(2)*	19.2263(19)	36.708(3)	13569(3)	8992.7	6989	~0.77
0.64(2)	19.1965(10)	36.699(2)	13523.9(16)	9031.8	9455	~1.04
1.12(2)	19.185(2)	36.720(2)	13515(2)	9080.1	9464	~1.04
1.67(2)	19.156(2)	36.710(2)	13471(3)	9054.4	9792	~1.08
2.26(2)	19.123(2)	36.648(3)	13401(3)	9023.6	10519	~1.16
2.45(2)*	19.083(4)	36.725(7)	13374(6)	8888.5	12365	~1.39
2.86(2)	19.086(2)	36.593(3)	13330(3)	8942	11046	~1.23
3.32(5)*	19.0287(13)	36.5400(17)	13230.8(19)	8825.8	9673	~1.09
4.20(5)	18.955(4)	36.464(4)	13101(5)	8712.1	9756	~1.12
4.71(5)*	18.933(3)	36.424(4)	13056(4)	8640.2	9979	~1.15
5.33(5)	18.857(3)	36.302(7)	12909(4)	8572.3	10360	~1.21

*measured upon decompression

3.5 Mechanical robustness and retention of crystallinity of MOF-520-BPDC under extreme pressure

Our next step was to study the mechanical response of the new modified framework to variations in hydrostatic pressure. Using theoretical calculations, it was hypothesized before that the introduction of the new linker may increase the rigidity of MOF toward the extreme pressure[28]. The single-crystalline sample of MOF-520-BPDC was placed into a DAC filled with a methanol/ethanol pressure medium, and single-crystal X-ray diffraction data were collected up to 5.5 GPa. It is worth noting that we did not collect the data at even higher pressures because of the size of the crystal: the distance between two culets of diamonds was almost equal to the longest dimension of the sample, and further compression could result in cracking of the MOF crystal. Additionally, the SXRD data were also collected on the subsequent decompression. Notably, the crystal structure of retrofitted MOF experiences only one regime of distortion. The installation of rigid girder removes the overhydration effect upon initial compression but also increases the stiffness of the framework. The relative decrease in unit cell volume at 1 GPa is just 0.3%, which is almost five times smaller than in the case of pristine MOF-520. More importantly, the existence of the girder between two SBUs does not hinder the solvent molecules from diffusion inside the pore. The amount of unassigned electron density within the pore increases from 8612 electrons after closing the DAC to 9455 electrons at 0.64(2) GPa. Despite the penetration of pressure medium into the MOF, the internal pressure created by these molecules is not enough to expand the framework from the inside. This is not surprising considering that, for expansion of the unit cell, the carbon−carbon bonds of the BPDC girder must be stretched. Further compression of the MOF crystal leads to the reduction of the pore volume by ∼500 $Å^3$, and the amount of unassigned electron density related to resident molecules of PTM within the pore increases from 9455 electrons at 0.34(2) GPa to 10360 electrons at 5.33(5) GPa. The anisotropy of compression of MOF-520-BPDC is shown in Figure 3.3. One can see that the structure compresses along all crystallographic directions monotonically. The linear strain reaches almost 2% along the *a* (and *b*) crystallographic axis and 1.5% along the *c* axis at 5.3 GPa. The relative volume change at 5.3 GPa is about 5.5%. Based on the collected data, the ellipsoid of strain was calculated, showing the median compressibility coefficients of 3 TPa^{-1} along all three crystallographic directions[26]. These values are almost

two times smaller than those of parent MOF-520, indicating the corresponding increase of stiffness due to the placement of the girders. The reason for the drastic difference of MOFs' response to mechanical stimuli is the removal of distortion of the unit cell between two SBUs along the shortest axes due to the girder. For example, the distance between carbon atoms of the formate ligands of two neighboring SBUs is 9.470(4) Å at 100 K, 10.25(2) Å after closing the DAC, 10.31(2) Å in MOF-520 at 0.86 GPa (regime of expansion), and 9.64(4) Å at 2.82 GPa (regime of compression). In contrast, in the retrofitted MOF, the distance between carboxylate carbon atoms in the girder only shortens by 0.37(2) Å at 5.33 GPa. While in previously studied MOFs, such as MOF-5 and HKUST-1, the weakest element of the structures is the metal-linker bonds in the metal−oxide SBU, in the MOF-520 and retrofitted MOF-520 the rotated phenylene units of the BTB linkers are the weak points responsible for the deformation of the framework (see Tables S3.21 and S3.22 in the Supporting Information). In other words, the structure of MOF-520 suffers from mechanical instability due to the organic linker rather than the inorganic SBU. This study showed how this framework instability can be turned into robustness by molecular retrofitting of MOF-520 with BPDC.

Supporting Information for Chapter 3

General Methods

Chemicals used in this work: Aluminum nitrate nonahydrate, $Al(NO_3)_3 \cdot 9H_2O$, *N*,*N*-dimethylformamide (DMF) (purity ≥ 99.9 %), biphenyl-4,4'-dicarboxylic acid (H_2BPDC), ethanol (purity ≥ 99.5 %), methanol (purity ≥ 99.8 %) were purchased form Sigma Aldrich Co. 1,3,5-benzenetribenzoic acid (H_3BTB) was purchased from TCI America. Formic acid (99.8 %) was obtained from EMD Chemicals. Anhydrous acetone (purity ≥ 99.8 %, extra dry with AcroSeal) was purchased from Acros Organics. All chemicals obtained were used without further purification.

Analytical Techniques: Powder X-ray diffraction data were collected using a Bruker D8-advance θ-θ diffractometer in parallel beam geometry employing Cu Kα1 line focused radiation at 1600 W (40 kV, 40 mA) power and equipped with a position sensitive detector with at 6.0 mm radiation entrance slit. Samples were mounted on zero background sample holders by dropping powders from a wide-blade spatula and then leveling the sample with a razor blade. Data were collected using a 0.02˚ 2θ step scan from 2 – 35˚ with exposure time of 3 s per step. Thermogravimetric analysis (TGA) curves were recorded on a TA Q500 thermal analysis system under nitrogen flow. Elemental microanalyses (EA) were performed in the Microanalytical Laboratory of the College of Chemistry at UC Berkeley, using a Perkin Elmer 2400 Series II CHNS elemental analyzer. FT-IR spectra were collected in-house using a Bruker ALPHA Platinum ATR-FT-IR Spectrometer equipped with a single reflection diamond ATR module. Low-pressure Ar adsorption isotherms were recorded on a Quantachrome Autosorb-1 volumetric gas adsorption analyzer. A liquid argon bath was used for the N_2 measurements at 77 K. Solution ^1H NMR spectra were acquired on a Bruker Advance-500 MHz NMR spectrometer in Molecular Foundry in LBNL. Single-crystal X-ray diffraction (SXRD) data at ambient conditions was collected using synchrotron radiation in beamline 11.3.1 of the Advanced Light Source, Lawrence Berkeley National Laboratory (LBNL), equipped with a PHOTO100 CMOS detector operating in shutterless mode equipped, and the radiation is monochromated using silicon (111). Single-crystal X-ray diffraction at non-ambient pressure was collected using synchrotron radiation in beamline 12.2.2 of the Advanced Light Source, Lawrence Berkeley National Laboratory (LBNL).

Synthesis and characterization of MOF-520 and MOF-520-BPDC samples

MOF-520, **$Al_8(OH)_8(HCOO)_4BTB_4$.** In a 20 mL scintillation vial, the mixture solution of $Al(NO_3)_3 \cdot 9H_2O$ (90.0 mg, 0.240 mmol), H_3BTB (75.0 mg, 0.170 mmol) in DMF (17 mL) was prepared. The solution was sonicated for 1 min and formic acid (1.40 mL, 0.0310 mol) was added to the solution. The vial was capped and placed in the preheated 140 °C oven. After 4 days, block shaped clear single crystals with size range 50 to 100 μm were obtained on the wall of the vial. Subtle temperature difference can affect the quality of the single crystals. The vial with the best single crystals was chosen and the single crystals were used for the inclusion of the biphenyl-4,4'-dicarboxylic acid molecules. For the characterization of MOF-520, the rest of the crystals were further processed.

MOF-520-BPDC, **$Al_8(OH)_8(BPDC)_2BTB_4$.** In a 20 mL scintillation vial, the solution of H_2BPDC (315.0 mg, 1.3 mmol) in DMF (8 mL) was prepared. MOF-520 single crystals (5.0 mg) impregnated with DMF were added to the solution. The vial was capped and placed in the preheated 100 °C oven for 5 days.

Solvent exchange and guest removal activation procedure for the full characterization: The single crystals were washed with DMF (10.0 mL) three times per day for three days to remove the unreacted reagents in the pores. DMF solvent in the pore was exchanged with anhydrous acetone by washing the crystals with anhydrous acetone (10.0 mL) three times per day for three days. For supercritical CO_2 drying (SCD) activation, the acetone was decanted and acetone in the crystals was thoroughly exchanged with liquid CO_2 in the chamber of a Tousimis Samdri PVT-3D critical point dryer. The sample was subsequently kept in a supercritical CO_2 atmosphere (typical conditions of 40 °C and 1200 psi) for 30 min and then the supercritical CO_2 was slowly vented over the course of 6 hours.

Solvent exchange for the high-pressure measurements: The single crystals were washed with DMF (10.0 mL) three times per day for three days to remove the unreacted reagents in the pores. DMF solvent in the pore was exchanged by washing the crystals with methanol/ethanol (4:1 ratio) solution (4 ml) three times per day for three days. After that, the crystals were kept in methanol/ethanol media for at least several weeks before the high-pressure SXRD measurements.

Argon isotherms at 87 K: 40 mg of activated samples in 9 mm bulb gas cell was charged with Ar to avoid air contamination and the cell was mounted on the instrument. Liquid argon bath was used for the measurements at 87 K. Helium was used for the estimation of dead space for gas adsorption measurements. Ultra-high-purity grade Ar and He gases (Praxair, 99.999% purity) were used throughout the adsorption experiments. 46 adsorption and 16 desorption points were collected.

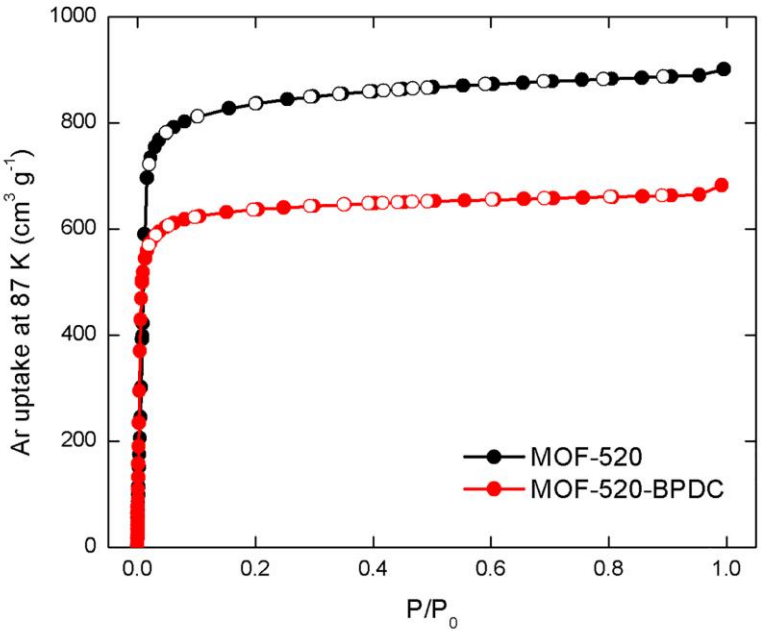

Figure S3.1. Comparison of MOF-520 and MOF-520-BPDC Ar isotherms at 87 K.

Thermogravimetric analysis: The activated sample was held in a platinum pan under nitrogen atmosphere with a flow rate of 40 mL/min. Temperature was controlled by the furnace heating from 25 °C up to 800 °C with a ramp rate of 5 °C/ min.

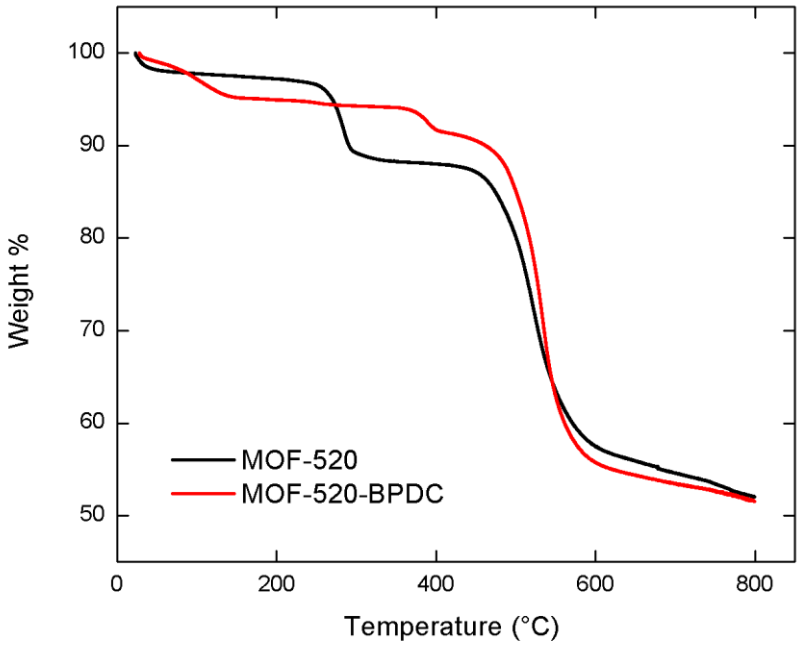

Figure S3.2. Comparison of activated MOF-520 and MOF-520-BPDC TGA traces under N_2 flow.

^{1}H NMR analysis: The activated sample (1 mg) was transferred to a 4 mL vial. Deuterated dimethyl sulfoxide (d_6-DMSO) (600 µL) was add to the vial followed by the addition of 20 µL of NaOH (1 M in D_2O). The solution was sonicated for 10 min to digest the crystals. The vial was capped and placed in a preheated 120 °C oven for 20 min to completely dissolve the crystals. The final clear solution was used for the ^{1}H NMR experiment. The integration ratio suggests the occupancy of BPDC linker to be about 70%. The deviation from 100% occupancy of BPDC in the single-crystalline sample used for high-pressure experiments can be explained by that the molecule incorporation in a single crystal does not represent the whole batch of the sample.

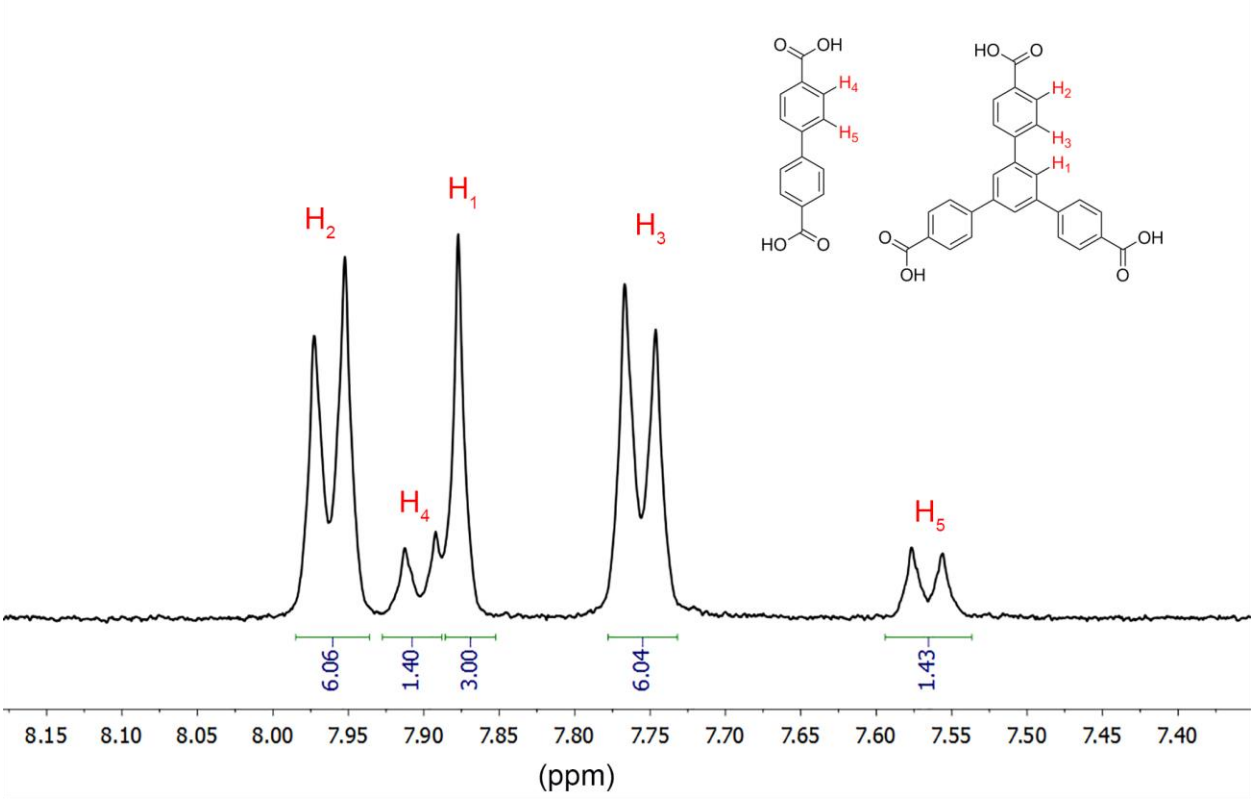

Figure S3.3. ^{1}H NMR data of digested activated MOF-520-BPDC in d_6-DMSO. The integration ratio suggests the occupancy of BPDC linker to be about 70%.

Powder X-ray diffraction analysis: The activated single crystals were used for PXRD experiment. Ground sample was placed on a quartz sample holder and was mounted on the diffractometer. The data was collected from 2 to 35 degrees by 0.02 step for total 60 minutes data collection time.

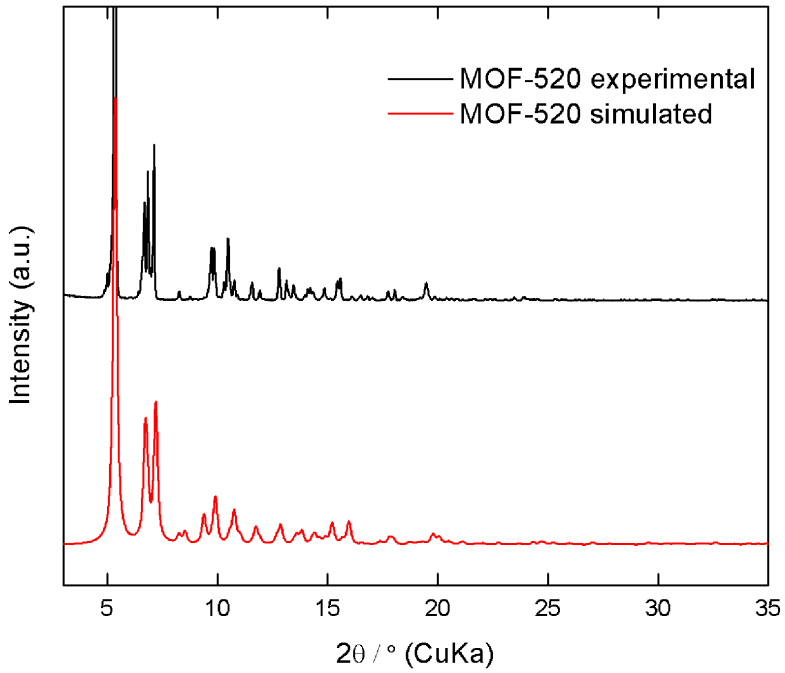

Figure S3.4. PXRD pattern of activated MOF-520 and the simulated pattern of MOF-520 structure from SXRD data.

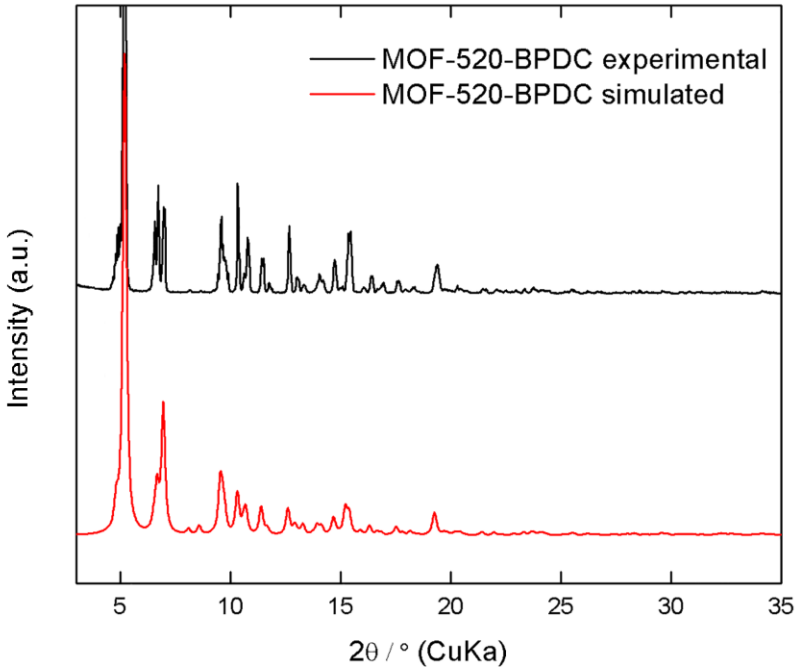

Figure S3.5. PXRD pattern of activated MOF-520-BPDC and the simulated pattern of MOF-520-BPDC structure from SXRD data.

Elemental analysis: MOF-520 ($Al_8C_{112}H_{72}O_{40}$) Found (wt %): C: 57.86; H: 3.24; N: < 0.2. Calculated (wt %): C: 59.17; H: 3.19; N: 0.0; MOF-520-BPDC ($Al_8C_{136}H_{84}O_{40}$) Found (wt %): C: 61.67; H: 3.36; N: < 0.2. Calculated (wt %): C: 63.46; H: 3.29; N: 0.0.

IR analysis:

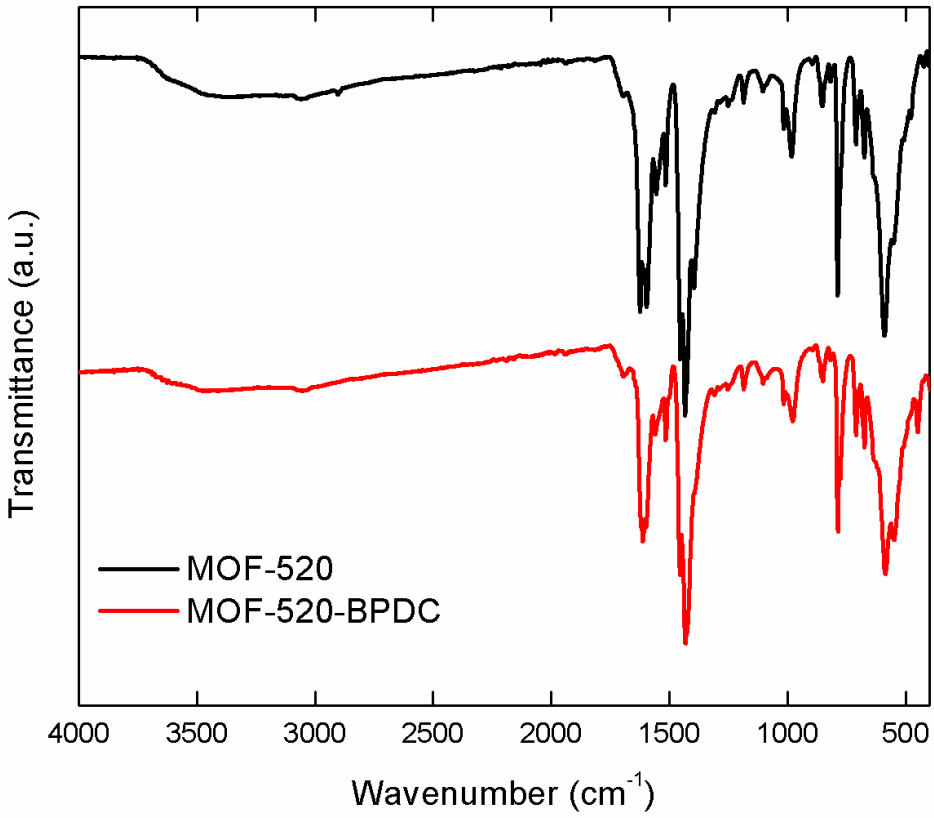

Figure S3.6. Comparison of activated MOF-520 and MOF-520-BPDC IR spectra.

Single crystal X-ray diffraction analysis at ambient conditions: Single-crystalline samples were mounted on MiTeGen® kapton loops in LV CryoOil®. In all cases, the raw data were processed with the Bruker APEX2 software package. The data were first integrated using the SAINT procedure and then corrected for absorption with SADABS procedure. The structures were solved by direct methods (XS-2008) and the refinement was done by full-matrix least squares on F^2 (SHELXL-2014), using the Olex2 software package[30]. Mercury software was used for structure visualization[31].

Δ-MOF-520. A block-shaped crystal (50 x 40 x 40 μm^3) of Δ-MOF-520 a was measured at beamline 11.3.1 at the ALS with radiation of λ = 1.0332 Å. According to intensity statistics table for the whole dataset (PRP file), the resolution was cut off to 0.83 Å. Solvent masking was applied during structure refinement. Before solvent masking instruction, structure was refined anisotropically and hydrogen atoms were placed into positions calculated geometrically. The

connected asymmetric unit was defined inside the unit cell: MOVE command was applied to all atoms. The void volume is estimated to be 8963 $Å^3$ with 9196 electrons removed during masking. Some reflections were omitted due to non-ideal solvent masking, beam stop clipping and the minor presence of diffuse scattering. The threshold $(I_{obs}-I_{calc})/\sigma(W)>10$ was chosen for omitting these reflections. Omission of these reflections did not affect the refinement; the fraction of omitted reflections is less than 0.1% of the whole dataset.

Table S3.1. Crystal data, data collection, and structure refinement parameters for Δ-MOF-520.

Name	Δ-MOF-520
Chemical composition of MOF per asymmetric unit	Al_2 C_{28} H_{18} O_{10}
Chemical formula of bound molecule	none
Formula mass	568.38
Crystal system	Tetragonal
Space group	$P4_22_12$
a, Å	18.3754(6)
c, Å	37.6893(12)
V, $Å^3$	12726.0(9)
d, g cm^{-3}	0.593
μ, mm^{-1}	0.190
Z	8
Measured reflections	107906
Independent reflections	11720
Observed reflections	10185
θ_{min} , º	2.250
θ_{max} , º	38.603
h	-22 to 21
k	-22 to 22
l	-45 to 45
R int	0.0414
R [$F^2>2\sigma(F^2)$]	0.0338
$wR(F^2)$	0.01066
S	1.058
Parameters	362
Flack parameter	0.086(15)
$\Delta\rho_{max}$, e $Å^{-3}$	0.227
$\Delta\rho_{min}$, e $Å^{-3}$	-0.219
Crystal size, mm^3	0.050 x 0.040 x 0.040
Radiation, Å	1.0332
Temperature, K	100
Pressure, GPa	0.0001

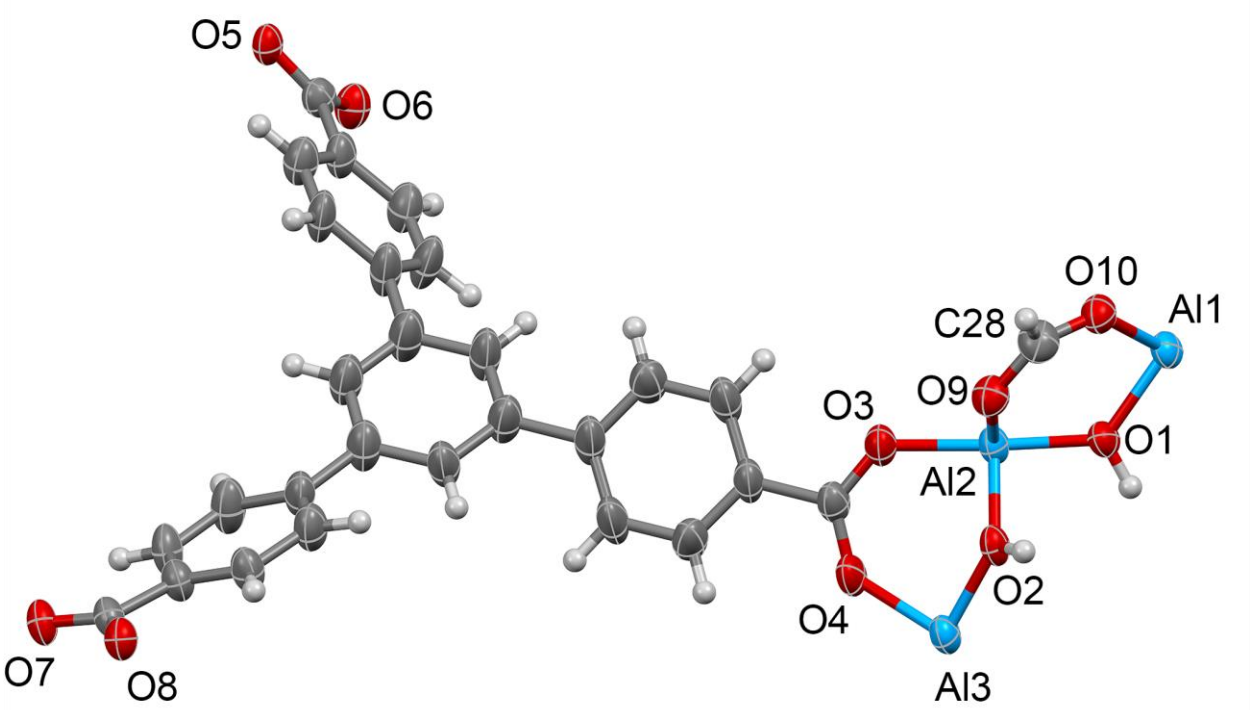

Figure S3.7. Asymmetric unit in the single crystal structure of Δ-MOF-520. Thermal ellipsoids are drawn with 50% probability. Same numbering scheme is used for all structures of MOF-520 under non-ambient conditions.

Δ-**MOF-520-BPDC.** A block-shaped crystal (80 x 60 x 60 μm^3) of as-synthesized Δ-MOF-520-BPDC was measured at beamline 11.3.1 at the ALS with radiation of λ = 1.0332 Å. According to intensity statistics table for the whole dataset (PRP file), the resolution was cut off to 0.83 Å. Solvent masking was applied during structure refinement. Before solvent masking instruction, structure was refined anisotropically and hydrogen atoms were placed into positions calculated geometrically. The occupancy of the BPDC linker is 1.0. The connected asymmetric unit was defined inside the unit cell: MOVE command was applied to all atoms. The void volume is estimated to be 9052.2 $Å^3$ with 5819.9 electrons removed during masking. Some reflections were omitted due to non-ideal solvent masking, beam stop clipping and the minor presence of diffuse scattering. The threshold $(I_{obs}-I_{calc})/\sigma(W)>10$ was chosen for omitting these reflections. Omission of these reflections did not affect the refinement; the fraction of omitted reflections is less than 0.1% of the whole dataset.

Table S3.2. Crystal data, data collection, and structure refinement parameters for Δ-MOF-520-BPDC.

Name	Δ-MOF-520-BPDC
Chemical composition of MOF per asymmetric unit	$Al_2\ C_{34}\ H_{21}\ O_{10}$
Formula mass	643.47
Crystal system	Tetragonal
Space group	$P4_22_12$
a, Å	19.1813(7)
c, Å	36.6658(13)
V, Å^3	13490.2(11)
d, g cm^{-3}	0.634
μ, mm^{-1}	0.190
Z	8
Measured reflections	46877
Independent reflections	11988
Observed reflections	10083
θ_{min} , º	2.183
θ_{max} , º	38.564
h	-18 to 23
k	-23 to 22
l	-43 to 37
R int	0.0335
$R\ [F^2>2\sigma(F^2)]$	0.0315
$wR(F^2)$	0.0732
S	1.045
Parameters	424
Flack parameter	0.08(2)
$\Delta\rho_{max}$, e Å^{-3}	0.174
$\Delta\rho_{min}$, e Å^{-3}	-0.179
Crystal size, mm^3	0.080 x 0.060 x 0.060
Radiation, Å	1.0332
Temperature, K	100
Pressure, GPa	0.0001

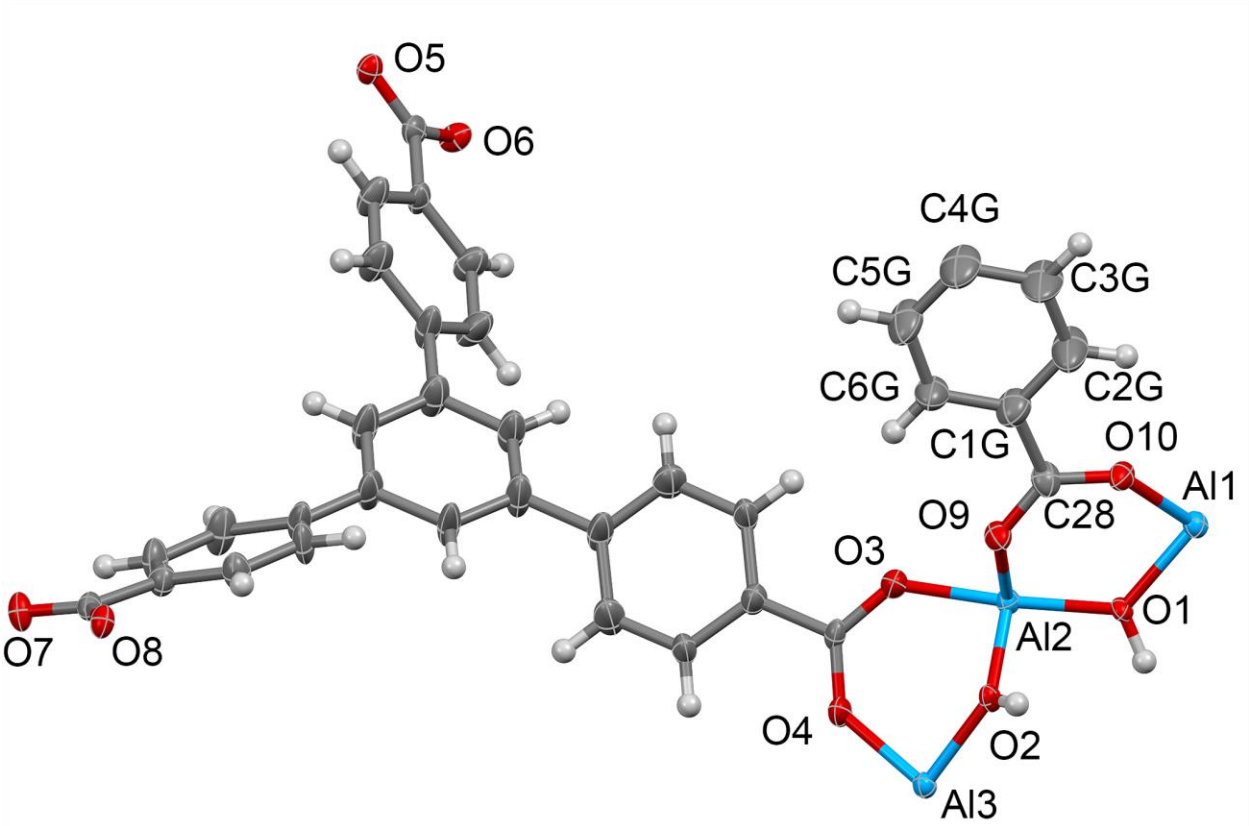

Figure S3.8. Asymmetric unit in the single crystal structure of Δ-MOF-520-BPDC. Thermal ellipsoids are drawn with 50% probability. Same numbering scheme is used for all structures of MOF-520-BPDC under non-ambient conditions.

High-pressure single-crystal diffraction setup and data collection procedure. PASCal calculations procedure.

The X-ray diffraction studies of MOF-520 and MOF-520-BPDC at variable pressure were performed on a single crystal samples. The samples of 0.040 x 0.040 x 0.030 mm^3 were loaded into a Merrill-Bassett-type diamond anvil cell (DAC) with Boehler-Almax cut diamonds, with culets of 500 μm and a tungsten gasket with hole diameter of 200 μm. Gasket holes were drilled using an Oxford Lasers Laser mill. A 4:1 methanol/ethanol mixture was used as the hydrostatic pressure medium. Once the single-crystalline sample was fixed on the culet of the diamond in the gasket hole, several rubies were placed next to it, and the pressure/medium was added right before closing the DAC. The pressure calibration was done using the Ruby fluorescence method.

The high-pressure SXRD data was collected using synchrotron radiation (λ = 0.49594 Å) in beamline 12.2.2 of the Advanced Light Source. The beamline is equipped with Perkin-Elmer CMOS detector. The DAC centering procedure and the geometry setup was performed according to literature[29]. To maximize the data collected, two datasets were collected in the typical experiment: a first ω-scan with a rotation of DAC from the front by 80 ° from -40 to 40 °, and the second ω-scan with a rotation of DAC from the front by 80 ° from 140 to 220 °. The exposure time was adjusted throughout the whole pressure range to achieve the highest possible resolution.

In all cases, the raw data were processed with the Bruker APEX2 software package. In order to find the orientation matrix of the MOF sample, all reflections from both diamonds were removed using cell_now command. The data were integrated using the SAINT procedure; the pre-determined masking procedure was applied. The shielding of the diffraction pattern by the DAC was taken into account by the generation of dynamic masks using Eclipse software (Parsons, Simon. 2010. ECLIPSE – Program for masking high pressure diffraction images and conversion between CCD image formats). The data were then corrected for absorption with SADABS multiscan procedure. The structures were solved by direct methods (XS-2008) and the refinement was done by full-matrix least squares on F^2 (SHELXL-2014), using the Olex2 software package[30]. Mercury software was used for structure visualization[31]. The resolution obtained for all samples was limited due to DAC-opening angle and in order to improve the refinement of the model, the resolution was cut off, according to intensity statistics table. DISP command was used to set the f′, f′′, and μ values for atoms in the structures.

All geometrical restraints, applied to non-hydrogen atoms are listed in the corresponding table of each structure.

Note that poor quality of the experimental data, including low resolution, non-ideal dynamic masking, overlap with the diamond reflections, overlap with the powder rings from the gasket, results in several alert of A and B level in CheckCif reports. In addition, because of very short wavelength ((λ = 0.49594 Å) and presence of light atoms in the structure, the flack parameter could not be estimated precisely.

A structural model refined at a previous pressure point served as a starting one for the next pressure. The atom positions. Olex2 software was used to monitor the quality of the structural models using convenient graphs. In case of severe distortion of the building units of MOF under pressure, we applied RIGU restraints to the whole framework. All hydrogen atoms were placed into geometrically calculated positions and refined using a riding model.

The principal axis strain calculations were conducted using PASCal web tool: pascal.chem.ox.ca.uk. The unit cell parameters for MOF-520 and MOF-520-BPDC were used to plot the ellipsoid of compression and to estimate the median compressibility coefficients in TPa^{-1}. Only the regime of compression was used in case of MOF-520. The error of 0.02 or 0.05 GPa in pressure data was used as an input. No error for the unit cell parameters was considered.

The median compressibilities for each principal directions were found from these calculations.

Table S3.3. Crystal data, data collection, and structure refinement parameters for MOF-520 at 10^{-4} GPa.

Name	MOF-520_10-4 GPa
Chemical composition of MOF per asymmetric unit	$Al_2\ C_{28}\ H_{18}\ O_{10}$
Formula mass	568.38
Crystal system	Tetragonal
Space group	$P4_22_12$
a, Å	18.920(3)
c, Å	37.190(7)
V, Å^3	13313(5)
d, g cm^{-3}	0.567
μ, mm^{-1}	0.029
Z	8
Measured reflections	13052
Independent reflections	5124
Observed reflections	2572
θ_{min} , º	1.062
θ_{max} , º	13.660
h	-17 to 17
k	-17 to 16
l	-30 to 26
R int	0.1343
$R\ [F^2>2\sigma(F^2)]$	0.0407
$wR(F^2)$	0.0737
S	0.672
Parameters	363
Restraints	324
Flack parameter	0.70(13)
$\Delta\rho_{max}$, e Å^{-3}	0.075
$\Delta\rho_{min}$, e Å^{-3}	-0.099
Crystal size, mm^3	0.040 x 0.040 x 0.030
Radiation, Å	0.49594
Temperature, K	298
Pressure, GPa	0.0001

Table S3.4. Crystal data, data collection, and structure refinement parameters for MOF-520 at 0.15 GPa.

Name	MOF-520_0.15 GPa
Chemical composition of MOF per asymmetric unit	$Al_2\ C_{28}\ H_{18}\ O_{10}$
Formula mass	568.38
Crystal system	Tetragonal
Space group	$P4_22_12$
a, Å	19.070(3)
c, Å	36.930(7)
V, Å^3	13430(5)
d, g cm^{-3}	0.563
μ, mm^{-1}	0.029
Z	8
Measured reflections	10435
Independent reflections	4641
Observed reflections	1888
θ_{min} , º	0.839
θ_{max} , º	13.025
h	-16 to 15
k	-17 to 17
l	-32 to 29
R int	0.1067
$R\ [F^2>2\sigma(F^2)]$	0.0628
$wR(F^2)$	0.1628
S	0.922
Parameters	329
Restraints	303
Flack parameter	0.6(7)
$\Delta\rho_{max}$, e Å^{-3}	0.153
$\Delta\rho_{min}$, e Å^{-3}	-0.351
Crystal size, mm^3	0.040 x 0.040 x 0.030
Radiation, Å	0.49594
Temperature, K	298
Pressure, GPa	0.15

Table S3.5. Crystal data, data collection, and structure refinement parameters for MOF-520 at 0.86 GPa.

Name	MOF-520_0.86 GPa
Chemical composition of MOF per asymmetric unit	$Al_2\ C_{28}\ H_{18}\ O_{10}$
Formula mass	568.38
Crystal system	Tetragonal
Space group	$P4_22_12$
a, Å	19.196(3)
c, Å	36.569(7)
V, Å^3	13475(5)
d, g cm^{-3}	0.560
μ, mm^{-1}	0.029
Z	8
Measured reflections	12386
Independent reflections	4730
Observed reflections	3219
θ_{min} , º	0.836
θ_{max} , º	13.027
h	-16 to 15
k	-17 to 16
l	-31 to 30
R int	0.0826
$R\ [F^2>2\sigma(F^2)]$	0.0396
$wR(F^2)$	0.0809
S	0.883
Parameters	362
Restraints	336
Flack parameter	0.50(9)
$\Delta\rho_{max}$, e Å^{-3}	0.097
$\Delta\rho_{min}$, e Å^{-3}	-0.219
Crystal size, mm^3	0.040 x 0.040 x 0.030
Radiation, Å	0.49594
Temperature, K	298
Pressure, GPa	0.86

Table S3.6. Crystal data, data collection, and structure refinement parameters for MOF-520 at 1.47 GPa.

Name	MOF-520_1.47 GPa
Chemical composition of MOF per asymmetric unit	$Al_2\ C_{28}\ H_{18}\ O_{10}$
Formula mass	568.38
Crystal system	Tetragonal
Space group	$P4_22_12$
a, Å	19.182(3)
c, Å	36.534(7)
V, Å^3	13443(5)
d, g cm^{-3}	0.562
μ, mm^{-1}	0.029
Z	8
Measured reflections	9518
Independent reflections	3850
Observed reflections	3381
θ_{min} , º	0.837
θ_{max} , º	11.925
h	-14 to 15
k	-15 to 15
l	-26 to 28
R int	0.0491
$R\ [F^2>2\sigma(F^2)]$	0.0361
$wR(F^2)$	0.1009
S	1.062
Parameters	362
Restraints	336
Flack parameter	0.1(3)
$\Delta\rho_{max}$, e Å^{-3}	0.115
$\Delta\rho_{min}$, e Å^{-3}	-0.185
Crystal size, mm^3	0.040 x 0.040 x 0.030
Radiation, Å	0.49594
Temperature, K	298
Pressure, GPa	1.47

Table S3.7. Crystal data, data collection, and structure refinement parameters for MOF-520 at 2.24 GPa.

Name	MOF-520_2.24 GPa
Chemical composition of MOF per asymmetric unit	$Al_2\ C_{28}\ H_{18}\ O_{10}$
Formula mass	568.38
Crystal system	Tetragonal
Space group	$P4_22_12$
a, Å	19.130(3)
c, Å	36.480(7)
V, Å^3	13350(5)
d, g cm^{-3}	0.566
μ, mm^{-1}	0.029
Z	8
Measured reflections	11629
Independent reflections	4366
Observed reflections	3499
θ_{min} , º	0.839
θ_{max} , º	12.449
h	-16 to 16
k	-15 to 15
l	-30 to 28
R int	0.0567
$R\ [F^2>2\sigma(F^2)]$	0.0465
$wR(F^2)$	0.1261
S	0.981
Parameters	362
Restraints	336
Flack parameter	-0.2(3)
$\Delta\rho_{max}$, e Å^{-3}	0.146
$\Delta\rho_{min}$, e Å^{-3}	-0.254
Crystal size, mm^3	0.040 x 0.040 x 0.030
Radiation, Å	0.49594
Temperature, K	298
Pressure, GPa	2.24

Table S3.8. Crystal data, data collection, and structure refinement parameters for MOF-520 at 2.82 GPa.

Name	MOF-520_2.82 GPa
Chemical composition of MOF per asymmetric unit	$Al_2\ C_{28}\ H_{18}\ O_{10}$
Formula mass	568.38
Crystal system	Tetragonal
Space group	$P4_22_12$
a, Å	19.070(3)
c, Å	36.409(7)
V, Å^3	13241(5)
d, g cm^{-3}	0.566
μ, mm^{-1}	0.029
Z	8
Measured reflections	19178
Independent reflections	7050
Observed reflections	3723
θ_{min} , º	0.841
θ_{max} , º	15.130
h	-18 to 19
k	-18 to 18
l	-36 to 35
R int	0.1082
$R\ [F^2>2\sigma(F^2)]$	0.0495
$wR(F^2)$	0.1101
S	0.863
Parameters	362
Restraints	336
Flack parameter	0.4(5)
$\Delta\rho_{max}$, e Å^{-3}	0.155
$\Delta\rho_{min}$, e Å^{-3}	-0.232
Crystal size, mm^3	0.040 x 0.040 x 0.030
Radiation, Å	0.49594
Temperature, K	298
Pressure, GPa	2.82

Table S3.9. Crystal data, data collection, and structure refinement parameters for MOF-520-BPDC at 10^{-4} GPa.

Name	MOF-520-BPDC_10^{-4} GPa
Chemical composition of MOF per asymmetric unit	$Al_2\ C_{34}\ H_{21}\ O_{10}$
Formula mass	643.47
Crystal system	Tetragonal
Space group	$P4_22_12$
a, Å	19.215(4)
c, Å	36.779(4)
V, Å^3	13580(6)
d, g cm^{-3}	0.629
μ, mm^{-1}	0.031
Z	8
Measured reflections	22070
Independent reflections	7973
Observed reflections	4948
θ_{min} , º	0.834
θ_{max} , º	15.998
h	-21 to 21
k	-9 to 9
l	-40 to 40
R int	0.1141
R [$F^2>2\sigma(F^2)$]	0.0404
$wR(F^2)$	0.0745
S	0.763
Parameters	424
Restraints	0
Flack parameter	0.4(5)
$\Delta\rho_{max}$, e Å^{-3}	0.093
$\Delta\rho_{min}$, e Å^{-3}	-0.133
Crystal size, mm^3	0.040 x 0.040 x 0.030
Radiation, Å	0.49594
Temperature, K	298
Pressure, GPa	0.0001

Table S3.10. Crystal data, data collection, and structure refinement parameters for MOF-520-BPDC at 0.64 GPa.

Name	MOF-520-BPDC_0.64 GPa
Chemical composition of MOF per asymmetric unit	$Al_2\ C_{34}\ H_{21}\ O_{10}$
Formula mass	643.47
Crystal system	Tetragonal
Space group	$P4_22_12$
a, Å	19.1965(10)
c, Å	36.699(2)
V, Å^3	13523.9(16)
d, g cm^{-3}	0.632
μ, mm^{-1}	0.031
Z	8
Measured reflections	22120
Independent reflections	9102
Observed reflections	7042
θ_{min} , º	0.835
θ_{max} , º	15.990
h	-21 to 21
k	-19 to 14
l	-38 to 35
R int	0.0642
R [F^2>2σ(F^2)]	0.0404
$wR(F^2)$	0.1171
S	1.293
Parameters	424
Restraints	0
Flack parameter	1.6(2)
$\Delta\rho_{max}$, e Å^{-3}	0.925
$\Delta\rho_{min}$, e Å^{-3}	-0.793
Crystal size, mm^3	0.040 x 0.040 x 0.030
Radiation, Å	0.49594
Temperature, K	298
Pressure, GPa	0.64

Table S3.11. Crystal data, data collection, and structure refinement parameters for MOF-520-BPDC at 1.12 GPa.

Name	MOF-520-BPDC_1.12 GPa
Chemical composition of MOF per asymmetric unit	$Al_2\ C_{34}\ H_{21}\ O_{10}$
Formula mass	643.47
Crystal system	Tetragonal
Space group	$P4_22_12$
a, Å	19.185(2)
c, Å	36.720(2)
V, Å^3	13515(3)
d, g cm^{-3}	0.632
μ, mm^{-1}	0.031
Z	8
Measured reflections	21306
Independent reflections	7387
Observed reflections	5614
θ_{min} , º	0.836
θ_{max} , º	15.993
h	-9 to 7
k	-21 to 21
l	-40 to 40
R int	0.0645
R [$F^2>2\sigma(F^2)$]	0.0343
$wR(F^2)$	0.0729
S	0.983
Parameters	416
Restraints	0
Flack parameter	0.8(3)
$\Delta\rho_{max}$, e Å^{-3}	0.087
$\Delta\rho_{min}$, e Å^{-3}	-0.126
Crystal size, mm^3	0.040 x 0.040 x 0.030
Radiation, Å	0.49594
Temperature, K	298
Pressure, GPa	1.12

Table S3.12. Crystal data, data collection, and structure refinement parameters for MOF-520-BPDC at 1.67 GPa.

Name	MOF-520-BPDC_1.67 GPa
Chemical composition of MOF per asymmetric unit	$Al_2\ C_{34}\ H_{21}\ O_{10}$
Formula mass	643.47
Crystal system	Tetragonal
Space group	$P4_22_12$
a, Å	19.156(2)
c, Å	36.710(2)
V, Å^3	13471(3)
d, g cm^{-3}	0.635
μ, mm^{-1}	0.031
Z	8
Measured reflections	22317
Independent reflections	7218
Observed reflections	5599
θ_{min} , º	0.837
θ_{max} , º	15.979
h	-7 to 8
k	-21 to 21
l	-40 to 40
R int	0.0654
R [F^2>2σ(F^2)]	0.0356
$wR(F^2)$	0.0855
S	1.007
Parameters	416
Restraints	36
Flack parameter	0.8(3)
$\Delta\rho_{max}$, e Å^{-3}	0.115
$\Delta\rho_{min}$, e Å^{-3}	-0.136
Crystal size, mm^3	0.040 x 0.040 x 0.030
Radiation, Å	0.49594
Temperature, K	298
Pressure, GPa	1.67

Table S3.13. Crystal data, data collection, and structure refinement parameters for MOF-520-BPDC at 2.26 GPa.

Name	MOF-520-BPDC_2.26 GPa
Chemical composition of MOF per asymmetric unit	$Al_2\ C_{34}\ H_{21}\ O_{10}$
Formula mass	643.47
Crystal system	Tetragonal
Space group	$P4_22_12$
a, Å	19.123(2)
c, Å	36.648(2)
V, Å^3	13401(3)
d, g cm^{-3}	0.638
μ, mm^{-1}	0.032
Z	8
Measured reflections	19345
Independent reflections	6198
Observed reflections	4987
θ_{min} , º	0.838
θ_{max} , º	15.124
h	-8 to 7
k	-20 to 20
l	-38 to 38
R int	0.0667
$R\ [F^2>2\sigma(F^2)]$	0.0361
$wR(F^2)$	0.0880
S	0.984
Parameters	416
Restraints	378
Flack parameter	1.1(3)
$\Delta\rho_{max}$, e Å^{-3}	0.125
$\Delta\rho_{min}$, e Å^{-3}	-0.142
Crystal size, mm^3	0.040 x 0.040 x 0.030
Radiation, Å	0.49594
Temperature, K	298
Pressure, GPa	2.26

Table S3.14. Crystal data, data collection, and structure refinement parameters for MOF-520-BPDC at 2.86 GPa.

Name	MOF-520-BPDC_2.86 GPa
Chemical composition of MOF per asymmetric unit	$Al_2\ C_{34}\ H_{21}\ O_{10}$
Formula mass	643.47
Crystal system	Tetragonal
Space group	$P4_22_12$
a, Å	19.086(2)
c, Å	36.593(3)
V, Å^3	13330(3)
d, g cm^{-3}	0.641
μ, mm^{-1}	0.032
Z	8
Measured reflections	16805
Independent reflections	5361
Observed reflections	4642
θ_{min} , º	0.840
θ_{max} , º	14.352
h	-7 to 8
k	-19 to 19
l	-36 to 36
R int	0.0528
R [$F^2>2\sigma(F^2)$]	0.0379
wR(F^2)	0.1037
S	1.062
Parameters	416
Restraints	387
Flack parameter	0.7(2)
$\Delta\rho_{max}$, e Å^{-3}	0.146
$\Delta\rho_{min}$, e Å^{-3}	-0. 169
Crystal size, mm^3	0.040 x 0.040 x 0.030
Radiation, Å	0.49594
Temperature, K	298
Pressure, GPa	2.86

Table S3.15. Crystal data, data collection, and structure refinement parameters for MOF-520-BPDC at 4.20 GPa.

Name	MOF-520-BPDC_4.20 GPa
Chemical composition of MOF per asymmetric unit	$Al_2\ C_{34}\ H_{21}\ O_{10}$
Formula mass	643.47
Crystal system	Tetragonal
Space group	$P4_22_12$
a, Å	18.955(4)
c, Å	36.464(4)
V, Å^3	13101(5)
d, g cm^{-3}	0.652
μ, mm^{-1}	0.032
Z	8
Measured reflections	18454
Independent reflections	6609
Observed reflections	4821
θ_{min} , º	0.845
θ_{max} , º	15.134
h	-7 to 9
k	-19 to 19
l	-38 to 38
R int	0.0962
R [$F^2>2\sigma(F^2)$]	0.0551
$wR(F^2)$	0.1385
S	0.969
Parameters	416
Restraints	387
Flack parameter	0.3(6)
$\Delta\rho_{max}$, e Å^{-3}	0.178
$\Delta\rho_{min}$, e Å^{-3}	-0.224
Crystal size, mm^3	0.040 x 0.040 x 0.030
Radiation, Å	0.49594
Temperature, K	298
Pressure, GPa	4.20

Table S3.16. Crystal data, data collection, and structure refinement parameters for MOF-520-BPDC at 5.33 GPa.

Name	MOF-520-BPDC_5.33 GPa
Chemical composition of MOF per asymmetric unit	$Al_2\ C_{34}\ H_{21}\ O_{10}$
Formula mass	643.47
Crystal system	Tetragonal
Space group	$P4_22_12$
a, Å	18.857(3)
c, Å	36.302(7)
V, Å^3	12909(4)
d, g cm^{-3}	0.662
μ, mm^{-1}	0.033
Z	8
Measured reflections	11848
Independent reflections	4477
Observed reflections	2732
θ_{min} , º	0.849
θ_{max} , º	13.027
h	-17 to 17
k	-9 to 7
l	-32 to 33
R int	0.1199
R [F^2>2σ(F^2)]	0.0967
$wR(F^2)$	0.1275
S	0.914
Parameters	416
Restraints	387
Flack parameter	-0.2(8)
$\Delta\rho_{max}$, e Å^{-3}	0.146
$\Delta\rho_{min}$, e Å^{-3}	-0.175
Crystal size, mm^3	0.040 x 0.040 x 0.030
Radiation, Å	0.49594
Temperature, K	298
Pressure, GPa	5.33

Table S3.17. Crystal data, data collection, and structure refinement parameters for MOF-520-BPDC at 4.71 GPa.

Name	MOF-520-BPDC_4.71 GPa
Chemical composition of MOF per asymmetric unit	$Al_2\ C_{34}\ H_{21}\ O_{10}$
Formula mass	643.47
Crystal system	Tetragonal
Space group	$P4_22_12$
a, Å	18.933(3)
c, Å	36.424(4)
V, Å^3	13056(4)
d, g cm^{-3}	0.655
μ, mm^{-1}	0.032
Z	8
Measured reflections	18321
Independent reflections	7030
Observed reflections	4836
θ_{min} , º	0.846
θ_{max} , º	15.128
h	-12 to 9
k	-19 to 19
l	-38 to 35
R int	0.0907
R [F^2>2σ(F^2)]	0.0519
$wR(F^2)$	0.1226
S	0.935
Parameters	416
Restraints	387
Flack parameter	1.9(5)
$\Delta\rho_{max}$, e Å^{-3}	0.166
$\Delta\rho_{min}$, e Å^{-3}	-0.272
Crystal size, mm^3	0.040 x 0.040 x 0.030
Radiation, Å	0.49594
Temperature, K	298
Pressure, GPa	4.71

Table S3.18. Crystal data, data collection, and structure refinement parameters for MOF-520-BPDC at 3.32 GPa.

Name	MOF-520-BPDC_3.32 GPa
Chemical composition of MOF per asymmetric unit	$Al_2\ C_{34}\ H_{21}\ O_{10}$
Formula mass	643.47
Crystal system	Tetragonal
Space group	$P4_22_12$
a, Å	19.0287(13)
c, Å	36.5400(17)
V, Å^3	13230.8(19)
d, g cm^{-3}	0.646
μ, mm^{-1}	0.032
Z	8
Measured reflections	19092
Independent reflections	6997
Observed reflections	5936
θ_{min} , º	0.846
θ_{max} , º	15.128
h	-20 to 20
k	-8 to 11
l	-38 to 36
R int	0.0514
$R\ [F^2>2\sigma(F^2)]$	0.0508
$wR(F^2)$	0.1443
S	1.084
Parameters	416
Restraints	387
Flack parameter	0.9(2)
$\Delta\rho_{max}$, e Å^{-3}	0.294
$\Delta\rho_{min}$, e Å^{-3}	-0.337
Crystal size, mm^3	0.040 x 0.040 x 0.030
Radiation, Å	0.49594
Temperature, K	298
Pressure, GPa	3.32

Table S3.19. Crystal data, data collection, and structure refinement parameters for MOF-520-BPDC at 2.45 GPa.

Name	MOF-520-BPDC_2.45 GPa
Chemical composition of MOF per asymmetric unit	$Al_2\ C_{34}\ H_{21}\ O_{10}$
Formula mass	643.47
Crystal system	Tetragonal
Space group	$P4_22_12$
a, Å	19.083(4)
c, Å	36.725(7)
V, Å^3	13374(6)
d, g cm^{-3}	0.637
μ, mm^{-1}	0.032
Z	8
Measured reflections	13071
Independent reflections	5012
Observed reflections	3377
θ_{min} , º	0.839
θ_{max} , º	13.031
h	-11 to 13
k	-17 to 17
l	-30 to 33
R int	0.1277
$R\ [F^2>2\sigma(F^2)]$	0.0557
$wR(F^2)$	0.1401
S	0.791
Parameters	416
Restraints	387
Flack parameter	1.1(8)
$\Delta\rho_{max}$, e Å^{-3}	0.179
$\Delta\rho_{min}$, e Å^{-3}	-0.197
Crystal size, mm^3	0.040 x 0.040 x 0.030
Radiation, Å	0.49594
Temperature, K	298
Pressure, GPa	2.45

Table S3.20. Crystal data, data collection, and structure refinement parameters for MOF-520-BPDC at 0.32 GPa.

Name	MOF-520-BPDC_0.32 GPa
Chemical composition of MOF per asymmetric unit	$Al_2\ C_{34}\ H_{21}\ O_{10}$
Formula mass	643.47
Crystal system	Tetragonal
Space group	$P4_22_12$
a, Å	19.2263(19)
c, Å	36.708(3)
V, Å^3	13569(3)
d, g cm^{-3}	0.629
μ, mm^{-1}	0.031
Z	8
Measured reflections	17486
Independent reflections	6205
Observed reflections	5044
θ_{min} , º	0.834
θ_{max} , º	14.357
h	-8 to 11
k	-19 to 19
l	-35 to 36
R int	0.0592
$R\ [F^2>2\sigma(F^2)]$	0.0323
$wR(F^2)$	0.0675
S	0.965
Parameters	416
Restraints	0
Flack parameter	0.9(3)
$\Delta\rho_{max}$, e Å^{-3}	0.079
$\Delta\rho_{min}$, e Å^{-3}	-0.091
Crystal size, mm^3	0.040 x 0.040 x 0.030
Radiation, Å	0.49594
Temperature, K	298
Pressure, GPa	0.32

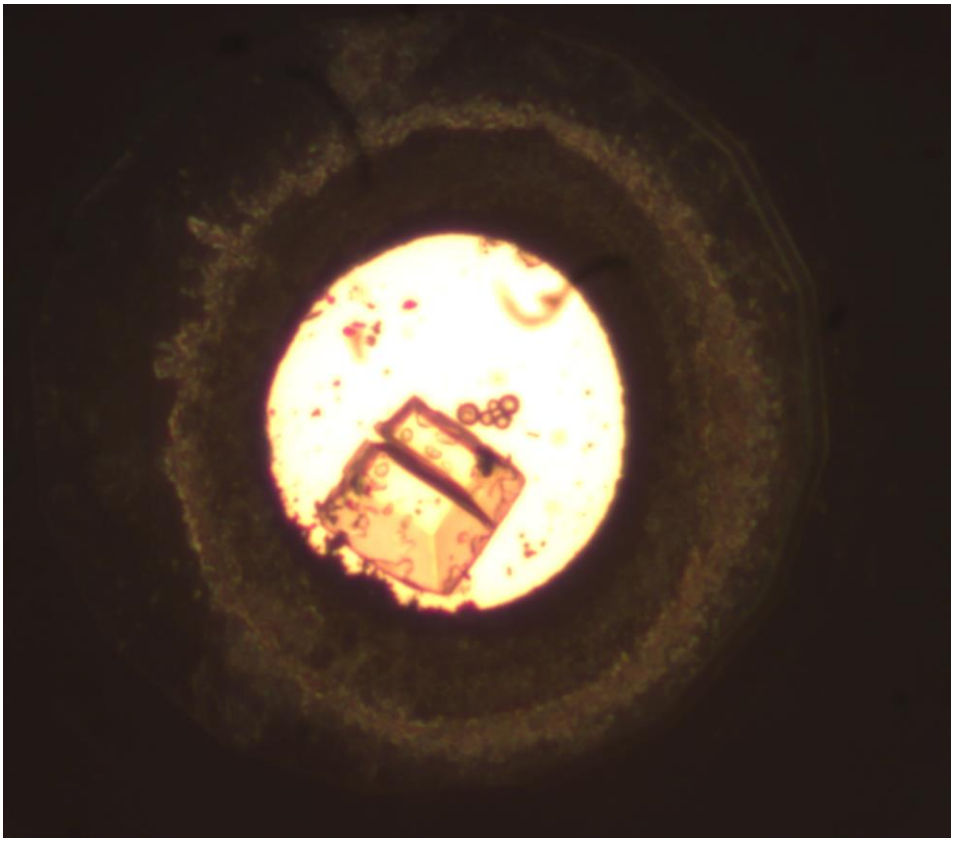

Figure S3.9. Degradation of pristine MOF-520 single crystal under high pressure. The cracking occurred at pressures higher than 3 GPa. At this point, the sample turned completely amorphous, preserving, however, its crystalline shape.

Summary of geometrical parameters for MOF-520 and MOF-520-BPDC under compression

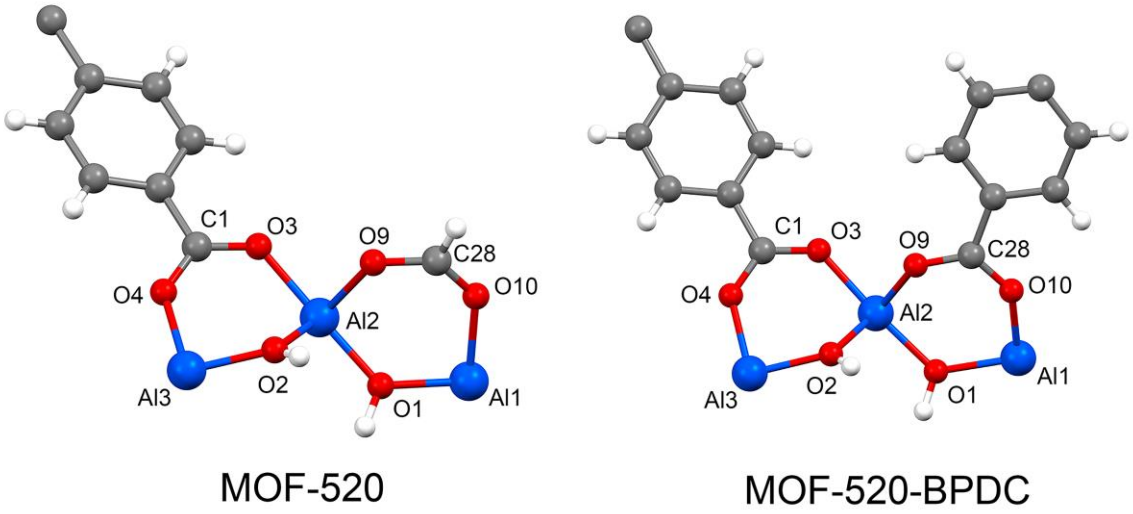

Figure S3.10. Crystal structures of MOF-520 and MOF-520-BPDC. Selected atoms are labeled for geometrical comparison clarity.

Table S3.21. List of Al-O bond lengths in the Al-based SBU in MOF-520 and MOF-520-BPDC at selected pressures.

MOF-520 Al-O bond lengths / Å					MOF-520-BPDC Al-O bond lengths / Å				
Pressure / GPa	Al3-O4	Al2-O3	Al2-O9	A1-O10	Pressure / GPa	Al3-O4	Al2-O3	Al2-O9	A1-O10
0.0001	1.907(2)	1.904(2)	1.909(2)	1.945(2)	0.0001	1.921(3)	1.909(3)	1.921(3)	1.881(3)
0.86(2)	1.893(5)	1.901(5)	1.885(4)	1.926(5)	0.64(2)	1.910(7)	1.896(7)	1.941(6)	1.875(6)
1.47(2)	1.888(5)	1.912(5)	1.857(4)	1.914(5)	1.67(2)	1.903(3)	1.920(2)	1.919(3)	1.877(3)
2.81(2)	1.860(4)	1.935(4)	1.878(4)	1.886(4)	2.86(2)	1.919(4)	1.937(3)	1.937(4)	1.878(3)

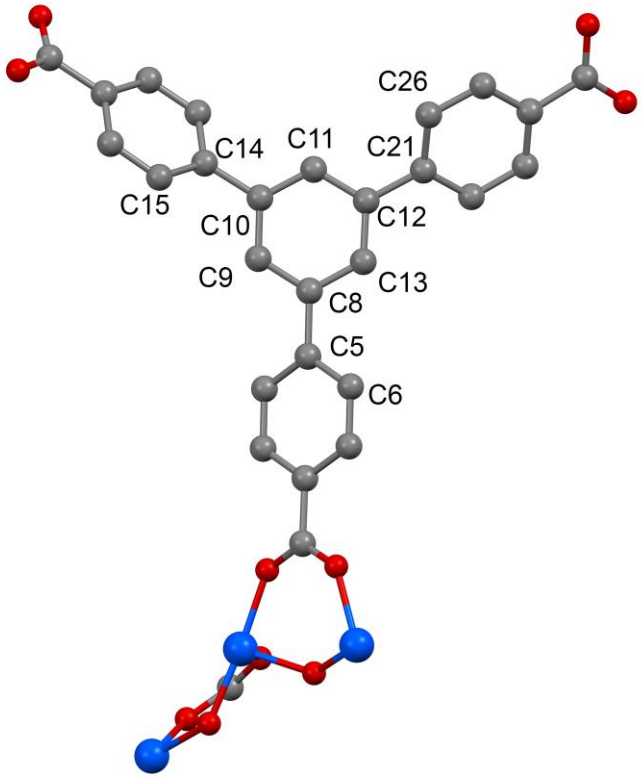

Figure S3.11. Crystal structures of MOF-520 and MOF-520-BPDC. Selected atoms are labeled for geometrical comparison clarity.

Table S3.22. List of torsion angles of BTB organic linkers in MOF-520 and MOF-520-BPDC at selected pressures.

MOF-520 BTB linker C-C-C-C torsion angle / °				MOF-520-BPDC BTB linker C-C-C-C torsion angle / °			
Pressure / GPa	6-5-8-13	11-12-21-26	9-10-14-15	Pressure / GPa	6-5-8-13	11-12-21-26	9-10-14-15
0.0001	24.9(3)	31.0(3)	28.5(3)	0.0001	35.9(4)	32.7(4)	42.3(4)
0.86(2)	20(1)	34(1)	25(1)	0.64(2)	35(1)	34(1)	41(1)
1.47(2)	21(1)	33(1)	31(1)	1.67(2)	37(1)	36(1)	33(1)
2.81(2)	27(1)	33(1)	17(1)	2.86(2)	29(1)	41(1)	32(1)

References for Chapter 3

(1) Lin, X.; Telepeni, I.; Blake, A. J.; Dailly, A.; Brown, C. M.; Simmons, J. M.; Zoppi, M.; Walker, G. S.; Thomas, K. M.; Mays, T. J.; Hubberstey, P.; Champness, N. R.; Schröder, M. *J. Am. Chem. Soc.* **2009**, *131*, 2159–2171.

(2) Furukawa, H.; Ko, N.; Go, Y. B.; Aratani, N.; Choi, S. B.; Choi, E.; Yazaydin, A. O.; Snurr, R. Q.; O'Keeffe, M.; Kim, J.; Yaghi, O. M. *Science* **2010**, *329*, 424–428.

(3) Farha, O. K.; Eryazici, I.; Jeong, N. C.; Hauser, B. G.; Wilmer, C. E.; Sarjeant, A. A.; Snurr, R. Q.; Nguyen, S. T.; Yazaydın, A. Ö.; Hupp, J. T. *J. Am. Chem. Soc.* **2012**, *134*, 15016–15021.

(4) Furukawa, H.; Cordova, K. E.; O'Keeffe, M.; Yaghi, O. M. *Science* **2013**, *341*, 123044.

(5) Seo, J. S.; Whang, D.; Lee, H.; Jun, S. I.; Oh, J.; Jeon, Y. J.; Kim, K. *Nature* **2000**, *404*, 982–986.

(6) Zhao, X.; Xiao, B.; Fletcher, A. J.; Thomas, K. M.; Bradshaw, D.; Rosseinsky, M. J. *Science* **2004**, *306*, 1012–1015.

(7) Nugent, P.; Belmabkhout, Y.; Burd, S. D.; Cairns, A. J.; Luebke, R.; Forrest, K.; Pham, T.; Ma, S.; Space, B.; Wojtas, L.; Eddaoudi, M.; Zaworotko, M. J. *Nature* **2013**, *495*, 80–84.

(8) Faust, T. *Nat. Chem.* **2016**, *811*.

(9) Gándara, F.; Furukawa, H.; Lee, S.; Yaghi, O. M. *J. Am. Chem. Soc.* **2014**, *136*, 5271–5274.

(10) Merrill, L.; Bassett, W. A. *Rev. Sci. Instrum.* **1974**, *45*, 290–294.

(11) Angel, R. J.; Bujak, M.; Zhao, J.; Gatta, G. D.; Jacobsen, S. D. *J. Appl. Crystallogr.* **2007**, *40*, 26–32.

(12) Gagnon, K. J.; Beavers, C. M.; Clearfield, A. *J. Am. Chem. Soc.* **2013**, *135*, 1252–1255.

(13) Bennett, T. D.; Cheetham, A. K. *Acc. Chem. Res.* **2014**, *47*, 1555–1562.

(14) Gándara, F.; Bennett, T. D. *IUCrJ* **2014**, *1*, 563–570.

(15) Coudert, F.-X. *Acta Crystallogr. Sect. B Struct. Sci. Cryst. Eng. Mater.* **2015**, *71*, 585–586.

(16) McKellar, S. C.; Moggach, S. A. *Acta Crystallogr. Sect. B Struct. Sci. Cryst. Eng. Mater.* **2015**, *71*, 587–607.

(17) Cai, W.; Gładysiak, A.; Anioła, M.; Smith, V. J.; Barbour, L. J.; Katrusiak, A. *J. Am. Chem. Soc.* **2015**, *137*, 9296–9301.

(18) Im, J.; Yim, N.; Kim, J.; Vogt, T.; Lee, Y. *J. Am. Chem. Soc.* **2016**, *138*, 11477–11480.

(19) Graham, A. J.; Allan, D. R.; Muszkiewicz, A.; Morrison, C. A.; Moggach, S. A. *Angew. Chemie Int. Ed.* **2011**, *50*, 11138–11141.

(20) Graham, A. J.; Tan, J.-C.; Allan, D. R.; Moggach, S. A. *Chem. Commun.* **2012**, *48*, 1535–1537.

(21) Moggach, S. A.; Bennett, T. D.; Cheetham, A. K. *Angew. Chemie Int. Ed.* **2009**, *48*, 7087–7089.

(22) Hobday, C. L.; Marshall, R. J.; Murphie, C. F.; Sotelo, J.; Richards, T.; Allan, D. R.; Düren, T.; Coudert, F.-X.; Forgan, R. S.; Morrison, C. A.; Moggach, S. A.; Bennett, T. D. *Angew. Chemie Int. Ed.* **2016**, *55*, 2401–2405.

(23) O'Keeffe, M.; Yaghi, O. M. *Chem. Rev.* **2012**, *112*, 675–702.

(24) Piermarini, G. J.; Block, S.; Barnett, J. D.; Forman, R. A. *J. Appl. Phys.* **1975**, *46*, 2774–2780.

(25) Spek, A. L. *Acta Crystallogr. Sect. C, Struct. Chem.* **2015**, *71*, 9–18.

(26) Cliffe, M. J.; Goodwin, A. L.; IUCr. *J. Appl. Crystallogr.* **2012**, *45*, 1321–1329.

(27) Lee, S.; Kapustin, E. A.; Yaghi, O. M. *Science* **2016**, *353*, 808–811.

(28) Ortiz, A. U.; Boutin, A.; Fuchs, A. H.; Coudert, F.-X. *J. Chem. Phys.* **2013**, *138*, 174703.

(29) Clark, S. M.; MacDowell, A. A.; Knight, J.; Kalkan, B.; Yan, J.; Chen, B.; Williams, Q. *Synchrotron Radiat. News* **2012**, *25*, 10–11.

(30) Dolomanov, O. V.; Bourhis, L. J.; Gildea, R. J.; Howard, J. A. K.; Puschmann, H. *J. Appl. Crystallogr.* **2009**, *42*, 339–341.

(31) Macrae, C. F.; Edgington, P. R.; McCabe, P.; Pidcock, E.; Shields, G. P.; Taylor, R.; Towler, M.; van de Streek, J. *J. Appl. Crystallogr.* **2006**, *39*, 453–457.

Chapter 4

Water Harvesting from Air with Metal–Organic Frameworks Powered by Natural Sunlight

Portions of this chapter have been previously published in:
Kim, H., Yang, S., Rao, R. S., Narayanan, S., Kapustin, E. A., Furukawa, H., Umans, A. S., Yaghi, O. M. & Wang, E. N. Water Harvesting from Air with Metal-Organic Frameworks Powered by Natural Sunlight *Science* **356**, 430–434. (2017).

4.1 Preface

In the previous Chapter 2, we discussed the importance of knowledge of structural parameters of guests in MOFs. In the previous Chapter 3, we went even further and demonstrated the applicability of this knowledge towards the retrofitting of the parent MOF with guests. In the following Chapters, we focus on the study and applications of the most common guest molecules in MOFs — water. Indubitably, water is the most important molecule of life, and atmospheric water in particular is a natural resource equivalent to ~10% of all fresh water in lakes on Earth. However, an efficient process for capturing and delivering water from air, especially at low humidity levels (down to 20%), has not been developed. In this Chapter, we described the design and demonstration of a device based on MOF-801 [$Zr_6O_4(OH)_4$(fumarate)$_6$]} that captures water from the atmosphere at ambient conditions by using low-grade heat from natural sunlight at a flux of less than 1 sun (1 kilowatt per square meter). This device is potentially capable of harvesting 2.8 liters of water per kilogram of MOF daily at relative humidity levels as low as 20% and requires no input of energy other than sunlight. This work was done in collaboration with Hyunho Lee, Sungwoo Yang, Sameer Rao, Shankar Narayanan, Hiroyasu Furukawa, Ari Umans, Evelyn N. Wang.

4.2 Introduction

Two-thirds of the world's population is experiencing water shortages[1]. The water in the form of vapor and droplets in the atmosphere, estimated to be about 13 thousand trillion liters[2], is a natural resource that could address the global water problem. Although there has been interest in dewing[3–6] from moist air and fog capture[7–9], these processes require either the frequent presence of 100% relative humidity (RH) or a large amount of energy and thus are not viable solutions for the capture of water from air. Ideally, a water harvesting system should operate with a material that can take up and release water with minimum energy requirements and that is powered by low-grade energy sources, such as sunlight, in order to potentially allow its deployment in households, especially those located in sunny regions. Here, we demonstrate water harvesting by vapor adsorption using a microcrystalline powder form of MOF-801 in ambient air with low RH typical of the levels found in most dry regions of the world (down to a RH of 20%)[10]. We also report a device based on this MOF that can harvest and deliver water (2.8 liters of water per kilogram of MOF per day at 20% RH) under a nonconcentrated solar flux less than 1 sun (1 kW m^{-2}), requiring no additional power input for producing water at ambient temperature outdoors.

4.3 Choice of material

Porous materials, such as zeolites, silica gels, and MOFs, can harvest water from air by adsorption over a wide range of humidity values[11–13]. However, conventional adsorbents (e.g., zeolites and silica gels) suffer from either low uptake of water or requiring high energy consumption to release water. Although MOFs have already been considered in numerous applications — including gas storage, separation, and catalysis[14–16]; heat pumps[17,18]; and dehumidification[19] — the use of MOFs for water harvesting has only recently been proposed[10]. The flexibility with which MOFs can be made and modified at the molecular level, coupled with their ultrahigh porosity, makes them ideally suited for overcoming the challenges mentioned above[20–22].

A critical step is the release of water from the MOF, for which we applied a low-grade heat–driven vapor-desorption process[23,24]. Solar energy is particularly promising because sunlight is often abundant in arid regions with low RH (>7 kilowatt-hours m^{-2} day^{-1}, equivalent to 7 hours of 1 sun per day) where water resources are limited and where a natural diurnal temperature swing thermally assists the process (adsorption of water during the cooler night and release during the warmer day). This strategy is much more energy-efficient compared with refrigeration-based dew-harvesting systems because heat is directly used for desorption. The amount of water that can be harvested with MOFs can be much greater than with dew-harvesting systems, which become impractical at RHs less than 50% (see the efficiency comparison in the Supporting Information for this Chapter).

To use MOFs to harvest water with maximum yield and minimal energy consumption, an isotherm with a steep increase in water uptake within a narrow range of RH is desired, which enables maximum regeneration with minimal temperature increase. Recent MOFs have exhibited such sorption characteristics (Figure 4.1A). In particular, MOF-801 is suitable for regions where RH is merely 20% (e.g., North Africa), and UiO-66[10,25] is suitable for regions with ~40% RH (e.g., northern India). We harvested water with MOF-801 and natural sunlight at <1 sun in an environment at regeneration temperatures of ~65°C. Once water vapor adsorbed into the MOF, solar energy was used to release the adsorbate. Water was then harvested using a condenser maintained at temperatures near that of the surrounding environment. For MOF-801, a temperature swing between 25° and 65°C can harvest more than 0.25 liters kg^{-1} at >0.6 kPa vapor pressure (20% RH at 25°C; Figure 4.1B). This water-harvesting strategy is completely passive, relying only on the high water uptake capacity, low-grade heat requirement for desorption, and ambient temperatures to condense and collect the water (Figure 4.1C).

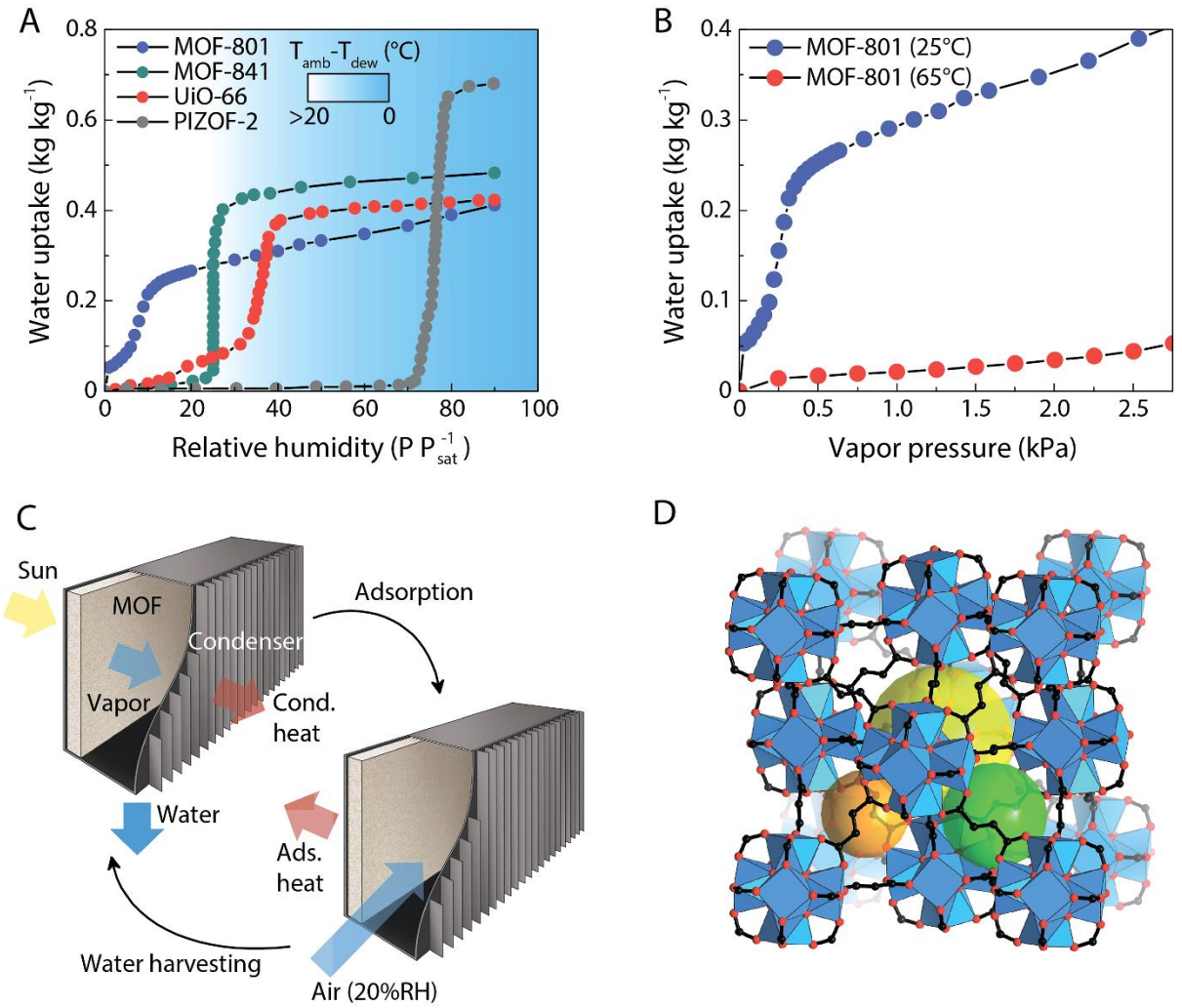

Figure 4.1. Working principle of water harvesting with MOFs. (**A**) Water-adsorption isotherms of Zr-based MOFs (MOF-801, MOF-841, UiO-66, and PIZOF-2) at 25°C, showing a rapid increase in adsorption capacities (in kilograms of water per kilogram of MOF) with a relatively small change in the relative humidity (RH) ($P\,P_{sat}^{-1}$, vapor pressure over saturation pressure)[10]. The background color map shows the minimum difference between the temperatures of the ambient air (T_{amb}) and the condenser (T_{dew}) required for dew collection with active cooling. (**B**) Water-adsorption isotherms of MOF-801, measured at 25° and 65°C, illustrating that the temperature swing can harvest greater than 0.25 kg kg^{-1} at >0.6 kPa vapor pressure (20% RH at 25°C). (**C**) A MOF water-harvesting system, composed of a MOF layer and a condenser, undergoing solar-assisted water-harvesting and adsorption processes. During water harvesting (left), the desorbed vapor is condensed at the ambient temperature and delivered through a passive heat sink, requiring no additional energy input. During water capture, the vapor is adsorbed on the MOF layer, transferring the heat to the ambient surroundings (right). Ads. and cond., adsorption and condensation, respectively. (**D**) $Zr_6O_4(OH)_4(\text{-}COO)_{12}$ secondary building units are linked together with fumarates to form MOF-801. The large yellow, orange, and green spheres are three different pores. Black, C; red, O; blue polyhedra, Zr.

For our approach, MOF-801 has several advantages: (i) well-studied water-adsorption behavior on a molecular level, (ii) good performance driven by aggregation of water molecules into clusters within the pores of the MOF, (iii) exceptional stability and recycling, and (iv) constituents that are widely available and low-cost. It is composed of 12-connected Zr-based clusters [$Zr_6O_4(OH)_4(\text{-}COO)_{12}$] joined by fumarate linkers into a three-dimensional, extended porous framework of face-centered cubic topology. The structure of MOF-801 contains three

symmetrically independent cavities into which water molecules can be captured and concentrated (Figure 4.1D).

4.4 Adsorption-desorption cycle under controlled conditions

We carried out the adsorption-desorption experiments for water harvesting with MOF-801 at 20% RH. A powder of MOF-801 was synthesized as reported before[10] and activated (solvent removal from the pores) by heating at 150°C under vacuum for 24 hours. The powder was infiltrated into a porous copper foam with a thickness of 0.41 cm and porosity of ~0.95, which was brazed on a copper substrate to create an adsorbent layer (5 by 5 by 0.41 cm) with 1.79 g of activated MOF-801, an average packing porosity of ~0.85 (Figure 4.2A), and enhanced structural rigidity and thermal transport. This particular geometry with a high ratio of layer area to thickness was selected to reduce parasitic heat loss.

Experiments were performed in a RH-controlled environmental chamber interfaced with a solar simulator. The fabricated MOF-801 layer was placed in the chamber (Figure 4.2A) and evacuated under high vacuum (less than 1 Pa) at 90°C. Water vapor was then introduced inside the chamber to maintain a condition equivalent to a partial vapor pressure of 20% RH at 35°C, matching the steep rise in water uptake for MOF-801 (Figure 4.1A). Vapor was adsorbed onto the sample surfaces by diffusion (Figure 4.2B). After saturation, the chamber was isolated from the vapor source. A solar flux (1 kW m^{-2}, air mass 1.5 spectrum) was introduced to the graphite-coated substrate layer with a solar absorptance of 0.91 to desorb water from the MOF. This water was then collected using a condenser interfaced with a thermoelectric cooler, which maintained the isobaric conditions of ~1.2 kPa (20% RH at 35°C, saturation temperature of ~10°C). By maintaining the isobaric conditions, all of the desorbed vapor was condensed and harvested by the condenser. During desorption, the water-harvesting rate (or vapor-desorption rate) was continuously monitored with a heat flux sensor interfaced to the condenser. The environmental temperature above standard ambient temperature was necessary to perform the experiments at >1 kPa; otherwise, a much lower condenser temperature would be needed (e.g., ~0.5°C for 20% RH at 25°C). Thermocouples were placed on both sides of the MOF-801 layer to monitor the dynamic temperature response.

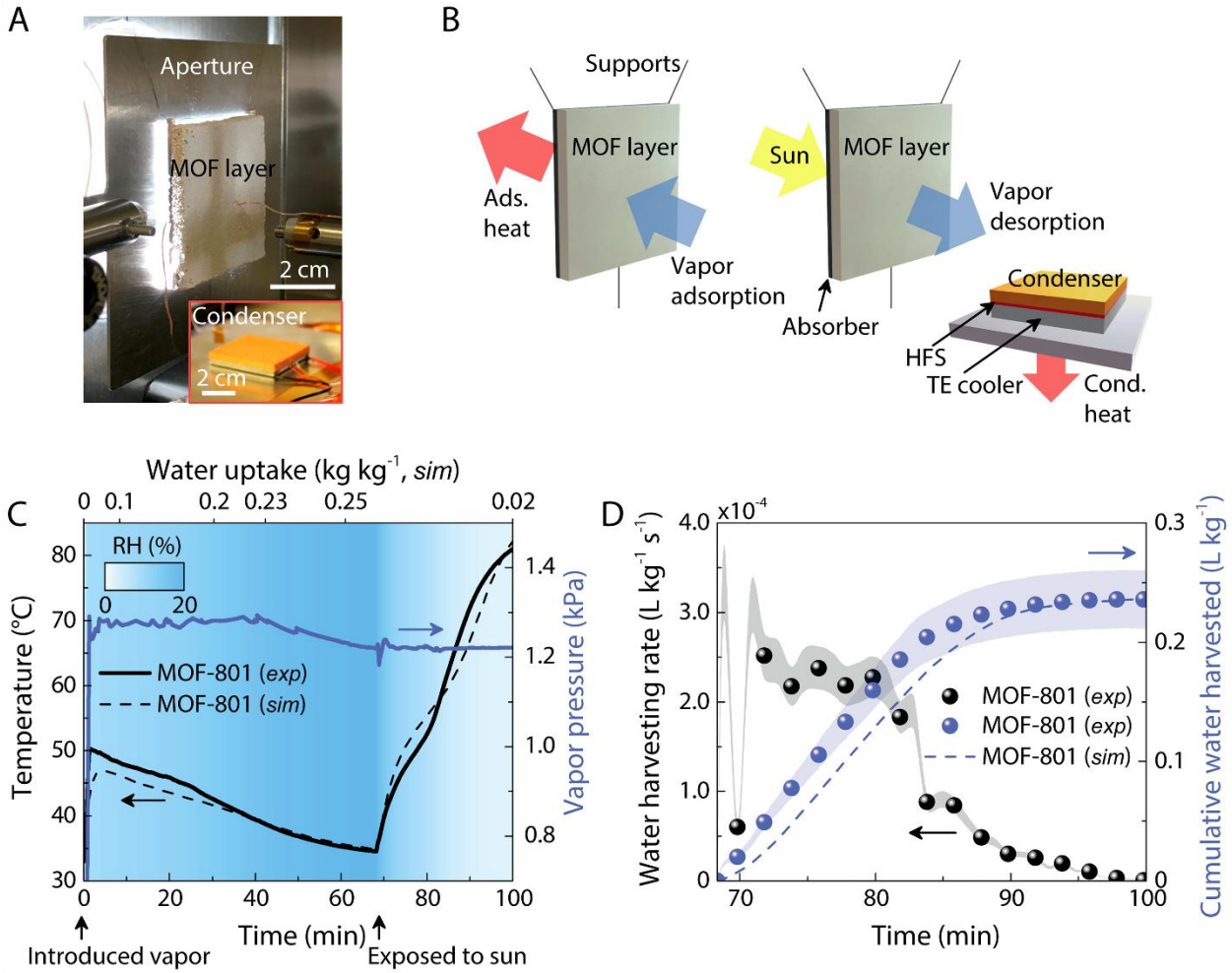

Figure 4.2. Experimental characterization of harvested water from an adsorption-desorption cycle with MOF-801. (**A**) Image of the MOF-801 layer and condenser. (**B**) The schematic illustrates the vapor adsorption and desorption experiments carried out under isobaric conditions. Vapor was adsorbed through the sample surface by diffusion. Desorption was achieved by applying an incident solar flux on an absorber with a solar absorptance of 0.91, and the desorbed vapor was condensed simultaneously in the condenser to harvest water. The condensation heat was monitored using a heat flux sensor (HFS) with active cooling through a thermoelectric (TE) cooler. (**C**) Layer temperature and chamber vapor pressure as functions of time during the water-harvesting cycle. The background color map represents the estimated RH from the chamber pressure and the layer temperature, and the upper abscissa represents the overall water uptake predicted from the theoretical model as a function of time (lower abscissa). (**D**) Experimentally characterized water-harvesting rate (liters per kilogram per second) and cumulative harvested water (liters per kilogram) during desorption. The shaded region represents the error based on uncertainties of the heat flux and MOF-801 weight measurements. The predicted temperature profile and cumulative water harvested are also included in (**C**) and (**D**), respectively, showing good agreement. The activated MOF-801 has a weight of 1.79 g, a layer thickness of 0.41 cm, and a packing porosity of ~0.85. *sim* and *exp*, simulated and experimental results, respectively.

Figure 4.2C shows the temperature of the MOF-801 layer and pressure inside the chamber during the adsorption and solar-assisted desorption experiments. During adsorption, the temperature of the MOF-801 layer first rapidly increased because of the exothermic adsorption process and then slowly decreased as heat was lost to the surroundings. After ~70 min of adsorption, the MOF-801 temperature equilibrated with the surrounding vapor temperature of ~35°C. At these adsorption conditions, the predicted water uptake, or potential harvestable

quantity of water, was estimated to be ~0.25 kg of water per kg of MOF, as shown in the upper abscissa of Figure 4.2C. Each water-harvesting cycle, ~0.24 liters kg^{-1} were harvested (Figure 4.2D), as determined by integrating the water-harvesting rate. We further confirmed the experimental result with an adsorption analyzer under identical adsorption-desorption conditions (Figure S4.2A in the Supporting Information).

4.5 Data validation of sorption kinetics using theoretical modelling

A theoretical model was developed to optimize the design of the water-harvesting process with MOF-801, which was further validated with the experimental data. The model framework was based on mass and energy conservation, incorporating adsorption dynamics parameters[26,27], and the analysis was carried out using COMSOL Multiphysics (see the theoretical modelling in the Supporting information). The inter- and intracrystalline vapor diffusion through the layer and within the crystals, as well as the thermal transport through the layer, were considered in the model. The theoretical model results agreed well with the experimental data (Figure 4.2, C and D). We then investigated the water-harvesting behavior under ambient air conditions by incorporating the diffusion and sorption characteristics of MOF-801 at ambient conditions into the theoretical model. We performed a parametric study, including varying the packing porosity (0.5, 0.7, and 0.9) and layer thickness (1, 3, 5, and 10 mm), and determined the time and amount of harvestable water for a solar flux of 1 sun. By considering both the adsorption and desorption dynamics, a porosity of 0.7 was predicted to yield the largest quantity of water. At a porosity of ~0.5 or less, the adsorption kinetics are limited by Knudsen diffusion because the crystal diameter of MOF-801 is only ~0.6 mm (Figure S4.5 in the Supporting information). The characteristic void spacing for Knudsen diffusion is a function of packing porosity and the crystal diameter. However, at higher porosities, a thicker MOF-801 layer is required to harvest a sufficient amount of water, but the time scale and transport resistance for inter-crystalline diffusion also scales with the MOF layer thickness as $t \sim L_c^2/D_v$, where, t, D_v, and L_c are the time scale, intercrystalline diffusivity, and characteristic length scale (*i.e.*, layer thickness), respectively.

Simulated adsorption-desorption dynamics for the MOF-801 layer with the optimized packing porosity of 0.7 are shown in Figure 4.3 for 1 sun and realistic boundary conditions for heat loss (a natural heat transfer coefficient of 10 W m^{-2} K^{-1} and standard ambient temperature). In this simulation, MOF-801 was initially equilibrated at 20% RH, and the vapor content in the air-vapor mixture that surrounds the layer during desorption increased rapidly from 20 to 100% RH at 25°C. This scenario is more realistic compared with the model experiment described above because water is harvested by a condenser at ambient temperature. Once solar irradiation was stopped, the air-vapor concentration reverted to 20% RH for vapor adsorption from ambient air, and the heat from the adsorption process was transferred to the surroundings. A detailed description of the boundary conditions and idealizations in the simulation is given in Supporting information for this Chapter (see the optimization and predictions of MOF-801 for water harvesting).

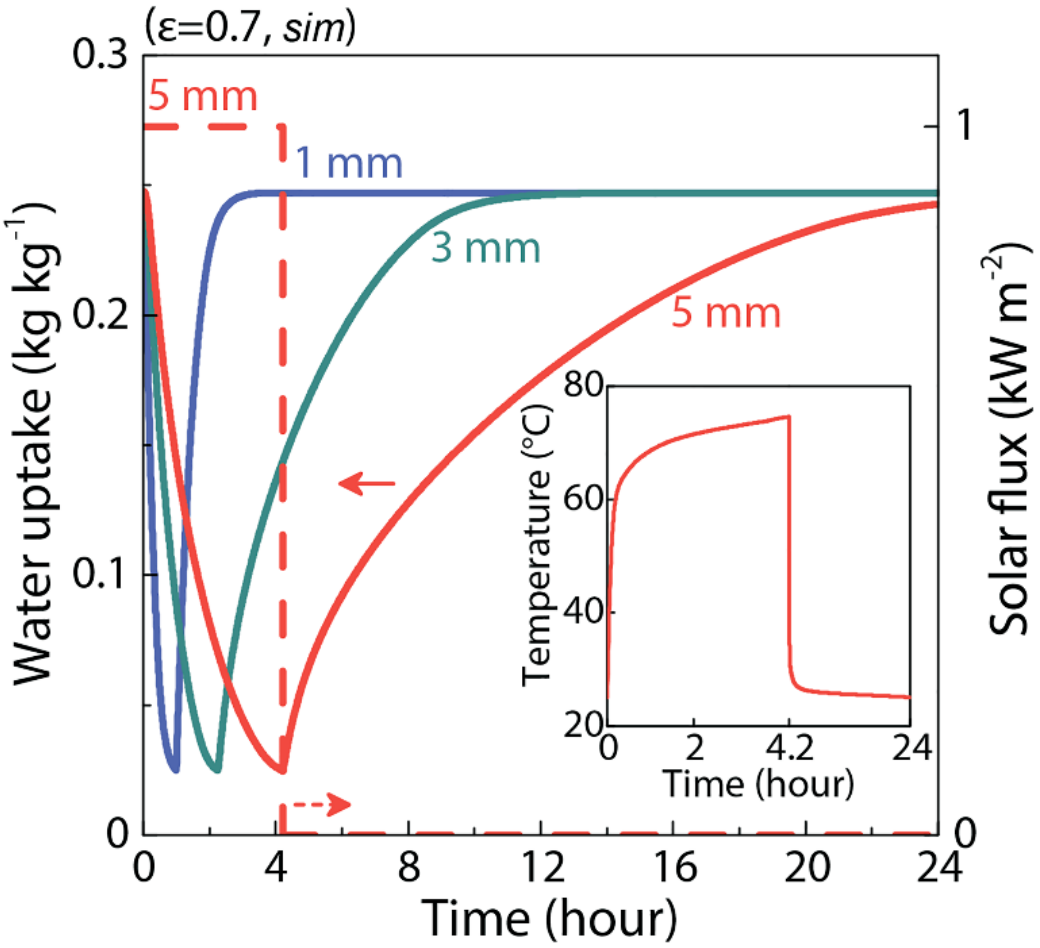

Figure 4.3. Adsorption-desorption dynamics of MOF-801 in ambient air with a flux of 1 sun. Predicted adsorption-desorption dynamics with a packing porosity (ε) of 0.7, solar flux of 1 sun (1 kW m^{-2}), and various thicknesses (1 to 5 mm). MOF-801 was initially equilibrated at 20% RH and 25°C, and the partial vapor pressure rapidly increased to 100% RH at 25°C during desorption for vapor condensation. After desorption, the surrounding air-vapor mixture reverted to 20% RH. The durations of solar exposure for thicknesses of 1, 3, and 5 mm were 1, 2.3, and 4.2 hours, respectively. The duration of solar exposure is plotted only for the 5-mm thick sample (red dashed line) for simplicity. The 1-mm, 3-mm, and 5-mm layers can harvest 0.08, 0.24, and 0.4 liters m^{-2} per complete water-harvesting cycle, respectively. More than 90% of the initially adsorbed water could be harvested under these conditions. The inset shows a predicted temperature profile of the 5-mm-thick layer during the adsorption-desorption processes.

First, water uptake decreased with time during solar heating and water condensation, then increased through adsorption, as shown by the simulated water uptake profiles for the MOF-801 layer at thicknesses of 1, 3, and 5 mm (Figure 4.3). The temperature correspondingly increased and then decreased with time. Continuously harvesting water in a cyclic manner for a 24-hour period with low-grade heat at 1 kW m^{-2} can yield ~2.8 liters kg^{-1} day^{-1} or ~0.9 liters m^{-2} day^{-1} with a 1-mm-thick layer. Alternatively, per one cycle, a 5-mm-thick layer of MOF-801 can harvest ~0.4 liters m^{-2}. Our findings indicate that MOFs with enhanced sorption capacity and high intracrystalline diffusivity — along with an optimized crystal diameter, crystal density, and thickness of the MOF layer — can further boost the daily quantity of water harvested from an arid environment.

4.6 Water harvesting outdoors (Cambridge, Massachusetts)

Last, a proof-of-concept MOF-801 water-harvesting prototype was built to demonstrate the viability of this approach outdoors (Figure 4.4A). This prototype includes a MOF-801 layer (packing porosity of ~0.85, 5 by 5 by 0.31 cm, containing 1.34 g of activated MOF), an acrylic enclosure, and a condenser, and it was tested on a roof at MIT (Cambridge, Massachusetts, United States). The spacing between the layer and condenser in the prototype was chosen to be large enough to enable ease of sample installation and visualization. The activated MOF-801 layer was left on the roof overnight for vapor adsorption from ambient air (day 1). The desorption process using natural sunlight was carried out on day 2 (ambient RH was ~65% at the start of the experiment). For visualization purposes, we used a condenser with a temperature controller to maintain the temperature slightly below ambient levels but above the dew point, in order to prevent vapor condensation on the inner walls of the enclosure. However, active cooling is not needed in a practical device because the hot desorbed vapor can condense at the cooler ambient temperature through a passive heat sink.

The formation, growth, and multiplication of water droplets on the condenser with the change in the MOF layer temperature and time are shown in Figure 4.4B. The temperature and solar flux (global horizontal irradiation) measurements during the solar-assisted desorption process revealed a rapid increase in the MOF-801 temperature, accompanied by the relatively low solar fluxes (Figure 4.4C). Because water harvesting with vapor condensation is done in the presence of noncondensables (air), transport of desorbed vapor from the layer to the condenser surface is by diffusion. Using the experimentally measured solar flux and environmental conditions, as well as the theoretical model incorporating the vapor diffusion resistance between the layer and condenser, we predicted the MOF layer temperature and water uptake profiles (Figure 4.4C). The RHs based on the MOF layer temperature before and after the solar-assisted desorption are ~65% at 25°C and ~10% at 66°C, and the corresponding equilibrium water uptakes under these conditions are ~0.35 kg kg^{-1} and ~0.05 kg kg^{-1}, respectively, at a 23°C condenser temperature (estimated from Figure S4.6B in the Supporting Information). By saturating the MOF layer with ambient air at a solar flux less than 1 sun, ~0.3 liters kg^{-1} potentially can be harvested.

Because of the large spacing between the layer and condenser and the orientation of the prototype, there was a delay in desorption. Therefore, to predict the prototype's water-harvesting potential under equilibrium conditions, we extended the desorption time for the simulation, the results of which match the prediction from the isotherm (~0.3 liters kg^{-1}, shown in the upper abscissa of Figure 4.4C). To fully utilize the steep step in water uptake in the MOF-801 isotherm, a temperature difference of ~45°C between the condenser and the layer is necessary to achieve desorption at 10% RH. For instance, if the initial RH is 20%, ~0.2 liters kg^{-1} can potentially be harvested with MOF-801, which is an order of magnitude greater than yields from conventional adsorbents estimated from isotherms[28,29].

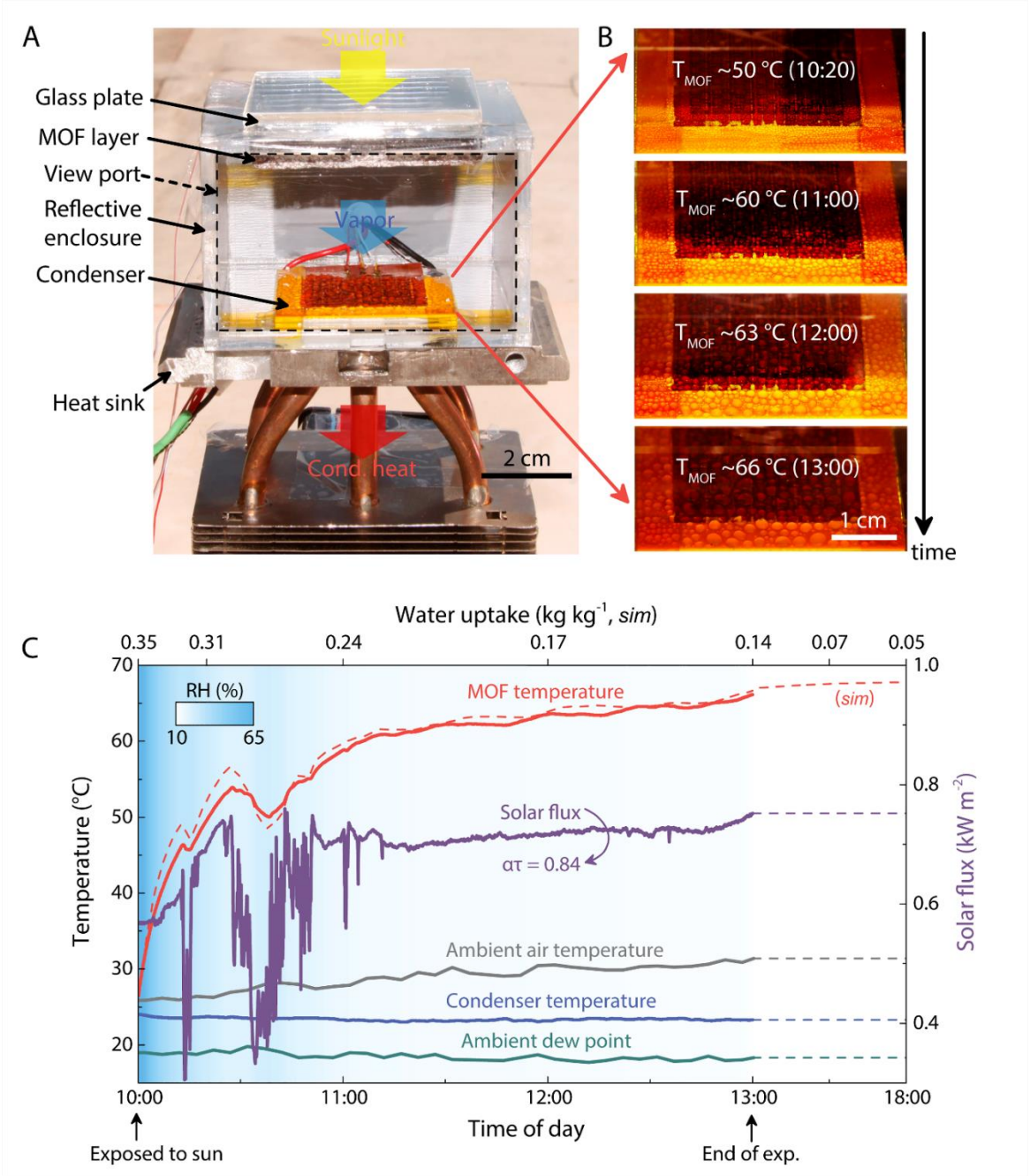

Figure 4.4. Proof-of-concept water-harvesting prototype. (**A**) Image of a water-harvesting prototype with activated MOF-801 with a weight of 1.34 g, a packing porosity of ~0.85, and outer dimensions of 7 by 7 by 4.5 cm. (**B**) Formation and growth of droplets of water as a function of MOF temperatures (T_{MOF}) and local time of day. (**C**) Representative temperature profiles for the MOF-801 layer (experimental, red solid line; predicted, red dashed line), ambient air (gray line), the condenser (blue line), and the ambient dew point (green line), as well as solar flux (purple line), as functions of time of day (14 September 2016). The background color map represents the estimated RH from the condenser saturation pressure and the layer temperature, and the upper abscissa represents the water uptake predicted from the theoretical model as a function of time (lower abscissa). Because of losses from the absorber solar absorptance (α, 0.91) and the glass plate solar transmittance (τ, 0.92), 84% of the solar flux shown in (**C**) was used for desorption. The layer temperature and full water-harvesting potential based on complete desorption were predicted using the solar flux and environmental conditions at the end of the experiment (dashed lines). The fluctuations of the solar flux from 10:20 to 11:00 were due to the presence of clouds.

Supporting Information for Chapter 4

Synthesis of microcrystalline powder MOF-801

In a 4 L glass bottle, 72 g (0.62 mol) of fumaric acid (Fluka, 99%) and 200 g (0.62 mol) of $ZrOCl_2 \cdot 8H_2O$ (Alfa Aesar, 98%) were dissolved in a mixed solvent of DMF and formic acid (2 L and 700 mL, respectively). The mixture was then heated in an isothermal oven at 130 ºC for 6 hours to give as-prepared MOF-801 as white precipitate. The precipitate was collected by filtration apparatus using a membrane filter (45 μm pore size), washed three times with 400 mL DMF, three times 400 mL methanol, and dried in air. Air-dried MOF sample was transferred to a vacuum chamber equipped with a magnetic stirring bar. The chamber was first evacuated at room temperature without stirring for 2 hours until the pressure dropped below 15 kPa. After that, with gentle stirring, the sample was further evacuated at room temperature for another 12 hours, heated in vacuum at 70 ºC for 6 hours, and then at 150 ºC for another 24 hours. This finally gave activated MOF-801 as a white powder (yield: 101 g). Further details can be found in a recent study[10].

Sample fabrication and experimental methodology: Vacuum chamber experiment

Activated MOF-801 was infiltrated in a copper porous foam (~100 ppi), 0.41 cm thick, brazed on a (5 by 5 cm) copper plate with a thickness of 1.7 mm by immersing the foam-plate structure in a MOF-801 suspension in DI water. Copper foam was used to enhance structural rigidity, and to overcome the intrinsically low thermal conductivity of the porous adsorbent[30]. The thermal conductivity, k, of the foam was estimated to be ~4 W m^{-1} K^{-1}. The conduction resistance with the metallic foam ($L\ k^{-1}$, L being thickness, ~4 mm, and k being the thermal conductivity of the MOF layer) was ~10^{-2} of the convective resistance (h^{-1}, h being a convective heat transfer coefficient). The weights of MOF-801 and copper foam-plate structures were 1.79 g and 41 g, respectively. Use of an ultra-light thermal and structural binder, such as carbon-based foam[31], can reduce the overall weight significantly. The packing density of infiltrated MOF-801 (170 kg m^{-3}) was characterized by letting it equilibrate in a laboratory environment for ~1 day and measuring the dehydrated weight of the surface powdered MOF-801 using an adsorption analyzer (DVS Vacuum, Surface Measurement Systems Ltd.) under high vacuum (<1E-4 Pa) at 120 °C. The back side of the sample (copper plate side) was coated with a graphite spray (dgf 123 dry graphite film lubricant, Miracle Power Products Corp.) to make the surface absorptive for solar irradiance. Solar-weighted absorptivity (in the 250-2,500 nm wavelength range) was characterized to be 0.91 using a UV-Vis-NIR spectrophotometer (Cary 5000, Agilent). The sample was hung on a stand supported with metallic wires to minimize conduction losses, and an aperture was placed next to the sample, as shown in Figure S4.2A. The condenser was fabricated by stacking the thermoelectric cooler (TE-127-1.0-1.5, TE technology), the heat flux sensor (HFS-4, Omega Engineering), and the copper foam using conductive pads (TFLEX 720, Laird Technologies). The copper foam attached to the condenser was used to promote condensation with a high surface area and to avoid water dripping from capillary pressure induced by the pores in the foam. Degassed reagent-grade water (Sigma-Aldrich, CAS:7732-18-5) was used during the water harvesting experiments. The simulated solar flux equivalent to 1 kW m^{-2} (AM1.5 spectrum; 92192, Newport Oriel) was measured at the absorber side of the sample plane using a thermopile detector (919P-040-50, Newport) with an active diameter of 5 cm. Thermocouples (J type 5TC series, Omega Engineering.) were used to measure both sides of the sample, and also vapor temperatures. Outgassing of each component during the experiments was found to be

negligible, and a schematic of the vacuum chamber system used for the water harvesting experiments is shown in Figure S4.1. The effective heat transfer coefficient inside the chamber was characterized to be 7 to 9 W m^{-2} K^{-1} with a Kapton heater (KHL kapton flexible heater, Omega) coated with the graphite spray.

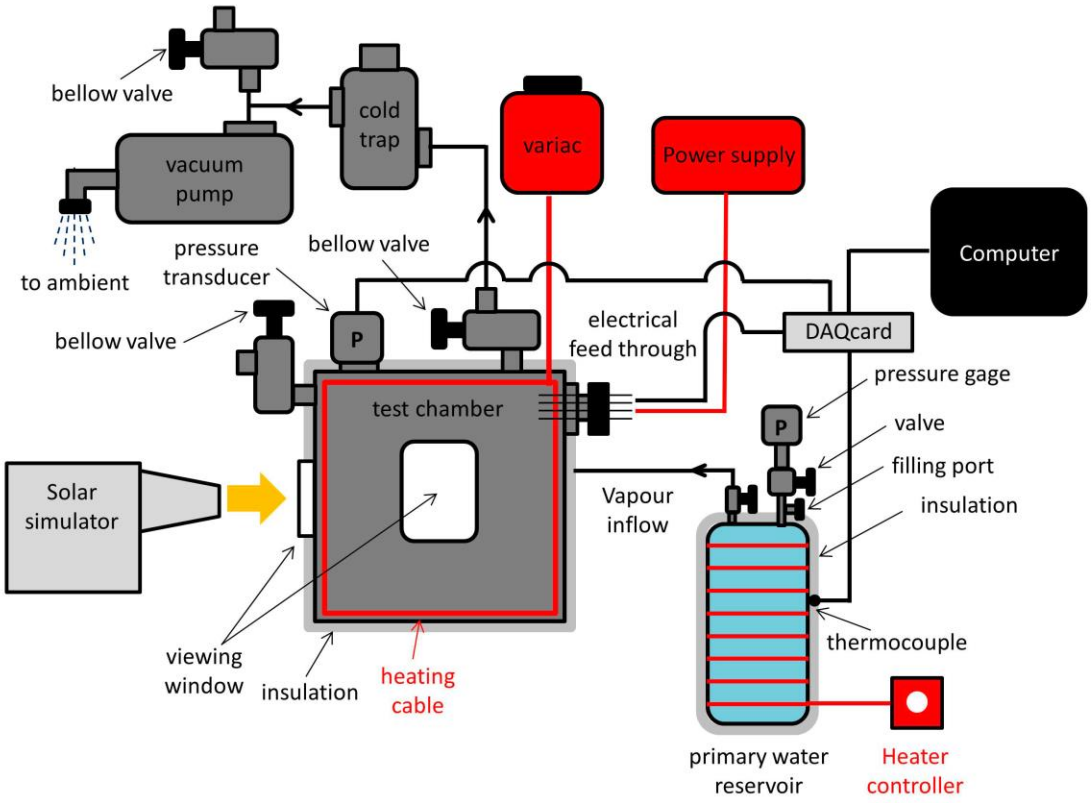

Figure S4.1. Schematic of vacuum chamber system used for water harvesting experiments. Degassed vapor was provided from a primary water reservoir and simulated solar flux was provided through a glass view port. The chamber temperature was controlled with a heating cable and variac power supply. A data acquisition system was used to measure the MOF-801 layer, vapor, and condenser temperatures, and the heat flux readings. A power supply was used to control the condenser temperature.

Prior to the experiments in the environmental chamber, the fabricated MOF-801 layer was evacuated at high vacuum (< 1 Pa) and high temperature (~90 °C) for ~1 hour to remove initially adsorbed vapor. The chamber walls were maintained at ~35 °C throughout the entire experiment. After the evacuation process, the sample was cooled down to a temperature ~35 °C through radiative heat exchange with the chamber wall. Once the sample was thermally equilibrated with the chamber, adsorption was carried out by introducing degassed water vapor into the chamber. The vapor pressure was maintained ~1.2 kPa, monitored using a pressure sensor (722B Baratron, MKS instruments), by regulating a valve connecting a vapor source and the chamber. This pressure corresponds to 20% RH at 35 °C, which allows the utilization of the steep rise in water uptake observed from the adsorption isotherm shown in Figure 4.1A (main text in Chapter 4). An isobaric condition was maintained for ~70 minutes; the sample

temperature reached ~35 °C and the reduction in pressure due to adsorption was negligibly small. Then, the desorption was carried out by isolating the chamber from the vapor source and introducing simulated solar flux equivalent to 1 kW m-2 (AM1.5 spectrum) to the graphite-coated substrate surface through a glass view port. During the desorption process, the condenser was maintained at a constant temperature of ~10 °C, a saturation temperature corresponding to ~1.2 kPa using a thermoelectric cooler (TE-127-1.0-1.5, TE technology), to actively ensure an isobaric environment in the chamber. Desorbed vapor from the sample was condensed on the condenser and the heat from the condensation process was monitored using the heat flux sensor. Desorption experiment was carried out until the heat flux readings reached the baseline, which was in ~30 minutes. The vapor temperature inside the chamber was also maintained constant at ~35 °C, monitored using multiple thermocouples, during the experiment.

Sample fabrication and experimental methodology: Outdoor proof-of-concept demonstration

The proof-of-concept prototype enclosure was fabricated with reflective acrylic sheets (coated with aluminum and 0.318 cm thick) to reflect incoming solar incidence during the experiment. One of the lateral faces was made of transparent plastic for visualization purposes as shown in Figure 4.4A (main text in Chapter 4). Vacuum grease (high vacuum grease, Dow Corning), acrylic cement (TAP Plastics), and transparent food-grade wrap, and adhesive tape were used to seal the enclosure. A thermal compound (340 heat sink compound, Dow Corning) was used to bond the condenser (TE-127-1.0-1.5, TE technology) side of the enclosure onto a heat sink. The MOF-801 layer was hung on the top wall of the enclosure with nylon threads. A glass plate (solar transmittance of 0.92, measured with the UV-Vis-NIR spectrophotometer) was placed on the top of the absorber to suppress convective losses during the experiment. The finished prototype measured 7 cm × 7 cm × 4.5 cm, excluding the heat sink. Thermocouples were used to measure both sides of the MOF-801 layer (center of the layer), as well as the condenser. The estimated effective heat transfer coefficient experienced by the MOF-801 layer during the outdoor demonstration was ~9 W m^{-2} K^{-1}. Further improvements can be made with an optimized spacing between the layer and the condenser (optimization of heat loss between the layer and condenser, and diffusion process for vapor condensation), and with a simple radiative insulation, such as using bubble wrap insulation for solar steamers[32], optically transparent and thermally insulating aerogels[33], or with highly absorptive coatings for solar irradiation (e.g., Pyromark coating).

For the outdoor experimental demonstration, the MOF-801 layer was left overnight on a roof at MIT overnight (day 1; September 13, 2016) for vapor adsorption from ambient air. The layer was incorporated into the enclosure and sealed the next day (at 9:30 AM with ~65% RH; day 2, September 14, 2016). The enclosure integrated with a heat sink was placed on a flat surface and the solar-assisted water harvesting experiment was carried out (10:00 AM – 1:00 PM; day 2). The condenser temperature was set slightly below the ambient air temperature at the start of the experiment using the thermoelectric cooler and a controller (TC-720, TE technology), and was always above the dew point temperature of ambient air. A pyranometer (LP02-C, Hukseflux) was used to measure the incident solar flux on the horizontal plane (global horizontal irradiation). The ambient air temperature and RH data were obtained from a weather station on the roof.

Efficiency comparison of MOF-based water harvesting system

We can determine the energy efficiency of our MOF-based water harvesting system to enable comparison with refrigeration enabled systems for water capture (dewing). From an energy balance on the MOF- and refrigeration-based water harvesting systems operating with a thermal or solar energy input (primary energy), the amount of harvested water can be defined as,

$$(m_w)_{MOF} = \frac{Q_{thermal} - Q_{loss}}{h_{ad}} \tag{4.1}$$

$$(m_w)_{REF} = \frac{Q_{thermal}\eta_{conv}COP_{REF} - Q_{gain}}{h_{fg}} \tag{4.2}$$

where m_w is the amount of harvested water, $Q_{thermal}$ is thermal energy input, Q_{loss} is heat loss from the MOF layer to the environment, h_{ad} is the enthalpy of adsorption, η_{conv} is thermal or solar energy to electricity conversion efficiency, COP_{REF} is coefficient of performance (COP) of refrigeration cycle, Q_{gain} is heat transfer from the environment to the dew collecting surface, and h_{fg} is the latent heat of evaporation. In Equation 4.1, sensible heat contribution is neglected, and in Equation 4.2, the maximum water harvesting is when Q_{gain} is minimal and this is possible only when relative humidity (RH) is high. Assuming the enthalpy of adsorption is approximately equal to the latent heat of evaporation, the ratio between the amounts of harvested water for the MOF as compared to a refrigeration cycle for equal input energy ($Q_{thermal}$) is

$$\frac{(m_w)_{MOF}}{(m_w)_{REF}} \approx \frac{Q_{thermal} - Q_{loss}}{Q_{thermal}\eta_{conv}COP_{REF} - Q_{gain}} \tag{4.3}$$

Heat loss (Q_{loss}) from the MOF layer can be minimized by using thermal insulation, and for a high RH condition, Q_{gain} can be negligible. Therefore, neglecting Q_{loss} and Q_{gain}, a first order estimation of Equation 4.3 for representative values of COP_{REF} (~2)[34] and η_{conv} (~20%)[35] is 2.5. The ratio drastically increases with decreasing RHs because the temperature requirement for the dew collection decreases substantially (increasing $Q_{gain} = hA\Delta T$, where h, A, and ΔT are convective heat transfer coefficient in W m^{-2} K^{-1}, area of dew collecting surface in m^2, and temperature difference between the surface and ambient air in K (>25 °C at 20% RH), respectively). Note that since the refrigeration-based dew harvesting systems require a fan to blow air over to the dew surface, h is significantly greater than natural convective heat transfer coefficients (~10 W m^{-2} K^{-1}) and air needs to be cooled well below the dew point[36]. The upper bound of the harvested water mass ratio is when there is no water harvested with the refrigeration-based system at a given environmental condition and thermal energy input (*i.e.*, $Q_{thermal}\eta_{conv}COP_{REF} = Q_{gain}$).

Amount of harvested water and hydrothermal stability of MOF-801

We investigated the hydrothermal stability of MOF-801. The amount of harvested water was ~0.24 L kg^{-1} for MOF-801 (Figure S4.2A) from the first water harvesting cycle. After the first cycle, the amount of harvested water decreased by ~10%, then remained approximately

constant for the subsequent cycles. This was also observed with the powdered MOF-801 characterized using the adsorption analyzer, as shown in Figure S4.2A. The adsorption and desorption conditions were 35 °C and 1.2 kPa, and 85 °C and 1.2 kPa, respectively. The x-ray diffraction (X'Pert PRO MRD, PANalytical) patterns of MOF-801, with Cu K radiation, before and after 10 adsorption-desorption cycles are shown in Figure S4.2B, indicate that the crystallinity of MOF-801 remained intact after 10 cycles.

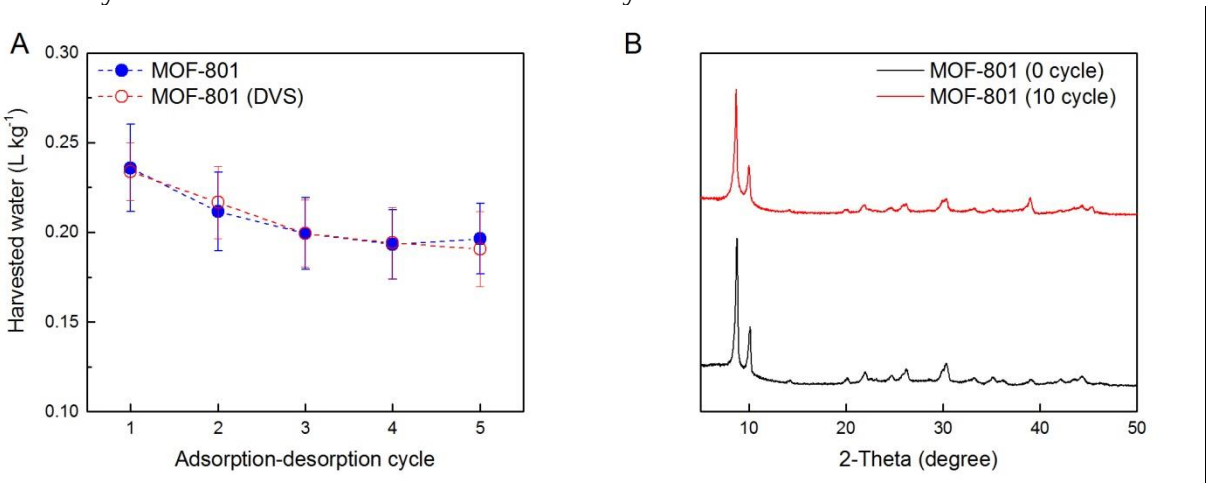

Figure S4.2. Experimentally characterized harvested water from multiple water harvesting cycles using MOF-801. (**A**) Amount of harvested water from the first five water harvesting cycles with a simulated solar flux of 1 kW m^{-2} (blue circles). Amount of harvested water of powdered MOF-801 characterized with the adsorption analyzer at 35 °C and 1.2 kPa for adsorption, and 85 °C and 1.2 kPa for desorption (red circles) averaged over three different runs with error bar representing +/- 1 SD. (**B**) XRD patterns of MOF-801 before and after 10 adsorption-desorption cycles.

The hydrothermal stability of MOF-801 over 80 adsorption-desorption cycles under flow of nitrogen-vapor mixture at ~30% relative humidity (at room temperature) is shown in Figure S4.3, characterized using a DSC-TGA instrument (Q600 SDT, TA instruments). While the sorption properties are not identical to the MOF-801 used in this study, the results demonstrate that MOF-801 is exceptionally stable towards the water adsorption and desorption.

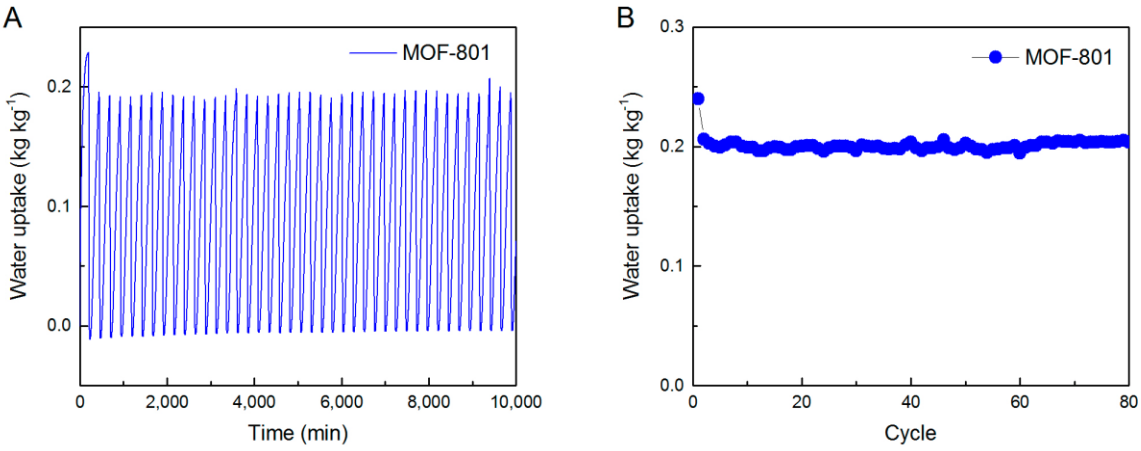

Figure S4.3. Hydrothermal stability of MOF-801. (**A**) Dynamic adsorption-desorption behavior of MOF-801 over 80 cycles. For each cycle, room temperature adsorption for 200 min and 85 °C desorption for 30 min (with 5 °C min^{-1} ramp rate) under a continuous flow of nitrogen-vapor mixture at ~30% RH. (**B**) Water uptake as a function of cycle number.

Theoretical modelling

A theoretical model based on mass and energy conservation was developed to understand and predict adsorption-desorption dynamics of MOF-801 using the following governing equations [26,27,37,38]:

$$\frac{\partial C}{\partial t} + \nabla \cdot (uC) = \nabla \cdot D_v \nabla C - \frac{(1-\varepsilon)}{\varepsilon} \frac{\partial C_\mu}{\partial t} \tag{4.4}$$

$$\rho c_p \frac{\partial T}{\partial t} = \nabla \cdot k \nabla T + h_{ad}(1-\varepsilon) \frac{\partial C_\mu}{\partial t} \tag{4.5}$$

Equation 4.4 is a mass conservation of the vapor due to diffusion within the packed adsorbent, where C, ε, and $\partial C_\mu / \partial t$ are vapor concentration (mol m^{-3}), porosity of packed adsorbent, and the average instantaneous rate of adsorption, respectively. The vapor concentration (mol m^{-3}) can be calculated using the ideal gas law, $C = PR^{-1}T^{-1}$, where P, R and T denote the pressure (Pa), universal gas constant (J mol^{-1} K^{-1}), and temperature (K) of the sample**.** D_v is the *inter*crystalline diffusivity of vapor (m^2 s^{-1}) through the packed MOF-801 crystals. The compressibility factor of water vapor at atmospheric pressure is nearly unity. Vapor transport due to advection ($\nabla \cdot (uC)$ in Equation 4.4) can be neglected by scaling the advection to diffusion transport using the Peclet number, $Pe = L_c u \cdot D_v^{-1}$. Here, L_c is the characteristic length scale (layer thickness), and the Darcian vapor velocity, $u = -K\nabla P / \mu$, can be calculated using the permeability, K, of the porous medium (packed adsorbent), $K = (2r_c)^2 \varepsilon^3 (36k_k(1-\varepsilon)^2)^{-1}$ [39], where μ, r_c, and k_k are the dynamic viscosity of vapor, MOF-801 crystal radius (Figure S4.5), and the Kozeny constant, respectively. The estimated Peclet number for water harvesting experiments under pure vapor condition is on the order of 10^{-2}. For the air-vapor mixture case where D_v is much lower than the case of pure vapor, advection can be neglected because the presence of air molecules can equilibrate the pressure gradients during adsorption and desorption processes. The energy equation shown in Equation 4.5 represents energy conservation within the packed adsorbent, neglecting the contribution from advection, where ρc_p, k, and h_{ad} are the locally averaged heat capacity (J m^{-3} K^{-1}), thermal conductivity (W m^{-1} K^{-1}), and enthalpy of adsorption (J mol^{-1}), ~55 kJ mol^{-1} [29]. The heat capacity and thermal conductivity terms incorporate the presence of the metallic foam, MOF-801 (specific heat capacity of 760 J kg^{-1} K^{-1} measured using a DSC, Discovery DSC TA Instruments), and adsorbed vapor (assumed liquid phase heat capacity). Due to the high thermal conductance of the metallic binder (copper foam), advection can be neglected. Based on the Knudsen number for vapor transport, D_v can be approximated as Knudsen diffusion, molecular diffusion, or a combination of both. The Knudsen number for vapor can be calculated using the mean free path of vapor and the characteristic void size of porous media (see below estimation of packing density and intercrystalline diffusivity). The effective vapor intercrystalline diffusivity, D_v, in an air-vapor mixture with consideration of both Knudsen and molecular diffusions in tortuous porous adsorbent can be estimated as [40–42],

$$D_v = \varepsilon^{3/2} \left(\frac{1}{D_{Vap}} + \frac{1}{D_{K,Vap}} \right)^{-1} \tag{4.6}$$

where D_{Vap}, $D_{K,Vap}$, and ε are vapor molecular diffusivity in air, Knudsen diffusivity of vapor, and porosity of packed adsorbent, respectively. Because water harvesting experiments (Figure 4.2) were conducted under pure vapor conditions at low pressures (~1.2 kPa), *inter*crystalline diffusivity in this case is expressed as $D_v = \varepsilon^{3/2} \cdot D_{K,Vap}$.

In Equations 4.4 and 4.5 C_μ is the vapor concentration within an adsorbent crystal, and the average instantaneous rate of adsorption, $\partial C_\mu / \partial t$, can be approximated with the linear driving force model[26,37,43].

$$\frac{\partial C_\mu}{\partial t} = \frac{15}{r_c^2} D_\mu (\mathrm{C}_{eq} - C_\mu) \tag{4.7}$$

In Equation 4.7, r_c, D_μ, and C_{eq} are, the adsorbent crystal radius (m), the intracrystalline diffusivity of vapor within adsorbent crystals, and the equilibrium vapor concentration based on the local temperature and vapor pressure, respectively. r_c and D_μ were characterized experimentally, and C_{eq} can be obtained from the adsorption isotherms measured in the range of temperatures considered in this study (Figure S4.5).

Packing density and intercrystalline diffusivities

The effective intercrystalline diffusion is a function of spacing between the adsorbent crystals. The characteristic void size of a random packing of spherical crystals of uniform size can be estimated using a probability distribution[26,44], as shown,

$$P(\chi) = 3(1+\chi)^2 \frac{\varepsilon(1-\varepsilon)(1-\varepsilon_{HCP})}{(\varepsilon-\varepsilon_{HCP})} \exp\left(-\frac{(1-\varepsilon)(1-\varepsilon_{HCP})}{(\varepsilon-\varepsilon_{HCP})} \left[(1+\chi)^3 - 1 \right] \right) \tag{4.8}$$

where ε and ε_{HCP} are the average porosity of packed adsorbent and the porosity corresponding to the maximum packing density of spheres arranged in a hexagonal close-packed structure. The characteristic void size is calculated as $d_P = 2 r_c \chi_{avg}$, where r_c is the adsorbent crystal radius, and χ_{avg} is calculated as:

$$\chi_{avg} = \frac{1}{\varepsilon} \int_0^\infty \chi P(\chi) d\chi \tag{4.9}$$

This was carried out using Equations 4.8 and 4.9, as shown in Figure 4.3A in the main text of this Chapter. The porosity of the adsorbent layer can be calculated with the following relation: $\varepsilon = 1 - \rho_{adsorbent} / \rho_{powder}$. The powdered particle density ρ_{powder} of activated MOF-801 was estimated to be 1200 ± 60 kg m^{-3} from the pycnometer (Micromeritics AccuPyc 1340) and BET pore volume measurements[10]. The crystal diameter of MOF-801 (~0.6 μm) was characterized using a scanning electron microscope (6010LA SEM, JEOL), as shown in Figure S4.5. The effective *inter*crystalline diffusivity can be computed using Equation 6, where the Knudsen diffusivity is $D_{K,Vap} = (d_p / 3)\sqrt{8RT / \pi M}$. The diffusion coefficient of vapor in air at atmospheric pressure as a function of temperature can be obtained using the following relation[40],

$$D_{vap,T} = D_{vap,ref}\left(\frac{T}{T_{ref}}\right)^{3/2}\left(\frac{\Omega_{D,ref}}{\Omega_{D,T}}\right) \tag{4.10}$$

where D_{vap} and Ω_D are the diffusion coefficient and collision integral based on the Lennard-Jones potential for molecular diffusion[45], respectively, and subscript *ref* denotes reference value. For the case of MOF-801, the effective *inter*crystalline diffusivities are plotted in Figure S4.4B as a function of the packed adsorbent porosity and temperature at atmospheric pressure.

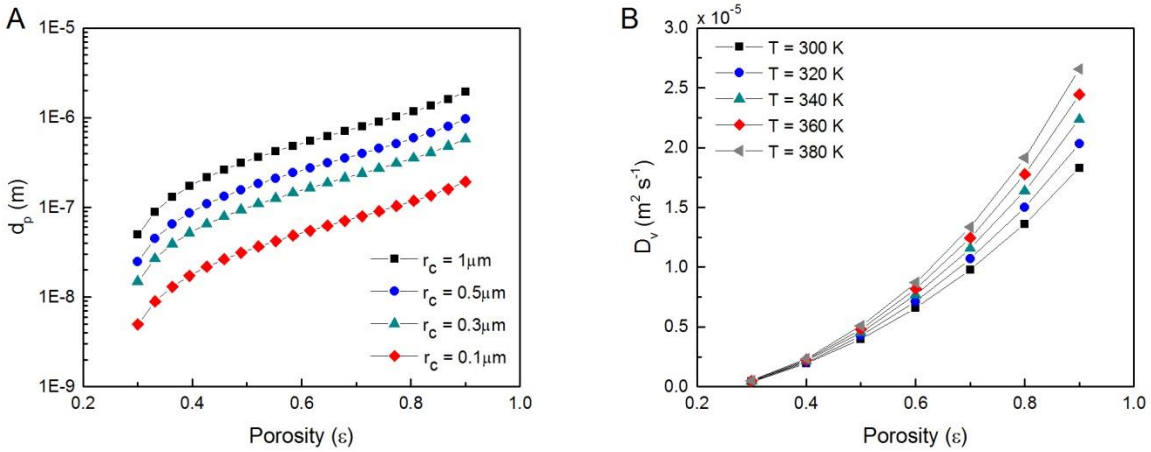

Figure S4.4. *Inter*crystalline vapor diffusivities of packed MOF-801 in air. (**A**) Characteristic void size as a function of packed adsorbent porosity and adsorbent crystal radius. (**B**) Effective *inter*crystalline diffusivities of vapor as functions of porosity and temperature estimated for MOF-801, crystal diameter of ~0.6 μm, at atmospheric pressure.

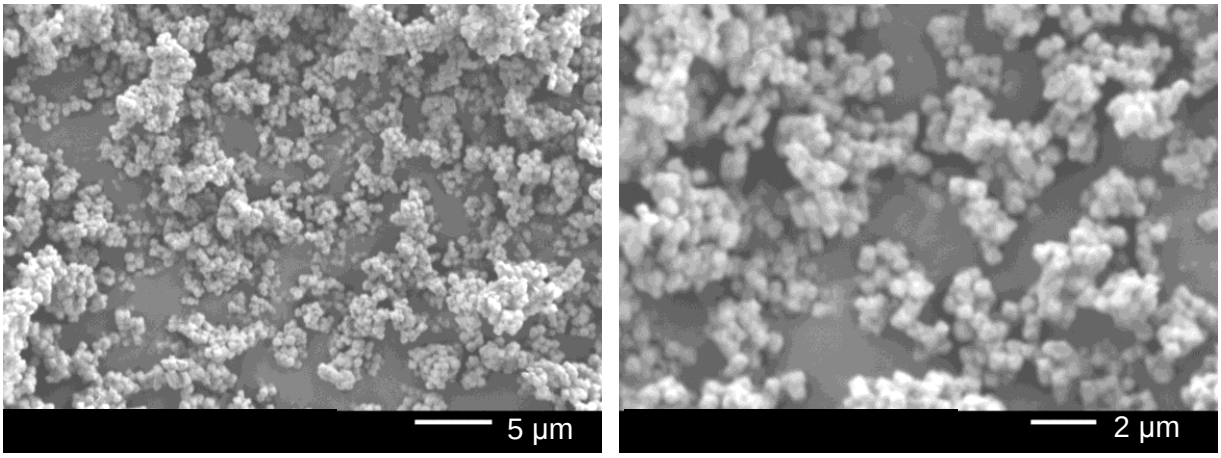

Figure S4.5. SEM images of powdered MOF-801. Crystal diameter of MOF-801 is ~0.6 μm.

Adsorption isotherms and *intra*crystalline diffusivities

Vapor adsorption isotherms of MOF-801 were characterized using dynamic adsorption analyzers (DVS adsorption analyzer and Q5000SA, TA Instruments) at 25 °C, 45 °C, and 65 °C, as shown in Figure 6 in the vapor and nitrogen-vapor mixture environments. Using dynamic behavior captured by these instruments, vapor *intra*crystalline diffusivities of MOF-801 were

estimated, with assumptions of spherical crystal and isothermal diffusion, using Fick's law of diffusion given by

$$\frac{\partial C}{\partial t} = \frac{1}{r^2}\frac{\partial}{\partial r}\left(D_\mu r^2 \frac{\partial C}{\partial r} \right) \tag{4.11}$$

where C, t, r, and D_μ are the vapor concentration, time, crystal radius, and *intra*-crystalline diffusivity, respectively. With assumptions of homogeneous pore structure, constant spherical adsorbent crystals of radius, r_c, and constant surface concentration and diffusivity (D_μ), the solution to Equation 4.11 is [46]:

$$\frac{m_t}{m_{eq}} = 1 - \frac{6}{\pi^2}\sum_{n=1}^{\infty}\left(\frac{1}{n^2}\right)\exp\left(-\frac{n^2\pi^2 D_\mu t}{r_c^{\,2}}\right) \tag{4.12}$$

where m_t / m_{eq} is the fractional water uptake with $m_t = 0$ at $t = 0$ and $m_t = m_{eq}$ as $t \to \infty$ for a sufficiently small pressure step. The effective *intra*crystalline (Fickian) diffusivities of MOF-801 were estimated by fitting Equation 4.12 with the experimental measurements, as shown in Figure S4.6, for the pure vapor and nitrogen-vapor mixture cases at 20% RH. The *intra*crystalline diffusivities for the mixture case are lower due to extra mass transfer resistances introduced by the presence of nitrogen gas. The *intra*crystalline diffusivities depend on temperature and adsorbate uptake[47,48], therefore, a description of the diffusivity with the Arrhenius behavior is only satisfactory for limited cases. However, for a macroscopic modelling using the linear driving force model, it is essential to define a characteristic diffusivity. This is permissible because the *intra*crystalline diffusion process is not a governing mechanism for vapor transport, and this becomes predominant for the case of air-vapor mixture where *inter*crystalline diffusion dictates the overall transport. Using a constant *intra*crystalline diffusivity of $5e^{-17}$ m^2 s^{-1} (as shown in Figure S4.7A) for the theoretical model, good agreement with the experiment was achieved (Figure 4.2, C and D, main text). The estimated *intra*crystalline diffusivities were found to be fairly constant, within the order of magnitude, for the range of vapor pressures and temperatures investigated (Figure S4.7C).

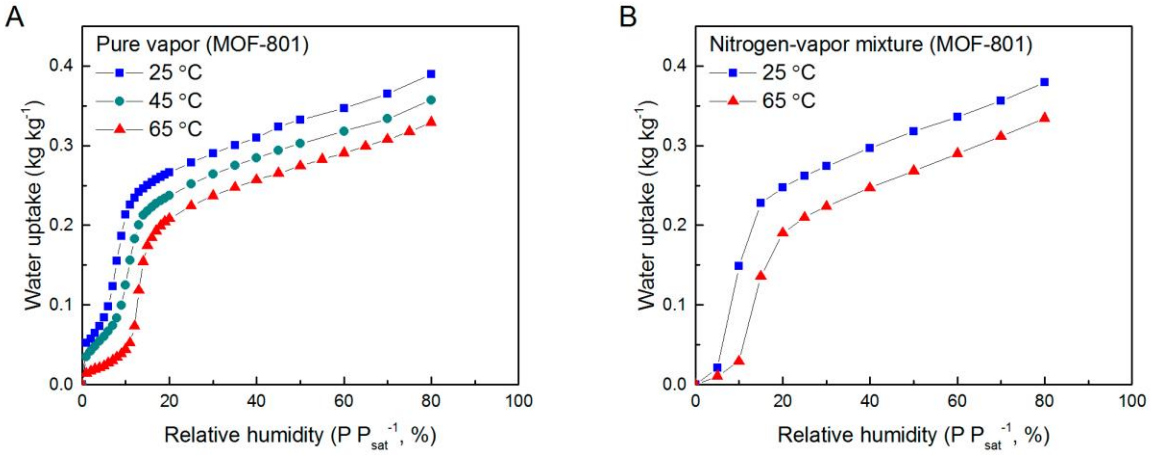

Figure S4.6. Adsorption isotherms of MOF-801 measured in a (**A**) pure vapor and (**B**) nitrogen- vapor mixture at atmospheric pressure at various temperatures.

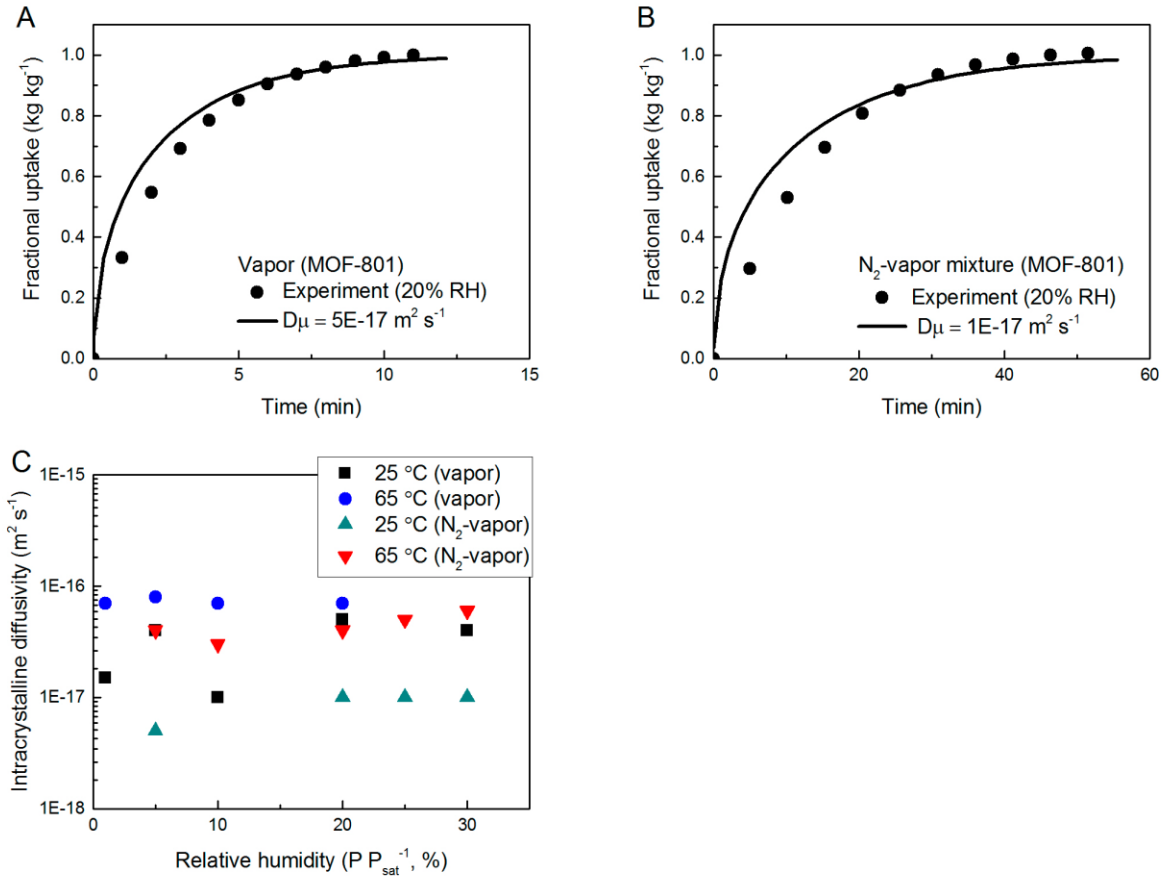

Figure S4.7. *Intra*crystalline vapor diffusivities of MOF-801. Fractional water uptake (kg kg^{-1}) as a function of time for MOF-801 in (**A**) pure vapor and in (**B**) nitrogen-vapor mixture characterized at 25 °C and 20% RH. The dynamic responses are recorded during the isotherm measurements shown in Figure S4.6. (**C**) Estimated *intra*crystalline diffusivities using Equation 4.12 as functions of relative humidity and temperature.

Optimization and predictions of MOF-801 for water harvesting

Using the developed model and characterized properties, computational analysis was carried out using COMSOL Multiphysics for MOF-801. Since MOF-801 is classified as a physisorbent for water sorption process[11], the hysteresis between the adsorption and desorption isotherms is assumed to be negligible. The advective vapor transport was neglected. Overall transport processes are governed by the *inter*crystalline diffusion in an air-vapor mixture. The variations in the *intra*crystalline diffusivity have marginal effects on the overall transport processes, therefore, the *intra*crystalline diffusivity value of $1e^{-17}$ m^2 s^{-1} is used for the simulation. For simplicity, we assumed the condenser is maintained at the ambient temperature of 25 °C, a negligible vapor pressure difference between the MOF layer and the condenser surface during desorption (*i.e.*, sufficiently small spacing between the layer and condenser), and negligible vapor pressure difference between the MOF layer surface and ambient during adsorption (*i.e.*, negligible depletion layer thickness with sufficiently high ambient air free stream velocity or mixing)[49].

The predicted desorption-adsorption behaviors of MOF-801 with various packing porosities and layer thicknesses with one sun (1 kW m^{-2}) under an atmospheric condition are shown in Figure 4.3, main text and Figure S4.7, supporting information. Among various porosities, ε of 0.7 yielded the most water. Note that the adsorption process takes considerably longer than the desorption process (at 1 kW m^{-2}); this becomes predominant with a decrease in porosity or increase in layer thickness. Both of these have significant effects on the *inter*crystalline diffusion ($D_v = f(\varepsilon, r_c) \sim L_c^{\,2} t^{-1}$). Because vapour condensation is done with presence of noncondensables (air), transport of desorbed vapour to the condenser surface is *via* diffusion. We can estimate the time-averaged vapor pressure difference between the layer and condenser using following relation[40],

$$L_s = \frac{C_t \cdot D_{vap} \cdot MW_w}{J_w} \ln\left(\frac{1 - y_{w,cond}}{1 - y_{w,layer}}\right) \tag{4.13}$$

Equation 4.13 assumes steady state vapor diffusion where L_s , C_t , MW_w , J_w , $y_{w,cond}$, $y_{w,layer}$ are the spacing between the layer and condenser (m), total molar concentration of gas (mol m^{-3}), molecular weight of water (kg mol^{-1}), time-averaged mass flux of desorbed vapor (kg m^{-2} s^{-1}), and mole fractions of vapor at the condenser surface and the layer surface, respectively. The time scale of vapor diffusion in few centimeters is significantly small compared to the time scale for complete desorption, therefore, steady state assumption is valid. For the case of porosity of 0.7 and 1 mm layer thickness, if the spacing is ~4 cm, the estimated time-averaged vapor pressure at the layer surface is ~2 times of the condenser vapor pressure. This will delay the desorption process as the driving potential for desorption decreases with increase in vapor pressure. However, RH is an exponential function of temperature and the adsorption isotherm shifts down with increase in temperature, therefore, we don't expect significant delay as the vapor pressure difference will ultimately vanish. Alternatively, vapor transport can be enhanced with density gradient, *i.e.*, buoyancy, with geometric orientation of the layer and condenser. In addition, heat loss from the layer to the condenser during desorption increases with the decreasing spacing, and there will be an optimum based on considerations of heat loss and pressure difference. Under a natural convection condition in air, heat transfer coefficients ranges between 3 and 25 W m^{-2} K^{-1}, and with forced convection, 10 and 200 W m^{-2} K^{-1} [50]. Therefore, a finned condenser can dissipate condensation heat with temperature difference between the condenser and ambient less than 5 °C. For all predicitons, we assumed MOF-801 composite thermal conductivity of 4 W m^{-1} K^{-1} (infiltrated in a copper foam binder), convective heat transfer coefficient of 10 W m^{-2} K^{-1}, temperature of surrounding air-vapour mixture of 25 °C, and black body solar absorber. In addition, temperature and water uptake profiles of the MOF prototype (Figure 4.4C, main text in this Chapter) were predicted using the theoretical model incorporating vapor diffusion resistance between the layer and condenser. Here, Fick's law of diffusion, 1-dimensional form of Equation 4.11, is used to correlate the vapor pressure at the layer surface from the condenser saturation pressure at ~23 °C. The experimentally measured solar flux (including solar transmittance and absorptance losses) and environmental conditions with effective heat transfer coefficient of ~9 W m^{-2} K^{-1} are used for the boundary conditions.

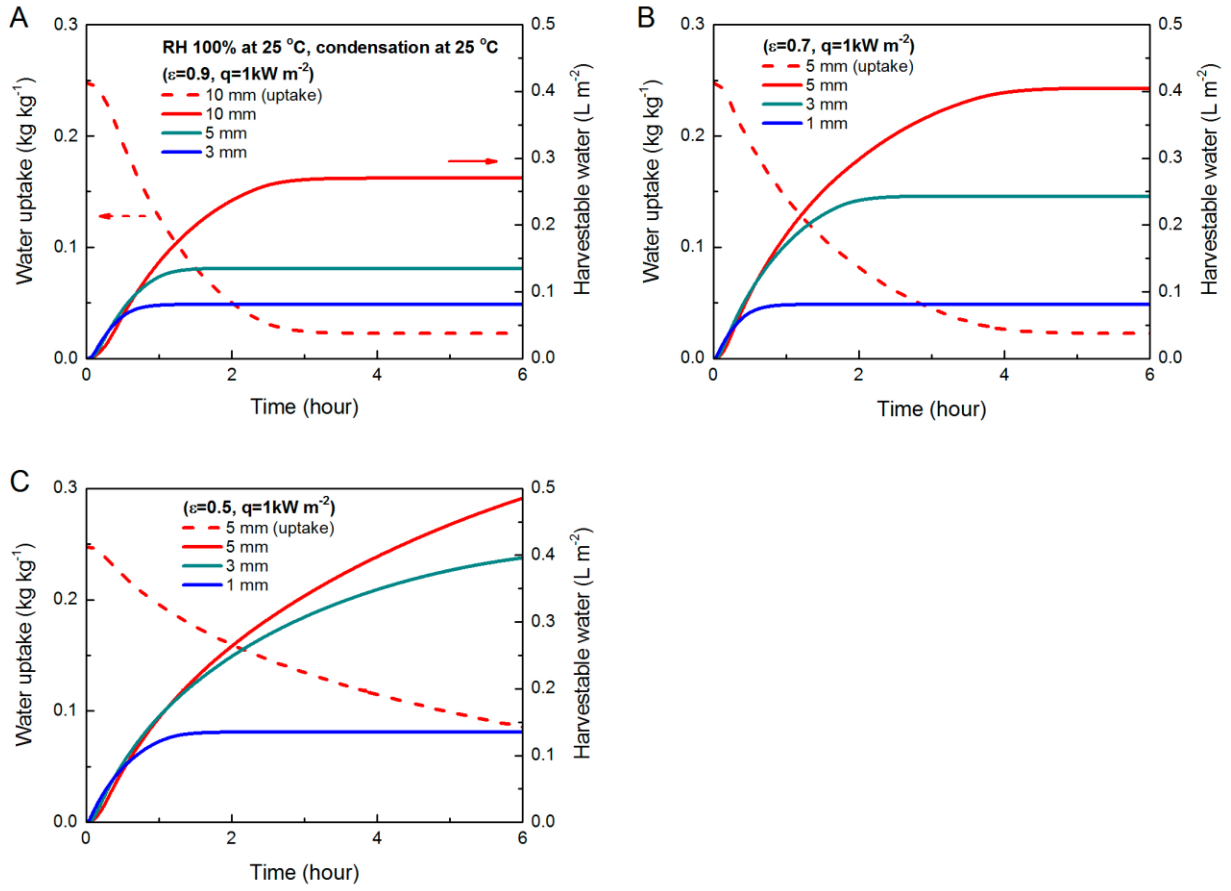

Figure S4.8. Predicted desorption dynamics of MOF-801 in humid air. Predicted desorption water uptake (kg kg^{-1}) and harvestable water (L m^{-2}) with solar flux of 1 kW m^{-2}. (**A**) porosity, ε, of 0.9 with layer thickness of 3, 5, 10 mm, (**B**) ε of 0.7 with layer thickness of 1, 3, 5 mm, and (**C**) ε of 0.5 with layer thickness of 1, 3, 5 mm. MOF-801 was initially equilibrated at 20% RH, at 25 °C, and the vapor partial pressure rapidly increased to 100% RH at 25 °C during desorption for vapour condensation. The mass transfer resistance is due to both Knudsen diffusion and the tortuosity of the porous media at ε of ~0.5.

References for Chapter 4

(1) Mekonnen, M. M.; Hoekstra, A. Y. *Sci. Adv.* **2016**, *2*, e1500323.

(2) Schneider, S. H. *Encyclopedia of Climate and Weather*; Oxford Univ. Press, 1996.

(3) Wahlgren, R. V. *Water Res.* **2001**, *35*, 1–22.

(4) Muselli, M.; Beysens, D.; Marcillat, J.; Milimouk, I.; Nilsson, T.; Louche, A. *Atmos. Res.* **2002**, *64*, 297–312.

(5) Clus, O.; Ortega, P.; Muselli, M.; Milimouk, I.; Beysens, D. *J. Hydrol.* **2008**, *361*, 159–171.

(6) Lee, A.; Moon, M.-W.; Lim, H.; Kim, W.-D.; Kim, H.-Y. *Langmuir* **2012**, *28*, 10183–10191.

(7) Schemenauer, R. S.; Cereceda, P.; Schemenauer, R. S.; Cereceda, P. *J. Appl. Meteorol.* **1994**, *33*, 1313–1322.

(8) Klemm, O.; Schemenauer, R. S.; Lummerich, A.; Cereceda, P.; Marzol, V.; Corell, D.; van Heerden, J.; Reinhard, D.; Gherezghiher, T.; Olivier, J.; Osses, P.; Sarsour, J.; Frost, E.; Estrela, M. J.; Valiente, J. A.; Fessehaye, G. M. *Ambio* **2012**, *41*, 221–234.

(9) Park, K.-C.; Chhatre, S. S.; Srinivasan, S.; Cohen, R. E.; McKinley, G. H. *Langmuir* **2013**, *29*, 13269–13277.

(10) Furukawa, H.; Gándara, F.; Zhang, Y.-B.; Jiang, J.; Queen, W. L.; Hudson, M. R.; Yaghi, O. M. *J. Am. Chem. Soc.* **2014**, *136*, 4369–4381.

(11) Canivet, J.; Fateeva, A.; Guo, Y.; Coasne, B.; Farrusseng, D. *Chem. Soc. Rev.* **2014**, *43*, 5594–5617.

(12) Burtch, N. C.; Jasuja, H.; Walton, K. S. *Chem. Rev.* **2014**, *114*, 10575–10612.

(13) Wang, C.; Liu, X.; Keser Demir, N.; Chen, J. P.; Li, K. *Chem. Soc. Rev.* **2016**, *45*, 5107–5134.

(14) Lee, J.; Farha, O. K.; Roberts, J.; Scheidt, K. A.; Nguyen, S. T.; Hupp, J. T. *Chem. Soc. Rev.* **2009**, *38*, 1450–1459.

(15) D'Alessandro, D. M.; Smit, B.; Long, J. R. *Angew. Chemie Int. Ed.* **2010**, *49*, 6058–6082.

(16) Zhou, H.-C.; Long, J. R.; Yaghi, O. M. *Chem. Rev.* **2012**, *112*, 673–674.

(17) Jeremias, F.; Fröhlich, D.; Janiak, C.; Henninger, S. K. *New J. Chem.* **2014**, *38*, 1846–1852.

(18) de Lange, M. F.; Verouden, K. J. F. M.; Vlugt, T. J. H.; Gascon, J.; Kapteijn, F. *Chem. Rev.* **2015**, *115*, 12205–12250.

(19) Seo, Y.-K.; Yoon, J. W.; Lee, J. S.; Hwang, Y. K.; Jun, C.-H.; Chang, J.-S.; Wuttke, S.; Bazin, P.; Vimont, A.; Daturi, M.; Bourrelly, S.; Llewellyn, P. L.; Horcajada, P.; Serre, C.; Férey, G. *Adv. Mater.* **2012**, *24*, 806–810.

(20) Eddaoudi, M.; Kim, J.; Rosi, N.; Vodak, D.; Wachter, J.; O'Keeffe, M.; Yaghi, O. M. *Science* **2002**, *295*, 469–472.

(21) Yaghi, O. M.; O'Keeffe, M.; Ockwig, N. W.; Chae, H. K.; Eddaoudi, M.; Kim, J. *Nature* **2003**, *423*, 705–714.

(22) Furukawa, H.; Cordova, K. E.; O'Keeffe, M.; Yaghi, O. M. *Science* **2013**, *341*, 1230444.

(23) Gur, I.; Sawyer, K.; Prasher, R. *Science* **2012**, *335*, 1454–1455.

(24) Chu, S.; Majumdar, A. *Nature* **2012**, *488*, 294–303.

(25) Cavka, J. H.; Jakobsen, S.; Olsbye, U.; Guillou, N.; Lamberti, C.; Bordiga, S.; Lillerud, K. P. *J. Am. Chem. Soc.* **2008**, *130*, 13850–13851.

(26) Narayanan, S.; Yang, S.; Kim, H.; Wang, E. N. *Int. J. Heat Mass Transf.* **2014**, *77*, 288–300.

(27) Narayanan, S.; Kim, H.; Umans, A.; Yang, S.; Li, X.; Schiffres, S. N.; Rao, S. R.; Mckay, I. S.; Rios Perez, C. A.; Hidrovo, C. H.; Wang, E. N.; Wang, E. N. *Appl. Energy* **2017**, *189*, 31–43.

(28) Ng, K. C.; Chua, H. T.; Chung, C. Y.; Loke, C. H.; Kashiwagi, T.; Akisawa, A.; Saha, B. B. *Appl. Therm. Eng.* **2001**, *21*, 1631–1642.

(29) Kim, H.; Cho, H. J.; Narayanan, S.; Yang, S.; Furukawa, H.; Schiffres, S.; Li, X.; Zhang, Y.-B.; Jiang, J.; Yaghi, O. M.; Wang, E. N. *Sci. Rep.* **2016**, *6*, 19097.

(30) Liu, D.; Purewal, J. J.; Yang, J.; Sudik, A.; Maurer, S.; Mueller, U.; Ni, J.; Siegel, D. J. *Int. J. Hydrogen Energy* **2012**, *37*, 6109–6117.

(31) Yang, S.; Huang, X.; Chen, G.; Wang, E. N. *J. Porous Mater.* **2016**, *23*, 1647–1652.

(32) Ni, G.; Li, G.; Boriskina, S. V; Li, H.; Yang, W.; Zhang, T.; Chen, G. *Nat. Energy* **2016**, *1*, 16126.

(33) Soleimani Dorcheh, A.; Abbasi, M. H. *J. Mater. Process. Technol.* **2008**, *199*, 10–26.

(34) R. Farrington, J. Rugh, paper presented at Earth Technologies Forum, Washington, DC, 31 October 2000 (National Renewable Energy Laboratory, 2000).

(35) P. J. Cousins, D. D. Smith, H. C. Luan, J. Manning, T. D. Dennis, A. Waldhauer, K. E. Wilson, G. Harley, W. P. Mulligan, in 35th IEEE Photovoltaic Specialists Conference (PVSC 2010) (Institute of Electrical and Electronics Engineers, 2010), 275–278.

(36) Beysens, D. *Atmos. Res.* **1995**, *39*, 215–237.

(37) Chan, K. C.; Chao, C. Y. H.; Sze-To, G. N.; Hui, K. S. *Int. J. Heat Mass Transf.* **2012**, *55*, 3214–3224.

(38) Solmuş, İ.; Andrew S. Rees, D.; Yamalı, C.; Baker, D. *Int. J. Heat Mass Transf.* **2012**, *55*, 5275–5288.

(39) M. Kaviany, *Principles of Heat Transfer in Porous Media*, Springer Science & Business Media, 2012.

(40) J. R. Welty, C. E. Wicks, G. Rorrer, R. E. Wilson, *Fundamentals of Momentum, Heat, and Mass Transfer*, John Wiley & Sons, 2009.

(41) Marshall, T. J. *J. Soil Sci.* **1959**, *10*, 79–82.

(42) Moldrup, P.; Olesen, T.; Gamst, J.; Schjønning, P.; Yamaguchi, T.; Rolston, D. E. *Soil Sci. Soc. Am. J.* **2000**, *64*, 1588.

(43) Sircar, S.; Hufton, J. R. *Adsorption* **2000**, *6*, 137–147.

(44) Alonso, M.; Sainz, E.; Lopez, F. A.; Shinohara, K. *Chem. Eng. Sci.* **1995**, *50*, 1983–1988.

(45) Hirschfelder, J. O.; Bird, R. B.; Spotz, E. L. *Chem. Rev.* **1949**, *44*, 205–231.

(46) J. Crank, *The Mathematics of Diffusion*, Oxford Univ. Press, 1979.

(47) Krishna, R. *J. Phys. Chem. C* **2009**, *113*, 19756–19781.

(48) Kärger, J.; Binder, T.; Chmelik, C.; Hibbe, F.; Krautscheid, H.; Krishna, R.; Weitkamp, J. *Nat. Mater.* **2014**, *13*, 333–343.

(49) Beysens, D. *Comptes Rendus Phys.* **2006**, *7*, 1082–1100.

(50) A. F. Mills, *Heat Transfer*, Prentice Hall, 1999.

Chapter 5

Adsorption-based atmospheric water harvesting device for arid climates

Portions of this chapter published in:
Kim, H., Rao, S. R., Kapustin, E. A., Zhao, L., Yang, S., Yaghi, O. M. & Wang, E. N. Adsorption-based atmospheric water harvesting device for arid climates *Nature Commun.*, **2018**, DOI: 10.1038/s41467-018-03162-7.

5.1 Preface

In the previous Chapter, we described for the first time the concept of water harvesting using MOFs from air at low relative humidity. The proof-of-concept was shown to deliver water without energy input except for direct sunlight. To fully utilize the MOF sorption properties, we performed the water harvesting with MOF-801 in an exceptionally arid climate of Arizona, Unites States. At the relative humidity levels of 10 to 40%, the dew point is sub-zero, thus any state-of-art dewing technologies cannot compete with the air-cooled MOF-based water harvesting device. We predicted that the device can produce up to 0.25 liters of water per kg of MOF daily driven by solar energy solely at the conditions where other atmospheric water generators fail to deliver water. This work was done in collaboration with Hyunho Lee, Sameer Rao, Sungwoo Yang, Lin Zhao, Evelyn N. Wang.

5.2 Introduction

As discussed earlier, enabling access to fresh potable water in desert and arid regions is a critical challenge and tightly coupled to social and economic development[1]. Water scarcity is difficult to address in areas that are landlocked and have limited infrastructure, such that mature water purification technologies, *i.e.*, reverse osmosis and multi-stage flash, are challenging to implement. Atmospheric water generators (AWGs) can take advantage of solar energy via photovoltaics (refrigeration-based)[2,3] or solar thermal (sorption-based)[4–6] to harvest moisture from air. Typical AWGs utilize refrigeration to cool large volumes of air well below the dew point to condense water. The amount of energy consumed to harvest water from the air dramatically increases as the humidity or ambient temperature decreases. Desert and arid regions, unfortunately, have day-time relative humidities (RH; P_{vap}/P_{sat}, vapor pressure over saturation pressure) as low as ~10% with a vapor content of approximately 3 L of liquid water for every one million liters of air. For these conditions, the dew point can be sub-zero, requiring a large amount of energy to freeze and collect water out of air. Though the typical night-time RH can be as high as ~40%, the lower ambient temperature (~20 °C) prevents water harvesting with refrigeration-based AWGs. As a result, the practical implementation of refrigeration-based AWGs is infeasible[3,7].

AWGs that take advantage of solar-thermal processes are a promising alternative to capture and deliver water in arid regions. In this approach, a sorbent is first saturated with water from air and subsequently heated to release and condense the water[4–6,8]. By selecting the desired sorbent characteristics (e.g., shape and step position of the isotherm, saturation capacity, and binding energy), solar-thermal-driven water harvesting is viable and efficient even in low RH conditions. In Chapter 5, we demonstrated that MOFs are particularly attractive because they can capture more water and require lower regeneration temperatures[4] for its release compared to conventional sorbents (e.g., zeolites/silica gels or liquid brines). In addition, their step-like isotherms suggest that a small change in temperature and/or RH can lead to a large change in uptake and water release. The proof-of-concept device showed that with MOF-801[4], water harvesting is possible (Cambridge, Massachusetts, United States, with ~65% RH), with a temperature differential of ~45 K between the MOF layer and condenser. While this demonstration as well as several prior studies[5,6,8] have shown that the approach is viable, demonstration under representative conditions of desert/arid climates has not been achieved. In this Chapter, we experimentally demonstrate an air-cooled MOF-801-based water harvesting device operating in the arid climate of south western United States (Tempe, Arizona, United

States) with a day-time RH as low as 10% and under sub-zero dew points. In addition, we analyzed the water from the adsorption−desorption/condensation process with MOF-801 and confirmed that the MOF compound is stable to water and the metal ions and organic linkers do not contaminate the produced water.

Cyclic water harvesting (*i.e.*, multiple adsorption−desorption cycles a day) is challenging in extremely arid regions due to the low day-time humidity (~10% RH) that prevents water adsorption, *i.e.*, the RH is lower than the adsorption step of MOF-801. Consequently, to achieve maximum water production for a single cycle, in this work, we implemented significant design improvements over our prior proof-of-concept. First, we optimized and engineered the device to completely saturate during the nighttime humidity swing (20-40% RH). Second, with an optical concentration of less than 2× and buoyancy-assisted vapor transport during condensation, the overall thermal efficiency (i.e., product of latent heat of water and mass of harvested water per unit input solar energy) was estimated to be ~14%. This corresponds to an increase of ~5× in comparison to operation without optical concentration and enabled complete regeneration with MOF-801.

Operation in such arid regions also opens an interesting avenue for increasing water harvesting output with passive radiative cooling by leveraging the typically clear sky. The clear night sky and low vapor content in the atmosphere enables dissipation of long-wavelength (infrared) thermal radiation from the device to the cold sky to cool it below its ambient temperature. By facing the device to the sky during adsorption, a ~3 K temperature drop was achieved, which corresponds to an increase in 5-7% RH experienced by the adsorbent. This passive cooling can lead to opportunities to utilize other adsorbents that have their adsorption steps located beyond the typical levels of RH in specific regions.

5.3 Device design and operation

Our operational principle involves a single daily cycle where adsorption occurs during night-time at a higher humidity (20-40% RH) and solar-assisted desorption/water production occurs during day-time at a lower humidity (10-20% RH), schematically described in Figure 5.1A. The device consists of two key components, an adsorbent layer (MOF) and an air-cooled condenser in an enclosure. The back side of the MOF layer is coated black and serves as a solar absorber. During night-time adsorption, the enclosure side walls are opened and the MOF layer is saturated with vapor from the natural flow of ambient air and passively cooled with radiation to the sky. During day-time water production, the enclosure is closed and the solar absorber side is covered with an optically transparent thermal insulator (OTTI aerogel)[9,10]. The MOF layer is heated by exposure to solar irradiance, causing water release (desorption). The desorbed water vapor diffuses from the MOF layer to the condenser due to a concentration gradient. Accumulation of vapor in the enclosure leads to saturation conditions and consequently, the condensation process occurs at ambient temperature. The heat of condensation is dissipated to the ambient by a heat sink. The adsorbents need to be selected based on the typically available ambient RH for water adsorption. MOF-801 was chosen in our study because it exhibits an adsorption step located around 20% RH and is well-suited for the specific climate tested (Tempe, Arizona, United States). Furthermore, MOF-801 is hydrothermally stable and well-characterized for water adsorption including having high stability to cycling water in and out of the pores[4,11].

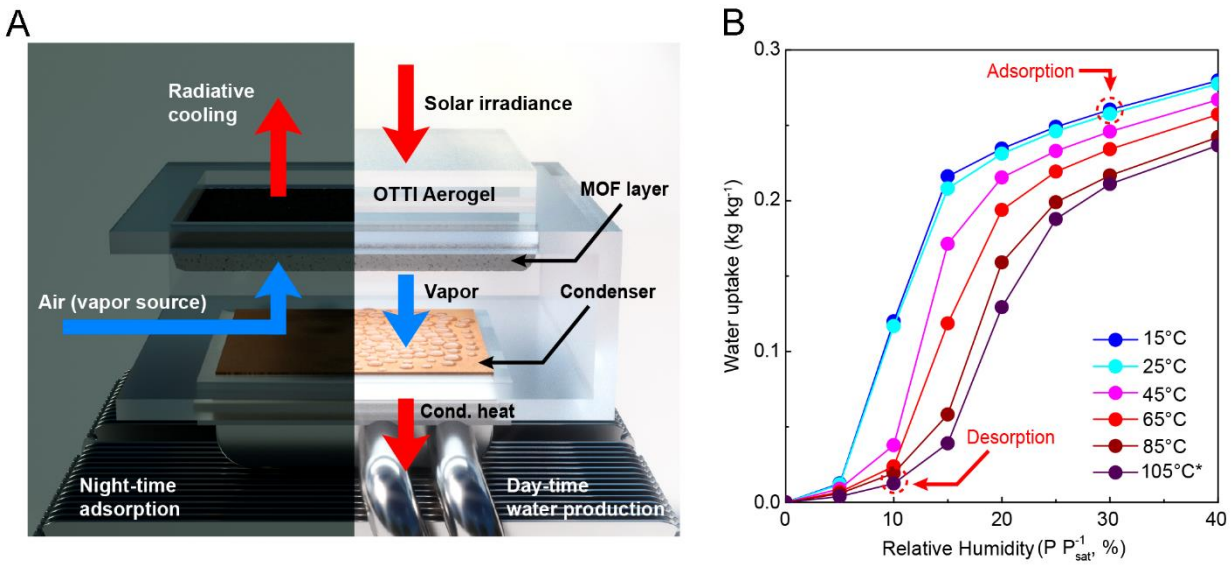

Figure 5.1. Working principle of MOF-801-based water harvesting device and adsorption isotherms. (**A**) Illustrative schematic of the water harvesting device undergoing adsorption (night-time, left half) and solar-assisted water production (day-time, right half) processes. During adsorption, air is circulated around the MOF layer and water from air is adsorbed. Passive radiative cooling lowers the MOF layer temperature below ambient by dissipating thermal radiation to clear cold sky to increase the effective RH for adsorption. During water production, the OTTI aerogel is stacked on top of the MOF layer to suppress convective heat loss from the solar absorber. The desorbed vapor is condensed on a condenser and heat of condensation is rejected to the ambient by a heat pipe heat sink. (**B**) Water adsorption isotherms of MOF-801 in kg kg^{-1} (kg of water per kg of MOF-801) as a function of relative humidity (P P_{sat}^{-1}, vapor pressure over saturation pressure) at temperatures of 15, 25, 45, 65 and 85 °C measured using a sorption analyzer (Q5000 SA, TA Instruments). *Isotherm at 105 °C was predicted using the characteristic curve based on the isotherm at 85 °C[12]. Dotted red circles indicate representative conditions achieved during night-time adsorption and day-time water production in Arizona, United States.

The amount of water that can be harvested in a single cycle using MOF-801 can be evaluated based on the adsorption isotherm shown in Figure 5.1B. For representative conditions in our test location, with a night-time ambient temperature of 15-25 °C and RH of ~30% during adsorption, the equilibrium uptake is estimated to be ~0.25 kg kg^{-1} (kg of water per kg of MOF-801). To achieve complete desorption (at ~10% RH, see Figure 5.1B), with a day-time ambient (condenser) temperature of 30 °C (saturation vapor pressure, P_{sat} = 4.2 kPa), the adsorbent must be heated to a minimum of 77 °C (P_{sat} = 42 kPa). This corresponds to a target temperature difference of ~45 K between the adsorber and the condenser.

To attain these operating conditions, based on the computational simulation (see theoretical modelling in Supporting Information for this Chapter), the prototype design described in our prior study was further optimized and engineered (see optimization of MOF layer in Supporting Information). An MOF layer (base of 5 cm by 5 cm with ~3 g of MOF-801) was fabricated using a porous copper foam. The solar absorber side of the MOF layer was coated with pyromark paint with a solar absorptance of ~0.95. The MOF layer density and thickness were optimized for operation in arid climates based on the transport properties of MOF-801. A packing porosity of 0.67 (or packing density of 464 kg m^{-3}) and thickness of 2.57 mm were chosen for the MOF layer (see Figure S5.7 in Supporting Information). These optimized parameters enable saturation within the limited time window, i.e., during the humidity swing (increase) in the night-time (roughly under 8 h in a 20−40% RH environment) and to maximize water harvesting capacity. Due to the fixed side walls of the small-scale device (unlike Figure

5.1A), which prevented access to air flow (vapor source), the MOF layer was secured in a separate enclosure that allowed adequate access to air (see Figure S5.1 in Supporting Information). The condenser of the device was fabricated with a copper plate (4 cm by 4 cm and 0.6 cm thick) attached to a commercial air-cooled heat sink (NH-L9x65, Noctua) to efficiently dissipate the heat from condensation to the ambient. The condenser was air-cooled throughout the entire experiment. To suppress convective heat loss from the solar absorber side of the MOF layer during solar-assisted desorption, an OTTI aerogel with a thermal conductivity of less than 0.03 W m^{-1} K^{-1} and solar transmittance of ~0.94 was stacked on the MOF layer as shown in Figures 5.1A, 5.2. The use of OTTI aerogel is well-suited for arid climates due to the inherently low RH and no degradation during testing was observed. In order to prevent vapor leak during desorption, a transparent plastic wrap (solar transmittance of ~0.93) was used to seal the device, leading to an overall solar transmittance and absorptance loss of ~17% (83% sun to thermal conversion efficiency) with an effective heat loss coefficient of 9-10W m^{-2} K^{-1}. To help overcome these solar thermal losses and improve water harvesting thermal efficiencies, experiments were also performed with a biconvex lens (9 cm diameter) that was used to achieve an optical concentration of 1.8× during desorption. The spacing between the MOF layer and condenser (~1.8 cm) was also reduced in comparison to our prior study to enable faster vapor diffusion during condensation while maintaining minimal heat loss from the MOF layer to the condenser. One of the lateral walls of the device was made transparent to serve as a view port for visualization.

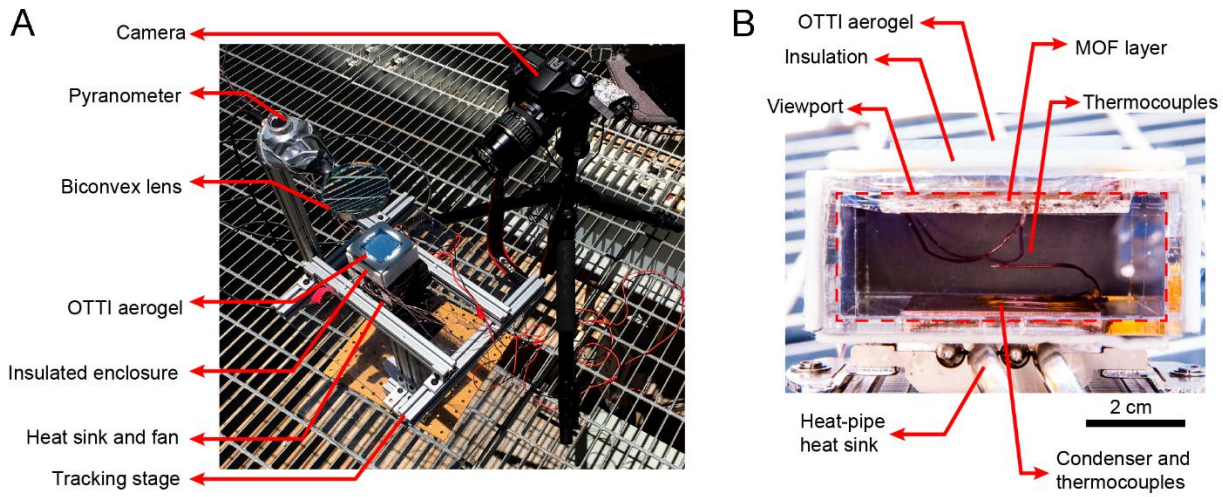

Figure 5.2. Water harvesting device test apparatus. (**A**) Photo of the device test apparatus during the solar-assisted water production with 1.8× optical concentration. Test location: Tempe, Arizona, United States. (**B**) Photo of the water harvesting device showing the MOF layer (5 cm by 5 cm base, porosity of 0.67 or packing density of 464 kg m^{-3} with 2.57 mm thickness), condenser (4 cm by 4 cm), and thermocouples through the view port. OTTI aerogel, heat pipe heat sink and insulation are also shown.

5.4 Water harvesting experiments

Five water harvesting cycles were performed between May 11 and May 18, 2017 (Tempe, Arizona, United States) with the same MOF layer. Prior to the first cycle, the MOF layer was heated and dehydrated under direct solar radiation to ~50 °C and in an ambient of 35 °C and RH less than 20% for ~1.5 h. The experimental procedures and measurement/instrumentation details are presented in Supporting Information for this Chapter. We initiated the water harvesting cycle

around 20:00 hours local time. The absorber (black) side was positioned to face the clear sky to enable passive radiative cooling, reducing the MOF layer temperature below its ambient. Temperature drops of ~3 K were consistently observed throughout the adsorption phase of the five consecutive water harvesting cycles. This reduction in temperature corresponds to a 5-7% increase in effective RH experienced by the MOF layer. While the ambient vapor pressure was constant in this case, the saturation pressure is now defined by the temperature of the cooler adsorbent layer. After the overnight adsorption process, the MOF layer was installed back into the device between 06:00 and 07:00 hours local time, before the ambient RH started to decrease. The solar-assisted desorption phase of the water harvesting cycle started typically between 10:00 and 11:00 hours local time. For water harvesting cycles with non-concentrated solar irradiance, the global horizontal irradiance (GHI) was measured directly using a pyranometer. Water harvesting cycles with 1.8× optical concentration and direct normal irradiance (DNI) was achieved by facing the sun, where the measured global normal irradiance (GNI) was used to evaluate DNI for a clear day in Arizona, United States (see Methods). In addition, the tilting of the device at the elevation angle of solar irradiance enhanced mass transfer due to buoyancy-assisted transport and condensation of the hot desorbed vapor (see details of water harvesting cycles in Supporting Information). Due to the limited quantity of MOF-801 used in the device (~3 g), accurate measurement of the quantity of harvested water was not possible, albeit we expected ~0.75 g of water production. Therefore, we used validated computational predictions[4] based on the measured conditions during the water harvesting cycles (ambient and condenser temperatures, RH, and solar flux) to evaluate deliverable water capacity.

Representative water harvesting cycles without optical concentration (May 14-15, 2017) and with concentration (May 17-18, 2017) with the associated temperature profiles (MOF layer, environmental, dew point and condenser), solar flux and RH measurements are shown in Figures 5.3A, B, respectively. In both figures, the upper abscissa indicates the measured RH at the local time of day (lower abscissa). The radiative cooling during the adsorption phase (between ~20:00 and 06:00 hours) is also shown. During the desorption phase (starting between ~10:00 and 11:00 hours the next day), the MOF layer temperature increased when exposed to incoming solar irradiation. Images taken during this phase are shown in Figures 5.3C, D. The desorption started immediately following exposure to the solar irradiation and water condensation was observed on both the view port (fogging) and the condenser. The amount of fogging reduced over time as the enclosure walls and the air-vapor mixture inside the device heated up.

For the cycles carried out with optical concentration, the higher desorption temperatures (or desorption driving potential) can be inferred from Figure 5.3B. In addition, the rate of regeneration was significantly faster than the predictions (see water harvesting cycles and Figure S5.10 in Supporting Information) due to buoyancy-assisted vapor transport during condensation (as the stage was tilted and faced the sun at the elevation and azimuth angles). The higher desorption temperatures associated with the concentrated case enabled complete desorption and this can be qualitatively deduced from the change in slope of the adsorber temperature in Figure 5.3B (~11:45 hours local time). After complete desorption, most of the incident solar energy was available for sensible temperature rise leading to the slope change.

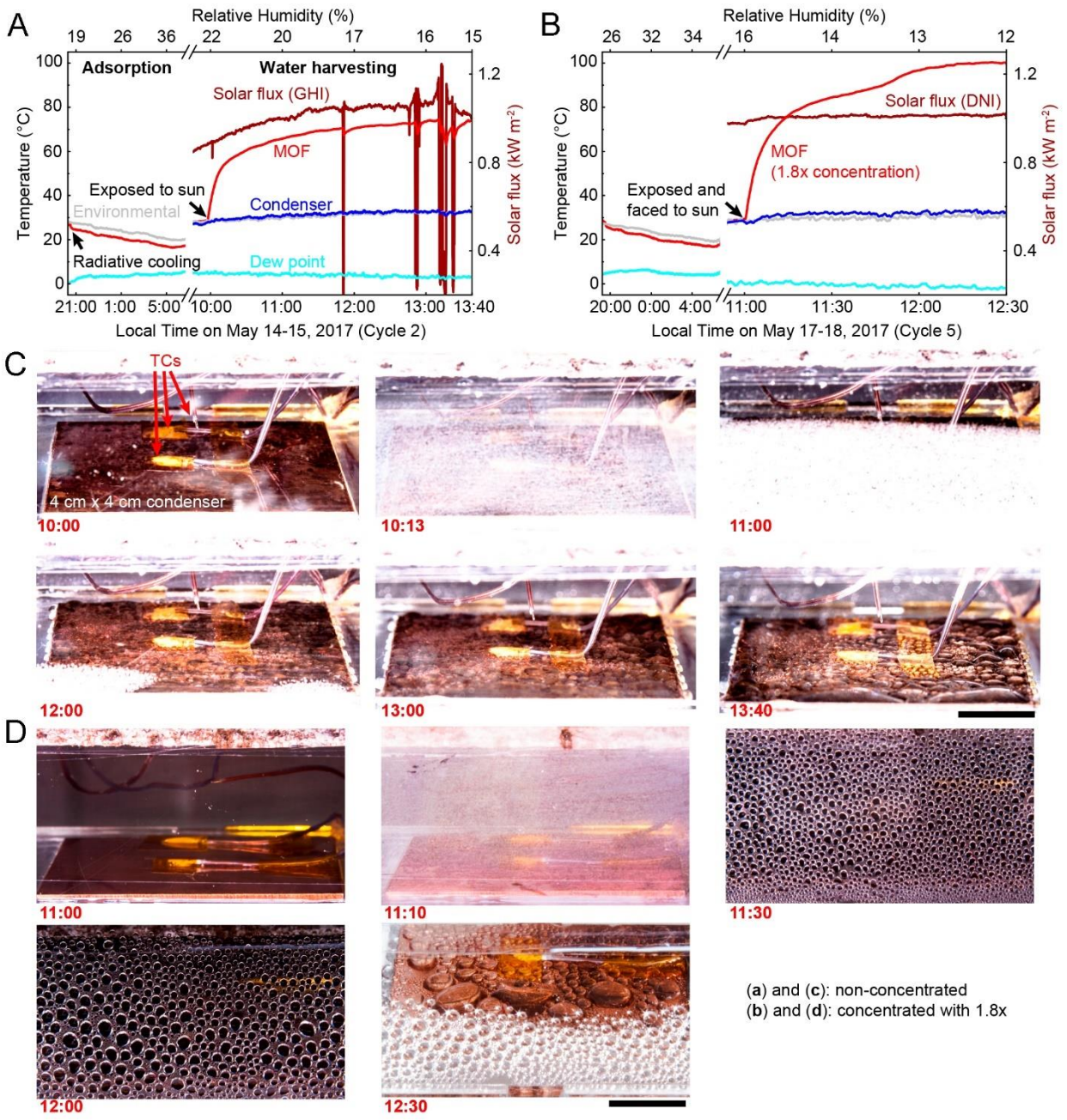

Figure 5.3 Water harvesting test results. (**A**, **B**) Representative temperature profiles (environmental, MOF layer, dew point and condenser) and solar flux (global horizontal irradiance (GHI) or direct normal irradiance (DNI)) as a function of local time for representative non-concentrated (Cycle 2, May 14-15, 2017) and concentrated with 1.8× (Cycle 5, May 17-18, 2017) cycles, respectively. (**C**, **D**) Representative photos illustrating droplet condensation on the copper plate condenser (4 cm by 4 cm) during the water harvesting process as a function of local time for representative non-concentrated (cycle 2) and concentrated (cycle 5) cycles, respectively. Shortly after the solar exposure, the view port fogged up due to condensation of desorbed vapor for both cycles. Thermocouples (TCs) measuring the condenser, air gap and the MOF layer temperatures are also shown. Due to the higher solar flux with the concentration, the rate of temperature increase of the MOF layer was significantly faster than the non-concentrated cycle, reducing the time required for desorption. The temperature slope change at ~11:45 hours local time indicates near completion of desorption. The predicted amount of harvested water for the non-concentrated (cycle 2) and concentrated (cycle 5) cycles were ~0.12 L and ~0.28 L per kg of MOF, respectively. Scale bars are 1 cm.

5.5 Prediction of harvested water

High-fidelity computational simulations based on the characteristics of MOF-801 (see Figures S5.9 and S5.10 in Supporting Information for this Chapter) were used to predict the water harvesting capacity of the device. Experimentally measured ambient and condenser temperatures, solar flux and RHs were used for the initial and boundary conditions. For the representative nonconcentrated cycle, ~0.12 L of water per kg of MOF-801 was delivered following saturation at 40% RH (equilibrium uptake of ~0.28 kg kg^{-1}). From the equilibrium considerations presented in Figure 5.1B, after the desorption phase, the residual uptake at ~13% RH (adsorber at 74 °C and P_{sat} of 37 kPa; condenser at 33 °C and P_{sat} of 5 kPa) was ~0.09 kg kg^{-1}, leading to a net water production capacity of ~0.19 L kg^{-1} (liters per kg of MOF). However, due to the kinetic limitations, the residual uptake at the end of the desorption was predicted to be only ~0.16 kg kg^{-1}, leading to ~0.12 L kg^{-1} water production capacity. The kinetic limitations are dictated by *intra*/*inter*crystalline diffusion within the MOF layer as well as the vapor diffusion between the MOF layer and condenser. Similarly, for a representative cycle with an optical concentration (1.8×), an adsorber temperature of 100 °C (P_{sat} of 101 kPa) and a condenser temperature of 33 °C (P_{sat} of 5 kPa), the water production capacity was predicted to be ~0.28 L kg^{-1}. This prediction is consistent with the estimate from the simulation (see Figure S5.10). Here, the kinetic limitations were overcome by the higher adsorber temperature as well as the buoyancy-assisted vapor transport during condensation.

As a result of the optical concentration and tilting of the device, we predicted a thermal efficiency gain of ~5× in comparison to the non-concentrated cycle. Accordingly, with the concentration, the thermal efficiency was ~14% with input solar energy (product of DNI and optical concentration; herein, DNI was ~93% of GNI for the test location) and was ~3% for the non-concentrated cycle with GHI. The present device configuration and ambient conditions can deliver over ~0.34 L m^{-2} $cycle^{-1}$ (liters per m^2 of MOF layer base area per cycle) with the 1.8× solar concentration.

5.6 Water quality analysis

Though hydrothermal stability of MOF-801 has been extensively studied and well-established, we quantitatively characterized the quality of the harvested water using a bench-top adsorption cycling system that enables sufficient water collection (see Figure S5.11, S5.12). Results from inductively coupled plasma-mass spectroscopy (ICP-MS) analysis indicate that the zirconium concentration in the water was found to be less than 1 ppb (parts per billion). In addition, the harvested water was analyzed using infrared spectroscopy and evidence of organic linkers (fumarate) was not found, indicating that the compositions from MOF-801 did not contaminate the harvested water.

5.7 Performance comparison

The concept of using night-time radiative cooling to increase the effective RH experienced by the adsorber layer is introduced and discussed in this work. This approach opens possibilities to use MOFs, such as MOF-841[11] or Co_2Cl_2BTDD[13] with adsorption step located at 25-30% RH, which have higher water uptake values and need even lower regeneration temperatures can be used in climates which offer ~20% RH for adsorption. FAM Z-series (functional adsorbent material zeolite), also referred as AQSOA series[14], offers step-like

isotherm located at 15–20% RH with adsorption capacity of ~0.2 kg kg^{-1} (AQSOA Z01). The device design and operation presented in this work can be similarly extended with such advanced zeolites. However, the synthetic flexibility and ability to tune adsorption properties are unique to MOFs[15] and, therefore, ideally suited for atmospheric water harvesting systems. While the chosen MOF-801 in this study can deliver ~0.34 L m^{-2} $cycle^{-1}$ (or ~0.25 L kg^{-1} $cycle^{-1}$), further improvements can be realized with the development of new MOFs. For instance, with an identical device design and optimization, a cobalt-based MOF (Co_2Cl_2BTDD) with an adsorption capacity greater than 0.8 kg kg^{-1} at ~30% RH can lead to ~1 L m^{-2} $cycle^{-1}$ of water output, potentially leapfrogging the water harvesting output of advanced zeolites. While sorption kinetics of this MOF is relatively slower than MOF-801, we envision that the development of new MOFs with enhanced sorption capacities and kinetics can ultimately lead to a significant increase in water harvesting output.

Passive operation can be enabled with concentrating thermal energy with larger absorber areas[16] or with stationary reflectors[17] that eliminates the need for solar tracking (see thermal analysis for passive operation in Supporting Information). Furthermore, considerations presented in this work can be extended to a higher output system by integrating multilayer adsorbent stacks into a compact bed-type architecture[18–20], common to many classes of adsorption systems. The merit of the bed-type architecture is that in addition to solar-thermal, waste heat or low-infrastructure sources of energy such as biomass can be used to drive the desorption process (eliminating the need for a planar adsorber). While such a system configuration can enable higher output, the limitation of this approach is the need for auxiliary components (e.g., pumps) and higher system complexity to efficiently route the thermal energy to the various layers in the bed. The required heat storage capacity and source temperatures would need to be determined based on the required temperature difference between the adsorber and the condenser, which can be inferred from the adsorption isotherm. Our demonstration in an exceptionally arid climate indicates that adsorption-based water harvesting strategy is a promising solution to solve water scarcity in these regions.

Supporting Information for Chapter 5

Synthesis and characterisation of microcrystalline powder MOF-801.

In a 500 mL screw-capped jar, 5.8 g (50 mmol) of fumaric acid (Fluka, 99%) and 16 g (50 mmol) of $ZrOCl_2 \cdot 8H_2O$ (Alfa Aesar, 98%) were dissolved in a mixed solvent of DMF and formic acid (200 and 70 mL, respectively). The mixture was then heated in an isothermal oven at 130 °C for 6 h to give as-prepared MOF-801 as white precipitate. The precipitate from three reaction jars was collected by filtration apparatus using a membrane filter (45 μm pore size), washed three times with 100 mL DMF, three times 100 mL methanol, and dried in air. Air-dried MOF sample was transferred to a vacuum chamber. The chamber was first evacuated at room temperature for 5 h until the pressure dropped below 1 kPa. After that, the sample was heated in vacuum at 70 °C for 12 h, and then at 150 °C for another 48 h. This finally gave activated MOF-801 as a white powder (yield: 30 g). Low-pressure gas (N_2 and Ar) adsorption isotherms were measured using volumetric gas adsorption analyser (Autosorb-1, Quantachrome). Liquid nitrogen and argon baths were used for the measurements at 77 and 87 K, respectively. The powdered particle density (ρ_p) of activated MOF-801 was estimated to be 1400 ± 20 kg m^{-3} from the pycnometer (Ultrapyc 1200e, Quantachrome) (skeletal density ρ_s = 2.6991 g cm^{-3}) and BET pore volume measurements (V_p = 0.3425 cm^{-3} g) using the following equation: $\rho_p = 1/(V_p + 1/\rho_s)$. The particle size and *inter*crystalline diffusion characteristics of the powder MOF-801 were characterized.

Synthesis and optical characterisation of OTTI aerogel.

The OTTI silica aerogel was synthesized by sol-gel polymerization of tetramethyl orthosilicate (TMOS, CAS 131903, Sigma Aldrich), using an ammonia solution (NH_3, 2.0 M in methanol, CAS 341428, Sigma Aldrich) as a catalyst to promote both hydrolysis and condensation reactions[9,10]. TMOS was diluted by methanol (MeOH, CAS 322415, Sigma Aldrich) followed by addition of NH_3 and water. The mixing molar ratio of chemicals was NH_3:TMOS:water:methanol = 0.004:1:4:6. Then, the solution was gelled in a disposable polystyrene container. After 2 weeks, the container was dissolved away using acetone. The mother solvent was replaced with ethanol (EtOH, CAS 89234-848, VWR) to be prepared for critical point drying (CPD, model 931, Tousimis) as EtOH is miscible with liquid CO_2. To dry the wet gels in EtOH without cracks, it is important to dry them slowly to minimize capillary pressure during the CPD process. A bleed rate of 100 psi h^{-1} was used to decrease the CPD chamber pressure from ~1300 psi to ambient pressure. After drying, the monolithic aerogels were annealed at 400 °C for 24 h to maximize their transmittance. The aerogel was cut to the final size using a laser cutter (Epilog Zing). Experimentally measured solar transmittance and predicted thermal conductivity[20,21] of the 8-mm-thick OTTI aerogel are shown in Figures S5.3A, B , respectively.

Device fabrication.

The adsorber layer was fabricated by first brazing a porous copper foam (~100 pores per inch or ppi), 0.26 cm thick, onto a copper plate (5 × 5 × 0.17 cm). The activated MOF-801 was infiltrated into this foam-plate structure by immersion drying in a ~50 wt. % aqueous dispersion. The copper foam provided structural rigidity and helped enhance the effective thermal conductivity of the layer, given the intrinsically low thermal conductivity of the porous MOF. The layer was then dried under vacuum for 4 h at the temperature of 70 °C and the total mass dehydrated MOF-801 was characterized to be 2.98 g. This corresponds to a packing density of

464 kg m^{-3} (dry) and a porosity of 0.67. In order to enhance solar absorption, the back side of the absorber was coated with Pyromark paint. This coating was optically characterized using a UV-Vis-NIR spectrophotometer (Cary 5000, Agilent) and found to have a solar-weighted absorptivity of 0.95.

The adsorber layer was then integrated into an enclosure constructed with acrylic sheets (0.318 cm thick). The top face was designed with a cut-out, equal in size to the adsorber layer (5 cm × 5 cm) and pilot holes to suspend the adsorber layer with nylon strings. Any gaps found between the side walls of the adsorber layer and the cut out were sealed with high temperature vacuum grease (Dow Corning). In addition, a layer of transparent polyethylene wrap was stretched over the entire top face and sealed against the side walls. Both these measures prevented leakage of any desorbed vapour. Thermal insulation (white in color) was attached on all side walls except the view port. The adsorber side was completed by placing a piece of OTTI aerogel measuring 5 × 5 × 1 cm. The bottom face of the enclosure was made with a 4 × 4 cm cut-out to enable integration with a condenser assembly. The condenser assembly comprised a 4 × 4 × 0.6 cm polished copper piece that was bonded with high conductivity thermal epoxy (Omega Therm, Omega Engineering) to a heat pipe heat sink (NH-L9x65, Noctua). The air-cooled heat sink consisted of a finned heat pipe array with a fan that consumed ~0.9 W of electrical power to dissipate the condensation heat. The finished device measured 7 × 7 × 3.2 cm (excluding the heat sink, fan, insulation and aerogel) and was mounted on a stage with adjustable tilt to enable experiments under both GHI (no optical concentration, no tilt) and GNI (with optical concentration of 1.8× and tilt at elevation angles of 55−75° and azimuth angles of 100−180°).

Experimental procedure.

The water harvesting experiment comprises two phases: night-time vapor adsorption and day-time water harvesting and condensation. During vapor adsorption, typically started at 20:00 hours local time (UTC/GMT—7 h), the adsorber layer with its acrylic frame was mounted into the cover of an air-tight food storage container with the pyromark coated side up for night-time radiative cooling (see Figure S5.1). The sides of the air-tight container were modified to fit a fan (0.9 W; 12 VDC) and enable cross flow of ambient air (vapor source). Two T-type thermocouple (5TC series, Omega Engineering) were used to measure the temperature of the adsorber layer during adsorption. In order to estimate the extent of radiative cooling and ambient temperature, another T-type thermocouple was placed in the air stream of another fan. Relative humidity measurements were made with a capacitive RH sensor (RH820U, Omega Engineering). Transparent polyethylene wrap was used to suppress convective heat loss on the black absorber side of the layer. Prior to the exposure to the clear sky, the container cover was wrapped in aluminum foil so that the MOF layer could equilibrate with the ambient air. Once the foil was removed, the MOF layer was exposed to the sky and an instant temperature drop of ~3 K below ambient was observed, as shown in Figures 5.3A and 5.3B (main text of this Chapter), due to radiative cooling. Adsorption was allowed to occur overnight and the sample was sealed into the device (between 06:00 and 07:00 hours local time) to prevent undesired loss of water due to the RH swing.

The procedure for water release and condensation typically started between 10:00 and 11:00 hours local time. In addition to the two T-type thermocouples embedded into the adsorption layer, three additional T-type thermocouples were used to measure temperatures: two for the copper condenser plate and one for the vapor space between the adsorber layer and the condenser plate. Ambient humidity and temperature conditions were recorded as described

during the adsorption phase. The heat of condensation was dissipated to the ambient through the heat sink and fan operating at 0.9 W. The incoming solar irradiation (both global horizontal (GHI) and global normal (GNI) irradiations) was measured with a pyranometer (LP02-C, Hukseflux). The measured GNI was used to evaluate the DNI as: DNI = GNI – DI (diffuse irradiance) according to the weather data available from a weather station in Tucson, Arizona, United States (available at NREL, SOLRMAP University of Arizona (OASIS)) for clear days in May 2017. The ratio between the GNI and DNI was found to be 0.93 and it matched well to an available correlation[22]. The area ratio between the lens and solar absorber surface was ~2.5; however, the achieved optical concentration of 1.8× was due to transmittance loss of the lens and the square solar absorber area being circumscribed by the circular concentrated solar irradiance (Figure 5.2A). The actual optical concentration achieved with the concentrating lens was characterized to be 1.8× for the focal distance during the outdoor experiments with a thermopile detector (919P-040-50, Newport) and a solar simulator (92192, Newport Oriel). Solar transmittance of the transparent polyethylene wrap, ~0.93, was characterized with the pyranometer under direct solar irradiance. Images were acquired with a digital camera (EOS DS126211, Canon) to visualize the condensation process (see Figure 5.3). At the end of desorption, the MOF layer and its acrylic frame were extracted from the device to prevent re-adsorption of condensed water and isolated in an air-tight box. The adsorber assembly was only removed in the evening time to restart the adsorption phase for the next cycle. A total of five water harvesting cycles are reported in this study: cycle 1 (Figure S5.8A,B), cycle 2 (Figure 5.3A,C), cycle 3 (Figure S5.8C,D), cycle 4 (Figure S5.8E,F), and cycle 5 (Figure 5.3B,D).

Water quality analysis.

In order to quantitatively characterize the harvested water, a bench-top adsorption cycling system was constructed. A schematic of the water collection apparatus for ICP-MS analysis is shown in Figure S5.11A. The system consists of five main components, namely, adsorption and condenser chambers, a glass flask that serves as a reservoir for HPLC water (OmniSolv HPLC grade water, VWR), two temperature-controlled thermoelectric stages (CP-200HT-TT, TE Tech), and a vacuum pump. The adsorption and con-denser chamber were custom-designed copper vacuum chambers (2 × 2 × 1 cm) with a removable lid. The adsorption chamber additionally had a layer of copper foam (2 × 2 × 0.8 cm) brazed to the bottom, which was infiltrated with activated MOF-801 (~1.5 g). These chambers were individually placed in thermal contact with a temperature-controlled thermoelectric stage that allowed for continuous cycling. Thermocouples (5TC series, Omega Engineering) were inserted into pilot holes made in the side walls of the copper chambers. For cycling, a pair of electronically controlled vacuum valves were used to link the adsorbent chamber to either the water reservoir during adsorption or the condenser chamber during desorption.

The adsorption−desorption cycles were performed under evacuated conditions to enable efficient transport of vapor across distances of ~0.5 m through the hoses and valves as shown in Figure S5.11A. The water in the glass flask was first degassed to remove non-condensable gases by connecting it to the vacuum pump and freezing the water. The flask was then heated to melt the ice under evacuation and reduce the solubility of non-condensable gasses. This cycle was repeated three times. The adsorption and condenser chambers were heated to 60 °C for 2 h under evacuated conditions to ensure there was no residual water in the system. The cycling experiments started with the adsorption phase, where the water reservoir was exposed to the adsorbent chamber. The dry adsorbent triggered evaporation and the generated vapor was

adsorbed. During adsorption, the chamber was held at a constant temperature of 30 °C to extract the adsorption heat as well as prevent any condensation of vapor from the reservoir kept at ~20 °C. After complete adsorption (~40 min), the adsorption chamber was isolated from the water reservoir and exposed to the condenser chamber. The thermoelectric stage of the adsorption chamber was programmed to ramp up to 60 °C at this stage while the condenser stage was always maintained at 0.5 °C. The desorption was allowed to continue for 40 min at the end of which the adsorption chamber was opened to the reservoir and simultaneously cooled to 30 °C for the next cycle. Representative temperature and pressure profiles for a desorption−adsorption cycle are shown in Figure S5.11B. This cycle was repeated 18 times and about 8 g of condensed water was collected (*i.e.*, ~0.3 L of water per kg of MOF per cycle).

The HPLC grade water from the reservoir was used as a control sample. The concentration of potentially contaminant elements was analyzed using an inductively coupled plasma–mass spectroscopy system (ICP-MS, Agilent 7900, 68403A). Both the harvested water and control sample were analyzed for the following elements: iron (from tubes/hoses), copper (from foam, chambers and braze alloy), silver, indium (both from braze alloy) and zirconium (from MOF compound). In addition, FT-IR spectra of control water (HPLC grade) and collected water from MOF-801 were collected in-house using a Bruker ALPHA Platinum ATR-FT-IR Spectrometer equipped with a single reflection diamond ATR module.

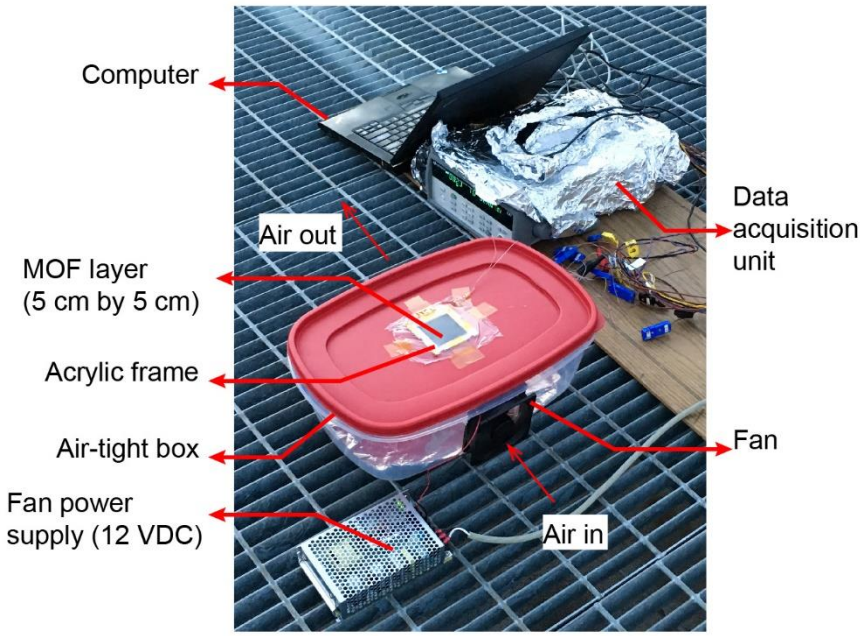

Figure S5.1. Photo of experimental setup during night-time adsorption. The MOF layer with its acrylic frame was mounted into cover of an air-tight plastic storage container with the pyromark coated side up for night-time radiative cooling. A ~5 kg metal block was placed inside to secure the apparatus against wind damage. The sides of the air-tight container were modified to fit a fan (0.9 W; 12 VDC) and enable cross flow of ambient air (vapor source). Initially, the black absorber side was covered with aluminum foil to reach thermal equilibrium with the ambient. At the start of the adsorption experiment, the aluminum foil was removed and a temperature drop due to the passive radiative cooling was observed.

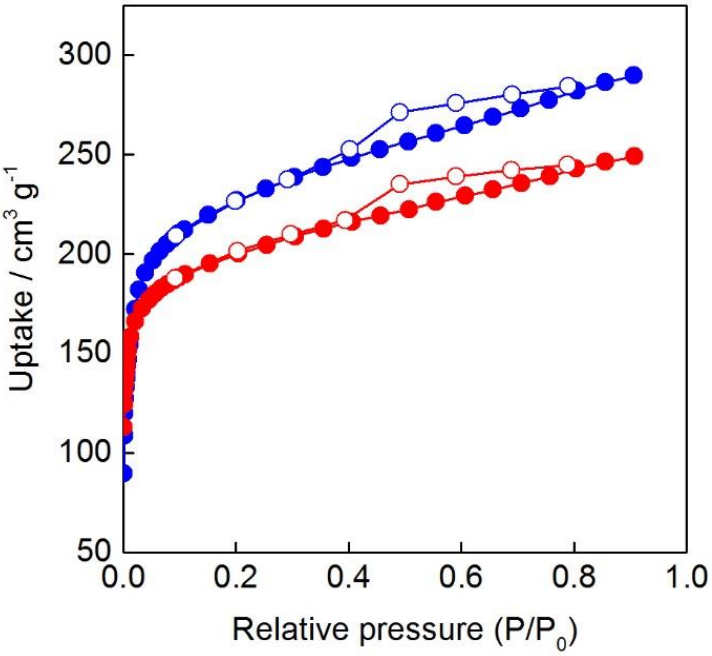

Figure S5.2. N_2 (red) and Ar (blue) adsorption isotherms of MOF-801 at 77 K and 87 K as functions of relative pressure, respectively.

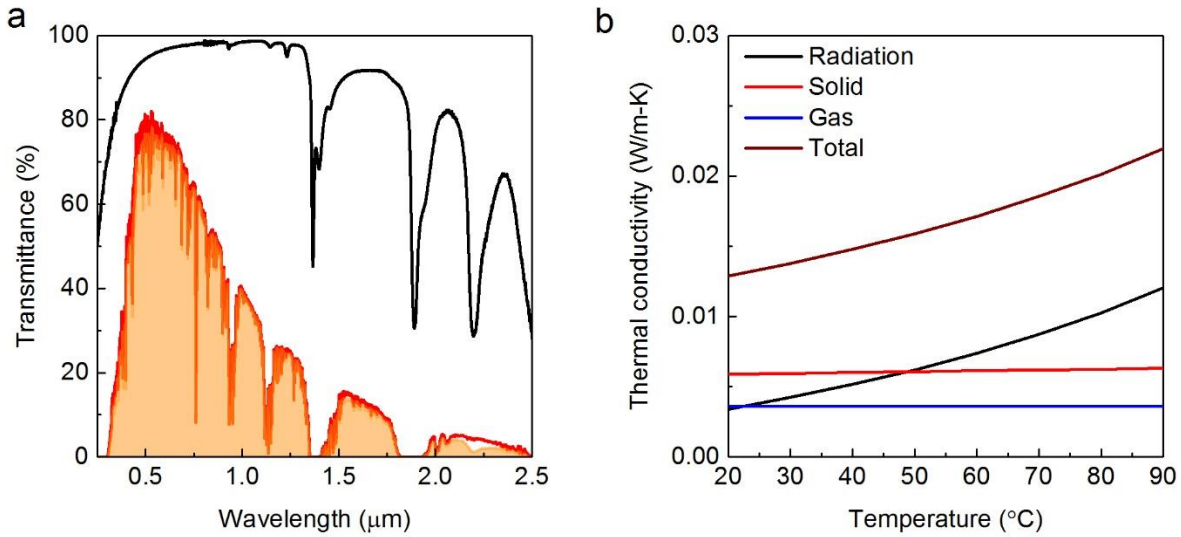

Figure S5.3. (**A**) Measured transmittance of an 8 mm thick aerogel sample using UV-Vis-NIR spectrophotometer (Cary 5000, Agilent). The AM1.5 solar spectrum is shown for comparison (red line). The orange area represents the transmitted spectrum by the aerogel. The solar weighted transmission of the sample is 94.5%. (**B**) Predicted thermal conductivity of an 8 mm thick aerogel sample. Contributions from radiation, solid conduction, and gas convection are also shown.

Theoretical modelling framework.

A theoretical model based on mass and energy conservation was used to predict the adsorption-desorption dynamics and the extent of regeneration for MOF-801 during the solar-assisted desorption process using the following governing equations[4,19,23]:

$$\frac{\partial C}{\partial t} = \nabla \cdot D_v \nabla C - \frac{(1-\varepsilon)}{\varepsilon} \frac{\partial C_\mu}{\partial t} \tag{5.1}$$

$$\rho c_p \frac{\partial T}{\partial t} = \nabla \cdot k \nabla T + h_{ad}(1-\varepsilon) \frac{\partial C_\mu}{\partial t} \tag{5.2}$$

Equation (5.1) describes mass conservation of the vapor during diffusion and adsorption/desorption within the packed MOF layer. Here, C, is the local vapour concentration (mol m^{-3}), $\partial C_\mu / \partial t$ is the average instantaneous rate of vapour adsorption/desorption, ε is the porosity, and D_v is the *inter*crystalline diffusivity of vapor (m^2 s^{-1}). The vapor concentration (mol m^{-3}) can be expressed from the ideal gas law, $C = PR^{-1}T^{-1}$, where P, R, and T denote the pressure (Pa), universal gas constant (J mol^{-1} K^{-1}), and temperature (K). The effective vapor *inter*crystalline diffusivity, D_v, in an air-vapor mixture with consideration of both Knudsen and molecular diffusions in tortuous porous media can be estimated as[24–26],

$$D_v = \varepsilon^{3/2} \left(\frac{1}{D_{vap}} + \frac{1}{D_{K,vap}} \right)^{-1} \tag{5.3}$$

where D_{vap} and $D_{K,vap}$ are vapour molecular diffusivity in air and Knudsen diffusivity of vapour, respectively.

In Equations 5.1 and 5.2, C_μ is the vapor concentration within an adsorbent crystal, and the average instantaneous rate of adsorption/desorption, $\partial C_\mu / \partial t$, can be approximated with the linear driving force model[4,19,23,26].

$$\frac{\partial C_\mu}{\partial t} = \frac{15}{r_c^2} D_\mu (C_{eq} - C_\mu) \tag{5.4}$$

In Equation 5.4(4.7), D_μ represents the diffusivity of vapor inside an adsorbent crystal (*intra*crystalline), r_c is adsorbent crystal radius (m), and C_{eq} is the equilibrium vapour concentration corresponding to instantaneous local temperature and vapour pressure. r_c and D_μ were characterized experimentally, and C_{eq} can be estimated from a linear interpolation of the adsorption isotherms (Figure S5.6A).

Equation 5.2 represents energy conservation within the MOF layer. Here, ρc_P represents the average heat capacity (J m^{-3} K^{-1}), k is the thermal conductivity (W m^{-1} K^{-1}), and h_{ad} is the enthalpy of adsorption (J mol^{-1}) for MOF-801 and water (~55 kJ mol^{-1})[27]. The effective thermophysical properties were evaluated to include the contributions from the metallic copper foam (~3 W m^{-1} K^{-1}, porosity of ~0.95), MOF-801 (specific heat capacity of 760 J kg^{-1} K^{-1})[4], and the adsorbed water (assumed to be in a liquid state). In Equation 5.2, the advection term is neglected due to the high effective thermal conductivity of the MOF layer owing to the metallic binder (copper foam).

During the solar-assisted desorption, desorbed vapor is transported and condensed *via* diffusion in air. For the orientation of the device described in Figure 1 (main text), diffusional vapor transport between the MOF layer and the condenser can be approximated using Fick's law of diffusion where x represents the spatial coordinate:

$$\frac{\partial C}{\partial t} = D_{vap} \frac{\partial^2 C}{\partial x^2} \tag{5.5}$$

Packing density and estimation of *inter*crystalline diffusivities

The effective *inter*crystalline diffusion is a function of spacing between the packed adsorbent particles and temperature. The characteristic void size of a random packing of spherical particles of uniform size can be estimated using a probability distribution[4,23,28], on the basis of its average packing porosity (ε) and the porosity corresponding to the maximum packing density of hexagonally packed spheres (ε_{HCP}) as:

$$P(\chi) = 3(1+\chi)^2 \frac{\varepsilon(1-\varepsilon)(1-\varepsilon_{HCP})}{(\varepsilon-\varepsilon_{HCP})} \exp\left(-\frac{(1-\varepsilon)(1-\varepsilon_{HCP})}{(\varepsilon-\varepsilon_{HCP})}\left[(1+\chi)^3-1\right]\right) \tag{5.6}$$

The average porosity (ε) was calculated from the measured MOF layer density (ρ_{layer}) and the estimated particle density (ρ_p) of the activated MOF-801 (1400± 20 kg m^{-3}) using Equation 5.7 The porosity of the MOF-801 layer is determined to be 0.67.

$$\varepsilon = 1 - \frac{\rho_{layer}}{\rho_p} \tag{5.7}$$

The characteristic void size (d_p) based on this distribution can be estimated as, $d_p = 2r_c X_{avg}$, where r_c is the MOF crystal radius, and X_{avg} is defined as:

$$\chi_{avg} = \frac{1}{\varepsilon}\int_0^\infty \chi P(\chi) d\chi \tag{5.8}$$

The average crystal diameter of MOF-801 (~1 μm) was characterized using a scanning electron microscope (6010LA SEM, JEOL), as shown in Figure S5.4, and assumed uniform for the estimation of the void size.

The effective *inter*crystalline diffusivity can be computed using Equation 5.3(4.6), where the Knudsen diffusivity is $D_{K,vap} = (d_p/3)\sqrt{8RT/\pi M}$**,** and the d_p is ~0.34 μm for the porosity of 0.67 and uniform crystal diameter of 1 μm. The diffusion coefficient of vapor in air at atmospheric pressure as a function of temperature can be obtained using the following relation[24],

$$D_{vap,T} = D_{vap,ref}\left(\frac{T}{T_{ref}}\right)^{3/2}\left(\frac{\Omega_{D,ref}}{\Omega_{D,T}}\right) \tag{5.9}$$

where D_{vap} and Ω_D are the vapor diffusion coefficient and collision integral, respectively, and subscript *ref* denotes reference value. Effective *inter*crystalline and vapor diffusivities in air are plotted in Figure S5.5 using Equations 5.3 and 5.9, respectively.

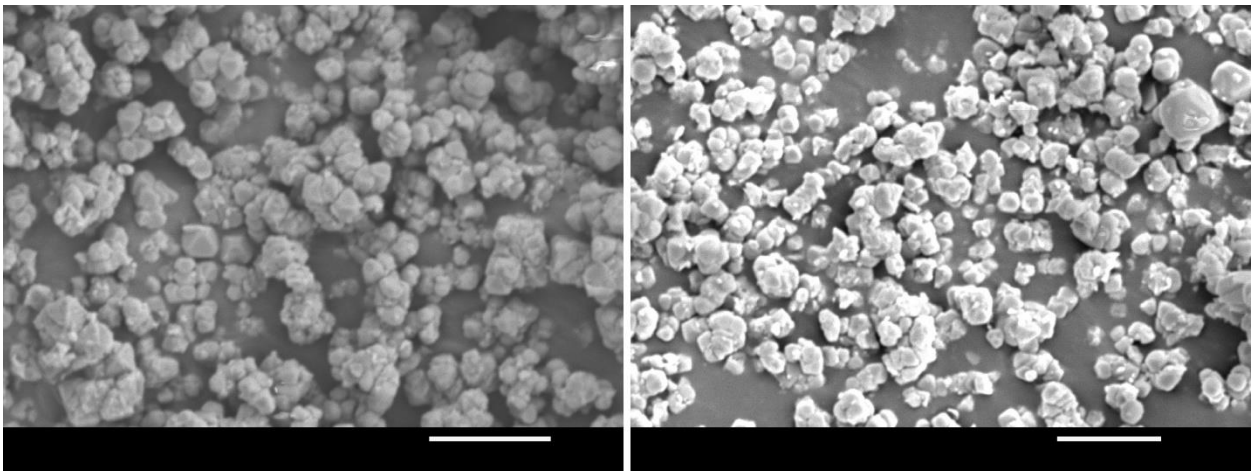

Figure S5.4. SEM images of powdered MOF-801. Crystal diameter of MOF-801 is 1 ± 0.15 μm, mean value and error (standard deviation) were obtained from image analysis using ImageJ software. Scale bars are 5 μm.

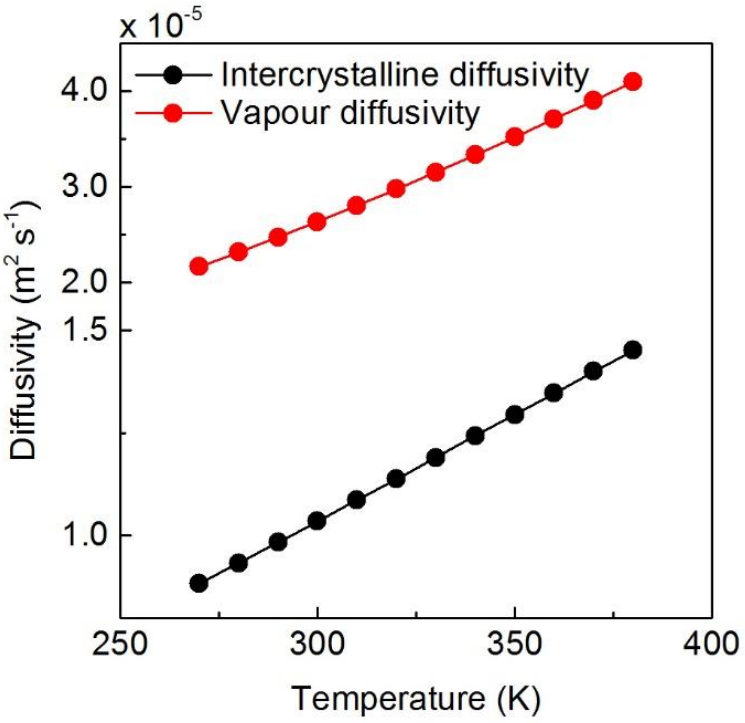

Figure S5.5. Effective *inter*crystalline vapor diffusivity of packed MOF-801 in air (black) as a function of temperature for the porosity of 0.67 and crystal diameter of 1 μm. Vapor diffusivity in air (red) as a function of temperature is also shown for comparison.

Adsorption isotherms and estimation of *intra*crystalline diffusivities of MOF-801

Vapor adsorption isotherms of MOF-801 were characterized using an adsorption analyzer (Q5000 SA, TA instruments) at 15, 25, 45, 65, and 85°C (see Figure S5.6A). The adsorption isotherm at 105°C was predicted using the characteristic curve based on the 85°C isotherm,

vapor uptake as a function of adsorption potential: $A = RT\ln(P_{sat}/P)$[12]. The vapor adsorption isotherm of MOF-801 before and after water harvesting cycles is also shown in Figure S5.6B, indicating the hydrothermal stability of MOF-801.

Using the dynamic adsorption behavior (*i.e.*, rate of mass adsorbed as a function of time), *intra*crystalline vapor diffusivity of MOF-801 was estimated using the following relation[29] where we assume homogeneous pore structure, constant spherical adsorbent crystals of radius (r_c), and constant surface concentration and diffusivity (D_μ),

$$\frac{m_t}{m_{eq}} = 1 - \frac{6}{\pi^2}\sum_{n=1}^{\infty}\left(\frac{1}{n^2}\right)\exp\left(-\frac{n^2\pi^2 D_\mu t}{r_c^{\,2}}\right) \tag{5.10}$$

where m_t/m_{eq} is the fractional water uptake with $m_t = 0$ at $t = 0$ and $m_t = m_{eq}$ as $t \longrightarrow \infty$ for a sufficiently small pressure and uptake step. The effective *intra*crystalline (Fickian) diffusivity of MOF-801 at 25 and 65°C were estimated by fitting Equation 5.10 with the experimental measurements, as shown in Figures S5.5C, and S5.5D, respectively. For the macroscopic modelling framework outlined, it is essential to define a characteristic *intra*crystalline diffusivity[4], therefore, constant *intra*crystalline diffusivities at 25°C or 65°C (25% RH) were used for the theoretical prediction.

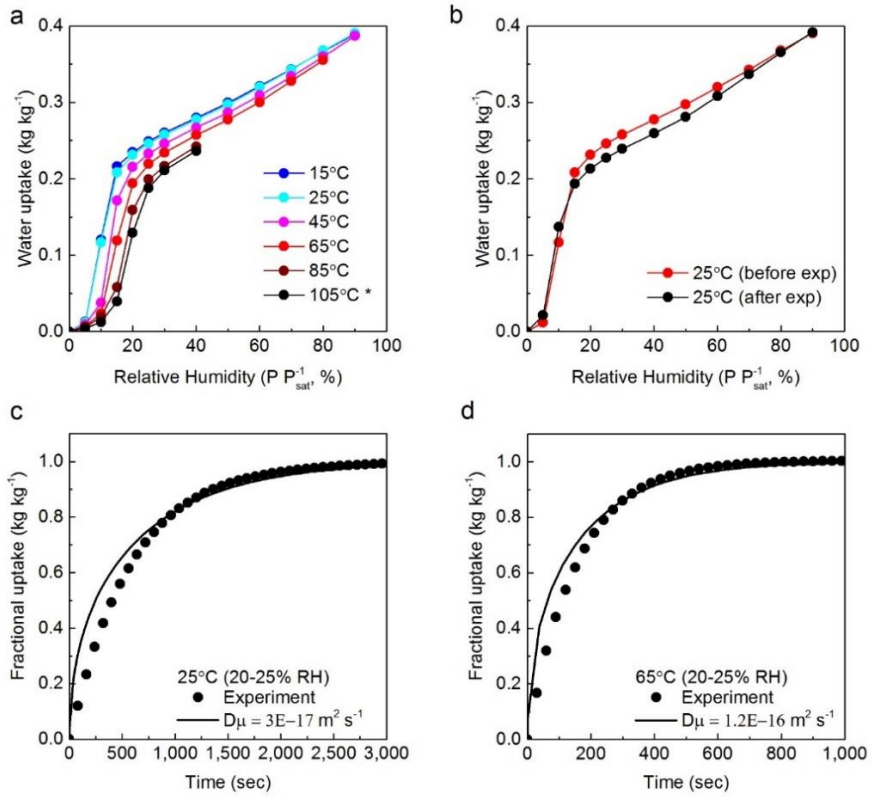

Figure S5.6. (**A**) Vapor adsorption isotherms of MOF-801 at 15, 25, 45, 65, and 85°C. *Isotherm at 105°C was predicted from the characteristic curve[12] based on the 85°C isotherm. (**B**) Vapor adsorption isotherms of MOF-801 at 25°C before (red) and after climate testing (black). (**C**) and (**D**) Fractional water uptake (kg kg^{-1}) as a function of time for MOF-801 characterized at 25 and 65°C at 25% RH, respectively. Dotted data (experimental) and solid line (fitting from Equation 5.10).

Optimization of MOF layer

To enable sufficient vapor diffusion kinetics along with reasonably high water production, findings from our recent study suggests that the optimum packing porosity for the MOF-801-based water harvesting device is ~0.7[4]. Using the theoretical framework presented and characterized properties, adsorption-desorption dynamics for MOF-801 were simulated, as shown in Figure S5.7, and used as a guideline for selecting the optimum MOF layer thickness.

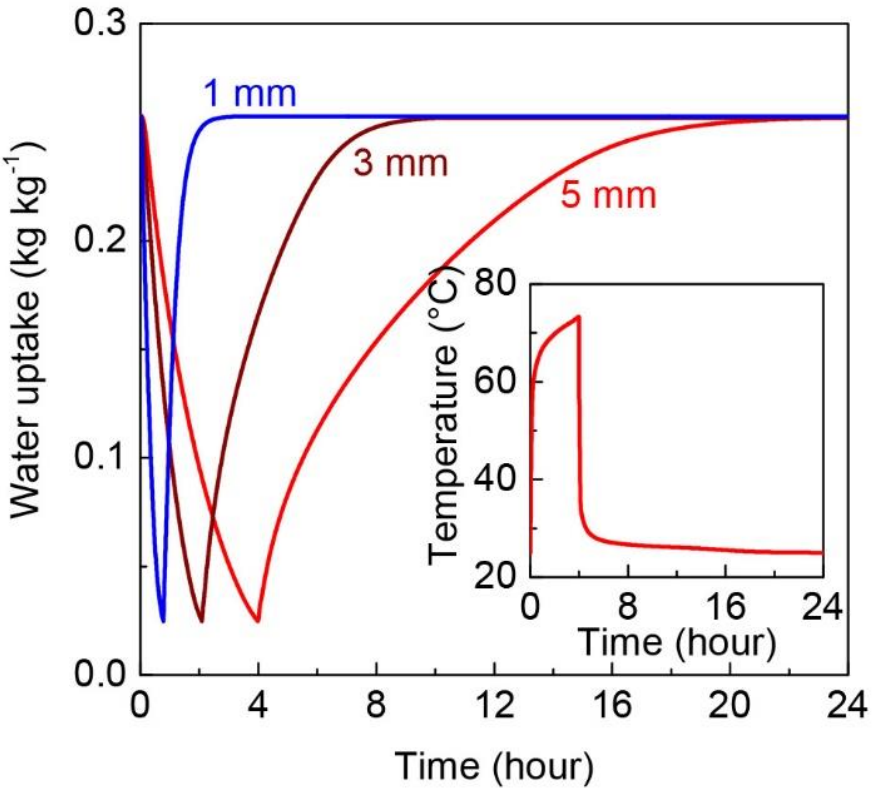

Figure S5.7. Adsorption-desorption dynamics of MOF-801 in ambient air at 30% RH. Predicted adsorption-desorption dynamics with a packing porosity of 0.67, desorption heat flux of 1 kW m^{-2}, natural convective heat transfer coefficient of 10 W m^{-2} K^{-1}, ambient temperature of 25°C, and thicknesses of 1, 3, and 5 mm. MOF-801 is initially equilibrated at 30% RH (25°C), and the partial vapor pressure rapidly increased from 30% RH to 100% RH (at 25°C) for condensation/water harvesting at 25°C with a desorption heat flux of 1 kW m^{-2}. Durations of solar exposure for 1, 3, and 5 mm thick MOF layer are 0.8, 2.1, and 4 hours, respectively. After desorption, solar exposure is stopped and the surrounding RH reverted to 30% RH for water adsorption from air. The temperature profile of a 5 mm thick MOF layer is also shown. Based on the predicted performance for the porosity of 0.67, the MOF layer thickness should be ~3 mm to enable complete saturation under the limited time window for adsorption (approximately under 8 hours in 20-40% RH environment). For simplicity, constant intracrystalline diffusion coefficient of $3e^{-17}$ m^2 s^{-1} is used for the simulation (Figure S5.6C) and sufficiently fast air freestream velocity is assumed to keep the RH of 30% at the MOF layer.

Water harvesting cycles: experiments and predictions

Using the theoretical framework outlined and characterized properties, computational simulations were carried out using COMSOL Multiphysics to evaluate the extent of regeneration during the solar-assisted water harvesting (Figures S5.9 and S5.10). Temperature (MOF layer, environmental, dew point, and condenser) and solar flux profiles, and photos of condensed

droplets of the water harvesting (adsorption-desorption) cycles for the cycle numbers 1, 3, and 4 are shown in Figure S5.8. Note that cycles 1 to 3 were carried out under global horizontal irradiance (GHI), and cycles 4 and 5 were carried out with 1.8x optical concentration with direct normal irradiance (DNI). For the cycle 4 and 5, due to buoyancy-assisted condensation with tilting of the stage, the regeneration was significantly faster than the predictions as evident in the change in temperature slope shown in Figure S5.10 after ~45 minutes of desorption. The thermal efficiency of the water harvesting cycle is defined as

$$\eta_{thermal} = \frac{m_{water} h_{fg}}{Q_{solar}} \tag{5.11}$$

where m_{water}, h_{fg}, and Q_{solar} are predicted amount of harvested water, latent heat, and input solar energy, respectively. For the non-concentrated cycle number 2, $\eta_{thermal}$ is predicted to be ~3% (with GHI) and for the concentrated cycle number 5, $\eta_{thermal}$ is predicted to be ~14% (with GNI times optical concentration of 1.8x). The efficiency for the concentrated cycle was evaluated on the basis of the time at which a change in the slope of the MOF temperature was observed. Despite the near complete desorption, at the time of the slope change, the simulation predicts ~0.1 kg kg^{-1} of residual uptake (Figure S5.10). This is due to fact that the simulation does not take into account the enhanced vapor transport due to buoyancy. Furthermore, the enhanced rate of desorption driven by the enhanced vapor transport (lower interface vapor pressure) is evident from the lower MOF layer temperature observed in comparison to the simulations. This can also be qualitatively deduced from the significantly greater amount of water condensation on the viewport compared to the non-concentrated cycles.

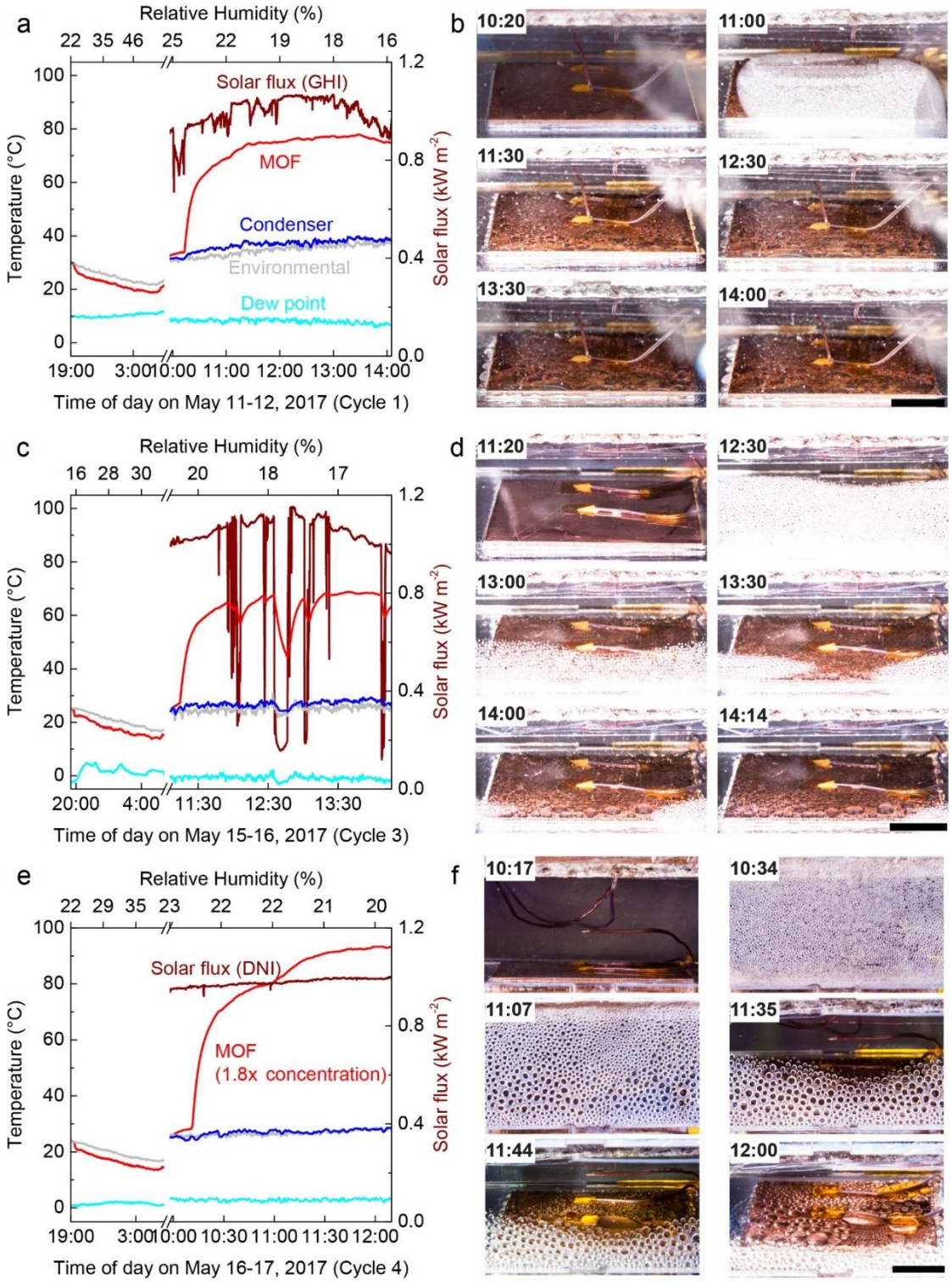

Figure S5.8. (**A**) Representative temperature profiles (environmental, MOF layer, dew point, and condenser) and solar flux (global horizontal irradiance (GHI)) as a function of local time for the cycle 1. (**B**) Representative photos illustrating droplet condensation on the copper condenser (4 cm by 4 cm) during desorption process as a function of local time for the cycle 1. (**C**) and (**D**), and (**E**) and (**F**) represent temperature profiles, solar flux (GHI for cycle 3 and direct normal irradiance (DNI) for cycle 4), and representative photos of droplet condensation for cycle number 3 and 4, respectively. Cycle 4 was carried out under DNI with optical concentration of 1.8x. Scale bars are 1 cm.

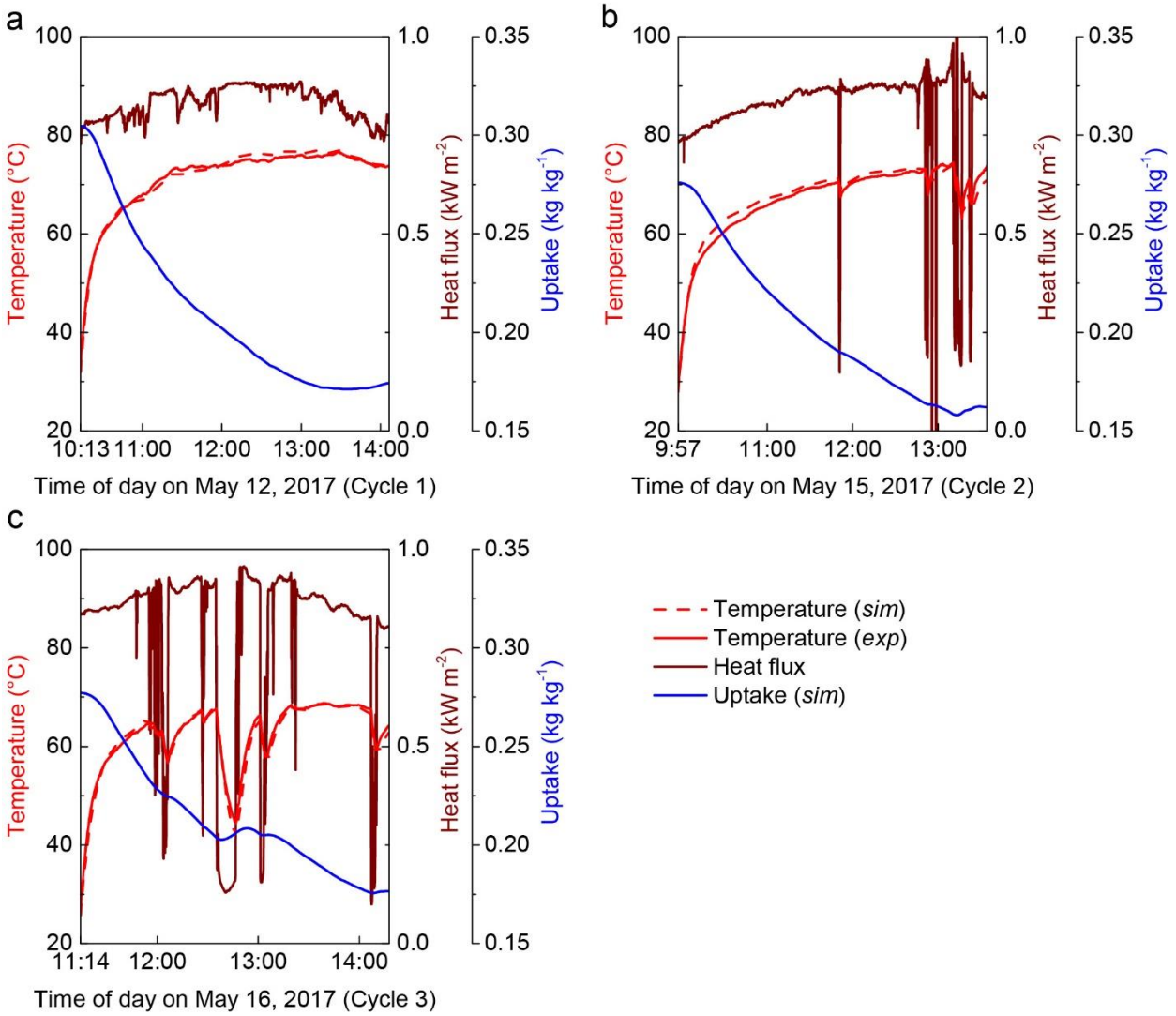

Figure S5.9. (**A-C**) Temperature profiles [Experimental (red solid line); predicted (red dotted line)], heat flux for desorption [(solar flux)*(optical and absorptance loss)], and predicted vapor uptake during the water harvesting as a function of time of day for cycles 1, 2, and 3, respectively. For cycle 1, an initial equilibrium RH of 55%, and for cycles 2 and 3, an initial RH of 40% was assumed based on the RH and radiative cooling measurements shown in Figure 5.3 (main text) and Figure S5.8. For simplicity, a constant *intra*crystalline diffusion coefficient of $1.2e^{-16}$ m^2 s^{-1} was used for the simulation (Figure S5.6D).

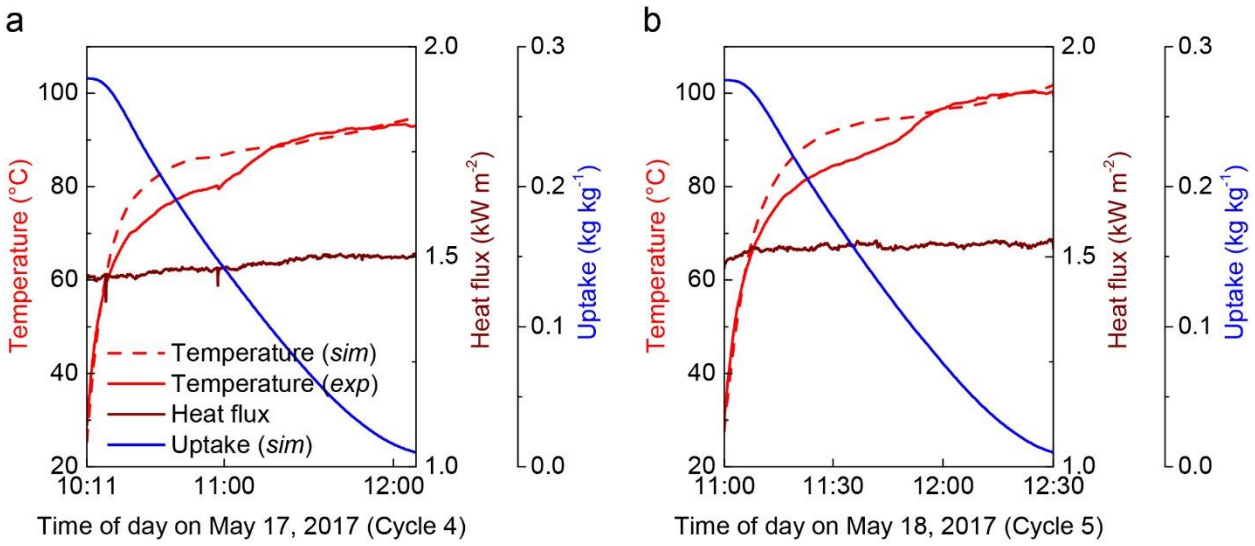

Figure S5.10. (**A-B**) Temperature profiles [Experimental (red solid line); predicted (red dotted line)], heat flux for desorption [(solar flux)*(optical and absorptance loss)*(optical concentration)], and predicted vapour uptake during water harvesting as a function of time of day for cycles 4 and 5, respectively. For both cycles, an initial equilibrium RH of 40% was assumed based on the RH and radiative cooling measurements shown in Figure 5.3 (main text) and Figure S5.8. For simplicity, a constant *intra*crystalline diffusion coefficient of $1.2e^{-16}$ m^2 s^{-1} was used for the simulation (Figure S5.6D).

Water quality analysis

Results shown in Figure S5.12 indicate that zirconium concentration in both the collected and control water was found to be indistinguishable and less than 1 ppb (part per billion), indicating that the metal ions (Zr) from MOF-801 did not leach the harvested water. The largest difference in composition was found in concentrations of iron and copper (which are both absent in MOF-801 compound) due to oxidation reactions occurring during the cycling experiments. While the concentration of iron (~3 ppb) in the harvested water was negligible, the concentration of copper (~2.6 ppm) can be eliminated through material choices. Copper was chosen in this study for its high thermal conductivity and ease of machinability (*i.e.*, milling and fabrication of chambers), which enabled an isothermal condenser. In a practical system, we envision the use of galvanized steel as a candidate material for the condenser and thermal binder. The FT-IR spectra indicated that signature of organic linkers (fumaric acid) was absent.

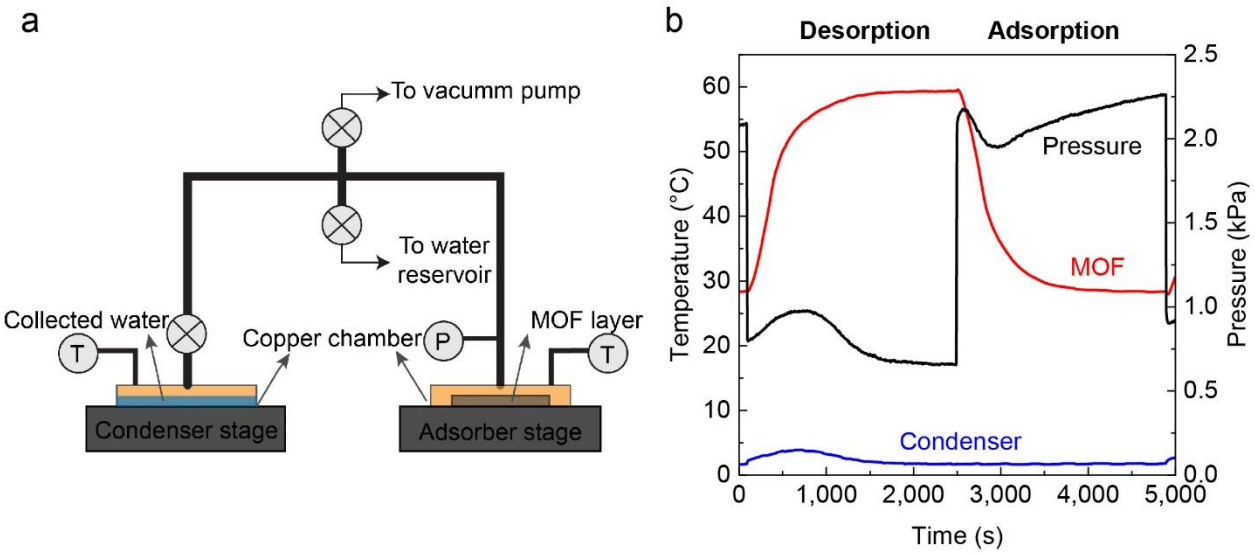

Figure S5.11. (**A)** Schematic of water collection apparatus with MOF-801 layer. (**B**) Representative temperature (MOF chamber and condenser chamber) and pressure profile (MOF chamber) for a desorption-adsorption cycle as a function of time.

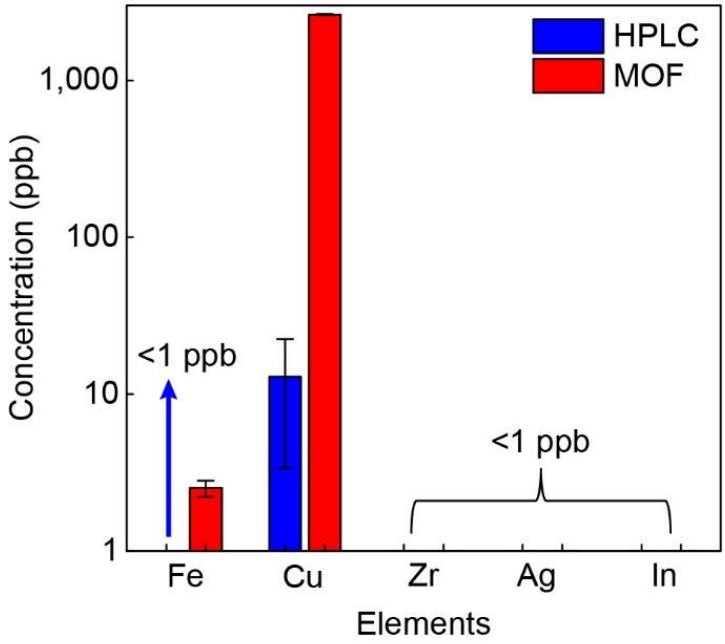

Figure S5.12. ICP-MS analysis of control water (HPLC) and water collected from MOF-801 (MOF). Iron (Fe; 56), copper (Cu; 63), zirconium (Zr; 90 and 91), silver (Ag; 107), and indium (In; 115) concentrations were analysed. Zirconium, silver, and indium concentrations in both HPLC and MOF samples were found to be less than 1 ppb (part per billion), indicating that the compositions from MOF-801 did not contaminate the harvested water. Iron concentrations in the harvested water (MOF) and control water (HPLC) were ~3 ppb and less than 1 ppb, respectively.

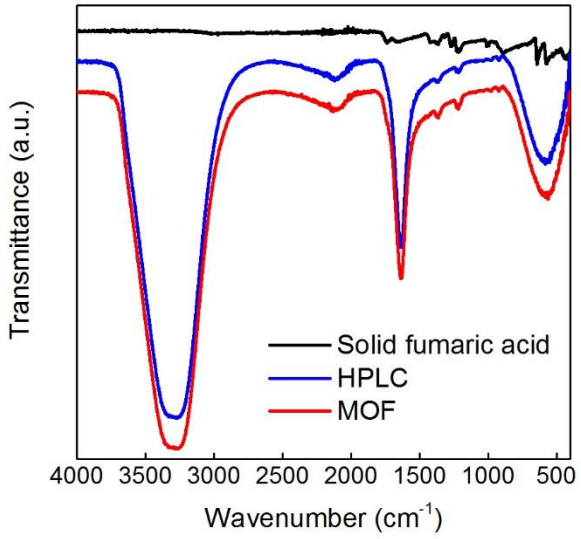

Figure S5.13. Comparison of FT-IR spectra (transmittance as a function of wavenumber) for solid fumaric acid, HPLC grade water (HPLC), and water collected from MOF-801 (MOF).

Thermal analysis for passive operation

Our proposed approach can harvest water solely based on solar-thermal energy without any additional input of electrical energy (*i.e.*, in a passive manner) for remote/arid climates. In this section, we present thermal analysis which shows that complete passive solar-thermal operation is realistic without any additional input of energy.

First, night-time adsorption and the processing of air can be managed through the natural flow of air encountered in open areas (wind). For instance, for the representative conditions for our experiments (30% RH and 25 °C) during night-time adsorption, the water content in air is approximately 0.006 kg of water per kg of air. Assuming the MOF layer is freely exposed to the natural flow of air at a calm wind speed of 0.3 m/s flowing onto the layer, the incident vapor flux at this condition is 0.003 kg $m^{-2}\,s^{-1}$ (or 10.8 kg $m^{-2}\,hour^{-1}$). For the optimized MOF layer porosity (0.67) and thickness (~3 mm) from Figure S5.7, the amount of MOF-801 is ~1.4 kg per m^2. The average flux of vapor adsorption shown in Figure S5.7 is ~$2e^{-5}$ kg $m^{-2}\,s^{-1}$. The approximately two orders of magnitude difference between the incident vapor and the vapor adsorption flux confirms that the natural flow of air is sufficient to ensure complete night-time adsorption.

During day-time operation, the dissipation of heat from the condenser to the ambient can also be managed by passive means of buoyant convection and the natural flow of air. Though, it is a common practice to assume ambient temperature condensers for thermodynamic analysis, we show a simple analysis to indicate that passive operation is possible. We start by developing an energy balance during the steady-state operation which can be expressed as:

$$\dot{Q}_{dissipation} = \dot{Q}_{condensation} + \dot{Q}_{gain} \tag{5.12}$$

where $\dot{Q}_{\text{dissipation}}$ is the rate of heat dissipation from a finned heatsink to the ambient, $\dot{Q}_{\text{condensation}}$ is the rate of heat released during the condensation of water, and $\dot{Q}_{\text{gain}}$ is the rate of heat addition from the MOF layer to the condenser. Equation (5.12) can be expressed as

$$h_{dissipation} A_{heat\sin k} (T_{condenser} - T_{ambient}) = \dot{m}_{water} h_{fg} + h_{gain} A_{condenser} (T_{MOF} - T_{condenser}) \qquad (5.13)$$

In Equation (5.13), h, A, and T are heat transfer coefficient in W m^{-2} K^{-1}, heat transfer area in m^2, and temperature, respectively. $\dot{m}_{water}$ is the rate of condensation. Here, we assume equal area of MOF layer and condenser. In order to estimate the required heat transfer coefficient ($h_{dissipation}$) to enable passive operation, we assume a reasonable area ratio ($A_{heatsink}/A_{condenser}$) of 20 [30], and a temperature difference of 5 K between the condenser and the ambient. $\dot{m}_{water}$ was estimated based on complete desorption in 1 hour (~$1e^{-4}$ kg m^{-2} s^{-1} or ~0.36 L m^{-2} $hour^{-1}$). Based on the experimentally measured temperatures shown in Figure 5.3, for T_{MOF} of 100°C, $T_{ambient}$ of 35°C and h_{gain} of 10 W m^{-2} K^{-1}, $T_{condenser}$ can be maintained at 40°C with an $h_{dissipation}$ of only ~10 W m^{-2} K^{-1}. This confirms that the passive operation is achievable with buoyant convection and naturally occurring flow of air.

References for Chapter 5

(1) Mekonnen, M. M.; Hoekstra, A. Y. *Sci. Adv.* **2016**, *2*, e1500323.

(2) Wahlgren, R. V. *Water Res.* **2001**, *35*, 1–22.

(3) Wikramanayake, E. D.; Ozkan, O.; Bahadur, V. *Energy* **2017**, *138*, 647–658.

(4) Kim, H.; Yang, S.; Rao, S. R.; Narayanan, S.; Kapustin, E. A.; Furukawa, H.; Umans, A. S.; Yaghi, O. M.; Wang, E. N. *Science* **2017**, *356*, 430–434.

(5) Ji, J. G.; Wang, R. Z.; Li, L. X. *Desalination* **2007**, *212*, 176–182.

(6) Wang, J. Y.; Liu, J. Y.; Wang, R. Z.; Wang, L. W. *Appl. Therm. Eng.* **2017**, *127*, 1608–1616.

(7) Kim, H.; Rao, S. R.; Narayanan, S.; Kapustin, E. A.; Yang, S.; Furukawa, H.; Umans, A. S.; Yaghi, O. M.; Wang, E. N. *Science* **2017**, *358*, eaao3139.

(8) Gad, H.; Hamed, A.; El-Sharkawy, I. *Renew. Energy* **2001**, *22*, 541–556.

(9) Zhao, L.; Yang, S.; Bhatia, B.; Strobach, E.; Wang, E. N. *AIP Adv.* **2016**, *6*, 025123.

(10) Strobach, E.; Bhatia, B.; Yang, S.; Zhao, L.; Wang, E. N. *J. Non. Cryst. Solids* **2017**, *462*, 72–77.

(11) Furukawa, H.; Gándara, F.; Zhang, Y.-B.; Jiang, J.; Queen, W. L.; Hudson, M. R.; Yaghi, O. M. *J. Am. Chem. Soc.* **2014**, *136*, 4369–4381.

(12) de Lange, M. F.; Verouden, K. J. F. M.; Vlugt, T. J. H.; Gascon, J.; Kapteijn, F. *Chem. Rev.* **2015**, *115*, 12205–12250.

(13) Rieth, A. J.; Yang, S.; Wang, E. N.; Dincă, M. *ACS Cent. Sci.* **2017**, *3*, 668–672.

(14) Mitsubishi Plastics. Zeolitic water vapor adsorbent: AQSOA. http://www.aaasaveenergy.com/products/001/pdf/AQSOA_1210E.pdf (accessed 21 November 2017).

(15) Furukawa, H.; Cordova, K. E.; O'Keeffe, M.; Yaghi, O. M. *Science* **2013**, *341*, 1230444.

(16) Ni, G.; Li, G.; Boriskina, S. V.; Li, H.; Yang, W.; Zhang, T.; Chen, G. *Nat. Energy* **2016**, *1*, 16126.

(17) Kalogirou, S. A. *Prog. Energy Combust. Sci.* **2004**, *30*, 231–295.

(18) Demir, H.; Mobedi, M.; Ülkü, S. *Renew. Sustain. Energy Rev.* **2008**, *12*, 2381–2403.

(19) Narayanan, S.; Kim, H.; Umans, A.; Yang, S.; Li, X.; Schiffres, S. N.; Rao, S. R.; McKay, I. S.; Rios Perez, C. A.; Hidrovo, C. H.; Wang, E. N. *Appl. Energy* **2017**, *189*, 31–43.

(20) Heinemann, U.; Caps, R.; Fricket, J. *Int. J. Heat Mass Transf.* **1996**, *39*, 2115–2130.

(21) Hrubesh, L. W.; Pekala, R. W. *J. Mater. Res.* **1994**, *9*, 731–738.

(22) Duffie, J. A.; Beckaman, W. A. *Solar Engineering of Thermal Processes*. John Wiley & Sons, Hoboken, New Jersey, 2013.

(23) Narayanan, S.; Yang, S.; Kim, H.; Wang, E. N. *Int. J. Heat Mass Transf.* **2014**, *77*, 288–300.

(24) Welty, J. R.; Wicks, C. E.; Rorrer, G.; Wilson, R. E.; *Fundamentals of Momentum, Heat, and Mass Transfer*, John Wiley & Sons, 2009.

(25) Moldrup, P.; Olesen, T.; Gamst, J.; Schjønning, P.; Yamaguchi, T.; Rolston, D. E. *Soil Sci. Soc. Am. J.* **2000**, *64*, 1588.

(26) Sircar, S.; Hufton, J. R. *Adsorption* **2000**, *6*, 137–147.

(27) Kim, H.; Cho, H. J.; Narayanan, S.; Yang, S.; Furukawa, H.; Schiffres, S.; Li, X.; Zhang, Y.-B.; Jiang, J.; Yaghi, O. M.; Wang, E. N. *Sci. Rep.* **2016**, *6*, 19097.

(28) Alonso, M.; Sainz, E.; Lopez, F. A.; Shinohara, K. *Chem. Eng. Sci.* **1995**, *50*, 1983–1988.

(29) Crank, J. *The Mathematics of Diffusion*, Oxford Univ. Press, 1979.

(30) Bar-Cohen, A.; Iyengar, M.; Benjaafar, S. *Int. J. Trans. Phenom*. **2002**, *4*, 43–58.

Chapter 6

Practical Water Production from Desert Air

Portions of this chapter will be published in:
Fathieh, F., Kalmutzki, M. J., Kapustin, E. A., Waller, P. J., Yang, J. & Yaghi, O. M. Practical Water Production from Desert Air *Science Advances* (accepted).

6.1 Preface

In the previous Chapters 4 and 5 we showed the feasibility of water harvesting from air with MOF. The proof-of-concept device based on these materials showed encouraging results, even in the arid environment of Arizona, United States during Spring. While this approach yielded water droplets, they were not of sufficient quantity to be collected and required a copper mesh to provide structural rigidity and heat transfer. To bring production of water into practice, in this chapter we addressed all these issues in a new design tested in the laboratory and the desert of Arizona, United States. The laboratory-to-desert study uncovered critical parameters concerning the interplay between water release, condensation, and material properties, and consequently led to water production under natural cooling and ambient sunlight, with no additional energy input. This work was done in collaboration with Dr. Farhad Fathieh, Dr. Markus J. Kalmutzki, Peter Waller, Jingjing Yang.

6.2 Energy, materials, and air requirements for the water harvesting cycle

As mentioned before, about thirteen sextillion (10^{21}) liters of water exist in the atmosphere at any given time[1]. This is a recyclable natural resource with potential to water the arid regions of the world. Methods to harvest water from humid air are known[2-6], but doing so at low humidity in desert climates is as yet undeveloped[7]. The difficulty in establishing a practical water harvesting cycle (WHC, Figure 6.1) for low humidity climates is two-fold: finding a material capable of facile water capture and release (capture cycle), and providing sufficient cooling energy such that the temperature of the condenser is lower than that of the released water vapor to allow for liquid water formation (collecting cycle). Although the two cycles have been shown to work with intensive energy input[8], it remains unknown whether they can produce water under natural cooling with energy only from ambient sunlight.

Our considerations in the design of the water production system took into account the energy, materials, and air requirements for the WHC. Figure 6.1A shows that the capture cycle starts with saturation of porous material (unsaturated MOF in this case) upon exposure to desert air at night time. This is followed by the release of captured water from the saturated MOF upon exposure to sunlight during day time. The collecting cycle takes place during day time when the released water vapor humidifies the air in the vicinity of the MOF. The hot humid air is subsequently cooled down, in our case by ambient cooling, to its dew point resulting in liquefied water at the condenser. The collecting cycle (release-condensation) continues until the end of the day time when the liquid water is collected and the next WHC starts.

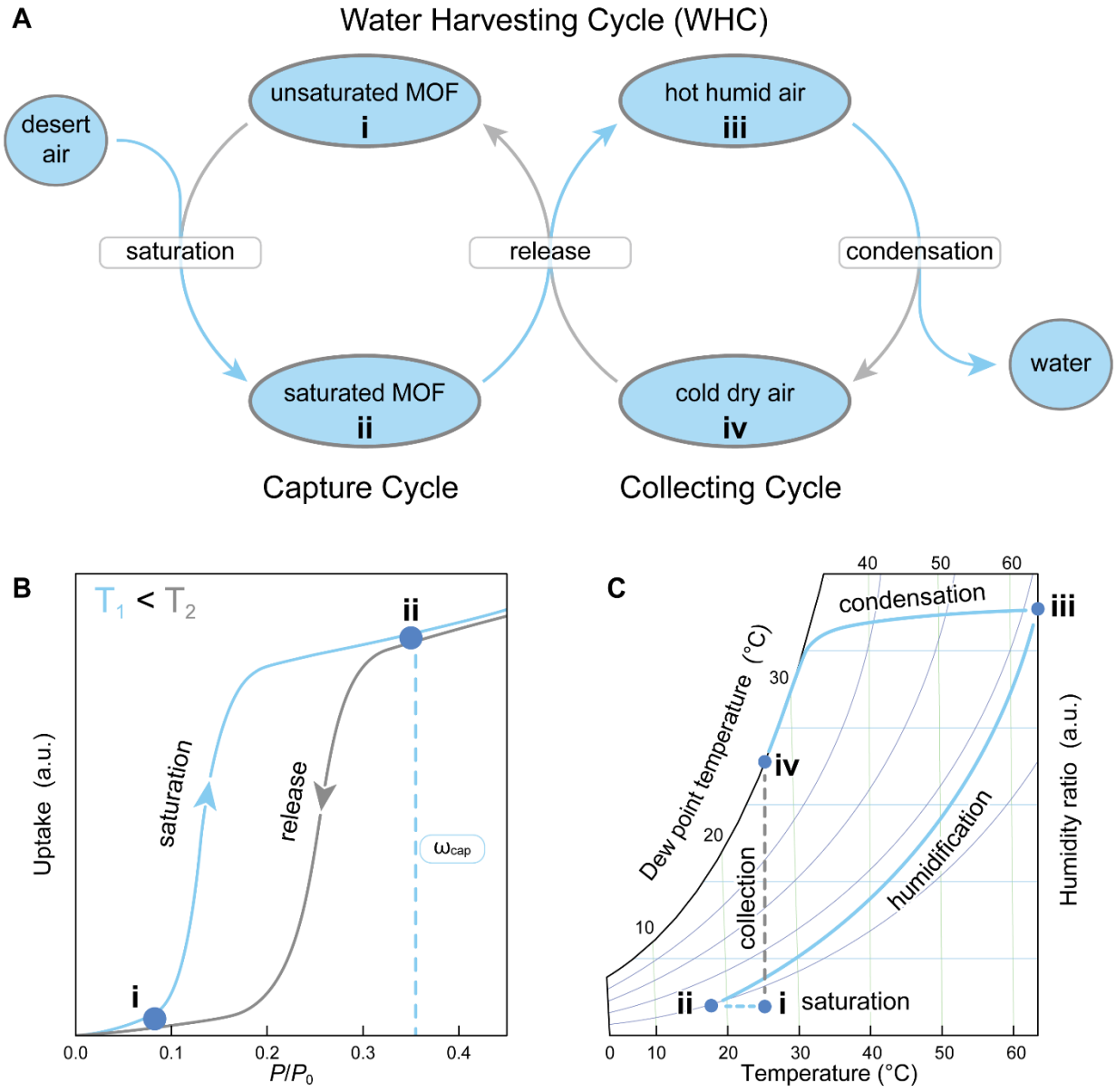

Figure 6.1. WHC for practical water production under natural cooling and ambient sunlight. (**A**) The WHC is composed of the capture and collecting cycles. (**B**) The capture cycle is defined by the sorption isotherm of the MOF and several prerequisites for high-performance water harvesting materials can be established therefrom; a Type IV or V isotherm with minimal or no hysteresis, a steep uptake below 25% RH, a high capture capacity ω_{cap} below 35% RH, and a significant shift of the inflection point for isotherms recorded at different temperatures are ideal. (**C**) The collecting cycle is defined by the psychrometric chart. During the release of captured water, the air is humidified and heated (ii→iii). Natural convection transports the hot humid air to the condenser, cooling it below its dew point (iii→iv). Concomitant condensation yields liquid water and dehumidified air. The collecting cycle can continue until the humidity ratio is too low for the dew point to be reached.

The saturation of the MOF is determined by the extent to which water fills the pores. This quantity is the water capture capacity (ω_{cap}: captured water per mass of MOF) at a given RH and it can be estimated from the water adsorption isotherm. Large values of ω_{cap} at low RH can be

achieved in hydrolytically stable MOFs with large pore volumes and hydrophilic pore environments. In addition to the MOF's sorption properties, a design optimizing the packing porosity is needed to enhance the *inter*crystalline diffusion and reach ω_{cap} within the 14-16 hours of night time.

The energy absorbed by the MOF is spent on three different processes: overcoming the MOF-water interactions $\left(q_{H,\,latent} = \omega_{cap} q_{st}\right)$, increasing the temperature of the MOF $\left(q_{H,sensible}\right)$, and dissipating due to heat loss $\left(q_{H,loss}\right)$. Considering $q_{H,sensible} \ll q_{H,latent}$ for MOFs and $q_{H,loss} \ll q_{H,sensible}$ for a thermally insulated adsorbent container, the majority of the absorbed energy is spent on breaking the MOF-water interactions to release water, and therefore, a MOF with low isosteric heat of adsorption (q_{st}) is desirable. A practical capture cycle with maximized water release should follow inequality (6.1), where we consider the minimum solar energy $(q_{H,min})$ that allows the release of the entire amount of captured water (see section S6.9 of Supporting Information for this Chapter).

The performance of the capture cycle can be evaluated by the release efficiency (η_R), equation (6.2), where $m_{released}$ and $m_{captured}$ are the absolute mass of released and captured water, respectively, and ω_{rel} is the mass of released water per unit mass of MOF $\left(\omega_{rel} \le \omega_{cap}\right)$. For a specific ω_{cap}, a maximum release efficiency can be achieved by using a MOF with high solar absorptivity, high thermal conductivity, small heat capacity, and sorbent containment with maximized surface to volume ratio (see section S6.9 of Supporting Information for this Chapter). The release of water from the MOF at elevated temperatures should be significantly faster than the capture from desert air due to the limited timeframe of the sunlight exposure.

$$q_{H,min} > \omega_{cap} q_{st} \tag{6.1}$$

$$\eta_R = \frac{m_{released}}{m_{captured}} = \frac{\omega_{rel}}{\omega_{cap}} \tag{6.2}$$

The cooling energy required to condense the water vapor released from the MOF is spent on three processes: decreasing the temperature of the air and released water vapor $\left(q_{C,sensible}\right)$, dewing $(q_{C,latent} = \omega_{cap} h_{fg})$, and dissipating due to heat loss $(q_{C,loss})$. Considering the large value of the specific heat of phase change $\left(h_{fg}\right)$ (*i.e.* enthalpy of condensation) for water, most of the cooling energy is spent on condensation rather than sensible cooling $(q_{C,sensible} \ll q_{C,latent})$. A practical collecting cycle with adequate cooling capacity should satisfy the following criterion:

$$q_{C,min} > \omega_{cap} h_{fg} \tag{6.3}$$

Inequality (6.3) states that any design for atmospheric water production should consider a minimum $q_{C,min}$ that theoretically allows for the condensation of the entire amount of released water. The performance of the collecting cycle is evaluated by the collecting efficiency (η_C),

$$\eta_C = \frac{m_{collected}}{\omega_{rel} m_{MOF}} \tag{6.4}$$

where $m_{collected}$ and m_{MOF} are the mass of collected water and MOF, respectively. The main challenge for water production in a desert climate is to maintain the condenser temperature below the dew point using only ambient cooling. This is possible by using an efficient condenser with a large cooling surface and enhanced convective heat and mass transfer. There is a theoretical maximum volume for the condenser beyond which the air saturation is not possible (see section S6.9 of Supporting Information for this Chapter).

The overall efficiency of the WHC is given by the harvesting efficiency (η_{WHC}) defined as:

$$\eta_{WHC} = \frac{m_{collected}}{\omega_{cap} m_{MOF}} = \eta_R \eta_C \tag{6.5}$$

According to equation (6.5), highly-efficient water production is only possible if the amount of water released from the MOF equals the captured amount $(\eta_R \to 1)$ and if all the released water is condensed $(\eta_C \to 1)$.

6.3 MOF-based water harvesting system

Based on this WHC and the considerations discussed above, a water harvesting system was designed using initially MOF-801 as the sorbent. MOF-801 was chosen for several reasons: (a) high hydrolytic stability, (b) well studied water sorption behavior, (c) good cycling stability, (d) low regeneration energy, and (e) a sorption isotherm that satisfies all mentioned prerequisites[7] for practical water production (Figure 6.2A).

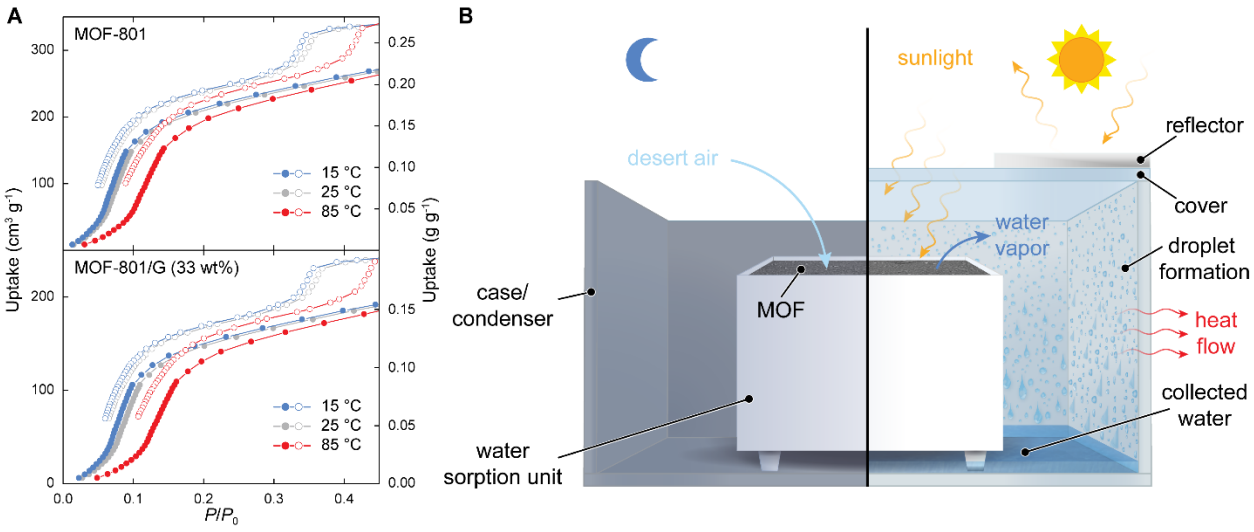

Figure 6.2. Isotherms of MOF-801 and design of the MOF-based water harvester for water production from desert air. (**A**) Water sorption isotherms (adsorption filled symbols, desorption open symbols) of MOF-801 and

MOF-801/G at 15 °C (blue), 25 °C (gray), and 85 °C (red). In comparison to previously reported isotherms for MOF-801, a shift of the inflection point to higher relative pressures, a lower maximum capacity, and hysteresis were observed. These findings are related to a high degree of single crystallinity of the material[9]. Blending MOF-801 with graphite led to a decrease of the gravimetric capacity corresponding to the added weight, while the general shape of the isotherm was fully retained. (**B**) Schematic of the water harvester consisting of a water sorption unit and a case. During the night, the cover of the case is opened, allowing the MOF to be saturated with moisture from desert air. During the day, the case is sealed to create a closed system. Humid hot air flows from the MOF to the condenser and is cooled down by heat rejection to the surroundings. When the dew point is reached, condensation occurs, and liquid water collects at the bottom of the case.

Like most MOFs, MOF-801 shows low absorptivity in the infra-red (IR) and near-IR region, low thermal conductivity[10], and high heat capacity[11] reducing direct heating using solar thermal energy. Hence, MOF-801 was blended with 33 wt% of non-porous graphite (termed MOF-801/G), to enhance its thermophysical[12] and absorptive properties (see section S6.6 of Supporting Information). The water harvester consists of two main components, a water sorption unit which holds the MOF, and the case which encloses it (Figure 6.2B). The water sorption unit is designed to retain up to 2945 cm^3 of sorbent, equaling 1.2 kg of MOF-801 (1.65 kg of MOF-801/G) assuming a packing porosity of 0.7, the ideal value for moisture transfer[13]. The geometry of the sorbent containment was chosen to facilitate a large surface to volume ratio (> 0.5) of the MOF. In the Chapter 4, we demonstrated that heating MOF-801 to 65 °C at 10% RH is sufficient for water release, however, under these conditions the condenser temperature should be below 20 °C to achieve condensation. This significant temperature gradient is created by designing the water sorption unit to act as a thermal insulator, capable of maintaining a low condenser temperature while heating the MOF. Solar thermal incalescence of the water sorption unit itself was minimized by applying an IR reflective coating to all exposed surfaces. The cubic case has a cover and encloses the water sorption unit (Figure 6.2B). The side walls of the case act as the condenser and provide surfaces for heat transfer with the surroundings. The case can be opened or closed for saturation during the night and release-condensation during the day. Finally, a reflector is attached to the cover to ensure that only the surface of the MOF is exposed to solar radiation. Temperature and humidity sensors are placed at the surface of and in the MOF powder, bottom of the case, and condenser. The data recorded with these sensors discussed below enable the calculations of the release, collecting, and WHC efficiencies.

6.4 Water production under controlled laboratory conditions

In a typical laboratory experiment, the sorbent was saturated overnight (RH = 30-50%, 18-25 °C, 16.5 h). After saturation, the case was sealed and exposed to artificial light (2700 K). Data were collected under low (558 W m^{-2}) and high radiant fluxes (792 W m^{-2}), representing the average solar irradiance over the course of one day and the peak solar irradiance in desert regions such as Arizona (33° N, 111° W), respectively. After 7.5 hours, the experiment was terminated, and liquid water was collected.

Initial experiments were performed using 1.65 kg of MOF-801/G under low and high radiant fluxes. While maintaining the condenser temperature at 20 °C, the formation of fog on the condenser was observed after approximately 30 minutes (Figure 6.3A).

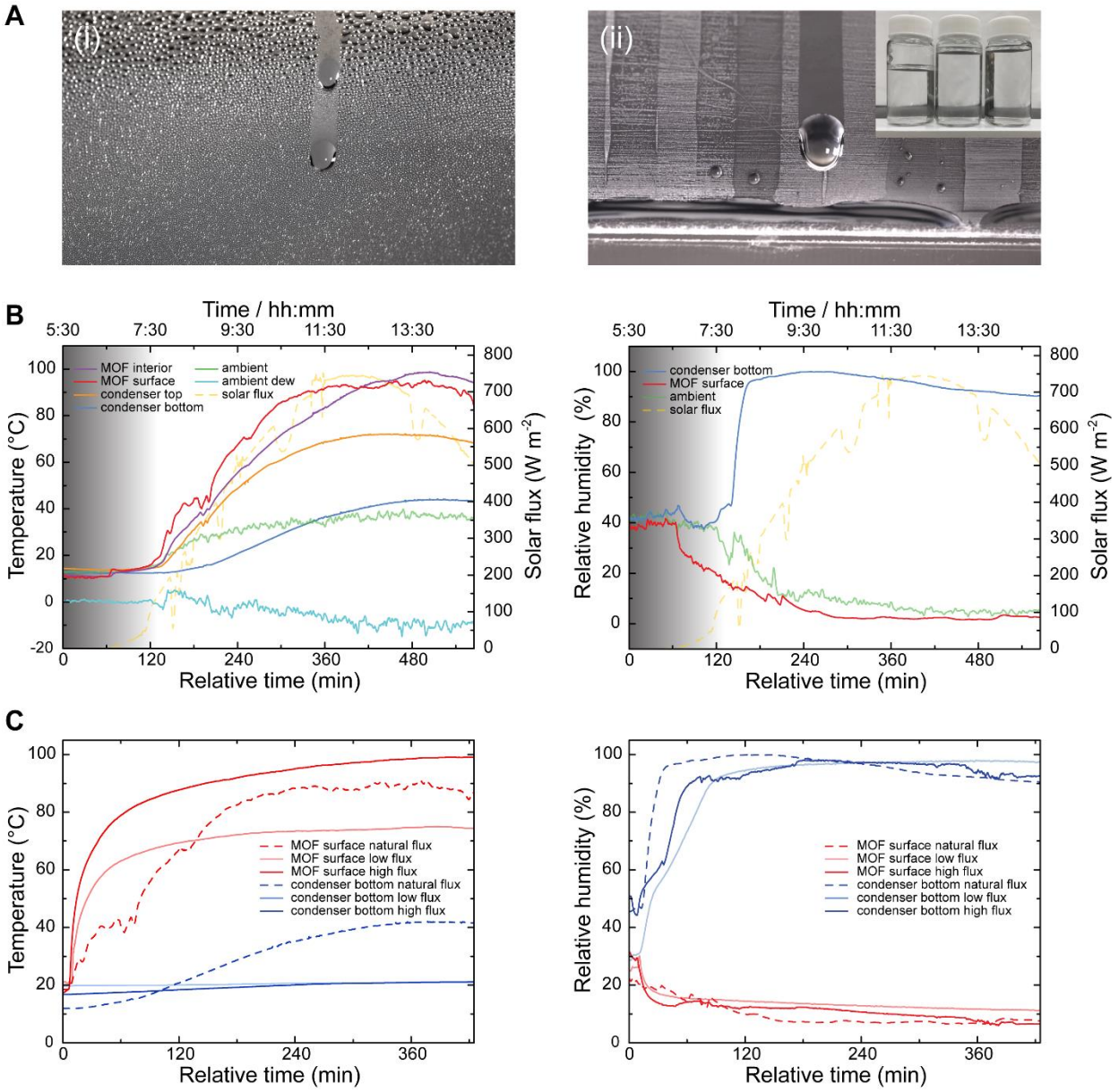

Figure 6.3. Water production and temperature, relative humidity, and solar flux profiles. (**A**) Photographs of the condenser showing (i) the formation of droplets (ii) flowing to make puddles (inset: water produced per day-and-night desert cycle). (**B**) Humidity and temperature profiles acquired during testing in the desert on 22nd of October 2017 in Scottsdale, Arizona, United States. Temperature and humidity sensors were placed at different positions within the water harvester; at the bottom (orange) and top of the condenser (blue), and at the surface of (red) and in the MOF powder (magenta). The solar flux was recorded using a pyranometer mounted on the reflector. Ambient temperature and relative humidity were monitored near to the water harvester and the ambient dew temperature (light blue) was calculated from these data. (**C**) Comparison of humidity and temperature profiles acquired under ambient solar flux during testing in the desert and under laboratory conditions using low (558 W m^{-2}) and high (792 W m^{-2}) fluxes. The origin represents when the complete surface of MOF-801/G was exposed to artificial or ambient solar radiation, for the laboratory experiments and the desert test, respectively.

Formation of water droplets that subsequently coalesced into larger puddles occurred 2-3 hours into the experiment. Water production with low and high radiant fluxes yielded 25 and 56

g of water, respectively. Using the humidity and temperature measurements, the efficiencies were found to be η_R = 39% and 76%, η_C = 30% and 43%, and η_{WHC} = 12% and 33%, for low and high fluxes, respectively. The low collecting efficiency suggests a mismatch between the amount of released water and the cooling capacity of the condenser (i.e. mismatch between the capture and collecting cycles). This issue was addressed by performing identical experiments using a half loading of MOF-801/G (0.825 kg). Remarkably, even though a smaller amount of sorbent was used, larger quantities of water were collected (37 and 78 g of water for low and high fluxes, respectively), leading to increased efficiencies of η_R = 44% and 86%, η_C = 93% and 92%, η_{WHC} = 41% and 79%, respectively. These major enhancements are attributed to improved water release ($\omega_{rel} \rightarrow \omega_{cap}$) due to a larger surface to volume ratio (~ 1), and faster energy transfer within the MOF resulting in a longer effective condensation time. While using even smaller amounts of MOF-801/G resulted in further improvement of η_C and η_{WHC}, the absolute yield of water decreased. Therefore, employing 0.825 kg of MOF-801/G provided us with a well-balanced water harvester with high values for η_R and η_C as well as a high nominal water yield that should be capable of operating under ambient cooling and on solar thermal energy solely (as in the desert). The chemical analysis of the produced water indicated the absence of contaminations originating from dissolution of the MOF for all experiments (see section S6.11 of Supporting Information).

6.5 Water production in desert conditions

We then transferred this device to Scottsdale, Arizona in late October 2017 to study its performance in desert conditions: as low as 5% RH at 35-40 °C during the day and up to 40% RH at 10-15 °C during the night and to validate the water harvesting principles discussed above. At these operating conditions the dew point is found to be at sub-zero temperatures, rendering refrigeration-based water production infeasible[13-14] (Figure 6.3B). Initial experiments using the water harvester under desert conditions, however, were unsuccessful and did not yield liquid water. The high ambient temperatures during the day resulted in dramatically increased condenser temperatures (42 °C) lowering the temperature difference between the MOF and the condenser to approximately 30 °C, hampering condensation (RH < 88% at the condenser). To circumvent warming of the condenser by heat transfer from the surroundings, exterior insulation (soil) with a high heat capacity and low thermal conductivity was used[15]. This modification facilitated a significant reduction of the condenser temperature by 10 °C and resulted in 94% RH at the condenser. Consequently, the formation of fog was observed, but the temperature difference between the MOF and the condenser (40 °C) still was not sufficient to reach the higher humidity ratio required to condense larger quantities of water. More solar energy was needed to further increase the temperature difference between the MOF and the condenser. During October, the altitude of the sun at Scottsdale (DMS Lat: 33° 30' 4.7664" N, DMS Long: 111° 55' 31.000" W) varies between 20° in the morning and late afternoon (9 am and 4 pm), and 45° at midday[16]. Thus, the water harvester was mounted on a stand and tilted by 37° to maximize the solar energy absorbed by the MOF. With this modification, MOF temperatures like those recorded under laboratory conditions could be reproduced and indeed, after 7 hours, liquid water was collected. More absorbed solar energy allowed for faster water release, as indicated by an instantaneous rise of RH at the condenser, which in combination with the delayed heating of the condenser itself, facilitated condensation (Figure 6.3B). Using 0.825 kg of MOF-801/G, 55 g of

water were collected, a value between those obtained under laboratory conditions for low flux (37 g) and high flux (78 g). This is in good agreement with the corresponding temperature and RH profiles as shown in Figure 6.3C.

6.6 Highly efficient water productions with a next generation MOF

To bring this development closer to practical use, we sought to make MOFs with enhanced water sorption properties potentially meeting the specification of industrial large-scale production. We developed the synthesis of next generation material MOF-303 [Al(OH)(HPDC): where HPDC = 1*H*-pyrazole-3,5-dicarboxylate], employing aluminum instead of zirconium as the metal and using water instead of organic solvents. It has a new structure based on the **xhh** topology and is built from infinite Al(OH)(-COO)$_2$ SBUs linked through HPDC linkers (Figure 6.4A)[17]. The structure of MOF-303 features hydrophilic 1D pores with 6 Å diameter and a free pore volume of 0.54 cm^3 g^{-1} facilitating a large maximum water capture capacity of 0.48 g g^{-1}. The water sorption isotherm satisfies all prerequisites for a high-performance water harvesting material outlined earlier: The Type IV isotherm has an inflection point at P/P_0 = 0.15, a plateau is reached at P/P_0 = 0.3, and good temperature response and minimal hysteresis are observed (Figure 6.4B).

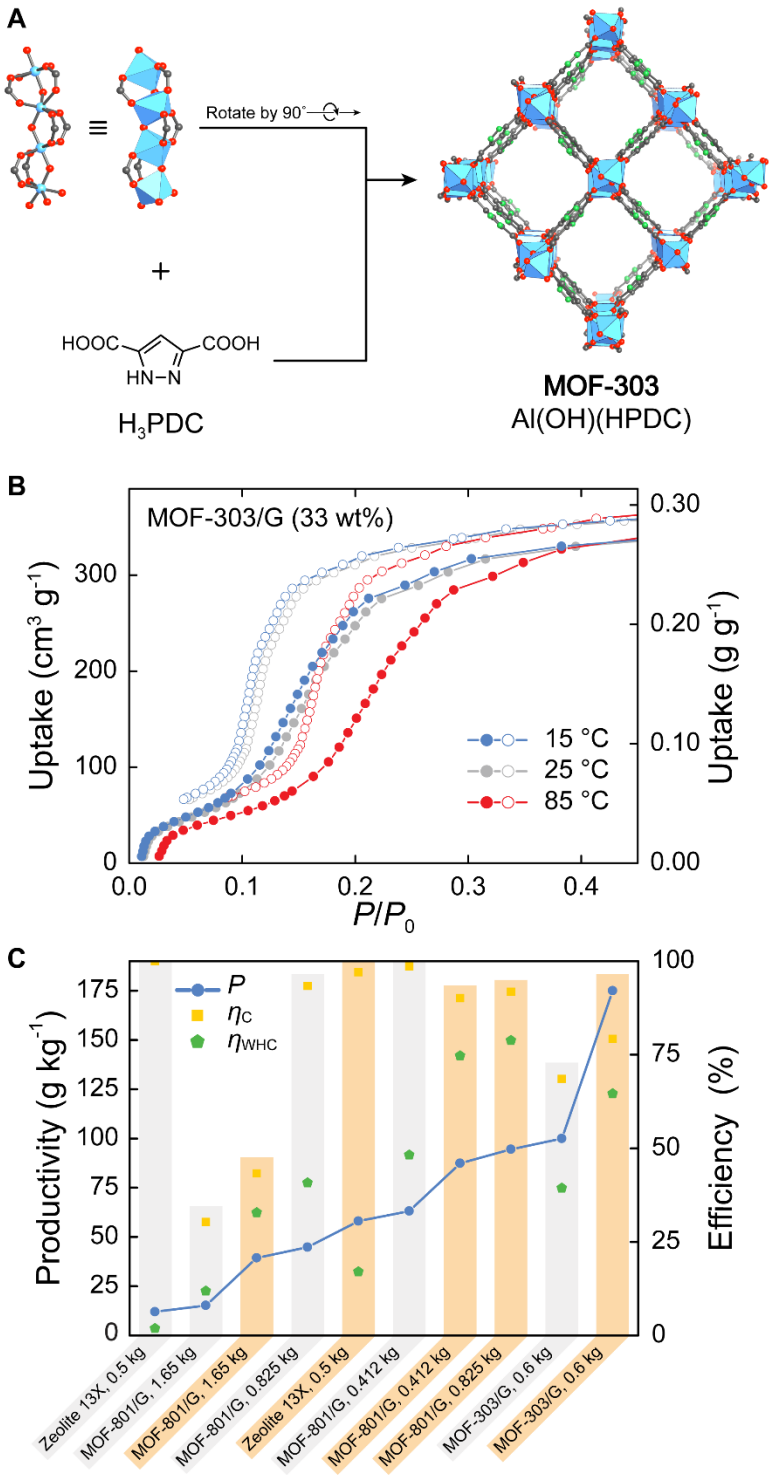

Figure 6.4. Next generation MOF with increased productivity. (**A**) Crystal structure of MOF-303 built from rod-like Al(OH)(-COO)$_2$ SBUs linked by HPDC linkers into an extended framework structure (**xhh** topology) with a 1D pore system. Gray, C; green, N; red, O; blue polyhedra, Al. (**B**) Water sorption isotherms for MOF-303/G at 15 °C (blue), 25 °C (gray) and 85 °C (red). (**C**) Comparison of parameters defining the efficiency and productivity of the water harvester. Gray and orange bars represent measurements under the low and high flux, respectively.

In addition, high hydrolytic stability was confirmed by carrying out 150 adsorption-desorption cycles without measurable degradation of the material (see Figure S6.24 in Supporting Information). Despite the larger ω_{cap} for MOF-303, both criteria are satisfied for $q_{H,min}$ and $q_{C,min}$ for operating conditions found in Arizona (RH at night, ambient temperature, and solar flux), thus making the present water harvester suitable for MOF-303. In a manner akin to that described for MOF-801, the thermophysical and absorptive properties of MOF-303 were enhanced by blending it with 33 wt% of non-porous graphite (termed MOF-303/G) (see section S6.6 of Supporting Information). MOF-303/G was tested under the same laboratory conditions described above and found to give a dramatic increase of 114% in water production.

Ultimately, the performance of a sorbent according to the WHC is defined by the productivity P (in g kg^{-1}):

$$P = \frac{m_{collected}}{m_{sorbent}} \tag{6.6}$$

where $m_{sorbent}$ is the amount of sorbent used (in kg). This parameter is useful in comparing the performance of various materials under identical conditions within the same water harvester. Zeolite 13X was chosen as a reference since it is a common microporous desiccant with a pore size and pore volume similar to those of MOF-801 and MOF-303. Figure 6.4C shows the comparison of productivities calculated for zeolite 13X, MOF-801/G, and MOF-303/G. This comparison is striking evidence, that the unique water sorption behavior of MOFs is key to water production from desert air under ambient cooling and solely driven by solar thermal energy. The ultrahigh productivity of MOF-303/G of up to 175 g_{water} kg^{-1}_{MOF} is encouraging in achieving practical water production from desert air. The development of the next generation MOF-303 highlights the prospect of MOFs with respect to this application arising from the flexibility of design and synthesis of such framework materials. This in combination with the design considerations outlined in this Chapter brings water production in desert climates one step closer to practical applications.

.

Supporting Information for Chapter 6

Section S6.1. Materials and analytical techniques for MOF synthesis and analysis

Materials

Zirconium oxychloride octahydrate ($ZrOCl_2 \cdot 8H_2O$, purity ≥ 99.8%), aluminum chloride hexahydrate ($AlCl_3 \cdot 6H_2O$, purity ≥ 99.8%), *N*,*N*-dimethylformamide (DMF) (HPLC grade), fumaric acid (purity ≥ 99%), 3,5-pyrazoledicarboxylic acid monohydrate (H_3PDC) (purity ≥ 97%), Zeolite 13X, sodium hydroxide were purchased form Sigma-Aldrich Co. Anhydrous DMF and formic acid (purity ≥ 99.8%) were obtained from EMD Millipore Chemicals. Extra-fine graphite powder was obtained from AGS Company. Methanol (HPLC grade) was purchased from Fisher Scientific. Deuterated solvents were obtained from Cambridge Isotope Laboratories. All chemicals obtained were used without further purification. Pyrex screw-capped media storage jars were used for synthesis, solvent exchange and storage.

Analytical techniques

Powder X-ray diffraction (PXRD) patterns were acquired with a Bruker D8 Advance diffractometer (Göbel-mirror monochromated Cu $K\alpha_1$ radiation, λ = 1.54056 Å). Single crystal X-ray diffraction (SXRD) data of MOF-303 was collected using as-synthesized crystals at beamline 11.3.1 of the Advanced Light Source at Lawrence Berkeley National Lab. N_2 adsorption isotherms were recorded on a Quantachrome Quadrasorb-SI volumetric gas adsorption analyzer. A liquid nitrogen bath was used for the measurements at 77 K. The framework density of all MOF and MOF/G samples was measured using a pycnometer (Ultrapyc 1200e, Quantachrome). Attenuated-total-reflectance Fourier-transform infrared (ATR-FTIR) spectra were recorded on a Bruker ALPHA Platinum ATR-FTIR Spectrometer. Thermogravimetric analysis (TGA) traces was measured on a TA Instruments SDT Q600 series thermal gravimetric analyze. Gases were humidified by bubbling dry air through a 2 L bubbler humidifier before advection into the TGA chamber. The humidity and temperature were monitored using high-accuracy thermocouples and humidity sensors upstream the TGA chamber. Water isotherms and cyclic stability test were measured on a BEL Japan BELSORP-aqua3, and the water uptake estimated in cubic centimeters per gram. Prior to the water adsorption measurements, water (analyte) was flash frozen under liquid nitrogen and then evacuated under dynamic vacuum for at least three times to remove any gases in the water reservoir. The measurement temperature was controlled using a water circulator. Helium was used to estimate the dead space for both, gas and water adsorption measurements. Ultrahigh purity N_2, and He (Praxair, 99.999% purity) were used throughout all experiments. Scanning electron microscope (SEM) and energy-dispersive X-ray spectroscopy (EDS) images were recorded on a FEI Quanta 3D scanning electron microscope with 10 kV accelerating voltage. ^{1}H-NMR spectra were recorded with a Bruker DRX-500 spectrometer operating at 500 MHz. The aluminum and zirconium content in samples of harvested water were analyzed using an ICP-AES spectroscope (Optima 7000 DV, Perkin Elmer). Diffuse reflectance spectra between 285 and 2500 nm were recorded on a Varian Cary 5000 spectrometer and absorption spectra between 285 and 3000 nm were recorded using a Shimadzu UV3600.

Section S6.2. MOF-801 synthesis and characterization

Synthesis of MOF-801 microcrystalline powder

Pre-scaled-up synthesis of MOF-801, $Zr_6O_4(OH)_4$(fumarate)$_6$: In a 100 mL screw-capped jar, 1.16 g (50 mmol) of fumaric acid and 3.2 g (50 mmol) of $ZrOCl_2 \cdot 8H_2O$ were dissolved in a mixed solvent of DMF and formic acid (40 mL and 14 mL, respectively). The mixture was then heated in an isothermal oven at 130 ºC for 10 hours to give as-prepared MOF-801 as a white precipitate. The precipitate was collected by filtration using a membrane filter (45 µm pore size), washed three times daily with 100 mL DMF for three days, then three times daily with 100 mL methanol for three days, and subsequently dried in air. The air-dried MOF sample was transferred to a vacuum chamber. The chamber was first evacuated at room temperature for 5 hours until the pressure dropped below 1 kPa. After that, the sample was heated in vacuum at 70 ºC for 12 hours, and then at 150 ºC for another 48 hours yielding activated MOF-801 as a white powder (yield: 2 g). This batch was further used to determine the water sorption characteristic curves and TGA kinetics for adsorption and desorption.

Scaled-up synthesis: In a typical procedure in a 500 mL screw-capped jar, 5.8 g (50 mmol) of fumaric acid and 16 g (50 mmol) of $ZrOCl_2 \cdot 8H_2O$ were dissolved in a mixed solvent of DMF and formic acid (200 mL and 70 mL, respectively). The mixture was then heated in an isothermal oven at 130 ºC overnight to give as-prepared MOF-801 as a white precipitate. Yield: ~10 g. The combined precipitate from five reaction jars was collected, washed three times daily with 500 mL DMF for three days, then three times daily with 500 mL methanol for three days, and subsequently dried in air.

MOF-801 scaled-up activation

Air-dried MOF sample was transferred into a vacuum chamber. The chamber was first evacuated at room temperature for 5 hours until the pressure dropped below 1 kPa. After that, the sample was heated in vacuum at 70 ºC for 12 hours, and then at 150 ºC for another 48 hours. The combined product from 140 jars was then placed in the drying oven on an aluminum pan at 160 ºC for 10 days prior to the water production experiment. Overall, the yield of activated microcrystalline MOF-801 powder was 1100 g.

Characterization of activated MOF-801

PXRD, EDS analysis, and SEM images: Activated microcrystalline MOF-801 was examined by PXRD. A ground sample was placed on a zero-background sample holder and mounted on the diffractometer. The data was collected from 3 to 50 degrees with a step width of 0.01 and total data collection time of 30 minutes. SEM and EDS measurements were performed to study the morphology and elemental composition of bulk MOF powder.

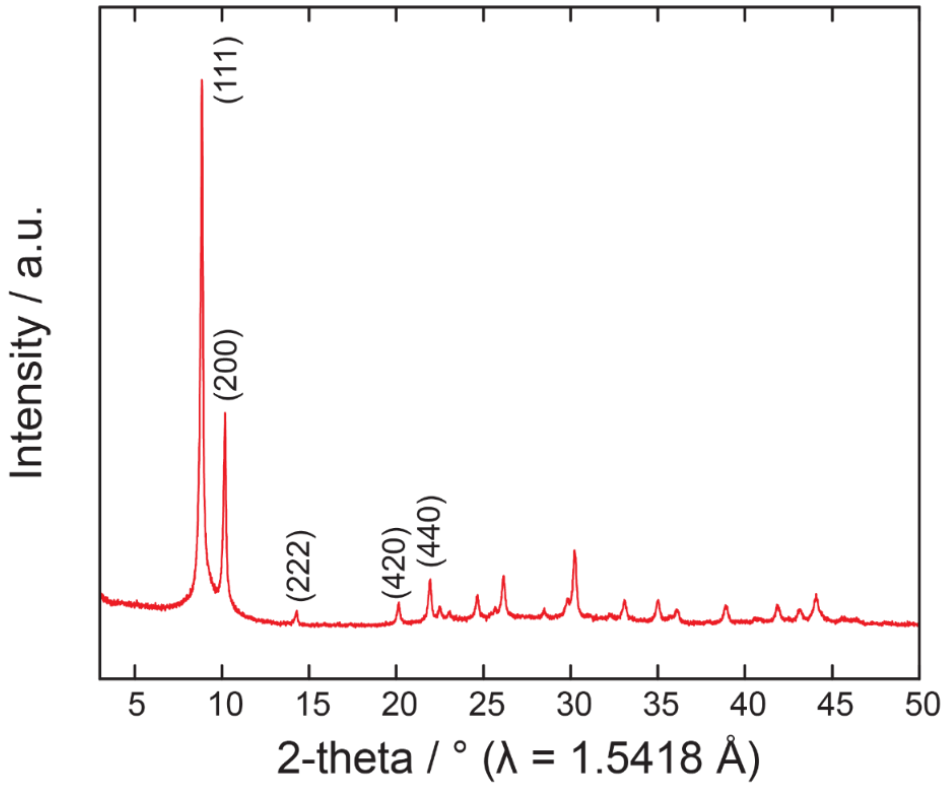

Figure S6.1. PXRD pattern of activated MOF-801.

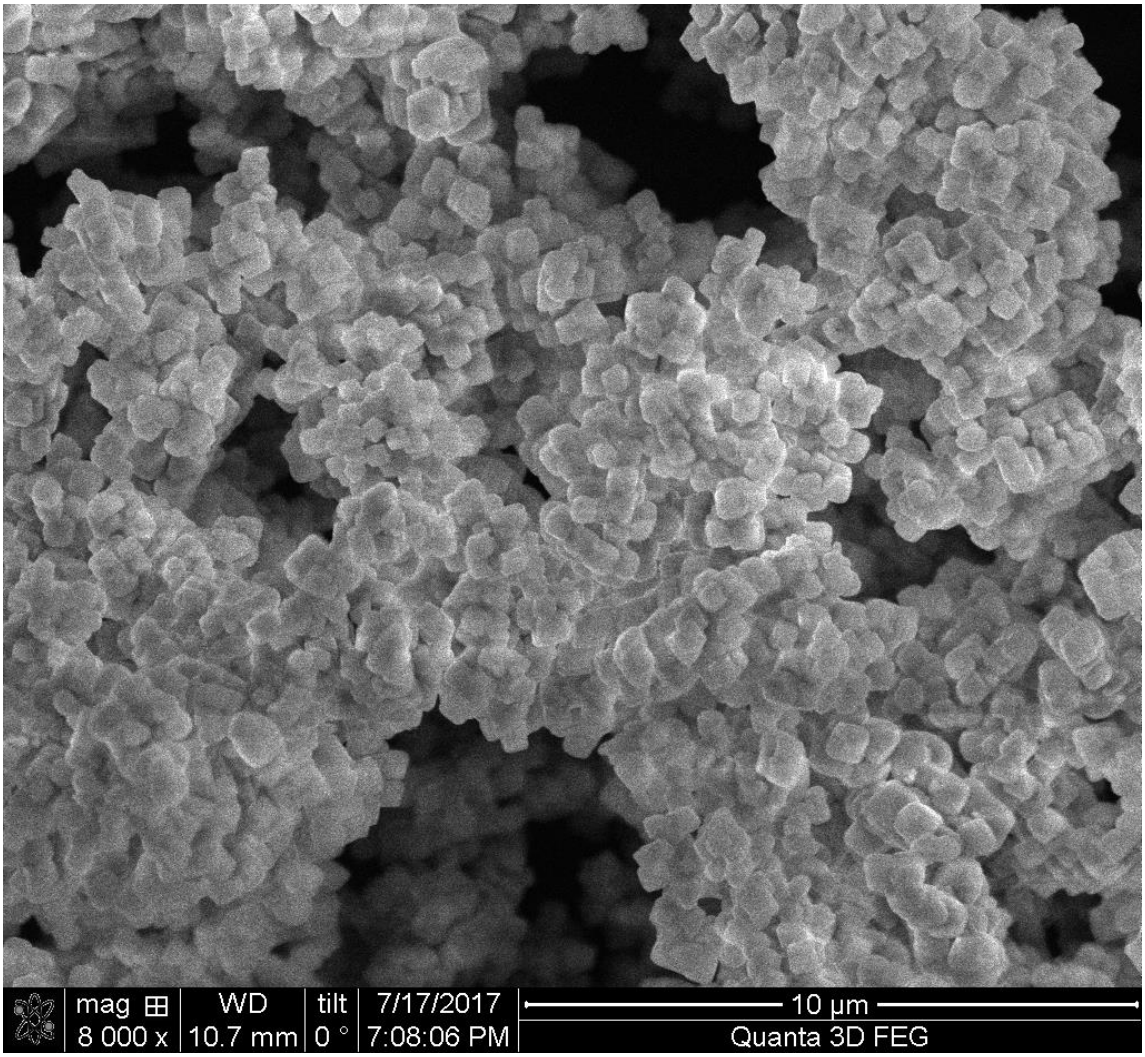

Figure S6.2. SEM image of activated MOF-801.

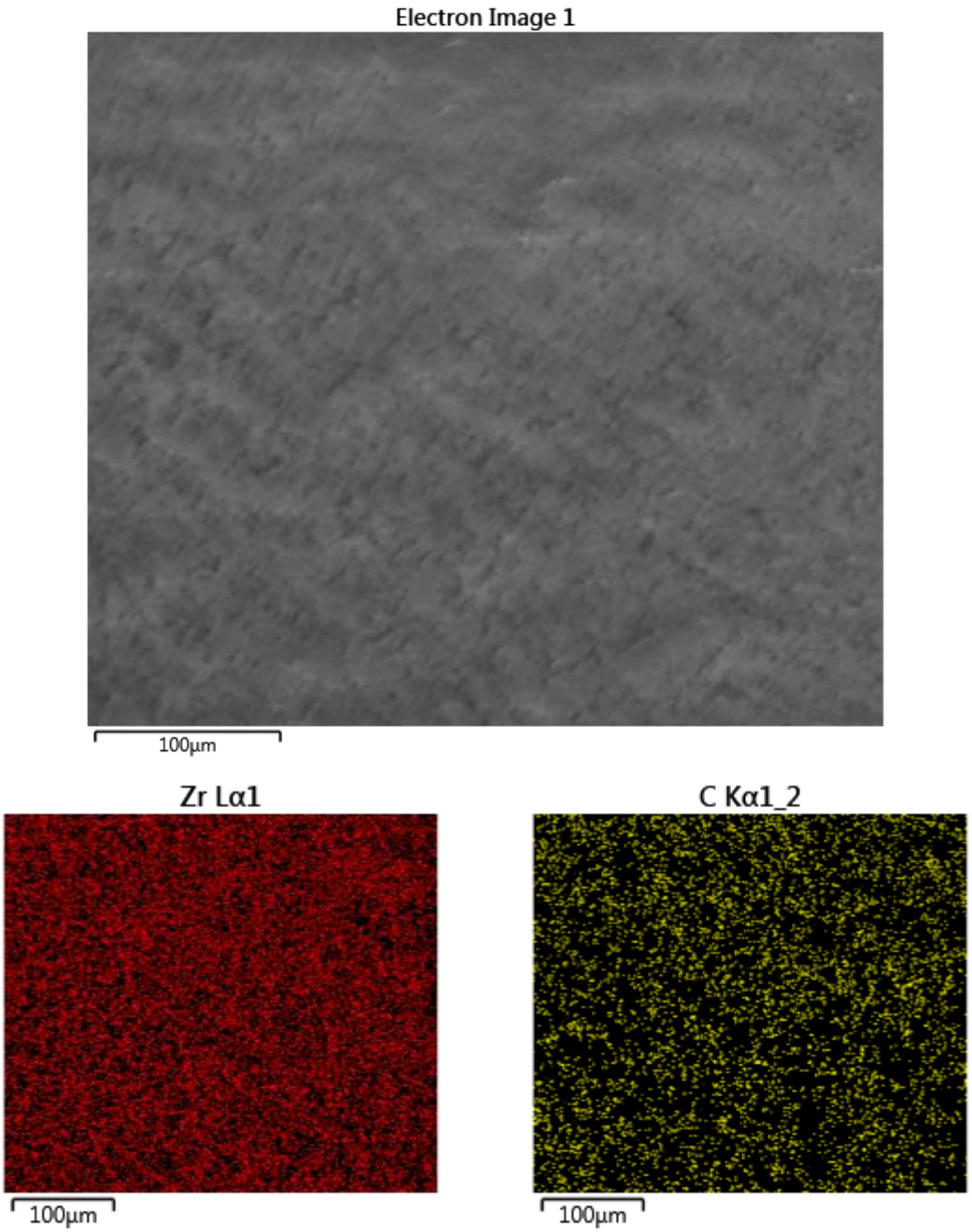

Figure S6.3. SEM image of activated MOF-801 (top). Carbon and Zirconium EDS images of the MOF-801 (bottom).

Porosity and packing density analysis: A 35 mg sample was taken from 1100 g of well-mixed activated microcrystalline powder MOF-801 and transferred into a 9 mm bulb gas cell and charged with N_2 to avoid air contamination, then the cell was mounted on the instrument. 26 adsorption and 11 desorption points were collected.

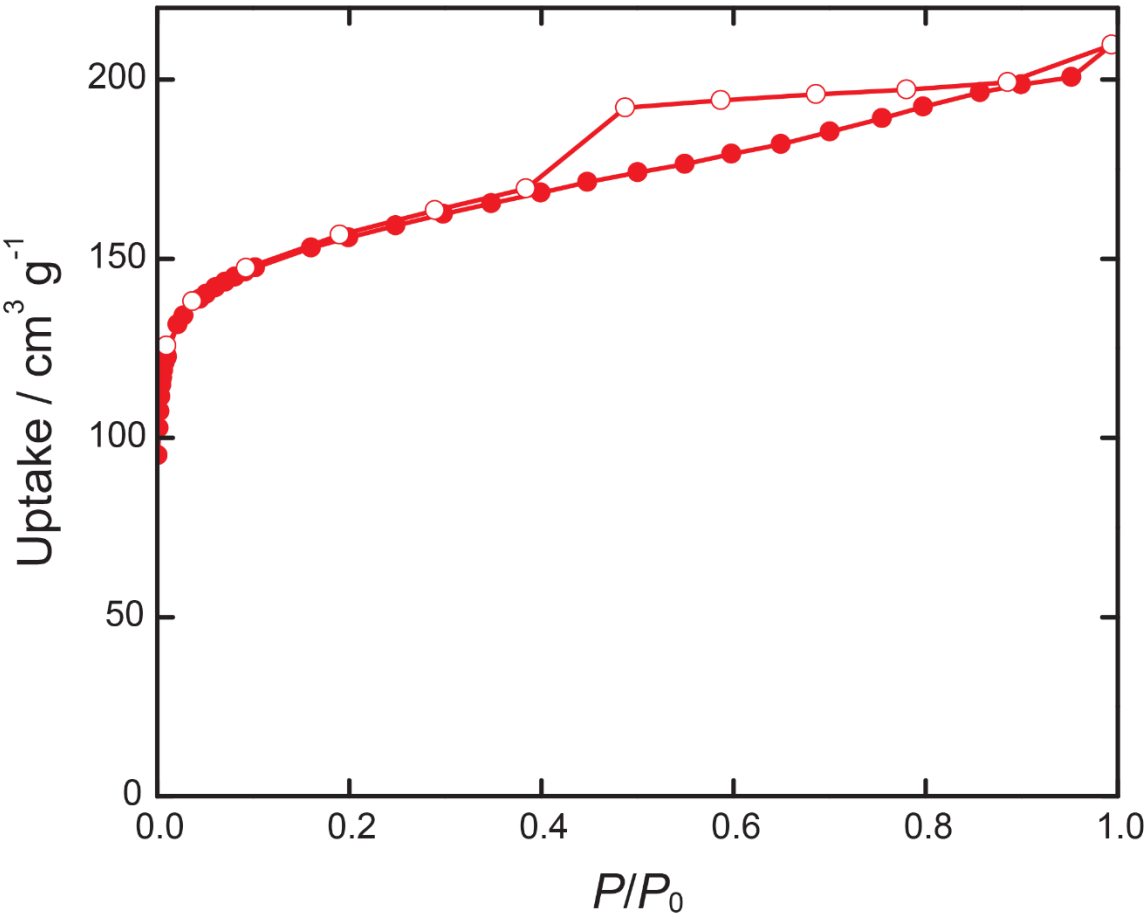

Figure S6.4. N_2 isotherm of activated MOF-801 recorded at 77 K. The BET surface area is 582 m^2 g^{-1}.

The powder particle density (ρ_p) of activated MOF-801 was estimated to be 1.401 g cm^{-3} from the pycnometer measurement (the framework density ρ_s = 2.3116 ± 0.0075 g cm^{-3}) and BET pore volume measurements (Vp = 0.2810 cm^3 g^{-1}) (see equation 6.7).

$$\rho_p = \frac{1}{\left(V_P + \frac{1}{\rho_s}\right)} \tag{6.7}$$

Evaluation of water capacity properties

A 34 mg sample was taken from an activated pre-scaled-up batch of MOF-801 and transferred to a 9 mm bulb gas cell and charged with N_2 to avoid air contamination, then the cell was mounted on the instrument. The temperature of the adsorbent was controlled using a water bath.

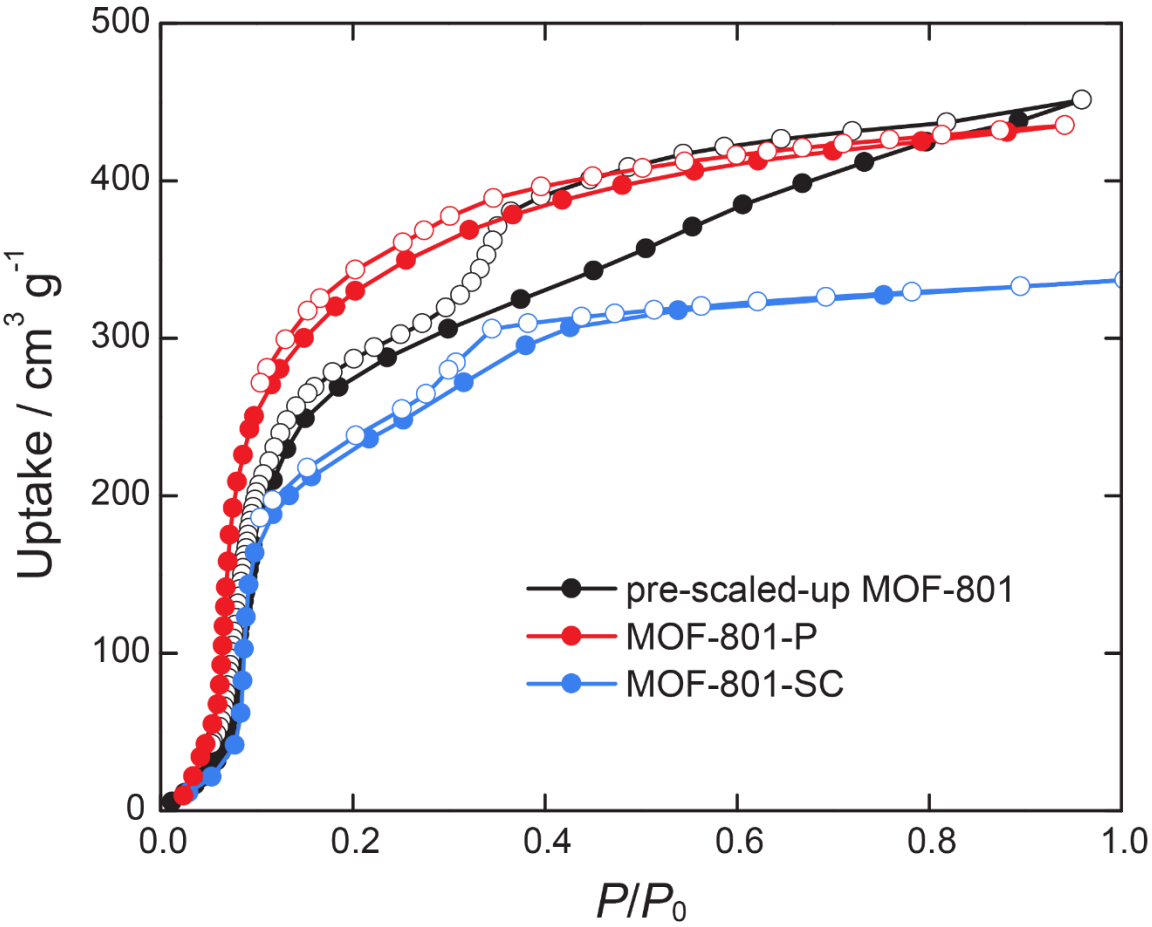

Figure S6.5. Water sorption isotherms of pre-scaled-up MOF-801 sample (black, this work), and MOF-801-P (red), MOF-801-SC (blue)[7].

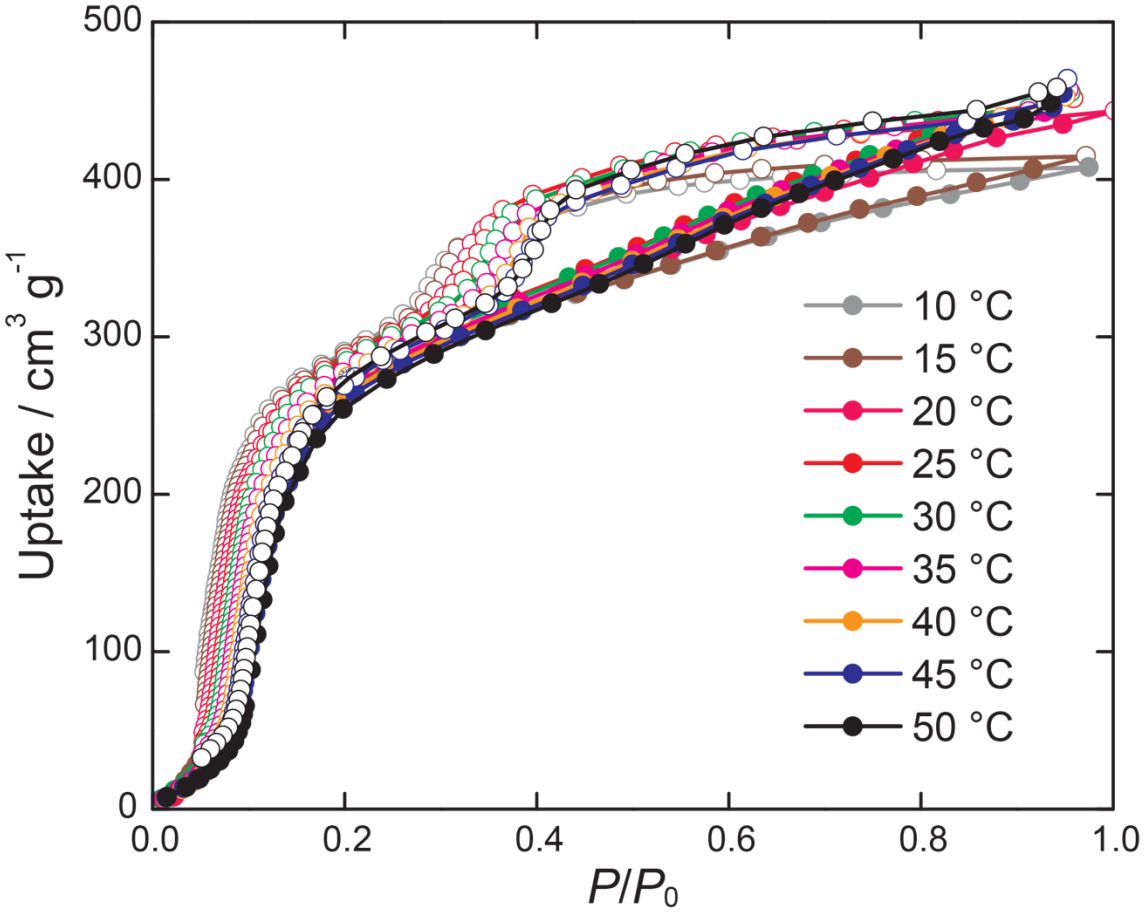

Figure S6.6. Water sorption isotherms of pre-scaled-up MOF-801 recorded at different temperatures.

Characteristic curves and isosteric heat of adsorption of activated MOF-801: The characteristic *A*-*W* water sorption curves were estimated using the Polanyi adsorption potential theory (equations (6.8, 6.9)),

$$A = RT \ln \frac{p_0(T)}{p} \tag{6.8}$$

$$W = \frac{q(p,T)}{\rho_{liq}^{wf}(T)} \tag{6.9}$$

where A is the molar Gibbs free energy of adsorption, p_0 is the temperature-dependent vapor pressure of water, W is the volume liquid adsorbed, q is the mass adsorbed, and ρ_{liq}^{wf} is the liquid density of water[18].

The isosteric heat of adsorption was estimated using the Clausius-Clapeyron relation.

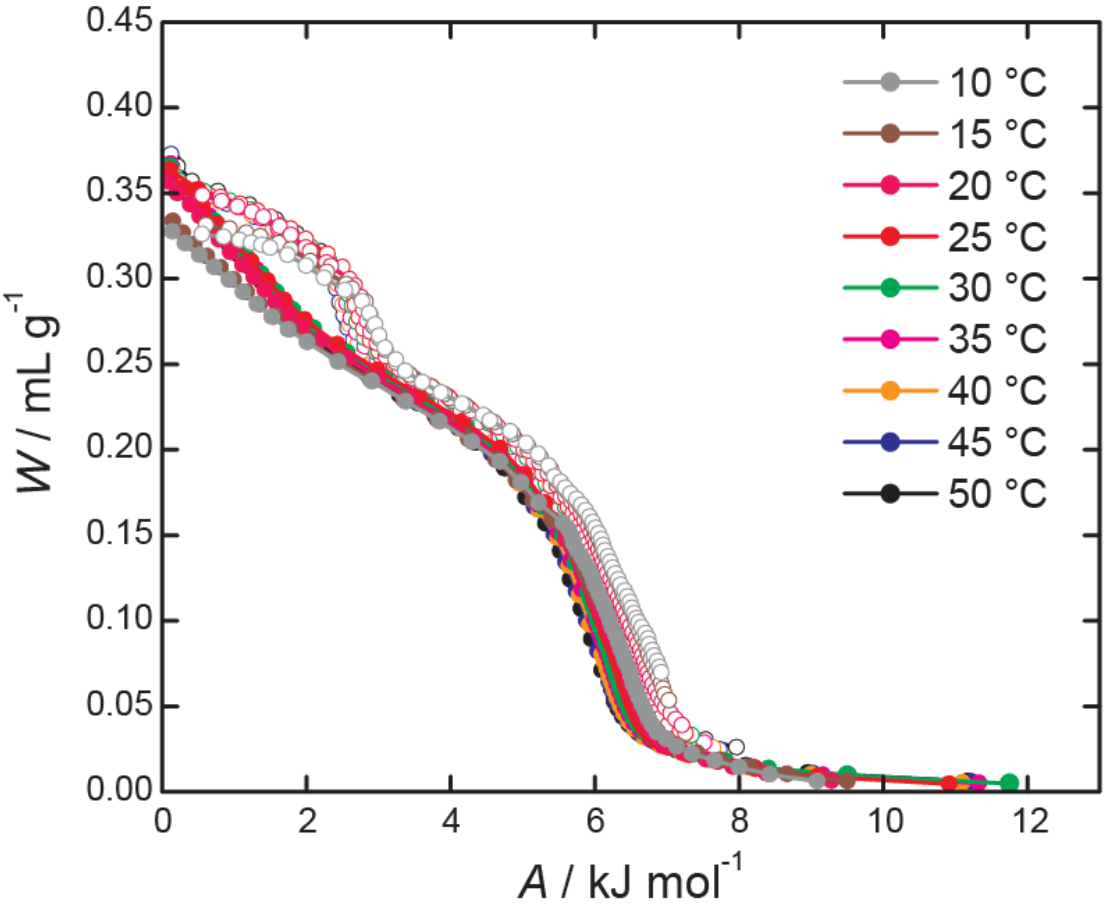

Figure S6.7. Characteristic curves for activated pre-scaled-up MOF-801 determined using equations (6.8, 6.9) based on the sorption isotherms measured at different temperatures.

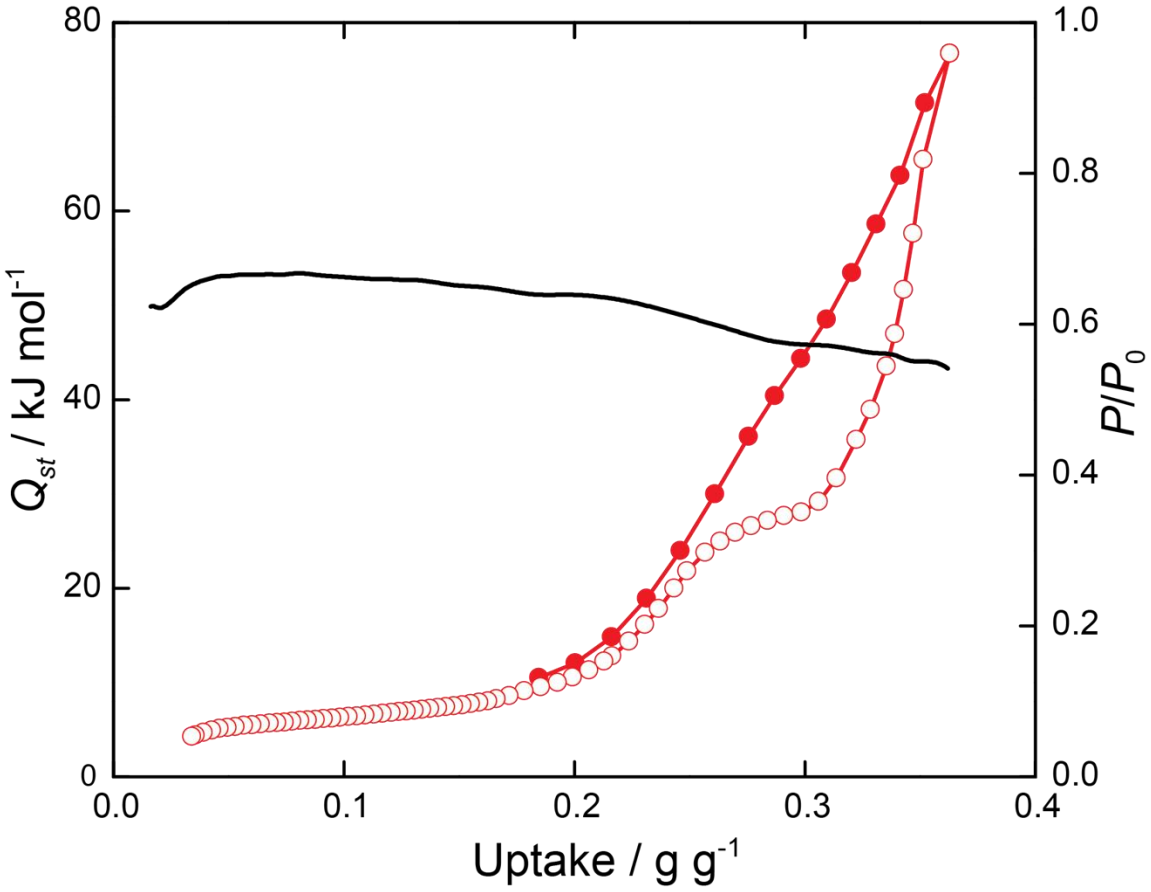

Figure S6.8. Isosteric heat of adsorption (black) and water sorption isotherm at 25 ºC (red) for activated MOF-801.

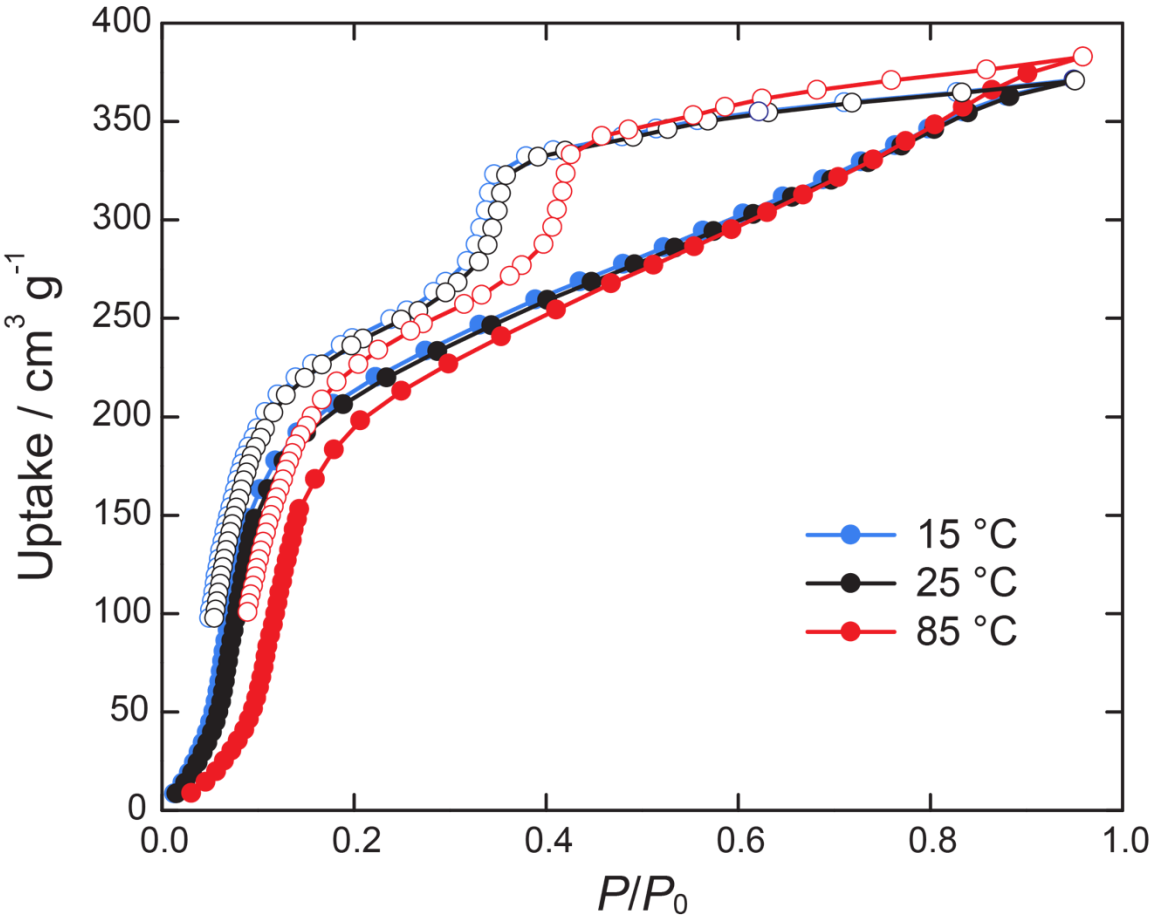

Figure S6.9. Experimental water sorption isotherm for activated scaled-up MOF-801 recorded at 25 °C and calculated water sorption isotherms at 15 and 85 °C. A 35 mg sample was taken from activated scaled-up MOF-801, transferred to a 9 mm bulb gas cell, and charged with N_2 to avoid air contamination. Then the cell was mounted on the instrument.

Section S6.3. MOF-801/G preparation and characterization

Preparation of the mixture

1100 g of activated scaled-up microcrystalline MOF-801powder was mixed with 550 g of graphite powder in the 2 L jar to produce 1650 g of 67:33 wt% MOF-801-graphite mixture, termed MOF-801/G. The resulting mixture was thoroughly mixed by shaking the jar until the MOF/G powder had a homogenous gray color. Aggregation of MOF-801 powder into large particles was observed, these aggregates were crushed using a spatula and remixed. The resulting mixture was further characterized in terms of crystallinity, powder density, porosity and water uptake properties without any additional activation.

Characterization of MOF-801/G

PXRD of graphite, and PXRD, EDS analysis, and SEM images of activated MOF-801/G: Commercially available graphite powder was used for PXRD experiment without any

modifications. A powder sample was placed on a zero-background sample holder and mounted on the diffractometer. The data was collected from 3 to 50 degrees with a step width of 0.01 and a total data collection time of 30 minutes. SEM and EDS images were taken to study the morphology and elemental composition of bulk MOF-801/G powder.

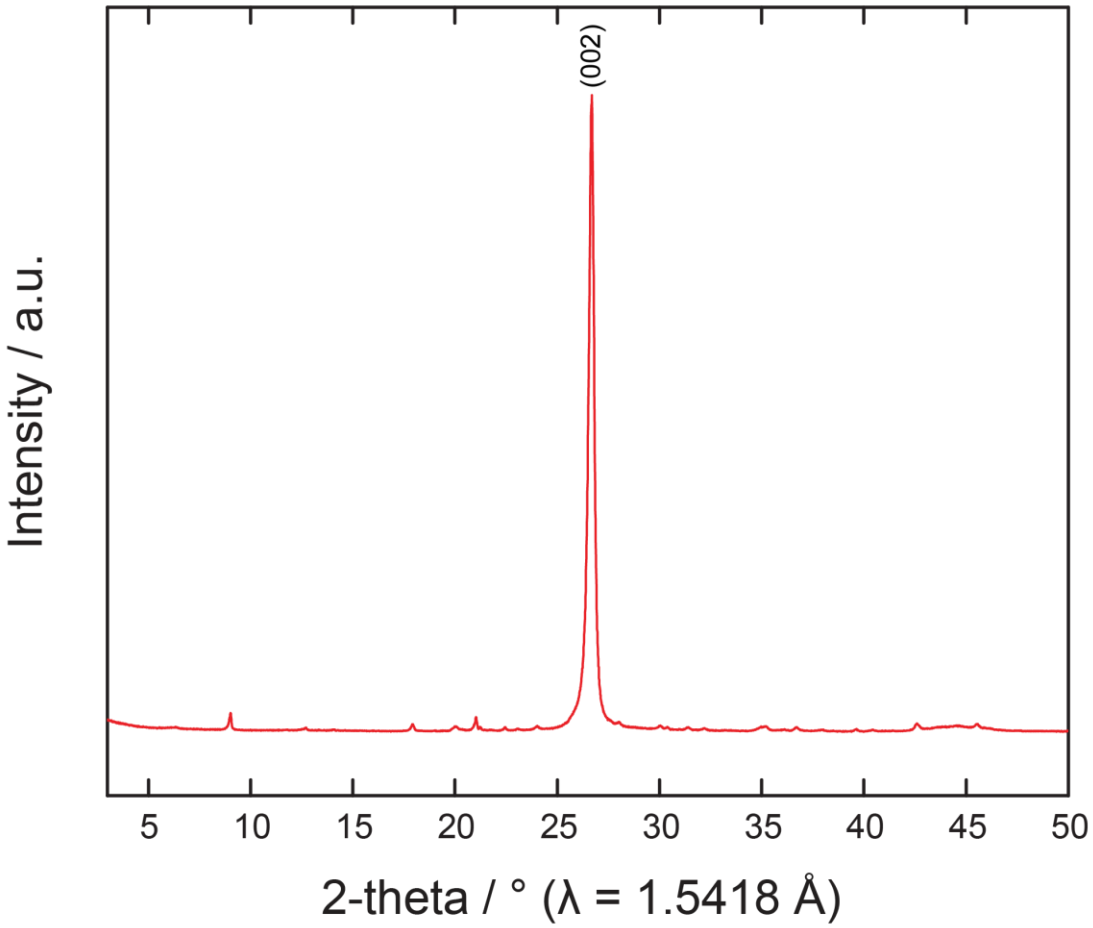

Figure S6.10. PXRD pattern of the graphite sample.

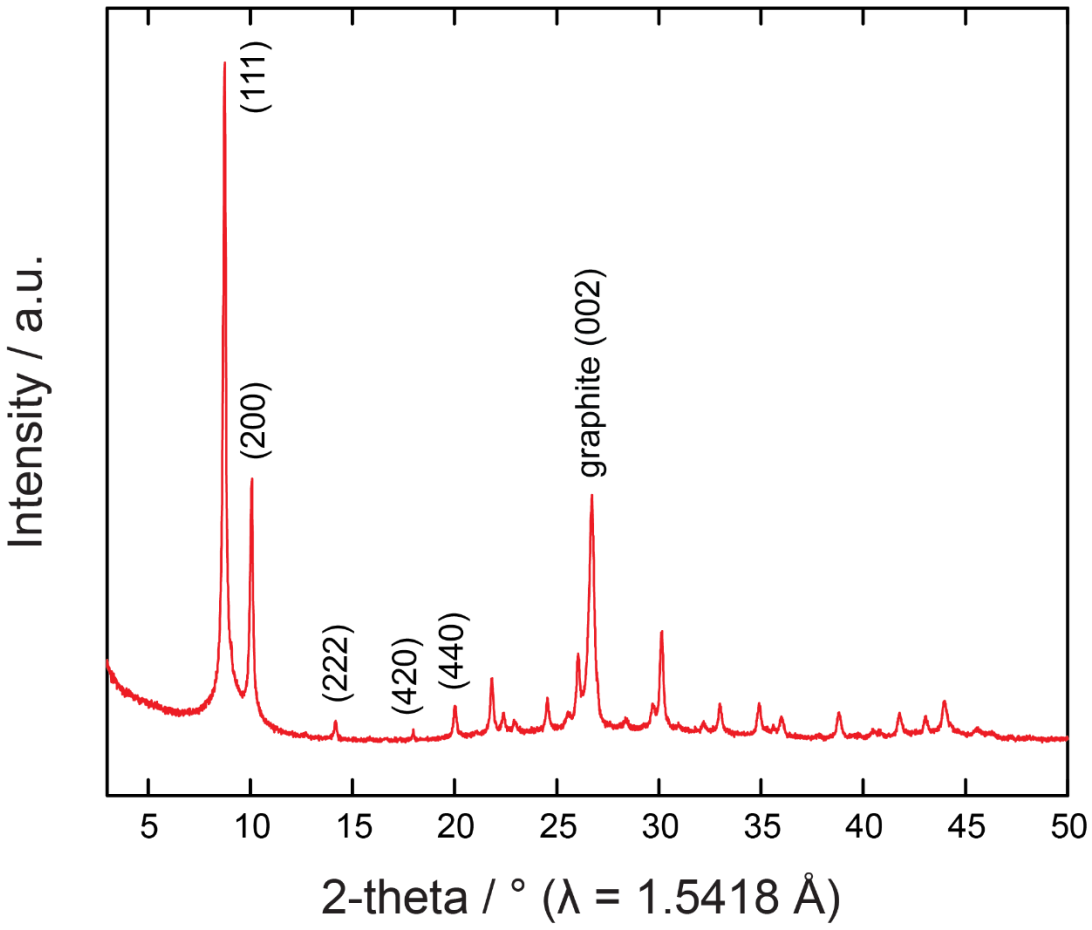

Figure S6.11. PXRD pattern of activated sample of MOF-801/G. A ground sample was placed on a zero-background sample holder and mounted on the diffractometer. The data was collected from 3-50 degrees with a step width of 0.01and a total data collection time of 30 minutes. The peak at 26.5º corresponds to the (002) reflection of graphite.

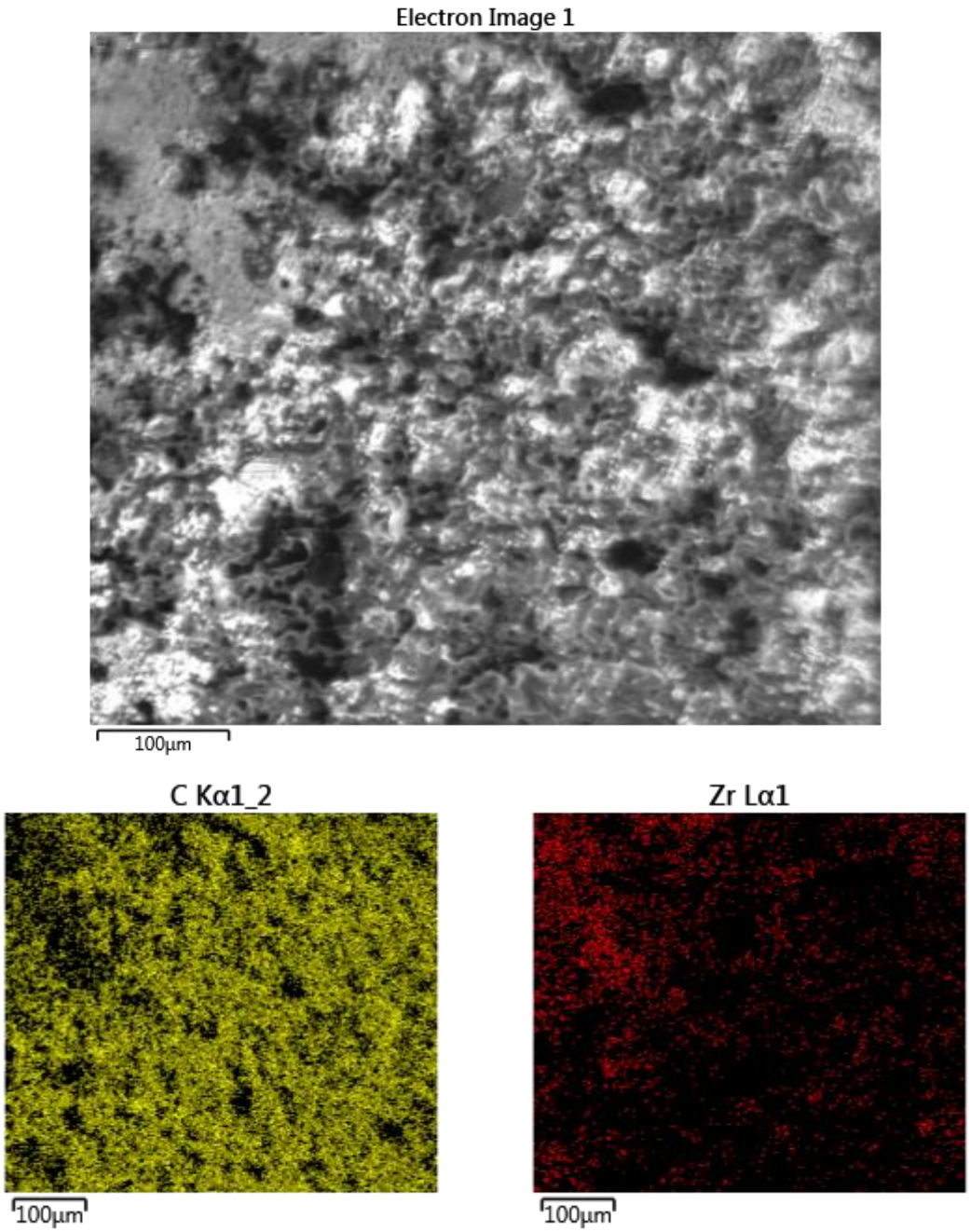

Figure S6.12. SEM image of activated MOF-801/G (top). Carbon and Zirconium EDS images of the MOF-801/G (bottom).

Porosity and packing density analysis: Due to the extremely low porosity of the graphite used in this work, the measurement of its N_2 isotherm at 77 K was complicated by large instrumental errors. Therefore, N_2 isotherms of pure graphite are not shown.

78 mg of well-mixed activated MOF-801/G were transferred to a 9 mm bulb gas cell and charged with N_2 to avoid air contamination, then the cell was mounted on the instrument. 26 adsorption and 11 desorption points were collected.

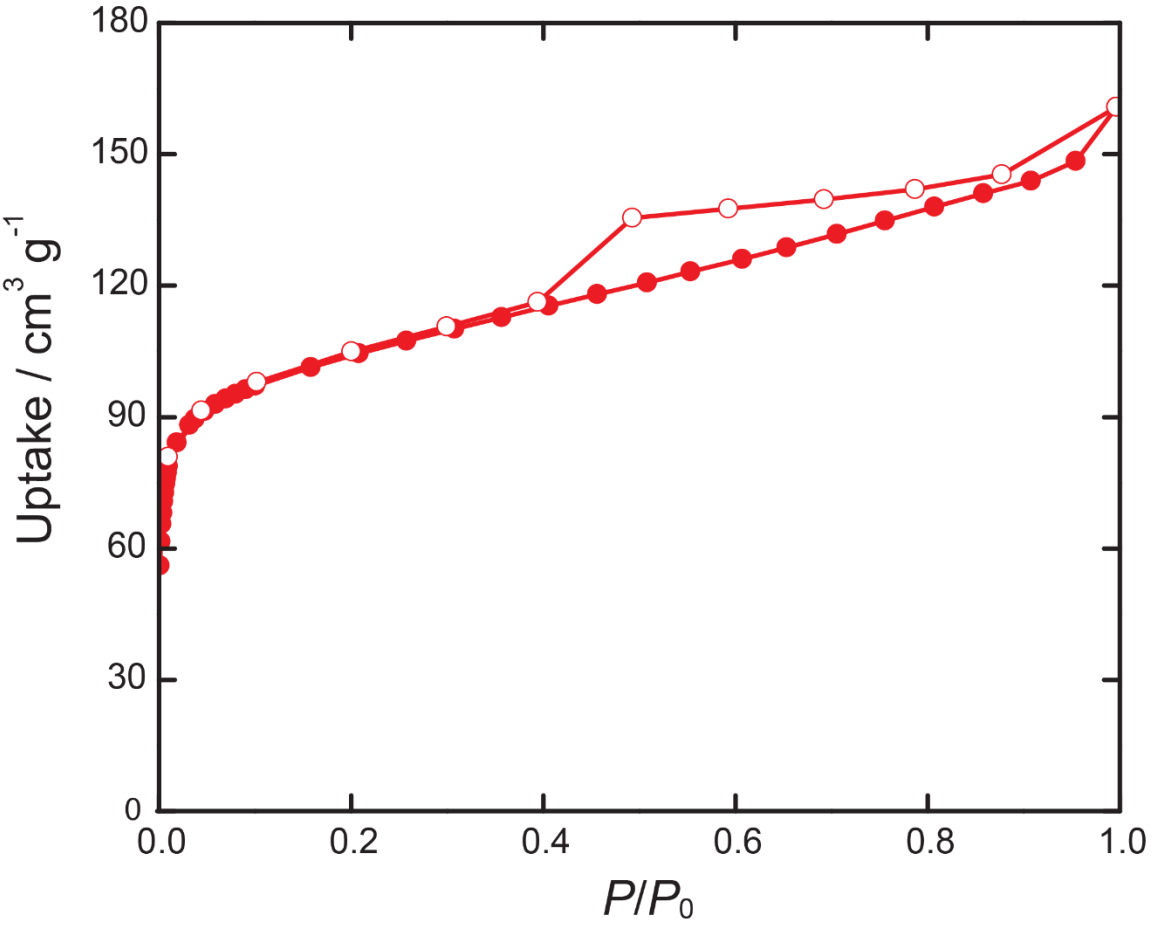

Figure S6.13. N_2 isotherm of the activated MOF-801/G recorded at 77 K. The BET surface area is 383 m^2 g^{-1}.

The expected BET surface area for the MOF-801/G was determined by multiplying the surface area of pure MOF-801 with the ratio of MOF within the mixture:
582 mg^{-1} × 67 wt% = 389 m^2 g^{-1}

The powder particle density (ρ_p) of activated MOF-801/G was estimated to be 1.552 g cm^{-3} from the pycnometer measurement (framework density ρ_s = 2.2822 ± 0.0105 g cm^{-3}) and BET pore volume measurements (V_p = 0.2060 cm^3 g^{-1}) (see equation (6.7)). The expected powder particle density was calculated as follows:

$$\rho_{MOF-801/G} = \frac{m_{MOF-801/G}}{\frac{m_{MOF-801}}{\rho_{MOF-801}} + \frac{m_{graphite}}{\rho_{graphite}}} = \frac{1650\,\text{g}}{\frac{1100\,\text{g}}{1.401\,\text{g cm}^{-3}} + \frac{550\,\text{g}}{2.16\,\text{g cm}^{-3}}} = 1.587\,\text{g cm}^{-3}$$

Evaluation of water sorption properties

A 78 mg sample of activated MOF-801/G was transferred to a 9 mm bulb gas cell and charged with N_2 to avoid air contamination. Subsequently the cell was mounted on the instrument.

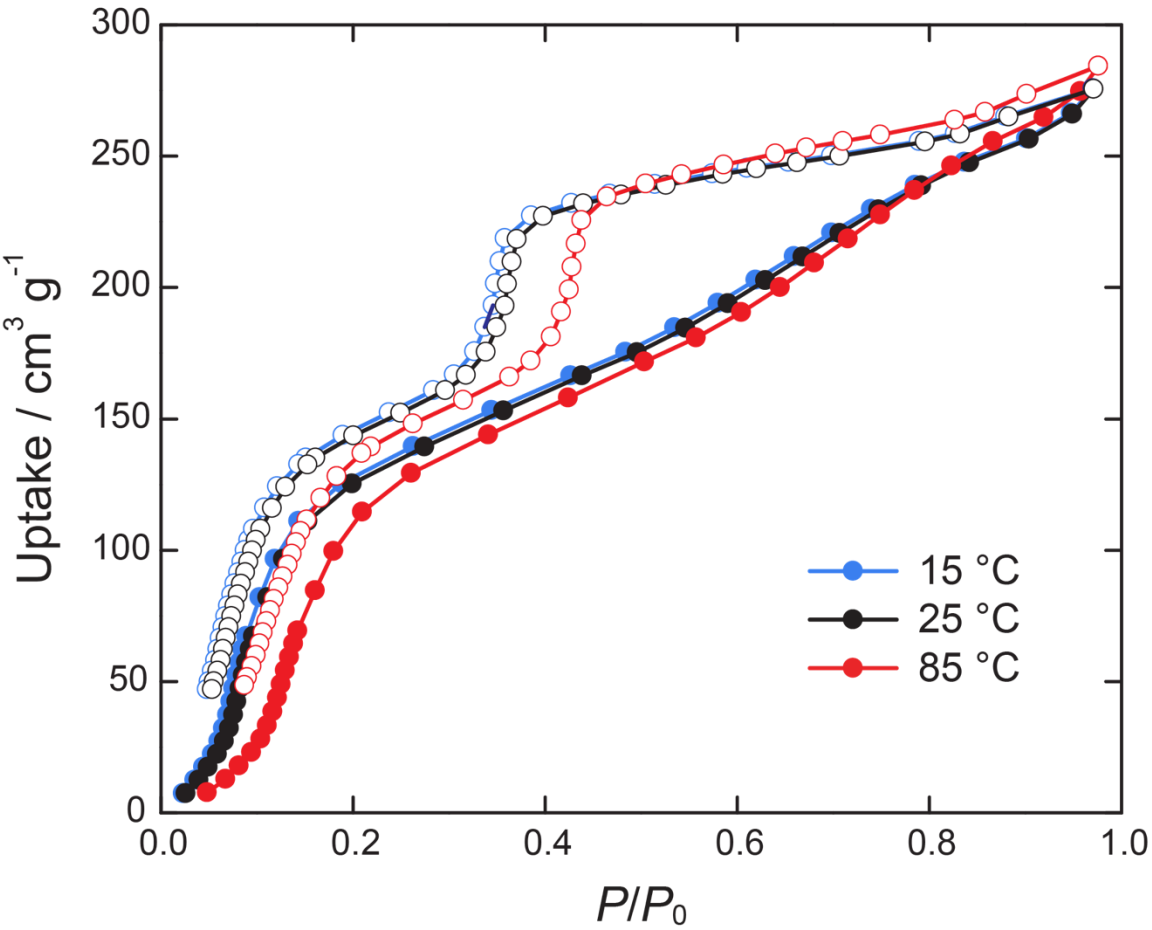

Figure S6.14. Experimental water sorption isotherm for MOF-801/G at 25 °C and calculated water sorption isotherms at 15 and 85 °C.

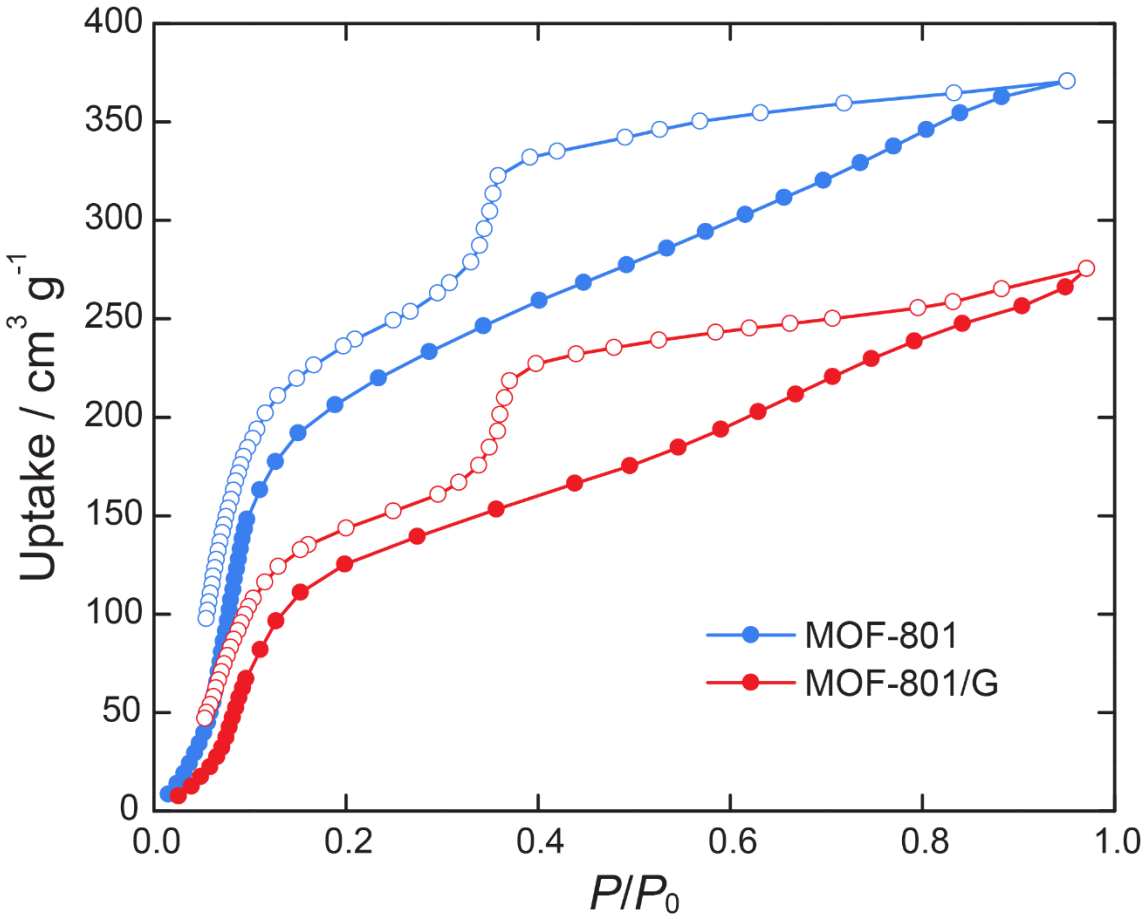

Figure S6.15. Comparison of water sorption isotherms for scaled-up MOF-801 and MOF-801/G at 25 °C. As expected, the water uptake drops by ~ 33 wt% after mixing with non-porous graphite, however, the general shape of the isotherm remains the same.

Section S6.4. MOF-303 synthesis and characterization

Synthesis of microcrystalline MOF-303 powder

MOF-303, Al(OH)(HPDC)(H_2O): 10.4 g Aluminum chloride hexahydrate ($AlCl_3 \cdot 6H_2O$, 43.08 mmol) and 7.5 g 3,5-pyrazoledicarboxylic acid monohydrate (H_3PDC, 43.08 mmol) were dissolved in 720 mL water in a 1 L glass jar, 30 mL aqueous NaOH (2.6 g, 65 mmol) were added dropwise to the above mixture under stirring. The jar was then sealed and heated in a 100 ºC isothermal oven for 24 h. (Yield: 3.0 g, 35% based on the linker). Single crystals suitable for X-ray diffraction study were prepared by combining 0.6 mmol $AlCl_3 \cdot 6H_2O$, 0.6 mmol H_3PDC, and 0.7 mmol NaOH in 4 mL H_2O. The resulting mixture was sealed in a 23 mL autoclave and placed in a 100 ºC isothermal oven for 7 days, EA: Calcd. for $Al(OH)(C_5H_2O_4N_2)(H_2O)$: C, 27.79; H, 2.33; N, 12.96%. Found: C, 27.62; H, 2.26; N, 12.74%. ATR-FTIR (4000-400 cm^{-1}): 1667(w), 1601(s), 1525(m), 1482(w), 1440(m), 1386(s), 1193(m), 1106(m), 998(s), 848(w), 791(s), 588(br), 456(s), 422(w).

MOF-303 activation

The white crystalline as-synthesized MOF-303 powder was collected by filtration and washed three times daily with water for three days, then with methanol three times daily for three days, and was then filtered and dried in air. The air-dried MOF sample was evacuated at room temperature until the pressure dropped below 1 kPa. After that, the sample was heated in vacuum at 100 ºC for 24 hours, and then at 150 ºC for another 48 hours. The combined MOF powder from 150 jars was then placed on an aluminum pan and transferred into a drying oven and heated at 160 ºC for 10 days prior to the characterization. Overall, 450 g of activated microcrystalline MOF-303 powder were prepared.

Characterization of single crystal and microcrystalline powder MOF-303

Single crystal X-ray diffraction analysis: Single crystal X-ray diffraction data were collected for a colorless plate-shaped (20 μm × 20 μm × 10 μm) crystal of as-synthesized MOF at beamline 11.3.1 of the ALS at LBNL, equipped with a Bruker Photon 100 CMOS area detector using synchrotron radiation (10-17 KeV), at 0.7749 Å. The crystal was mounted on a MiTeGen® kapton loop and placed under a 100 (2) K nitrogen cold stream. Data were processed using the Bruker APEX2 software package[19], integrated using SAINT v8.34A and corrected for the absorption by SADABS routines (no correction was made for extinction or decay). The structures were solved by intrinsic phasing (SHELXT) and refined by full-matrix least squares on F^2 (SHELXL)[20]. Atomic positions of MOF-303 were obtained from the single crystal data, but the anisotropic refinement remains unstable due to the poor diffraction of the crystals. Based on the structural model obtained from single-crystal data, the Pawley structural refinement was performed using the *Reflex* module in BIOVIA Materials Studio 7.0[21]. Selected crystal data and atomic position are given in Table S6.1,6.2.

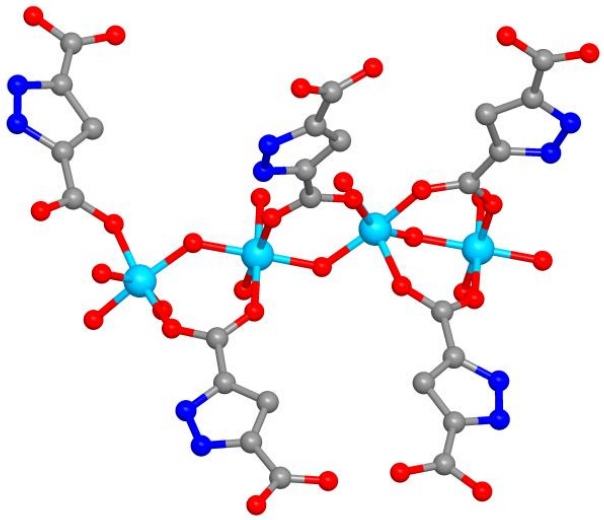

Figure S6.16. Asymmetric unit in the single-crystal structure of MOF-303 (atoms are shown isotropically). Hydrogen atoms are omitted for clarity. Color code: C, gray; N, blue; O, red; Al, cyan.

Table S6.1. Crystal data and structure determination for MOF-303 with single crystal data set.

Compound	**MOF-303**
Chemical formula	$C_{20}H_{12}O_{20}N_8Al_4$
Formula mass	792.30
Crystal system	monoclinic
Space group	$P2_1$
λ (Å)	0.7749(1)
a (Å)	12.2714(16)
b (Å)	14.572(2)
c (Å)	14.253(2)
β (°)	101.787(10)
Z	4
V (Å^3)	2495.0(6)
Temperature (K)	100(2)
Size (mm^3)	0.01 × 0.02 × 0.02
Density (g cm^{-3})	1.159
Measured reflections	16277
Unique reflections	3425
Parameters	209
Restraints	1
R_{int}	0.172
θ range (°)	2.2-19.7
R_1, wR_2	0.2948 0.6525
S (GOF)	2.86
Max/min res. dens. (e Å^{-3})	2.32/-1.38

Table S6.2. Atomic positions for MOF-303 from the Pawley refinement model. Space group $P2_1$. a = 12.2943 Å; b = 14.9784 Å; c = 14.6004 Å, β = 104.8238°

Atom name	Atom	*x* (Å)	*y* (Å)	*z* (Å)
Al1	Al	-2.5E-4	0.41685	0.73197
Al2	Al	0.5052	0.41616	0.7551
Al3	Al	0.26447	0.46312	0.79057
O4	O	0.14515	0.39394	0.75591
Al5	Al	0.74609	0.36962	0.71973
O6	O	0.65215	0.40091	0.78631
N7	N	0.65911	0.58781	0.4947
C8	C	0.0777	0.72771	0.46665
O9	O	0.02071	0.48883	0.83088
O10	O	0.35992	0.54594	0.8577
O11	O	0.51428	0.48687	0.65752
O12	O	0.65113	0.28639	0.65304
O13	O	0.20455	0.79397	0.38367
O14	O	0.99421	0.32564	0.85138
O15	O	0.52653	0.5122	0.82915
O16	O	0.68747	0.86186	1.12576
O17	O	0.80737	0.29639	0.8177
O18	O	0.20357	0.53672	0.69279
O19	O	0.20467	0.52545	0.87179
O20	O	0.68679	0.45674	0.63717
C21	C	0.58013	0.74842	1.02908
O22	O	0.51482	0.8318	1.14595
O23	O	0.35832	0.4318	0.72388
C24	C	0.48855	0.62779	0.50452
C25	C	0.10427	0.7884	0.39472
O26	O	0.01647	0.50848	0.65931
C27	C	0.14816	0.67003	0.53056
C28	C	0.52411	0.63714	0.92751
C29	C	0.07584	0.62466	0.57419
C30	C	0.59392	0.81827	1.10442
N31	N	0.62682	0.65447	0.43447
N32	N	0.62957	0.66206	0.92768
N33	N	-0.02885	0.71705	0.47343
O34	O	0.02097	0.8318	0.34361
C35	C	0.52304	0.68081	0.43799
C36	C	0.46556	0.56083	0.86836
C37	C	0.10124	0.55222	0.6462
C38	C	0.59316	0.50019	0.61568
O39	O	-0.14575	0.43922	0.70804

N40	N	-0.02924	0.65543	0.538
C41	C	0.10416	0.53187	0.8822
C42	C	0.90971	0.28167	0.86469
C43	C	0.8626	0.16279	0.97928
O44	O	0.48424	0.31984	0.68133
C45	C	0.93541	0.21017	0.93777
N46	N	0.66352	0.72837	0.98804
C47	C	0.4886	0.69163	0.99217
C48	C	0.57862	0.5694	0.53944
C49	C	0.54559	1.2441	0.64244
H50	H	0.68419	0.41194	0.84501
H51	H	0.32626	0.42087	0.66517
H52	H	0.16077	0.3388	0.74793
H53	H	0.73686	0.55587	0.50546
H54	H	0.41136	0.63246	0.52626
H55	H	0.23757	0.66099	0.54205
H56	H	0.67951	0.63378	0.88722
H57	H	-0.10175	0.63464	0.55666
H58	H	0.40953	0.6893	1.01121
C59	C	0.07726	0.59351	0.9532
N60	N	-0.02996	0.60721	0.95675
N61	N	-0.03044	0.66888	1.02125
H62	H	0.84905	0.49433	0.76191
H63	H	0.77244	0.16904	0.96483
H64	H	-0.10353	0.69193	1.0374

PXRD, EDS analysis, and SEM images: Activated microcrystalline MOF-303 was used for PXRD experiments. A ground sample was placed on a zero-background sample holder and mounted on the diffractometer. The data was collected from 3 to 50 degrees with a step width of 0.01 and a total data collection time of 30 minutes. SEM and EDS images were taken to study the morphology and elemental composition of bulk MOF-303 powder.

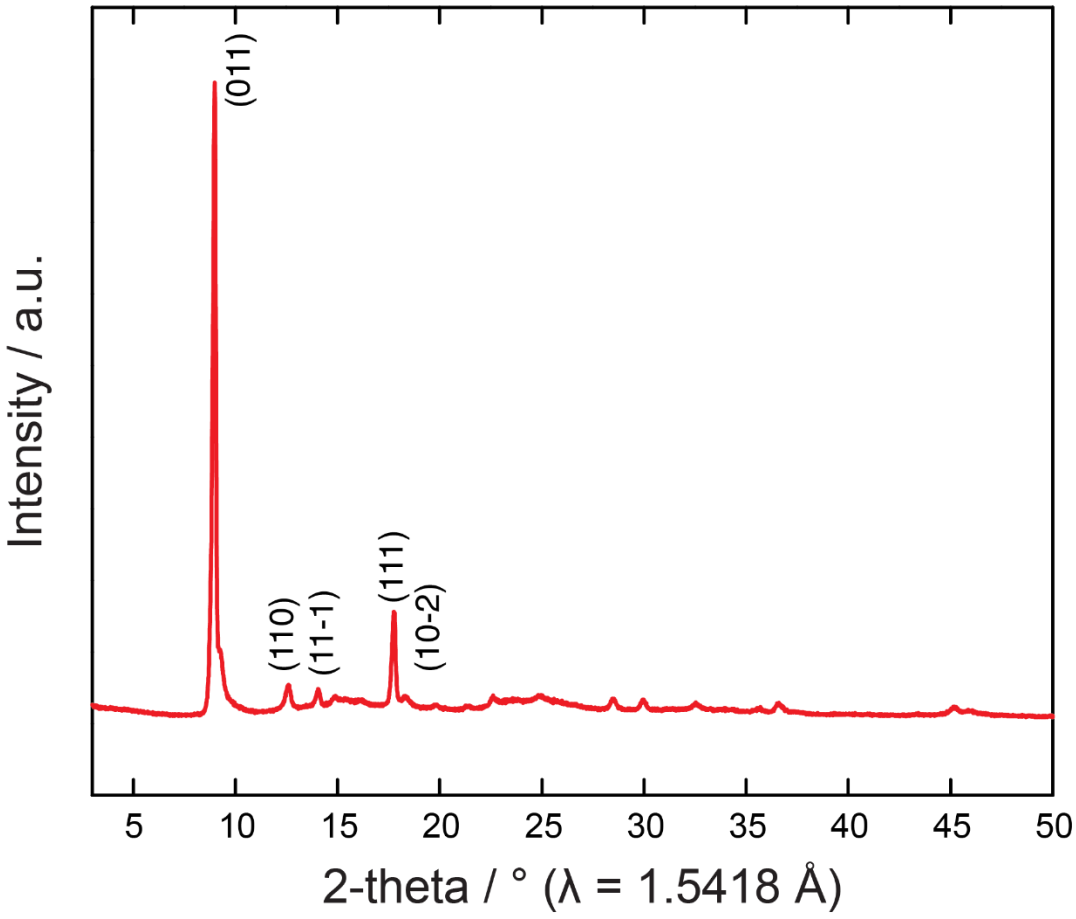

Figure S6.17. PXRD pattern of activated MOF-303.

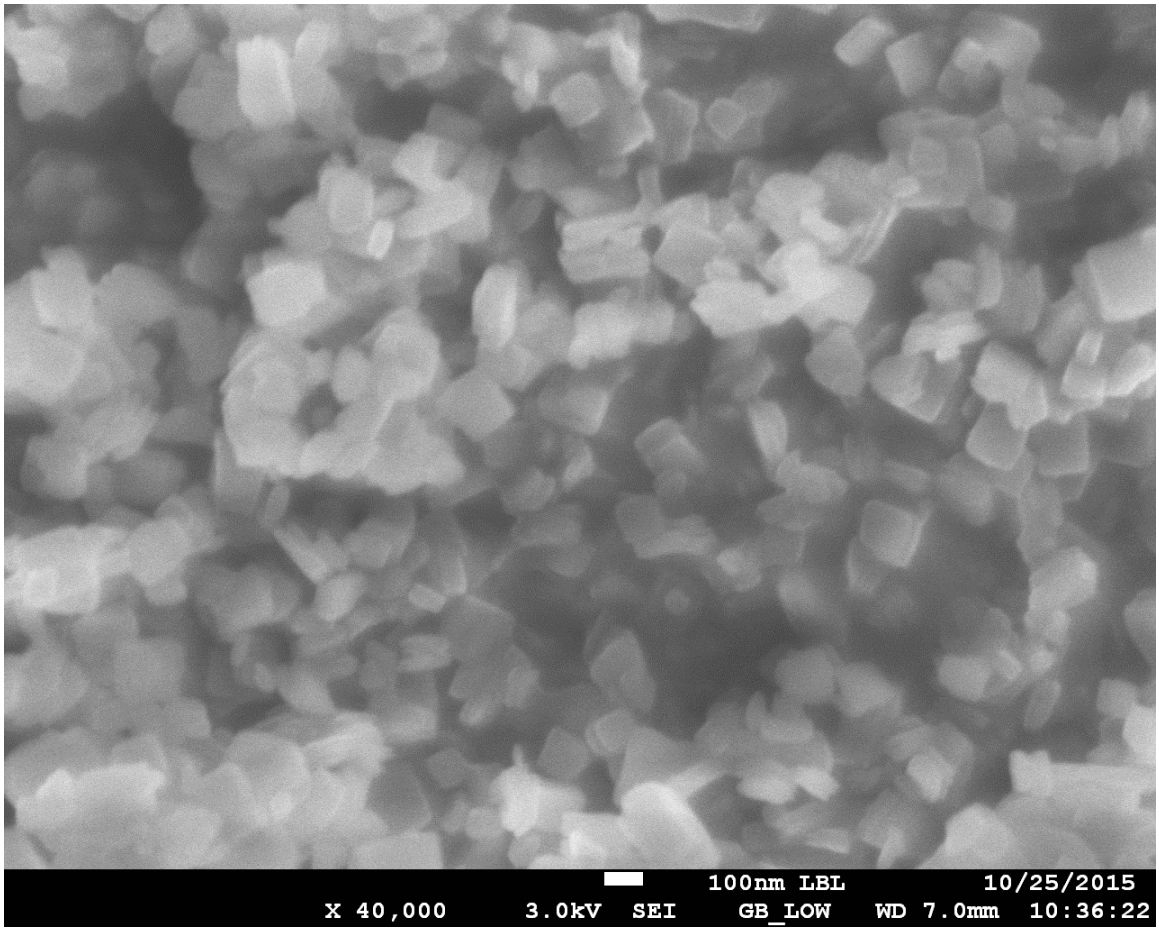

Figure S6.18. SEM image of activated MOF-303.

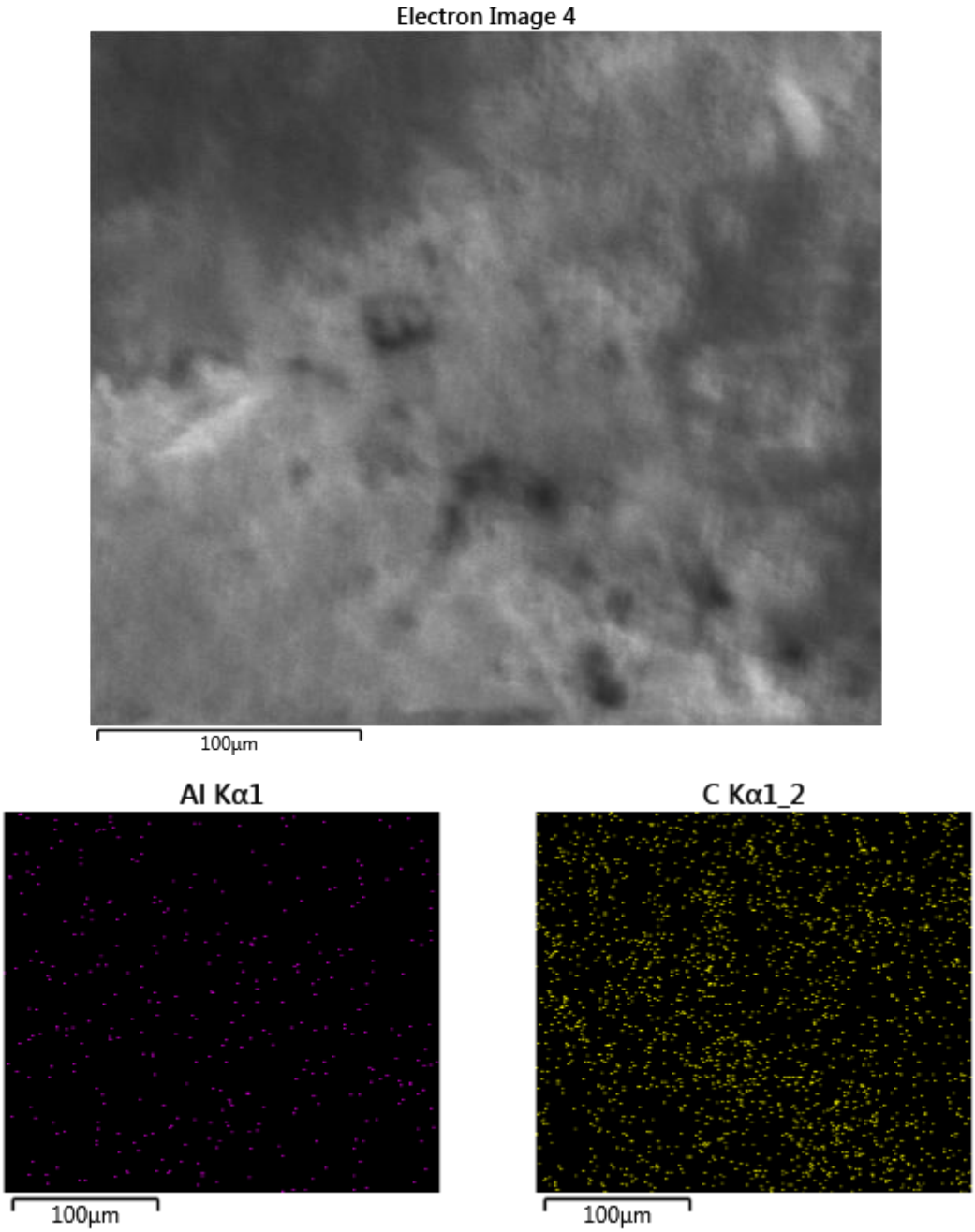

Figure S6.19. SEM image of activated MOF-303 (top). Carbon and Aluminum EDS images of the activated MOF-303 (bottom).

Porosity and packing density analysis: A 45 mg sample was taken from 450 g of well-mixed activated MOF-303, transferred to a 9 mm bulb gas cell and charged with N_2 to avoid air contamination. Then, the cell was mounted on the instrument. 26 adsorption and 11 desorption points were collected.

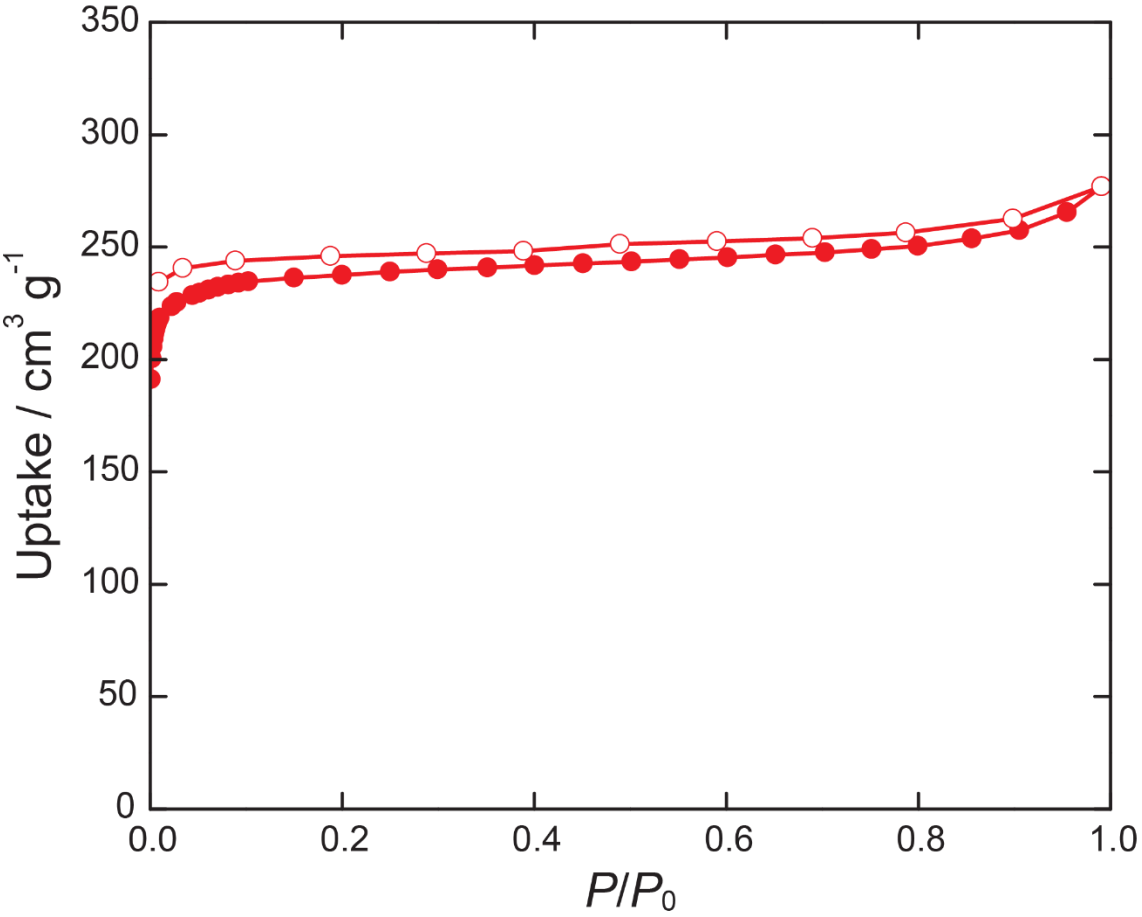

Figure S6.20. N_2 isotherm of activated scaled-up MOF-303 at 77 K. BET surface area is 989 $m^2 g^{-1}$.

The powder particle density (ρ_p) of activated scaled-up MOF-303 was estimated to be 1.293 g cm^{-3} from the pycnometer measurement (framework density ρ_s = 2.4591 ± 0.0037 g cm^{-3}) and BET pore volume measurements (V_p = 0.3670 $cm^3 g^{-1}$) (see equation (6.7)).

Evaluation of water capacity properties

A 38 mg sample was taken from the activated scaled-up MOF-303, transferred to a 9 mm bulb gas cell, and charged with N_2 to avoid air contamination. Then the cell was mounted on the instrument. The temperature of the adsorbent was controlled using a water bath. In case of pre-scaled-up MOF-303, 27 mg of sample was analyzed.

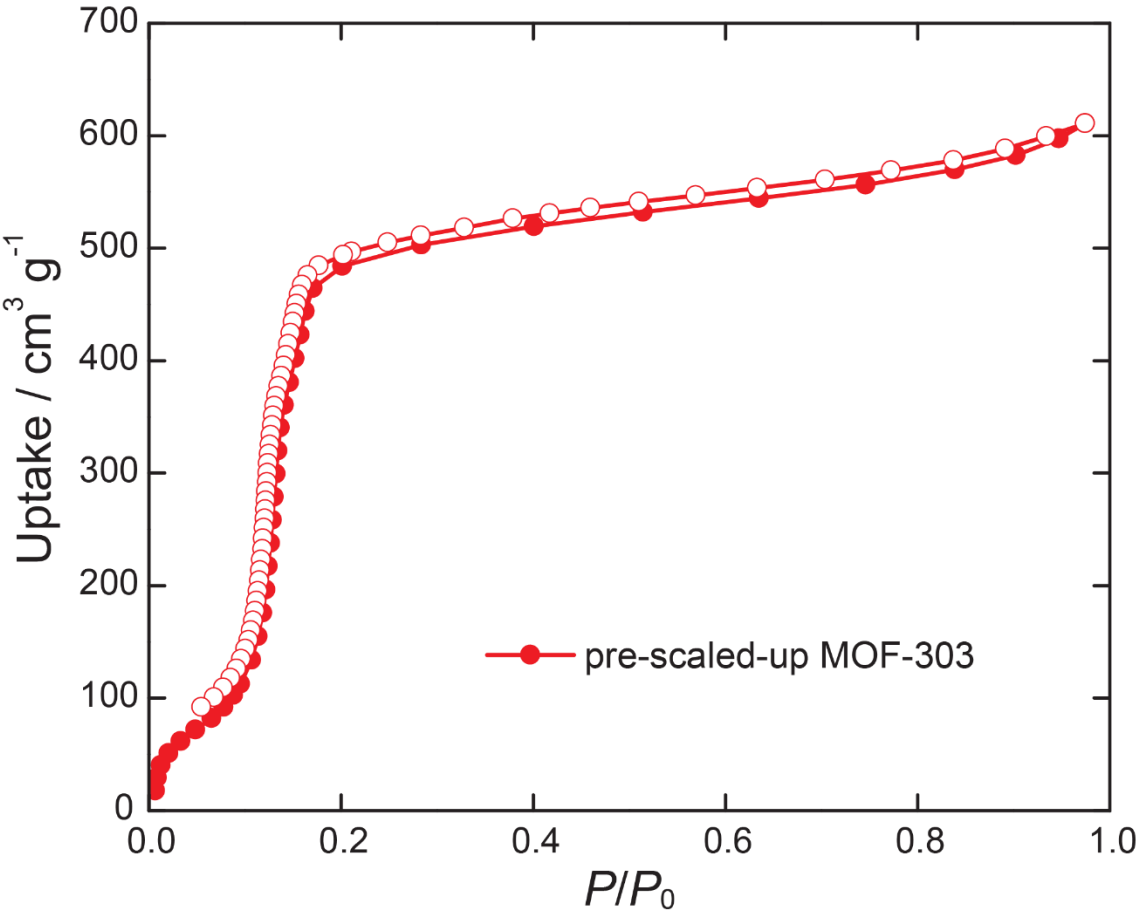

Figure S6.21. Water sorption isotherm of pre-scaled-up activated MOF-303 recorded at 25 °C.

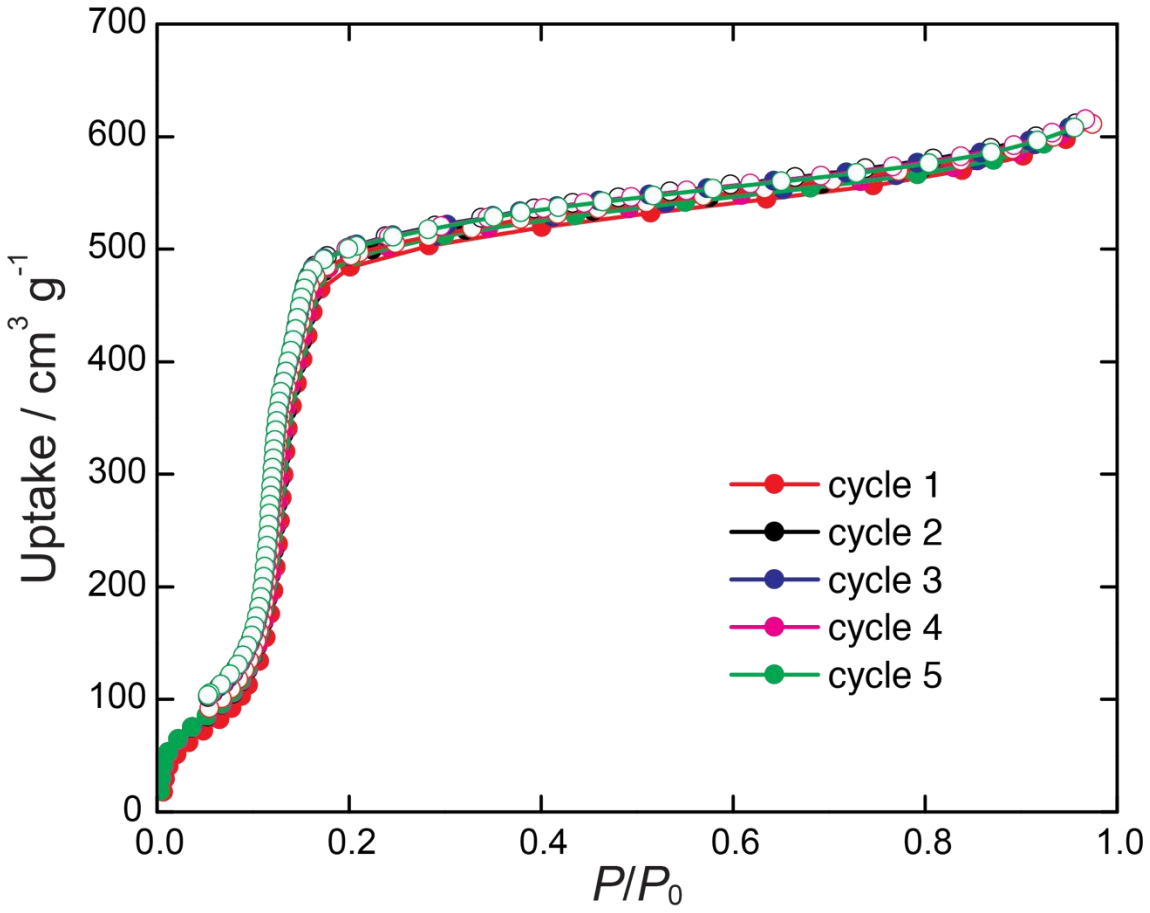

Figure S6.22 Cycling experiment of MOF-303. Five subsequent adsorption-desorption cycles recorded 25 °C are shown.

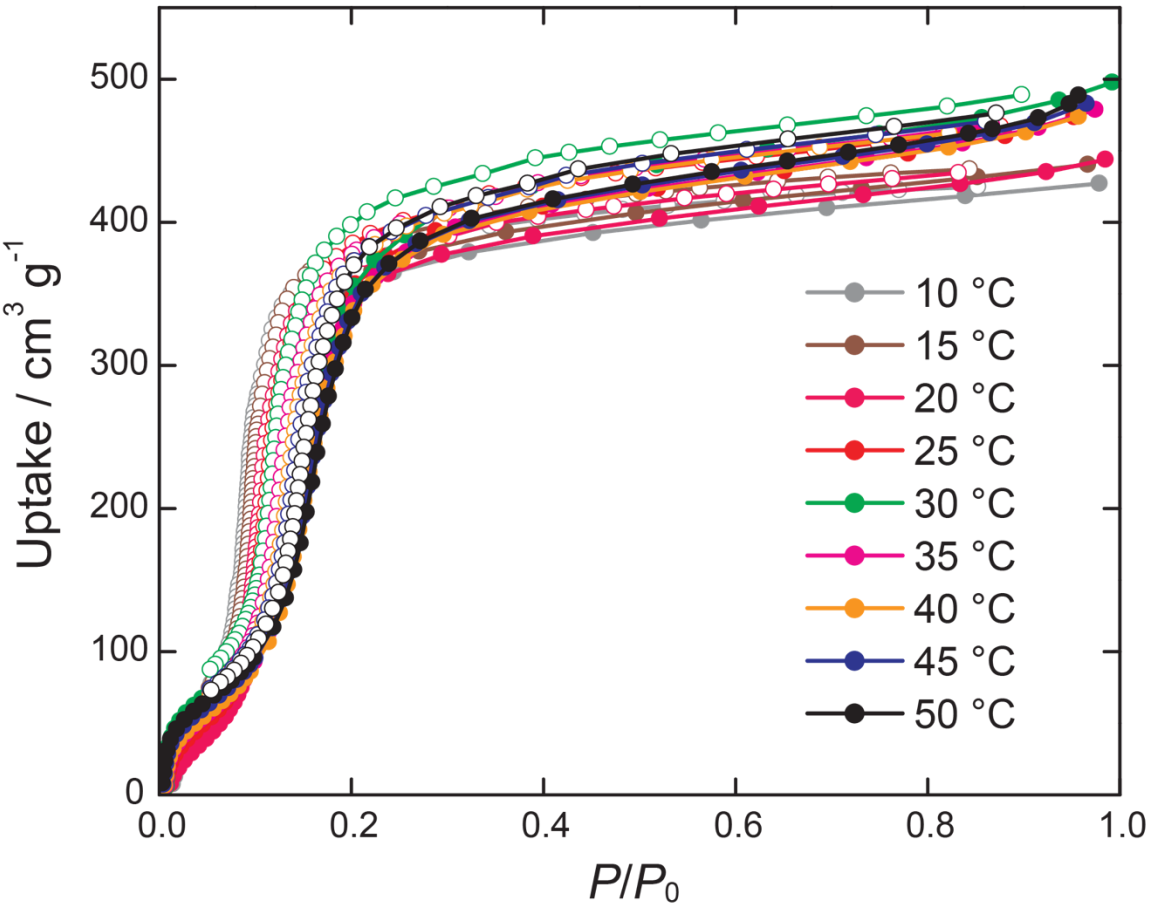

Figure S6.23. Water sorption isotherms of activated scaled-up MOF-303 at different temperatures.

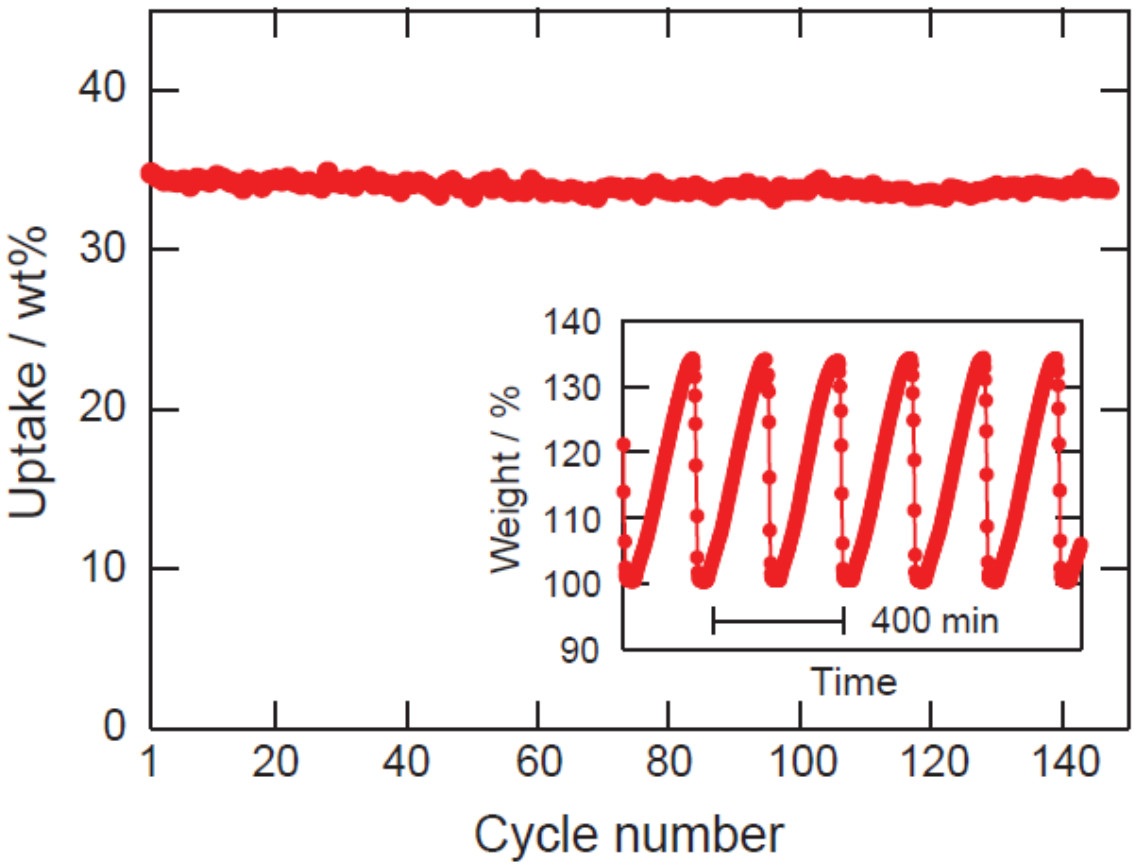

Figure S6.24. 150 cycles of relative humidity swing cycling of scaled-up activated MOF-303 at 25 °C in a TGA. The sample was purged a N_2 flow with 40% RH and then regenerated after saturation by purging with a dry N_2 flow at 85 °C for 30 minutes before commencing the next cycle. Weight percentage was estimated as (mass of activated material + mass of adsorbed water) / (mass of activated material).

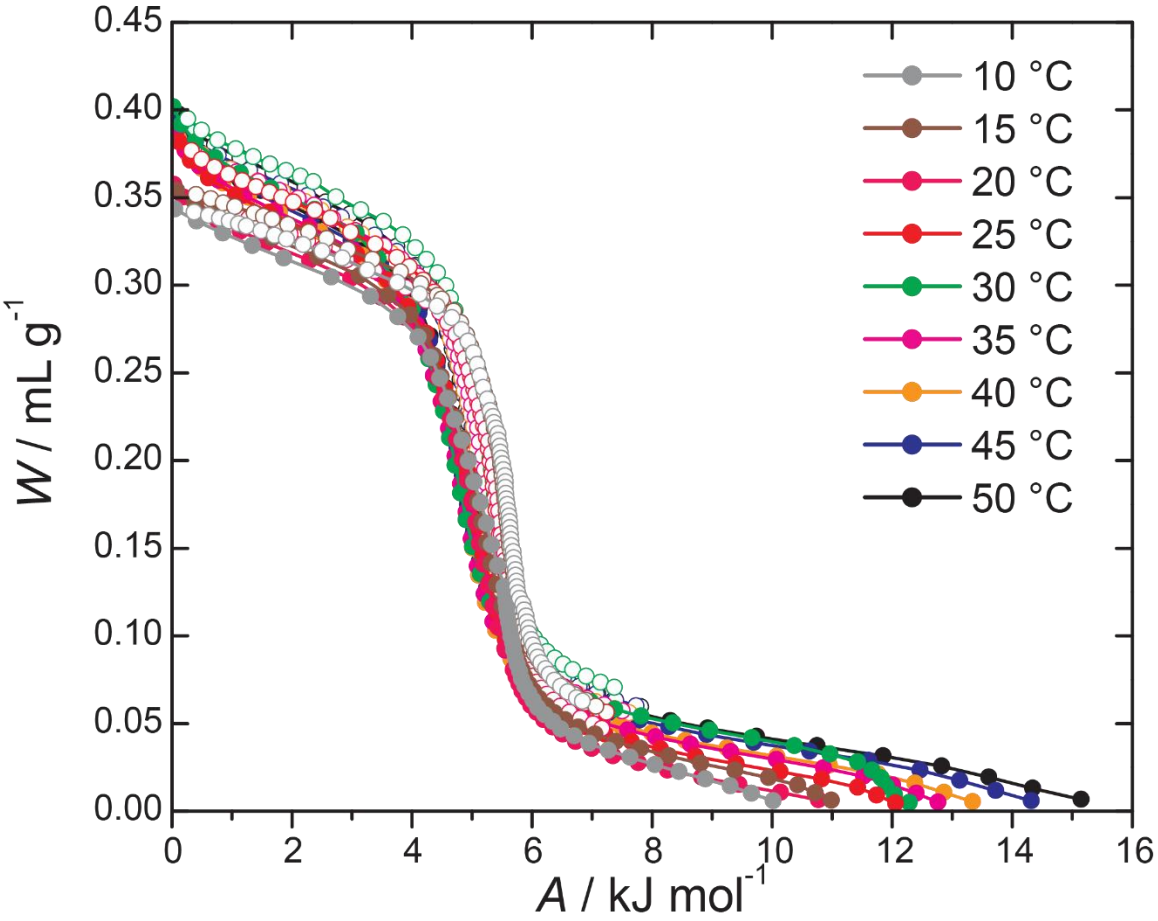

Figure S6.25. Characteristic curves determined using equations (6.8,6.9) based on sorption isotherms for MOF-303 measured at different temperatures.

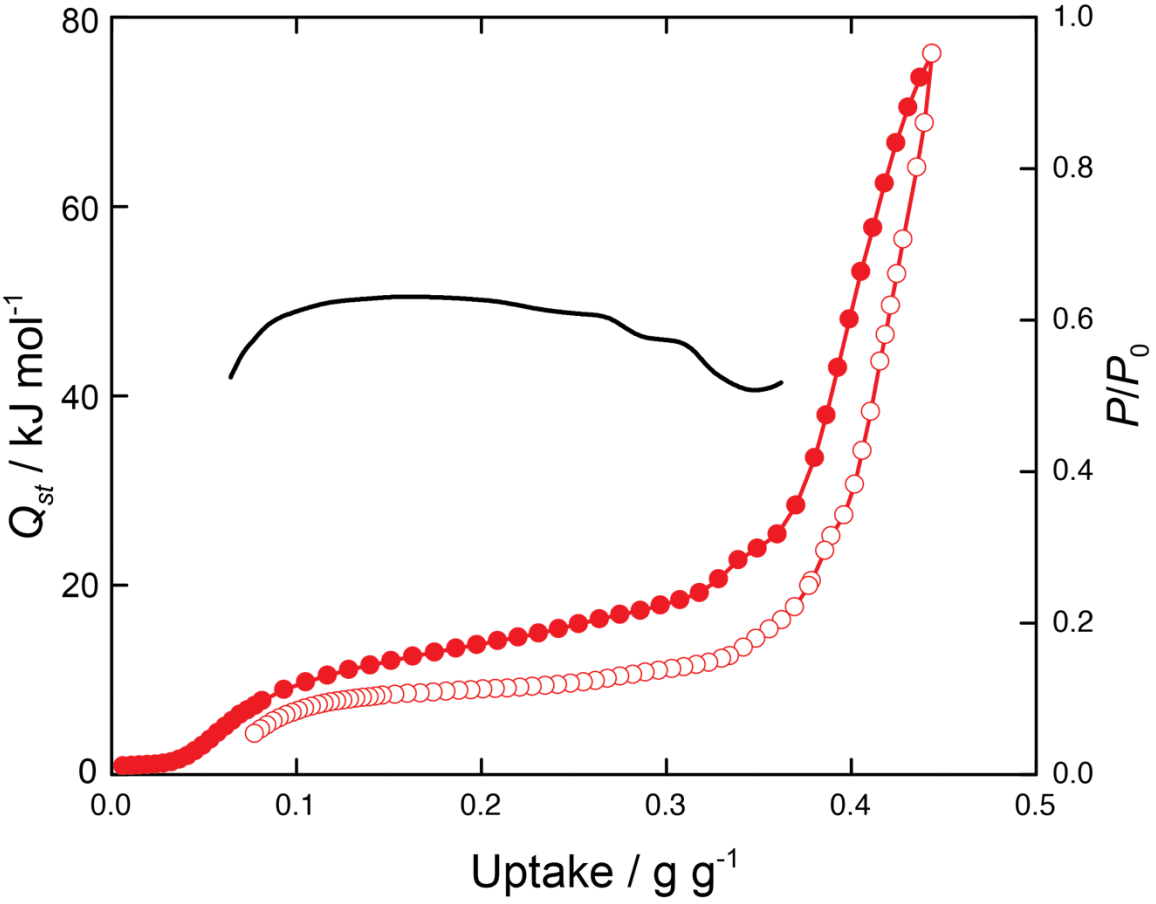

Figure S6.26. Isosteric heat of adsorption (black) vs. water sorption isotherm at 25 ºC (red) for activated MOF-303.

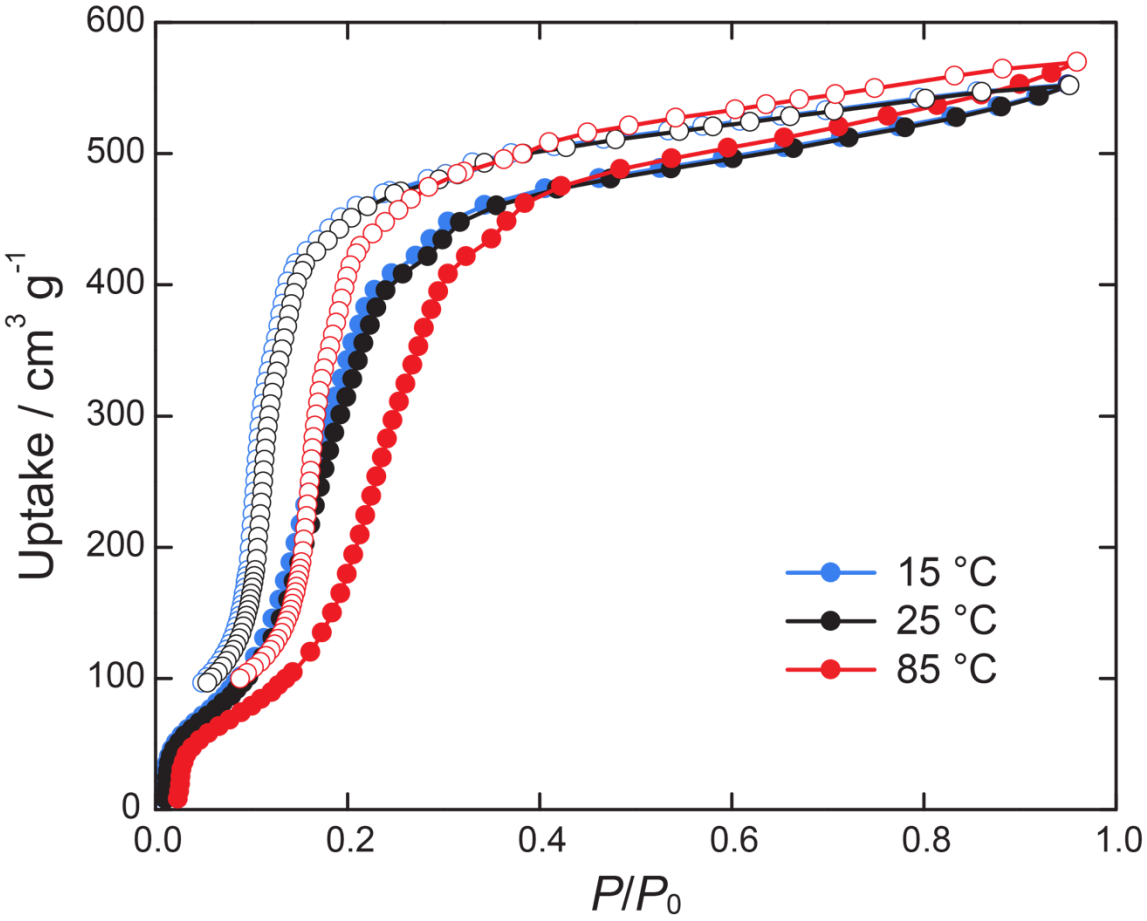

Figure S6.27. Experimental water sorption isotherm for activated scaled-up MOF-303 at 25 °C and calculated water isotherms at 15 and 85 °C. A 45 mg sample was taken from 450 g of activated scaled-up microcrystalline powder MOF-303, transferred to a 9 mm bulb gas cell, and charged with N_2 to avoid air contamination. Then the cell was mounted on the instrument.

Section S6.5. MOF-303/G preparation and characterization

Preparation of the mixture

450 g of activated scaled-up MOF-303 was mixed with 150 g of graphite powder in the 2 L jar to produce 600 g of 67:33 wt% MOF-303/G. The resulting mixture was thoroughly mixed by shaking the jar until the MOF-303/G mixture had homogenous gray color. Aggregation of MOF-303 powder into large particles was observed. These aggregates were further crushed using a spatula and remixed. The resulting mixture was further characterized in terms of crystallinity, powder density, porosity and water uptake properties without any additional activation.

Characterization of MOF-303/G

PXRD, EDS analysis, and SEM images of activated MOF-303/G: A powder sample was placed on a zero-background sample holder and was mounted on the diffractometer. The data was collected from 3 to 50 degrees with a step width of 0.01 and a total data collection time

of 30 minutes. SEM and EDS images were taken to study the morphology and elemental composition of bulk MOF-303/G powder.

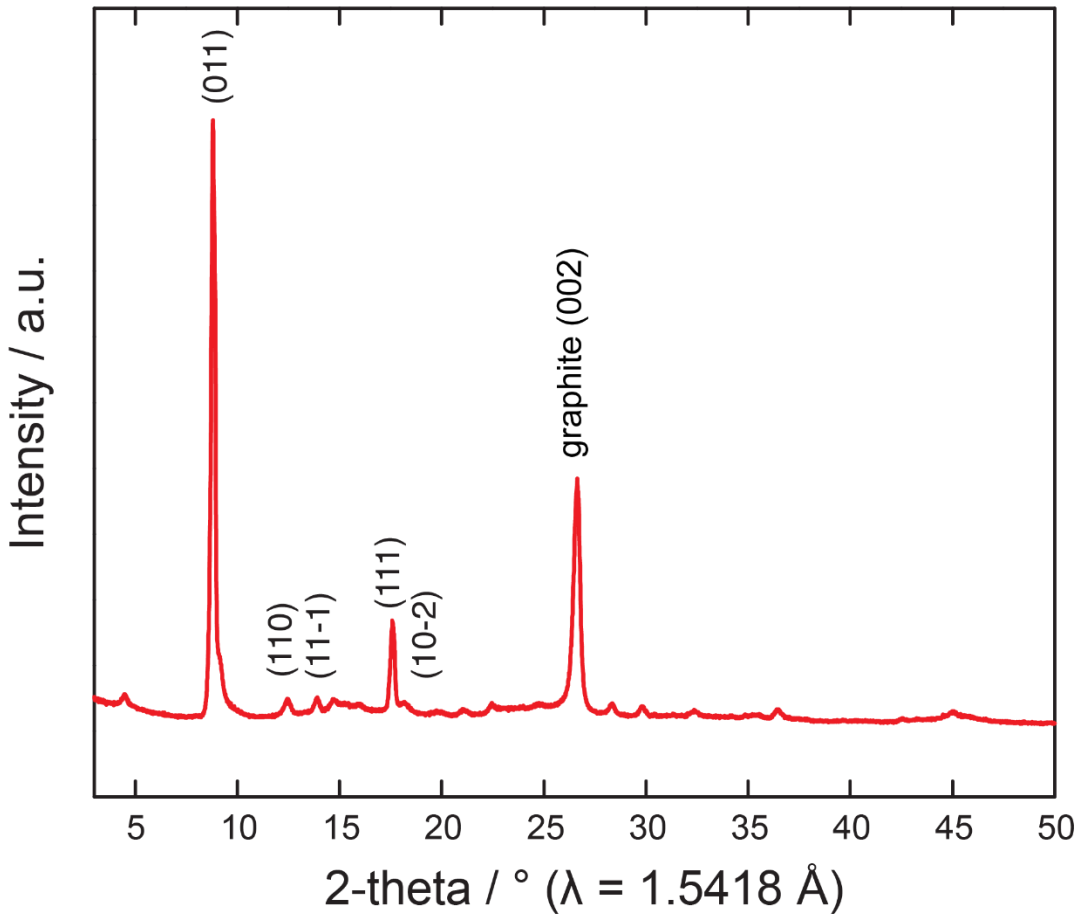

Figure S6.28. PXRD pattern of activated sample of MOF-303/G. The peak at 26.5º corresponds to the (002) reflection of graphite.

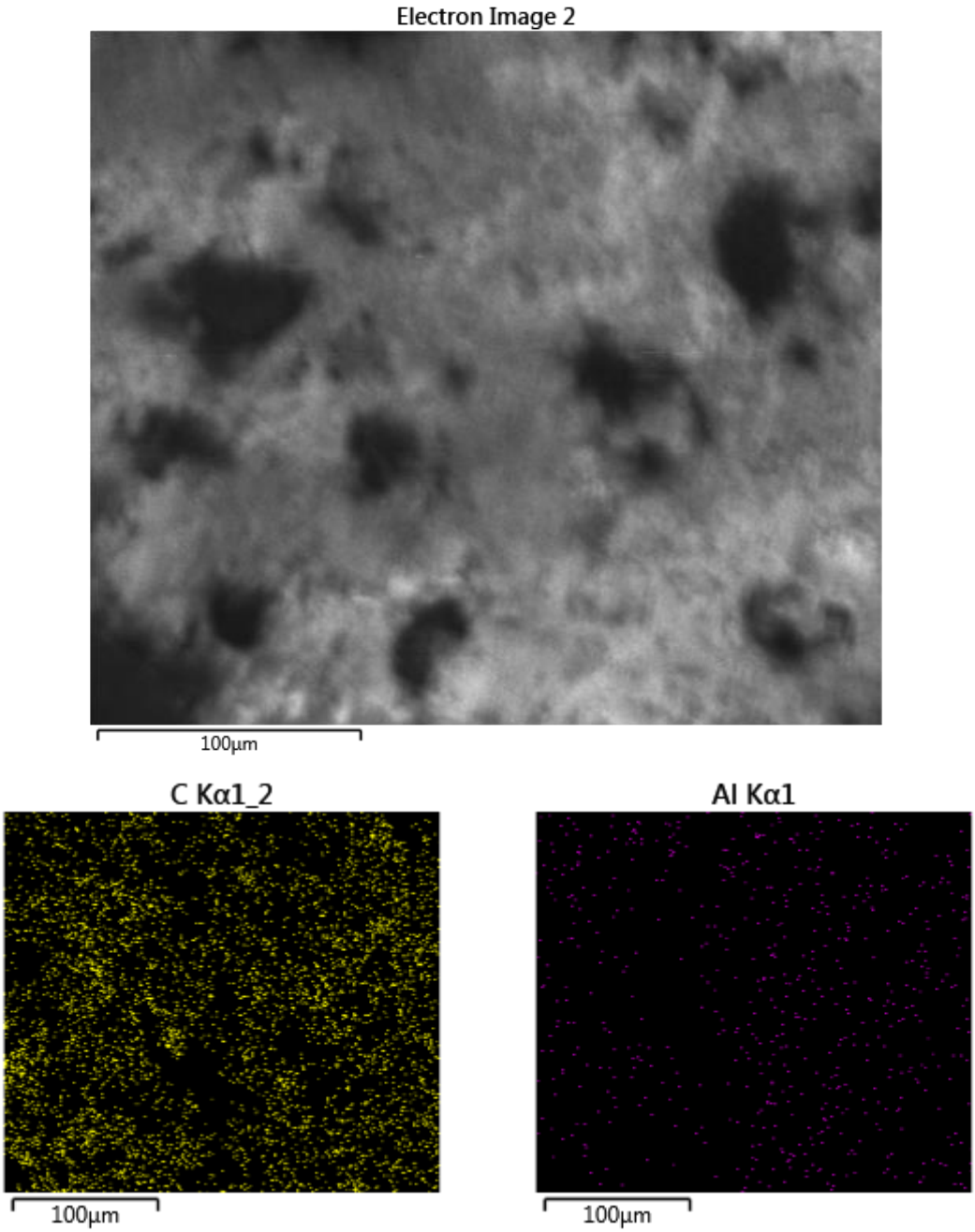

Figure S6.29. SEM image of activated MOF-303/G (top). Carbon and Aluminum EDS images of the MOF-303/G (bottom).

Porosity and packing density analysis: A 65 mg sample was taken from 600 g of well-mixed activated MOF-303/G, transferred to a 9 mm bulb gas cell and charged with N_2 to avoid air contamination. Then the cell was mounted on the instrument. 26 adsorption and 11 desorption points were collected.

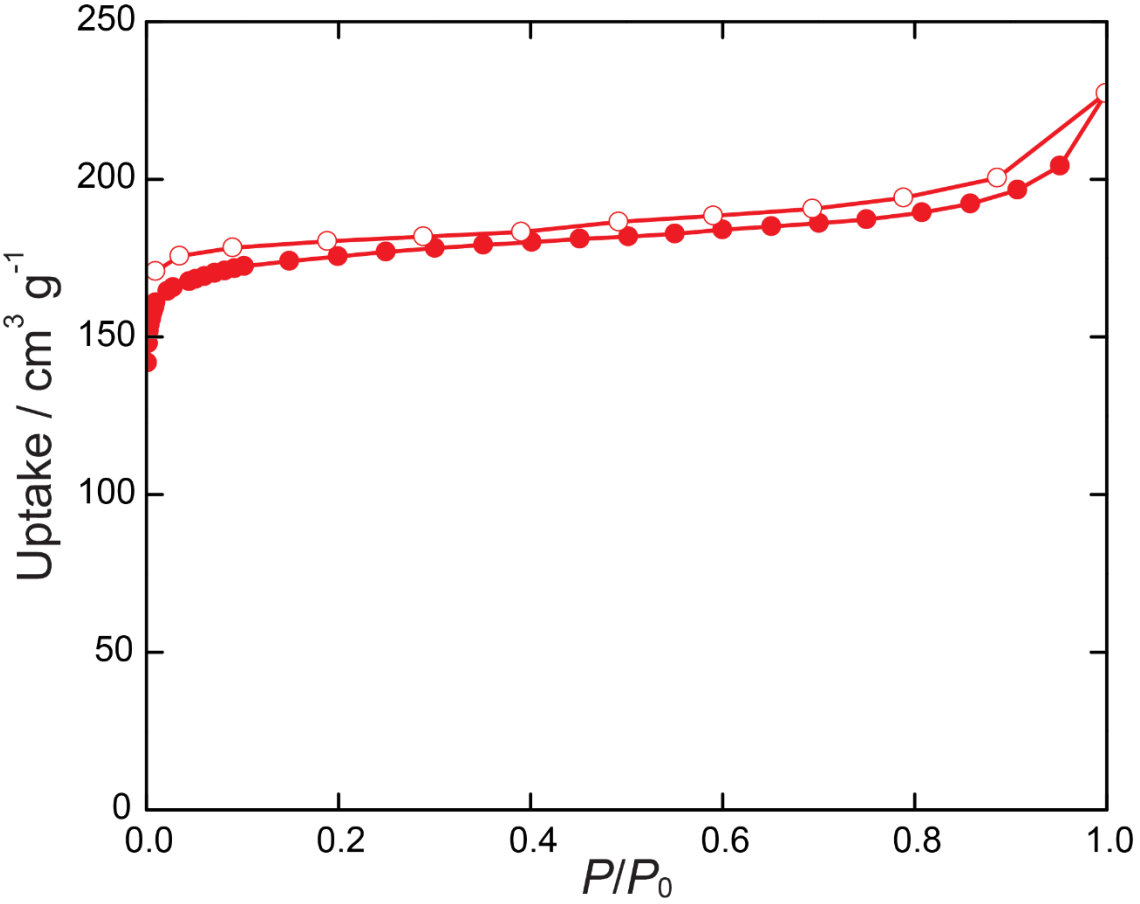

Figure S6.30. N_2 isotherm of activated MOF-303/G at 77 K. The BET surface area is 701 $m^2\ g^{-1}$.

The expected BET surface area for MOF-303/G was determined by multiplying the surface area of pure MOF-303 with the ratio of MOF within in the mixture: 989 $m^2\ g^{-1}$ × 67 wt% = 662 $m^2\ g^{-1}$.

The powder particle density (ρ_p) of activated MOF-303/G was estimated to be 1.482 g cm^{-3} from the pycnometer measurement (framework density ρ_s = 2.5452 ± 0.0015 g cm^{-3}) and BET pore volume measurements (V_p = 0.2820 $cm^3\ g^{-1}$) (see equation (6.7)). The expected powdered particle density is calculated as follows:

$$\rho_{MOF-303/G} = \frac{m_{MOF-303/G}}{\frac{m_{MOF-303}}{\rho_{MOF-303}} + \frac{m_{graphite}}{\rho_{graphite}}} = \frac{600\,\text{g}}{\frac{450\,\text{g}}{1.293\,\text{g cm}^{-3}} + \frac{150\,\text{g}}{2.16\,\text{g cm}^{-3}}} = 1.437\ \text{g cm}^{-3}.$$

Evaluation of water capacity properties

A 65 mg sample was taken from the activated MOF-303/G, transferred to a 9 mm bulb gas cell and charged with N_2 to avoid air contamination. Then, the cell was mounted on the instrument.

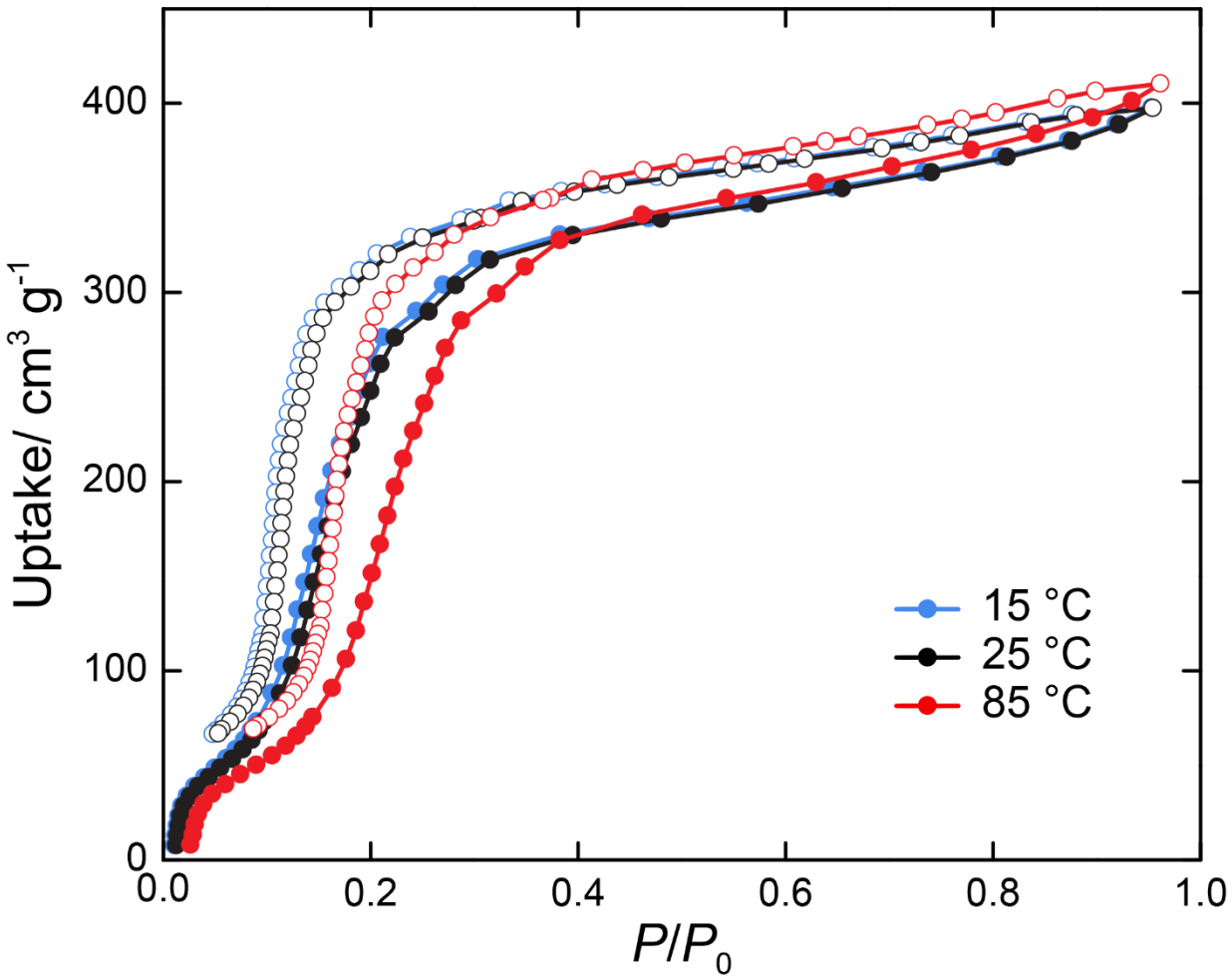

Figure S6.31. Experimental water sorption isotherm for MOF-303/G at 25 °C and calculated water isotherms at 15 and 85 °C.

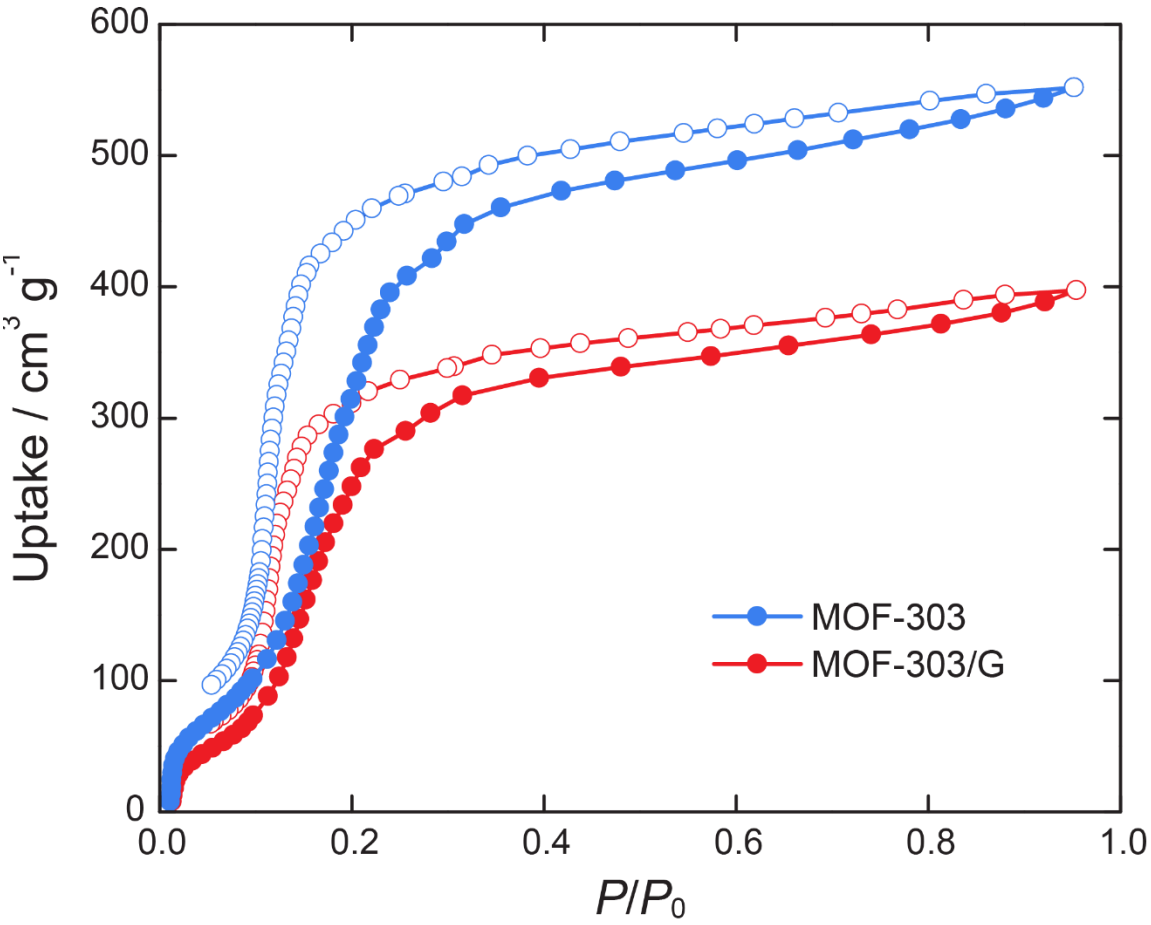

Figure S6.32. Comparison of water sorption isotherms of scaled-up MOF-303 and MOF-303/G at 25 °C. As expected, the water uptake drops by ~ 33 wt% after mixing MOF-303 with 33 wt% of non-porous graphite sample, however, the general shape of the isotherm remains the same.

Section S6.6. Comparison of sorbents

Characterization of Zeolite 13X

A commercially available Zeolite 13X sample was used without any modifications prior PXRD measurement. A powder sample was placed on a zero-background sample holder and was mounted on the diffractometer. The data was collected from 3 to 50 degrees with a step width of 0.01 and a total data collection time of 30 minutes.

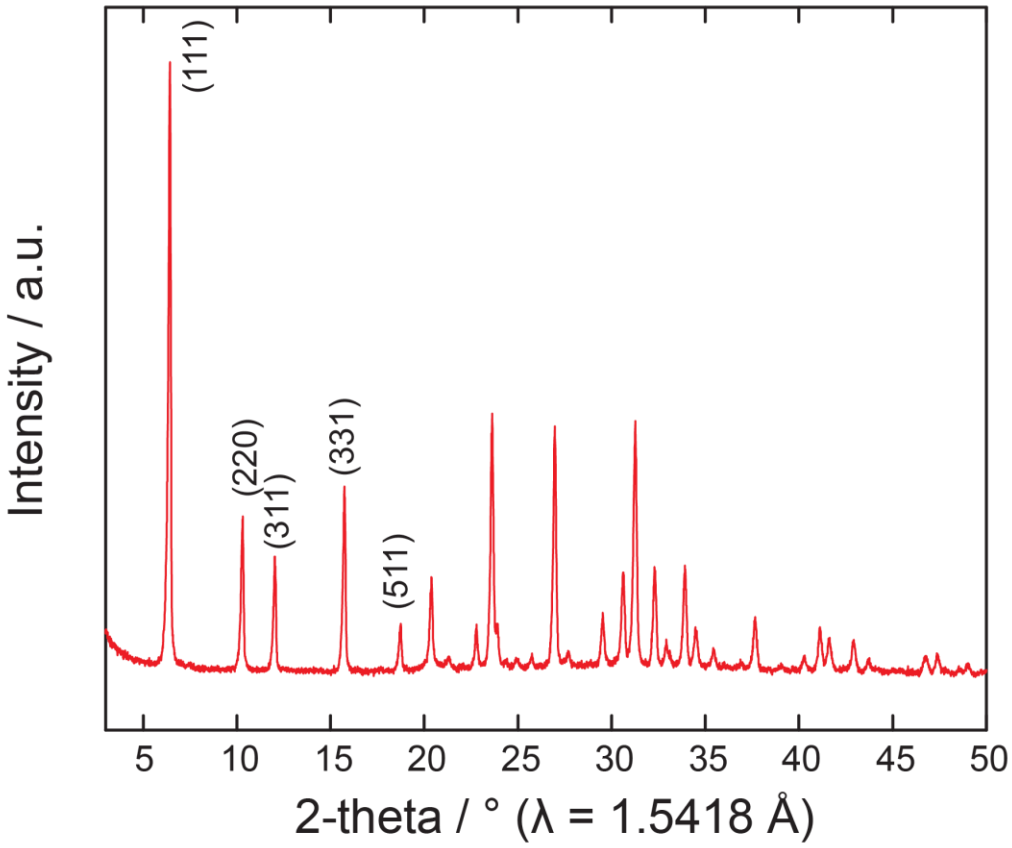

Figure S6.33. PXRD pattern of Zeolite 13X.

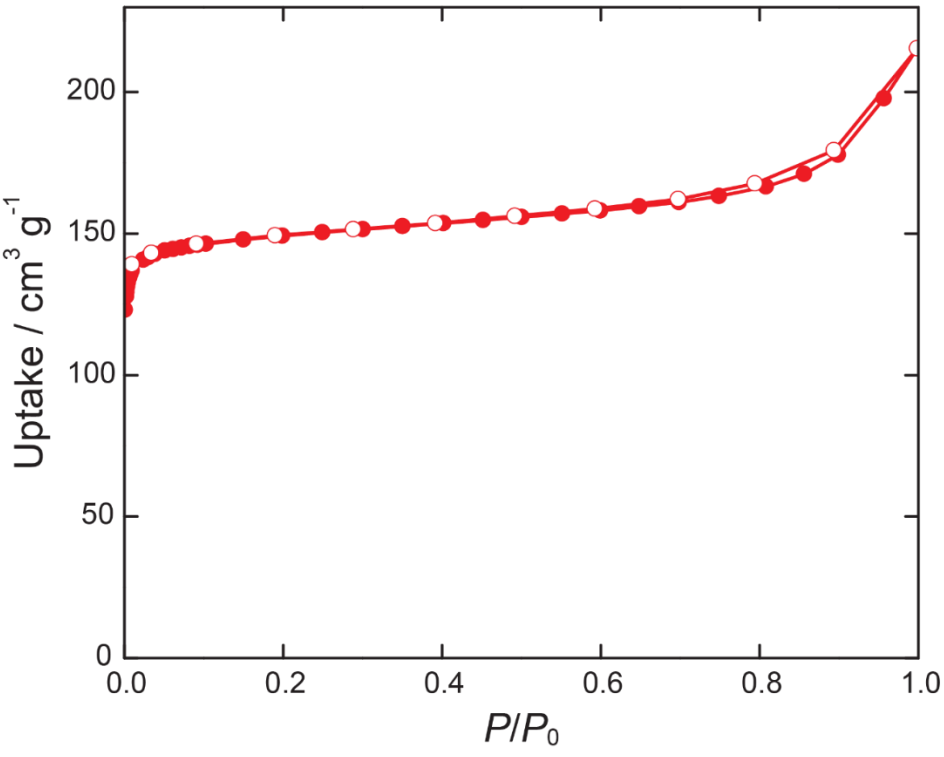

Figure S6.34. N_2 isotherm of Zeolite 13X recorded at 77 K. The BET surface area is 602 m^2 g^{-1}. 53 mg of activated Zeolite 13X were transferred to a 9 mm bulb gas cell and charged with N_2 to avoid air contamination. Then the cell was mounted on the instrument. 26 adsorption and 11 desorption points were collected.

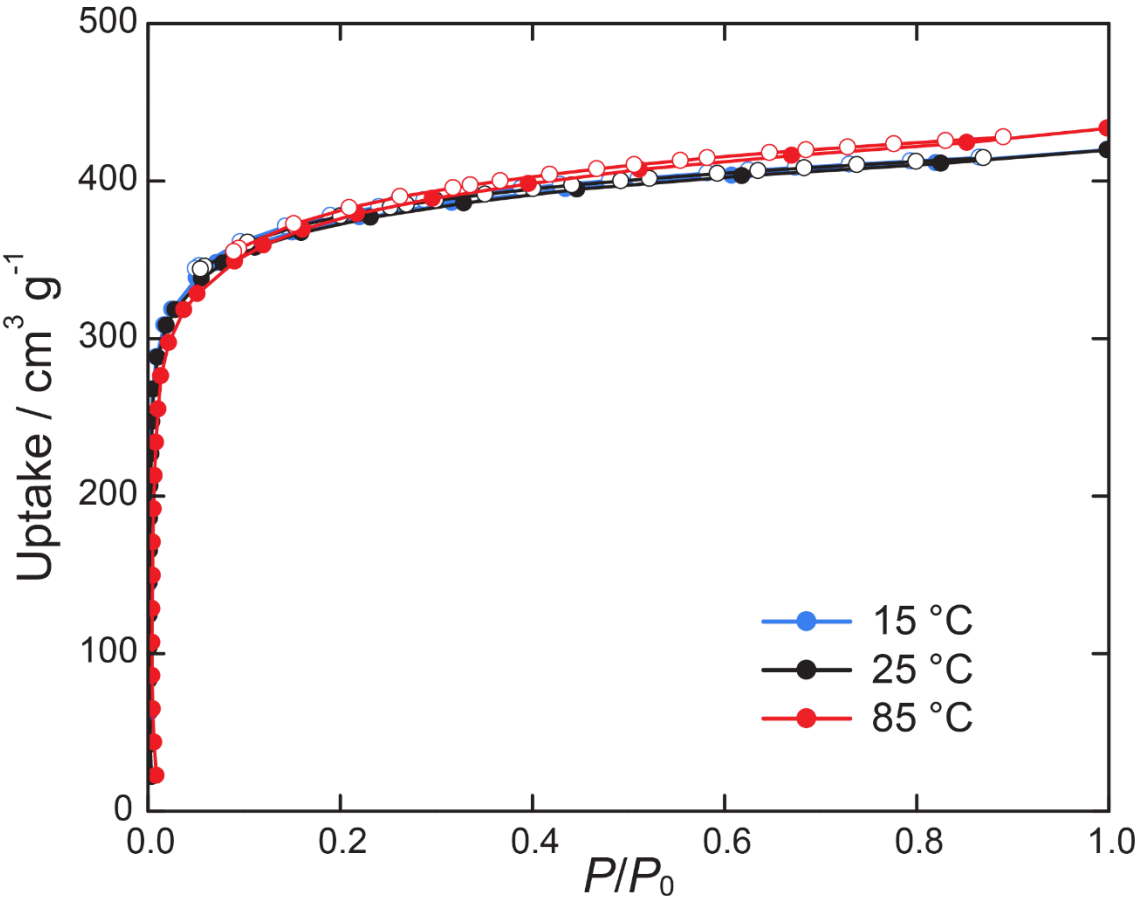

Figure S6.35. Experimental water sorption isotherm for Zeolite 13X at 25 °C and calculated water isotherms at 15 and 85 °C. 53 mg of activated Zeolite 13X were transferred to a 9 mm bulb gas cell and charged with N_2 to avoid air contamination. Then, the cell was mounted on the instrument to measure the water uptake capacity at 25 °C.

Solar flux response

The powder samples were packed in the insulation cell made of extruded polystyrene foam. An incandescent lamp (150 W) was placed 60 cm above the cell to ensure the flux of 1000 ± 30 W m^{-2} with ideal vertical exposure of the cell. The cell temperature was equilibrated with the surroundings prior the flux exposure. The pyranometer was used to monitor the solar flux and the temperature readings were taken at the bottom of the cell. The measurement was done at ambient temperature of 25 ± 0.5 °C. 1 g of powder sample was used in all measurements.

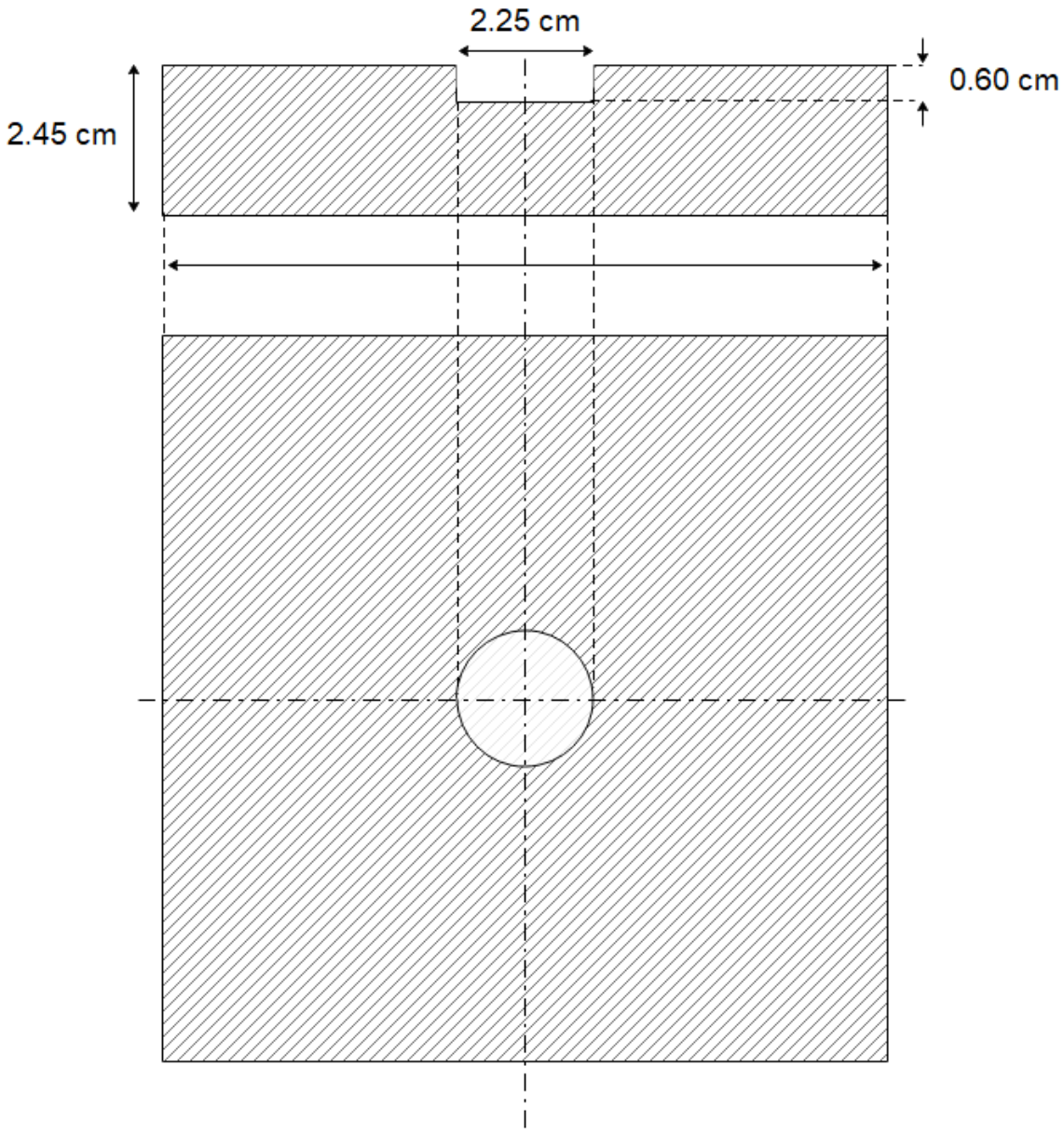

Figure S6.36. Schematic of insulation cell used for solar flux-temperature response measurements.

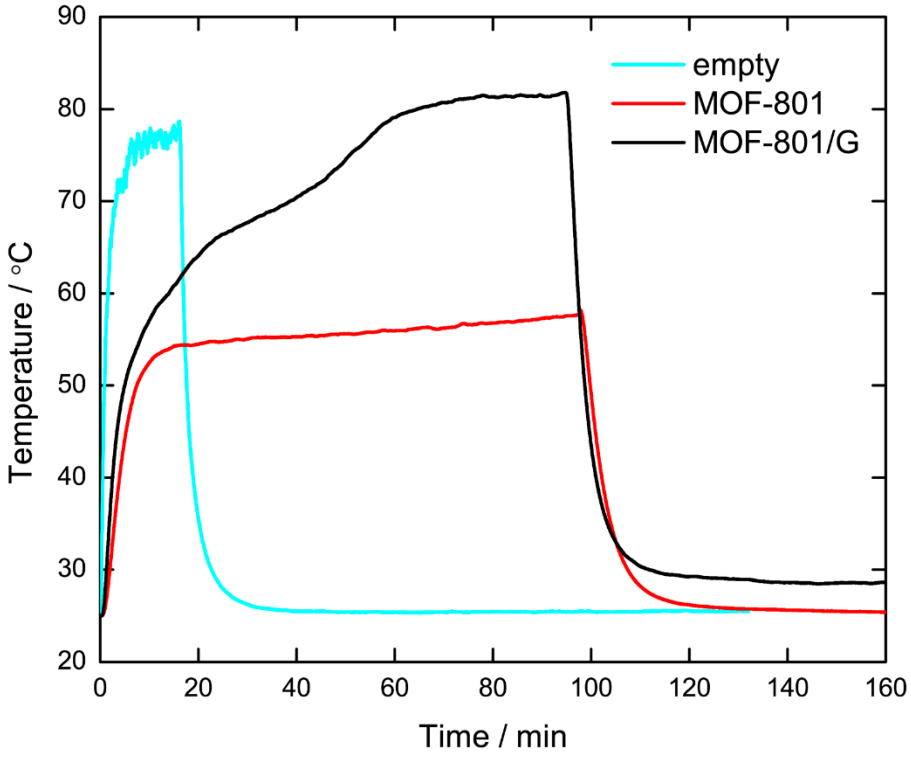

Figure S6.37. The increase of the sample temperature with time under a flux of 1000 W m^{-2} for MOF-801 and MOF-801/G. The measurement of an empty cell is shown for comparison. The sudden change in temperature increase for MOF-801/G at 70 °C is due to desorption of water.

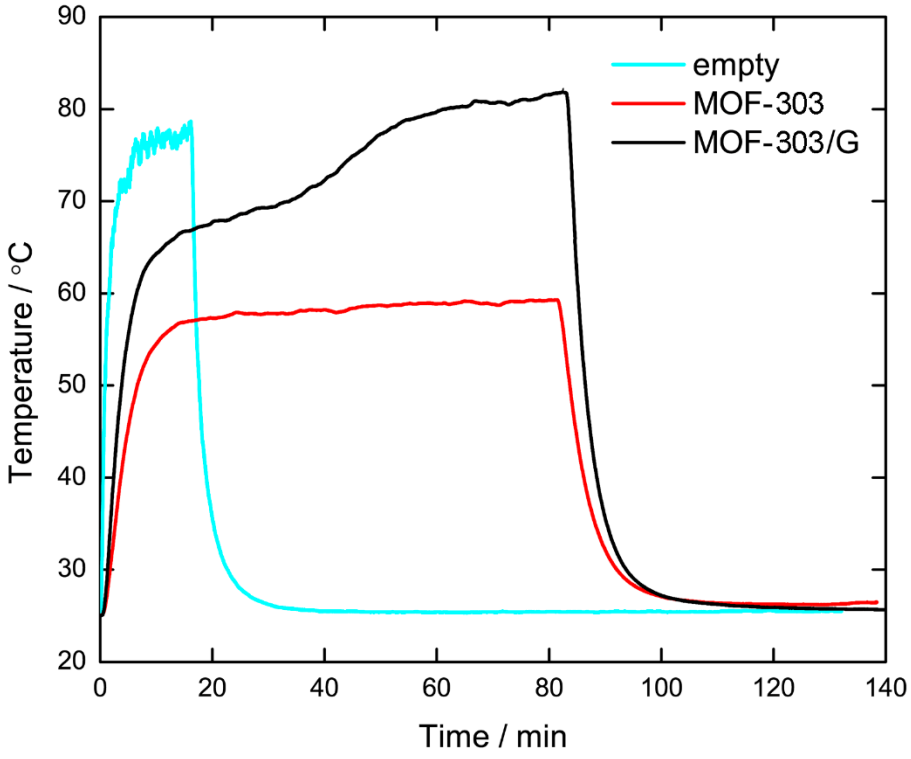

Figure S6.38. The increase of the sample temperature with time under a flux of 1000 W m^{-2} for MOF-303 and MOF-303/G. The measurement of empty cell is shown for comparison. The sudden change in temperature increase for MOF-303/G at 70 °C is due to desorption of water.

Near-IR properties

For the measured samples, a transmission of zero was assumed and the reflectance was transformed into absorption according to equations (6.10) or (6.11) for samples of high or low absorption, respectively,

$$\alpha = log_{10}\left(\frac{1}{R}\right) \tag{6.10}$$

$$\alpha = \frac{(1-R)^2}{2R} \tag{6.11}$$

where α is the absorption, R is the reflectance. A significant increase of the absorption was observed for both MOF-801/G and MOF-303/G compared to the pure samples.

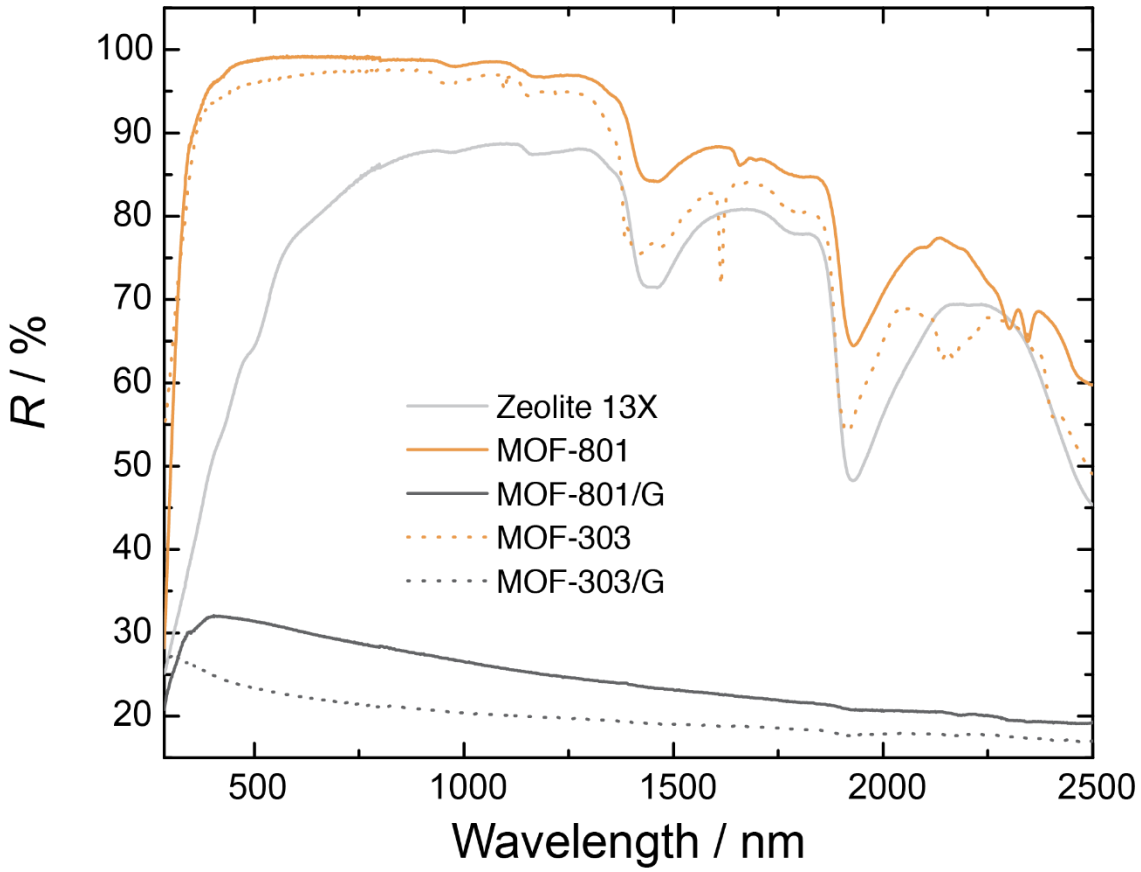

Figure S6.39. Diffuse reflectance spectra of Zeolite 13X, MOF-801, MOF-801/G, MOF-303, and MOF-303/G recorded between 285 and 2500 nm.

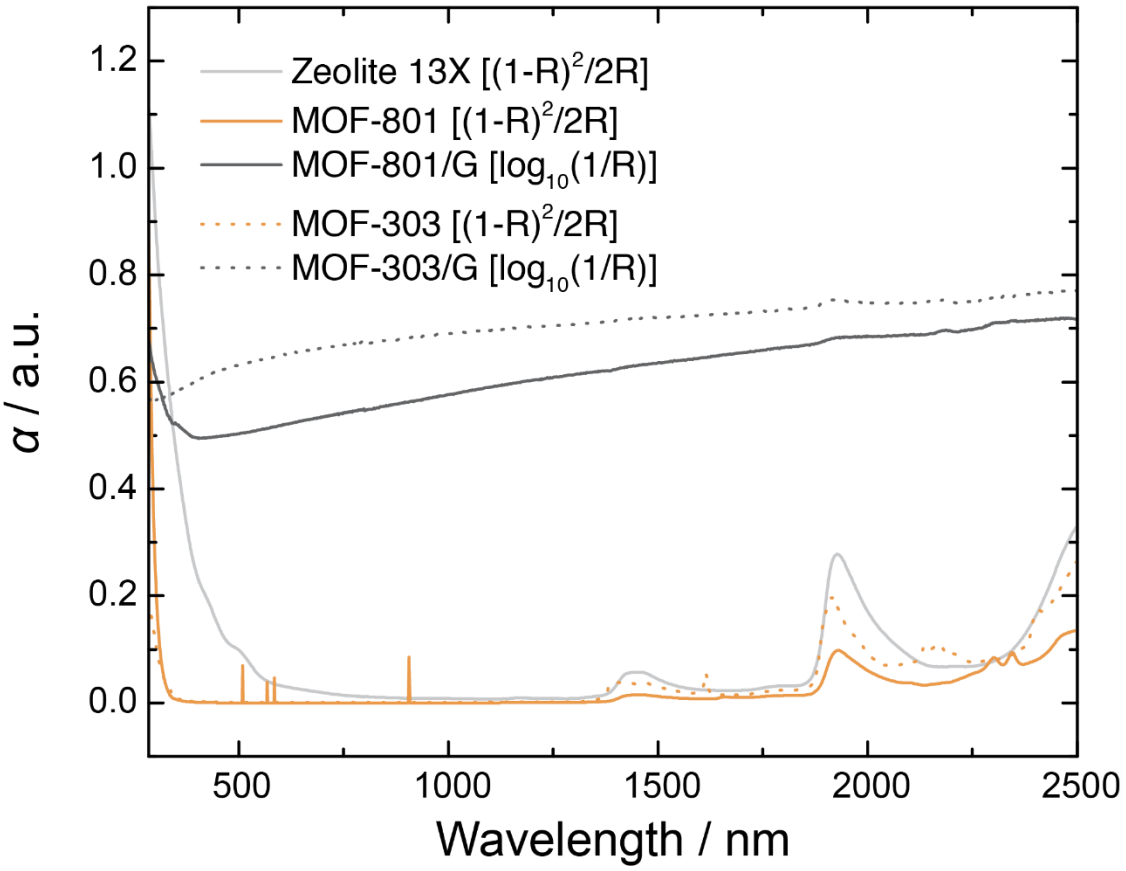

Figure S6.40. Absorption spectra of Zeolite 13X, MOF-801, MOF-801/G, MOF-303, and MOF-303/G between 285 and 2500 nm. The spectra are calculated from the diffuse reflectance data presented in Figure S6.39 using equations (6.10) or (6.11).

Comparison of water kinetics

The powder samples were placed into a platinum pan and heated to 150 °C at 0% RH (dry air). Then, the temperature was allowed to equilibrate for 24 hours at 25 °C and 0% RH. The adsorption measurement was performed at 25 °C and 40% RH; the desorption measurement was performed at 85 °C and 0% RH. Weight percentage was estimated as (mass of activated material + mass of adsorbed water) / (mass of activated material).

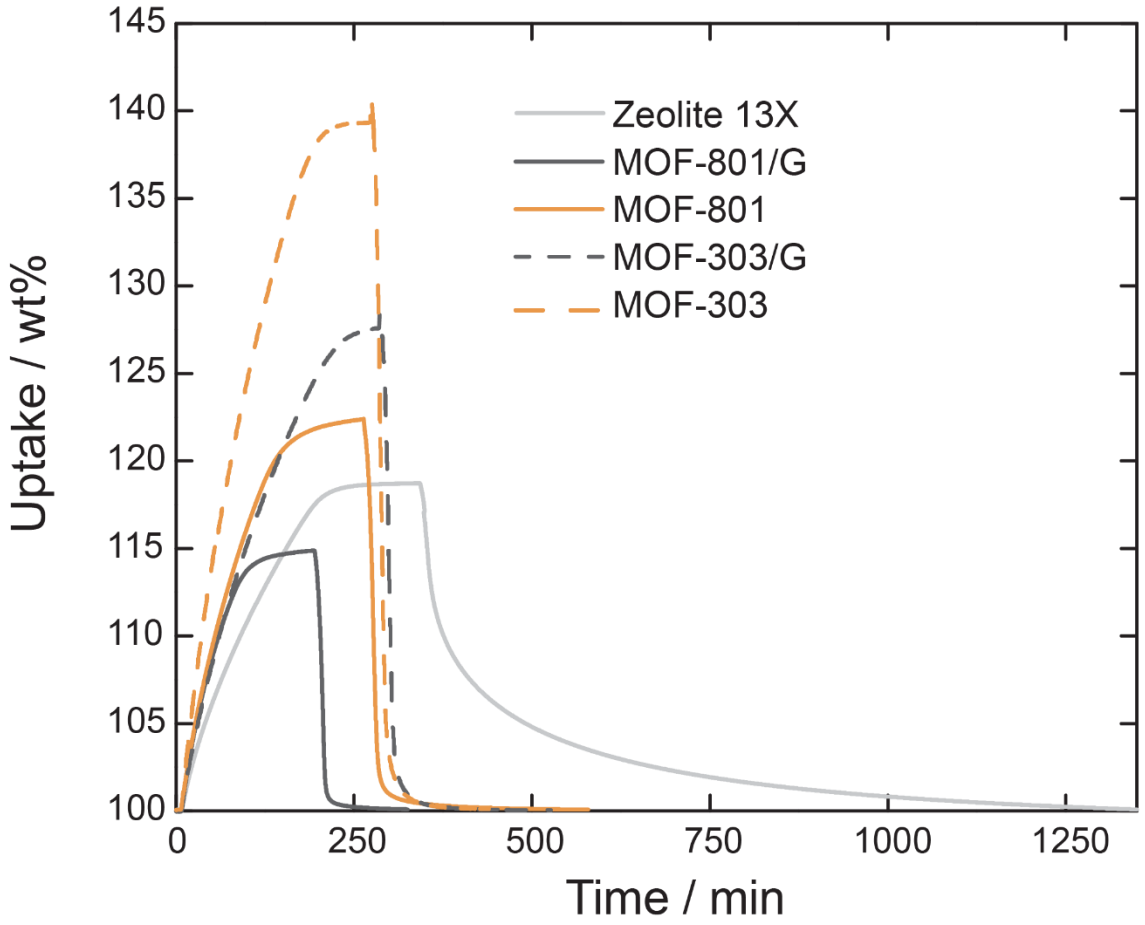

Figure S6.41. Comparison of water sorption kinetics for Zeolite 13X, MOF-801, MOF-303, MOF-801/G and MOF-303/G.

Section S6.7. Water harvester

Materials

Transparent plexiglass/PMMA (0.5" and 0.25" thick) and T-slotted aluminum framing (Single Rail, Silver, 1-1/2" high × 1-1/2" wide) with connections joins were purchased from McMaster-Carr. The solar absorptive coating (Pyromark 1200 high-temperature paint) was purchased from LA-CO®. High lumen incandescent bulbs (150 watts, 2,710 lumens, 100 CRI) were manufactured by Bulbrite. Extruded polystyrene foams (24" × 24" wide, 1" thick) was purchased from Owens Corning®. Acrylic cement was manufactured by Scigrip. Primer, white and clear gloss 2X paints were manufactured by Rust-Oleum.

Solar flux response

Circular poly(methyl methacrylate) (PMMA) pieces were packed in the insulation cell made of extruded polystyrene foam. The lamp was placed 60 cm above the cell to ensure a flux of 1000 ± 30 W m^{-2} with ideal vertical exposure of the cell. The cell temperature was equilibrated with the surroundings prior the flux exposure. The pyranometer was used to monitor

the flux and the temperature readings were taken at the bottom of the cell. All the measurements were carried out at the ambient temperature of 25 ± 0.5 °C.

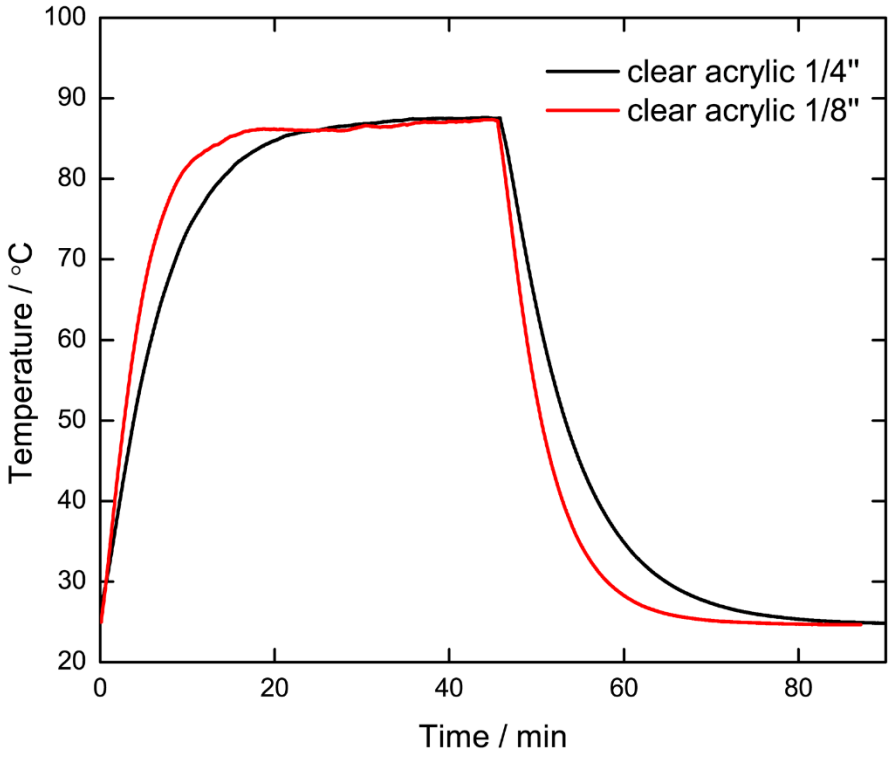

Figure S6.42. The temperature response with time under a flux of 1000 W m^{-2} measured for circular pieces of PMMA (diameter 20 mm) with a thickness of 1/4" and 1/8".

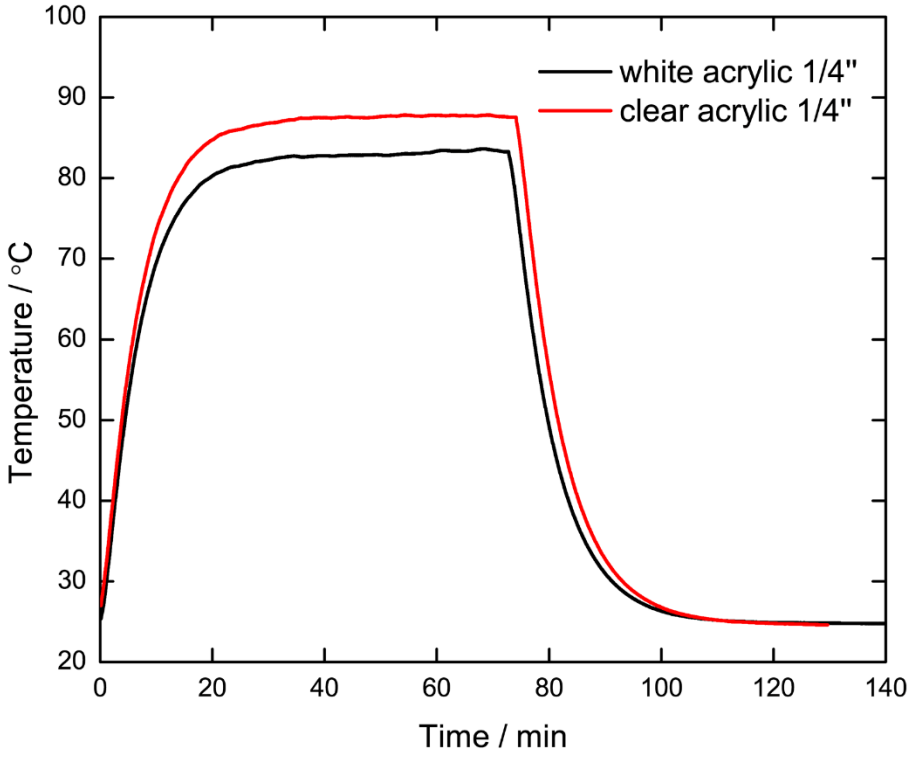

Figure S6.43. The temperature response with time under a flux of 1000 W m^{-2} measured for circular pieces of PMMA (diameter 20 mm) of the same thickness (1/4") coated with a white (red) and clear coating (black). A 7 °C lower temperature was observed in case of the PMMA sample with white coating.

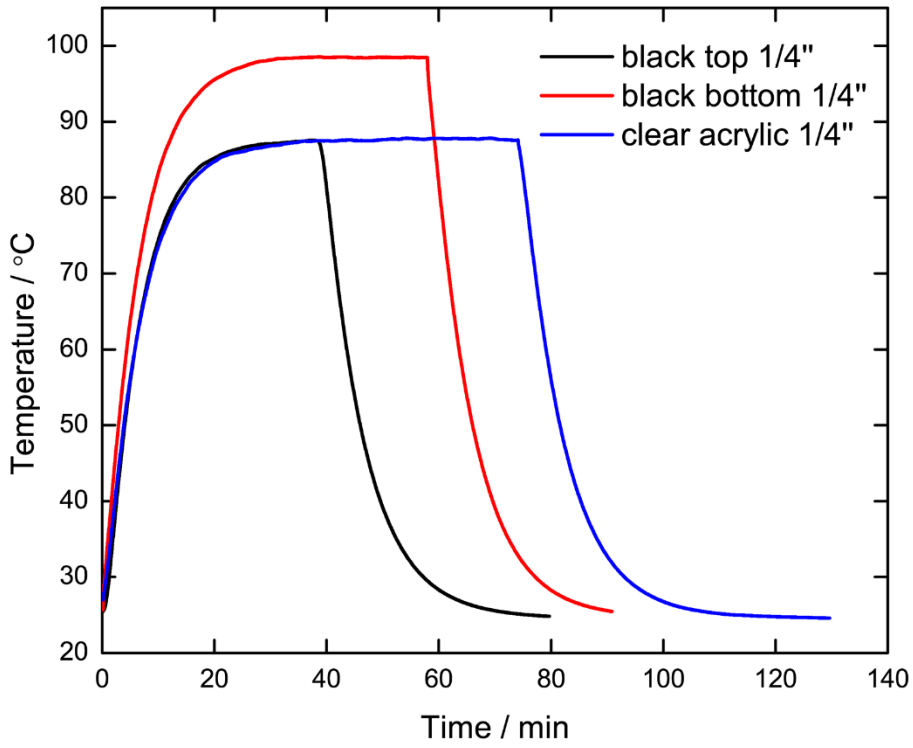

Figure S6.44. The temperature response with time under a flux of 1000 W m^{-2} measured for circular pieces of PMMA (diameter 20 mm) of the same thickness (1/4") coated with solar absorber coating (Pyromark paint). A comparison of a clear disc of PMMA (blue), and a coated disk in two different orientations, to coated (black) and bottom coated (red) is shown. A 13 °C higher temperature was observed for the PMMA disc with pyromark coating on the bottom. The identical profile of temperature variation in the case of the transparent disc of PMMA and that coated on the top implies the preferable direction for heat transfer.

Near-IR properties

Absorption spectra of PMMA were recorded on a Shimadzu UV3600 between 285 and 3000 nm. A PMT detector was used in the UV and visible region, and an InGaAs and cooled PbS detector for long-wavelength detection. The spectrophotometer is equipped with a double monochromator with a wavelength range of 185 to 3300 nm. PMMA identical to that used for the construction of the cover (1/8") was used in all experiments. PMMA was measured uncoated and with thin coats of primer and white paint. For both, primer and white paint, an increase in the absorption in the visible and IR region is observed, which is explained by a higher reflectivity.

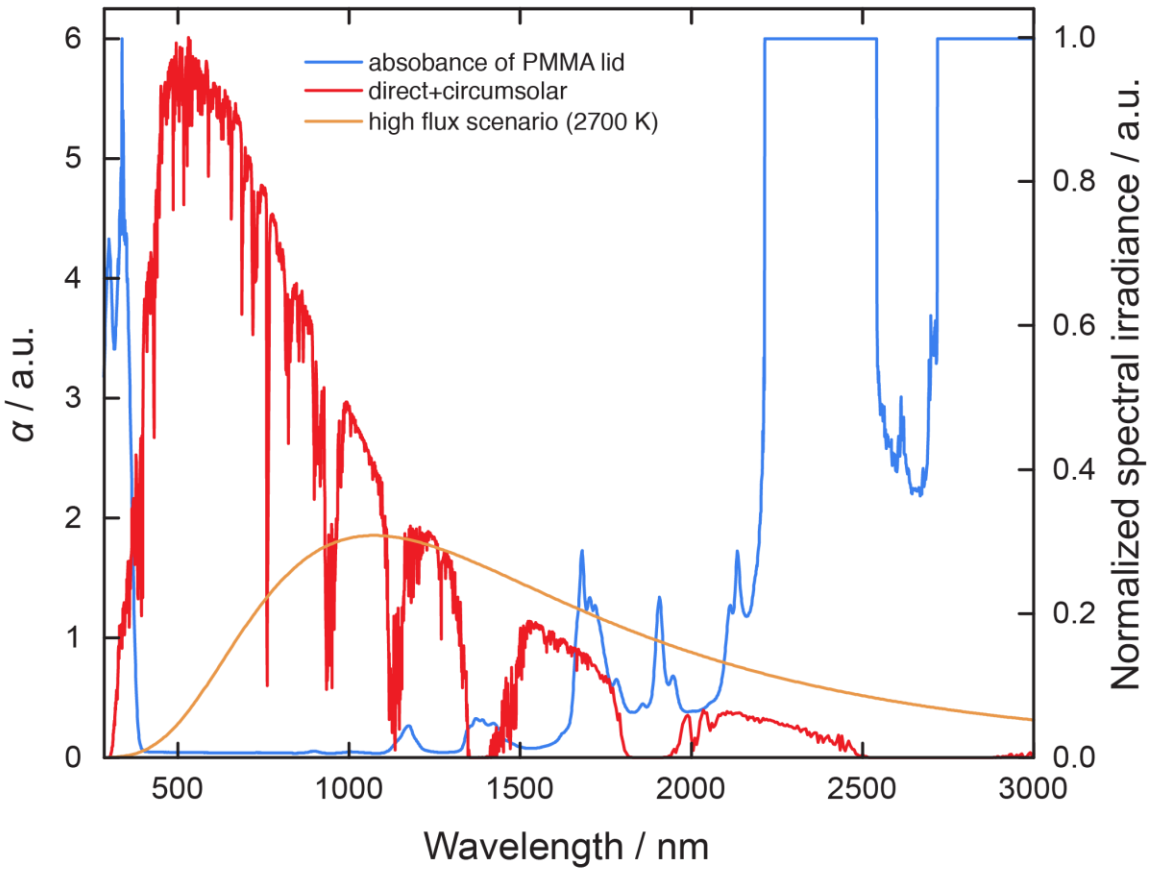

Figure S6.45. Absorption of PMMA (blue) compared to the spectral irradiance of the sun (red) and an incandescent lamps (orange) between 285 and 3000 nm. PMMA shows strong absorption below 400 and above 2300 nm.

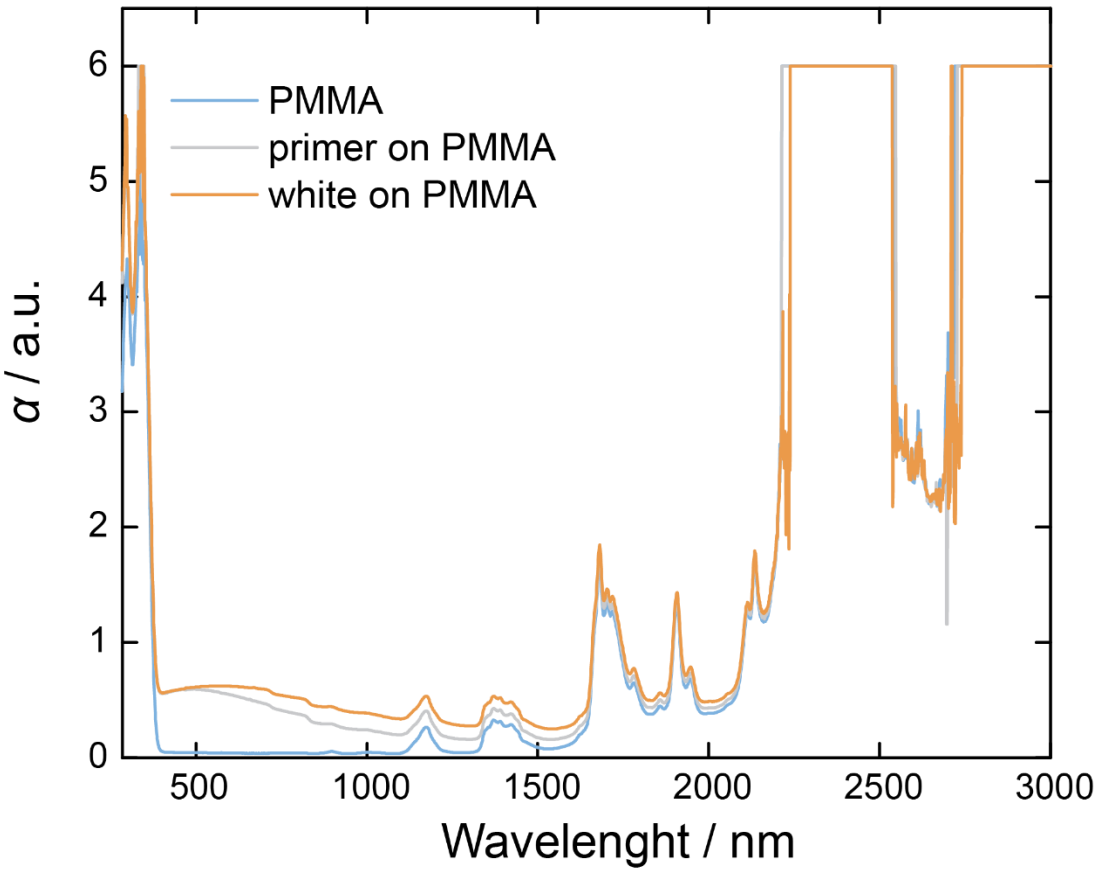

Figure S6.46. Comparison of absorption spectra for PMMA (light blue), PMMA coated with primer (light gray), and PMMA coated with white paint (orange). For both coated samples, an increase of the absorption in the visible and IR region is observed, arguably due to a higher reflectivity of the surface within the particular spectral range.

Water sorption unit

The water sorption unit is comprised of a sorbent container, support walls, and a thermal insulation compartment. The support walls are four rectangular transparent pieces (18.25" × 8.00" × 0.25") installed onto a bottom acrylic support plate (18.50" × 18.50" × 0.25") to hold the sorbent container at the desired position during the water capture/release. The sorbent container (16" × 16" × 1" deep) is subsequently glued to the upper side of the support walls to create a well-sealed enclosure eliminating water transfer to the thermal insulation.

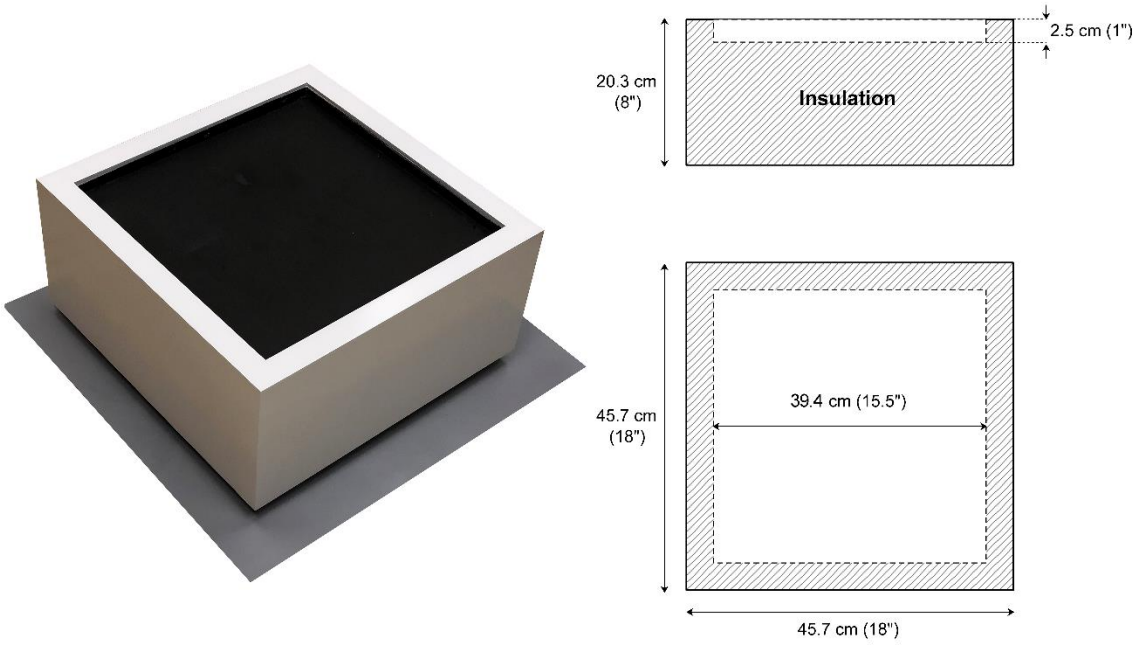

Figure S6.47. Photo of the water sorption unit (left) and schematic representation with dimensions (right).

To increase the temperature of the sorbent during the release period, the bottom surface and the side walls of the sorbent container was coated with a high solar absorptive black coating.

The thermal insulation compartment was packed with extruded polystyrene foam having of thermal conductivity and high heat capacity to minimize heat loss from the side and bottom surface of the container. Fiber glass was also placed between the side walls and the extruded polystyrene foam to avoid any buoyant air circulation within the water sorption unit and minimize the convective heat transfer in the thermal insulation compartment. The exterior surface of the support walls was coated with a white paint with high reflectivity in the infrared region of the solar spectrum to minimize irradiative heating of the water sorption unit and helped to maintain the condenser temperature below the dew point.

Case

The case is comprised of acrylic walls (22" × 22" × 0.25"). The side walls of the case prevent water transfer to/from the surroundings, and they participate in heat transfer occurring within the condenser and the pre-cooled airflow passages. The upper side of the case provides a rigid base for the installation of the cover and the solar reflector while the bottom acrylic plate (22" × 22" × 0.25") of the case is attached to the support frame and the stage (for the desert experiments). The cover is made of a transparent acrylic (24" × 24" × 0.125") with high transmissivity in the visible and near infrared range. The cover is screwed to the top of the case using 12 screws and sealed using a moisture resistant and water impermeable gasket to eliminate any potential gaps and thus prevent leakage.

During the release process, the vapor and heated air flow through airflow passages to the bottom of the case. Condensation is mainly observed on the side walls. The airflow passages are 45 mm wide and allow buoyant air circulation within the closed system. Heat transfer between the air and the side walls of the case is mainly due to convection, while the rejected heat is

conducted to the surroundings through the side walls of the case. The droplets on the side walls gradually slide down and accumulate at the bottom of the case separated from the water sorption unit by 2.45 cm spacers.

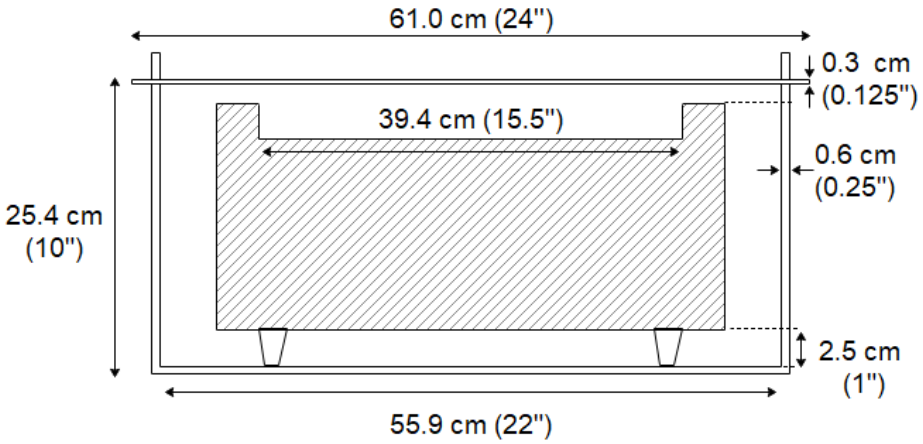

Figure S6.48. Schematic of the case, cover, and water sorption unit with dimensions.

Solar reflector

A solar reflector is positioned on top of the cover which facilitates (i) collection and deflection of solar radiation onto the sorbent and (ii) shading of the condenser, the exposed surfaces of the water sorption unit, the airflow passages, and the bottom of the case.

Section S6.8. Data acquisition and sensors

Temperature and humidity readings were recorded during the harvesting experiment at various locations insides the case. In addition, the humidity and temperature of the ambient air were measured in close proximity to the water harvester.

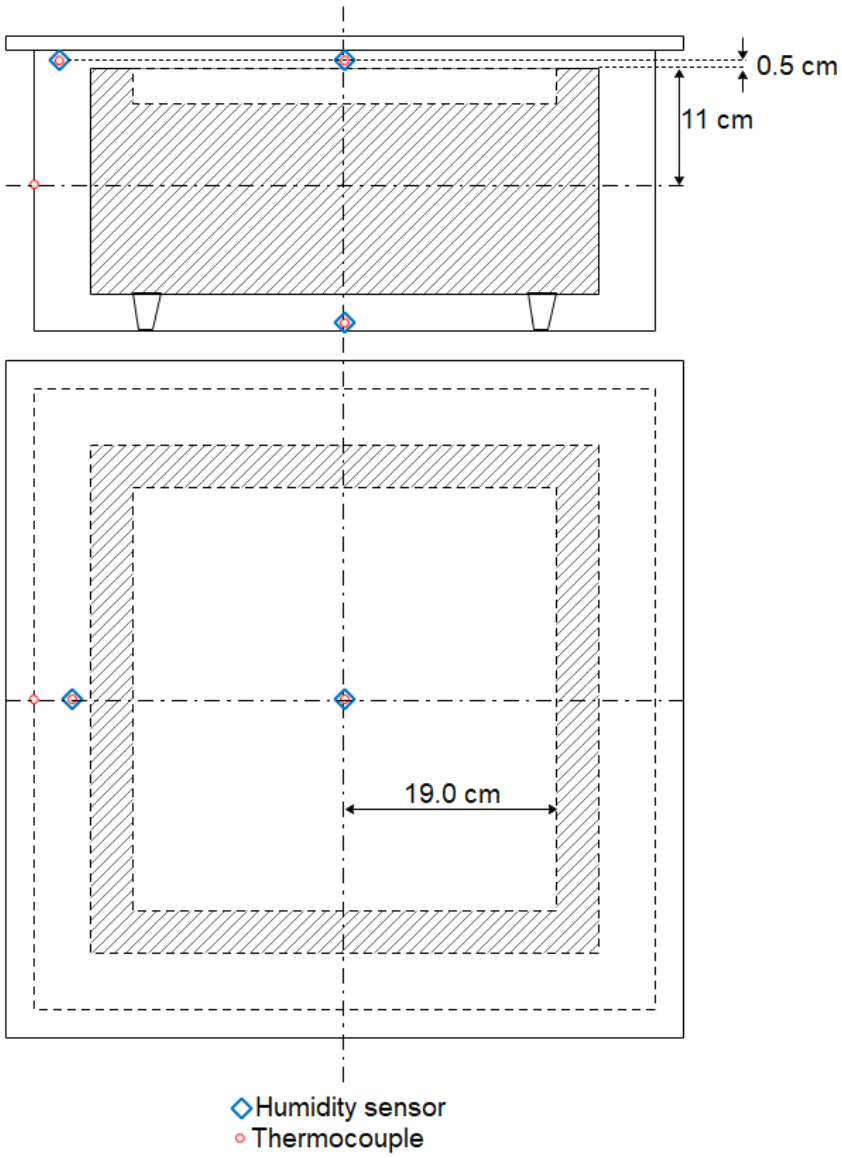

Figure S6.49. Locations of thermocouples and humidity sensors inside the case.

Humidity measurements

Humidity readings were recorded using integrated circuit sensors (Honeywell HIH-4021) with thermoset polymer capacitive sensing elements. The sensors were relatively small (12 mm × 4 mm × 2 mm) so that they did not significantly interact with the airflow inside the box. The voltage output of the humidity sensors was recorded using a National Instruments data acquisition system (cDAQ-9174 with NI 9205 32-Channel analog input module) and processed using LabView 2016 to collect and visualize the data[22]. The humidity sensors were calibrated within a range of RH (5% < RH < 90%, with 5% RH increments and at T = 25 °C) by using a HygroCal100 humidity generator (Michell Inc, MA, USA). Seven HygroSmart HS3 capacitive humidity sensors (with ±0.8% accuracy) were used to ensure humidity uniformity (less than ±0.5%) across the HygroCal 100 humidity chamber. The bias error was eliminated by using an external standard reference precision dew-point meter (the Optidew Vision precision, Michell Inc, MA, USA) with ±0.2 $°C_{dew\text{-}point}$ and 0.5% RH accuracy within the relative humidity range of 0.5 to 100%. At each humidity level, the voltage output of the humidity sensors was measured 50 times with a sampling frequency of 30 seconds while the hysteresis effects were determined through a loop of increasing (5% to 90%) and decreasing (95% to 5%) humidity. The precision uncertainty (U_p) of the humidity sensors at each humidity level was calculated using equation (6.12):

$$U_p = S \times t \tag{6.12}$$

where S is the precision index, i.e. the square root of standard deviation of analog readings and t the two-tailed student's t-factor (2 for 50 data points). The maximum precision uncertainty for the humidity sensors was found to be ±0.01%. Linear regression was applied to convert sensor voltage output (0.5-3.0 V) to relative humidity (0-100%) (Figure S6.50). The large coefficient of determination (R^2 > 0.99) confirmed the linear response of the sensor at constant temperature resulting in a bias uncertainty of the data reduction, U_{fit}, of less than ±0.6%. The total bias uncertainty (U_B) of 0.7%, coming from the bias uncertainty in the reference humidity (U_{ref} = 0.5%) and the bias uncertainty of the data reduction (U_{fit} = 0.6%), was calculated using equation (6.13):

$$U_B = \left(U_{fit}^2 + U_{ref}^2\right)^{1/2} \tag{6.13}$$

The total uncertainty (U_T) in the humidity measurements was found to be less than ±1% according to equation (6.14).

$$U_T = \left(U_P^2 + U_B^2\right)^{1/2} \tag{6.14}$$

A temperature compensation relation, equation (6.15), provided by the manufacturer was used to adjust the relative humidity values at different temperature.

$$RH\left(T\right) = \frac{RH\left(25°C\right)}{\left(1.0546 - 0.00216T\right)} \tag{6.15}$$

where T is the working temperature in degrees Celsius. It should be noted that although the temperature compensation relation can be used to determine the relative humidity at elevated temperatures, the uncertainty in humidity readings may increase drastically at higher temperature and relative humidity (e.g. ±5% RH when RH = 80% and T = 85 °C).

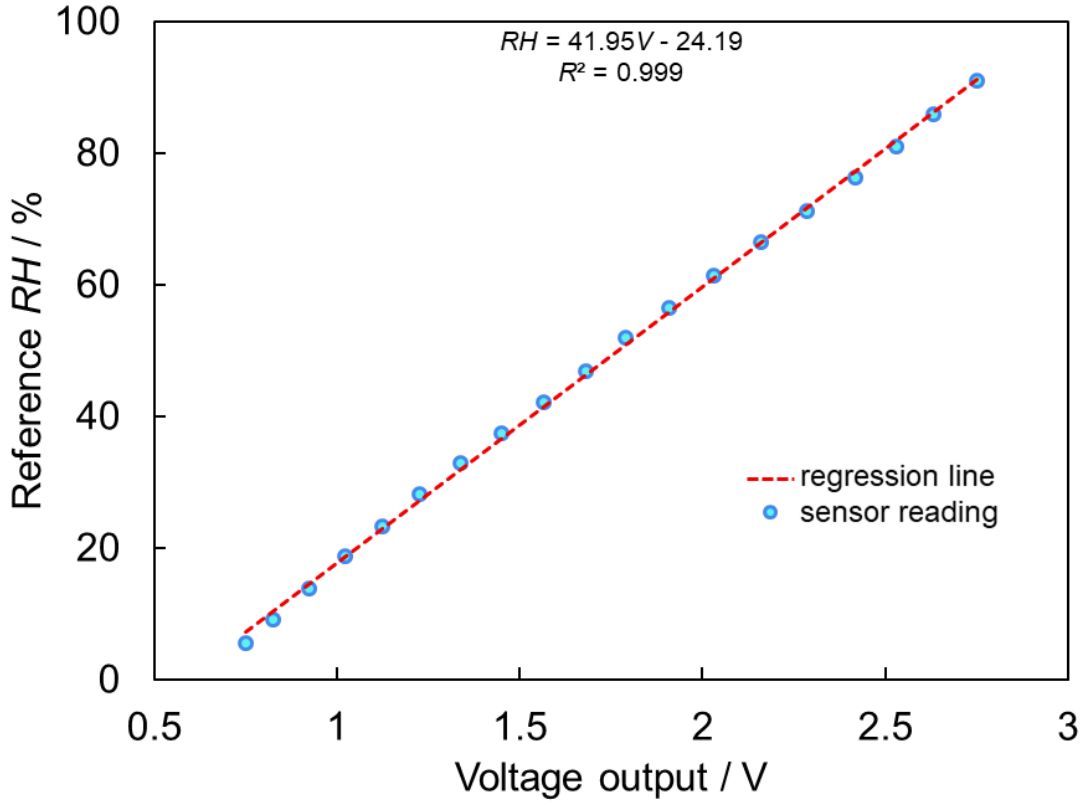

Figure S6.50. Calibration curve for humidity sensor converting the voltage output readings into the corresponding relative humidity.

Temperature measurements

T-type thermocouples (Neoflon PFA, American Wire Gauge 40, Omega Eng.) were used for temperature measurements. The output signal of the thermocouples was acquired using a National Instruments data acquisition system (cDAQ-9174 with NI 9214 16-Ch Isothermal TC module) and processed using LabView 2016 to collect and visualize the data. The thermocouples were calibrated within the range of 15-105 °C with 5 °C increments using a Hart Scientific 9103 dry-well calibrator with the accuracy of ±0.25 °C. At each reference temperature, 40 readings with a sampling rate of 5 s were taken while hysteresis effects were determined through an increasing and decreasing temperature loop. Using equation (6.12) with the student's t-factor of 2, the precision uncertainty was found to be less than ±0.01 °C. A linear regression curve was used for data reduction which resulted in a bias error of ±0.04 °C. Using equation (6.14) the maximum total uncertainty in the temperature readings was found to be less than ±0.25 °C.

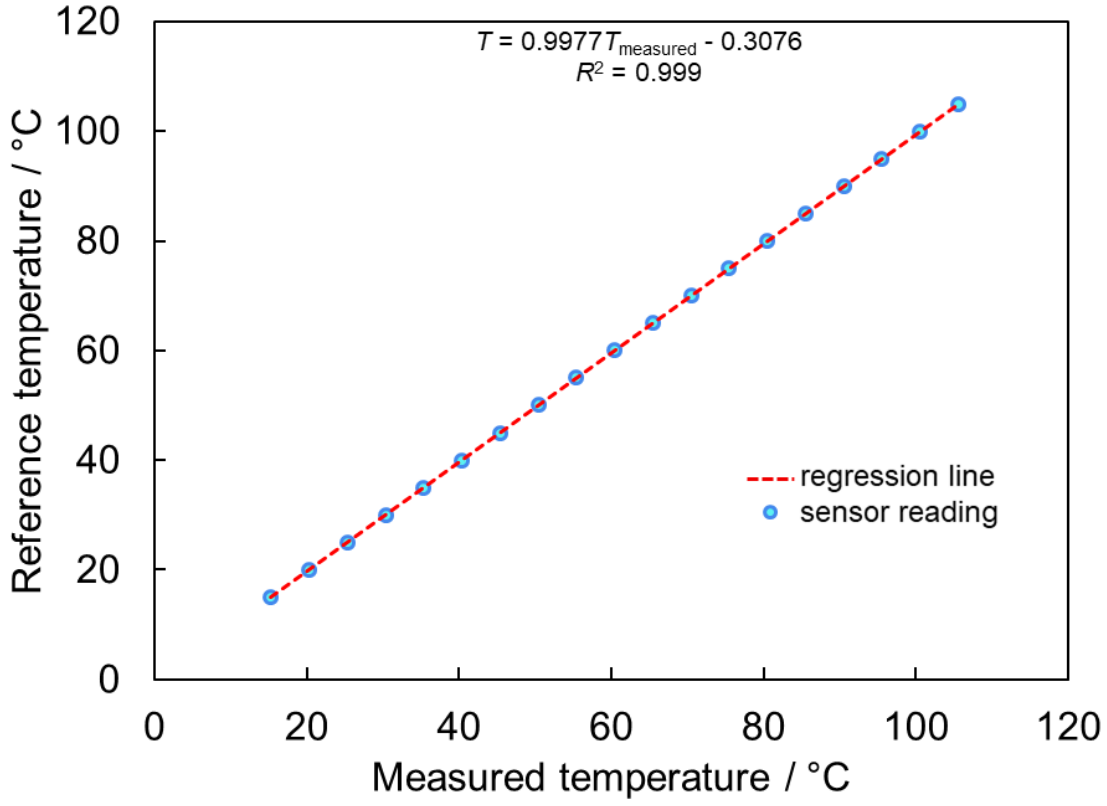

Figure S6.51. Calibration curve for temperature sensor.

Section S6.9. WHC under laboratory conditions

Artificial flux generator

In order to compare the irradiation under natural sunlight and that recorded for the harvesting experiment at laboratory conditions, the irradiance for the exposed top surface of the water harvester was scanned. For this purpose, two lamp configurations were tested (two and three lamps) and 25 data points were collected per run. The lamps were adjusted so that the pyranometer reading in the center of the cover of the case was within the range of the readings during the lab experiments reported in this work (830 W m^{-2} and 1140 W m^{-2} for two and three lamps, respectively). Two runs were performed for the two lamp-, and four runs for the four-lamp configuration. Based on these measurements, a correction factor for both configurations was calculated. The average irradiance (W m^{-2}) calculated for two lamps equals 67.25% and that calculated for three lamps equals 69.56% of the value measured in the center of the cover. For every run, two orientations, rotated by 90° with respect to each other were used (100 data points). This correction factor allows for a qualitative comparison of the solar irradiance (based on data provided by ASTM G173-03 Reference Spectra Derived from SMARTS v. 2.9.2, direct + circumsolar) and the theoretical spectra of the lamps, calculated using Planck's radiation law (see equation (6.16)) and a temperature of 2700 K, within the range of 285-3000 nm (the spectral range recorded by the pyranometer),

$$\dot{E}_{lab}(\lambda) = \frac{c_1}{\lambda^5} \frac{1}{e^{c_2/\lambda T} - 1} \tag{6.16}$$

where c_1 is $3.741832 \cdot 10^{-16}$ W m^2, c_2 is $438786 \cdot 10^{-2}$ K m, λ is the wavelength, T the temperature of the black body, and $\dot{E}_{lab}$ is the spectral irradiance. The resulting spectra are shown in Fig. S52 (two lamps) and Figure S6.53 (three lamps). The distribution of incident flux measured for one orientation and an average of all orientations are given in Figures S6.52 and S6.53 for two and three lamps, respectively.

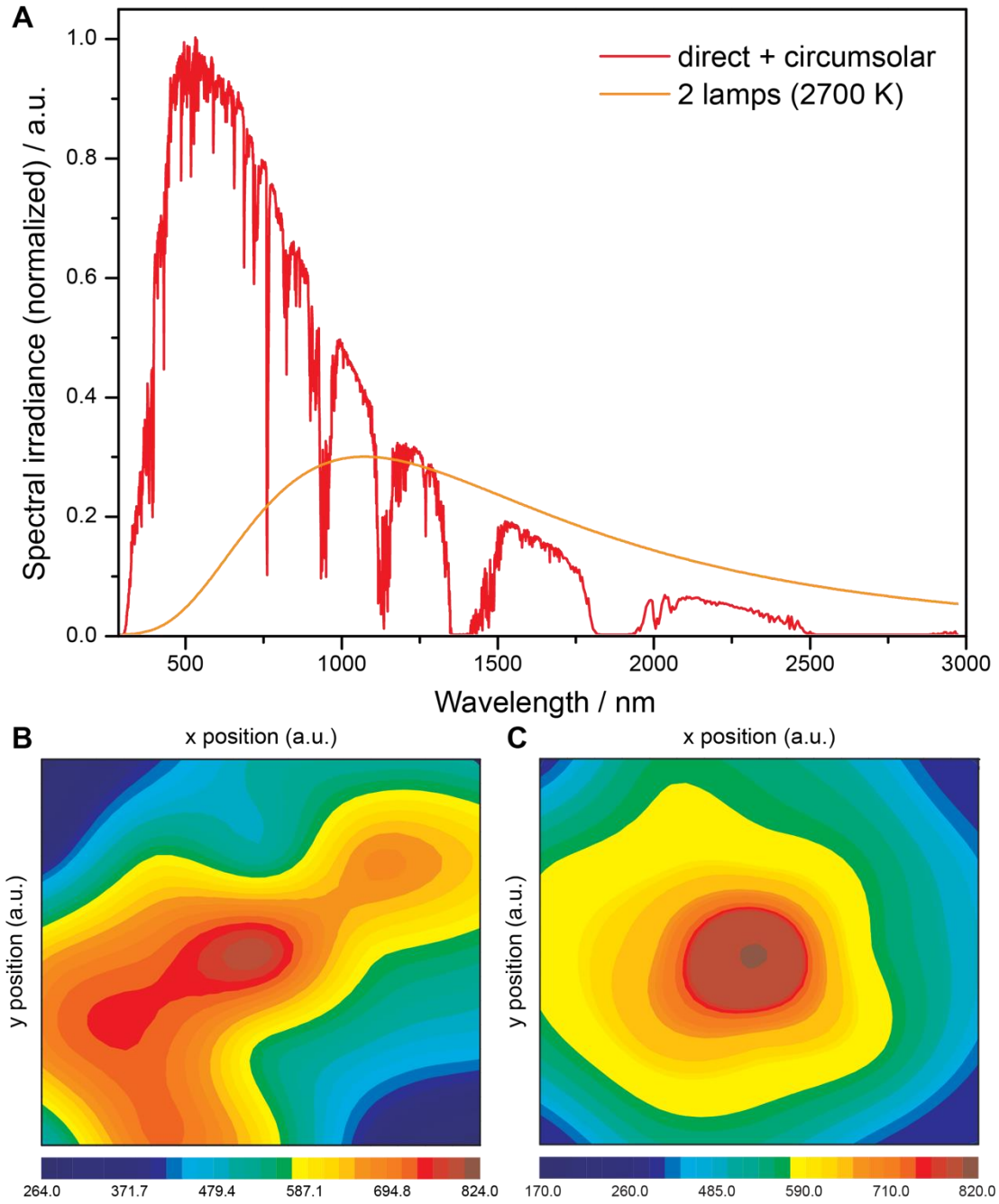

Figure S6.52. (**A**) Comparison of the solar irradiance (red) and the irradiance for a two-lamp configuration (orange line) with a color temperature of 2700 K. (**B**) Contour diagram of the distribution of the irradiance measured on the cover of the case for a two-lamp configuration in one orientation using 25 data points (lamps located at the bottom left and top right). (**C**) Contour diagram of the distribution of the irradiance on the cover of the case for a two-lamp configuration and two different orientations with lamps located at the bottom left and top right, or on the top left and bottom right.

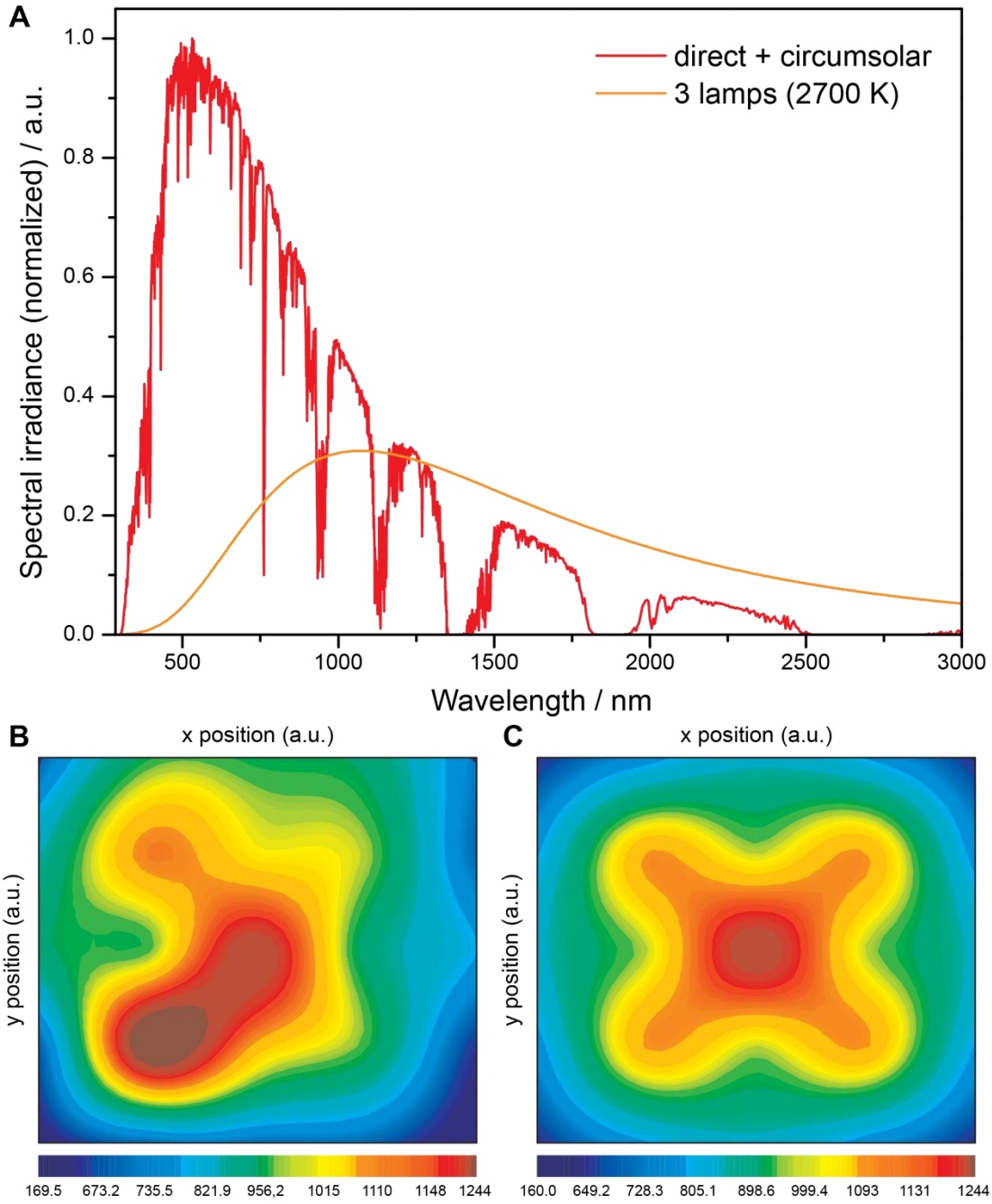

Figure S6.53. (**A**) Comparison of the solar irradiance (red) and the irradiance for a three-lamp configuration (orange line) with a color temperature of 2700 K. (**B**) Contour diagram of the distribution of the irradiance measured on the cover of the case for a three-lamp configuration in one orientation using 25 data points (lamps located at the bottom left, bottom right, and top right). (**C**) Contour diagram of the distribution of the irradiance on the cover of the case for a three-lamp configuration and four different constellations of lamps.

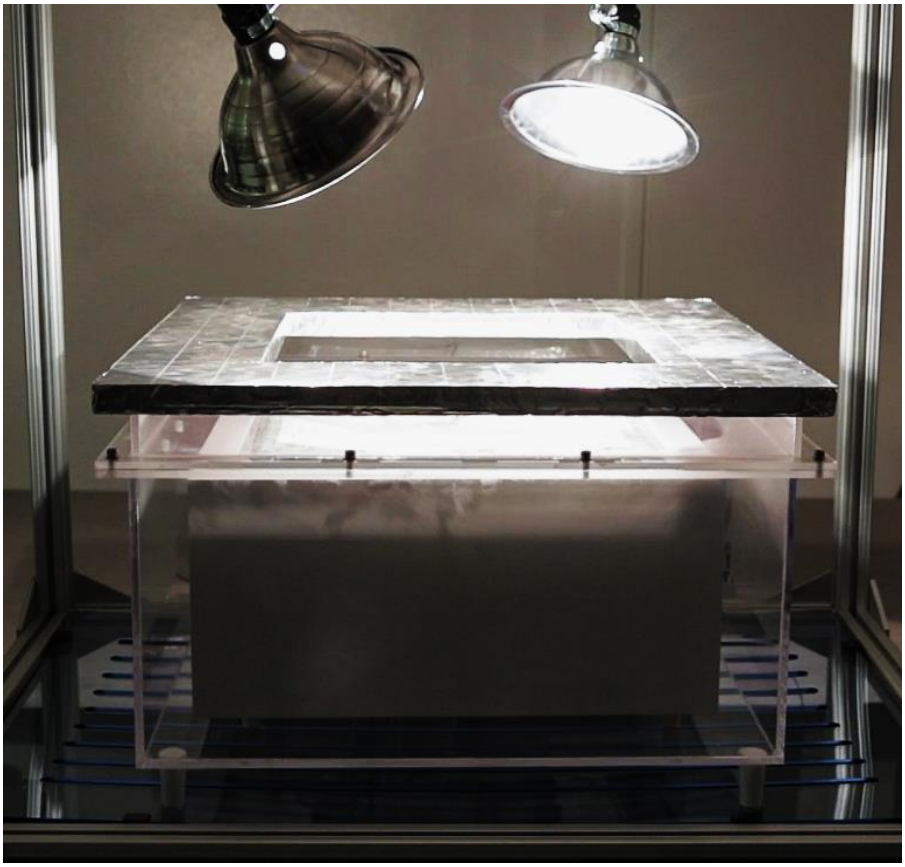

Figure S6.54. Image of the artificial flux generator in two lamps configuration.

The average hemispherical absorptivity (α) of the sorbents and transmissivity (τ) of the cover for artificial radiation were determined using the following equations:

$$\alpha \approx \frac{\int_{285}^{2500} \alpha_{\lambda}(\lambda)\dot{E}_{lab}(\lambda)d\lambda}{\int_{285}^{2500} \dot{E}_{lab}(\lambda)d\lambda} \tag{6.17}$$

$$\tau \approx \frac{\int_{285}^{2500} \tau_{\lambda}(\lambda)\dot{E}_{lab}(\lambda)d\lambda}{\int_{285}^{2500} \dot{E}_{lab}(\lambda)d\lambda} \tag{6.18}$$

where $\alpha_{\lambda}(\lambda)$ and $\tau_{\lambda}(\lambda)$, are the spectral directional absorptivity and transmissivity, respectively, and $\dot{E}(\lambda)$ is spectral distribution of solar or artificial radiation (shown in Figure S6.52). The numerical integration was done using MATLAB R2017a[23], and the values calculated for α and τ are listed in the Table S6.3.

Table S6.3. The average hemispherical absorptivity and transmissivity of materials for artificial and solar radiation within the range of 285-2500 nm.

Material	Solar radiation	Artificial radiation
Zeolite-13X	α_{solar} = 0.10	α_{lab} = 0.04
MOF-801	α_{solar} = 0.01	α_{lab} = 0.02
MOF-801/G	α_{solar} = 0.56	α_{lab} = 0.62
MOF-303	α_{solar} = 0.01	α_{lab} = 0.03
MOF-303/G	α_{solar} = 0.67	α_{lab} = 0.71
Cover	τ_{solar} = 0.92	τ_{lab} = 0.83

Water production under laboratory conditions

A set of water harvesting experiments was performed on Zeolite 13X, MOF-801/G, MOF-303/G under controlled laboratory conditions. To exclude error originating from humidity remaining in the water sorption unit, the case, and in between the graphite particles, harvesting experiments were conducted with an empty sorbent container and graphite. Table S6.4 summarizes the amount of sorbent used in the experiment as well as the adsorption/desorption conditions.

Table S6.4. Test conditions for the water harvesting in the laboratory.

# Test	Sorbent	Test conditions
1	no sorbent	adsorption: night conditions (30-50% RH, 18-25 °C) desorption: low flux radiation (7.5 h)
2	graphite (0.25 kg)	adsorption: night conditions (30-50% RH, 18-25 °C) desorption: low flux radiation (7.5 h)
3	Zeolite 13X (0.5 kg)	adsorption: night conditions (30-50% RH, 18-25 °C) desorption: low flux radiation (7.5 h)
4	Zeolite 13X (0.5 kg)	adsorption: night conditions (30-50% RH, 18-25 °C) desorption: high flux radiation (7.5 h)
5	MOF-801/G (1.650 kg)	adsorption: night conditions (30-50% RH, 18-25 °C) desorption: low flux radiation (7.5 h)
6	MOF-801/G (1.650 kg)	adsorption: night conditions (30-50% RH, 18-25 °C) desorption: high flux radiation (7.5 h)
7	MOF-801/G (0.825 kg)	adsorption: night conditions (30-50% RH, 18-25 °C) desorption: low flux radiation (7.5 h)
8	MOF-801/G (0.825 kg)	adsorption: night conditions (30-50% RH, 18-25 °C) desorption: high flux radiation (7.5 h)
9	MOF-801/G (0.412 kg,)	adsorption: night conditions (30-50% RH, 18-25 °C) desorption: low flux radiation (7.5 h)
10	MOF-801/G (0.412 kg)	adsorption: night conditions (30-50% RH, 18-25 °C) desorption: high flux radiation (7.5 h)
11	MOF-303/G (0.600 kg)	adsorption: night conditions (30-50% RH, 18-25 °C) desorption: low flux radiation (7.5 h)
12	MOF-303/G (0.600 kg)	adsorption: night conditions (30-50% RH, 18-25 °C) desorption: high flux radiation (7.5 h)
13	MOF-801/G (0.600 kg)	adsorption: controlled conditions (35% RH, 15 °C) desorption: low flux radiation (7.5 h)
14	MOF-303/G (0.600 kg)	adsorption: controlled conditions (35% RH, 15 °C) desorption: low flux radiation (7.5 h)

Relative humidity/temperature experimental data for water harvesting under laboratory conditions

The temperature and relative humidity profiles for all laboratory water harvesting cycles are shown in Figures S6.55-6.68. The amount of collected liquid water is given for each experiment. The last 30 minutes of saturation are shown to evaluate the saturation conditions. Low and high fluxes are 558 and 792 W m^{-2}, respectively. The temperature sensors were placed at the surface of the sorbent (sorbent surface), in the sorbent (sorbent interior), at side wall of the case (exterior side wall), at the bottom of the condenser (condenser), and outside (ambient). The ambient dew temperature was estimated from the ambient RH and temperature readings. The relative humidity sensors were placed at the top of the sorbent surface (sorbent surface), at the bottom of the case in the proximity of the condenser (condenser) and outside (ambient).

For experiment 13 and 14 (Table S6.4**)**, the saturation was carried out using an Espec environmental chamber. After the sorbent was taken out of the chamber and transferred to the water sorption unit, the case was sealed and the release process was started immediately.

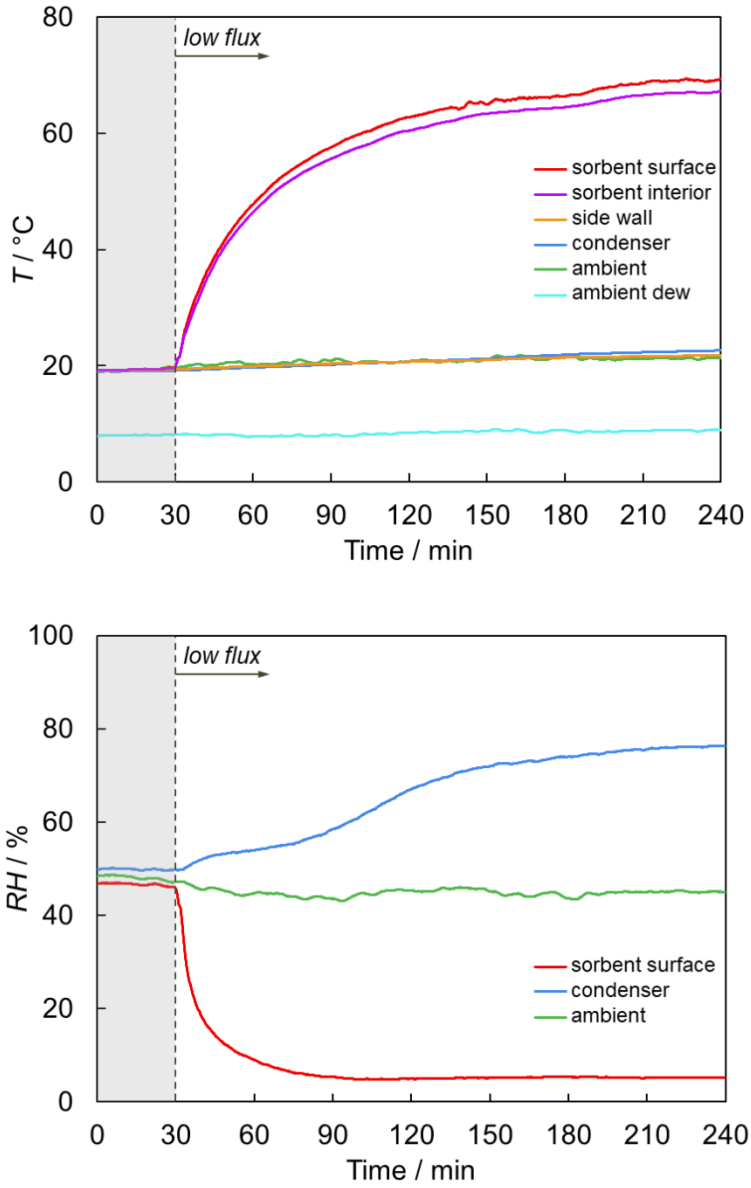

Figure S6.55. The temperature (top) and relative humidity (bottom) profiles during water harvesting without material (*i.e.* empty sorbent container). Water harvesting was performed under low flux for 7.5 h. No condensation was observed.

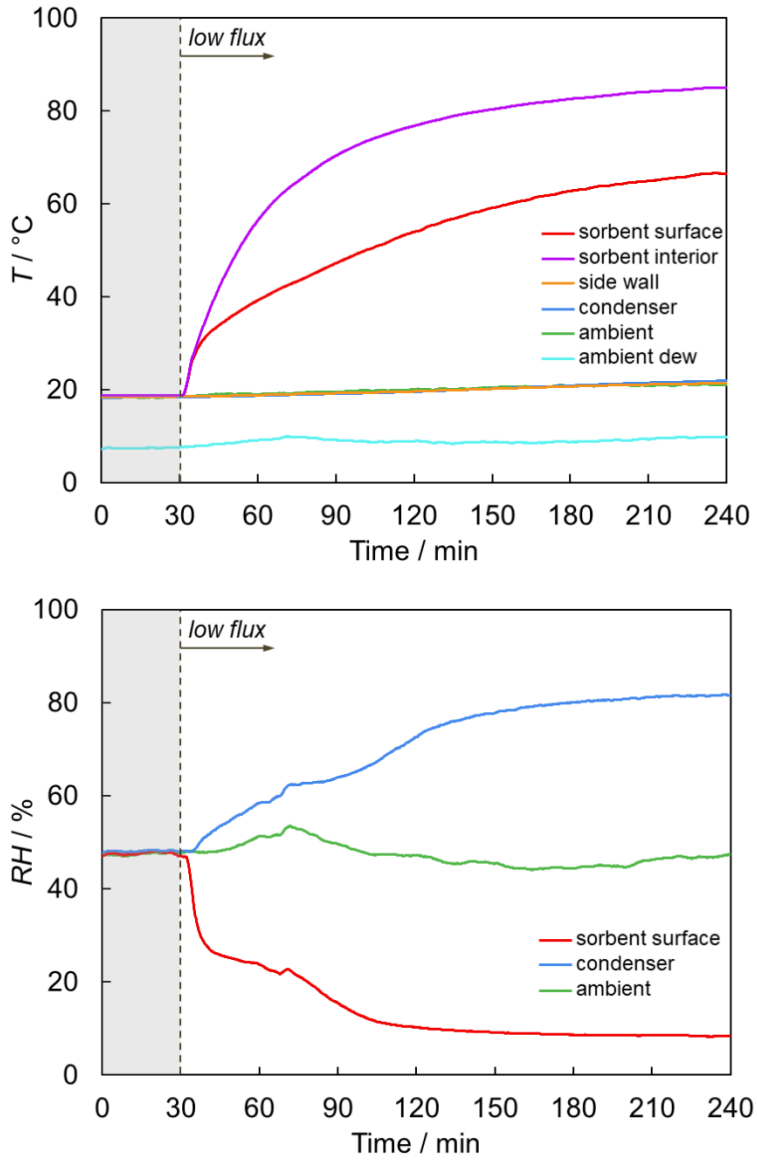

Figure S6.56. The temperature (top) and relative humidity (bottom) profiles during water harvesting using 0.25 kg graphite. Water harvesting was performed under low flux for 7.5 h. A small amount of fog formation was observed.

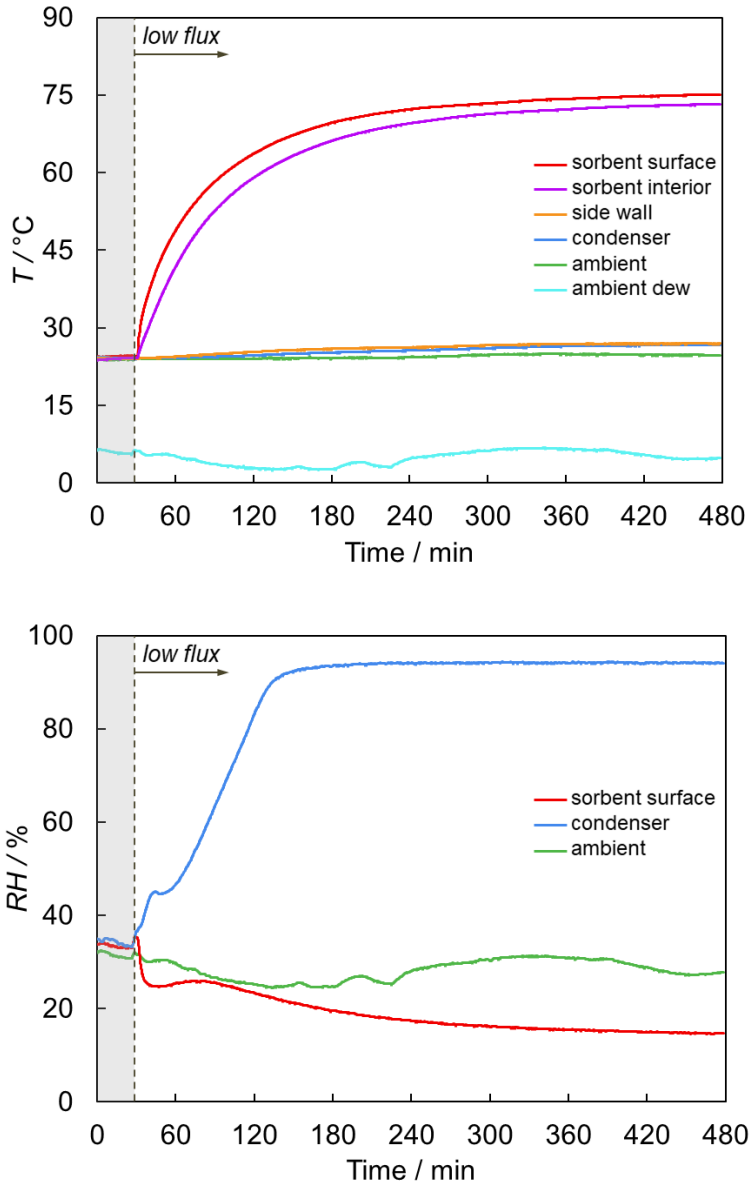

Figure S6.57. The temperature (top) and relative humidity (bottom) profiles during water harvesting using 0.5 kg of Zeolite 13X. Water harvesting was performed under low flux for 7.5 h. 6 g of liquid water was collected.

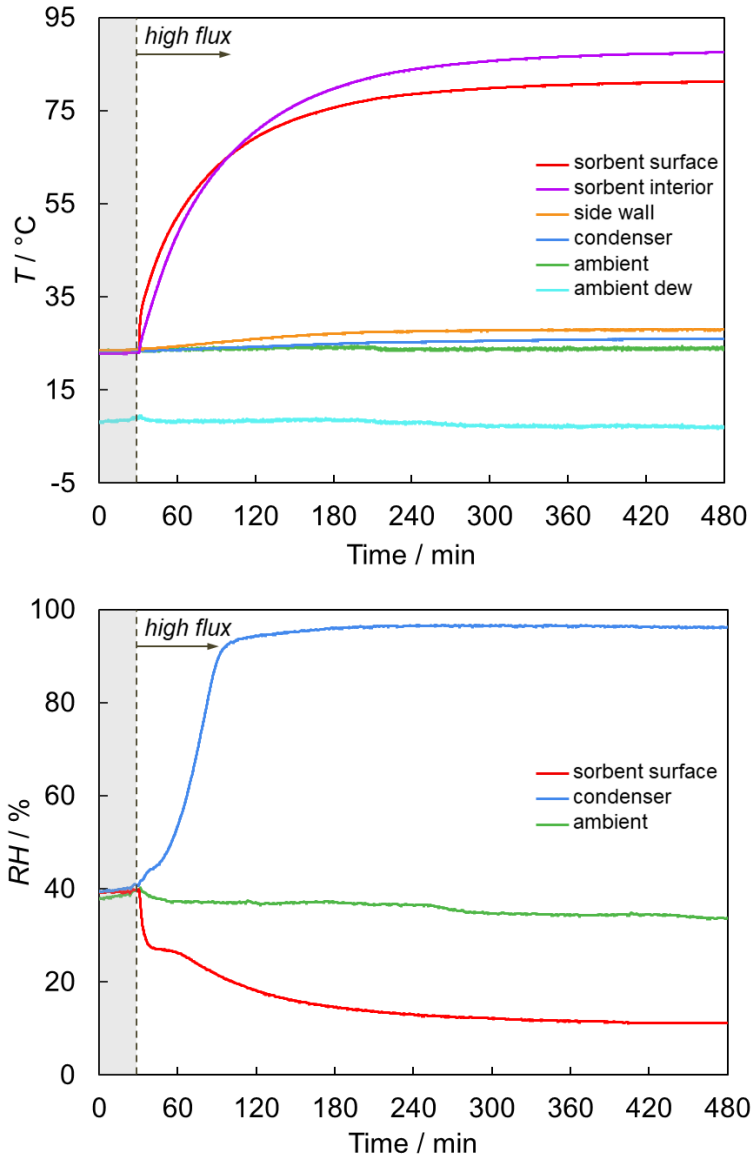

Figure S6.58. The temperature (top) and relative humidity (bottom) profiles during water harvesting using 0.5 kg of Zeolite 13X. Water harvesting was performed under high flux for 7.5 h. 16 g of liquid water was collected.

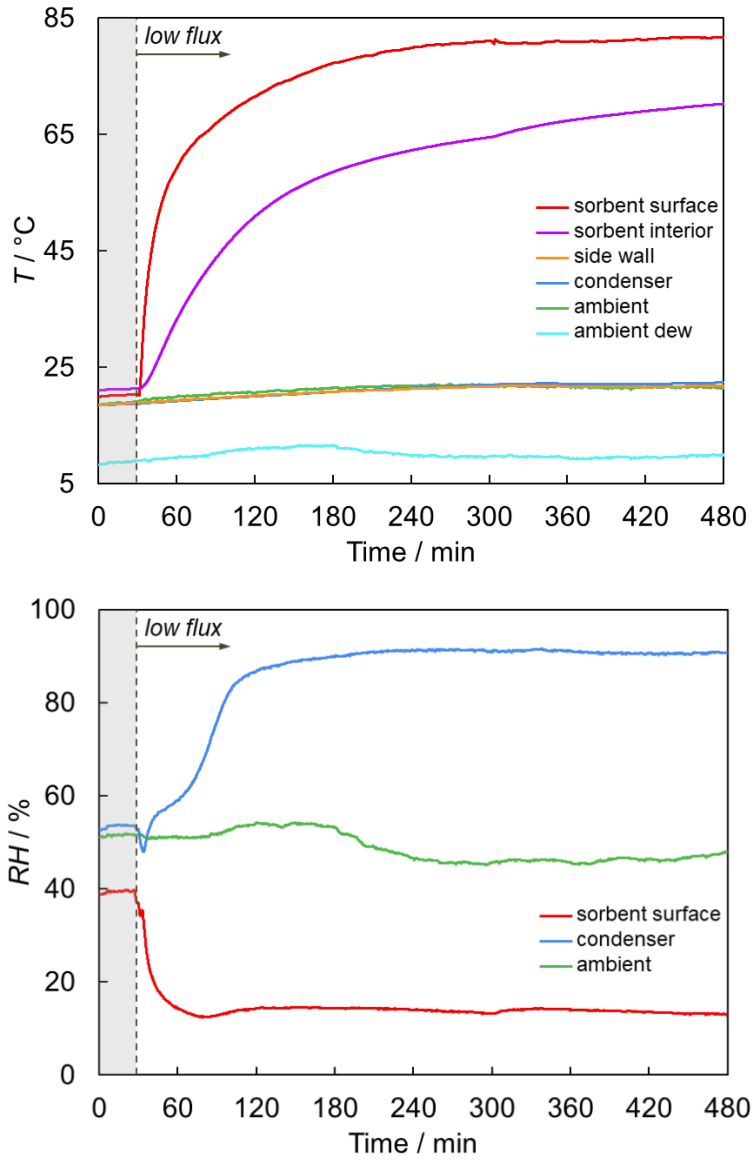

Figure S6.59. The temperature (top) and relative humidity (bottom) profiles during water harvesting using 1.65 kg of MOF-801/G. Water harvesting was performed under low flux for 7.5 h. 25 g of liquid water was collected.

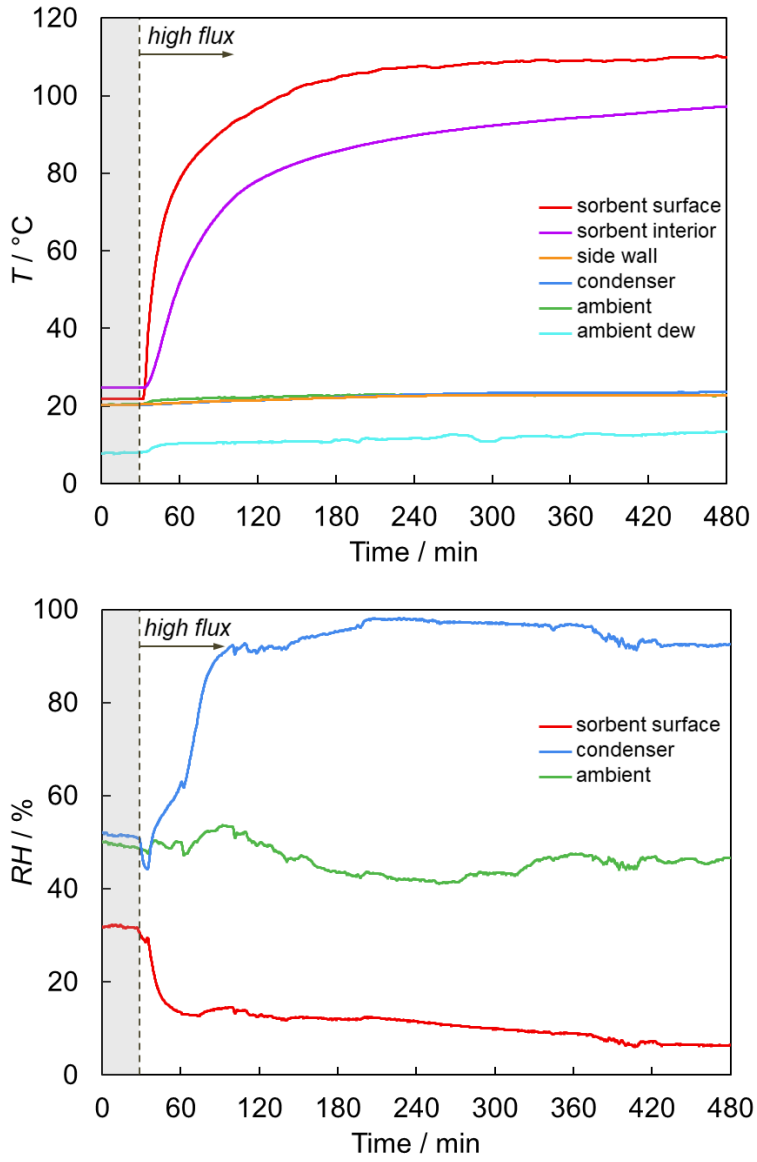

Figure S6.60. The temperature (top) and relative humidity (bottom) profiles during water harvesting using 1.65 kg of MOF-801/G. Water harvesting was performed under high flux for 7.5 h. 63 g of liquid water was collected.

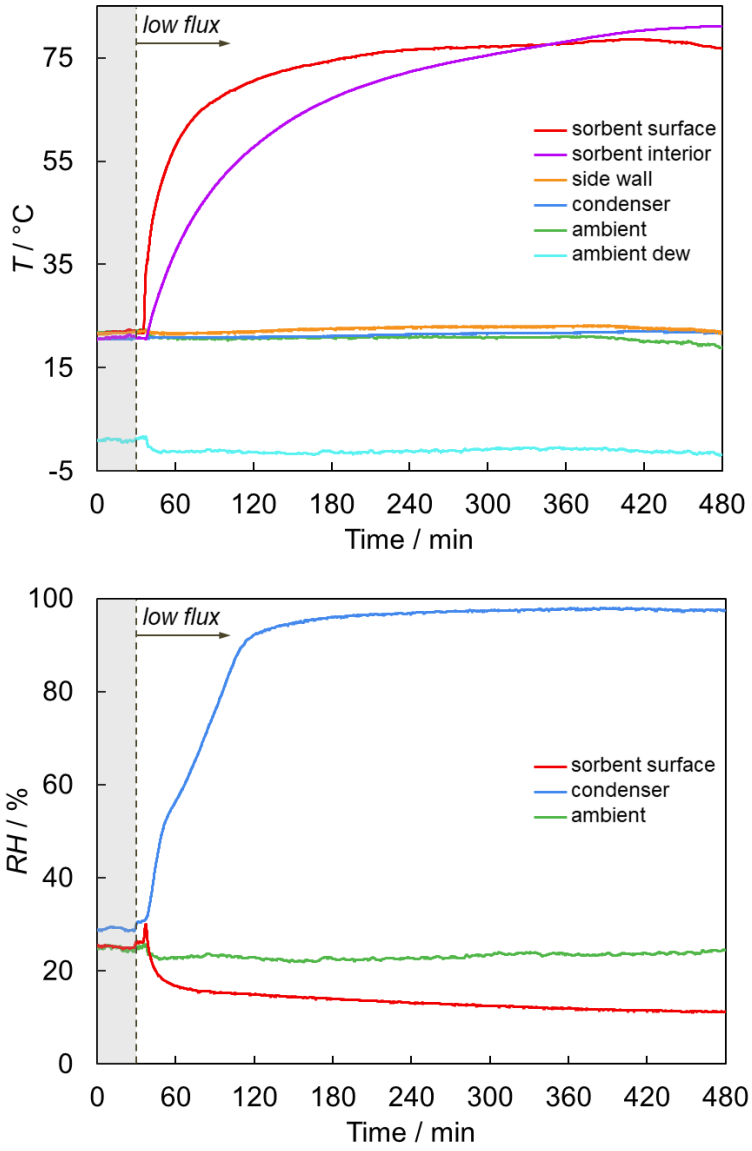

Figure S6.61. The temperature (top) and relative humidity (bottom) profiles during water harvesting using 0.825 kg of MOF-801/G. Water harvesting was performed under low flux for 7.5 h. 37 g of liquid water was collected.

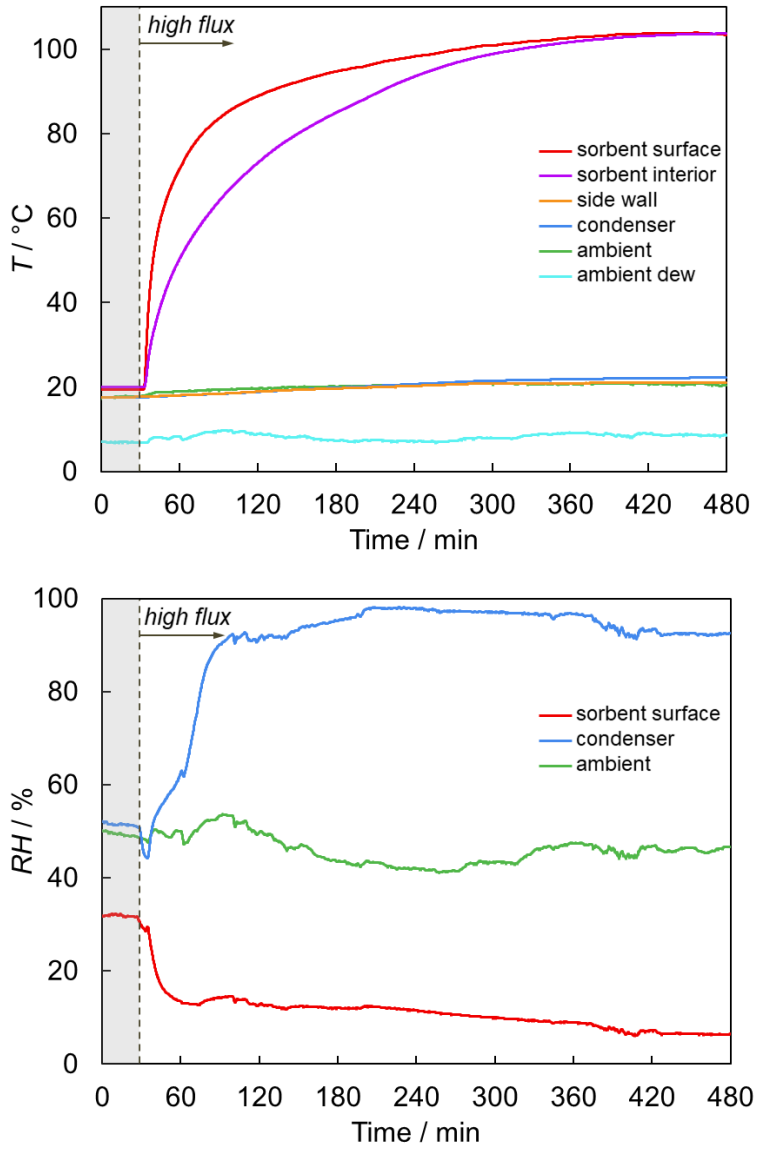

Figure S6.62. The temperature (top) and relative humidity (bottom) profiles during water harvesting using 0.825 kg of MOF-801/G. Water harvesting was performed under high flux for 7.5 h. 78 g of liquid water was collected.

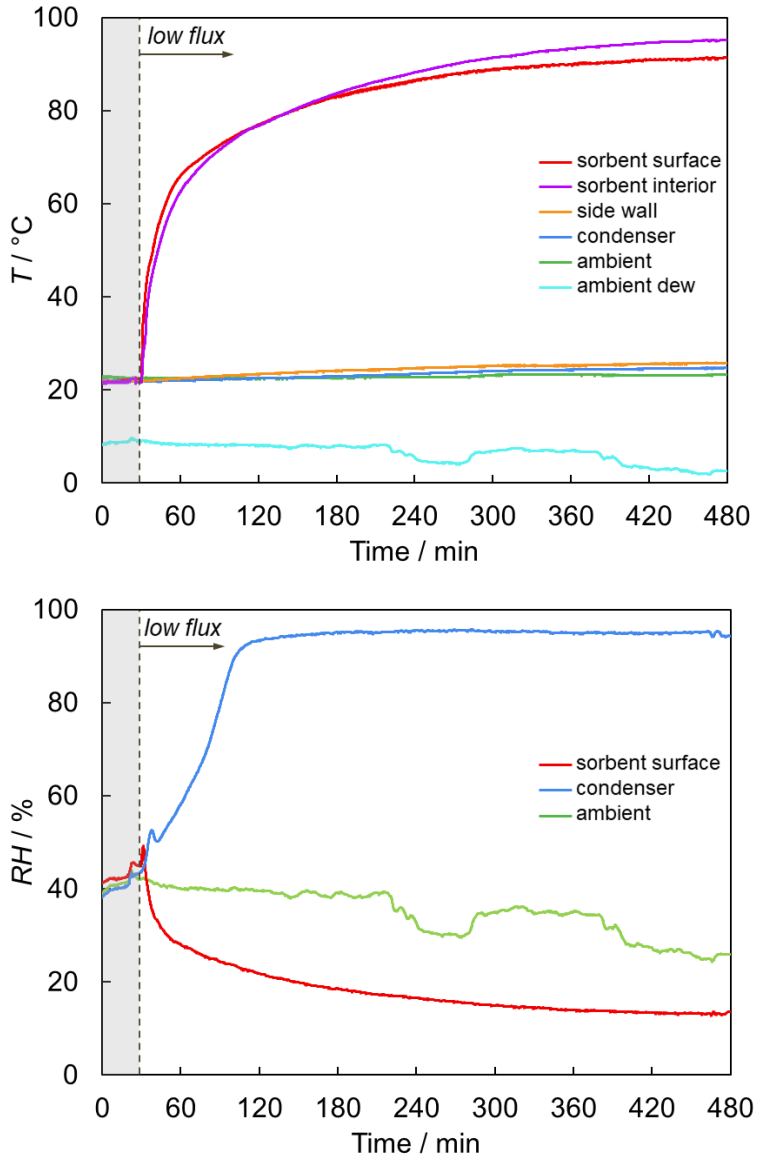

Figure S6.63. The temperature (top) and relative humidity (bottom) profiles during water harvesting using 0.412 kg of MOF-801/G. Water harvesting was performed under low flux for 7.5 h. 26 g of liquid water was collected.

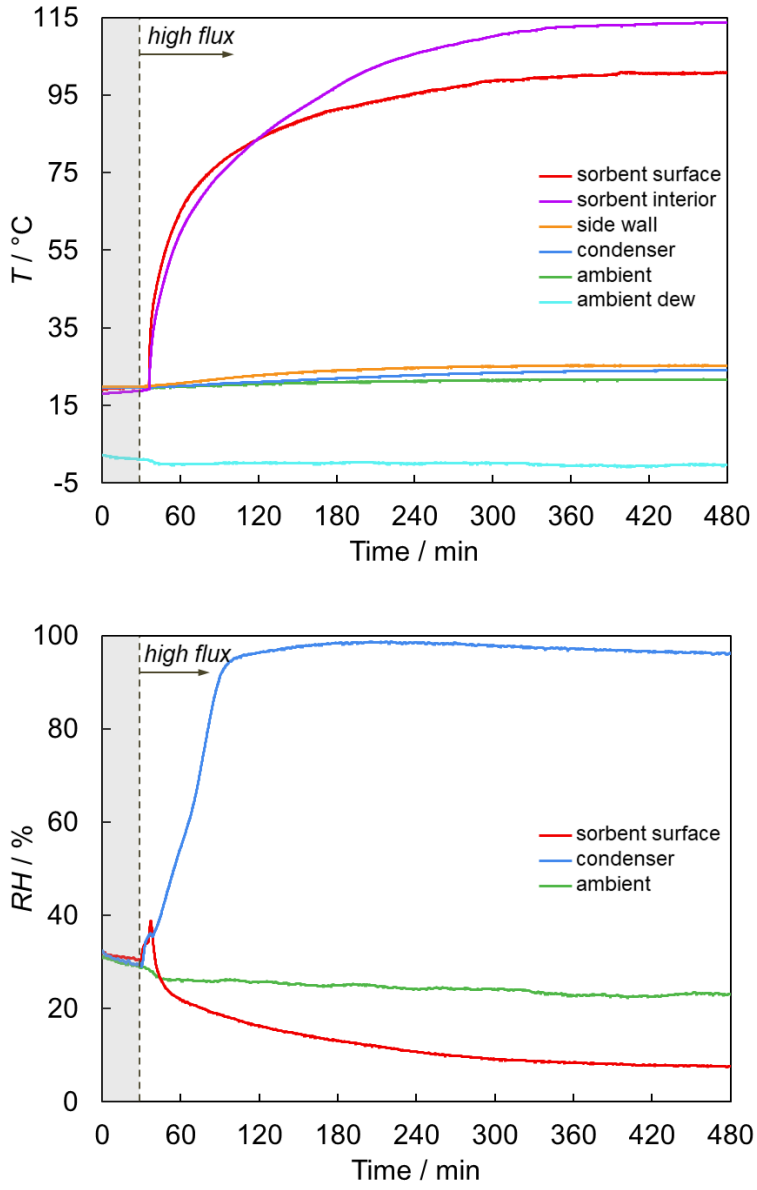

Figure S6.64. The temperature (top) and relative humidity (bottom) profiles during water harvesting using 0.412 kg of MOF-801/G. Water harvesting was performed under high flux for 7.5 h. 36 g of liquid water was collected.

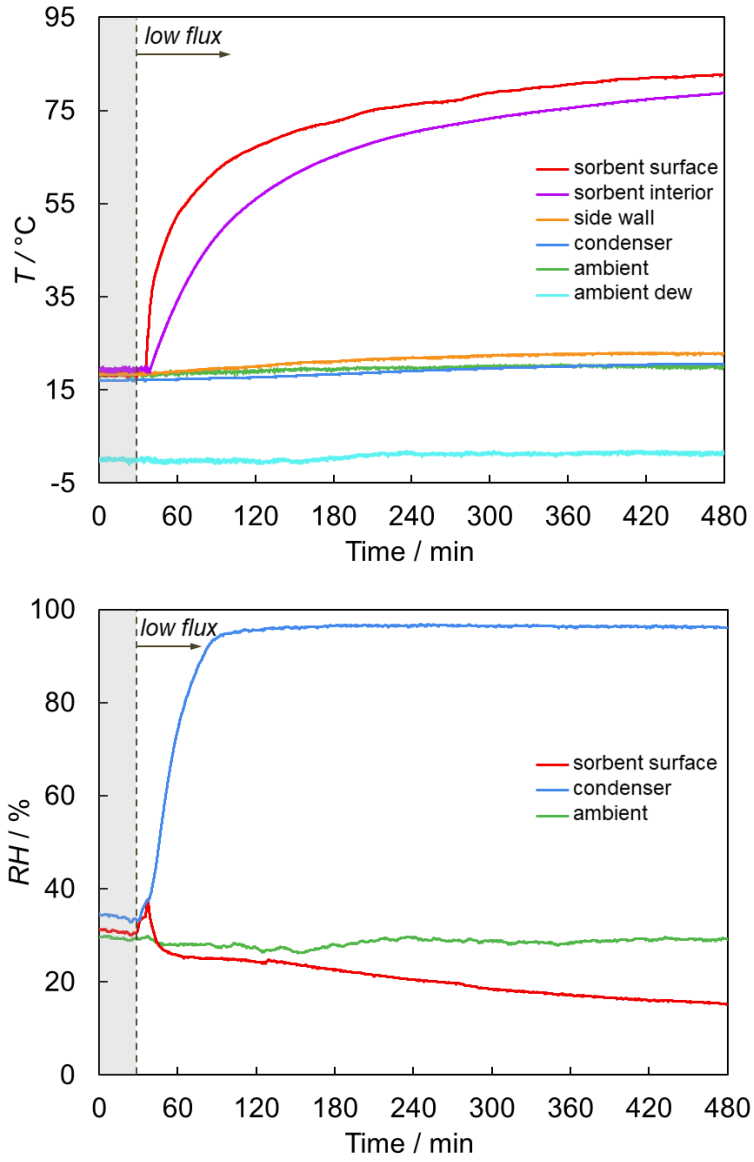

Figure S6.65. The temperature (top) and relative humidity (bottom) profiles during water harvesting using 0.600 kg of MOF-303/G. Water harvesting was performed under low flux for 7.5 h. 60 g of liquid water was collected.

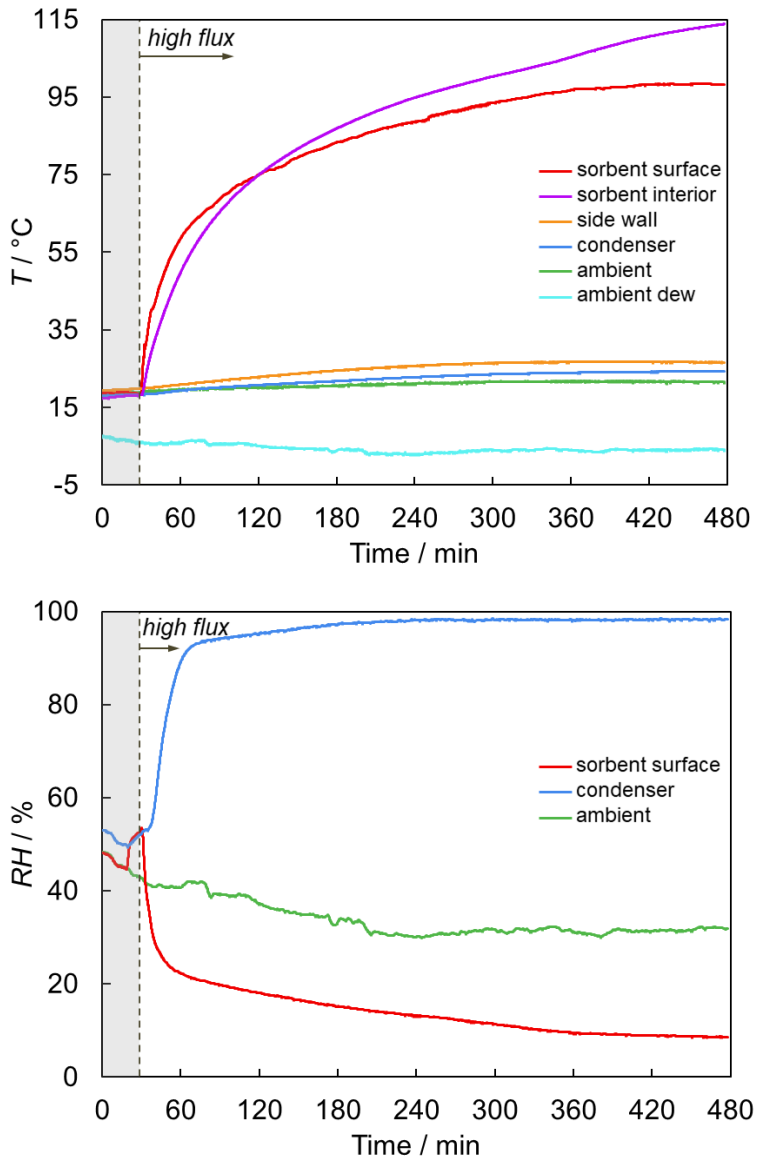

Figure S6.66. The temperature (top) and relative humidity (bottom) profiles during water harvesting using 0.600 kg of MOF-303/G. Water harvesting was performed under high flux for 7.5 h. 105 g of liquid water was collected.

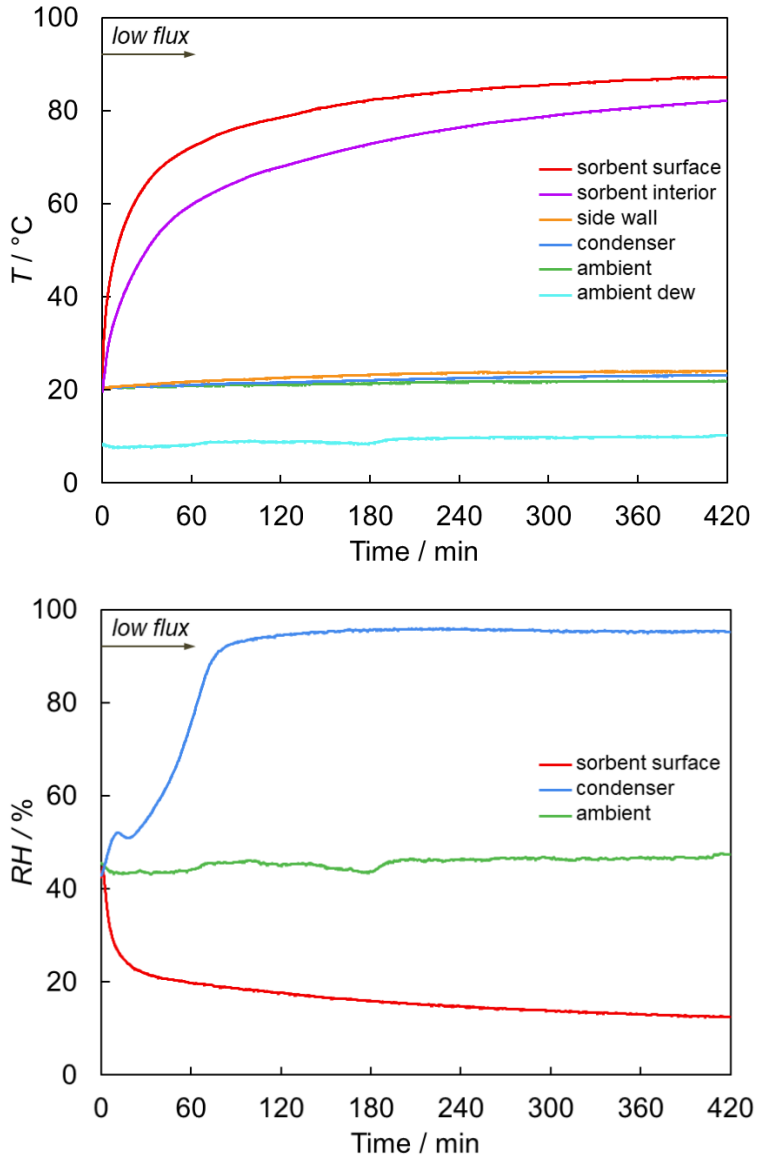

Figure S6.67. The temperature (top) and relative humidity (bottom) profiles during water harvesting using 0.600 kg of MOF-801/G. Saturation was performed in an environmental chamber at 35% RH and 15 °C for 5 days. Water harvesting was performed under low flux for 7.5 h. 28 g of liquid water was collected.

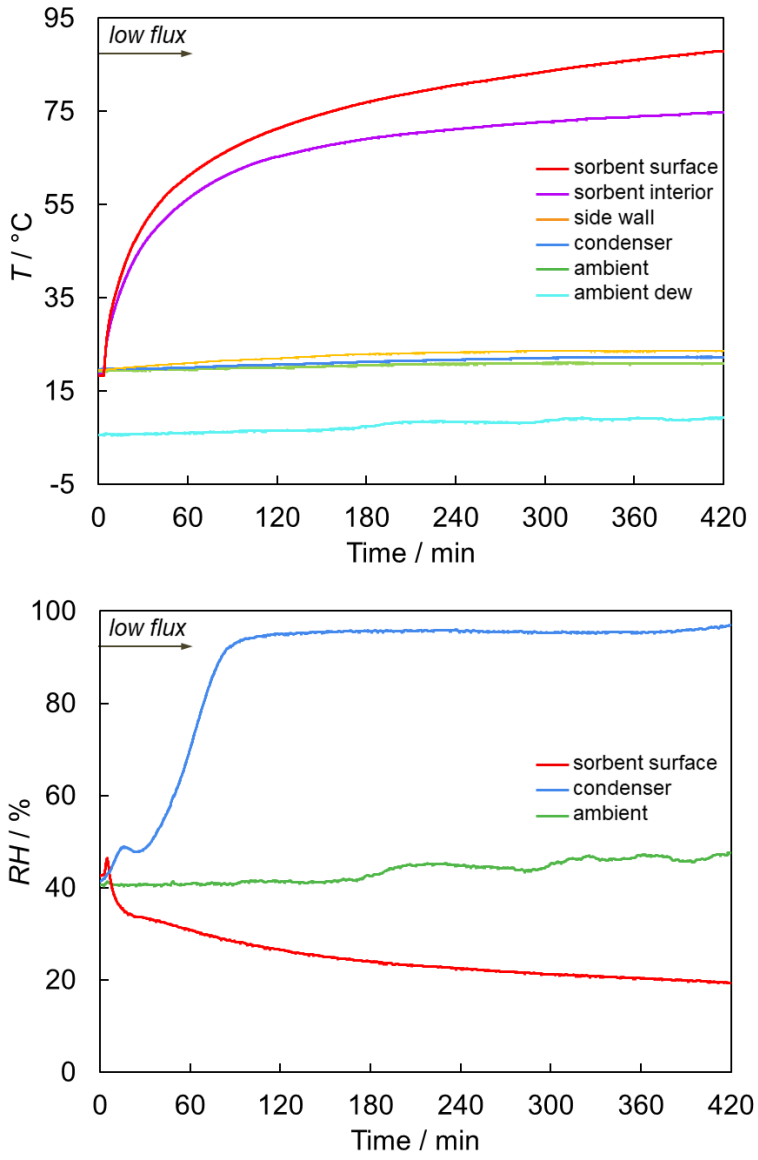

Figure S6.68. The temperature (top) and relative humidity (bottom) profiles during water harvesting using 0.600 kg of MOF-303/G. Saturation was performed in an environmental chamber at 35% RH and 15 °C for 5 days. Water harvesting was performed under low flux for 7.5 h. 60 g of liquid water was collected.

Evaluation of water harvesting cycle performance

The capture capacity ω_{cap} was estimated from the temperature and RH profiles for last 30 minutes of saturation. Final capacity ω_{fin} was estimated from the temperature and RH profiles assuming that the sorbent and air are in equilibrium with each other i.e. the change in RH and temperature values are smaller than their uncertainties for last 30 minutes of the harvesting experiment before liquid water collection. The amount of released water per mass of sorbent, ω_{rel}, is the difference between ω_{cap} and ω_{fin}. The capture, release, and water harvesting cycle efficiencies as well as the productivity are shown in Table S6.5.

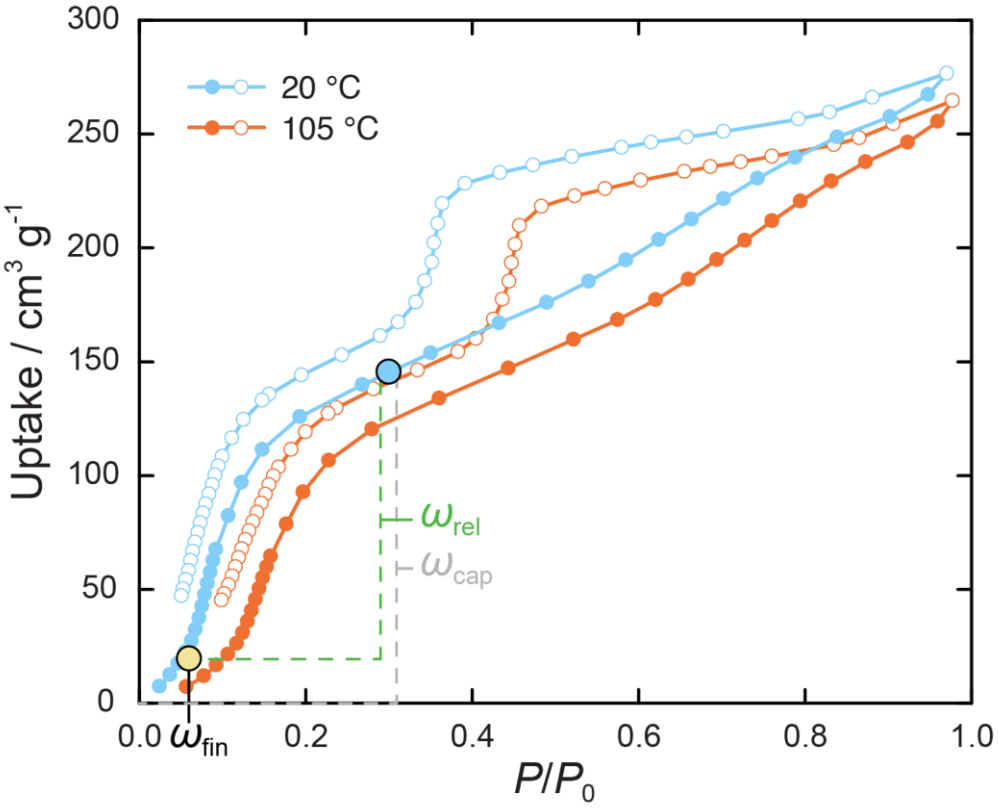

Figure S6.69. Water sorption isotherms for MOF-801/G. Blue and yellow points indicate the conditions for saturation and release for 1.65 kg of MOF-801/G at high flux during water harvesting experiment #6 (Table S6.4).

Table S6.5. The performance parameters for water production under laboratory conditions

Sorbent	Test condition	Collected water (g)	ω_{cap}	ω_{rel}	η_R (%)	η_C (%)	η_{WHC} (%)	P (g.kg^{-1})
No sorbent (empty pan)	Low flux	0	–	–	–	–	–	–
Graphite (0.25 kg)	Low flux	0	–	–	–	–	–	–
Zeolite 13X (0.5 kg)	Low flux	6	0.31	0.01	4	100	4	12
Zeolite 13X (0.5 kg)	High flux	16	0.32	0.03	10	100	10	32
MOF801/G (1.650 kg)	Low flux	25	0.13	0.05	39	30	12	15
MOF801/G (1.650 kg)	High flux	65	0.12	0.09	76	43	33	39
MOF801/G (0.825 kg)	Low flux	37	0.11	0.05	44	93	41	45
MOF801/G (0.825 kg)	High flux	78	0.12	0.10	86	92	79	95
MOF801/G (0.412 kg)	Low flux	26	0.13	0.64	49	99	48	63
MOF801/G (0.412 kg)	High flux	36	0.12	0.10	83	90	75	87
MOF303/G (0.600 kg)	Low flux	60	0.25	0.15	57	68	39	100
MOF303/G (0.600 kg)	High flux	105	0.27	0.22	81	79	65	175
MOF801/G (0.600 kg)	Low flux controlled	28	0.12	0.05	42	88	37	47
MOF303/G (0.600 kg)	Low flux controlled	60	0.27	0.15	55	67	37	100

Design considerations for water release

In this section, a theoretical approach to estimate the energy requirements for release of water from the MOF and subsequent condensation is discussed.

Figure S6.70 shows the incident radiation flux $\left(\dot{E}\right)$, a portion of it passing through the transparent cover, which is subsequently absorbed by a unit mass of MOF ($\dot{q}_{abs}$). A fraction of this energy is lost in the forms of the radiative heat loss ($\dot{q}_{radiation}$) and convective heat loss ($\dot{q}_{convection}$). The thermal radiation emitted by cover was neglected and it is assumed that the conducive heat loss is minimized by using extruded polystyrene foam with low thermal conductivity (0.027 W m^{-1} K^{-1}).

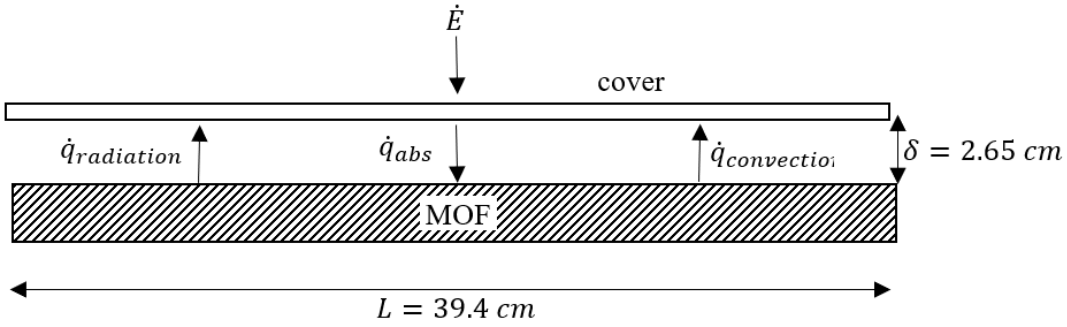

Figure S6.70. Schematic of energy flow on the top surface of the water sorption unit.

Considering the uniform temperature distribution within the MOF ($Bi = \frac{hL_c}{k} < 0.1$) at any given time, the energy balance for a control volume including the MOF is:

$$\rho_{eff} c_{p,eff} \frac{dT}{dt} - \rho_{MOF} q_{st} \frac{d\omega}{dt} = \left(\frac{A}{V_{bed}}\right)\left(\dot{q}_{abs} - \dot{q}_{radiation} - \dot{q}_{convection}\right) \tag{6.19}$$

Time-dependent effective properties of the sorbent packing are defined by the following equations,

$$\rho_{eff} = \rho_{MOF}\left(1-\varepsilon\right)\left(1+\omega\right) + \rho_{air}\varepsilon \tag{6.20}$$

and

$$c_{p,eff} = \frac{\rho_{MOF,dry}\left(1-\varepsilon\right)\left(c_{p,MOF,dry} + \omega c_{p,water}\right) + \rho_{air} c_{p,air}\varepsilon}{\rho_{eff}} \tag{6.21}$$

, where ε, c_p, ρ are the packing porosity (excluding the MOF internal pore volume), heat capacity, and density, respectively. Replacing the effective properties in equation (6.19) with equations (6.20) and (6.21) and integrating equation (6.19) over the release period results in:

$$\int_{T_{cap}}^{T_{rel}} \left(\rho_{MOF,dry}\left(1-\varepsilon\right)(c_{p,MOF,dry}+\omega c_{p,water})+\rho_{air}c_{p,air}\varepsilon\right)dT$$
$$-\int_{\omega_{cap}}^{\omega_{rel}} \rho_{MOF}q_{st}d\omega=\left(\frac{A}{V_{bed}}\right)\int_{sunrise}^{sunset}\left(\dot{q}_{abs}-\dot{q}_{radiation}-\dot{q}_{convection}\right)dt \quad (6.22)$$

Assuming that the entire amount of captured water is desorbed during the release process at the release temperature, the released water vapor is in thermal equilibrium with the MOF, and assuming that the variations of density and heat capacity with temperature are small, equation (6.22) becomes:

$$\left[\left(c_{p,MOF,dry}+\omega_{cap}c_{p,water}\right)\left(1-\varepsilon\right)+\left(\rho_{air}\Big/\rho_{MOF,dry}\right)c_{p,air}\varepsilon\right]\left(T_{rel}-T_{cap}\right)$$
$$+\omega_{cap}q_{st}=\left(\frac{1}{\rho_{MOF,dry}}\right)\left(\frac{A}{V_{bed}}\right)\int_{sunrise}^{sunset}\left(\dot{q}_{abs}-\dot{q}_{radiation}-\dot{q}_{convection}\right)dt \quad (6.23)$$

The total received energy per mass of MOF is defined:

$$q_H=\left(\frac{1}{\rho_{MOF,dry}}\right)\left(\frac{A}{V_{bed}}\right)\int_{sunrise}^{sunset}\left(\dot{q}_{abs}-\dot{q}_{radiation}-\dot{q}_{convection}\right)dt \quad (6.24)$$

The total sensible energy is defined as the amount of energy per unit mass of MOF spent to increase the temperature of MOF from the capture temperature to the release temperature as:

$$q_{sensible}=\left[\left(c_{p,MOF,dry}+\omega_{cap}c_{p,water}\right)\left(1-\varepsilon\right)+\left(\frac{\rho_{air}}{\rho_{MOF,dry}}\right)c_{p,air}\varepsilon\right]\left(T_{rel}-T_{cap}\right) \quad (6.25)$$

The total latent energy is defined as the amount of energy per unit mass of MOF spent to desorb the entire amount of captured water from the MOF as:

$$q_{latent}=\omega_{cap}q_{st} \quad (6.26)$$

$q_{sensible}$ and q_{latent} considerations: In this section, a comparison between the $q_{sensible}$ and q_{latent} for the designed water harvester is provided based on our preliminary laboratory data on MOF-801/G. The RH of 35% at 25 °C was considered for the water capture process which results in ω_{cap} = 0.14. The average value of $q_{st,801}$ = 3000 kJ kg^{-1} was determined from the sorption isotherms resulting in q_{latent} = 420 kJ kg^{-1}. With $c_{p,801}$ = 760 J kg^{-1} K^{-1} and $\rho_{p,801}$ = 1400 kg m^{-3} [13], $c_{p,G}$ = 760 J kg^{-1} K^{-1} and 2150 kg m^{-3} [24], then the density and heat capacity of the mixture are $\rho_{p,801/G}$ = 1584 kg m^{-3} and $c_{p,801/G}$ = 743 J kg^{-1} K^{-1}, respectively. The values of $q_{sensible}$ and $q_{sensible}/q_{latent}$ for different $\Delta T_{WH}=T_{rel}-T_{cap}$ are shown in the Figure S6.71 where the water and air properties were calculated at the mean release and capture temperatures. The results indicate that the $q_{sensible} << q_{latent}$ during the release process, therefore, almost all the incident energy is spent on overcoming the MOF-water interactions.

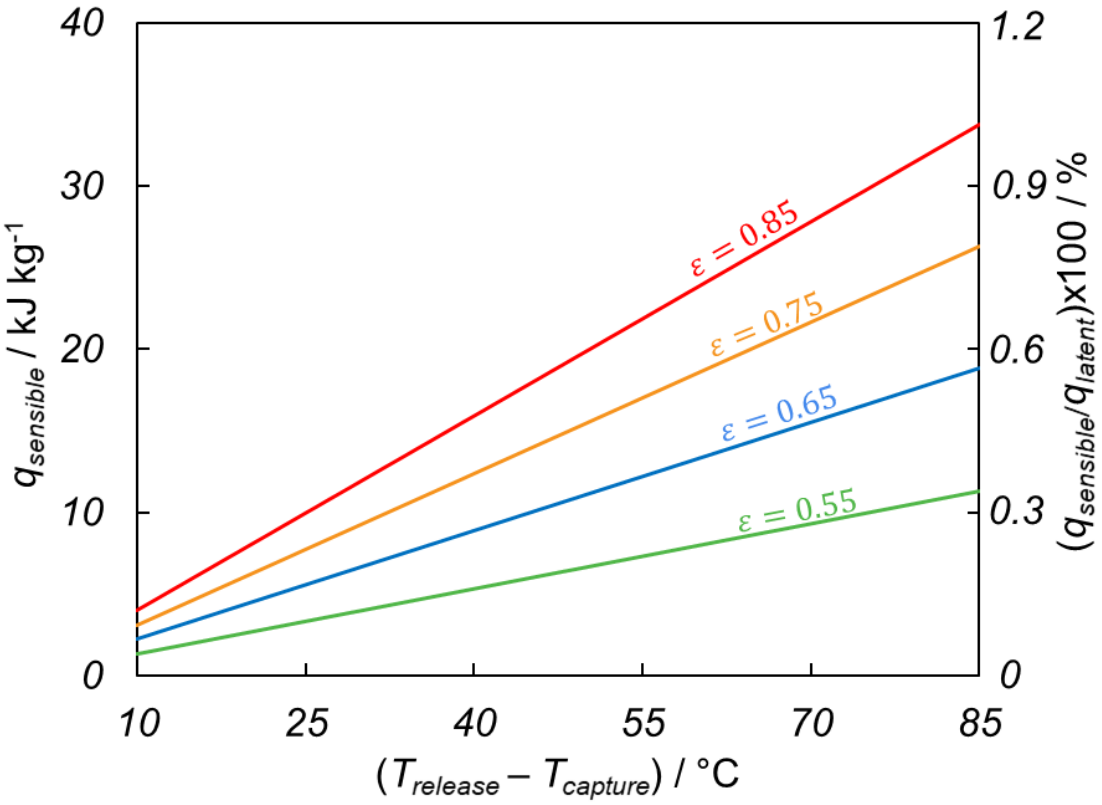

Figure S6.71. Variations of $q_{sensible}$ with the release and capture temperature for four values of packing porosities of 0.85, 0.75, 0.65, and 0.55. $q_{sensible}$ was calculated for a capture temperature of 20 °C. The ratio of sensible to latent energy reveals that the majority of the energy is spent on breaking the MOF-water interactions, rather than increasing the temperature of the MOF during the release process.

$\dot{q}_H$ considerations: To determine $\dot{q}_H$, it is required to quantify $\dot{q}_{abs}$, $\dot{q}_{radiation}$, and $\dot{q}_{convection}$. For the laboratory experiment with artificial flux,

$$\dot{q}_{abs} = \alpha_{MOF,lamp}\tau_{cover,lamp}\dot{E}_{lamp} \quad (6.27)$$

where α_λ and τ_λ are absorptivity of the MOF-801/G and transmissivity of the cover, respectively, and $\dot{E}_{lamp}$ is the measured incident radiation flux on the surface of the cover. With the average constant low and high fluxes $\dot{E}_{lamp}$ = 558 and 792 W m^{-2}, and the values of $\alpha_{MOF,lamp}$ and $\tau_{cover,lamp}$ taken from Section S6.7, the total radiant flux received by a unit mass of MOF-801/G was determined and listed in Table S6.6.

Table S6.6. Total flux received by different sorbents for the laboratory experiment using low and high fluxes

Sorbent	$\dot{q}_{abs}$ / W m^{-2}	
	Low flux	High flux
Zeolite 13X	18	28
MOF-801/G	277	430
MOF-303/G	317	492

The radiative heat loss from the sorbent surface can be determined by,

$$\dot{q}_{radiation} = \varepsilon_m \sigma T_{MOF}^4 \tag{6.28}$$

where $\sigma = 5.670 \times 10^{-8}$ / W m^{-3} K^4 is the Stefan-Boltzmann constant and ε_m is the hemispherical emissivity of the sorbent. Variations of $\dot{q}_{radiation}$ with the temperature and emissivity are shown in Figure S6.72. It can be observed that for the range of temperature required for the release of water from MOF ($T_{release}$ < 80 °C), the heat loss due to radiation is negligible (< 4 W m^{-2}) compared to the received flux (~ 250-500 W m^{-2}), even if the MOF is considered a blackbody emitter $(\varepsilon = 1)$. In the calculations of incident flux, the maximum value of 4 W m^{-2} was considered for the radiative heat loss.

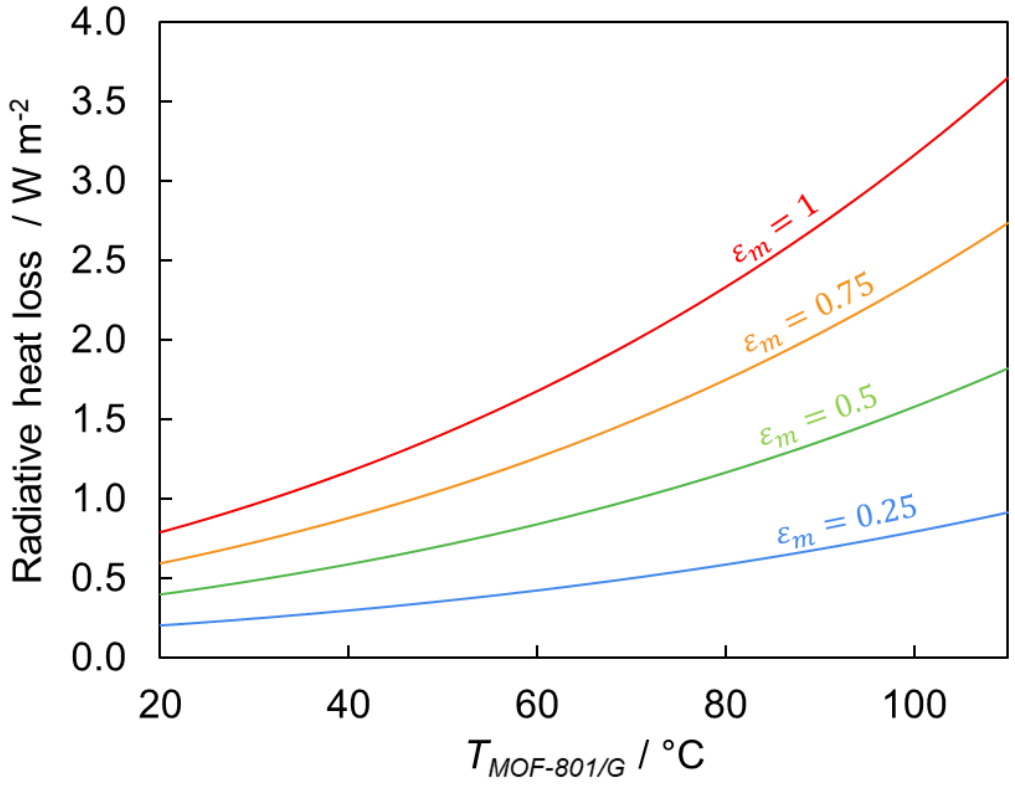

Figure S6.72. Variations of radiative heat loss with MOF-801/G temperature for different values of emissivity.

The heat loss from the MOF surface to the cover due to convection was determined by,

$$\dot{q}_{convection} = \bar{h}\left(T_{MOF} - T_{cover}\right) \tag{6.29}$$

where $\bar{h}$ is the average convective heat transfer coefficient over the length of the MOF surface and T_{cover} is the surface temperature of the cover. The Rayleigh number was calculated using the following equation,

$$Ra_L = \frac{g\rho\beta\left(T_{MOF} - T_{cover}\right)\delta^3}{\alpha_T \mu} \tag{6.30}$$

where β, α_T, and μ are the volumetric thermal expansion coefficient, thermal diffusivity, and dynamic viscosity of the air, respectively, and g is the gravitational acceleration. To determine the value of β, α_T, and μ, air was considered as an ideal gas and the following relations and correlations were used,

$$\rho = \frac{P}{RT} \tag{6.31}$$

$$\beta = \frac{1}{T} \tag{6.32}$$

$$\mu = \mu_{ref}\left(\frac{T}{T_{ref}}\right)^{3/2}\left(\frac{T_{ref} + 110.4}{T + 110.4}\right) \tag{6.33}$$

where $\mu_{ref} = 1.8205\times10^{-5}$ kg m^{-1} s^{-1} at $T_{ref} = 293.15$ K, and

$$c_p\left[\text{kJ kg}^{-1}\ \text{K}^{-1}\right] = 1.05 - 0.365\left(\frac{T}{1000}\right) + 0.85\left(\frac{T}{1000}\right)^2 - 0.39\left(\frac{T}{1000}\right)^3 \quad (6.34)$$

$$k\left[\text{W m}^{-1}\ \text{K}^{-1}\right] = 10^{-4}\times\left[1.52\times10^{-7}T^3 - 4.86\times10^{-4}T^2 + 1.02T - 3.93\right] \quad (6.35)$$

and

$$\alpha_T = \frac{k}{\rho c_p} \quad (6.36)$$

The Rayleigh number was estimated by taking the temporal measurement of the temperature of the MOF and the inner surface of the cover under low flux radiation. The temperature profile and instantaneous value of *Ra* are shown in Figure S6.73.

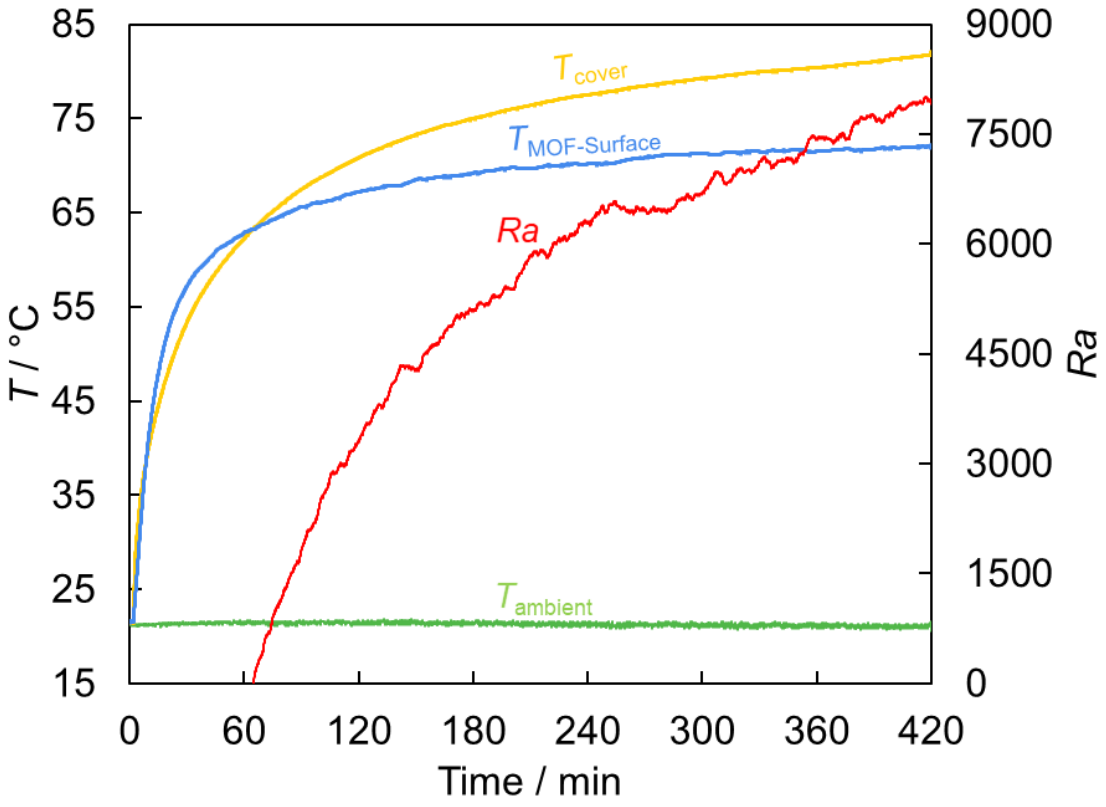

Figure S6.73. Variations of the temperature of MOF-801/G and the cover. Increase in the Rayleigh number is observed due to the increase in temperature difference. During the first 60 minutes, the cover temperature was higher than that of the MOF with no heat loss.

For $\delta/L > 12$ ($\delta/L = 14.2$ in the current design), the following correlation[25] was used to determine the Nusselt number (*Nu*),

$$\overline{Nu} = \begin{cases} 1.44\left(1-\frac{1708}{Ra}\right)+\left(\frac{Ra}{5830}\right)^{\frac{1}{3}} & 1708 < Ra <\sim 10000 \\ 1 & Ra < 1708 \end{cases} \quad (6.37)$$

where the critical Rayleigh number ($Ra_c = 1708$) determines whether buoyancy forces can overcome the resistance imposed by the viscous forces or not. With the known $\overline{Nu}$, $\bar{h}$ as a function of time was found using:

$$\bar{h} = \frac{k\overline{Nu}}{\delta} \quad (6.38)$$

The total energy absorbed by MOF-801/G for the case of low flux is:

$$q_{abs} = \int_{t=0}^{t=end} \dot{q}_{abs} dt = 277 W\, m^{-2} \times 7.5 h \times 3600 s\, h^{-1} = 7479 kJ\, m^{-2} \quad (6.39)$$

The radiative heat loss from the sorbent surface was determined by:

$$q_{radiation} = \int_{t=0}^{t=end} \dot{q}_{radiation} dt = 4 W\, m^{-2} \times 7.5 h \times 3600 s\, h^{-1} = 108 kJ\, m^{-2} \quad (6.40)$$

Total heat loss per unit area during the entire release cycle was found by numerical integration of the measured data and calculated $\bar{h}$ using MATLAB R2017a:

$$q_{convection} = \int_{t=0}^{t=end} \bar{h}\left(T_{MOF} - T_{cover}\right) dt = 3.4 kJ\, m^{-2} \quad (6.41)$$

Therefore, the total radiative heat loss and the total convective heat loss from the MOF surface are less than 1.5% and 0.05%, respectively. This would result in the total heat loss of less than 1.6%.

The total energy required for the release of water (q_H) was plotted versus the amount of MOF-801/G with and without the heat losses for and exposed surface of 0.155 m^2 (see Figure S6.74).

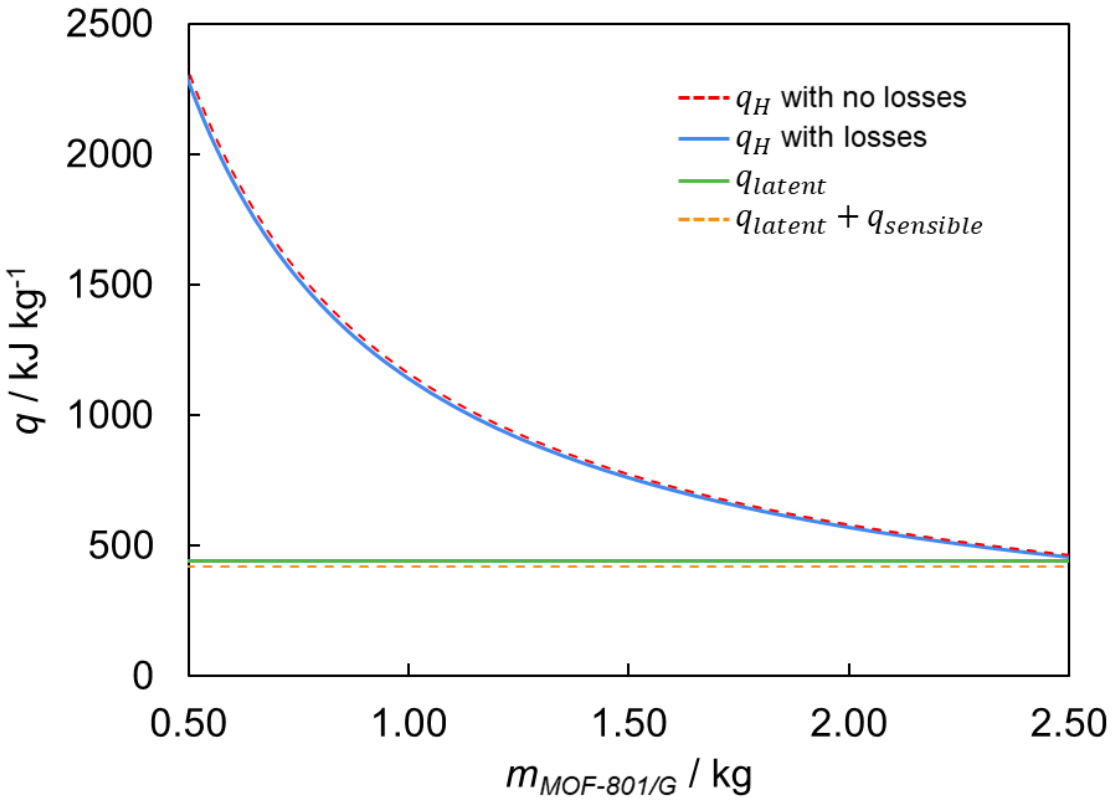

Figure S6.74. Comparison of q_H (with and without heat losses) and the amount of MOF-801/G to the latent and sensible energy per kg of MOF-801/G.

In addition, the total energy required to heat up the MOF and release the captured water $(q_{latent} + q_{sensible})$ is also plotted and compared to q_{latent}. The results reveal that up to 2.5 kg of MOF-801/G can be used in this water harvester; below this mass, the incident radiant energy is sufficient to fully release the captured water from the MOF. It should be noted that the same result is achieved by considering no energy losses from the MOF to the surroundings and neglecting the sensible energy. This eliminates the complication in the calculation and allows a simple criterion to be defined,

$$q_H \geq q_{latent} \tag{6.42}$$

or

$$\left(\frac{1}{\rho_{MOF,dry}}\right)\left(\frac{A}{V_{bed}}\right)\int_{sunrise}^{sunset}\left(\dot{q}_{abs}\right)dt \geq \omega_{cap} q_{st} \tag{6.43}$$

Design considerations for water condensation

In this section, a theoretical approach to estimate the energy requirements for condensation of water released from the MOF is discussed.

$\dot{q}_C$ considerations: The energy required for condensation of water vapor is used to decrease the temperature of the released water vapor ($q_{sensible}$), and liquefy water vapor (q_{latent}) with a portion of it being lost to the surroundings. Thus, the conservation of energy within the condenser over the condensation period is,

$$q_{c,sensible} + q_{c,latent} + q_{c,loss} = \omega_{rel} c_{p,wv} \left(T_{wv} - T_{dew}\right) + \frac{m_{air}}{m_{MOF}} c_{p,a} \left(T_a - T_{dew}\right) + \omega_{rel} h_{fg} + q_{c,loss} \quad (6.44)$$

where T_{wv}, T_a, and T_{dew} are the temperature of the water vapor, dry air, and dew temperature, respectively. $c_{p,wv}$ and $c_{p,a}$ are the heat capacity of water vapor and air, respectively. Considering the heat loss to be negligible, thermal equilibrium between the water vapor and dry air ($T_a = T_w$), maximum possible water release, and subsequent condensation of the released water ($\omega_{rel} = \omega_{cap}$), then:

$$q_{c,sensible} + q_{c,latent} = \left(T_a - T_{dew}\right)\left(\omega_{cap} c_{p,w} + \frac{m_{air}}{m_{MOF}} c_{p,a}\right) + \omega_{cap} h_{fg} \quad (6.45)$$

In the case that the condensation process relies solely on natural cooling, the cooling energy can be estimated as follows,

$$q_c = \int_{sunrise}^{sunset} \dot{q}_c(t)\, dt = A_c \int_{sunrise}^{sunset} \bar{h}\left[T_a - T_c\right] dt \quad (6.46)$$

where $\bar{h}$ is the average convective heat transfer coefficient within the condenser at any given time. Considering that $\frac{m_{air}}{m_{MOF}} c_{p,a} << \omega_{cap} c_{p,w}$, the following relation can be obtained:

$$\frac{A_c}{m_{MOF}} \int_{sunrise}^{sunset} \bar{h}\left[T_a - T_c\right] dt = \left(T_a - T_{dew}\right)\left(\omega_{cap} c_{p,w}\right) + \omega_{cap} h_{fg} \quad (6.47)$$

Here, to ensure a sufficiently large condenser surface, a minimum value of $\bar{h}$ was assumed for the case of film condensation (rather than dropwise condensation with higher heat transfer rate) on a vertical channel by using $Nu = 3.36$ throughout the condensation period using a correlation in the literature[26]. It should be noted that accurate calculation of $\bar{h}$ is possible through advanced numerical simulation or experimental measurement with the identical geometrical constrains and boundary conditions which would result in a better estimation of the required cooling energy and condenser design. Here, we considered that the release of water occurred at 65 °C and the condenser temperature was the same as the dew point ($T_c = T_a$). The total area required for condensation versus amount of MOF was calculated for different condenser temperatures and two Nusselt numbers ($Nu = 3.36$ and $Nu = 1.18$) which are plotted in the Figure S6.75. In the current design, the total area of 3100 cm^2 allowed for a sufficiently large case to enclose the water sorption unit and provided an adequately large surface for the condensation of the released water from up to 2.5 kg of MOF-801/G. Less than 1% variation in cooling area was observed by neglecting the sensible cooling. This implies that the minimum cooling energy required for the condensation of released water can be determined by neglecting the sensible cooling as follows:

$$q_{c.min} \geq m_{MOF}\omega_{cap}h_{fg} \tag{6.48}$$

Although increasing the size of the cooling surface provides more cooling energy for condensation, there is a theoretical limit for the volume of the condenser. The humidity ratio (w in $kg_{(water)}$ $kg_{(dry\ air)}^{-1}$) in the vicinity of the condenser can be related to the relative humidity according to:

$$w = 10^4\, RH \,/\left[e^{5294/(T_c+273.15)} - 1.61\times10^4\, RH \right] \tag{6.49}$$

Considering that the RH of 100% is required for the condensation, then:

$$\frac{\omega_{cap} m_{MOF}}{\rho_{air} V_c} = 10^6 \,/\left[e^{5294/(T_c+273.15)} - 1.61\times10^6 \right] \tag{6.50}$$

With the ratio known for A_c and m_{MOF} from equation (6.45), the maximum length of the condenser ($L_{c,max}$) can be expressed as follows:

$$L_{c,max} = \frac{\omega_{cap} m_{MOF}\left[e^{5294/(T_c+273.15)} - 1.61\times10^6 \right]}{A_c \rho_{air} 10^6} \tag{6.51}$$

Considering the minimum amount of the MOF of 0.4 kg, ω_{cap} = 0.14, A_c = 3100 cm^2, T_c = 30 °C, then $L_{c,max}$ = 3.16 m. In the current design, L_c = 25.4 cm which allowed to fully saturate the condenser when $\omega_{rel} = 0.08\,\omega_{cap}$.

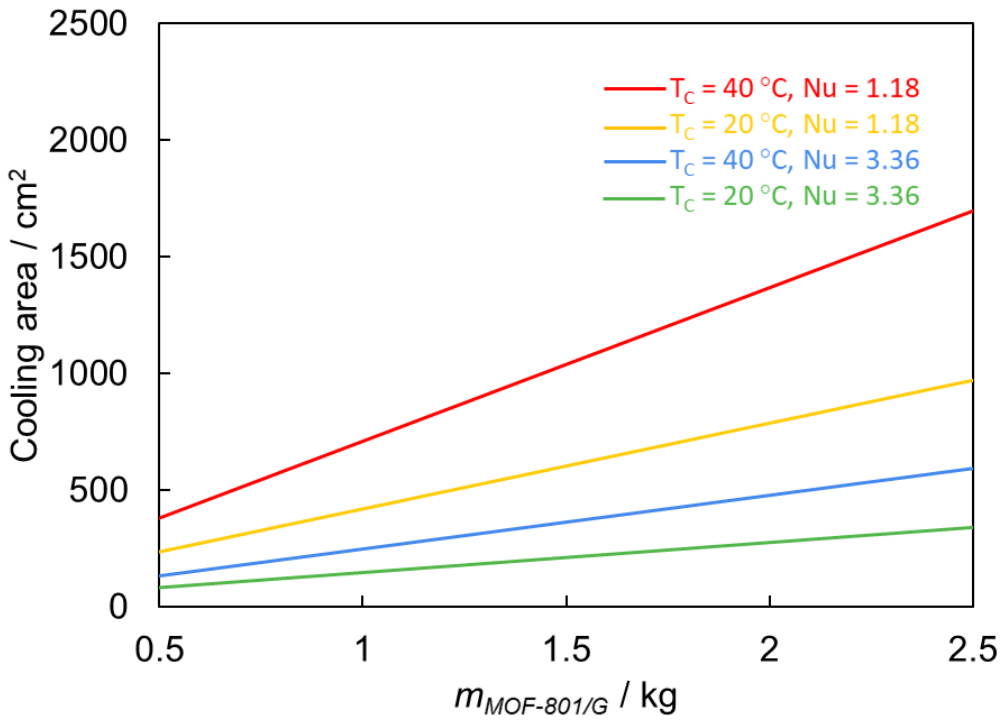

Figure S6.75. Variations of the size of the cooling surface with the amount of MOF-810/G for a temperature of 65 °C for the released water, a condenser temperature of 20 and 40 °C, and average heat condensation Nusselt number of 3.36 and 1.18. The cooling surface of 3100 cm^2 ensure enough cooling energy at the high condenser temperature (40 °C) and low heat transfer rate (Nu = 1.18).

Section S6.10. Harvesting experiments at Scottsdale, Arizona under desert conditions

The description of the setup for the harvesting experiment conducted at Scottsdale, Arizona, United States in late October is described in the main text. Figures S6.76-S6.77 show the temperature and relative humidity profile for two runs using 1.65 and 0.825 kg of MOF-801/G, respectively. Figure S6.78 describes the exterior insulation used in these experiments.

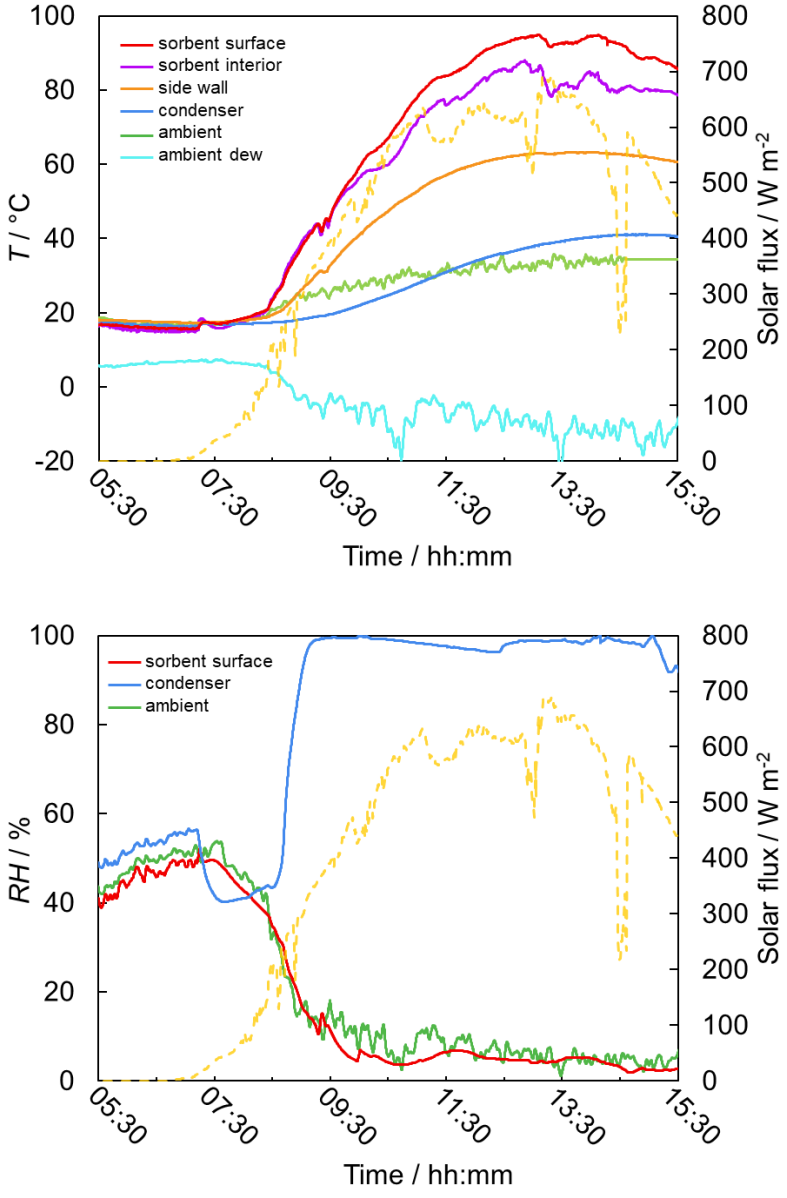

Figure S6.76. The temperature (top) and relative humidity (bottom) profiles recorded during water harvesting under desert conditions using 1.65 kg of MOF-801/G. 55 g of liquid water was collected. Release efficiency: 94%, collection efficiency: 25%, WHC efficiency: 24%, productivity: 33 g kg^{-1}.

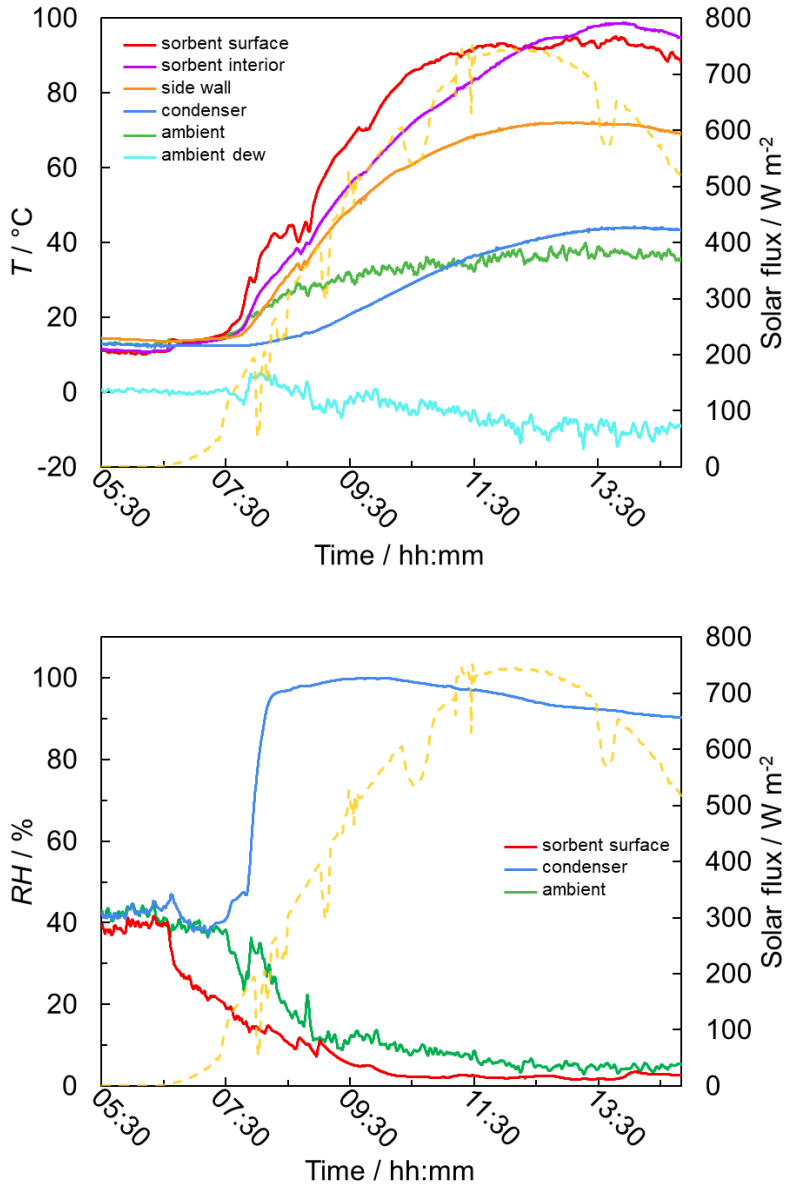

Figure S6.77. The temperature (top)and relative humidity (bottom) profiles recorded during water harvesting under desert conditions using 0.825 kg of MOF-801/G. 55 g of liquid water was collected. Release efficiency: 92%, collection efficiency: 56%, WHC efficiency: 51%, productivity: 67 g kg^{-1}.

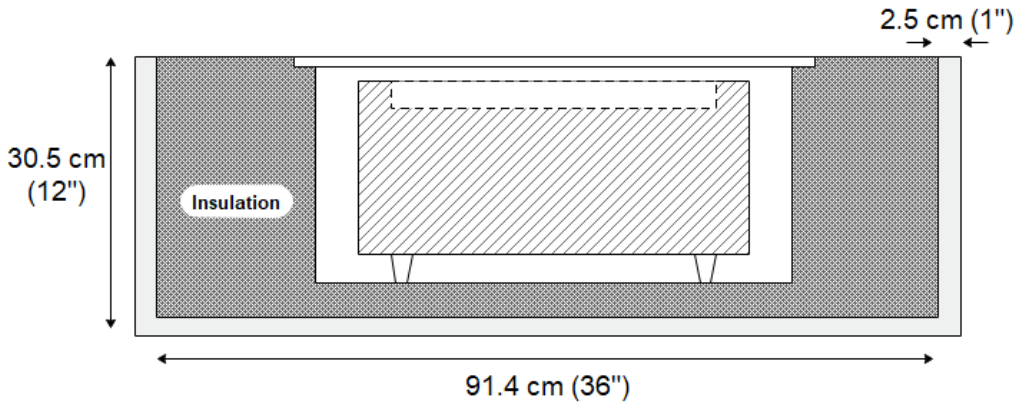

Figure S6.78. Schematic of the exterior insulation (soil) surrounding the case of the water harvester in desert climate.

Section 11. Chemical analysis of collected water samples and MOF chemical stability

Activated microcrystalline powder MOF-801 was placed into an NMR tube with D_2O. ^{1}H-NMR spectra were recorded prior to heating the NMR tube for two hours at 85 C and after heating. Chemical shifts are reported in parts per million (ppm) with reference to the appropriate residual solvent signal from deuterated solvents. ^{1}H NMR: D_2O δ: 4.79 ppm, DMSO-d_6 δ: 2.50 ppm. Traces of *N*,*N*-dimethylformamide, *N*,*N*-dimethylamine and formic acid were found to be present in the sample, presumably due to non-ideal activation procedures. After heating the MOF powder in deuterated water, traces of these compounds remained unchanged. No traces of fumaric acid were found leaching out of the MOF, confirming its hydrolytic stability.

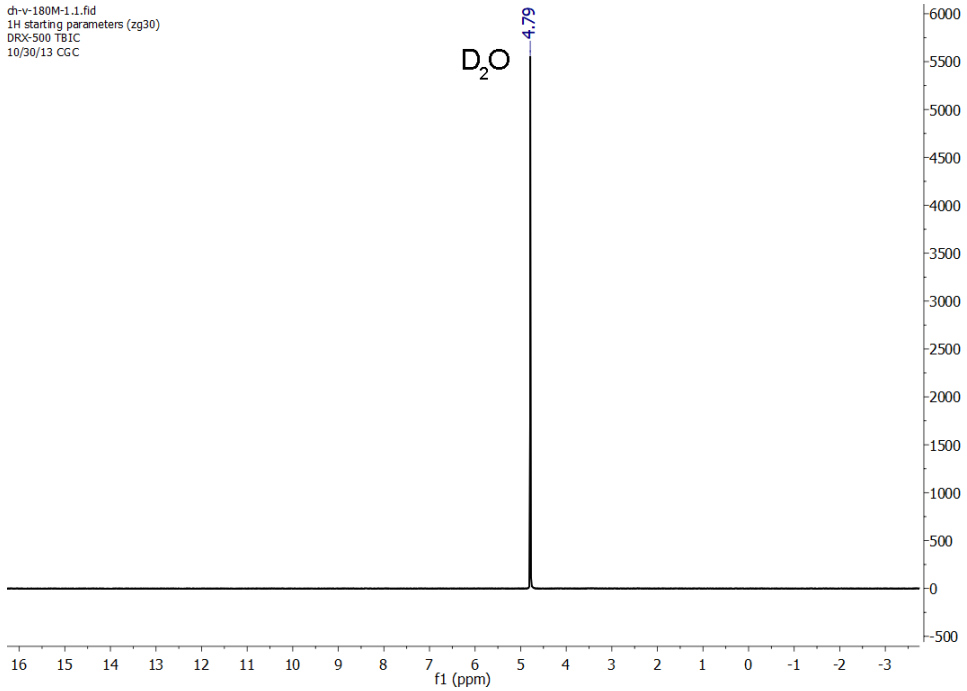

Figure S6.79. ^{1}H-NMR spectrum of pure D_2O before heating.

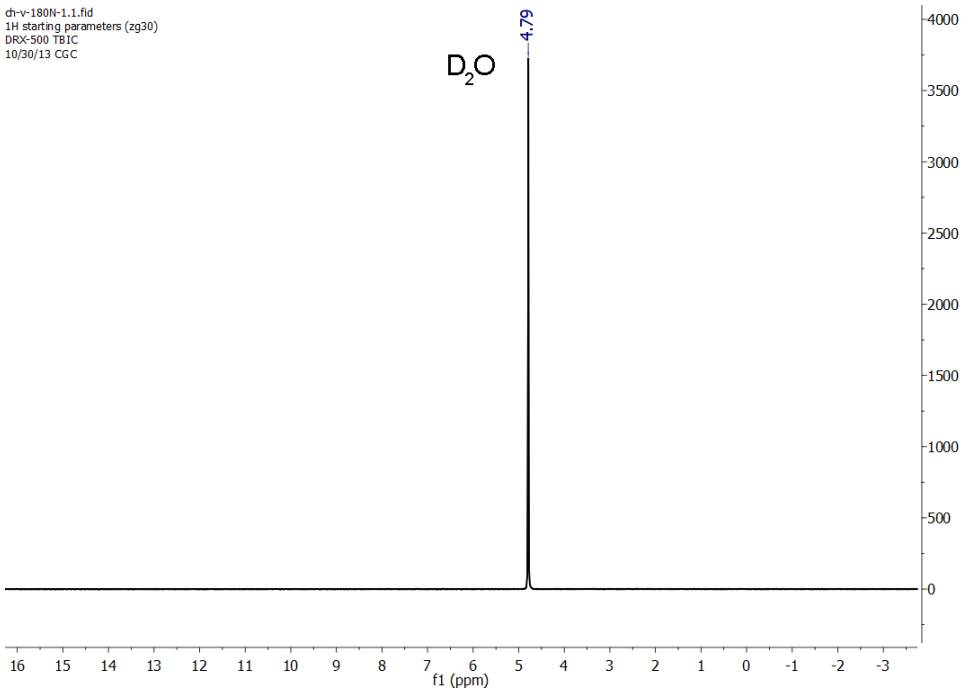

Figure S6.80. ^{1}H-NMR spectrum of pure D_2O after heating.

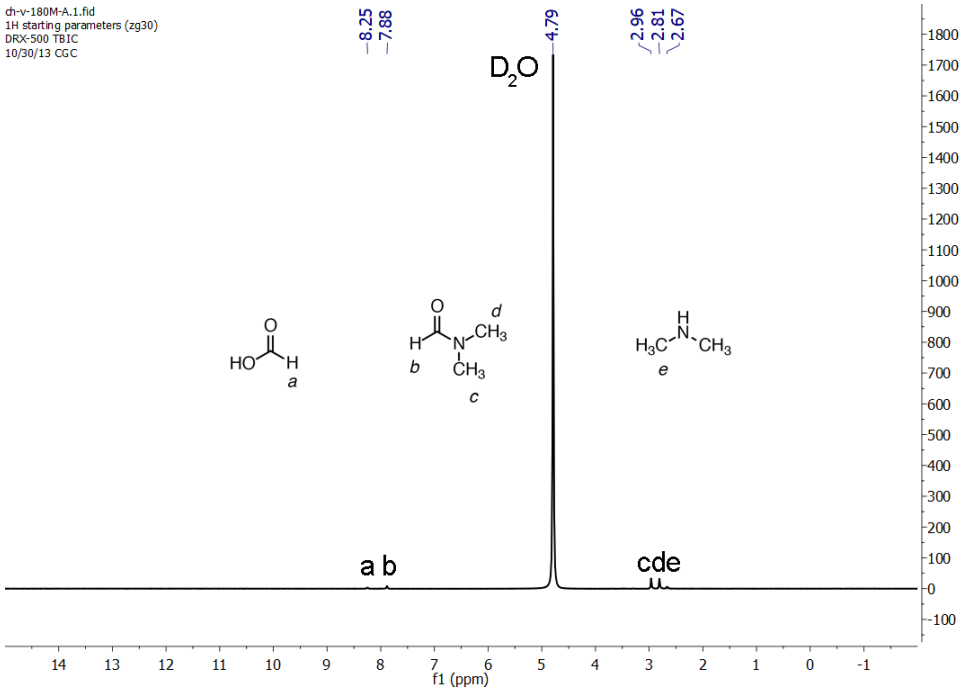

Figure S6.81. ^{1}H-NMR spectrum of MOF-801 in D_2O before heating. Observed signals: formic acid (8.25 ppm), *N*,*N*-dimethylformamide (7.88, 2.96, 2.81 ppm), *N*,*N*-dimethylamine (2.67 ppm).

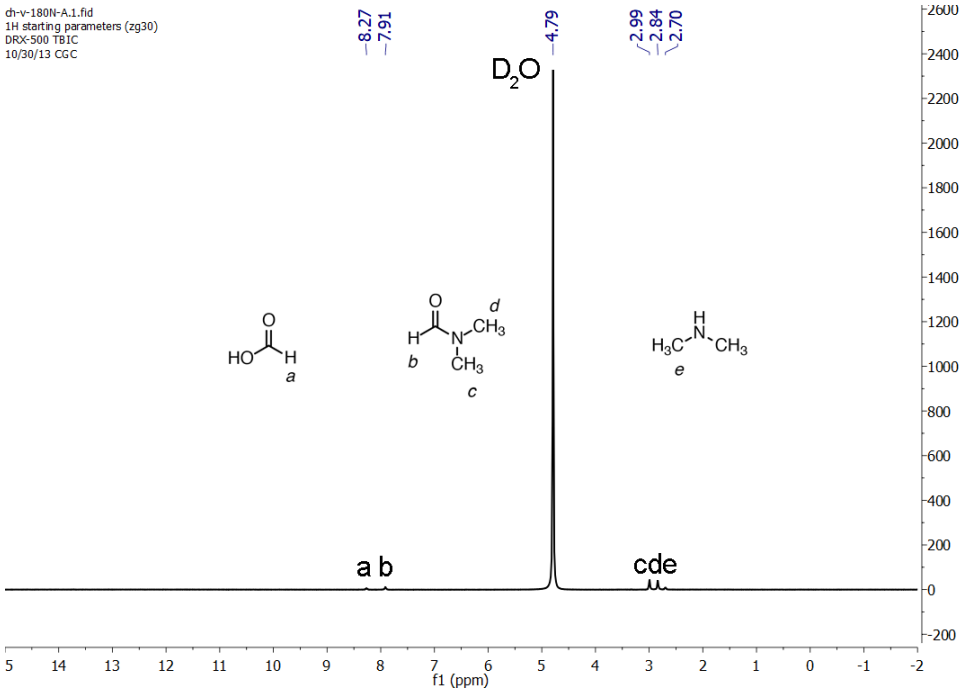

Figure S6.82. ^{1}H-NMR spectrum of MOF-801 in D_2O after heating. Observed signals: formic acid (8.27 ppm), *N*,*N*-dimethylformamide (7.91, 2.99, 2.84 ppm), *N*,*N*-dimethylamine (2.70 ppm).

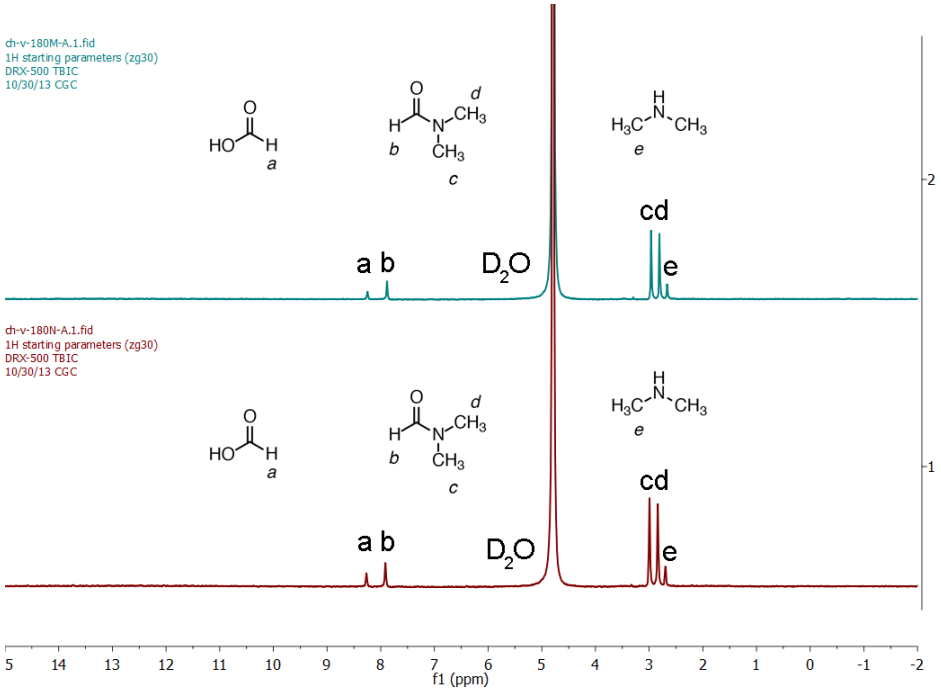

Figure S6.83. ^{1}H-NMR spectra of MOF-801 in D_2O: overlay of before/after heating.

4 ml of water were taken out of a 37 ml batch of water collected using 0.825 kg of MOF-801/G under low flux, and placed into a 4 ml vial. The water was evaporated overnight at 100 °C. The vial was rinsed with 0.6 ml of DMSO-d_6 and an ^{1}H-NMR spectrum was recorded. No organic impurities soluble in DMSO were found.

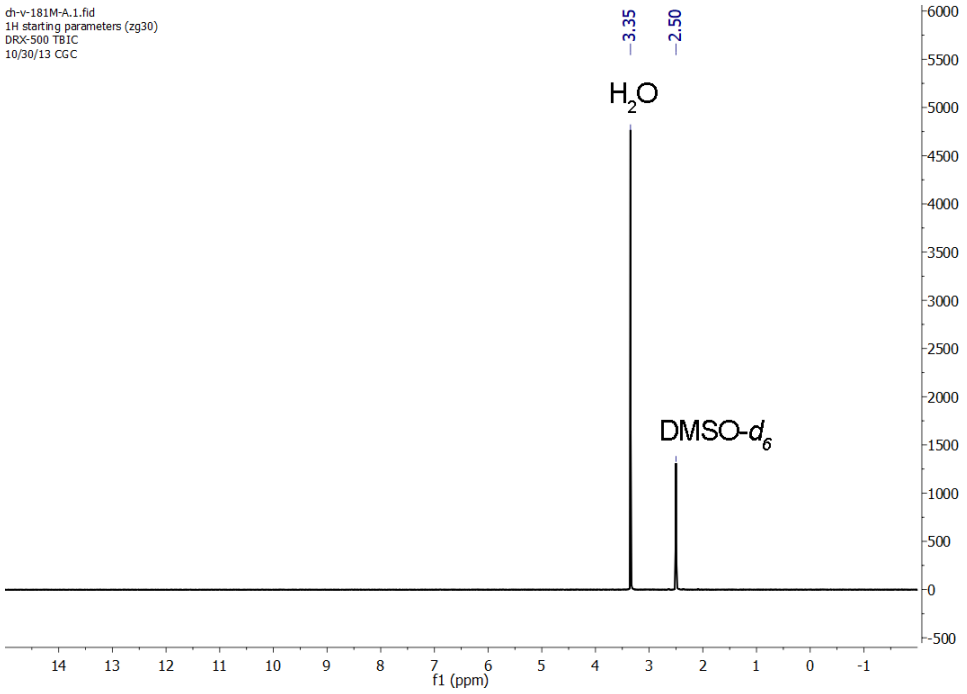

Figure S6.84. ^{1}H-NMR spectrum of water collected using 0.825 kg of MOF-801/G. Observed signal: water (3.35 ppm).

Activated microcrystalline MOF-303 powder was placed into an NMR tube with D_2O. ^{1}H-NMR spectra were recorded prior to heating the NMR tube for two hours at 85 °C and after heating. Chemical shifts are reported in parts per million (ppm) with reference to appropriate residual solvent signal from the deuterated solvents. ^{1}H NMR: D_2O δ: 4.79 ppm, DMSO-d_6 δ: 2.50 ppm. Traces of methanol were found to be present in the sample, presumably due to non-ideal activation procedure. After heating the MOF powder in deuterated water, the traces of compounds mentioned above remained. No traces of 3,5-pyrazoledicarboxylic acid were found leaching out of the MOF, confirming its hydrolytic stability.

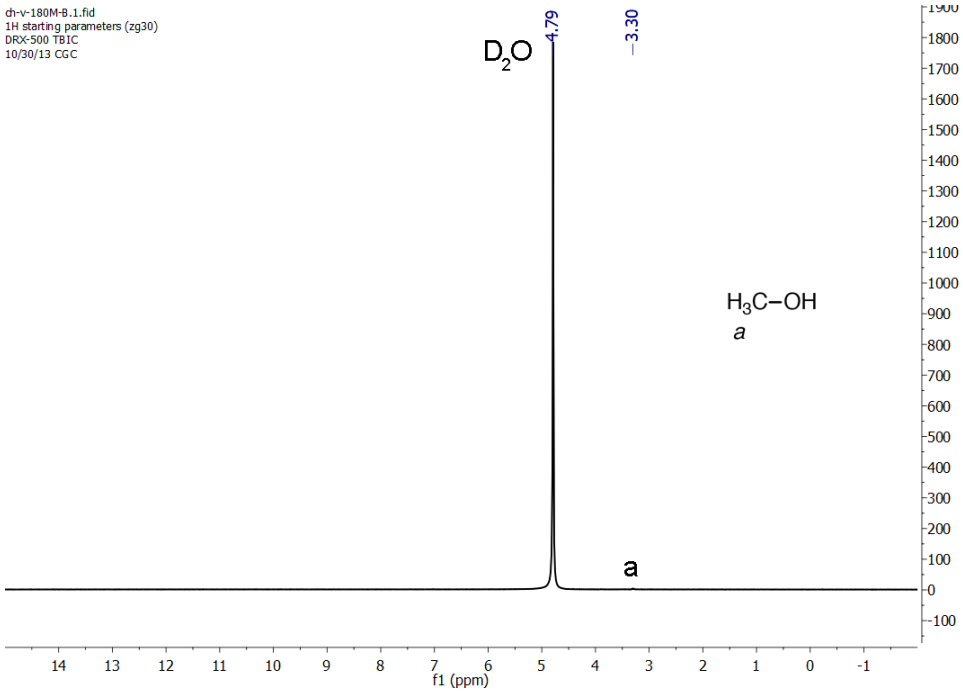

Figure S6.85. [1]H-NMR spectrum of MOF-303 in D_2O before heating. Observed signal: methanol (3.30 ppm).

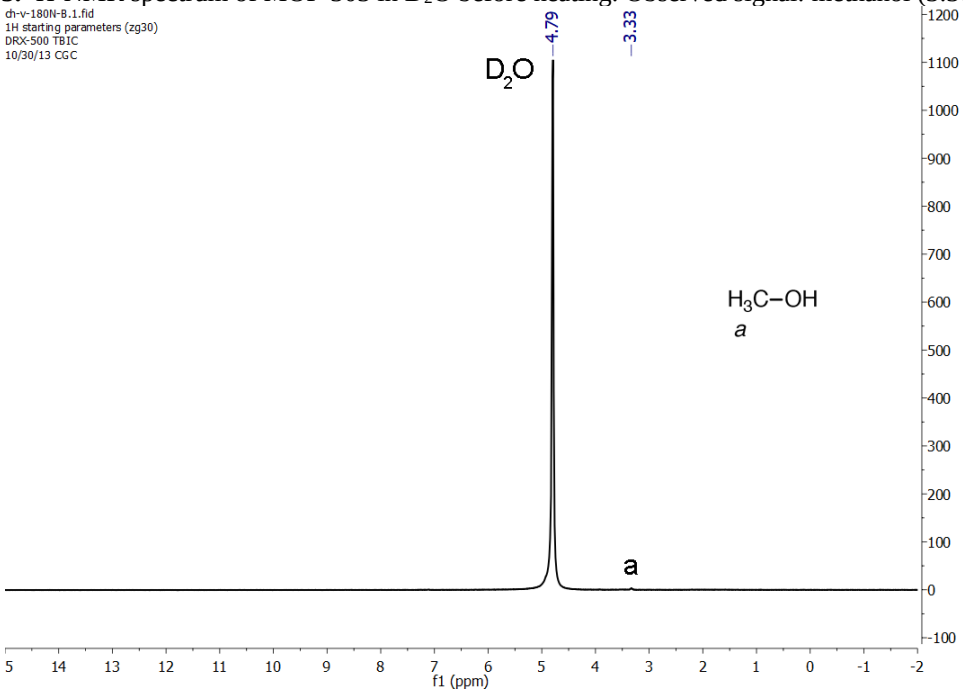

Figure S6.86. [1]H-NMR spectrum of MOF-303 in D_2O after heating. Observed signal: methanol (3.33 ppm).

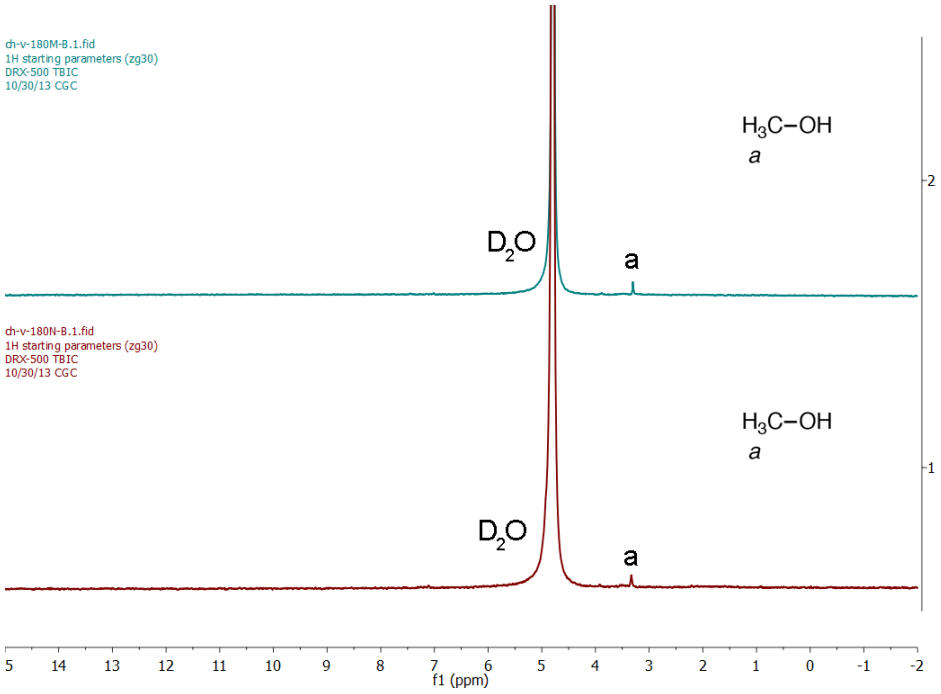

Figure S6.87. ^{1}H-NMR spectra of MOF-303 in D_2O: overlay of before/after heating.

4 ml of water were taken out of a 105 ml batch of water collected using 0.600 kg of MOF-303/G under high flux, and placed into a 4 ml vial. The water was evaporated overnight at 100 °C. The vial was rinsed with 0.6 ml DMSO-d_6 and an ^{1}H-NMR spectrum was recorded. No organic impurities soluble in DMSO were found.

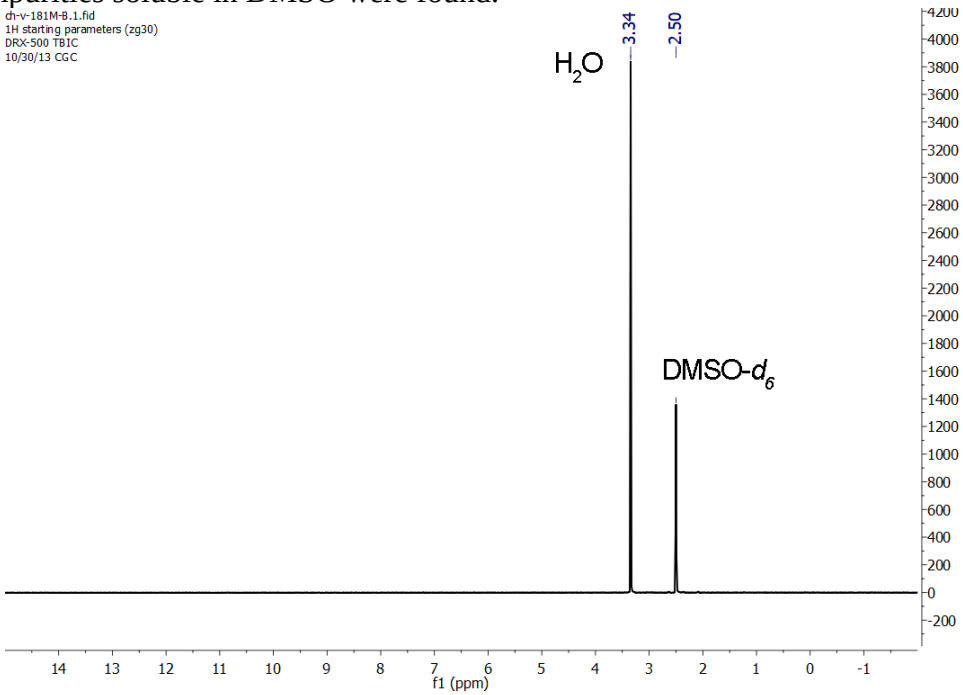

Figure S6.88. ^{1}H-NMR spectrum of water collected using 0.600 kg of MOF-303/G. Observed signal: water (3.34 ppm).

20 ml of water were taken out of a 65 ml batch of water collected using 1.65g of MOF-801/G under high flux, and placed into a 45 ml centrifuge tube. The sample was centrifuged for 30 minutes at 12000 rpm. The supernatant was collected and placed into a 20 ml scintillation vial, and the water was evaporated overnight at 100 °C. The vial was rinsed with 10 ml of 2% v/v aqueous nitric solution and analyzed with ICP. Next, concentrations of standard zirconium solutions were used for the signal vs. concentration calibration curve: 0, 0.005, 0.05, 0.5, 5 ppm. The amount of zirconium in analyzed sample was found to be 0.009 ppm, indicating that the MOF-801 sample does not decompose during water harvesting.

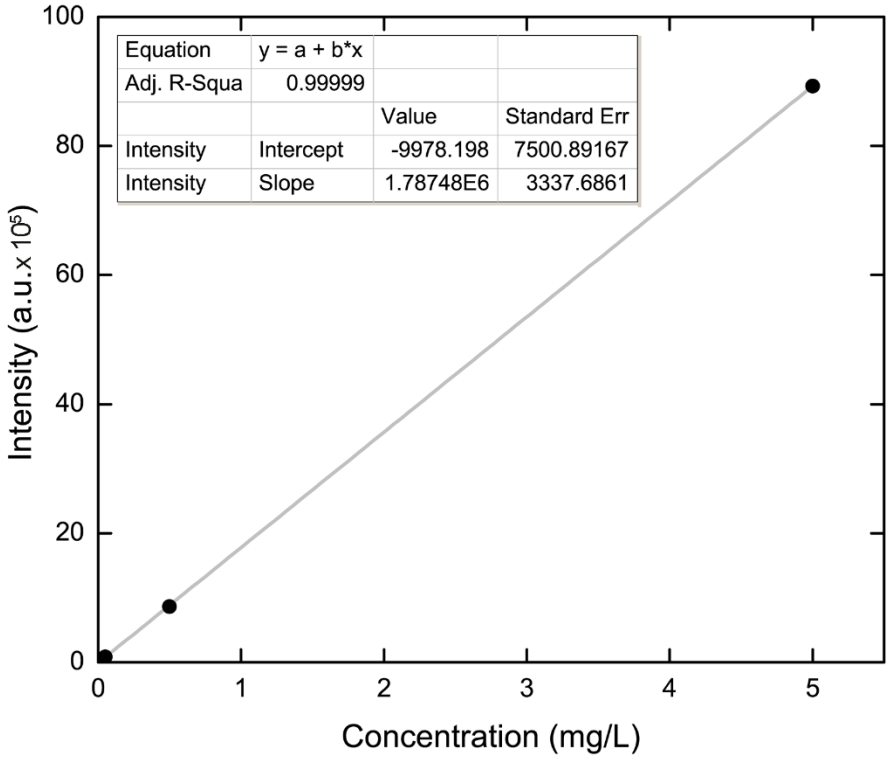

Figure S6.89. The calibration curve for zirconium standard solutions. The intensity of zirconium signal for the analyzed sample is 22639.7 a.u.

20 ml of water were taken out of a 105 ml batch of water collected using 0.600 kg of MOF-303/G under high flux, and placed into a 45 ml centrifuge tube. The sample was centrifuged for 30 minutes at 12000 rpm. The supernatant was collected and placed into a 20 ml scintillation vial, and the water was evaporated overnight at 100 °C. The vial was rinsed with 10 ml of 2% v/v aqueous nitric solution and analyzed with ICP. Next concentrations of standard aluminum solutions were used for the signal vs. concentration calibration curve: 0, 0.005, 0.05, 0.5, 5 ppm. The amount of aluminum in analyzed sample was found to be 0.005 ppm, indicating that the MOF-303 sample does not decompose during water harvesting.

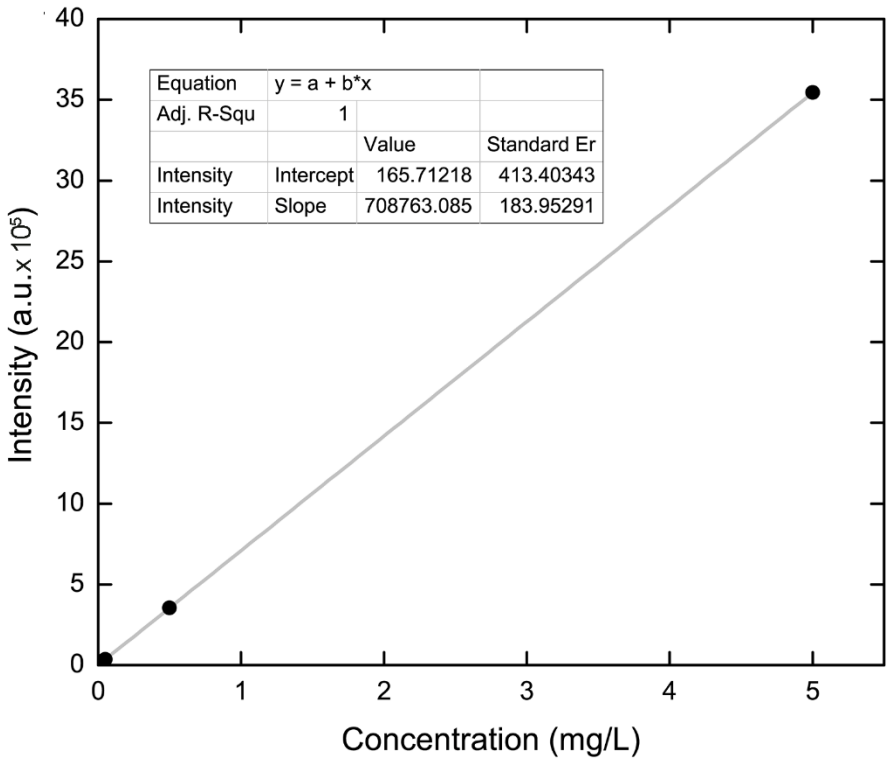

Figure S6.90. The calibration curve for aluminum standard solutions. The intensity of aluminum signal for the analyzed sample is 7739.6 a.u.

References for Chapter 6

(1) Gleick, P. H.; *Water in crisis: a guide to the worlds fresh water resources*, Oxford University Press, New York, 1993.

(2) Park, K. C.; Chhatre, S. S.; Srinivasan, S.; Cohen, R. E.; McKinley, G. H. *Langmuir* **2013**, *29*, 13269–13277.

(3) Klemm, O.; Schemenauer, R. S.; Lummerich, A.; Cereceda, P.; Marzol, V.; Corell, D.; van Heerden, J.; Reinhard, D.; Gherezghiher, T.; Olivier, J.; Osses, P.; Sarsour, J.; Frost, E.; Estrela, M. J.; Valiente, J. A.; Fessehaye, G. M. *Ambio* **2012**, *41* (3), 221–234.

(4) Schemenauer, R. S.; Cereceda, P.; Schemenauer, R. S.; Cereceda, P. *J. Appl. Meteorol.* **1994**, *33*, 1313–1322.

(5) Muselli, M.; Beysens, D.; Marcillat, J.; Milimouk, I.; Nilsson, T.; Louche, A. *Atmos. Res.* **2002**, *64*, 297–312.

(6) Wahlgren, R. V. *Water Res.* **2001**, *35*, 1–22.

(7) Furukawa, H.; Gándara, F.; Zhang, Y.-B.; Jiang, J.; Queen, W. L.; Hudson, M. R.; Yaghi, O. M. *J. Am. Chem. Soc.* **2014**, *136*, 4369–4381.

(8) SunToWater Technologies LLC, Two-stage desiccant system (2508 Highlander Way, Carrollton, TX 75006, USA); suntowater.com (2017).

(9) Ghosh, P.; Colon, Y. J.; Snurr, R. Q. *Chem. Commun.* **2014**, *50*, 11329–11331.

(10) Huang, B. L.; Ni, Z.; Millward, A.; McGaughey, A. J. H.; Uher, C.; Kaviany, M.; Yaghi, O. M. *Int. J. Heat Mass Transf.* **2007**, *50*, 405–411.

(11) Kloutse, F. A.; Zacharia, R.; Cossement, D.; Chahine, R. *Micropor. Mesopor. Mat.* **2015**, *217*, 1–5.

(12) Yang, S.; Huang, X.; Chen, G.; Wang, E. N. *J. Porous Mat.* **2016**, *23*, 1647–1652.

(13) Kim, H.; Yang, S.; Rao, S. R.; Narayanan, S.; Kapustin, E. A.; Furukawa, H.; Umans, A. S.; Yaghi, O. M.; Wang, E. N. *Science* **2017**, *356*, 430–434.

(14) Wikramanayake, E. D.; Ozkan, O.; Bahadur, V. *Energy* **2017**, *138*, 647–658.

(15) Farouki, O. T. *Thermal Properties of Soil*, U.S. Army Corps of Engineers, Cold Regions Research and Engineering Laboratory, 1986.

(16) Handbook-Fundamentals, A. IP edn. *American Society of Heating, Refrigerating and Air-Conditioning Engineers, Inc*, 2009.

(17) O'Keeffe, M.; Peskov, M. A.; Ramsden, S. J.; Yaghi, O. M. *Acc. Chem. Res.* **2008**, *41*, 1782–1789.

(18) de Lange, M. F.; Verouden, K. J. F. M.; Vlugt, T. J. H.; Gascon, J.; Kapteijn, F. *Chem. Rev.* **2015**, *115*, 12205–12250.

(19) Bruker, *APEX2*, Bruker AXS Inc., Madison, Wisconsin, USA, 2010.

(20) Sheldrick, G. M. *Acta Crystallogr. Sect. A Found. Crystallogr.* **2008**, *64*, 112–122.

(21) Discovery Studio Modeling Environment, Release 7.0, Accelrys Software Inc., San Diego, California, USA, 2006.

(22) Laboratory Virtual Instrument Engineering Workbench (LabVIEW), release 2016, National Instrument, Austin, Texas, USA, 2016.

(23) Matrix Laboratory (MATLAB), Release 2017a, The MathWorks, Inc., Natick, Massachusetts, USA, 2017.

(24) Domalski, E.S.; Hearing, E.D. Condensed Phase Heat Capacity Data in Eds. P.J. Linstrom, G. Mallard, *NIST Chemistry WebBook, NIST Standard Reference Database Number 69* National Institute of Standards and Technology, Gaithersburg MD, 20899, retrieved January 17, 2018.

(25) Hollands, K. G. T.; Raithby, G. D.; Konicek, L. *Int. J. Heat Mass Transf.* **1975**, *18*, 879–884.

(26) Giri, A.; Bhuyan, D.; Das, B. *Int. J. Therm. Sci.* **2015**, *98*, 165–178.